SYNERGISTIC DEVELOPMENT OF AN ENGINEERED BIODEGRADABLE THERANOSTIC
PROBE AND LYMPH NODE ORGAN-ON-A-CHIP TO STUDY NANOPARTICLE-LYMPHATIC
INTERACTIONS

BY

PARINAZ FATHI

DISSERTATION

Submitted in partial fulfillment of the requirements
for the degree of Doctor of Philosophy in Bioengineering
with a concentration in Cancer Nanotechnology
in the Graduate College of the
University of Illinois at Urbana-Champaign, 2020

Urbana, Illinois

Doctoral Committee:

      Professor Dipanjan Pan, Chair and Director of Research
      Dr. Mandy Esch, National Institute of Standards and Technology, Co-Director of Research
      Professor Shuming Nie
      Associate Professor Gregory Underhill
      Assistant Professor Jefferson Chan

ABSTRACT

The lymphatic system plays a vital role in controlling immune response. Despite this, cancer often reshapes the lymphatic microenvironment and metastasizes into lymph nodes. Theranostic (therapeutic + diagnostic) nanoparticles have been used in a variety of applications, including the detection and treatment of cancer metastases in lymph nodes. However, accumulation in the liver remains a major concern with any nanoparticle-based intervention. We have developed biodegradable nanoparticles made of biliverdin, an endogenous fluorophore that results from the breakdown of hemoglobin. We demonstrated the degradation of biliverdin nanoparticles (BVNPs) in the presence of biliverdin reductase, as well as the use of BVNPs in photoacoustic imaging of sentinel lymph nodes. Fundamental studies on BVNPs demonstrated shifts in their spectral properties as a response to various stimuli, including pH changes, metal chelation, and UV irradiation. BVNPs loaded with doxorubicin (Dox-BVNPs) were used for treatment of triple-negative breast cancer. BVNPs were further modified via metal chelation for use as a magnetic resonance imaging contrast agent. Finally, hybrid biliverdin-silica particles were developed for use in fluorescence imaging in the near-infrared I and II windows. At the same time, microfluidic models were created to recapitulate the lymph node tissue microenvironment. We first developed a lymphatic vessel on-a-chip that achieved long-term culture of primary human lymphatic endothelial cells (HLECs) under gravity-driven flow. We then developed a lymphatic system on-a-chip, comprised of multiple units that each model the lymph node subscapsular sinus, high endothelial venules, and lymph nodules. This device allows for the exploration of transport of nanoparticles, cancer cells, and immune cells to and from lymph nodes.

carbon dots project. Thank you to undergraduate researcher Sofie Schwink for your help with the silica-biliverdin hybrid nanoparticle project. Thank you to all the other students and postdocs in the Pan and Esch Labs for making my graduate school years enjoyable.

There were also many collaborators who played a role in my projects. Thank you to Glenn Holland from NIST for helping us develop the rotating platforms. Thank you to Professor Jeff Chan's lab, especially graduate students Hailey Knox and Nick Pino, for all of their help with the photoacoustic imaging and in vivo experiments. Thank you to Professor Kai Zhang's lab, especially graduate students John Khamo and Kritika Mehta, for their help with the single-particle imaging experiments. Thank you to Professor Liang Gao and his graduate student, Jorge Tordera Mora, for helping us with cellular PA imaging. Thank you to Professor Fan Lam for helping us with the MR imaging of our nanoparticles. Thank you to my committee members for taking the time to serve on my committee and provide me with guidance and feedback on my work.

I'm deeply grateful to my dear family for their endless love, encouragement, and support. As a child, I may not have enjoyed spending the first day of spring, our cultural new year, attending the county science fair every year for three years in a row, but I often wonder where I would be now if you hadn't forced me to do that all those years ago. I'm so thankful to have wonderful parents who always put so much emphasis on the importance of education. Thank you Maman and Baba for having my back every step of the way for my entire life. Any achievement I have is because of you and is a reflection of the values you've instilled in me. To my brother Payam, thank you for always pushing me to be my best. To my husband Hassan, thank you for being supportive and enthusiastic about my work and career.

I've been blessed to have wonderful friends in Illinois and further away to accompany me during grad school. Maryam S., thank you for always reminding of occasions in which my

stubbornness has helped me succeed. Carlos, Cheri, Elizabeth, Zach, and Craig, thank you for the memes, jokes, and cute pictures of animals, which always brought a smile to my face. Ramona and Hamideh, thank you for your friendship and encouragement throughout this grad school journey.

Thank you to Cathy Tingley and LaRhonda Jackson for helping schedule meetings and keeping the lab organized. Thank you to Krista Smith for all of your guidance and advice about graduate school these past few years. Thank you to Dr. Tor Jensen for keeping the BRC organized and training me on the fluorescence microscope. Thank you to the staff at the shared facilities in the Beckman Institute and the Materials Research Laboratory. I am especially grateful to Scott Robinson, Cate Wallace, and Dr. Wacek Swiech for their guidance on SEM and TEM.

I'm also grateful to the organizations and programs that have supported me through their fellowships and trainings. I'm very thankful to the National Institute of Standards and Technology (NIST) for providing me with three years of support through the National Physical Science Consortium (NPSC)/Graduate Measurement Science and Engineering (GMSE) Fellowship. I'm also thankful to have been supported by the Nadine Barrie Smith Memorial Fellowship, the Mavis Future Faculty Fellowship, and the NIH T32 Tissue Microenvironment Training Program.

This thesis is dedicated to my parents, Farahnaz Lotfi and Hamid Reza Fathi, for their never-ending support and encouragement. I love you both very much and would never have gotten to this point without you. Merci Maman va Baba.

TABLE OF CONTENTS

CHAPTER 1: INTRODUCTION

1.1 PROBLEM STATEMENT

Cancer metastasis is responsible for 90% of all cancer-related deaths [1]. In breast cancer, 10-15% of patients develop metastases within three years of initial diagnosis [2]. For metastasis staging purposes, a sentinel lymph node biopsy (SLNB) is performed to locate and resect the first few lymph nodes into which a tumor drains [3,4]. A dye is injected near the original tumor and drains into the SLNs, allowing them to be identified [5]. The SLN closest to the tumor is surgically removed and histologically examined for the presence of tumor cells [5]. Detection of tumor cells in the SLN results in further surgeries involving the removal of axillary lymph nodes for cancer staging [5,6]. Ideally, the number of lymph nodes removed should be limited to prevent complications from reduced lymphatic system functionality [6,7]. However, even in experienced hands the identification rates and sensitivities of this technique are < 95% [8–10]. Moreover, SLNB can lead to seroma formation, lymphedema, sensory nerve injury, and limitation in the range of motion [11]. Minimally invasive detection methods such as percutaneous fine-needle aspiration biopsies (FNAB) exist, but these suffer from low sensitivity and low accuracy [12,13]. An alternative noninvasive method to identify sentinel lymph nodes (SLNs) in conjunction with either minimally invasive or completely noninvasive molecular techniques is a clear unmet clinical need for noninvasive staging of breast cancer.

Non-invasive detection of SLN is an emerging area of research for breast cancer staging [14]. Due to the absence of intrinsic contrast inside the lymph nodes, exogenous contrast agents are used for real-time detection. Clinically approved dyes such as methylene blue and indocyanine green can be utilized [15–18], but they are not specific to lymph nodes which contain cancer cells. As a result, clinicians are often put in a situation in which they can either resect multiple sentinel and

axillary lymph nodes at once while risking complications, or resect only the sentinel lymph node and risk having to perform further surgeries. Specificity for metastases can be obtained by designing nanoprobes, however, the safety and efficacy of nanoparticles is typically influenced by multiple parameters which create a major bottleneck for their clinical translation. The complexity of nanomedicine presented by the multi-component three dimensional constructs demands vigilant design and engineering to achieve intended physicochemical characteristics and biological behaviors. Designing a targeted nanoparticle that 'disappears' completely from the biological system after use could offer a potential strategy to accelerate the translation of these agents. Noninvasive imaging modalities, e.g., magnetic resonance imaging (MRI), optical imaging, and photoacoustic tomography (PAT) in combination with nanoprobes show promise in improved detection of metastases. Among these, PAT is a hybrid biomedical imaging modality which combines the high contrast of optical imaging with the high resolution of ultrasonic imaging. PAT has been used for various biomedical applications, such as breast cancer imaging, brain structural and functional imaging, blood-oxygenation and hemoglobin monitoring, tumor angiogenesis, and molecular imaging [19–23]. The use of a completely biodegradable nanoprobe with PAT can be considered as a giant step towards breast cancer staging.

Animal models and traditional cell culture have been used for many years to study metastases and have contributed significantly to the development of powerful new therapies. However, limitations of animal studies are well evidenced due to their differences with human metabolism and diseases [24,25]. Furthermore, conventional in-vitro models have been unsuccessful in mimicking the biochemical and mechanical complexities of disease microenvironments [26–29]. Due to the complexity of lymph nodes and the lack of animal models that can accurately replicate the lymphatic functionality of humans, there is a need for a human-based lymph node model that

can aid in the evaluation of any such proposed treatments. A microfluidic model is needed because circulating tumor cells settle within the microvasculature under fluidic flow [30]. Thus, the flow-dependent behavior of metastases can best be modeled in a fluidic system. There are currently few published microfluidic lymph node models, and the majority of published models use low shear flow. A microfluidic lymph node model that mimics the shear conditions in metastatic lymph nodes can provide a valuable fundamental understanding of lymph node transport properties, aiding in the discovery and development of treatments that can travel through the lymph nodes. A multifunctional 'lymph node on a chip' opens up better possibilities to realistically simulate the flow processes in the lymphatic system.

1.2 APPROACH

Photoacoustic nanoparticles [31,32,41–44,33–40] are a class of contrast agents that hold great potential for multiscale diagnostic applications [45–50]. However, a majority of these nanoparticles are based on polymeric or metallic designs and therefore may remain in the body for extended time periods. Since nanoparticles are considered 'foreign' objects, they are easily captured by the mononuclear phagocytic system (MPS) and approx. 30–99% of administered nanoparticles have been reported to sequester in the liver [51]. This often leads to reduced delivery to the diseased tissue and causes toxicity at the hepatic cellular level [52–58], barriers which must be overcome for clinical translation. We hypothesized that the use of an endogenously available molecule as the primary building block for nanoparticles would take advantage of the body's inherent clearing mechanisms to prevent nanoparticle accumulation in the liver. Biliverdin is a bile pigment that results from the breakdown of heme [59]. During this process, biliverdin is reduced to bilirubin through the action of an enzyme, biliverdin reductase [59–61]. The breakdown pathway of biliverdin led me to hypothesize that nanoparticles composed of biliverdin would be entirely biodegradable in-vivo. Biliverdin has

3

an absorbance peak between 600 nm and 700 nm [62]. Absorbance above 650 nm is important for in vivo applications because interference from the surrounding tissue is minimal between 650-900 nm (i.e., the first biological imaging window) [63].

Drug-loaded nanoparticles provide the chance for targeting of the drug, reducing systemic side effects and increasing drug concentration within the tumor [64–67]. At the same time, the use of imageable and biodegradable nanoparticles can allow for tracking of the drug delivery and eventual systemic clearance of the particles. The use of biliverdin nanoparticles for drug delivery is a logical step towards utilizing nanoparticles for sentinel lymph node metastasis detection and treatment.

The lymphatic microenvironment is constantly undergoing shear stress due to the flow of lymph throughout the lymphatic system [68]. Lymphatic endothelial cells, which line lymphatic vessels and form the subcapsular sinus, have been shown to have altered production of TNF-alpha and other cytokines under high shear conditions [69]. IL-6, IL-8, and TNF-alpha levels have been shown to directly correlate with disease stage in breast cancer, with high TNF-alpha and IL-8 levels corresponding to the development of lymph node metastases [70]. Furthermore, lymphatic endothelial cells have been shown to support breast cancer tumor growth through the secretion of high levels of EGF and PDGF-BB [71]. It is apparent that shear stresses applied to lymphatic endothelial cells will have a major impact on the development of lymph node metastases in breast cancer patients, and subsequent invasion of these metastases across the subcapsular sinus and into the lymph nodules. While measuring shear stress in human lymph nodes proves challenging, in-vivo experiments in rodents have found peak shear stresses of up to 12 dyne/cm^2 [72], and increased flow in tumor-draining lymph nodes [73]. Computer-based simulations have predicted shear stresses of 6 dyne/cm^2 under baseline conditions [74]. Despite this, much of the research on the effects of

shear on lymphatic cells has utilized shear values of 1 dyne/cm^2 or less [68,75], or has focused on the use of human dermal endothelial cells [76]. There is a critical need for a better understanding of the lymphatic microenvironment, which can only be provided by moving beyond low-shear devices, 2D cell culture, and in-vivo rodent models. As such, we proposed the use of a fluidic device for the culture of primary human lymphatic endothelial cells and the eventual co-culture of these cells with metastatic breast cancer cells. Our design utilizes a 3D-printed rotating platform to obtain unidirectional pumpless (gravity-driven) flow. This removes the barrier of high-cost pumps while still allowing for physiologically relevant unidirectional flow which is not easily obtainable in gravity-driven devices that use commercially available rocker platforms.

1.3 OVERVIEW OF RESEARCH

My PhD research has primarily focused on studying sentinel lymph node metastases from breast cancer. To this end, we have taken two approaches. The first was to develop biodegradable biliverdin nanoparticles that could provide simultaneous image contrast and therapeutic benefit. The second was to develop a microfluidic lymph node organ-on-a-chip model to better understand the formation and treatment of metastases. Finally, both of these approaches can be combined to utilize the lymph node on-a-chip model in evaluating the biliverdin nanoparticles. An overview is provided in **Fig. 1.1**.

In preliminary experiments, biliverdin nanoparticles (BVNPs) were synthesized over different time ranges in a variety of solutions (Chapter 2). The goal in these experiments was to understand the effect of synthesis solvent and synthesis time on particle behavior. These particles were utilized in in-vivo photoacoustic imaging of sentinel lymph nodes. This work was then expanded with the incorporation of doxorubicin, a chemotherapeutic drug, within the BVNPs (Chapter 7). The doxorubicin-loaded BVNPs are being utilized for treatment of triple-negative

breast cancer. Along the way, we realized many interesting fundamental properties of biliverdin. For example, it had pH-dependent absorption, fluorescence, and photoacoustic behavior. We utilized this for cell-level photoacoustic and fluorescent pH sensing (Chapter 4). We also serendipitously found that rather than degrading as a result of long-term UV irradiation, biliverdin underwent a UV-induced conformational change that led to higher fluorescence emission intensity. When coupled with metal chelation in biliverdin's tetrapyrrole ring, this led to interesting fluorescent behaviors for both biliverdin and biliverdin nanoparticles (Chapter 3). The chelation of metals within biliverdin nanoparticles also allowed for the application of biliverdin nanoparticles as a magnetic resonance imaging contrast agent (Chapter 5). Finally, biliverdin nanoparticles were also adapted for use in near-infrared II imaging through a modified synthesis procedure involving the incorporation of silica (Chapter 6). These experiments altogether established the utility of biliverdin nanoparticles in a variety of imaging, therapeutic, and fundamental applications.

For the lymph node chip, we developed two generations of devices. In the first generation of the device, we sought to establish the effects of high-shear flow on the lymphatic endothelial cells lining lymphatic vessels (Chapter 8, Chapter 9). We developed a microfluidic device that utilized pumpless gravity-driven flow to apply adjustable cyclic shear flow to primary human lymphatic endothelial cells. We then explored the effects of flow on cell size, shape, alignment, viability, and the expression of inflammatory cytokines that contribute to the formation of lymph node metastases. In the second generation of the device, we utilized multiple cell types to model the lymph node subcapsular sinus and high endothelial venules in order to explore their permeability to nanoparticles, cancer cells, and lymphocytes (Chapter 10).

While working on these projects, I also had many opportunities to work on other projects. A number of these projects focused on the development of carbon dots from a variety of carbon sources. In the first of these projects, I explored the effect of carbon dot precursor and reaction temperature on the fluorescence behavior of these particles (Chapter 12). In the second of these projects, I utilized biliverdin and bilirubin to synthesize carbon dots (Chapter 11). We demonstrated that the particles retained some behaviors from their precursors, including their response to stimuli such as enzymes and UV irradiation. Ultimately, we utilized the bilirubin-derived carbon dots for ex-vivo fluorescence tissue contrast. In the third of these projects, I explored the use of methylene blue as a carbon dot precursor (Chapter 14).
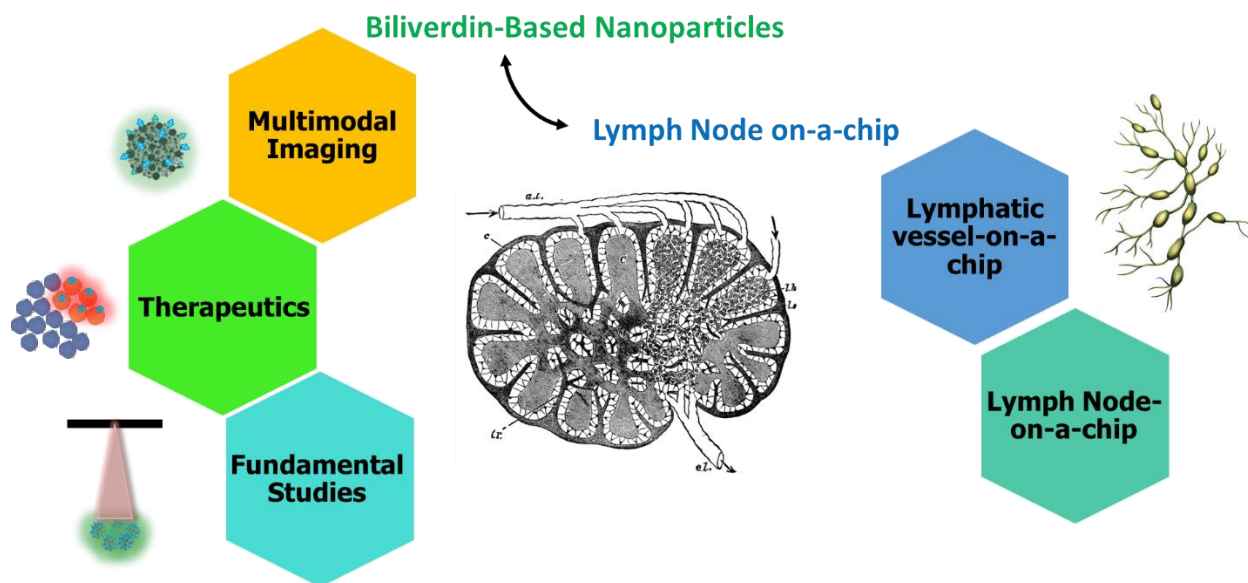
Figure 1.1. Overview of graduate research. The lymph nodes are a central focus of this work. Biodegradable nanoparticles composed of biliverdin, an endogenous bile pigment, were developed for sentinel lymph node imaging. Biliverdin nanoparticles were further characterized through fundamental studies, and were used for a variety of applications in multimodal imaging and cancer therapy. At the same time, microfluidic devices to were created to model the lymphatic system and develop a better understanding of nanoparticle-lymphatic interactions. This involved the development of lymphatic vessel-on-a-chip devices and lymph node on-a-chip devices.

While working on the biliverdin nanoparticle project, I accidentally discovered that the addition of diluted HCl onto a copper surface (such as that of a TEM grid or copper tape) results in the formation of beautiful hexagonally-shaped copper chloride nanocrystals (Chapter 13). This was highly repeatable across a variety of copper substrates, and we ultimately utilized this in treating antibiotic-resistant bacteria.

1.4 REVIEW OF PYRROLE-BASED THERANOSTIC NANOPARTICLES

1.4.1 Nano Theranostics

Small molecule heterocycles have been extensively utilized for imaging and therapeutic applications for many years [77–80]. The use of contrast agents such as methylene blue and indocyanine green is well-documented[81–88]. The inspiration of using nitrogen-containing heterocycles come perhaps directly from the red colour of haem in blood. Blood has served as a biomarker for assessing injury since ancient times, establishing an important role for porphyrins in diagnosis of human diseases. The last decade has also witnessed the advent of advanced imaging techniques, such as functional magnetic resonance imaging (fMRI) for interpretation of neural activity based on blood oxygenation[89]. The iron-containing haem can switch from diamagnetic oxyhaemoglobin to paramagnetic deoxyhaemoglobin allowing us to use these properties to probe *in vivo* activities. Interestingly, porphyrins and related compounds also offer inherent optical activity which can be chemically tuned for wide ranges of light-based imaging techniques. Despite this, systemic administration of small molecule contrast agents and drugs suffers from shortcomings such as unintended off-target side effects, toxicity issues, and inherent solubility issues making these agents poorly bioavailable for target tissues.

Nanoparticles have shown great promise for diagnostic imaging and disease therapy [90–95]. Major advantages of nanoparticle-based approaches have included the ability of nanoparticle

surfaces to be functionalized for selective uptake in organs or tissues of interest [96,97,106,98–105], ability to load therapeutic cargo within nanoparticles [107–110], and the potential for stimuli-responsive therapeutic effects [111–118]. This has allowed for targeted imaging of diseases such as cancer and atherosclerosis, loading and release of water-insoluble drugs [119], tumour microenvironment triggered drug delivery , and selective ablation of lesions . In particular, nanoparticles that provide simultaneous therapeutic and diagnostic ("theranostic") capabilities are of great interest for their multifunctionality and promise in identifying the need for therapeutic interventions and tracking their efficacy post-deployment [120,121]. An overview of theranostic applications of pyrrole-derived nanoparticles is provided in **Fig. 1.2**.

1.4.2 Imaging Modalities

A number of imaging modalities have been utilized for diagnostic imaging of diseases. Commonly used clinical imaging modalities include X-ray imaging and computed tomography (CT), ultrasound imaging, magnetic resonance imaging, positron emission tomography (PET), and single photon emission computed tomography (SPECT). An in-depth exploration of each imaging modality is beyond the scope of this review, but we will provide a brief overview of their operating principles. X-ray imaging utilizes electromagnetic radiation of frequencies ranging from 10^{16} Hz to 10^{19} Hz. Samples of interest are exposed to X-rays, which can travel through the entire thickness of the body. A detector on the other side of the sample collects the X-rays which have passed through the sample. The density of tissues affects the ability of the radiation to pass through the sample, with samples that are denser leading to greater attenuation of the X-rays. In CT imaging, X-rays are collected for individual slices of a sample, and then combined to form a 3D tomographic

9

image. CT and X-ray imaging are commonly used for detection of cancer, bone damage, abnormalities in organs such as the heart and lungs, and a variety of other applications [93,122–127].

In ultrasound imaging, a probe which generates sound in the range of 20 kHz to 200 MHz is applied to the sample. The sound waves are reflected by tissues within the body and are detected using the probe. The time taken for the sound waves to return to the probe corresponds to the distance between the probe and the tissue, allowing for the formation of an image.

Magnetic resonance imaging utilizes a strong magnetic field to align protons within the body. When the alignment of the protons is briefly disturbed using radio waves, the subsequent realignment of the protons leads to the generation of radio waves which can be detected and used in image formation. Unlike X-ray based imaging, MRI contrast agents are considered 'indirect' since they do not appear visible by themselves [128,129]. Paramagnetic and superparamagnetic metal ions are used to generate high resolution (<10 µm) images in spatial resolution as well as cellular processes at a molecular level. Typically, the efficiency of the contrast metals relies on longitudinal (r1) and transverse (r2) relaxivity. Paramagnetic metals shorten the longitudinal relaxation time (T1), and thereby increase the relaxation rate (1/T1) of solvent water protons. Accumulating organs become bright in a T1-weighted (T1w) MRI sequence. Iron oxide nanoparticles have been widely utilized as contrast agents in MR imaging and have been translated to clinical use for treatment of iron deficiency [130–133]. Similarly, Gd, Mn and Copper based agents have been used as a paramagnetic contrast agent. Manganese ion (Mn^{2+}) works similarly as other paramagnetic ions, i.e. gadolinium (Gd^{3+}) and copper (Cu^{+2}), which can shorten the T1 of water protons, thus increasing the signal intensity of T1w MR images.
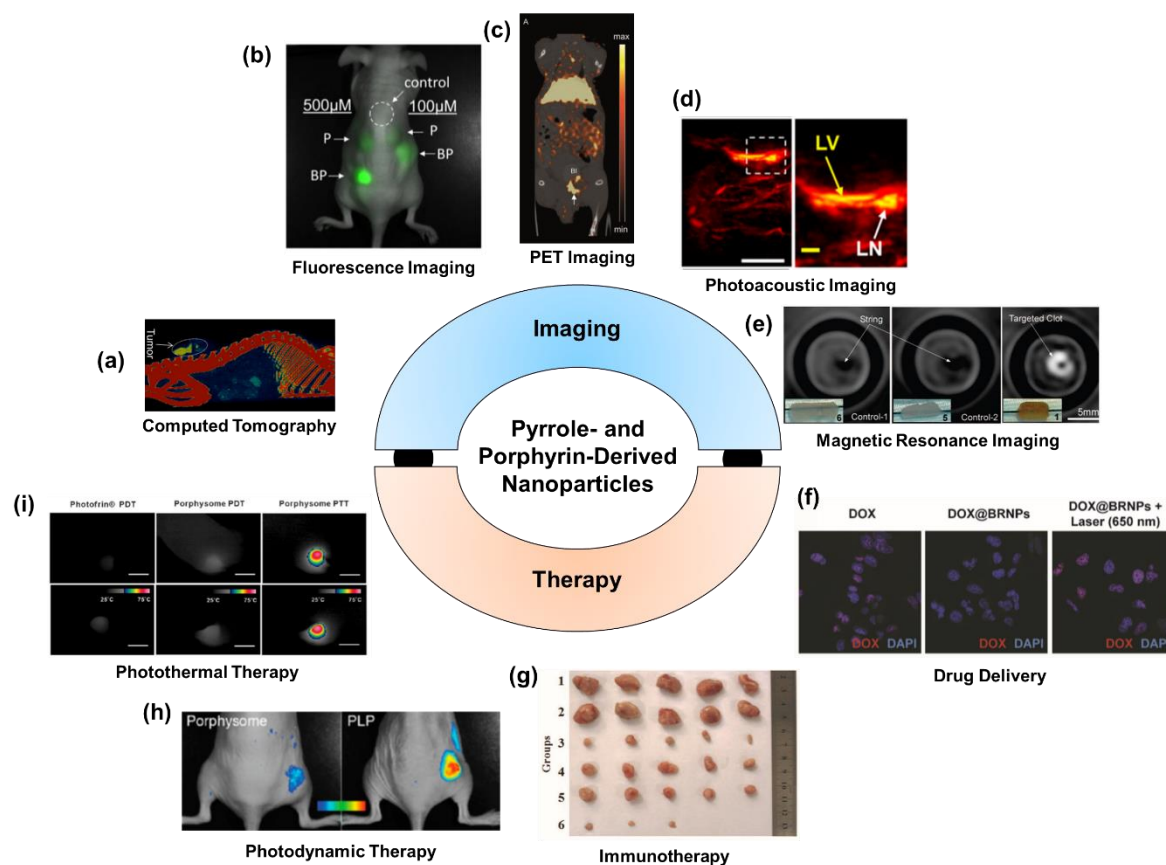
Figure 1.2. Applications of pyrrole- and porphyrin-derived nanoparticles. **(a)** Computed tomographic image of folic acid-conjugated iodinated silica-porphyrin hybrid nanoparticles accumulated in a multiple myeloma tumour[210]. **(b)** Fluorescence image of Matrigel embedded with porphysomes (P) and Bchl-lipid doped porphysomes (BP), injected into a mouse [220]. **(c)** PET imaging of a prostate cancer tumour-bearing mouse 24 h after injection with ^{64}Cu-porphysomes. **(d)** Photoacoustic imaging of lymphatic vessel and lymph node of a mouse 10 min after injection of biliverdin nanoparticles [137]. **(e)** Magnetic resonance imaging of blood clots using fibrin-targeted manganese-chelated nanobialys particles for contrast [230]. **(f)** Confocal fluorescence images of A549 cells treated with doxorubicin-loaded bilirubin nanoparticles with and without laser irradiation [200]. **(g)** Breast cancer tumours from mice treated with Janus nanobullets integrating chlorine e6 (Ce6) loaded, disulfide-bridged mesoporous organosilica bodies with magnetic heads. Magnetothermal therapy (group 3) and combined magnetothermal therapy/immunotherapy (group 6) led to a decrease in tumor size [104]. **(h)** Fluorescence imaging of activation of porphysomes vs. porphyliproprotein particles 24 h after intravenous injection in KB-xenograft mice [278]. **(i)** Temperature of tumours in mice treated with porphysomes and photodynamic therapy or photothermal therapy, illustrating that photothermal therapy (right) leads to high temperatures in tumours [217].

Positron Emission Tomography (PET) imaging makes use of radioactive nuclides to provide image contrast. As the radionuclides degrade, positrons are emitted, eventually making contact with electrons in the native tissue. The annihilation event caused by collision of the positrons and electrons leads to the generation of gamma rays in two opposite directions. The gamma rays are then simultaneously by two different detectors spaced 180 degrees apart, leading to the recording of an incident event. This information is then reconstructed into images. Single Photon Emitted Computed Tomography (SPECT) imaging detects gamma rays emitted directly from an injected radionuclide.

X-rays and gamma rays are both considered ionizing radiation, which means that they can generate free radicals that lead to tissue damage. Since exposure to ionizing radiation can lead to cell death [134–136], the use of these imaging techniques is carefully considered.

Emerging preclinical imaging techniques include fluorescence imaging and photoacoustic imaging (PAI) [45–47,92,95,137–141]. Fluorescence imaging utilizes light of particular wavelengths to excite a fluorophore, or fluorescent molecule. The absorbed light leads to excitation of the fluorophore's electrons from their ground state to a higher energy level. The subsequent return of the electrons to their ground state leads to the emission of lower-energy (higher wavelength) light. A major drawback of fluorescence imaging is in-vivo autofluorescence from haemoglobin in blood, which absorb light at wavelengths below 600 [142]. Thus, fluorescence imaging is often conducted in the first near-infrared (NIR-I) wavelength range of 650 nm-950 nm. More recently, fluorescence imaging in the second near-infrared (NIR-II) range of 1,000 and 1,350 nm has grown in popularity due to reduced interference from biological tissue within this wavelength range [125,143,144].

Like fluorescence imaging, photoacoustic imaging utilizes interrogation with light to excite a light-absorbing molecule. However, in photoacoustic imaging the energy is not released through light emission upon return of excited electrons to their ground state. Instead, the absorbance of light leads to slight increases in temperature which cause thermal expansion of the material. This thermal expansion leads to the generation of sound waves which can be detected with ultrasound imaging to generate a tomographic image. Photoacoustic imaging has gained interest due to its higher spatial resolution and depth of penetration compared to fluorescence imaging. Despite this, photoacoustic imaging is still limited to a penetration depth of approximately 6 cm[145–147]. Photoacoustic signal generated from biologically available molecules such as haemoglobin and melanin leads to some interference in the NIR-I region [148–155]. Thus, photoacoustic imaging in the NIR-II region has also grown in popularity [156–158].

1.4.3 Nanotherapeutics

In addition to surgical interventions, a major approach in disease therapy is the administration of drugs which can lead to diseased cell death, the use of laser irradiation or magnetic fields to induce cell death, or the generation of an immune response to diseased cells through the administration of immunotherapeutic agents. Nanoparticle agents can be utilized for the encapsulation and eventual release of drugs. Nanoparticle-based drug delivery allows for the delivery of drugs with poor solubility, gradual, stimuli-responsive, or on-demand release of drugs, and enhanced delivery of drugs to the site of interest through passive or active targeting mechanisms. In photothermal therapy [159–162], laser irradiation is utilized to irradiate a site containing nanoparticles which absorb light of the specified laser wavelength. The nanoparticles dissipate the energy from the laser through releasing heat, thus thermally ablating the surrounding tissue. In photodynamic therapy [163,164], a similar approach is taken, but the use of photosensitizers leads to the production of reactive

13

oxygen species (ROS) in response to the laser irradiation, leading to cell and tissue death due to the ROS. Another therapeutic approach is the use of magnetothermal therapy [165–167], which utilizes alternating magnetic fields to induce heating within the tissue. In immunotherapy [168–170], administered nanoparticles can present antigens, sometimes in combination with an adjuvant, in order to activate an immune response against the diseased cells to be eradicated. Other work has focused on photoimmunotherapy for selective removal of regulatory immune cells, which leads to a subsequent increase in immune response to tumour cells [171].

1.4.4 Porphyrin and pyrrole characteristics

Pyrroles are organic compounds composed of a five-membered ring containing four carbons and a nitrogen. Porphyrins are composed of four modified pyrrole subunits interconnected at their α carbon atoms via methine bridges (=CH−) Other non-cyclic tetrapyrrole molecules also exist. Pyrrole-derived molecules **(Fig. 1.3)** have drawn interest due to their high absorbance and strong fluorescent or photoacoustic contrast, as well as their abilities to act as photosensitizers and metal chelators [123,125,177,132,134,150,172–176].

1.4.5 Fluorescence and Absorbance Properties

UV-visible absorbance spectra of porphyrin typically contain a Soret band (400-436 nm) Q bands (490-650 nm), and N, L, and M bands (200-350 nm)[178,179]. The Soret band, which has greater intensity than the Q bands, is attributed to the strong transition from S_0 to the second excited state S_2, whereas the Q bands are attributed to the weak transition from S_0 to the first excited state S_1[178,179]. In addition, fluorescence yields for metal-chelated porphyrins have been shown to depend

on the central metal, and the radiative efficiency has been shown to depend on the presence or absence of metals[173].

1.4.6 Photosensitizing Behaviour

The photosensitizing behaviour of tetrapyrroles and porphyrins has long been the topic of much research. Initial studies primarily focused on utilizing hematoporphyrin-derived photosensitizers, but other photosensitizers have been explored more recently[163,174,180,181]. The mechanism behind the photosensitizing behaviour of porphyrins is explained by the excitation of a singlet photosensitizer electron caused by light, leading to excitation of a single electron into a higher-energy orbital. Through intersystem crossing, the excited singlet photosensitizer can then form an excited triplet state with a longer lifetime than the singlet state. Collision with oxygen then results in the formation of ROS and a return of the photosensitizer to its ground state [163].

1.4.7 Metal Chelation

Porphyrins and tetrapyrroles have the potential to form coordination complexes with a variety of metals. Bivalent manganese can be chelated to porphyrins, e.g. sulfonatoporphyrins, where it undergoes rapid oxidation to Mn(III) [176]. Manganese (III) tetra-(4-sulfonatophenyl) porphyrin (TPPS4) and its analogues with progressively fewer sulfonate functionalities (TPPS3, TPPS2) are also known [182,183]. Similar examples of manganese complexes include uroporphyrin (UROP-1), mesoporphyrin, hematoporphyrin and metalloporphyrin (ATN-10)[184–188]. Paramagnetic porphyrin-Mn has been reported to produce sustained tumour T1w enhancement up to at least 24 h following contrast injection in tumour-bearing (SCC-VII) mice[186]. HOP-8 P (α-Aqua-13,17-bis(1-carboxypropionyl)carbamoylethyl-3,8   bis(1phenethyloxyethyl)-β-hydroxy-2,7,12,18-

tetramethylporphyrinato manganese (III)) represents an example of a tumour specific manganese based agent which has been evaluated in a tumour-bearing mouse model [189]. Such metalloporphyrins also exist naturally. Chlorophyll, the plant pigment used in photosynthesis, is a magnesium-chelated porphyrin. Haem, the oxygen-binding domain of haemoglobin, is composed on an iron-chelated porphyrin. Metal coordination complexes have also been reported with other tetrapyrroles[190–192].

1.4.8 Porphyrins and pyrroles as functional building blocks

Nanoparticles derived from porphyrins and other pyrrolic compounds have been utilized in a variety of applications including fluorescence imaging, photoacoustic imaging, magnetic resonance imaging, computed tomography, positron emission tomography, photothermal therapy, drug delivery, and biosensing. Other reviews have focused on metalloporphyrin nanoparticles [171], porphyrin-loaded nanoparticles for cancer therapy [193], polypyrrole nanoparticles for photothermal therapy [194], nanoparticles derived from organic dyes[195], and porphysomes [196–198]. In this review, we have classified porphyrin and polypyrrole-derived nanoparticles into categories of cross-linked or self-assembled particles, carbon dots, and coated particles. We will provide an overview of the different synthetic strategies for each class of particle and will provide examples of the wide variety of applications each class of nanoparticle has been used for.
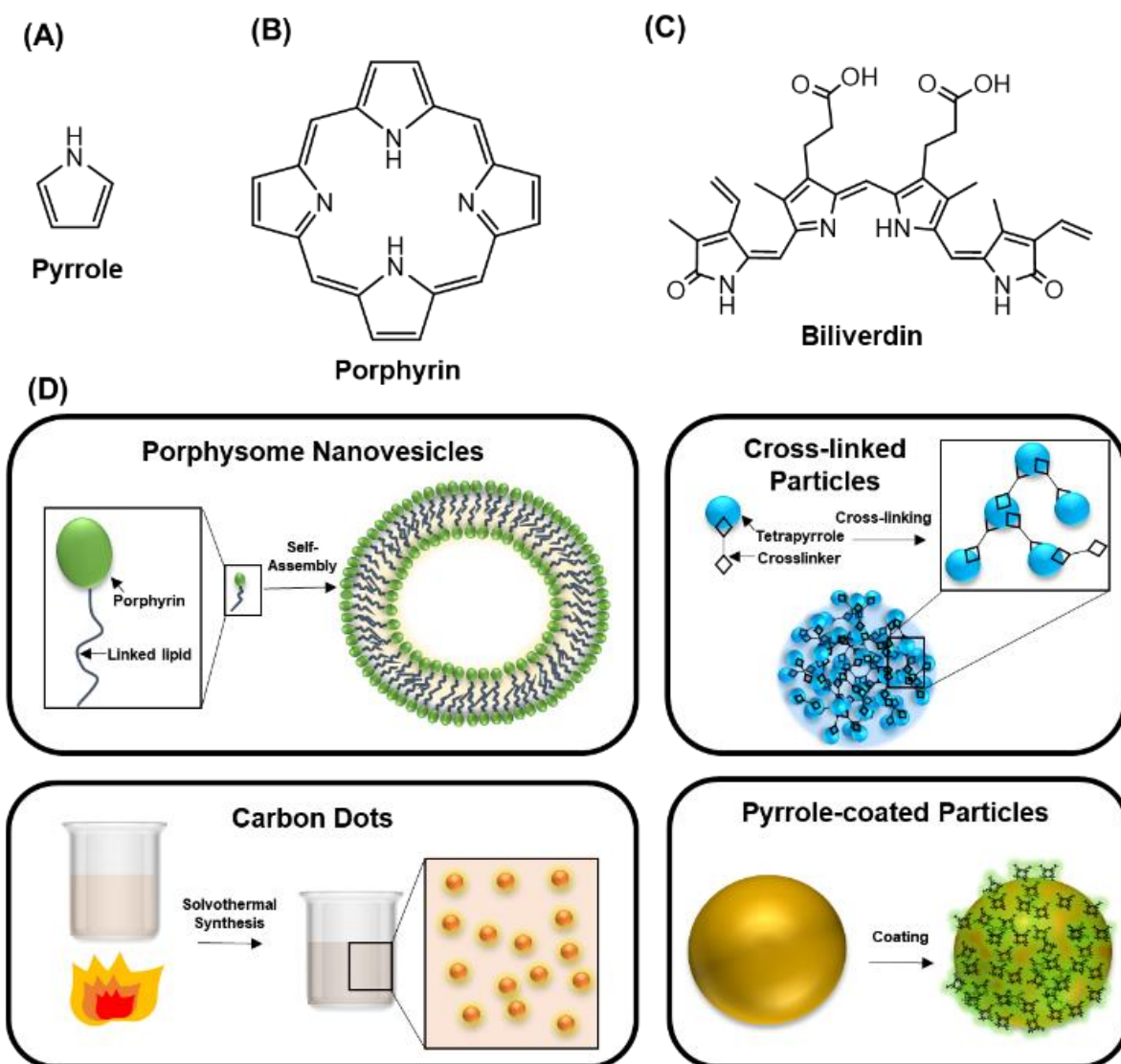
Figure 1.3: Pyrrole and polypyrrole molecules and nanoparticles. (A) Pyrrole molecule composed of a cyclic ring containing four carbons and a nitrogen. (B) Porphyrin, a cyclic molecule composed of four linked pyrrole groups. (C) Biliverdin, a non-cyclic tetrapyrrole molecule. (D) Synthesis of polypyrrole nanoparticles.

1.4.9 Self-assembled particles

One synthetic strategy for polypyrrole and porphyrin nanoparticles has involved exploiting the multiplicity of their functional groups along with polymeric or short homo multifunctional crosslinkers to cross-link multiple molecules or attach ligands which would allow for self-assembly.

1.4.9.1 Naturally-derived porphyrins and pyrroles. Naturally-derived porphyrins and polypyrroles are commonly used for nanoparticles. Haemoglobin, a naturally occurring blood protein contains haem, an iron-chelated porphyrin which is utilized for oxygen transport. Haem-derived pigments have been a popular source of tetrapyrroles for such self-assembled nanoparticles. One such example, bilirubin, an endogenous molecule with poor water solubility, has been extensively utilized by Jon et al. as a precursor for nanoparticle synthesis. In their preliminary work, Lee et al. took advantage of bilirubin's dual carboxylic acid groups to attach amine-terminated polyethylene glycol to bilirubin via carbodiimide coupling, eliminating bilirubin's insolubility in water **(Fig. 1.4)** [199]. This amphiphilic pegylated bilirubin then self-assembled into nanoparticles (BRNPs) with a hydrodynamic size of 136±9 nm. Lee et al. examined the use of BRNPs as reactive oxygen species scavengers, demonstrating the selective uptake of these particles in inflamed colons in-vivo in mice. In addition, they found that BRNPs prevented an increase in myeloperoxidase, a marker of irritable bowel disease severity, and led to a decreased expression of proinflammatory cytokines in a colitis mouse model, compared to controls which were treated with saline.

In further work, Lee et al. examined the use of BRNPs for stimuli-responsive anticancer therapy [200]. They determined that BRNPs experience a switch in solubility upon exposure to ROS or UV irradiation, leading to their subsequent disassembly. They demonstrated the use of this phenomenon for triggered release of doxorubicin, a chemotherapeutic drug. Mice bearing human lung adenocarcinoma xenograft tumours were shown to have reduced tumour volumes when treated with both doxorubicin-loaded BRNPs and 650 nm irradiation, compared to mice treated with doxorubicin or doxorubicin-loaded BRNPs alone. Kim et al. utilized BRNPs for the prevention of hepatic ischemia reperfusion injury[201]. They reasoned that since bilirubin has been

shown to reduce ischemia reperfusion injury, BRNPs would have a similar preventative effect, with the added benefit of water solubility. Biocompatibility of BRNPs was demonstrated in-vivo in mice through histopathological analysis and measurement of ALT, a hepatocellular damage marker, after intravenous injection of particles. In addition, the ability of BRNPs to reduce hepatocellular ischemia reperfusion injury were examined in mice. Mice that received an intravenous injection of BRNPs prior to periods of ischemia and reperfusion were found to have lower levels of serum ALT and AST compared to mice that received injections of PBS or peritoneal injections of unconjugated bilirubin. Such BRNP preconditioning was also found to lead to lower apoptosis and necrosis compared to preconditioning with unconjugated bilirubin,
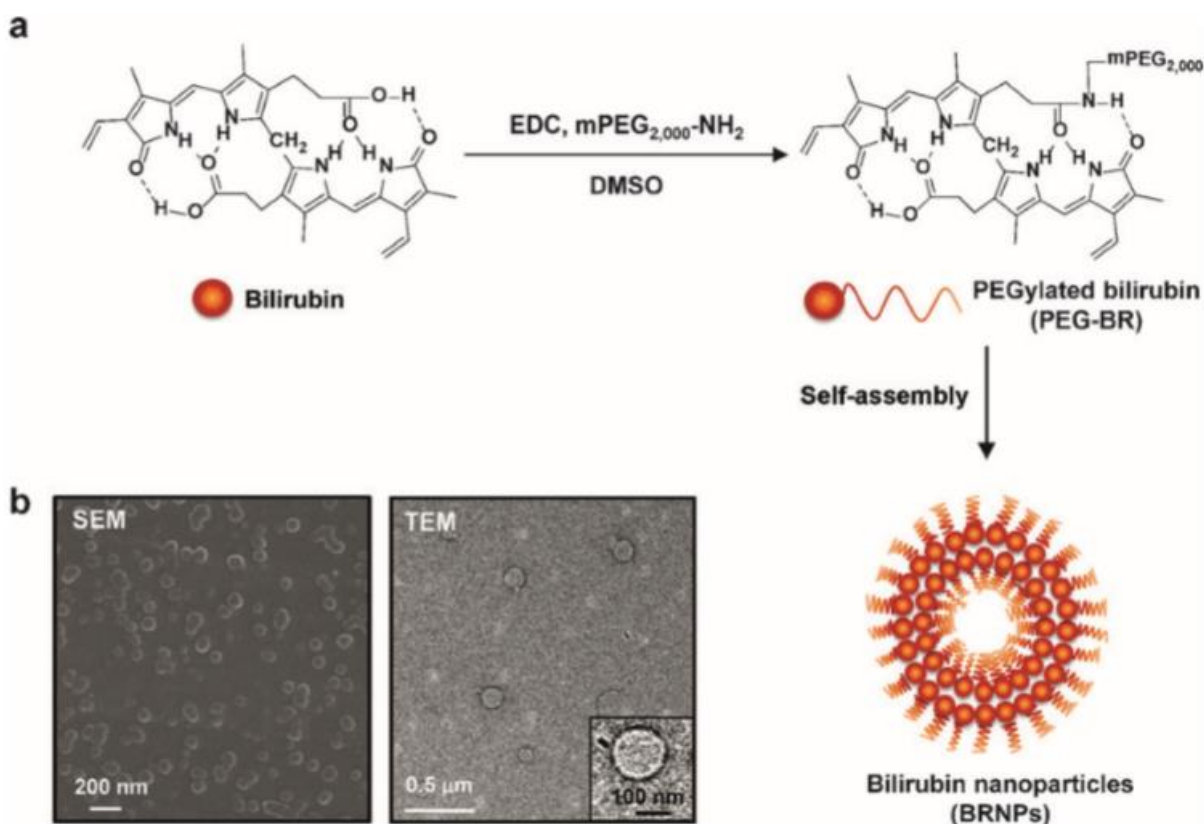
Figure 1.4. **(a)** Synthesis process for BRNPs. **(b)** Scanning electron microscopy and transmission electron microscopy images of BRNPs. Reproduced from Lee et al. 2016, Angew. Chemie Int. Ed.

19

reduced expression of pro-inflammatory cytokines, chemokines, and cell adhesion molecules from ischemia reperfusion injury, and inhibition of neutrophil infiltration after ischemia reperfusion.

BRNPs were found to prolong pancreatic islet graft survival in a diabetic rat model [202]. They were also demonstrated to scavenge ROS to protect islet cells from oxidative stress and supress cytokine release to protect islet cells from activated macrophages. The anti-inflammatory properties of BRNPs also allowed for their use as an anti-asthmatic in a mouse model of allergen-induced asthma [203]. BRNPs were found to possess immunomodulatory behaviour which reduced lung inflammation and asthma symptoms. The chelation of cisplatin into BRNPs has also been explored, allowing for their use for drug delivery, photoacoustic imaging, and photothermal therapy of mice bearing HT-29 human colorectal carcinoma tumours [204].

Biliverdin is another haem-derived tetrapyrrole molecule which has been utilized for nanoparticle synthesis. Recently, Fathi et al. reported the crosslinking of biliverdin molecules using a bifunctional amine linker to form biliverdin nanoparticles (BVNPs) with hydrodynamic diameters of approximately 100 nm (**Fig. 1.5**) [137]. They found that the particles had high absorbance at 365 nm and 680 nm and could be utilized for fluorescence imaging with UV wavelengths and photoacoustic imaging with NIR wavelengths. They utilized BVNPs for sentinel lymph node imaging and demonstrated the complete biodegradation of these particles in the presence of biliverdin reductase. Xing et al. utilized biliverdin and a metal-binding peptide, Z-Histidine-Obzl, to form self-assembled biliverdin nanoparticles which contained Mn^{2+} [205]. They demonstrated the ability of these particles to be used in MR imaging, photoacoustic imaging, and photothermal therapy of MCF-7 tumours in mice.

Hemin, a haem-derived porphyrin, has also been utilized in the formation of nanoparticles. Yang et al. utilized dialysis of hemin dissolved in acidified acetone to form the nanoparticles [206].

They experimented with different temperatures, volume ratios, and incubation times, finding that higher initial concentrations of hemin led to the formation of spherical particles, while lower initial concentrations of hemin led to the formation of tadpole-shaped particles. Hemin nanoparticles were also found to have a higher solubility than pure hemin. In a separate report, Liu et al. reported self-assembled nanoparticles from hemin, guanine-rich DNA, and histidine-rich peptides [207]. These nanoparticles utilized hemin as the cofactor to exhibit peroxidase-mimicking activity and were shown to oxidize reducing substrates. A summary of naturally-derived porphyrin and tetrapyrrole particles is provided in **Table 1.1**.

Table 1.1: Summary of naturally-derived porphyrin and tetrapyrrole particles

Porphyrin or Tetrapyrrole	Reference	Particle Type	Application
Bilirubin (tetrapyrrole)	Lee et al. [199]	Self-assembled	ROS scavengers, decreased inflammation in a colitis mouse model
	Lee et al. [200]	Self-assembled	Triggered release of doxorubicin in mice bearing human lung adenocarcinoma xenograft tumours
	Kim et al. [201]	Self-assembled	Prevention of ischemia reperfusion injury
	Kim et al. [202]	Self-assembled	Prolong pancreatic islet graft survival in diabetic rats
	Kim et al. [203]	Self-assembled	Reduced lung inflammation and asthma symptoms in allergen-induced asthma
	Lee et al. [204]	Self-assembled	Cisplatin delivery, photoacoustic imaging, and photothermal therapy in mouse HT-29 tumours
Biliverdin (tetrapyrrole)	Fathi et al. [137].	Self-assembled and stabilized by cross-linking	Photoacoustic sentinel lymph node imaging, Fluorescence imaging, biodegradability
	Xing et al. [205]	Self-assembled	Photothermal therapy, MR imaging, photoacoustic imaging, MCF-7 tumour treatment
Hemin (porphyrin)	Yang et al. [206]	Self-assembled	Increased solubility compared to pure hemin
	Liu et al. [207]	Self-assembled	Peroxidase-mimicking activity
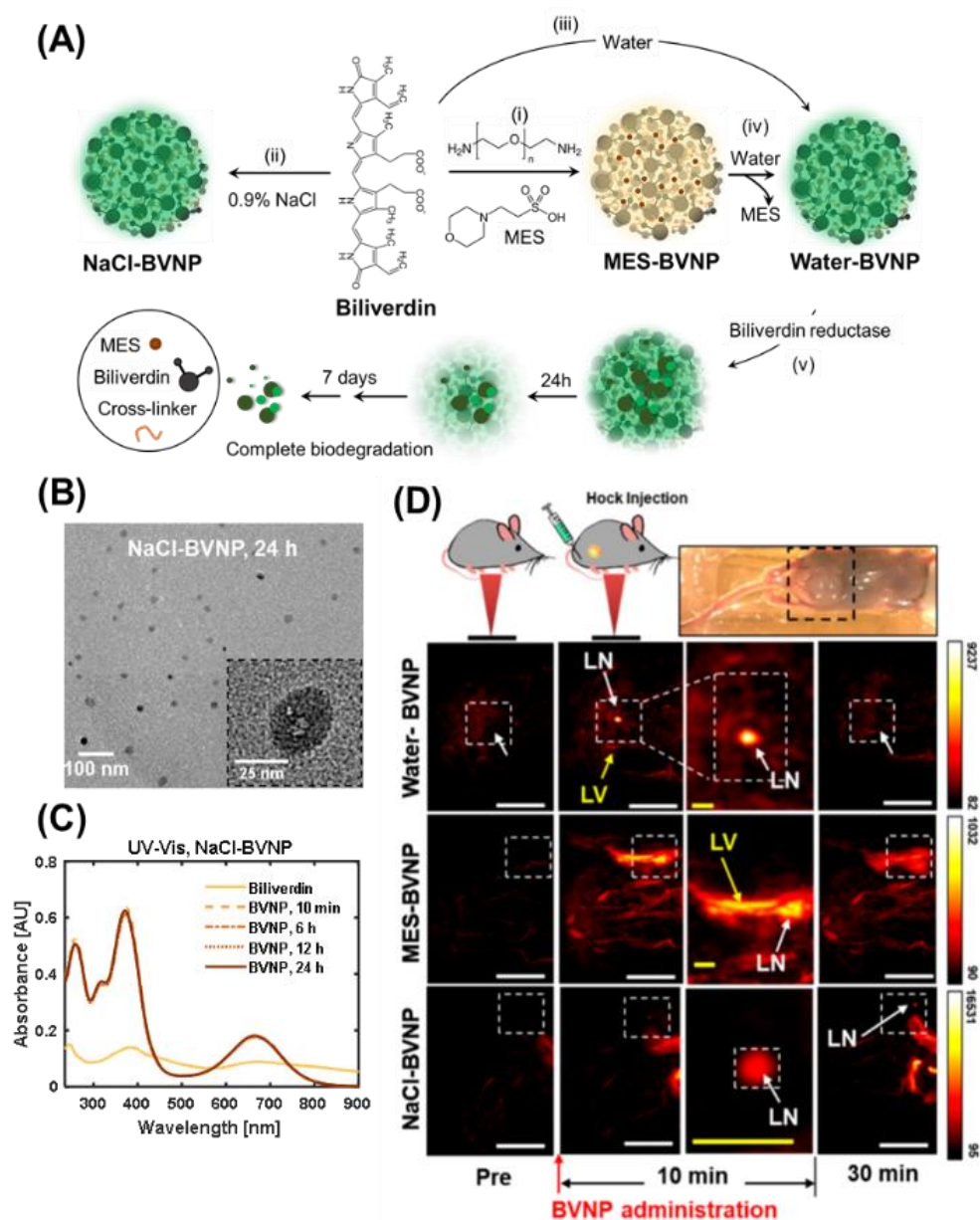
Figure 1.5. (**A**) Synthesis of BVNPs (**B**) Transmission electron microscopy images of BVNPs synthesized in NaCl solution. (**C**) UV-visible absorption spectra of BVNPs synthesized in NaCl solution. (**D**) Photoacoustic sentinel lymph node imaging using three different types of biliverdin nanoparticles. LN=lymph node, LV= lymphatic vessel. Reproduced from Fathi et al., ACS Nano, 2019.

1.4.9.2 Silica-Containing Porphyrin and Tetrapyrrole Hybrids. In addition to the formation of amide bonds, another mechanism of nanoparticle crosslinking has been the formation of siloxane

bonds. Hayashi et al. utilized tetrakis (4-carboxyphenyl)porphyrin (TCPP), a porphyrin, to form silica-porphyrin hybrid nanorings [208]. They utilized the carboxylic acid groups on TCPP to form amide bonds with 3-aminopropyltriethoxysilane (APTES). They then utilized APTES and tetraethylorthosilicate (TEOS) for polycondensation of TCPP-APTES into nanorings, and coated the nanoparticle surface with polyethylene glycol, obtaining a final hydrodynamic diameter of 98 ± 37 nm. When injected intravenously in mice bearing tumours from human myeloma cells, these particles were found to accumulate within the tumours, which was attributed to the enhanced permeability and retention (EPR) effect.

In a separate work, Hayashi et al. developed iodinated silica/porphyrin hybrid nanoparticles (ISP HNPs) by sol-gel reaction of porphyrin-containing silicon alkoxide (PCSA) with (3-iodopropyl)trimethoxysilane (IPTMS) [209]. ISP HNPs had an anhydrous size of 47 ± 12 nm and were utilized for fluorescence imaging, photothermal therapy, and photodynamic therapy in mice bearing human myeloma tumours. Treatment of mice with ISP HNPs and LED irradiation led to a lower tumour volume compared to mice which received no treatment or received only ISP HNPs or only LED irradiation. Mice treated with ISP HNPs and LED irradiation also had a 100% survival rate 10 weeks post-treatment. Hayashi et al. also utilized ISP HNPs modified with PEG and targeted with folic acid to conduct in-vivo fluorescence and CT imaging on multiple myeloma tumours in mice **(Figure 1.6)** [210].

Others have also developed silica-porphyrin nanohybrid structures. Ohulchanskyy et al. synthesized iodobenzyl-pyro-silane, which they then co-precipitated with vinyltriethoxysilane to form porphyrin-containing organically modified silica nanoparticles[211]. The photosensitizing and fluorescence capabilities of these particles were demonstrated in-vitro. Qiu et al. reported the formation of chiral mesostructured porphyrin–silica hybrids[212], and Hayashi et al. reported the

formation of silica–porphyrin hybrid nanotubes for in-vivo cell tracking[213]. A summary of porphyrin-silica hybrid nanoparticles is provided in **Table 1.2**.

Table 1.2. Summary of porphyrin-silica hybrid nanoparticles

Porphyrin building block	Crosslinker	Reference	Application
tetrakis (4-carboxyphenyl)porphyrin (TCPP)	3-aminopropyltriethoxysilane (APTES) and tetraethylorthosilicate (TEOS)	Hayashi et al. [208]	NIR fluorescence imaging of human myeloma tumours in mice
	trimethyl[3-(triethoxysilyl)-propyl]ammonium chloride (TMAPS)	Hayashi et al. [213]	In-vivo macrophage tracking
Porphyrin-containing silicon alkoxide	(3-iodopropyl)trimethoxysilane (IPTMS)	Hayashi et al. [209]	Fluorescence imaging, photothermal therapy, and photodynamic therapy in mice bearing human myeloma tumours
		Hayashi et al. [210]	Targeted in-vivo fluorescence and CT imaging on multiple myeloma tumours in mice
iodobenzyl-pyro-silane	vinyltriethoxysilane	Ohulchanskyy et al. [211]	In-vitro photosensitizing and fluorescence imaging
meso-tetra(4-sulfonatophenyl) porphyrin (TSPP)	N-Trimethoxy silylpropyl-N,N,N-trimethylammonium chloride (TMAPS) tetraethoxysilane (TEOS)	Qui et al. [212]	--
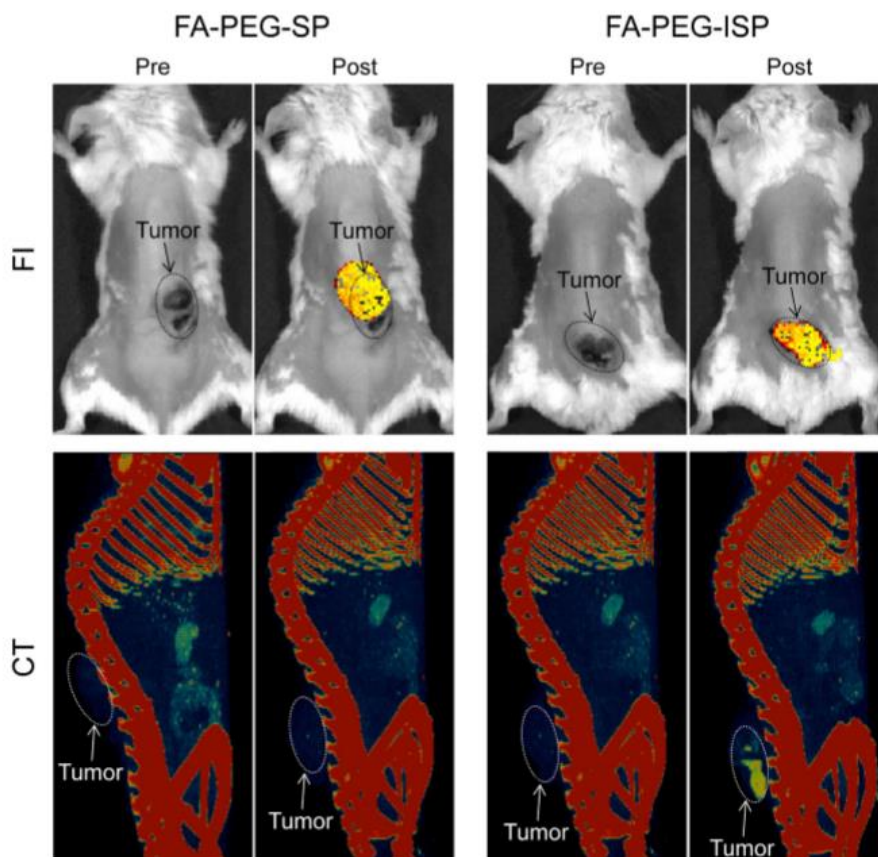
Figure 1.6. Fluorescence and CT images of mice before and after nanoparticle injection. FA-PEG-SP particles were synthesized without iodine incorporation, while FA-PEG-ISP particles were synthesized with iodine incorporation. Reproduced from Hayashi et al., 2014, Journal of Asian Ceramic Societies.

1.4.9.3 Porphysomes. Porphysomes are self-assembled nanovesicles formed from porphyrin bilayers, and are a class of nanoparticle extensively studied by Lovell et al. and Zheng et al. Lovell et al. reported the synthesis of porphysomes using an acylation reaction to attach pyropheophorbide to lysophosphatidylcholine **(Fig. 1.7)** [214]. The structures self-assembled and were extruded to form porphysomes of approximately 100 nm diameter. They also separately formed porphysomes of zinc-pyropheophorbide and bacteriochlorophyll. The porphysomes were utilized in photoacoustic sentinel lymph node imaging, as well as fluorescence imaging and photothermal therapy evaluated in KB cell mouse xenografts. The enzymatic degradation of

25

porphysomes was demonstrated, and porphysomes were also found to have minimal in-vivo toxicity.
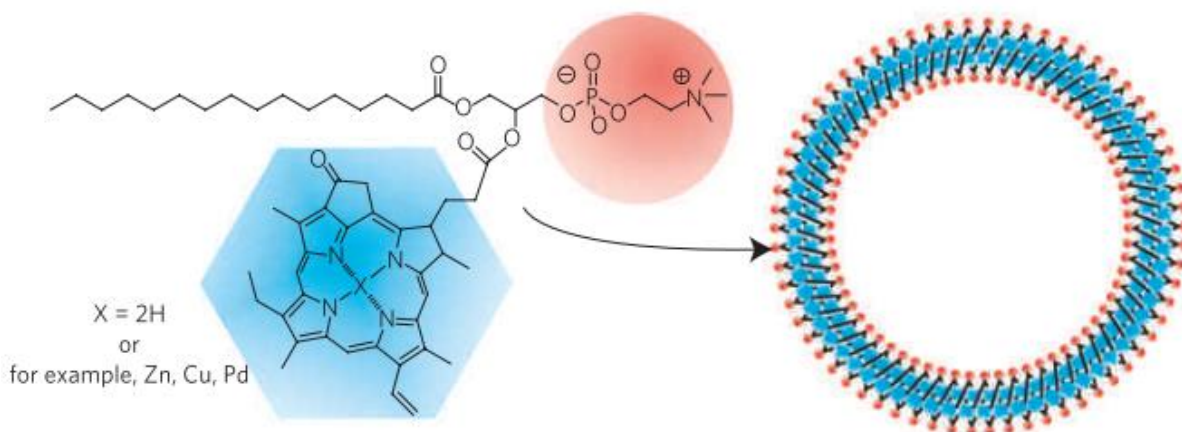
Figure 1.7. Self-assembly of Porphysomes. Reproduced from Lovell et al., Nature Materials, 2011.

Liu et al. reported the use of ^{64}Cu-chelated porphysomes for PET imaging[215]. Radio-labelling was conducted after porphysome formation, and particles were used for combined PET and CT imaging in an orthotopic PC3 prostate cancer model by taking advantage of leaky tumour vasculature. Liu et al. later reported the use of ^{64}Cu-chelated porphysomes for imaging prostate tumour bony metastases[216]. Jin et al. conducted comparative experiments the use of porphysomes and porphyrin monomers (Photofrin) for photodynamic and photothermal therapy of hypoxic and hyperoxic KB xenograft tumours **(Fig. 1.8)** [217]. They demonstrated that since photodynamic therapy relies on the presence of oxygen, porphysome-based photodynamic therapy was only effective under hyperoxic conditions. However, photothermal therapy was found to be effective under both hypoxic and hyperoxic conditions. MacLaughlin et al. also utilized porphysomes for photothermal therapy in a patient-derived pancreatic cancer xenograft model[218].

MacDonald et al. chelated Mn^{3+} into porphysomes to provide MR imaging contrast[219]. These particles were found to have high photostability and retained the potential for use in photothermal therapy. Ng et al. doped porphysomes with a bacteriopheophorbide−lipid to allow

for energy transfer (FRET) between pyropheophorbide and bacteriopheophorbide[220]. This was necessary because of the self-quenching behaviour of regular porphysomes, which did not allow for fluorescence detection of intact porphysomes. Doping with bacteriopheophorbide allowed for fluorescence emission detection of bacteriopheophorbide for intact porphysomes, and fluorescence emission detection of pyropheophorbide for disrupted porphysomes. This allowed fluorescence imaging to be utilized to determine whether the porphysomes were intact or disrupted in-vivo.

Muhanna et al. used ^{64}Cu-chelated porphysomes for imaging of head and neck cancer in a rabbit model[221]. The use of ^{64}Cu-chelated porphysomes allowed for PET mapping of vascular and lymphatic vessels between the tumour and metastatic lymph nodes. Porphysome accumulation in the tumour and lymph nodes was also confirmed with fluorescence imaging. Jin et al. used ^{64}Cu-chelated porphysomes for MRI-guided focal photothermal therapy of prostate tumours[222]. Porphysomes demonstrated high tumour selectivity, and the temperature change induced by photothermal therapy was monitored with MR thermometry.

Ng et al. demonstrated the role of chlorin modification with a methoxy group and chelated with zinc in forming an assembled chlorin nanovesicle[223]. The chlorin-based porphysomes were utilized in photoacoustic imaging of hamster cheek pouch tumours. Philp et al. utilized porphysomes for detection of primary tumour, lymph node metastases, and abdominal metastases in a rabbit model of endometrial cancer[224]. This method of cancer detection was found to have a sensitivity of 98.4% and specificity of 80.0%.

Liu et al. utilized a redox-activatable linkage to form a porphyrin-phospholipids conjugate used in the self-assembly of porphysomes for photoimmunotherapy[225]. This provided the porphysomes with sensitivity to the elevated glutathione level in tumours. The additional encapsulation of an indoleamine 2,3dioxygenase (IDO) inhibitor allowed the porphysomes to serve a dual purpose as

photosensitizers which could induce immunogenic cell death to provoke a systemic immune response. A summary of porphysomes is provided in **Table 1.3**.

Table 1.3. Summary of porphysomes.

Porphysome Modification	Reference	Application
Various porphyrin sources: Pyropheophorbide, zinc-pyropheophorbide, bacteriochlorophyll	Lovell et al. [214]	Fluorescence imaging, photoacoustic imaging, photothermal therapy of KB cell xenografts
^{64}Cu chelation	Liu at al. [215]	PET-CT imaging in orthotopic PC3 prostate cancer model
	Liu et al. [216]	PET-CT imaging of prostate cancer bone metastases
	Muhanna et al. [221]	PET-CT imaging of head and neck cancer and metastases in a rabbit model
	Jin et al. [222]	MRI-guided focal photothermal therapy of prostate tumours
	Philp et al. [224]	Fluorescence detection of tumour and metastases in rabbit endometrial cancer model
None	Jin et al. [217]	Photothermal therapy of hypoxic and hyperoxic KB xenograft tumours
	MacLaughlin et al. [218]	Photothermal therapy in a patient-derived pancreatic cancer xenograft model
Mn^{3+} chelation	MacDonald et al. [219]	MR imaging and photothermal therapy
Doping with bacteriopheophorbide−lipid	Ng et al. [220]	FRET to determine intactness of porphysomes
Utilized chlorin derivatives (including zinc chelate) as porphyrin source	Ng et al. [223]	Photoacoustic imaging of hamster cheek pouch tumour
Incorporation of redox-sensitive linkage and encapsulation of indoleamine 2,3dioxygenase (IDO)	Liu et al. [225]	Photoimmunotherapy of breast cancer

1.4.9.4 Dendritic nanostructures from porphyrins. Dendrimers are repetitively branched macromolecules consisting of a core and spherical three-dimensional morphology. They are typically derived from a single functional entity known as dendrons. Dendrimers carrying porphyrins were first reported by Jin et al[226]. Porphyrin-based photosensitizers have been attached to the branches or encapsulated in the core of the dendrimers mimicking natural haem-containing proteins[227]. Dendritic porphyrins nanoprecipitate into tiny 5-20nm sized particles. These particles have been widely used in imaging and therapeutic application preclinically.
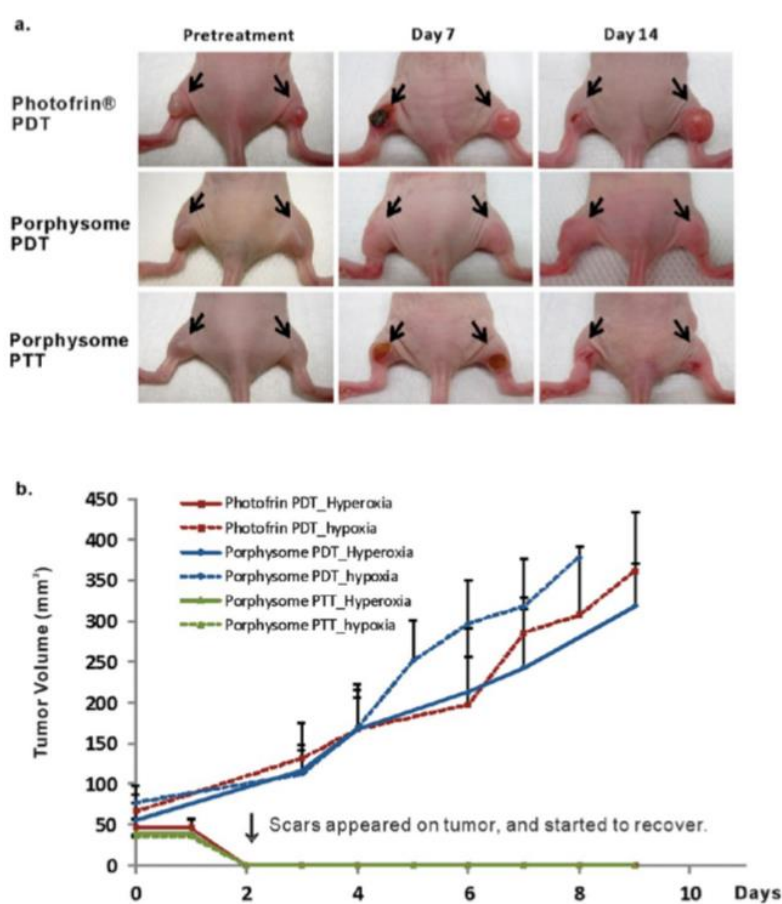
Figure 1.8. Porphysome-based treatment of hypoxic tumours. **(a)** Photodynamic and photothermal therapy using phorphysomes. **(b)** tumour volume in mice treated with photothermal therapy or photodynamic therapy. Reproduced from Jin et al., ACS Nano, 2013.

1.4.9.5 Other Crosslinked and Self-Assembled Systems from Porphyrins. In addition to the aforementioned examples of assembling porphyrin and tetrapyrrole-based nanoparticles, other particles have been formed from a variety of crosslinking and self-assembly methods[228,229].

Pan et al. reported one of the first examples of MR imaging with porphyrin-chelated trivalent manganese which self assembles into a morphology that resembles red blood cells[230]. Toroidal "nanobialys" was developed as a polymer-lipid particle which showed potential as a targeted MR theranostic agent. Nanobialys (~200 nm) were prepared through spontaneous self-assembly of amphiphilic hyperbranched polyethylenimine. Hyperbranched polyethyleneimine (MW=10kDa) was subjected to hydrophobically modify with palmitic acid through a nominal 55% conjugation of the 1° amines. In presence of anhydrous chloroform, the amphiphilic polymer assumed inverted micellar structures that successfully transferred a contrast agent Mn(III)-protoporphyrin chloride (Mn-PPC) in a kinetically stable complex. Biotin was used as a homing agent for targeting these particles to fibrin clots through classic avidin-biotin interactions and a well-characterized biotinylated fibrin-specific monoclonal antibody (NIB5F3). Extensive MRI studies produced ionic r1 and r2 relaxivities of 3.7 ± 1.1 mmol^{-1} s^{-1} and 5.2 ± 1.1 mmol^{-1} s^{-1} per Mn ion and particulate relaxivities of $612,307 \pm 7213$ mmol^{-1} s^{-1} and $866,989 \pm 10,704$ mmol^{-1}s^{-1} per particle, respectively.

Wu et al. developed porphyrin−diketopyrrolopyrrole (Por−DPP), an organic compound that utilizes porphyrin as a donor molecule and diketopyrrolopyrrole as the acceptor molecule[231]. The synthesized compound possessed a red-shifted and broadened absorbance spectrum, and its amphiphilic structure allowed for its spontaneous self-assembly into nanoparticles which were used for imaging and photothermal therapy of cervical cancer tumours in mice. Yang et al. were able to achieve red-shifted and broadened absorption spectra in self-assembled nanoparticles

composed of synthesized porphyrin-based molecules Por and ZnPor[232]. The nanoparticle self-assembly was facilitated by the introduction of hydrophilic polyethylene glycol chains and pentafluorobenzene. The Por and ZnPor nanoparticles were found to have good biocompatibility in the absence of light, and successfully killed HeLa cervical cancer cells when exposed to laser irradiation.

Wang et al. formed particles of zinc meso-tetra(4-pyridyl)porphyrin (ZnTPyP) through non-covalent self-assembly[233]. Through coordination with the zinc, they were able to entrap nitric oxide within the nanoparticles. Upon exposure to light, the nanoparticles produced ROS and released nitric oxide, leading to the death of Escherichia coli (E. coli) and Staphylococcus aureus (S. aureus) bacteria. Wang et al. synthesized porphyrin-containing covalent organic frameworks (COF-366) from tetra (p-amino-phenyl) porphyrin (TAPP)[234]. COF-366 NPs were formed by ultrasonic dispersion of COF-366, and were utilized for photoacoustic imaging, photothermal therapy, and photodynamic therapy in 4T1 breast cancer tumours.

Pan et al. showed that Zn-metalation and phenyl ethynyl functionalization remarkably improves the NIR absorbance of porphyrins through strong intramolecular and intermolecular π–π interactions of porphyrin macrocycles[235]. They synthesized two novel Zn-metalated porphyrins functionalized with symmetrical two phenyl ethynyl groups. Corresponding nanoparticles (60-80nm) were obtained through solvent-exchange based self-assembly approach. The particles displayed good biocompatibility, excellent photostability, and strong $^1O_2$ generation ability.

Other emerging applications also include application of metallo-porphyrin particles in surface enhanced Raman spectroscopic (SERS) application. Tam et al. synthesized gold nanoparticles embedded into Mn-pyro-lipid porphysomes and demonstrated the potential of in SERS based tissue imaging application[236]. In addition to these, other micro-sized porphyrin-lipid

complexes have been developed including nanodisc particles derived from ApoA-1 and porphyrin-lipid **(Fig. 1.9)**[237].

Other work has involved more fundamental studies of porphyrin behaviours. Trapani et al. formed hybrid gold-porphyrin nanoparticles by mixing ten-atom gold clusters (Au_{10}) with tetrakis(4-sulfonatophenyl)porphyrin (TPPS) J-aggregates under mildly acidic conditions[238]. Summerfield et al. formed cyclic nanorings of Zn porphyrin in a directed self-assembly process. They found that the number of porphyrin subunits had a direct impact on the arrangement of the nanorings[239]. A summary of these particles can be found in **Table 1.4**.
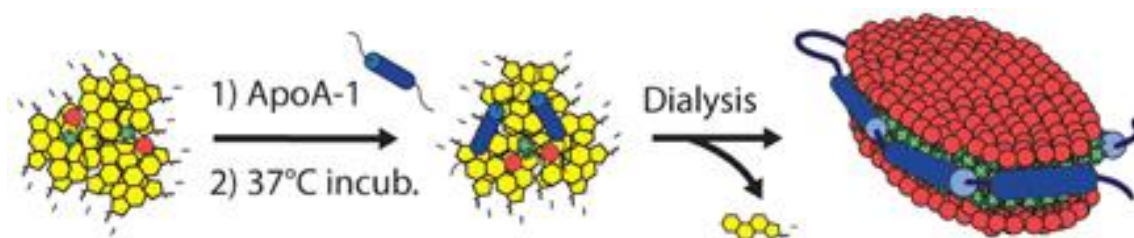
Figure 1.9. Synthesis of self-assembled porphysome nanodics (Adapted with permission from Ng et al. ACS Nano, 2013.

1.4.10 Carbon Dots

Carbon dots, or carbon nanoparticles, are a class of nanomaterial typically formed by burning a carbon-containing material at high temperatures. These particles are known for their biocompatibility, fluorescence, and ease of synthesis[240–242]. In recent years, a number of papers have been published on carbon dot fundamental properties[243,244], as well as applications in bioimaging[138,245–252],drug and gene delivery[253–258], and photothermal therapy[245,259–261]. Despite this, there have been few reports focusing on the use of porphyrins and polypyrroles as precursors in carbon dot synthesis.

Table 1.4. Summary of other porphyrin-based cross-linked and self-assembled particles.

Particle Description	Reference	Application
Toroidal "Nanobialys" with porphyrin-chelated manganese	Pan et al. [230]	Targeted MR imaging of fibrin clots
Self-assembled porphyrin−diketopyrrolopyrrole (Por−DPP) particles	Wu et al. [231]	Photoacoustic imaging and photothermal therapy of HeLa tumours in mice
Self-assembled particles formed by synthesized Por and ZnPor molecules	Yang et al. [232]	Fluorescence imaging and in vitro photothermal ablation of HeLa cells
Nitric oxide-entrapped particles of zinc meso-tetra(4-pyridyl)porphyrin (ZnTPyP)	Wang et al. [233]	ROS generation and nitric oxide release to fight E. Coli and S. Aureus bacteria
COF-366 NPs formed from COFs containing tetra (p-amino-phenyl) porphyrin (TAPP)	Wang et al. [234]	Photoacoustic imaging, photodynamic therapy, and photothermal therapy of 4T1 tumours.
Nanoparticles formed from solvent exchange based self-assembly of novel Zn-metalated porphyrins	Pan et al. [235]	Singlet oxygen generation
Mn-pyro-lipid porphysomes encapsulating gold nanoparticles	Tam et al. [236]	SERS probe for cellular imaging
Porphyrin nanodiscs formed by linking apolipoproteins to pyro-lipid	Ng et al. [237]	In vitro singlet oxygen generation, diffusion into collagen-rich environment
Gold-porphyrin hybrid nanoparticles from tetrakis(4-sulfonatophenyl)porphyrin and Au_{10}	Trapani et al. [238]	-
Cyclic nanorings of Zn porphyrin	Summerfield et al. [239]	-

Wen et al. utilized pheophytin, a chlorophyll derivative, for microwave synthesis of carbon dots [262]. These carbon dots were initially hydrophobic, had an anhydrous size of 5.5 nm, and had a fluorescence emission maximum of approximately 680 nm. They also demonstrated the use of pheophytin carbon dots for in-vivo photodynamic therapy and fluorescence imaging in 4T1-tumour bearing mice. Wu et al. utilized tetraphenylporphyrin and its transition metal complexes with palladium and platinum to form carbon dots [263]. These carbon dots were found to have strong

blue fluorescence which was quenched in the presence of Fe^{3+} ions and were utilized in sensing these ions with a limit of detection of 3.7 µM.

Li et al. formed porphyrin carbon dots (TPP CDs) from hydrothermal synthesis using mono-hydroxylphenyl triphenylporphyrin and chitosan **(Fig. 1.10)** [264]. TPP CDs had a size of 2.6 nm and were utilized in photodynamic therapy of hepatocarcinoma in a Hepatocarcinoma 22 (H22) mouse xenograft model. Wu et al. formed carbon dots from 5,10,15,20-tetrakis(4-aminophenyl)porphyrin (TAPP) and citric acid [265]. These particles exhibited UV−visible and near-infrared absorption, which was utilized for photoacoustic imaging of breast cancer tumours treated with particles targeted using centuximab. The utility of these nanoparticles in inducing tumour cell death was also demonstrated using two-photon photodynamic therapy.
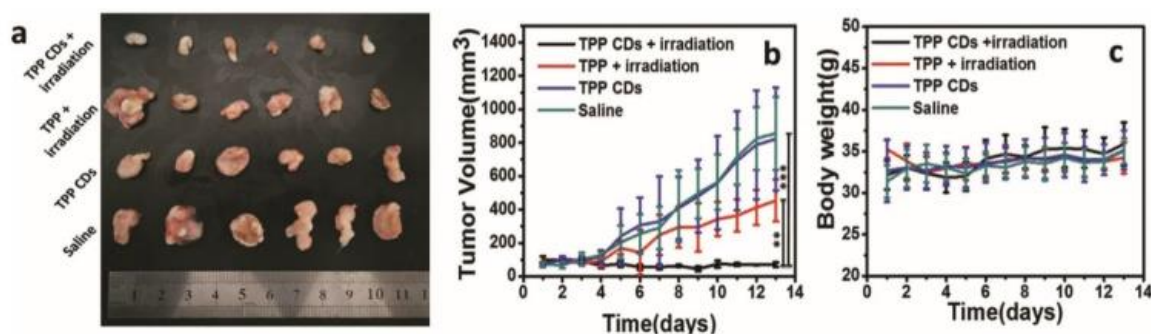
Figure 1.10. Tumours from mice with hepatocarcinoma treated with TPP CDs and photodynamic therapy. Reproduced from Li et al., Adv. Healthc. Mater., 2017

Zhao et al. reported the synthesis of near-infrared carbon dots from corn bract, reasoning that the carbon dot behaviour may stem from chlorophyll-derived porphyrins which were present in the precursor material [266]. The authors demonstrated that these carbon dots could be used in ratiometric detection of mercury ions. Li et al. utilized polypyrrole nanoparticles as the precursor for carbon dot synthesis [267]. The carbon dots exhibited smaller sizes (30 to 70 nm) and higher conductivity compared to the initial polypyrrole nanoparticles. A summary of porphyrin and tetrapyrrole-based carbon dots is provided in **Table 1.5**.

Table 1.5. Summary of porphyrin and tetrapyrrole-derived carbon dots.

Carbon Source	Reference	Application
Pheophytin	Wen et al. [262]	Photodynamic therapy and fluorescence imaging in 4T1-tumour bearing mice
Tetraphenylporphyrin (and its complexes with palladium and platinum)	Wu et al. [263]	Fe^{3+} ion sensing
Mono-hydroxylphenyl triphenylporphyrin and chitosan	Li et al. [264]	Photodynamic therapy of hepatocarcinoma in a mouse xenograft model
5,10,15,20-tetrakis(4-aminophenyl)porphyrin and citric acid	Wu et al. [265]	Targeted photoacoustic imaging of breast cancer tumours, two-photon photodynamic therapy
Corn bract	Zhao et al. [266]	Ratiometric detection of mercury ions
Polypyrrole nanoparticles	Li et al. [267]	Improved conductivity compared to regular polypyrrole nanoparticles

1.4.11 Porphyrin and Polypyrrole coatings

In addition to utilizing porphyrins and tetrapyrroles as precursors for nanoparticle synthesis, other nanoparticles have been functionalized with porphyrin or tetrapyrrole coatings to make use of their unique properties.

Wang et al. utilized coated candle soot-derived carbon dots with porphyrin through electrostatic and π-stacking interactions[268]. They demonstrated that these particles had could be used for labelling of E. Coli bacteria and 293T cells. Additionally, the particles were found to have peroxidase-like activity, which was utilized in the development of a colourimetric glucose sensor. Arcudi et al. coated nitrogen-doped carbon dots with porphyrin through coupling carboxylic acid groups with amine groups[269]. In a similar approach, Huang et al. coated carbon dots through surface passivation with an amine-terminated poly(ethyleneglycol) followed by EDC-NHS cross-coupling with chlorin e6[270]. The coating and carbon dots interacted via Forster Resonance Energy

Transfer (FRET) to provide strong fluorescence emission in the near-infrared region. This allowed for their application in image-guided PDT in an *in vivo* mouse model of gastric cancer.

Shan et al. developed organosilica- based hollow mesoporous bilirubin nanoparticles for the coencapsulation of graphene oxide and tirapazamine (TPZ), a bioreactive prodrug[271]. The resulting particles possessed a core-shell structure, where the core consisted of a mesoporous silica nanoparticle and the shell was composed of bilirubin-silane. The particles were utilized to scavenge H_2O_2 byproducts of aerobic glycometabolism caused by graphene oxide aerobic glycometabolism. This allowed for the protection of normal tissues from oxidative damage while inducing tumour hypoxia to convert nontoxic TPZ into a highly toxic radical. In vivo application of these particles for PET imaging, ultrasound imaging, photoacoustic imaging, and cancer therapy was demonstrated in a U87MG brain cancer model.

Other efforts have focused on coating metallic nanoparticles with polypyrroles. Yang et al. developed a core-shell structure in which the shell consisted of a polypyrrole and the core consisted of silver nanoparticles [272]. Takahashi et al. utilized plasmon induced charge separation to coat gold nanoparticles with polypyrrole[273], while Zotti et al. formed self-assembled monolayers on gold nanoparticles[274]. A summary of porphyrin- and tetrapyrrole-derived nanoparticle coatings is presented in **Table 1.6**.

1.4.12 Limitations

Porphyrins and pyrrole-derived nanomaterials find widespread preclinical use because of their large extinction coefficients, excellent biocompatibility, and negligible adverse effects on organisms. Despite the many advantages of utilizing porphyrins and tetrapyrroles for nanomedicine, a number of drawbacks exist. First, a majority of these materials are used for fluorescence imaging, which faces inherent limitations in depth of penetration and spatial

Table 1.6. Porphyrin- and tetrapyrrole-derived nanoparticle coatings

Particle Core	Coating (method)	Reference	Application
Carbon nanoparticles from candle soot	Porphyrin (electrostatic and π-stacking)	Wang et al.[239]	Colourimetric glucose sensor
Nitrogen-doped carbon nanodots	Covalent linkage	Arcudi et al. [269]	-
Carbon dots	Chlorin e6 (EDC-NHS covalent linkage)	Huang et al. [270]	Fluorescence image-guided PDT of MGC803 mouse gastric cancer
Mesoporous silica nanoparticles	Bilirubin (nitrogen-protected silica template method)	Shan et al. [271]	Brain cancer imaging (PET, photoacoustic, ultrasound) and therapy
Silver nanoparticles	polyvinylpyrrolidone (UV-induced polymerization)	Yang et al. [272]	-
Gold nanoparticles on TiO₂ substrate	Polypyrrole (plasmon induced charge separation)	Takahashi et al. [273]	-
Gold nanoparticles	alkyl-substituted pyrrole, bithiophene, and terthiophene thiols, terthiophene and sexithiophene dithiols, and polythiophene polythiol (self-assembly)	Zotti et al. [274]	-

resolution. Second, the overlap of porphyrin and tetrapyrrole absorbance and fluorescence spectra with those of biological components such as blood can lead to difficulties in distinguishing between background signal and the signal from contrast agents. Third, for many metal-chelated compounds, including porphyrins and tetrapyrroles, the possibility for unintended release of metal ions must be taken into consideration.

Strong efforts are being devoted to address these issues. For example, although porphyrin derivatives have been extensively used for fluorescence imaging, PDT and PTT, the absorption maxima of many porphyrin derivatives are generally below 700 nm[275] and they typically exhibited poor photostability in NIR treatment which limits their shelf-life and long-term use[276]. A possible

way to counter these issues is to redshift the Q band absorption to near 800 nm through enhancing their π-conjugated system. For example, introducing functionalities such as diketopyrrolopyrrole (DPP) that can enhance their molar absorption coefficient and photostability. DPP offers a unique electron-deficient feature, and once conjugated with electron-donating components to form a donor–acceptor (D–A) structure, it enhances their NIR absorption[277].

Further studies must be conducted to better explore the use of porphyrins and tetrapyrroles in clinically-available imaging modalities while taking into consideration the potential toxicity issues that may arise from the introduction of these materials into the body. For example, the development of PEGylation-free porphyrin-based nanoparticles allows for reduced concern about immunogenicity of poly(ethylene glycol) coatings that are often used to increase nanoparticle circulation time[278]. The use of these porphyrin-high-density-lipoprotein particles has been demonstrated for lung cancer therapy[275]. Additional efforts must be undertaken to utilize nanoparticle synthesis methods that take advantage of biocompatible and biodegradable materials that prevent long-term accumulation and immunogenicity.

1.4.13 Conclusions

Porphyrin- and tetrapyrrole-based nanoparticles are promising tools for bioimaging, therapeutic, and sensing applications. These particles can be made through a variety of synthesis methods including cross-linking, self-assembly, hydrothermal synthesis, and other techniques. Porphyrin- and tetrapyrrole-based nanoparticles have been demonstrated to have a variety of applications in fluorescence imaging, photoacoustic imaging, MR imaging, CT imaging, PET imaging, photothermal therapy, photodynamic therapy, and drug delivery. In addition, these nanoparticles have been shown in some cases to exhibit biodegradability and stimuli-responsive behaviours

which make them a promising platform with some inherent advantages over traditional nanoparticles.

1.5 LYMPH NODE STRUCTURE AND FUNCTION

Lymph nodes are complex organs that play an important role in regulating immune response to stimuli. Each lymph node is engulfed in a capsule. Lymph enters this capsule from the afferent lymphatic vessel, and exits at the efferent lymphatic vessel. The flow rate of lymph within lymph nodes is approximately 0.05 mm^3/s[279] . Lymph that has entered the capsule travels through the subcapsular sinus, interacting with lymph nodules before exiting the lymph node. Each nodule is composed of a cortex surrounding a lymphoid follicle, which can be classified as a primary or secondary lymphoid follicle based on the absence or presence of immune stimulation respectively. The cortex primarily contains B cells. The paracortical area borders the cortex, and is composed mostly of T cells. This is in turn bordered by the Medullary chords, which are composed of macrophages, dendritic cells, and plasma cells. Immune cells in the lymph node are programmed to respond to stimuli, filtering out harmful substances. A representative schematic of a lymph node is provided in **Fig. 1.11**.

The subcapsular sinus is lined with lymphatic endothelial cells, and controls the flow of cells and antigens into and out of the lymph nodules. Antigens less than 70 kDa in size (corresponding to a hydrodynamic radius of 4 to 5 nm) can enter a conduit system at the interface between the subcapsular sinus and the nodules[280], allowing them direct entry to the nodules. These conduits intersect the subcapsular sinus with Diaphragms composed of PLVAP, which creates a sieve with a cartwheel structure that can filter out antigens above the size limit[281]. Other interactions that exceed this size limit, for example the transmigration of leukocytes between the

sinus and the nodules, must take place across the lymphatic endothelial cell layer of the subcapsular sinus[282].
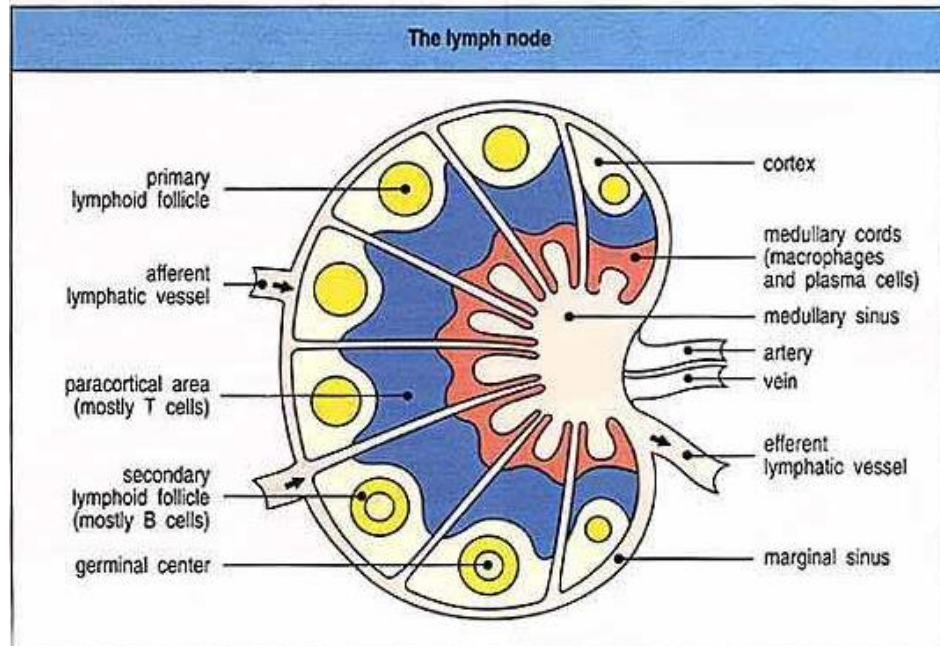
Figure 1.11. A representative diagram of the lymph node[283]

The flow of lymph between lymph nodes throughout the lymphatic system allows for the development and propagation of immune responses to foreign antigens. Lymph nodes are comprised of an outer layer known as the capsule, which envelopes the subcapsular sinus. The subcapsular sinus further envelopes the lymph nodules, which contain B cells, T cells, and dendritic cells. High endothelial venules located throughout the lymph node allow lymphocytes to travel from blood into the lymph nodes[284]. The immune cells are activated in response to antigens in the lymph, and can then travel throughout the body to carry out an immune response to these antigens[284]. The flow of antigens and cells from lymph into the nodules occurs across the subcapsular sinus, which is composed of human lymphatic endothelial cells and subcapsular sinus macrophages[285].

40

Antigens below 70 kDa in size cross the subcapsular sinus through a conduit system that utilizes sieves to filter antigens by size[280,281,286,287]. Other antigens and cells must cross the lymphatic endothelial cell layer to access the nodules[280,281,286,287]. Subcapsular sinus macrophages aid in the transport of pathogens across the subcapsular sinus[288–291], and their ability to do so is directly dependant on factors secreted by lymphatic endothelial cells[285]. Lymph solute transport across the subcapsular sinus has also been shown to occur both paracellularly and intracellularly within lymphatic endothelial cells[292].

Flow in the lymph nodes is unidirectional due to a complex valving system[293–296], ensuring that lymph travels only from the afferent lymphatics to the efferent lymphatics. Lymph node shear values of up to 1.2 Pa (12 dyn/cm^2) have been reported in rodents[72], and computer simulations have predicted shears of up to 0.6 Pa (6 dyn/cm^2) in human lymph nodes[74].

Lymph nodes are also a common site of cancer metastases from skin, breast, prostate, gastric, and other cancers[297–302] because tumors can drain directly into neighboring lymph nodes. In a VEGF-C-expressing breast cancer mouse tumor model, increased flow velocity was observed in tumor-draining lymph nodes.[73] Additionally, decreased flow velocity was observed in lymph nodes containing metastases.[73] Application of shear stress to lymphatic endothelial cells has been found to increase expression of ICAM-1, which can contribute to the formation of metastases[68]. Flow behavior in lymph nodes has further been linked to cytokine expression. Cessation of lymph flow has been found to lead to an increase in TNF-α and interleukin 6 (IL6) production.[303] When administered, these cytokines were also found to lead to reduced contraction/pumping in the lymphatic system.[303] In breast cancer patients, a higher expression of TNF-α expression has been correlated with the presence of lymph node metastases, and a correlation between TNF-α and IL8

levels has also been demonstrated.[70] Importantly, although cancer metastases can travel from one lymph node to another via the lymphatic system, studies in mouse models of breast cancer have determined that cancer cell extravasation across the high endothelial venules is the main route through which tumor cells can enter the blood circulation to metastasize to other parts of the body.[304]

1.6 REVIEW OF MICROFLUIDIC MODELS OF THE LYMPHATIC SYSTEM

The goal of this chapter is to provide a brief overview of currently existing microfluidic lymph node chip models. A number of detailed reviews that are related to the importance of microfluidic organ-on-a-chip devices have already been published,[305–308] so we will not discuss the argument for use of such devices. There have also been a few published review articles on subjects tangential to what we will be discussing in this chapter. Greenlee et al. extensively reviewed the use of microfluidics in studying lymphatic cancer metastasis, although the focus of their review was not only on organ-on-a-chip devices but also the application of microfluidics in fundamental studies of lymphatic cell behaviors.[309] Shanti et al. touched on some of the contemporary organ-on-a-chip models of the lymphatic system in their 2018 review.[310] Kim et al. discussed various 3D culture and materials-based approaches to the development of lymphoid organs.[311] Sun et al. reviewed various organ-on-a-chip models related to cancer and immune organs, including briefly discussing lymph node models.[312] A recent review from Henderson et al. describes organ-on-a-chip models of blood and lymphatic vasculature.[313]

One of the earliest microfluidic lymph node devices was reported by Mitra et al. (**Figure 1.12**).[314] The goal of their work was to develop an in vitro model that incorporated dendritic cell migration with T cell activation. Their device incorporated two layers. The first layer was comprised of a chemotaxis compartment for studying the migration of dendritic cells. The second

layer contained a T cell compartment. They demonstrated that mature dendritic cells would respond to a gradient of CCL19, a chemokine that is believed to regulate the migration of dendritic cells towards lymph nodes. The dendritic cells exposed to the CCL19 gradient migrated towards the T cell compartment and led to T cell activation, which was confirmed by measuring calcium levels within the T cells. This is characteristic of lymph node behavior, as dendritic cells typically migrate to lymph nodes in order to present antigens to T cells.
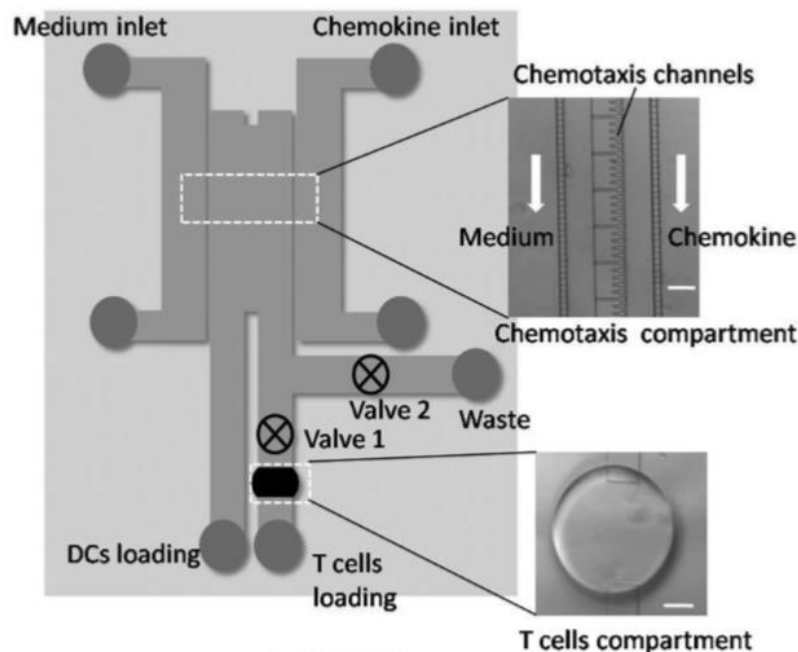
Figure 1.12. Design of a microfluidic device combining dendritic cell migration with T call activation. Adapted from Mitra et al. [314]

Gopalakrishnan et al. utilized a microfluidic device to study the activation and migration of immune cells in response to infections and other immune stimuli (**Fig. 1.13**).[315] The device allowed for coculture of migratory immune cells and activator cells. Microfluidic channels connected the migratory cell chambers with the activator cell chambers, allowing immune cells to be exposed to cytokines produced by the activator cells and migrate in response to these cytokines. When the activator chamber was loaded with T cells and mature dendritic cells, it led to migration

of immature dendritic cells from the migratory cell chamber. When the activator chamber was loaded with mature dendritic cells that were stimulated with bacterial infection, immature dendritic cells again migrated towards the activator chamber. When the activator chamber was loaded with lipopolysaccharide, peptide-loaded macrophages, and I-Ab-peptide restricted T cells, and the migratory cell compartment was loaded with T cells, the T cells from the migratory chamber migrated towards the activator chamber. These experiments illustrate the utility of microfluidic devices in examining immune cell interactions. However, they did not examine the effect of flow on the cell kinetics.
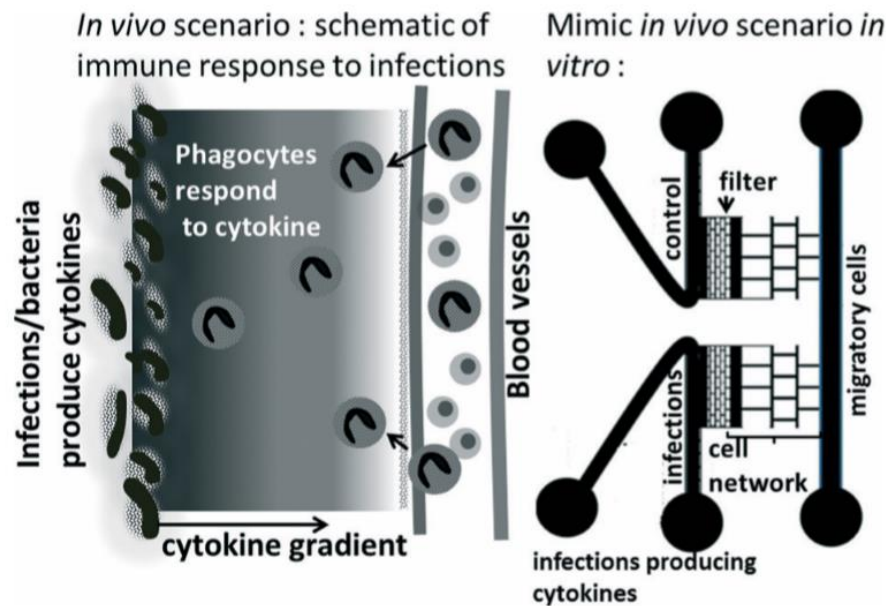
Figure 1.13. A microfluidic device that mimics the response of immune cells to infections. Adapted from Gopalakrishnan et al.[315]

Pisano et al. reported a fluidic flow chamber-based device that was used to study the effects of transmural and apical flow on MDA-MB-231 cells migration across a lymphatic endothelial cell layer **(Fig. 1.14)**.[75] Their device combined transwell inserts (8 µm pore size) with fluidic flow both across the transwell membrane and beneath the surface of the transwells. This was meant to mimic the transmural and apical flows that occur within lymph nodes. Transmural flows of 0 or 1

μm/s and luminal shear stresses of 0, 0.01 or 1 dyn/cm^2 were utilized within the device. The results demonstrated that transmural flow and luminal shear stress each play a role in cancer cell migration, with the concurrent application of these two flows increasing cancer cell invasion (i.e. transport) compared to the application of individual flows.
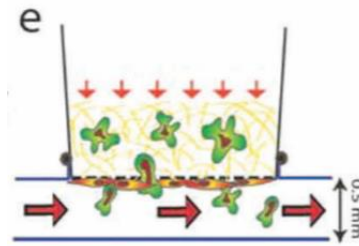
Figure 1.14. A fluidic flow chamber to evaluate the effects of transmural and apical flow on tumor cell invasion across the subcapsular sinus. Arrows depict directions of flow. Orange cells represent lymphatic endothelial cells, while green cells represent breast cancer cells. Adapted from Pisano et al.[75]

Sato et al. reported a microfluidic device for co-culture of cells representing lymphatic endothelial cells and blood vascular endothelial cells **(Fig. 1.15)**.[316] The two channels within the device were separated by a porous membrane. Lymphatic endothelial cells were grown on the bottom of the membrane, and blood vascular endothelial cells were grown on the top of the membrane. Cells were grown under static conditions, 1-μL/h pulsating flow, or 1-μL/h continuous flow (0.01 dyn/cm^2 shear). Transport across the cell layers was evaluated, demonstrating that cells grown under flow allowed for lower transport across the endothelial cell layers than those grown under static conditions. This was attributed to the development of endothelial cell tight junctions in cells grown under flow conditions. The device was further utilized to assess the vascular damage resulting from snake venom.
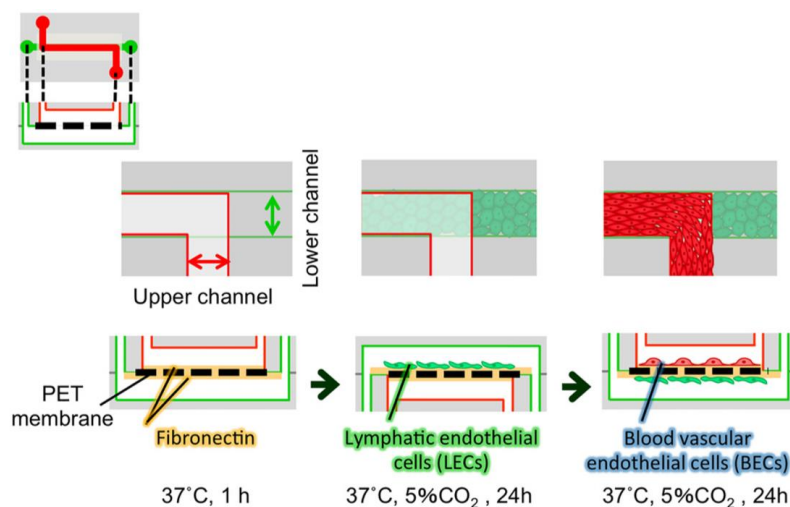
Figure 1.15. Coculture of lymphatic endothelial cells and blood endothelial cells in a microfluidic chip. Reproduced from Sato et al.[316]

Ross et al. developed a microfluidic device that allowed for culture of live tissue slices from rodent lymph nodes **(Fig. 1.16)**.[317] The device consisted of three layers, one of which contained a perfusion chamber, the second contained ports to interface with the channels, and the third contained channels for delivery of stimuli to the perfusion chamber. The perfusion chamber allowed for perfusion of media into the lymph node tissue slice. The device design allowed for local chemical stimulation within the lymph node tissue slice. Glucose-conjugated albumin, a model therapeutic, was delivered directly to regions of interest within the lymph node tissue slice, and used to demonstrate that the B-cell zone had higher drug retention than the T-cell zone did. In follow-up work, Shim et al. developed a microfluidic device that allowed for co-culture of lymph node slices with tumor slices under recirculating flow.[318] They demonstrated that lymph node slices co-cultured with tumors had a decreased immune response (as determined by IFN-γ secretion) than slices that were co-cultured with sections of fat pad. They additionally demonstrated that the microfluidic chip allowed for exchange of proteins between the various tissue slices.
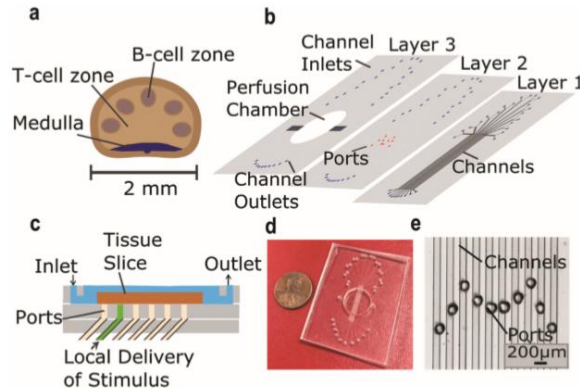
Figure 1.16. Design of a microfluidic device that allows for stimulation of lymph node tissue slices. Adapted from Ross et al. [317]

In a preprint, Goyal et al. describe a microfluidic lymph node chip device that allows for the assembly of B cells and T cells into lymph node follicles.[319] The device is comprised of two layers, each of which contains a channel. The two channels are separated by a porous membrane. T and B cells were co-cultured in a Matrigel-collagen gel in the bottom channel, and the top channel was used for media perfusion into the device. The authors demonstrated that perfusion led to follicle formation within 3-4 days of culture, and that although follicles formed in 3D culture without perfusion, media perfusion led to the formation of a greater number of follicles and a greater follicle size. When dendritic cells were included within the 3D matrix in addition to T and B cells, the device could be used for evaluation of a clinically-available quadrivalent flu vaccine. The authors demonstrated that the lymph node chip could be immunized with the flu vaccine. Vaccination led to the production of anti-influenza hemagglutinin antibodies and plasma cells. Multiple cytokines produced on-chip were also compared to those produced by humans immunized with the flu vaccine.

Recently, Ayuso et al. reported a microfluidic model of tumor-lymphatic interactions (**Fig. 1.17**).[317] They embedded two adjacent channels in a gel matrix, growing human lymphatic endothelial cells in one of the channels, and MCF-7 or MDA-MB-231 cells in the other. Using this

device, it was demonstrated that conditioning of the lymphatic endothelial cells through co-culture with cancer cells led to increased vessel permeability. Additionally, transcriptional analysis of the lymphatic endothelial cells co-cultured with cancer cells demonstrated that conditioning with MCF-7 cells led to the development of pro-lymphangiogenic and hypoxic phenotypes. In addition, co-culture with MCF-7 cells led to the upregulation of genes that were linked to cell metabolism, migratory capacity, and cell proliferation. Co-culture of human lymphatic endothelial cells with MDA-MB-231 cells was found to lead to a less drastic change in lymphatic endothelial cell transcriptional properties. Co-culture with the cancer cells was also demonstrated to lead to lymphangiogenic sprouting. A summary of all discussed devices can be found in **Table 1.7.**
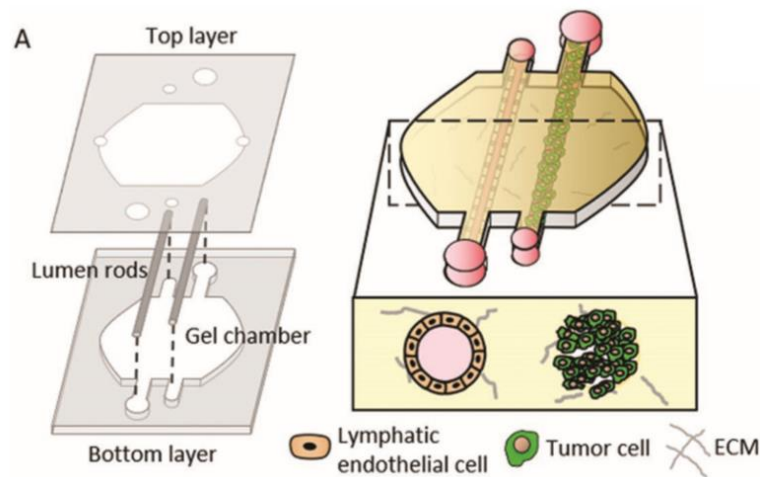
Figure 1.17. Device for co-culture of lymphatic endothelial cells and tumor cells. Adapted from Ayuso et al.[317]

Table 1.7. Overview of microfluidic models of lymph nodes

Author	Cell Types Used	Description of Device
Mitra et al. (2013)[314]	- Mature dendritic cells - Immature dendritic cells - T cells (from PBMCs)	Two-layer device with chemotaxis compartment to study migration of dendritic cells, and T cell compartment to evaluate dendritic cell-induced T cell activation
Gopalakrishnan et al. (2015) [315]	- MF2.2D9 T cell hybridomas - IC-21 macrophages - B6 macrophages - Dendritic cells - Mycobacterium avium	Migratory cell chamber and activator cell chamber, separated from each other by filters and a channel network. The cytokines secreted by cells in the activator cell chamber could induce migration of the migratory immune cells towards the activator cells.
Pisano et al. (2015) [75]	- Human dermal lymphatic endothelial cells from neonatal foreskin - MDA-MB-231 breast cancer cells	Fluidic flow chamber with transwell inserts. Flow occurred within the channel beneath the transwell inserts, as well as across the transwell membrane surface.
Sato et al. (2015) [316]	- Human lymphatic microvascular endothelial cells (as a model of lymphatic endothelial cells) - human dermal microvascular endothelial cells (as a model of blood endothelial cells)	Two-layer device with an upper and lower channel that partially overlapped, separated only by a porous membrane. Blood endothelial cells were cultured in the top channel, and lymphatic endothelial cells were cultured in the bottom channel.
Ross et al. (2017)[317]	- Lymph node tissue slices	Multilayer device that incorporates a perfusion chamber and microfluidic channels for perfusion and stimulation of lymph node tissue slices.
Shim et al. (2019)[318]	- Lymph node tissue slices - 4T1 Breast cancer tumor tissue slices	Device that has multiple perfusion chambers for perfusion of lymph node tissue slices and tumor tissue slices through recirculating flow.
Goyal et al. (2019, pre-print)[319]	- Primary T cells - Primary B cells - Dendritic cells differentiated from primary monocytes	Device with two channels separated by a membrane. The top channel is used for perfusion, while the bottom channel is used for formation of lymphatic follicles
Ayuso et al. (2020) [317]	- Human lymphatic endothelial cells - MCF-7 breast cancer cells - MDA-MB-231 breast cancer cells	Two adjacent channels embedded in a gel matrix. One channel is seeded with human lymphatic endothelial cells, while the other is seeded with breast cancer cells.

1.6.1 Potential for Future Research Directions

Although the various described models have managed to recapitulate some aspects of lymph node function **(Table 1.8)**, there remains much work to be done in this field. First, there are currently no reports of devices that incorporate channels representing both high endothelial venules and the subcapsular sinus, both of which are important routes of transport to and from lymph nodes. Second, the study of immune cell behavior in the reported chips has mostly been lacking in discussion of the roles of lymph node 3D structure in cell behavior, as well as the roles of interactions between immune cells and lymphatic endothelial cells in lymph node behavior. Although some aspects of this can be mimicked through the use of lymph node tissue slices, the potential for difference between murine lymph node behavior and human lymph node behavior may always cast doubt on the utility of animal-based microfluidic models in predicting the response of human lymph nodes. Further research must be conducted to identify the effects of lymphatic cell spatial organization on parameters of interest. Third, many of the microfluidic devices discussed lack flow. Since flow is present in the lymph nodes, the role of flow in cell behavior must be carefully considered in the design of devices that seek to mimic lymph node structure and function.

Table 1.8. Elements incorporated into microfluidic lymph node models.

	Shear Flow	Cancer Cells	Chemokines	Immune cells	Cell Migration	Endothelial cells	Tissue Slices
Mitra et al	-	-	X	X	X	-	-
Gopalakrishnan et al	-	-	X	X	X	-	-
Pisano et al	X	X	-	-	X	X	-
Sato et al	X	-	-	-	-	X	-
Ross et al		-	-	X	-	X	X
Shim et al		X	-	X	-	X	X
Ayuso et al	-	X	-	-	-	X	-

1.7 DESIGN PRINCIPLES OF PUMPLESS MICROFLUIDIC DEVICES

Pumpless microfluidic devices allow end users to obtain fluidic flow within devices without the need for expensive pump setups. This can enable the operation of many devices in parallel, allowing for higher-throughput experimentation. Gravity-driven flow is one method of obtaining flow in pumpless devices. In gravity-driven flow, the device is tilted to allow gravitational acceleration to act in the direction of desired flow. The device can be placed on an inclined rocker plate to change the direction of the flow by changing the position of the rocker plate (**Fig. 1.18**). This causes flow to occur without the use of pump systems, reducing cost and allowing for the simultaneous operation of many devices, which would not have been possible with the use of pump systems. Alternative methods of obtaining gravity-driven flow, such as the use of a rotating platform can also be utilized.[320]
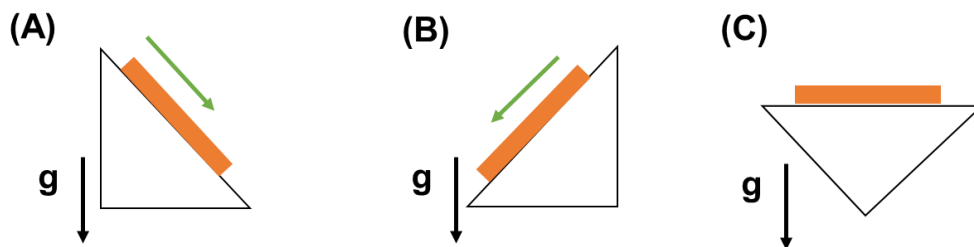
Figure 1.18 Effect of rocker plate position on direction of fluidic flow within devices. (A-B) Fluid flow (green) occurs due to gravity when the devices (orange) are placed at an angle. (C) Fluid flow doesn't occur when devices are laid flat.

One important factor to consider in organ-on-a-chip devices is the direction of flow within the devices. For some cell types, flow must be unidirectional in order to accurately mimic physiological conditions within the body. This means that the flow should not travel back along the same path even when the rocker plate position has changed, but it instead should continue to travel in the same direction along the remainder of the path even with a change in rocker plate position (**Fig. 1.19**). Gravity-driven devices typically rely on bidirectional flow rather than

unidirectional flow, but bidirectional flow has been known to cause complications for endothelial cell culture. Thus, pumpless microfluidic devices must be designed carefully to achieve unidirectional flow if desired. Another important parameter in the use of pumpless organ-on-a-chip devices is obtaining the desired physiologically-relevant shear flows. Shear has been shown to be an important factor in the culture of cells such as endothelial cells, and the ability to control the shear experienced by cells makes microfluidic devices a desirable alternative to 2D cell culture.
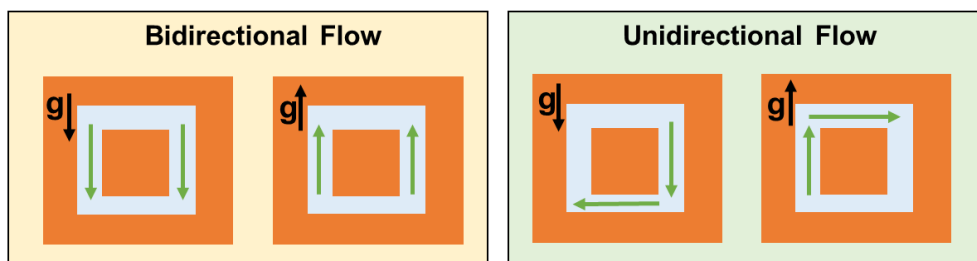
Figure 1.19. Difference between unidirectional flow and bidirectional flow in a microfluidic device.

The aforementioned design considerations governed the development of our microfluidic devices in this work. We sought to combine a pumpless chip design with an in-house fabricated and programmed rotating platform that would enable cyclic unidirectional flow with desired shear levels within the device **(Fig. 1.20)**.
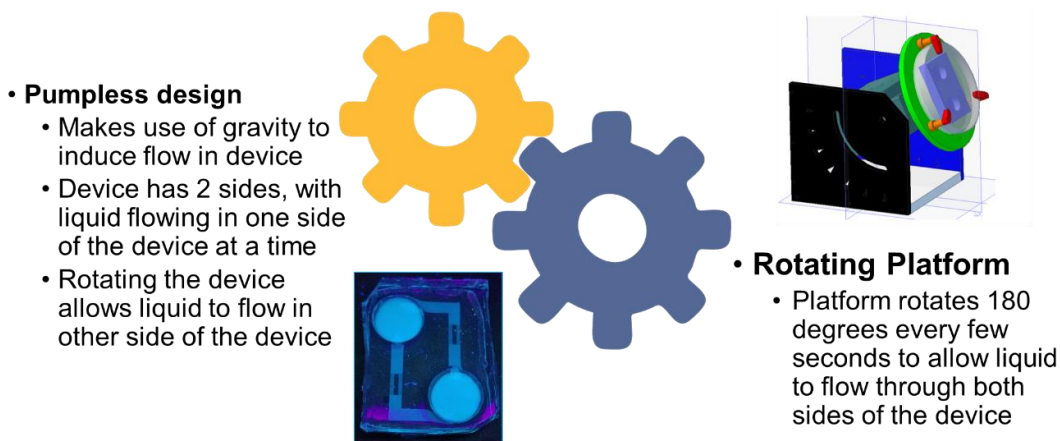
Figure 1.20. Approach to microfluidic device design in this work.

CHAPTER 2: DESIGN AND PHYSICOCHEMICAL CHARACTERIZATION OF BIODEGRADABLE NANOPARTICLES FROM ENDOGENOUS BILIVERDIN MOLECULES

2.1 ABSTRACT

Photoacoustic imaging has emerged as a promising imaging platform with a high tissue penetration depth. However, biodegradable nanoparticles, especially those for photoacoustic imaging, are rare and limited to a few polymeric agents. The development of such nanoparticles holds great promise for clinically translatable diagnostic imaging with high biocompatibility. Metabolically digestible and inherently photoacoustic imaging probes can be developed from nanoprecipitation of biliverdin, a naturally occurring heme-based pigment. The synthesis of nanoparticles composed of a biliverdin network, cross-linked with a bifunctional amine linker, is achieved where spectral tuning relies on the choice of reaction media. Nanoparticles synthesized in water or water containing sodium chloride exhibit higher absorbance and lower fluorescence compared to nanoparticles synthesized in 2-(*N*-morpholino) ethane sulfonic acid (MES) buffer. All nanoparticles display high absorbance at 365 nm and 680 nm. Excitation at near-infrared wavelengths leads to a strong photoacoustic signal, while excitation with ultraviolet wavelengths results in fluorescence emission. *In vivo* photoacoustic imaging experiments in mice demonstrated that the nanoparticles accumulate in lymph nodes, highlighting their potential utility as photoacoustic agents for sentinel lymph node detection. The biotransformation of these agents was studied using mass spectroscopy and they were found to be completely biodegraded in the presence of biliverdin reductase, a ubiquitous enzyme found in the body. Degradation of these particles was also confirmed *in vivo*. Thus, the nanoparticles developed here are a promising platform for

biocompatible biological imaging due to their inherent photoacoustic and fluorescent properties, as well as their complete metabolic digestion.

2.2 INTRODUCTION

Photoacoustic (PA) imaging is a technique that combines optical excitation with ultrasound detection to achieve superior depth of penetration compared to fluorescence imaging.[321] Nanoparticle-based imaging probes have been utilized as an alternative to small-molecule probes due to advantages such as the ability to tune their surface characteristics, increase circulation time, and target tissues of interest. Nanoparticles with photoacoustic properties[31,32,41–44,33–40] are a class of contrast agents that hold great potential for multiscale diagnostic applications.[45–50] However, a majority of these nanoparticles are based on polymeric or metallic designs and therefore may remain in the body for extended time periods. In fact, 30-99% of nanoparticles will accumulate in the liver,[51] and a variety of nanoparticles have been shown to negatively impact liver cells.[52–58] With the exception of a few classes (*e.g.* iron oxide), only several examples of nanoparticles have been translated to a clinical setting.[322–327] One of the key determinants that would improve translational potential of nanoparticles is to improve their biodegradation profile. Specifically, there is a need for the development of photoacoustic nanoparticles that can be degraded in the body after the imaging session has been performed. The goal of the present work is to utilize endogenous molecules for designing inherently photoacoustic nanoparticles that, at the same time, could offer a solution to the issue of biodegradation.

In order to develop biodegradable nanoparticles with inherent photoacoustic imaging capabilities, we proposed the use of biliverdin, a water-soluble, naturally-occurring bile pigment that results from the breakdown of heme.[59] During this process, biliverdin is reduced to water-insoluble bilirubin through the action of an enzyme, biliverdin reductase.[59–61] The inherent

breakdown pathway of biliverdin led us to hypothesize that nanoparticles composed of biliverdin would be entirely biodegradable *in vivo*. Biliverdin has two main absorbance bands; one between 350 nm and 400 nm, and the other between 600 nm and 700 nm.[62] The absorbance above 650 nm is important for *in vivo* applications because interference from the surrounding tissue is minimal between 650-900 nm (*i.e.*, the first biological imaging window).[63]

Many photoacoustic nanoparticles obtain their photoacoustic properties through the incorporation of dyes or metals,[35,36,39,44] rather than through selection of intrinsically photoacoustic building blocks. These approaches pose a challenge due to the potential for toxicity of the metals, or premature release of the incorporated dyes. There are very few examples reported in the literature of nanoparticles derived entirely from endogenous species. For instance, a recent report revealed the synthesis of cisplatin-chelated bilirubin nanoparticles for photoacoustic imaging and photothermal therapy.[328] An important distinction is that while biliverdin has strong absorbance in the near-infrared region, bilirubin does not. Thus, in order for bilirubin-based nanoparticles to exhibit their favorable photoacoustic properties, it was necessary for cisplatin, a xenobiotic metal-based anti-cancer drug, to be incorporated. Additionally, the enzymatic degradation of these nanoparticles has not been reported

Here we report the synthesis of fully biodegradable nanoparticles that do not require the chelation of metals to exhibit photoacoustic properties suitable for *in vivo* imaging. Importantly, we expand the utility of these nanoparticles further by leveraging the blue-shifted absorbance for fluorescence imaging. The utility of these nanoparticles for bioimaging was demonstrated through application as a sentinel lymph node imaging probe. Finally, we demonstrate that the nanoparticles can be completely degraded both *in vitro* and *in vivo* by biliverdin reductase, an enzyme present throughout the body, and especially in the liver.[60,329]

55

2.3 RESULTS AND DISCUSSION

2.3.1 Synthesis

To develop biliverdin nanoparticles (BVNPs), biliverdin hydrochloride ($C_{33}H_{34}N_4O_6$ •HCl) was nano-precipitated using stoichiometric amounts of 1-ethyl-3-(3-dimethylaminopropyl) carbodiimide (EDC) and 2,2' ethylenedioxy bis(ethylamine) (henceforth referred to as diamine). The products obtained from this reaction were found to be highly dependent on the nature of the reaction media. We conducted the reactions in water, in 0.1 M 2-(N-morpholino) ethanesulfonic acid (MES) buffer, and in 0.15 M aqueous NaCl solution. The resultant BVNPs are designated water-BVNPs, MES-BVNPs, and NaCl-BVNPs, respectively **(Scheme 2.1)**.

The sizes of the nanoparticles were determined using transmission electron microscopy (TEM). We found that the addition of EDC, N-hydroxysuccinimide (NHS), and diamine to biliverdin dissolved in water led to the formation of small nanoparticles with an average diameter of 2.3 nm at 10 min, and larger nanoparticles with an average diameter of 105 nm when the components were allowed to react for 24 h **(Figure 2.1A)**. Water-BVNPs and NaCl-BVNPs showed an immediate color change upon addition of the diamine, while the color of the MES-BVNPs remained unchanged. The absorbance peaks of the BVNPs was markedly different with respect to free biliverdin, indicating successful particle self-assembly **(Figure 2.1B)**. The synthesis that was conducted in the NaCl solution exhibited similar absorbance characteristics to that of water-BVNPs **(Figure 2.1B)** and resulted in spherical nanoparticles with an average diameter of 14.2 nm after 24 h **(Figure 2.1A)**. In contrast, when the synthesis was performed in MES buffer, nanoparticles with diameters of 26.5 nm and 43.8 nm were observed at the 10-min and 24-h time points, respectively **(Figure 2.1A)**. These particles did not show a significant change in size when

the reaction time was extended, indicating that the reaction in MES was controlled and had formed

stable particles.
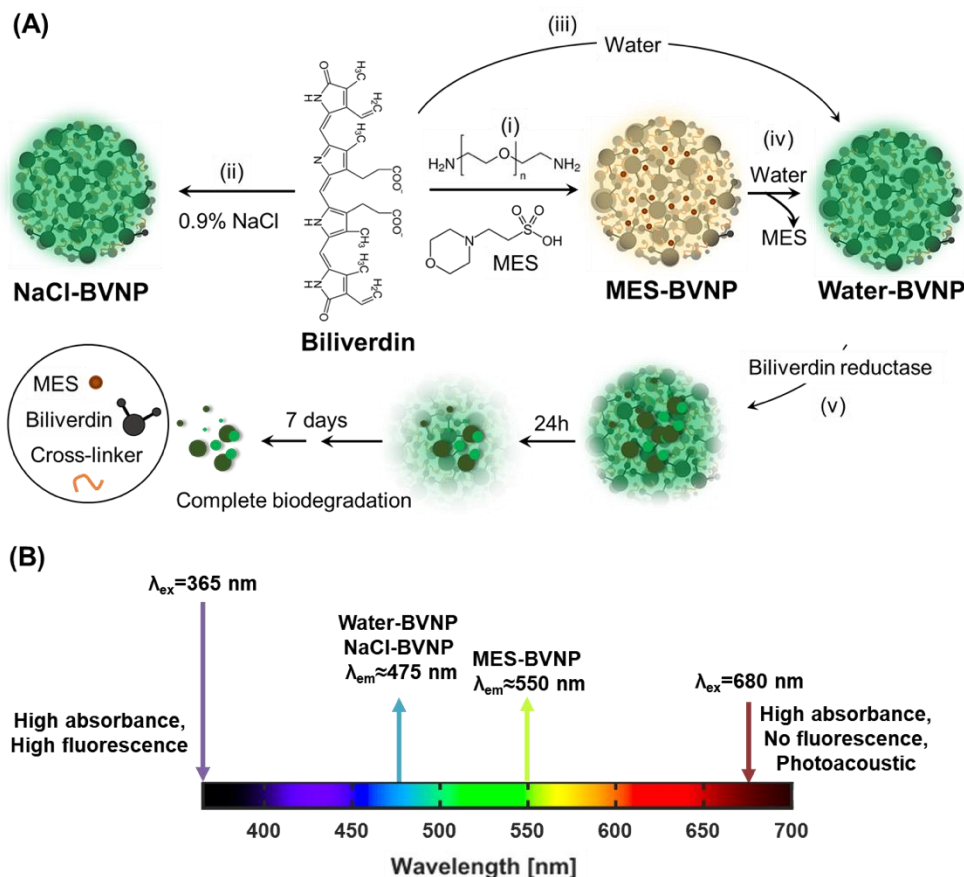
Scheme 2.1. (A) BVNP synthesis schematic. The synthesis solvent determines BVNP composition and spectral properties. The use of water, MES, and NaCl results in water-BVNPs **(iii)**, MES-BVNPs **(i)**, and NaCl-BVNPs **(ii),** respectively. Dialysis of MES-BVNPs with water **(iv)** results in water-BVNPs. Nanoparticles degrade in the presence of biliverdin reductase **(v)**. **(B)** MES-BVNPs have a red-shifted fluorescence compared to the Water-BVNPs and NaCl-BVNPs. All compositions exhibit high absorbance at 365 nm and 680 nm, resulting in fluorescent and photoacoustic properties respectively.

2.3.2 Photophysical Characterization

The photophysical properties of the nanoparticles were characterized using a full suite of

techniques including UV-Vis spectroscopy, Fourier transform infrared spectroscopy (FT-IR),

mass spectrometry, zeta potential measurements, fluorescence spectroscopy, fluorescence

imaging, and photoacoustic tomography. The MES-BVNPs showed a broadening of the UV-Vis peak at ≈650 nm, as well as a decrease in overall absorbance at all wavelengths compared to water-BVNPs and NaCl-BVNPs **(Figure 2.1B)**.

FT-IR spectroscopy **(Figure 2.1C, Figure D1)** revealed that the crosslinker had peaks at 1585 cm^{-1} (peak 1, N-H bend), 1305 cm^{-1} (peak 2, C-N stretch), and 1130 cm^{-1} (peak 3, C-N stretch). Unincorporated biliverdin had C-N stretches at 1330 cm^{-1} (peak 6), 1305 cm^{-1} (peak 2), 1280 cm^{-1} (peak 7), 1260 cm^{-1} (peak 8), and 1120 cm^{-1} (peak 9). The formation of amide bonds as a result of EDC-NHS crosslinking was confirmed by the appearance of peaks at 1678 and 1653 cm^{-1} (peaks 10 and 11) for the BVNPs. MES-BVNPs exhibited a unique set of peaks in the range of 800 cm^{-1} -1500 cm^{-1} compared to the water-BVNPs and the NaCl-BVNPs. The sharp peak near 1030 cm^{-1} (peak 12) can be attributed to the S=O in MES,[330] while the peak near 910 cm^{-1} (peak 13) can be attributed to the S-OH bond in MES, indicating that it is plausible that MES molecules were entrapped within the nanoparticle. 24 h MES-BVNPs dialyzed with MES retained the peaks at 1030 cm^{-1} and 910 cm^{-1}, while 24 h MES-BVNPs dialyzed with water no longer had these peaks, indicating that dialysis with water led to the removal of MES from the particles **(Figure D1 B)**. All three nanoparticle types were found to have negative zeta potentials, with no statistically significant difference in zeta potential between the 10-min and 24-h time points for any of the types **(Figure 2.1D)**. The reduction in zeta potential magnitude of 24-h MES-BVNPs compared to 24-h water-BVNPs further suggests a relationship between the reaction media and nanoprecipitation.

When the 10-min and 24-h samples were excited at 365 nm, all three nanoparticle types were fluorescent **(Figure 2.2A)**. However, the MES-BVNPs showed the highest fluorescence, with a maximum intensity over ten-fold greater than that of the water-BVNPs and NaCl-BVNPs. This
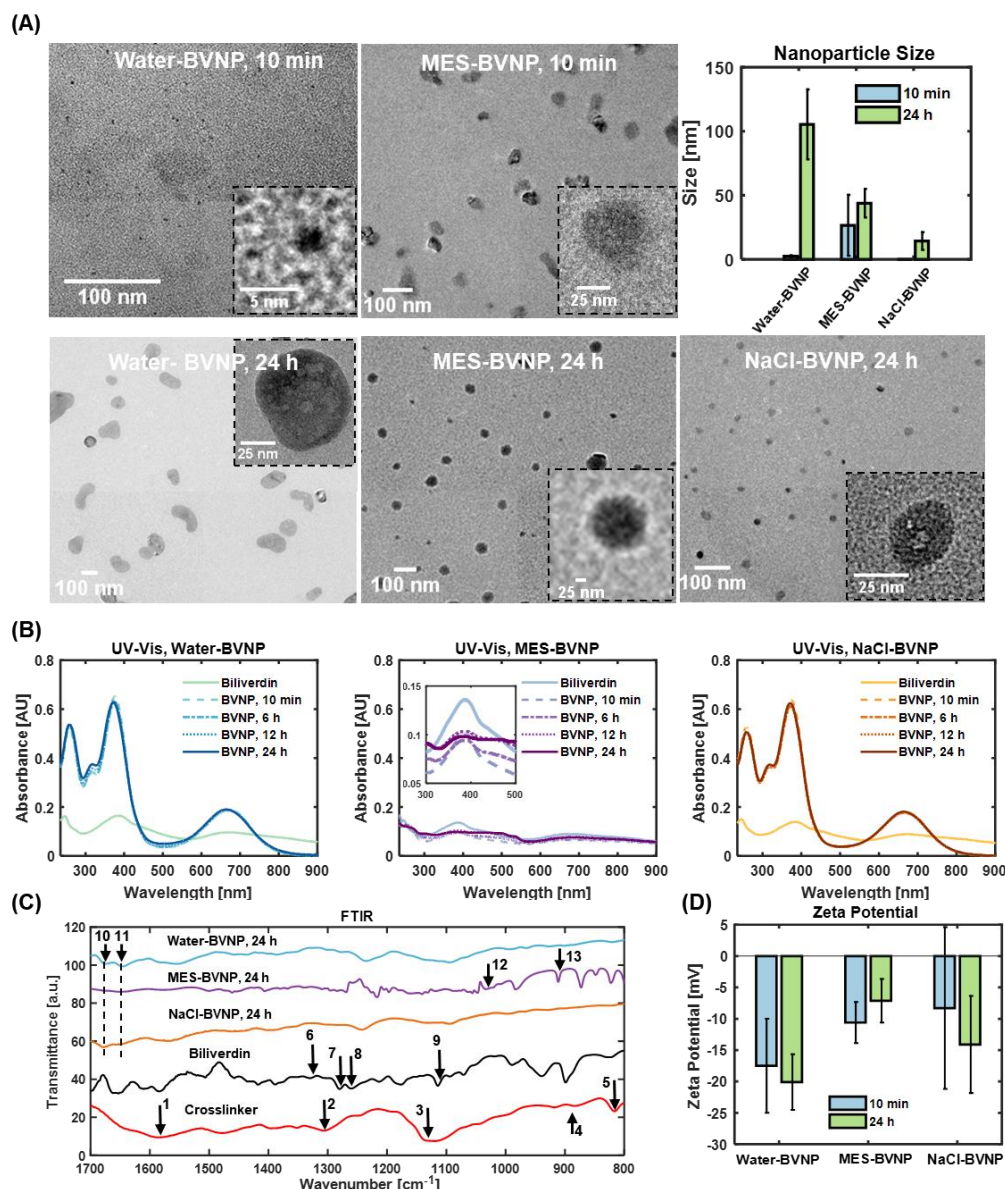
Figure 2.1. Physicochemical characterization of BVNPs. **(A)** TEM micrographs of different BVNP compositions. Spherical nanoparticles were found to be formed for each composition. Size was determined using ImageJ, and error bars represent standard deviation across all nanoparticles in a representative image for each nanoparticle type. **(B)** UV-Vis spectra for BVNPs. Water-BVNPs and NaCl-BVNPs display higher absorbance than MES-BVNPs. High absorbance is observed near 365 nm and 680 nm. **(C)** FT-IR spectra confirms the presence of differences between MES-BVNPs and other compositions, with peaks resulting from MES. **(D)** Zeta potential measurements indicate no significant zeta potential differences between Water-BVNPs, MES-BVNPs, and NaCl-BVNPs. Error bars represent standard deviation across twelve or more runs as automatically determined by the Malvern Zeta sizer software.

finding prompted us to determine the possible influence of MES. We dialyzed 10-min MES-

BVNPs and water-BVNPs with water using dialysis cassettes with a size cutoff of 10 kDa. We

hypothesized that if MES was influencing the photophysical properties, a greater change in MES-BVNP fluorescence would be observed compared to that of the water-BVNPs, which served as a control. Indeed, we found a larger fluorescence intensity fold change for the MES-BVNPs after dialysis with water. This suggested to us that the entrapped MES molecules were inducing a change in the fluorescence properties. Upon dialysis with water, the MES molecules were unloaded, resulting in a decreased fluorescence. Another interesting property is that the emission wavelength changed as a function of reaction time for the MES-BVNPs but not the Water-BVNPs and NaCl-BVNPs. In particular, the MES-BVNPs emission changed from blue (10-min) to yellow-green (24-h). The difference in fluorescence emission based on synthesis solvent was also observed under a 365 nm UV lamp for 24-h samples **(Figure 2.2A)**. When observed under the UV lamp, MES alone did not exhibit any fluorescence **(Figure D2)**. This finding suggests that it is possible to fine tune spectral properties of biliverdin nanoparticles through careful selection of the reaction media and synthesis time.

When excited at 680 nm, none of the three nanoparticle types exhibited fluorescence. A Spectrum *In vivo* Imaging System (IVIS) was used to perform further fluorescence imaging experiments **(Figure 2.2B, Figure D2)**. The MES-BVNPs showed greater radiant efficiency than the other nanoparticle types and exhibited some fluorescence in the near-IR region for excitation wavelengths of 430 nm, 465 nm, and 500 nm. In all cases, the BVNPs showed no fluorescence at an excitation wavelength of 675 nm.

We conducted further experiments with multiple time-points between 10 min and 24 h to investigate MES-BVNP fluorescence change with synthesis time. For 365 nm excitation **(Figure 2.2C)**, fluorescence intensity dropped between 10 min and 5 h. At 5 h the appearance of a second
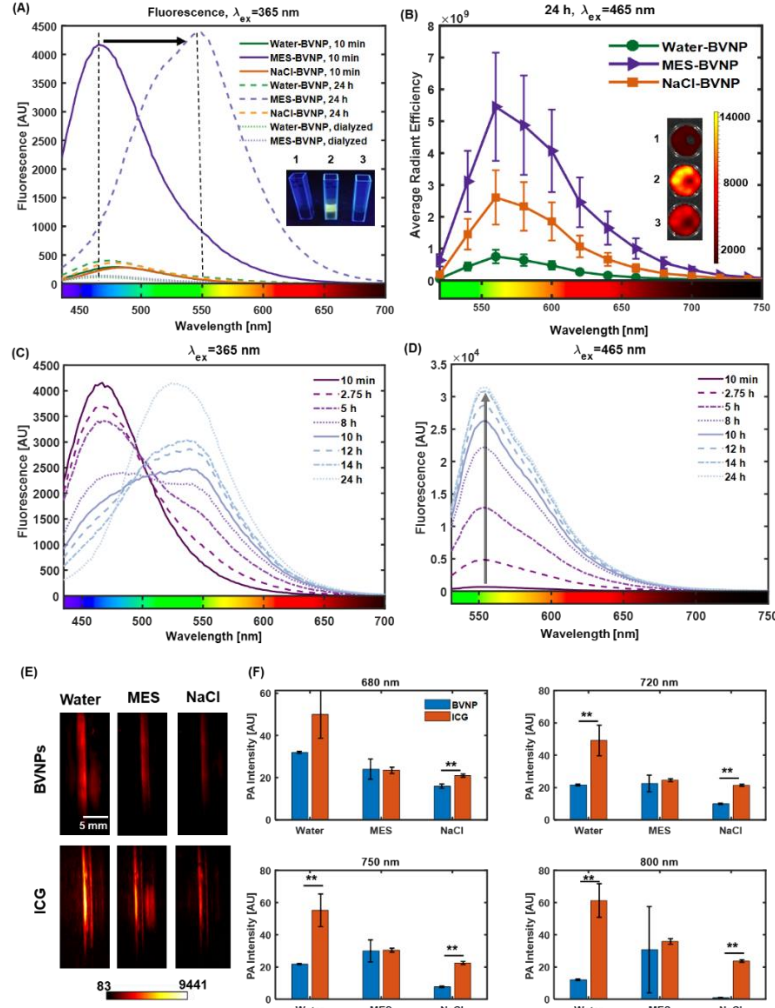
Figure 2.2. Spectral properties of BVNPs. (**A**) Fluorescence spectra for an excitation wavelength of 365 nm. MES-BVNPs exhibit red-shifting fluorescence with time, resulting in yellow-green fluorescence at 24 h. MES-BVNPs have the greatest fluorescence intensity. MES-BVNPs dialyzed with water lose their fluorescence advantage. Inset depicts 24-h BVNPs under a 365 nm lamp. 1, 2, and 3 correspond to Water-BVNP, MES-BVNP, and NaCl-BVNP respectively (**B**) Average Radiant efficiency for 24-h BVNPs at an excitation wavelength of 465 nm. MES-BVNPs were found to have higher radiant efficiency than Water-BVNPs and NaCl-BVNPs. Inset depicts IVIS image of BVNPs for an excitation wavelength of 500 nm and an emission wavelength of 680 nm. 1, 2, and 3 correspond to Water-BVNP, MES-BVNP, and NaCl-BVNP respectively. (**C**) MES-BVNP fluorescence change with time for an excitation wavelength of 365 nm. A decrease in fluorescence intensity is observed, followed by a fluorescence red-shifting and subsequent increase in fluorescence intensity to its initial magnitude. (**D**) MES-BVNP fluorescence change with time for an excitation wavelength of 465 nm. A steady increase in fluorescence intensity is observed with synthesis time. (**E**) Photoacoustic tissue phantom imaging of dialyzed BVNPs, compared to ICG dissolved in water at the same concentration. ICG concentrations were 0.51 mg/mL, 0.93 mg/mL, and 0.31 mg/mL respectively. An excitation wavelength of 680 nm was used. (**F**) ROI quantification of photoacoustic tissue phantom images. ** indicates statistical significance with $P<0.05$.

red-shifted peak is observed. By 10 h, the 2nd peak becomes more prominent than the first peak. The intensity then increases with time until 24 h, at which point it is the same intensity as that of the 10 min particles. The results suggest that the MES-BVNP synthesis takes place in two distinct steps. Over the first 10 min, nanoparticles are formed. Over time, the fluorescence of these nanoparticles is quenched and then slowly red-shifts until it regains its fluorescence intensity. For 465 nm excitation (**Figure 2.2D**), fluorescence intensity increased with synthesis time. These behaviors are likely due to pi-pi stacking of the biliverdin molecules and their aggregation under the influence of MES, although further elucidation of this mechanism is beyond the scope of this work.

The high absorbance and lack of fluorescence upon excitation at 680 nm was exploited for photoacoustic imaging. Tissue phantoms for photoacoustic imaging were prepared as previously reported[331], and the protocol is briefly described in the Methods section. Images of tissue phantoms and example ROIs are provided in **Figure D3**. Photoacoustic images of dialyzed BVNPs in a tissue phantom were acquired, and compared to the reference dye indocyanine green (ICG) dissolved in water at the same final mass concentration (**Figure 2.2E**). ROI analysis in ImageJ was used to quantify the average photoacoustic intensity of each sample (**Figure 2.2F**). MES-BVNPs were found to have a comparable photoacoustic intensity to ICG at the same concentration for excitation wavelengths of 680 nm, 720 nm, 750 nm, and 800 nm. These results suggest that BVNP imaging performance is comparable to that of ICG, and BVNPs may be used as a nanoparticle-based alternative to ICG, which has been known to elicit adverse events such as allergic reactions[332,333]. The use of a biliverdin-based nanoparticle may reduce the occurrence of such reactions as biliverdin should not be recognized by the immune system as a foreign antigen. Statistical comparisons of photoacoustic intensity between the different types of BVNPs were not conducted

as the final concentration of biliverdin in each type of particle will have a direct impact on the PA signal intensity. Additionally, our findings agree with previous reports that PA intensity is not necessarily directly correlated with absorption and fluorescence spectra.[334] The mechanisms behind this behavior are not well-understood, but nonradiative deactivation, triplet state contribution, and photobleaching are believed to contribute to this behavior.[334–336] Further tissue phantom imaging experiments were conducted to determine the effects of synthesis time on photoacoustic signal intensity (**Figure D4**). These experiments demonstrated that water-BVNP and NaCl-BVNP photoacoustic intensity increased with synthesis time, while MES-BVNP photoacoustic intensity did not significantly change with synthesis time.

2.3.3 Hydrodynamic Size and Particle Concentration

Nanoparticle hydrodynamic size, particle concentration, and size distributions were determined using a Malvern Panalytical NanoSight NS300, which records videos of nanoparticles under flow. 10 1-minute videos were recorded for dialyzed 24 h water-BVNPs, MES-BVNPs, and NaCl-BVNPs. All BVNP types were found to have a high concentration of particles at or below 100 nm in size (**Figure 2.3A**) with some peaks at higher sizes, which potentially results from the formation of aggregates composed of multiple nanoparticles. D10, D50, and D90 values indicate that on average 10% of particles in each particle population (water-BVNPs, MES-BVNPs, and NaCl-BVNPs) are below 70 nm in size, 50% are below 100 nm in size, and 90% are below 200 nm in size (**Figure 2.3B**). The average hydrodynamic size of all three nanoparticle types was approximately 100 nm (**Figure 2.3C**), with no significant difference in size between the particle types. This is in contrast to the different nanoparticle anhydrous sizes as determined by TEM imaging, suggesting a relationship between the dialysis solvent and the hydration layer around the nanoparticles. NaCl-BVNPs have the smallest anhydrous nanoparticle size, while Water-BVNPs

have the largest anhydrous nanoparticle size, indicating that water may lead to the formation of a

smaller hydration layer around the nanoparticles compared to MES buffer or NaCl solution. The

mode nanoparticle size detected across 10 videos for each nanoparticle type was found to typically

fall between 50 and 100 nm for Water-BVNPs and NaCl-BVNPs **(Figure 2.3D)**. The concentration

of nanoparticles per mL of final dialyzed particle solution was also determined **(Figure 2.3E)**,
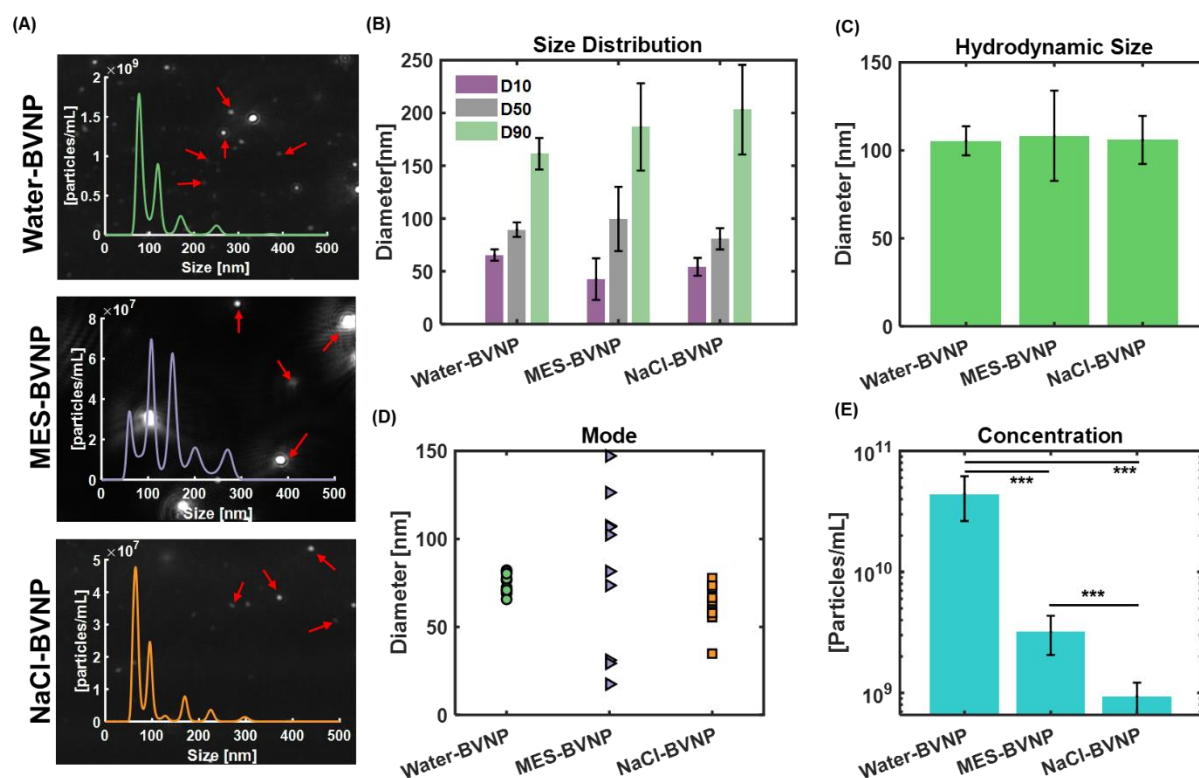
Figure 2.3. Nanoparticle Hydrodynamic size. **(A)** Screenshots from videos collected by Nanosight for size analysis. Red arrows point to some examples of nanoparticles. Overlays depict representative nanoparticle size distributions (concentration vs. size). **(B)** Hydrodynamic size distribution. 10% of detected nanoparticles are have sizes below the D10 value, 50% of detected nanoparticles are have sizes below the D50 value, and 90% of detected nanoparticles are have sizes below the D90 value. **(C)** Average hydrodynamic size for each type of particle. **(D)** The mode nanoparticle size (nanoparticle size with highest frequency of occurrence) for each type of particle. Each mode is calculated from one 1-minute Nanosight video. **(E)** Nanoparticle concentration post-dialysis, as determined by Nanosight video analysis. *** indicates statistical significance with P<0.001.

with water-BVNPs having an average final concentration of 4.41 x 10^{10} particles per mL, MES-BVNPs having an average final concentration of 3.20 x 10^9 particles per mL, and NaCl-BVNPs having an average final concentration of 9.37 x 10^8 particles per mL. Since the final amount of biliverdin in each particle was determined as described in the previous section, this information was combined with the nanoparticle concentration to determine the number of biliverdin molecules in each particle. A detailed explanation of the calculations is provided in the Methods section. We determined that Water-BVNPs had an average of 1.196 x 10^7 biliverdin molecules per particle, MES-BVNPs had an average of 3.002 x 10^8 biliverdin molecules per particle, and NaCl-BVNPs had an average of 3.420 x 10^8 biliverdin molecules per particle. This suggests that the EDC-NHS reaction kinetics may differ based on the synthesis solvent, which leads to the formation of greater or fewer particles with greater or fewer biliverdin molecules incorporated in each particle.

2.3.4 Biocompatibility

Blood smear experiments and 3-(4,5-dimethylthiazol-2-yl)-2,5-diphenyltetrazolium bromide (MTT) cell viability assays were utilized to assess BVNP biocompatibility. For blood smear experiments, samples of whole pig blood were exposed to BVNPs (10% by volume) for 30 min, after which the blood was imaged using an optical microscope. Observation of morphological changes in nanoparticle-treated samples compared to an untreated control would indicate potential adverse reactions to the nanoparticles. No morphological changes were observed in nanoparticle-treated samples compared to the control, indicating a lack of adverse interactions between the nanoparticles and blood cells **(Figure D5 A)**.

MTT experiments were separately conducted on MCF-7 cells, a metastatic breast cancer cell line, and MDA-MB-231 cells, a triple-negative metastatic breast cancer cell line. We chose

these cells because breast cancer is a type of cancer that metastasizes to lymph nodes. We reasoned that in sentinel lymph node biopsies, the nanoparticles would first be injected at the tumor site, after which they would drain into the surrounding lymph nodes. MTT experiments were conducted with nanoparticle concentrations of 5 % and 10 % by volume for 10 min and 24 h water-BVNPs, MES-BVNPs, and NaCl-BVNPs. Particle-treated cells typically had comparable or greater viability than untreated control cells **(Figure D5 B, Figure D5 C)**. The increase in viability compared to control cells may indicate increased metabolic activity of cells exposed to the BVNPs, rather than an increase in cell proliferation.

2.3.5 *In vivo* **Photoacoustic Imaging and** *Ex vivo* **Fluorescence Imaging**

To evaluate the feasibility of using these BVNPs as a diagnostic imaging probe for the lymphatic system, experiments were performed in live mice. Four groups of mice were administered water-BVNPs, MES-BVNPs, NaCl-BVNPs or a vehicle control *via* hock injection in the hindlimb. No adverse reactions were observed in the tissue from injection of the nanoparticles. Mice were imaged at 5, 10, 15, and 30 min post-injection, using 680 nm, 720 nm, and 750 nm excitation. *In vivo* photoacoustic imaging at 680 nm **(Figure 2.4)**, 720 nm **(Figure D6)**, and 750 nm **(Figure D7)** showed a marked increase in the signal as a result of nanoparticle injection. Importantly, all three nanoparticle types showed passive accumulation in the lymph nodes.[45,337–339] This was confirmed using *ex vivo* tissue analysis (*vide infra*). The PA signal intensity was also found to vary with time, indicating a time-dependent nanoparticle uptake within, and clearance from, the lymphatic system.

Following euthanization, the major organs were collected from the animals and photoacoustic imaging was performed to visualize the heart, lung, liver, kidneys, spleen, and

lymph nodes. Our analysis indicated some nanoparticle accumulation in the liver and spleen. There was also some accumulation in the lymph nodes, but consistent with our *in vivo* experiments, the particles appeared to have mostly cleared from the lymphatic system 30 minutes post-injection **(Figure 2.5A)**. These findings were further corroborated using fluorescence imaging of the various organs **(Figure 2.5B)**. The organs dissected from nanoparticle-treated animals exhibited higher signal overall compared to the control water-treated animal, indicating the distribution of BVNPs
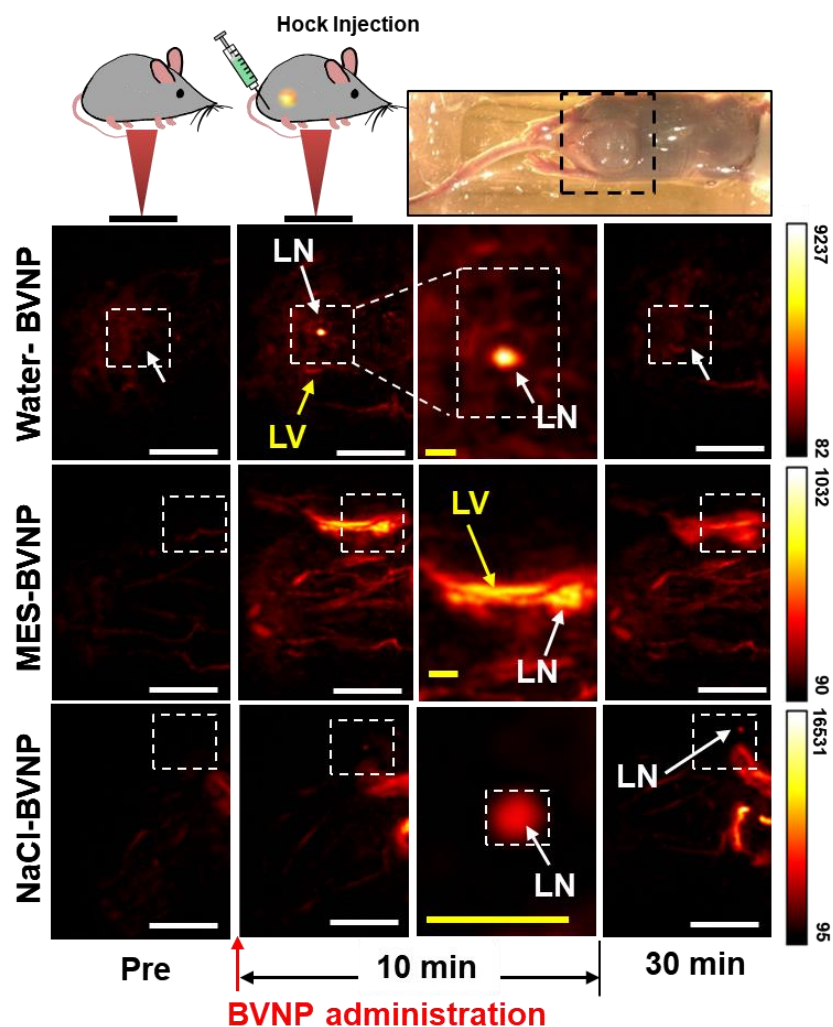
Figure 2.4. Photoacoustic Imaging of sentinel lymph nodes using BVNPs. 680 nm wavelength photoacoustic images of mice before nanoparticle injection, 10 min after injection, and 30 min after injection. An increase in PA signal intensity is observed post-injection, and nonspecific accumulation of BVNPs can be observed in lymph nodes. White scale bars represent 5 mm, and yellow scale bars represent 1 mm. LN=lymph node; LV= lymphatic vessel.

throughout the body. As in any *in vivo* experiment, biological variability from one animal to another likely played a role in this result. The high error bar in MES-BVNP lymph nodes suggests that the particles may have taken greater than 30 minutes to clear from the lymphatic system in some of the mice. Since the animals were sacrificed 30 min post-injection, these particles may not have fully cleared from the lymphatic system by then, and this in turn led to a high error bar in the fluorescence signal quantification. The ability of these nanoparticles to be detected with fluorescence imaging using an excitation wavelength of 675 nm can be attributed to an aggregation-induced effect, which has been observed in other fluorescent molecules and particles.[340,341]

2.3.6 *In Vitro* Biodegradation

As mentioned previously, one of the major barriers that must be overcome when using nanoparticles for diagnostic imaging is the issue of liver accumulation. We reasoned that the nanoparticles we have prepared can by biodegraded by biliverdin reductase, which is found in many organs[60,329] but has the highest expression in the liver. When degradation experiments were conducted using biliverdin reductase, we were able to establish the biodegradation profile of these nanoparticles. Degradation experiments were carried out on water-BVNPs and NaCl-BVNPs over a period of seven days, with biotransformation being tracked by UV-Vis spectroscopy and matrix-assisted laser desorption/ionization (MALDI) mass spectrometry. The magnitude of UV-Vis absorbance at 670 nm was used as an indicator for degradation as reported previously.[62] When exposed to biliverdin reductase and its cofactor, nicotinamide adenine dinucleotide hydride (NADH), the absorbance at 670 nm decreased steadily as a function of time (**Figure 2.6A, Figure D8**). After seven days of degradation of the 10-min and 24-h water-BVNPs, their absorbances had decreased to 8% and 17% of their initial absorbances respectively. Similarly, the NaCl-BVNP 10-
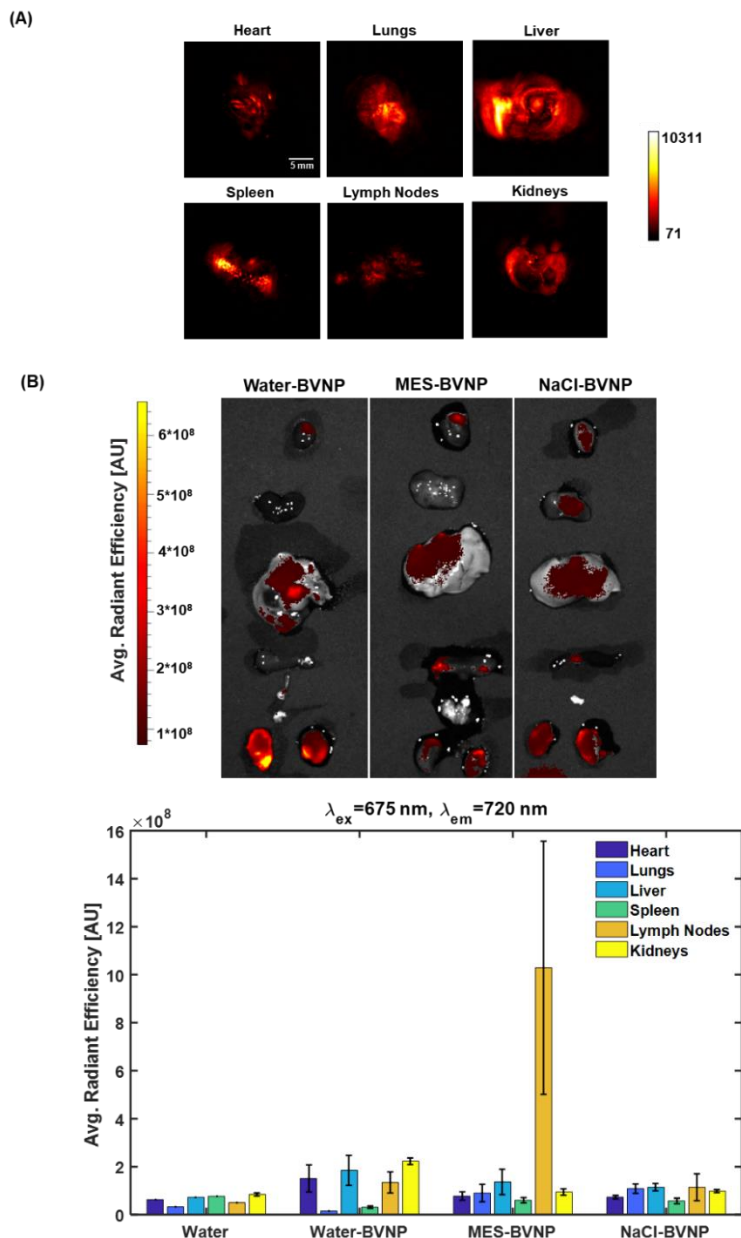
Figure 2.5. BVNP organ distribution. **(A)** Representative Photoacoustic images of dissected organs from mice treated with NaCl-BVNPs. Generally, similar accumulation was observed in the organs of mice treated with water-BVNPs MES-BVNPs, and NaCl-BVNPs. Here, some nanoparticle accumulation is seen in all organs, with very high nanoparticle accumulation in the liver. **(B)** IVIS fluorescence imaging of dissected organs from mice treated with Water-BVNPs, MES-BVNPs, and NaCl-BVNPs. The majority of accumulation in BVNP-treated animals was observed in the liver, kidneys, and lungs, with only minor accumulation in the spleen and most lymph nodes. Top to bottom: heart, lungs, liver, spleen, lymph nodes, and kidneys. Aggregation-induced fluorescence shifting resulted in a fluorescence response from BVNPs in organs for an excitation wavelength of 675 nm. Error bars represent standard error across all animals for each nanoparticle type.

min and 24-h absorbances fell to 9% and 13% of their initial values respectively. A visible color change from a blue-green color for the BVNPs to a yellow color for all degraded nanoparticles was also observed (**Figure 2.6B**).

MALDI/TOF spectrometry of water-BVNPs showed peaks at a mass to charge (m/z) value of 583 for the 10-min and 24-h nanoparticles, corresponding to the presence of biliverdin (**Figure 2.6C**). These peaks were no longer present after five days of nanoparticle degradation, further confirming the breakdown of the nanoparticles as a result of enzymatic degradation. Additionally, peaks at m/z values of 713 and 1277 were present in both the 10-min and 24-h nanoparticles (**Figure 2.6C, Figure D9-10**), indicating the covalent linkage of a biliverdin molecule with a single diamine, and the linkage of two biliverdin molecules with a single diamine, respectively. These peaks were found to disappear after five days of degradation. The results indicated biotransformation of BVNPs to bilirubin *via* biliverdin reductase, followed by further degradation by oxidation to produce compounds A, B, C, and D (**Figure 2.6D**), which correspond to m/z values of 178, 137, 177, and 135, as confirmed by Electrospray ionization (ESI) mass spectroscopy. The products corresponding to m/z values of 177 and 135 are identified as the keto-enol tautomer of compounds A and B. After five days of degradation of 10-min nanoparticles, several new mass peaks at m/z values of 428 to 1950 were identified, indicative of A, B, C, and D. The products corresponding to m/z values of 550, 666 and 805 were observed over the course of five days degradation of 24-h nanoparticles, indicating the formation of A, B, C, and D. Degradation by the same mechanism was also confirmed *via* mass spectrometry for NaCl-BVNPs (**Figures S11-S13**).
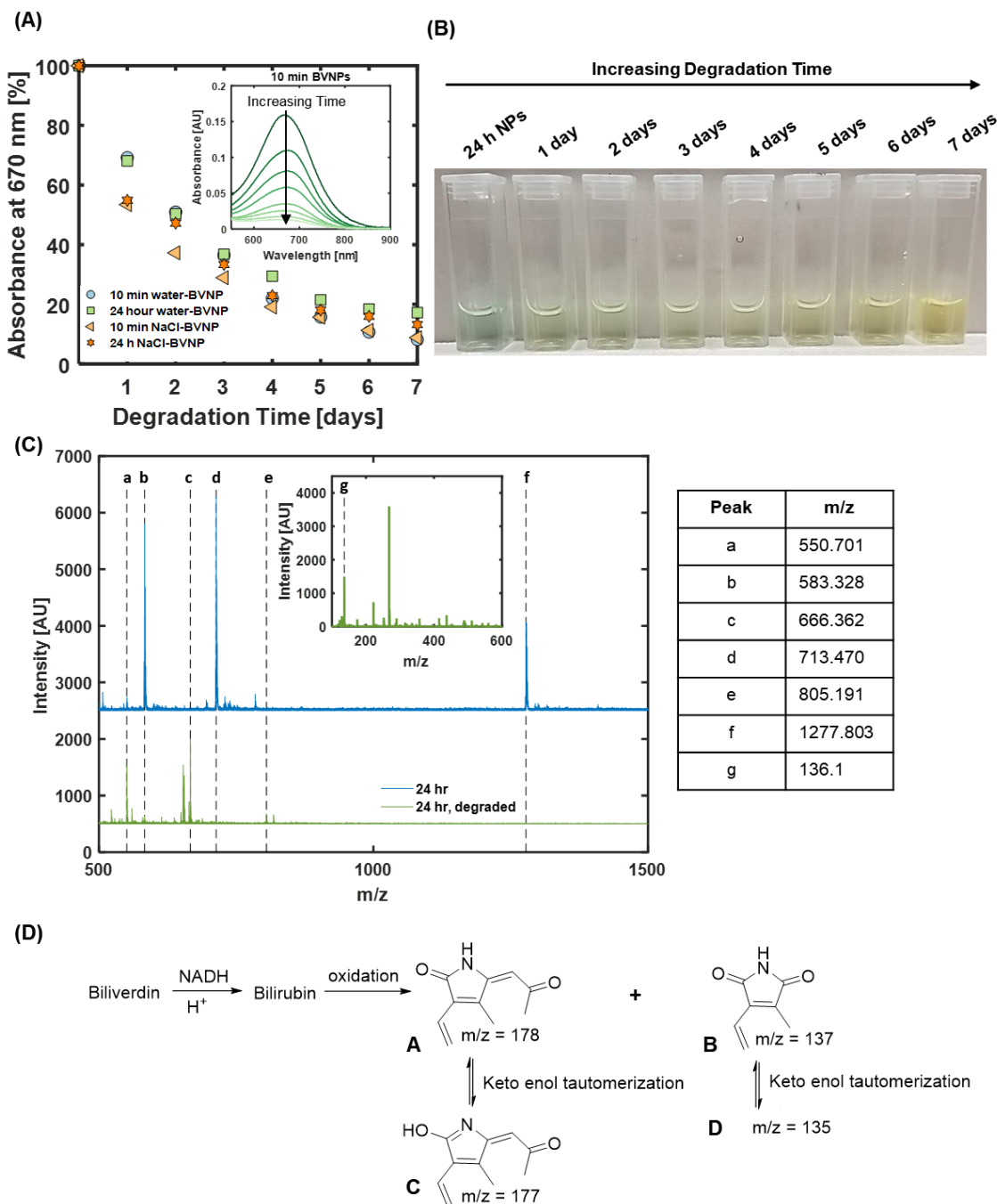
Figure 2.6. Degradation of water-BVNPs and NaCl-BVNPs. **(A)** UV-Vis absorbance at 670 nm for degraded BVNPs as a percentage of UV-Vis absorbance at 670 nm for BVNPs prior to degradation. Inset depicts 550 nm to 900 nm UV-Vis spectra collected for 10-min water-BVNPs. **(B)** Color change in diluted 24-h BVNPs as a result of increasing degradation time. A shift from blue-green to yellow is observed with an increase in degradation time. **(C)** Mass Spectrometry results for 24-h water-BVNPs. **(D)** Proposed BVNP degradation process.

Degradation experiments carried out on MES-BVNPs in the presence of biliverdin reductase and nicotinamide adenine dinucleotide phosphate (NADPH) **(Figure 2.7A)** showed that the MES-BVNPs degrade at a slower rate than that of water-BVNPs and NaCl-BVNPs **(Figure 2.7B)**, with 10-min and 24-h MES-BVNPs reaching 60.3 and 53.1% of initial MES-BVNP absorbance after 13 days of degradation. This slower degradation is likely due to both a higher BVNP crosslinking efficiency when synthesized in MES, and a change in the enzyme activity due to the lower pH of MES compared to the pH of water and the NaCl solution. The degradation
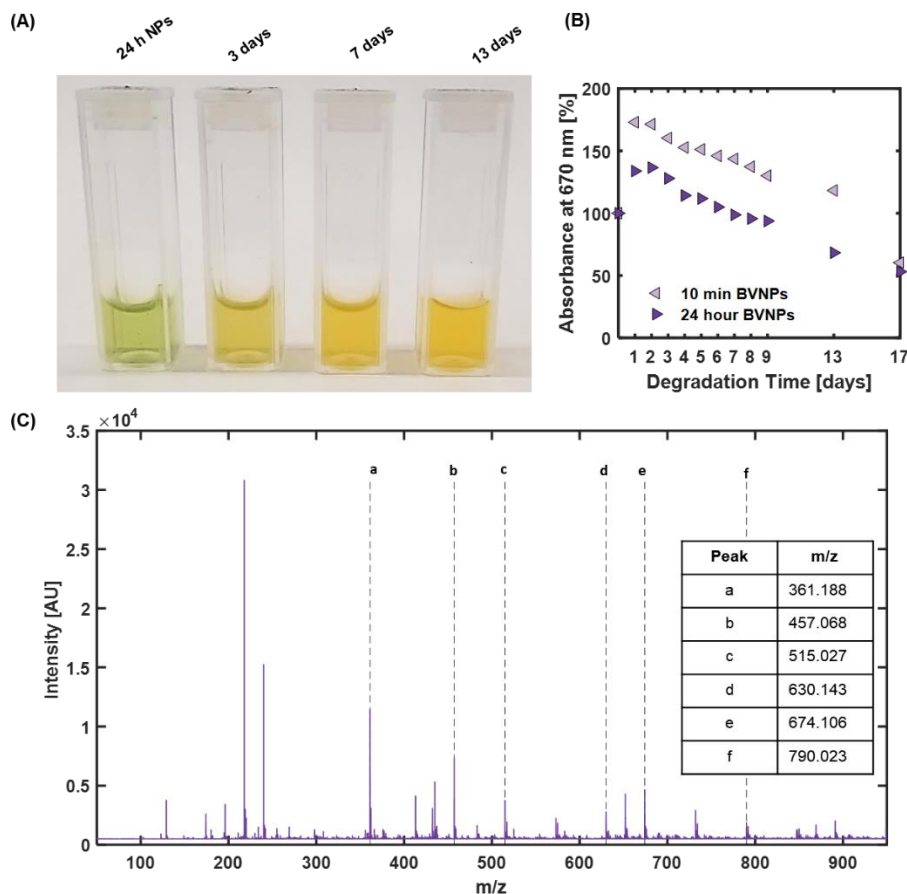
Figure 2.7. Degradation of MES-BVNPs. **(A)** Color change in diluted 24 h MES-BVNPs as a result of increasing degradation time. A shift from green to yellow is observed with an increase in degradation time. **(B)** UV-Vis absorbance at 670 nm for degraded MES-BVNPs (13 days degradation) as a percentage of UV-Vis absorbance at 670 nm for MES-BVNPs prior to degradation. **(C)** Mass Spectrometry results for degraded 24 h MES-BVNPs.

mechanism for MES-BVNPs was confirmed to be the same as that of water-BVNPs and NaCl-BVNPs *via* mass spectrometry **(Figure 2.7C, Figures S14-S16)**. Calculations for all spectra are provided in the supplementary information. These results are especially promising because biliverdin reductase occurs naturally in the liver and other organs, pointing towards facile biometabolism of BVNPs.

2.3.7 *In Vivo* Biodegradation

In vivo biodegradation experiments were conducted in order to confirm that the favorable *in vitro* degradation results could be replicated in living organisms. Mice were each administered with water-BVNPs, MES-BVNPs, or NaCl-BVNPs *via* a flank injection. Flank injections were utilized instead of hock injections because the lymphatic system is constantly draining, so any signal decrease with time in the lymph nodes could be attributed to clearance of the nanoparticles by flow through the lymph nodes, rather than degradation of the particles themselves. The flank injections allowed for high accumulation of the nanoparticles in one location rather than their dispersal with flow. This allowed us to study the degradation of the nanoparticles with time. Photoacoustic images of the mice were taken prior to injection, and at 5 min, 24 h, and 96 h after injection for wavelengths of 680 nm **(Figure *2*.8A)**, 720 nm **(Figure D17 A)**, and 750 nm **(Figure D17 B)**. The differences in PA intensity across multiple wavelengths for each particle type can be explained by the nonlinear relationship between absorbance and PA intensity. ROI analysis was conducted in ImageJ to quantify the signal increase after nanoparticle injection, and decrease as a result of degradation **(Figure *2*.8B)**. PA signal increased by at least three-fold upon injection of BVNPs, and then returned to values close to the initial value within 24 h, indicating that the BVNPs had almost completely degraded within 24 h. This was also apparent visually, as the flanks injected

73

with water-BVNPs and NaCl-BVNPs exhibited a visible green color after administration, and this

green color was no longer apparent 24 h post-injection. MES-BVNPs
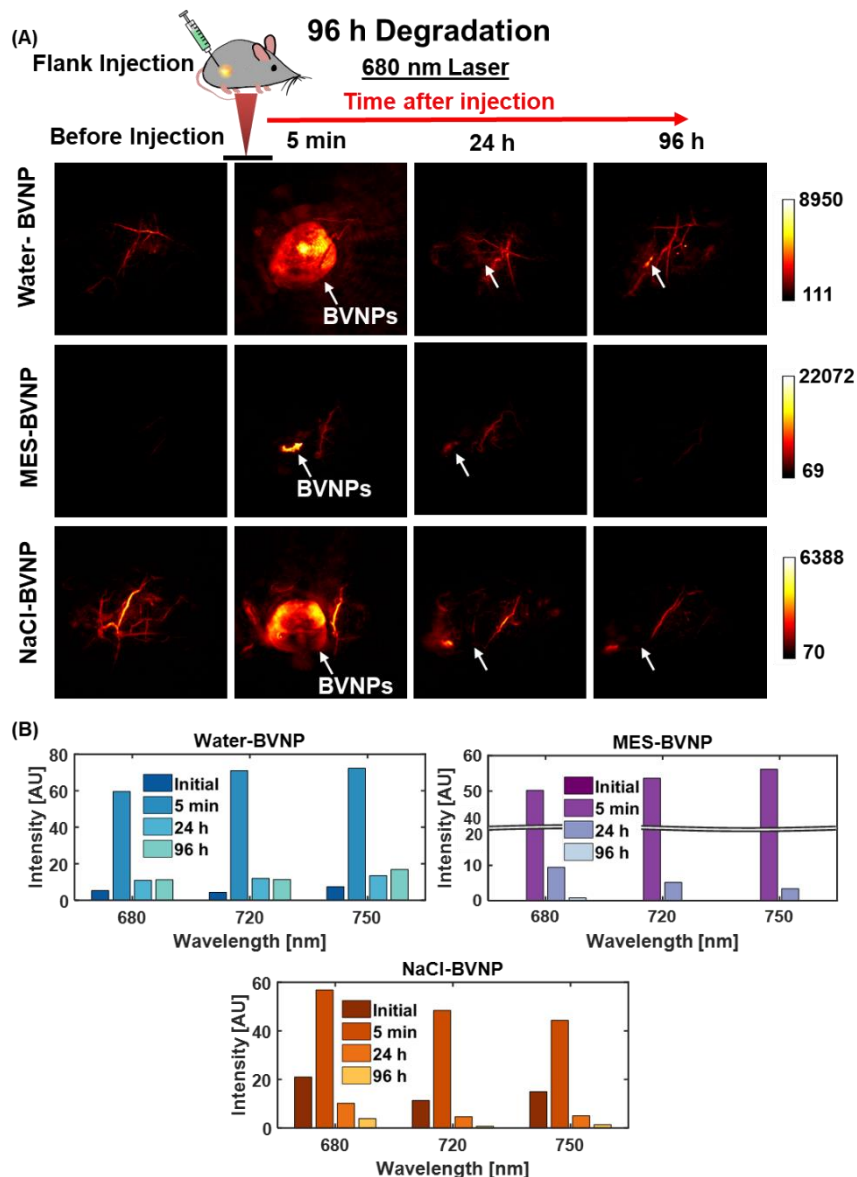
Figure 2.8. *In vivo* BVNP Degradation over a period of 96 h. **(A)** Photoacoustic images take prior to nanoparticle injection in mouse flanks, and 5 min, 24 h, and 96 h after injection. An increase in signal as a result of BVNP injection, and decrease in signal as a result of BVNP degradation, is observed. Arrows indicate locations of signal increase and decrease as a result of BVNP injection and degradation **(B)** ROI analysis of *in vivo* degradation for each type of BVNP for photoacoustic imaging acquisition wavelengths of 680 nm, 720 nm, and 750 nm. A sharp decrease in signal 24 h post-injection indicates quick *in vivo* degradation.
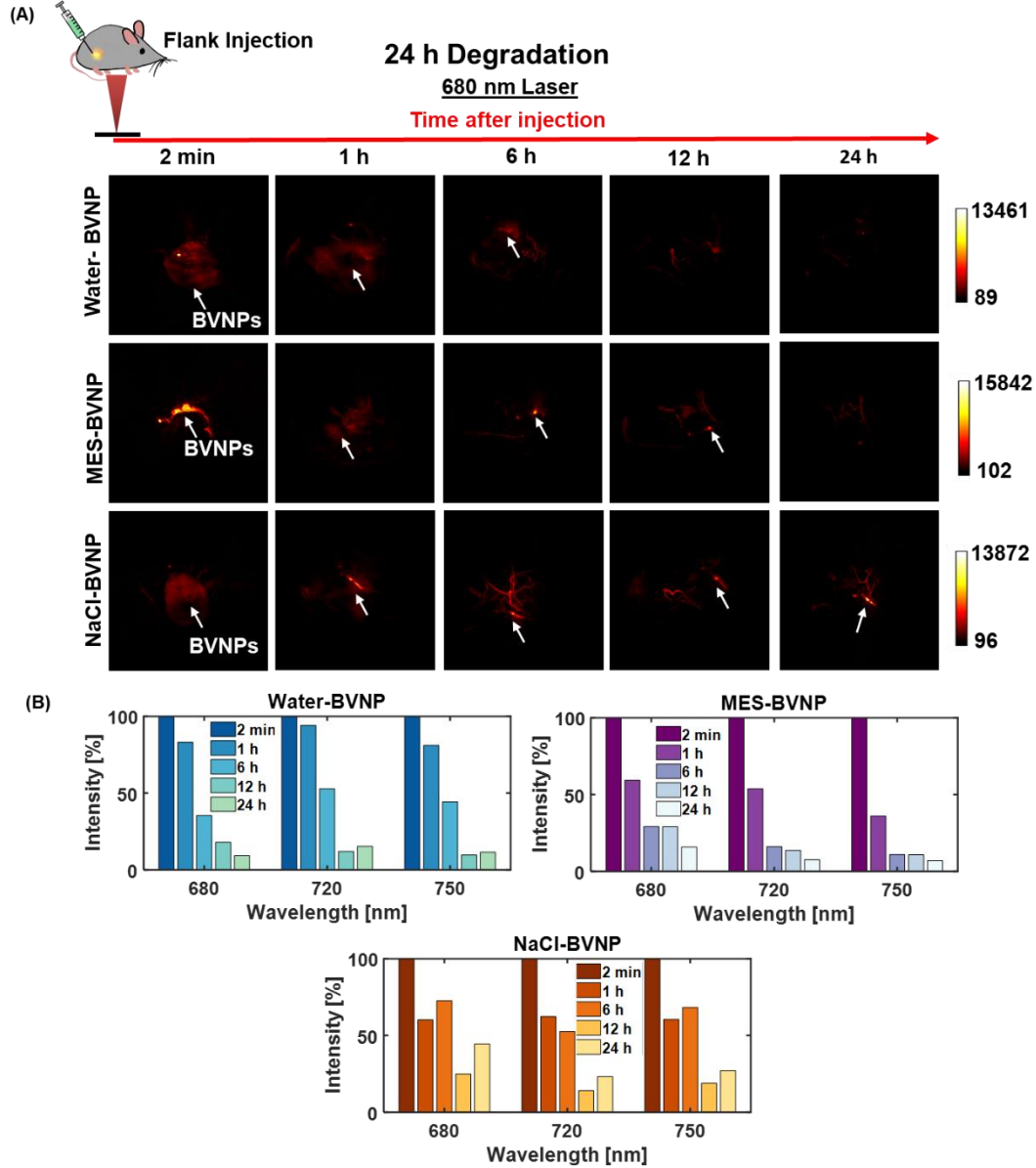
Figure 2.9. *In vivo* BVNP Degradation over a period of 24 h. **(A)** Photoacoustic images take 2 min, 1 h, 6 h, 12 h, and 24 h after injection in mouse flanks. A decrease in signal as a result of BVNP degradation is observed. Arrows indicate locations of signal increase and decrease as a result of BVNP injection and degradation **(B)** ROI analysis of *in vivo* degradation for each type of BVNP for photoacoustic imaging acquisition wavelengths of 680 nm, 720 nm, and 750 nm. A steady decrease in BVNP signal is observed over a period of 24 h, indicating BVNP degradation with time.

did not appear as widely distributed immediately after injection as the water-BVNPs and NaCl-BVNPs did, which is likely a result of the properties of the MES solvent. Despite the initially high accumulation of MES-BVNPs at the injection site, the MES-BVNPs also show a favorable *in vivo* degradation profile.

We further sought to explore the degradation behavior of these nanoparticles during the first 24 h after injection. Degradation experiments were repeated with multiple time-points (2 min, 1 h, 6 h, 12 h, 24 h) from initial injection through 24 h after injection. Images were collected at 680 nm **(Figure *2*.9A)**, 720 nm **(Figure D16 A)**, and 750 nm **(Figure D18 B)**. The BVNP signals were found to steadily decrease with time based on ROI analysis **(Figure *2*.9B)**. Taking the initial signal 2 min post-injection to be 100 %, after 24 hours Water-BVNPs, MES-BVNPs, and NaCl-BVNPs had degraded to 44, 23, and 27 % of their initial values respectively. These results indicate that BVNPs are entirely biometabolizable *in vivo*.

2.4 CONCLUSIONS

Overall, we show that nanoprecipitation of endogenous molecules can lead to spectral tuning based on the choice of reaction media. Due to the inherent water solubility of biliverdin, a simple synthetic process has been developed to synthesize a nano-platform that is fully biodegradable. Water-BVNPs and NaCl-BVNPs displayed high absorbance and low fluorescence in the UV region, while MES-BVNPs had low absorbance and high fluorescence in the UV region, in addition to a fluorescence red-shifting as a function of synthesis time. MES-BVNPs were found to have a higher fluorescence intensity and radiant efficiency than other nanoparticle types, and were also found to have comparable photoacoustic intensity to ICG. Water-BVNP and NaCl-BVNP PA intensity increased with synthesis time, while MES-BVNP PA intensity was unaffected.

Biocompatibility of BVNPs was demonstrated through blood smear experiments in addition to MTT assays in MCF-7 and MDA-MB-231 cells.

Injection of BVNPs was found to lead to an increased photoacoustic signal *in vivo* in mice, with some non-specific accumulation in the lymph nodes as expected based on the use of hock injections. The nanoparticles were also found to be biodegradable, degrading in the presence of biliverdin reductase and NADH or NADPH. The complete biodegradation of BVNPs was also demonstrated *in vivo*. BVNPs provide a promising platform for biological imaging due to their inherent photoacoustic and fluorescent properties, as well as their biodegradability. The safety and efficacy of nanomedicines is typically influenced by multiple parameters to create a major bottleneck for translating these agents. The complexity of nanomedicine presented by the multi-component three dimensional constructs demands vigilant design and engineering to achieve the intended physicochemical characteristics and biological behaviors. Designing a system that 'disappears' completely from the biological system could offer a potential strategy to accelerate the translation of these agents and accelerate the growth of this critical field.

2.5 METHODS

2.5.1 Materials

Biliverdin hydrochloride was purchased from Sigma-Aldrich and Frontier Scientific. EDC and Sodium Chloride were purchased from Fisher Scientific. N-hydroxysuccinimide (NHS), 2,2' ethylenedioxy bis(ethylamine), Biliverdin Reductase A human, NADPH tetrasodium salt, and NADH disodium salt were purchased from Sigma Aldrich. MES buffer was purchased from Thermo Scientific.

2.5.2 Synthesis

Biliverdin was dissolved overnight at a concentration of 1 mg/mL using 10 mL of the chosen solvent (filtered water, 0.1 M MES buffer, or 0.9% NaCl solution) in a 20 mL scintillation vial on a stir plate at 500 rpm. The carboxylic acid group on the Biliverdin was then activated using 6.7 mg EDC and 4 mg NHS for 10 min, after which 3.5 µL of the diamine was added to commence the cross-linking reaction. The resulting nanoparticles are referred to as water-BVNPs, MES-BVNPs, and NaCl-BVNPs depending on the respective solvent used for nanoparticle synthesis. Samples were collected at 10 min, 6 h, 12 h, and 24 h. Unless otherwise noted, in experiments for which dialyzed BVNPs were used, BVNPs were dialyzed against 500 mL of their respective synthesis solvents using dialysis cassettes with a cutoff of 10 kDa, and sample size of 3 mL.

2.5.3 Microscopy

TEM samples were prepared immediately *via* drop-casting of 2.5 µL diluted nanoparticle solution (10 µL of the nanoparticle solution diluted with 90 µL filtered water) on copper TEM grids. Excess moisture was wicked away after 2 minutes. TEM images were taken on a JEOL Cryo 2100 TEM using an acceleration voltage of 200 keV. Nanoparticle size was determined using ImageJ.

2.5.4 Spectroscopy

UV-Vis measurements were performed on samples using a Thermo Scientific Genesys 10S UV-Vis Spectrophotometer immediately after sample collection and dilution. For these measurements, 10 µL of the nanoparticle solution was diluted with 990 µL of the synthesis solvent, and the baseline measurement was taken using the synthesis solvent for each nanoparticle type. The UV-Vis spectra were collected over the 225 nm to 800 nm range.

Fluorescence measurements were taken using a TECAN infinite M200 PRO fluorescence spectrometer at excitation wavelengths of 365 nm and 680 nm, with a measured emission range of 365-850 nm and 680-680 nm respectively. Images were also taken of undiluted 24 h time point BVNPs under a 365 nm wavelength UV lamp. Zeta potential measurements were taken for the 10-min and 24-h time points using a Malvern Zetasizer.

FT-IR samples were prepared by dropping 500 µL of the nanoparticle solution onto Kevley MirrIR Corner Frosted FT-IR slides and allowing sit overnight, after which they were placed under vacuum until they had completely dried. FT-IR measurements were taken using a Thermo Nicolet Nexus 670 FT-IR.

2.5.5 Hydrodynamic Size, particle concentration, and calculations

Nanoparticle hydrodynamic size, size distribution, and concentration were measured using a Malvern Panalytical NanoSight NS300. Dialyzed nanoparticles were utilized for these experiments. 10 1-minute videos were recorded for each nanoparticle type, with average hydrodynamic size, mode hydrodynamic size, size distributions, and concentrations calculated for each nanoparticle type. 10 µL of Water-BVNPs and MES-BVNPs were diluted in 990 µL of their respective synthesis solvents for these measurements. For NaCl-BVNPs, 100 µL of the particles were diluted in 900 µL NaCl solution. These dilution factors were taken into consideration for calculation of the final concentrations. Taking into consideration the remaining mass of biliverdin in each type of particle (as determined by UV-Vis spectroscopy), the average mass of each nanoparticle type and the average number of biliverdin molecules were then calculated using the following equations:

$$Average\ Particle\ Mass\ [mg] = \frac{Incorporated\ biliverdin\ \left[\frac{mg}{mL}\right]}{Particle\ concentration\ [mL^{-1}]}$$

(Equation 2.1)

$$Number\ of\ biliverdin\ molecules\ per\ particle$$
$$= \frac{Average\ Particle\ Mass\ [mg]}{BIliverdin\ molecular\ weight\ \left[\frac{mg}{mol}\right]} * 6.022 * 10^{23} \left[\frac{molecules}{mol}\right]$$

(Equation 2.2)

2.5.6 Photoacoustic Imaging

Photoacoustic imaging was conducted using an Endra Nexus 128 photoacoustic tomographer with excitation wavelengths of 680 nm, 720 nm, 750 nm, and 800 nm (continuous rotation mode, 6 second rotation time).

Tissue-mimicking Phantom Preparation. Agarose (2 g) was dissolved in a solution containing deionized water (39 mL) and 2% milk (1 mL). The solution was heated in a microwave oven for 30 seconds, removed and stirred, and then heated for an additional 15 sections to produce a viscous gel. The mixture was then poured into a custom Teflon mold designed with the same specifications as the Endra Nexus 128 PA tomographer bowl **(Figure D3)**. For *in vitro* phantom studies, hypodermic steel tubing was inserted into the Teflon mold as a placeholder for fluorinated ethylene propylene tubing used to contain the samples.

Comparison with ICG. Tissue phantom imaging was conducted on 24-h water-BVNPs, MES-BVNPs, and NaCl-BVNPs which were dialyzed with their respective synthesis solvents. ICG at the same final mass concentrations was used for comparison. The final mass concentration of biliverdin in each type of BVNP was determined by taking the ratio of 365 nm absorbance after dialysis to before dialysis. Two 200 μL samples were used in each tissue phantom experiment, with a total of 3 technical replicates for each type of particle.

Comparison of 10 min and 24 h BVNPs. Tissue phantom imaging was conducted as before, but with 200-µL 10 min water-BVNPs, 24 h water-BVNPs, 10 min MES-BVNPs, 24 h MES-BVNPs, 10 min NaCl-BVNPs, and 24 h NaCl-BVNPs, each of which were dialyzed with their respective synthesis solvents. In addition, imaging was conducted on 24 h MES-BVNPs which were dialyzed with water. Three technical replicates were used for each sample. ROI analysis in ImageJ was used to determine the average PA intensity for each sample.

2.5.7 Blood Smear

Fresh whole pig blood was collected from the UIUC Meat Laboratory in citrate-coated blood collection tubes. Samples were stored until use, at which time any coagulated blood was removed through centrifugation at 1000 rpm for 1 minute. 180 µL of uncoagulated blood was placed in each of 7 0.7-mL centrifuge tubes. For experimental samples, 20 µL of BVNP solution (10 min water-BVNPs, 24 h water-BVNPs, 10 min MES-BVNPs, 24 h MES-BVNPs, 10 min NaCl-BVNPs, or 24 h NaCl-BVNPs) was added to the blood sample. All particles used were dialyzed with their respective synthesis solvents. The blood-nanoparticle solution was gently mixed through repeated pipetting, after which samples were incubated at room temperature for 30 min. Following this incubation period, 50 µL of each sample was deposited on individual glass slides, and a second clean glass slide was used to spread these samples uniformly across the slides. Optical microscopy was conducted immediately after slide preparation.

2.5.8 Cell Viability

MTT assays were separately conducted on MCF-7 cells and MDA-MB-231 cells exposed to 5 % by volume, and 10 % by volume of 10 min and 24 h water-BVNPs, MES-BVNPs, and NaCl-BVNPs dialyzed with their respective synthesis solvents. Cells were cultured in T-25 flasks using

DMEM completed with 10 % fetal bovine serum (FBS) and 1 % penicillin-streptomycin. Cells were plated in 96-well plates at a density of 10,000 cells/well, with 100 µL of cells added to each well. Cells were allowed to grow for 24 h, after which media was removed and replaced with 100 µL fresh media containing 5 % by volume or 10 % by volume BVNP solution. 4 wells were used for each experimental sample, and 12 wells were used for the control (untreated) samples. Cells were incubated with these solutions for 24 h at 37 °C, after which media was removed and cells were rinsed with DPBS. 100 µL fresh media was then added to each well, followed by 15 µL MTT (MCF-7 cells) or 10 µL MTT (MDA-MB-231 cells). Cells were then incubated at 37 °C for 4 h. The media-MTT solution was then removed and 100 µL DMSO was added to each well to dissolve the formazan crystals. Viability was assessed by measuring the absorbance of each well at 570 nm and 630 nm on a Biotek Cytation 5 plate reader. Cell viability as a percentage of control cell viability was determined using the following equation:

$$\% \, Viability = \left(\frac{Sample \, Abs_{570} - Sample \, Abs_{630}}{Control \, Abs_{570} - Control \, Abs_{630}} \right) * 100\%$$

(Equation 2.3)

2.5.9 Fluorescence Imaging

Fluorescence imaging was conducted using an IVIS imaging system. Excitation wavelengths ranging from 430 nm to 710 nm were used, and as-prepared 10-min and 24-h water-BVNPs, MES-BVNPs, and NaCl-BVNPs were imaged.

2.5.10 *In Vivo* Studies

To evaluate the *in vivo* imaging ability of the BVNPs in different solvent systems, animal experiments were performed with the minimum required number of animals. The experimental

protocol was approved by the Institutional Animal Care and Use Committee (IACUC), University of Illinois, Urbana−Champaign, and satisfied all University and National Institutes of Health (NIH) rules for the humane use of laboratory animals. Athymic mice were bought from Charles River Laboratories International, Inc. U.S.A. Upon arrival, athymic mice were allowed one week for acclimation. Animals were single-cage housed and had free access to food and water. Animals were housed in Beckman Institute, University of Illinois at Urbana-Champaign.

Lymph Node Imaging. A total of three groups of nude mice were used for *in vivo* demonstration of photoacoustic imaging, and one animal was used as the control. Animals in group one were treated with Water-BVNPs (n=3), animals in group two were treated with MES-BVNPs (n=3), and animals in group three were treated with NaCl-BVNPs (n=3). All nanoparticles were used post-dialysis of the 24-h timepoint. The mice were injected *via* a hock injection with 50 µL of the respective BVNP type in their rear leg. The control mouse was injected with water alone. Photoacoustic images were taken prior to injection, and 5 min, 10 min, 15 min, and 30 min post-injection. Images were acquired for wavelengths of 680 nm, 720 nm, and 750 nm. Mice were sacrificed after image acquisition at 30 minutes, and their organs were subsequently dissected. Photoacoustic images were taken of the dissected organs (heart, lungs, liver, spleen, lymph nodes, and kidneys). Fluorescence imaging of these organs was also conducted with an excitation wavelength of 675 nm.

In Vivo Degradation. Three mice were used for *in vivo* demonstration of biodegradation, one for each BVNP type. All nanoparticles were used post-dialysis of the 24-h timepoint. 50 µL of nanoparticle solution was injected subcutaneously in the flank of each mouse. Images were taken prior to injection, 5 min, 24 h, and 96 h after injection. In further experiments, images were taken 2 min, 1 h, 6 h, 12 h, and 24 h after injection. ROI analysis was conducted in ImageJ.

2.5.11 Water-BVNP and NaCl-BVNP Degradation Experiments

Degradation experiments were conducted on 1 mL each of 10-min and 24-h as-prepared water-BVNPs and NaCl-BVNPs. The nanoparticles were placed in 4 mL glass vials on a stirplate at 500 rpm with a temperature of 40 ˚C. 40 mg of NADH was then added to each vial, and allowed to dissolve for 10 min. 2 μL of the Biliverdin Reductase were then added to each vial, beginning the degradation experiment. 12 μL samples were taken from each vial every 24 h. Of these 12 μL, 10 μL was diluted with 990 μL of water in one UV-Vis cuvette, and the remaining 2 μL was diluted with 998 μL of water in another UV-Vis cuvette. UV-Vis measurements were taken in the range of 300 to 900 nm for the 2:998 μL dilution, and in the range of 550 to 900 nm for the 10:990 dilution. These ranges and dilutions were chosen because the NADH itself caused an increase in absorbance at 340 nm, which led to an absorbance of greater than one for the regular 10:990 dilution when the spectra were collected in the range of 300 to 900 nm. After UV-Vis measurements were taken, 50 μL of each 10:990 dilution were collected for mass spectrometry. The degradation experiment was conducted for a total of 7 days, with mass spectrometry being conducted for the first and fifth days.

2.5.12 MES-BVNP Degradation Experiments

Degradation experiments were conducted on MES-BVNPs as was conducted for water-BVNPs and NaCl-BVNPs. However, 47 mg NADPH was utilized in place of NADH for each mL of MES-BVNPs to be degraded. 50 μL samples were collected for UV-Vis analysis every 24 h for the first 9 days, and then at 13 and 17 days. UV-Vis spectra were collected between 550 and 900 nm, with a dilution of 50 μL nanoparticles to 950 μL MES buffer. This concentration was selected due to the lower absorbance of MES-BVNPs in this region compared to the water-BVNPs and NaCl-

BVNPs. 30-50 μL samples were collected for mass spectrometry prior to degradation and after 13 days of degradation.

2.5.13 Statistical Analysis

All statistical tests were conducted using Student's T-tests assuming unequal variances.

CHAPTER 3: UV-TRAINED AND METAL-ENHANCED FLUORESCENCE OF BILIVERDIN AND BILIVERDIN NANOPARTICLES

3.1 ABSTRACT

Tetrapyrroles (TP) such as biliverdin (BV) undergo conformational changes in response to stimuli such as metal chelation or UV irradiation. However, in contrast to previous reports of TP photodegradation, and in agreement with some reports of hemoglobin fluorescence enhancement with UV irradiation, we have determined that the conformational changes in BV as a result of UV irradiation actually lead to enhanced fluorescence emission without degradation into other products. This enhanced fluorescence can be further altered by chelating BV with metals. These observations were further evaluated in biliverdin nanoparticles (BVNPs), at the bulk state and at the single-particle level. Following 72 h of 365 nm UV irradiation and/or metal chelation, BV and BVNPs were characterized using UV-visible spectroscopy, fluorescence spectroscopy, transmission electron microscopy, mass spectrometry, circular dichroism, and fourier transform infrared spectroscopy. Density functional theory (DFT) simulations were utilized to determine the effects of metal chelation on BV conformation and near-infrared absorbance. BV conformational change was confirmed with circular dichroism, and the abilities of BV and BVNP to withstand photodegradation were confirmed with mass spectrometry. Single-particle imaging revealed the effects of metal chelation and UV irradiation on BVNP photoblinking behavior. Altogether, these findings suggest that UV irradiation and metal chelation can be utilized alone or in combination to tailor the fluorescence behavior of BV and BVNPs at selected wavelengths.

3.2 INTRODUCTION

Tetrapyrroles are known for their absorbance, fluorescence, and ability to form complexes with a variety of metals. Naturally-occurring tetrapyrroles include heme, bilirubin and biliverdin (bile

pigments resulting from the break-down of heme from hemoglobin), and chlorophyll, among others. The use of tetrapyrroles as building blocks of self-assembled nanoparticles has been increasingly explored for a variety of applications in diagnosis and treatment of diseases.[137,199–205] Biliverdin is a water-soluble tetrapyrrolic molecule of particular interest due to its near-infrared absorbance,[62] which allows for its use as a photoacoustic contrast agent, in addition to its biodegradation in response to biliverdin reductase, an enzyme available throughout the body and especially in the liver.[60,329] Recently, we reported the synthesis of self-assembled biliverdin nanoparticles (BVNPs) for use in fluorescence and photoacoustic imaging.[137] BVNPs were found to be enzyme-responsive due to biliverdin's inherent biodegradation pathway, which allowed for the complete degradation of biliverdin nanoparticles *in vitro* and *in vivo*.

The response of tetrapyrroles to external stimuli has long been of interest in developing a better understanding of these biologically-active molecules. A number of studies have examined some of the effects of these stimuli on spectral and conformational behavior. Goncharova et al. determined the effect of metal chelation on circular dichroism spectra of biliverdin and bilirubin in chiral matrices.[192] Wagniére et al. examined the effect of conformational structure on the absorbance behavior of biliverdin-human serum albumin complexes.[342] Dimitrijević et al. examined the effect of copper chelation on spectral properties of biliverdin.[191] Ostrow et al. reported that biliverdin undergoes photodegradation *in vitro*, finding that a higher pH led to faster photodecomposition in the presence of fluorescent daylight lamps, with photodecomposition tracked over six hours.[343] The effect of illumination of light on other tetrapyrroles has also been examined,[344,345] and short-term exposure to UV irradiation has been shown to lead to enhancement of hemoglobin fluorescence emission[346]. Interestingly, Rotomskis et al. proposed that

hematoporphyrin undergoes two competing processes in response to illumination: photodegradation and the formation of stable photoproducts.[345]

Despite this, a systematic study on the individual and combined effects of metal chelation and UV irradiation on biliverdin's spectral properties and conformational structure has not been explored. Additionally, the ability of these altered spectral properties to be transferred to tetrapyrrole-based nanoparticles has also not been reported. With the increasing use of tetrapyrrolic nanoparticles for biomedical applications, a better understanding of their response to stimuli would provide a clear path to manipulating the spectroscopic properties of these particles for applications in bioimaging. The goal of this work was to determine the effects of UV irradiation and metal chelation on biliverdin's spectral properties, and whether these effects could be exploited for use in enhancing the spectral properties of biliverdin nanoparticles **(Scheme 3.1)**. The effects of UV irradiation were of particular interest because in contrast to what we expected based on previous reports, we found that not only did UV irradiation not lead to photodegradation of biliverdin, it additionally led to enhancement of biliverdin's fluorescence emission for select wavelengths. We also examined the effects of metal chelation and UV irradiation on BVNP behavior at the single-particle level, including studying the photoblinking and photobleaching behavior of these particles. To the best of our knowledge, this is the first report of the photophysical behavior of tetrapyrrole-derived nanoparticles at the single-particle level.
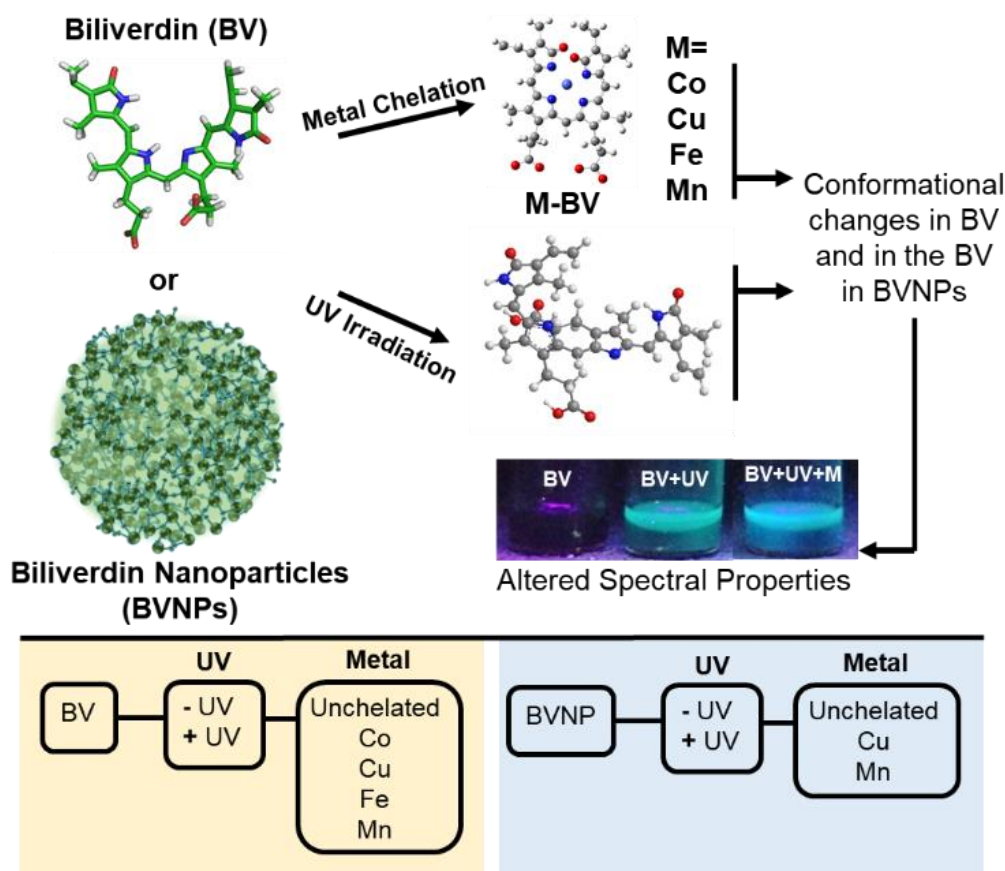
Scheme 3.1. Biliverdin (BV) undergoes conformational changes as a result of metal chelation or 72 h of 365 nm UV irradiation. These conformational changes lead to ehnanced fluorescence emission. Similarly, the biliverdin in biliverdin nanoparticles (BVNPs) can also undergo conformational changes in response to these stimuli, leading to alterations in BVNP spectral properties.

3.3 RESULTS AND DISCUSSION

In order to establish the separate and combined effects of metal chelation and UV irradiation on the spectral properties of molecular biliverdin (BV) and self-assembled biliverdin nanoparticles (BVNPs), we conducted a series of experiments in which molecular biliverdin and biliverdin nanoparticles were exposed to metal chloride solutions and subsequently illuminated with 365 nm UV irradiation for 72 hours. Detailed methods are provided in the Supplementary Information. BV and BVNPs were then spectroscopically characterized to determine the roles of metal chelation and UV irradiation in inducing conformational changes that led to altered spectral properties.

BVNPs were further imaged using single-particle imaging to allow for comparison of bulk-state and single-particle properties of these nanoparticles.

3.3.1 Effects of metal chelation and UV irradiation on BV absorbance and fluorescence

BV was exposed to cobalt (II) chloride, copper (II) chloride, iron (III) chloride, or manganese (II) chloride and subsequently irradiated with UV light for 72 h. The effects of metal chelation alone, UV irradiation alone, and the combined effects of metal chelation and subsequent UV irradiation on the spectroscopic properties of BV were apparent upon visual examination. Under white light, the color of BV samples that were chelated with metals changed based on the metal used **(Fig. 3.1A)**. There were no visible differences in sample color under white light for samples treated with 72 h of UV irradiation and those not treated with UV irradiation. When BV and metal-chelated BV samples were UV irradiated for 72 h, they exhibited a bright fluorescence when illuminated with 365 nm light **(Fig. 3.1A)**. The fluorescence emission of unchelated BV appeared green, while the fluorescence emission of cobalt-chelated BV (Co-BV), copper-chelated BV (Cu-BV), iron-chelated BV (Fe-BV), and manganese-chelated BV (Mn-BV) appeared blue.

Chelation of BV with all tested metals generally decreased UV-visible light absorption between 230 nm and 450 nm, as well as between 550 nm and 800 nm **(Fig. 3.1B).** Mn-BV and Co-BV in particular exhibited not only a dramatic decrease in absorption, but also caused the appearance of new absorption peaks between 230 nm and 450 nm, as well as between 550 nm and 800 nm. In contrast, UV irradiation of both BV and metal-chelated BV samples did not significantly alter UV-visible light absorption **(Fig. 3.1B)**. Ratios of final (after UV irradiation) to initial (without UV irradiation) 365 nm absorbance and 680 nm absorbance confirm that finding
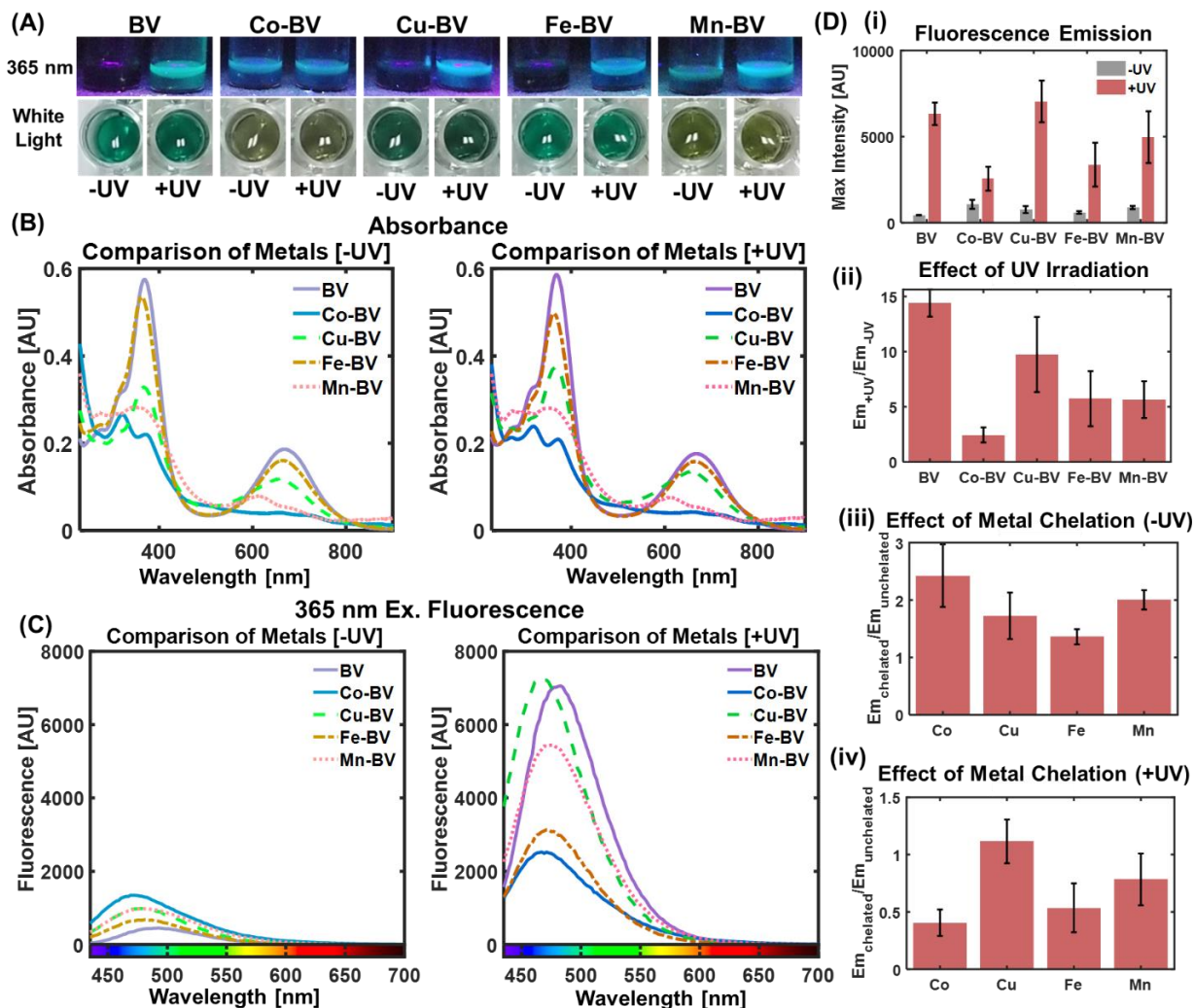
Figure 3.1. Absorbance and fluorescence behavior of BV. **(A)** Visual appearance of samples with and without metal chelation, and with and without 72 h UV irradiation. Samples are illuminated with ambient white light (bottom) and 365 nm light (top). Ambient light images are of samples diluted to 25% of their final concentration in order to better show their colors. **(B)** UV-visible absorption spectra of BV samples without UV irradiation and after 72 h of UV irradiation. Metal chelation leads to decreased absorbance. **(C)** Fluorescence spectra of BV samples without UV irradiation and after 72 h of UV irradiation. UV irradiation enhances fluorescence intensity. An excitation wavelength of 365 nm and gain of 100 was used. **(D)** Effects of metal chelation and UV irradiation on the fluorescence emission of BV. Error bars represent standard deviation obtained with three separate experiments. **(i)** Average fluorescence intensity for BV with and without 72 h UV irradiation. **(ii)** Average ratio of fluorescence intensity with UV irradiation to fluorescence intensity without UV irradiation. **(iii)** Average ratio of fluorescence intensity with metal chelation to fluorescence intensity without metal chelation, in the absence of UV irradiation. **(iv)** Average ratio of fluorescence intensity with metal chelation to fluorescence intensity without metal chelation, after 72 h UV irradiation.

(Fig. E1). Importantly, the effects of metals on the absorbance ratios remained similar, regardless of whether or not the samples were exposed to UV irradiation. This suggests that any conformational changes resulting from UV irradiation do not remove the chelated metals from BV. Fe-BV absorbance was the most similar to BV absorbance, while Cu-BV, Mn-BV, and Co-BV had decreased absorbances.

72 h of UV irradiation dramatically increased the fluorescence of both BV and metal-chelated BV samples **(Fig. 3.1C, Fig. 3.1D (i))**. However, the fluorescence intensities did not scale with the 365 nm absorbance, which suggests that metal chelation and UV irradiation each alter the quantum yield of biliverdin. We observed the largest increase in fluorescence intensity for BV (14-fold) and Cu-BV (10-fold) (**Fig. 3.1D (ii)**). The changes in Fe-BV and Mn-BV fluorescence intensities (approximately 5-fold each) were lower than that of unchelated BV. Without 72 h of UV irradiation, metal-chelated BV samples exhibited a 1.3 to 2-fold greater fluorescence than unchelated BV when excited at 365 nm **(Fig. 3.1D (iii))**. Notably, metal-chelated samples that were also UV-irradiated showed fluorescence intensities comparable to, or less than, the fluorescence intensity of unchelated BV **(Fig. 3.1D (iv))**. In addition, 72 h UV irradiation also caused a slight blue-shifted fluorescence emission in all samples **(Fig. E2)**.

Our results suggest that biliverdin's 365 nm fluorescence emission can be separately enhanced by either metal chelation or UV irradiation. While metal chelation causes a small increase in fluorescence (1.3 to 3-fold), UV irradiation has a much greater effect (2 to 14-fold). However, metal chelation attenuates the effects of UV irradiation on BV fluorescence intensity.

For an excitation wavelength of 488 nm, the fluorescence trends differ from those at an excitation wavelength of 365 nm **(Fig. E3)**. With 488 nm excitation, 72 h of 365 nm UV irradiation results in a decrease in BV fluorescence intensity, with no apparent effect on the fluorescence

intensity of BV metal chelates. Chelation with Mn and Co led to an enhancement of fluorescence, while chelation with Cu and Fe led to a quenching of fluorescence. Furthermore, the fluorescence emission peak for 488 nm excitation appears unaffected by the application or absence of 72 h of UV irradiation **(Fig. E4)**. These results suggest that the excitation wavelength utilized for the 72 h UV irradiation may play a role in what excitation wavelengths can be utilized when taking advantage of the UV-induced fluorescence enhancement. Thus, it is possible to "train" BV for an enhanced response to 365 nm excitation, by long-term exposure of BV to that wavelength.

3.3.2 Evaluation of BV Stability and Conformational Changes

To confirm that the observed changes, especially those caused by the UV irradiation, were not simply caused by degradation of biliverdin in the presence of UV irradiation, we conducted mass spectrometry on BV samples before and after UV irradiation **(Fig. 3.2A)**. In both cases, the peak characteristic for $BV + H^+$ at an m/z value of approximately 583 is observed. There are no new peaks that appear after 72 h of UV irradiation, which confirms that BV has not degraded as a result of the treatment. FT-IR studies were further utilized to confirm that BV composition is maintained even after UV irradiation and that metals are chelated within the BV **(Fig. 3.2B)**. The FT-IR spectra exhibited little or no change as a result of UV irradiation. Additionally, the characteristic peak between $1050\,cm^{-1}$ and $1200\,cm^{-1}$ exhibited a sharpening which correlated with the peaks observed for the metal salt solutions. We then collected circular dichroism (CD) spectra for BV and BV metal chelates with and without 72 h of 365 nm UV irradiation **(Fig. 3.2C)**. Since circular dichroism depends on differential absorption of circularly-polarized light, it is widely used to determine the conformation of molecules, with changes in CD spectra corresponding to changes in conformation. It is apparent that UV irradiation leads to a conformational change in BV,
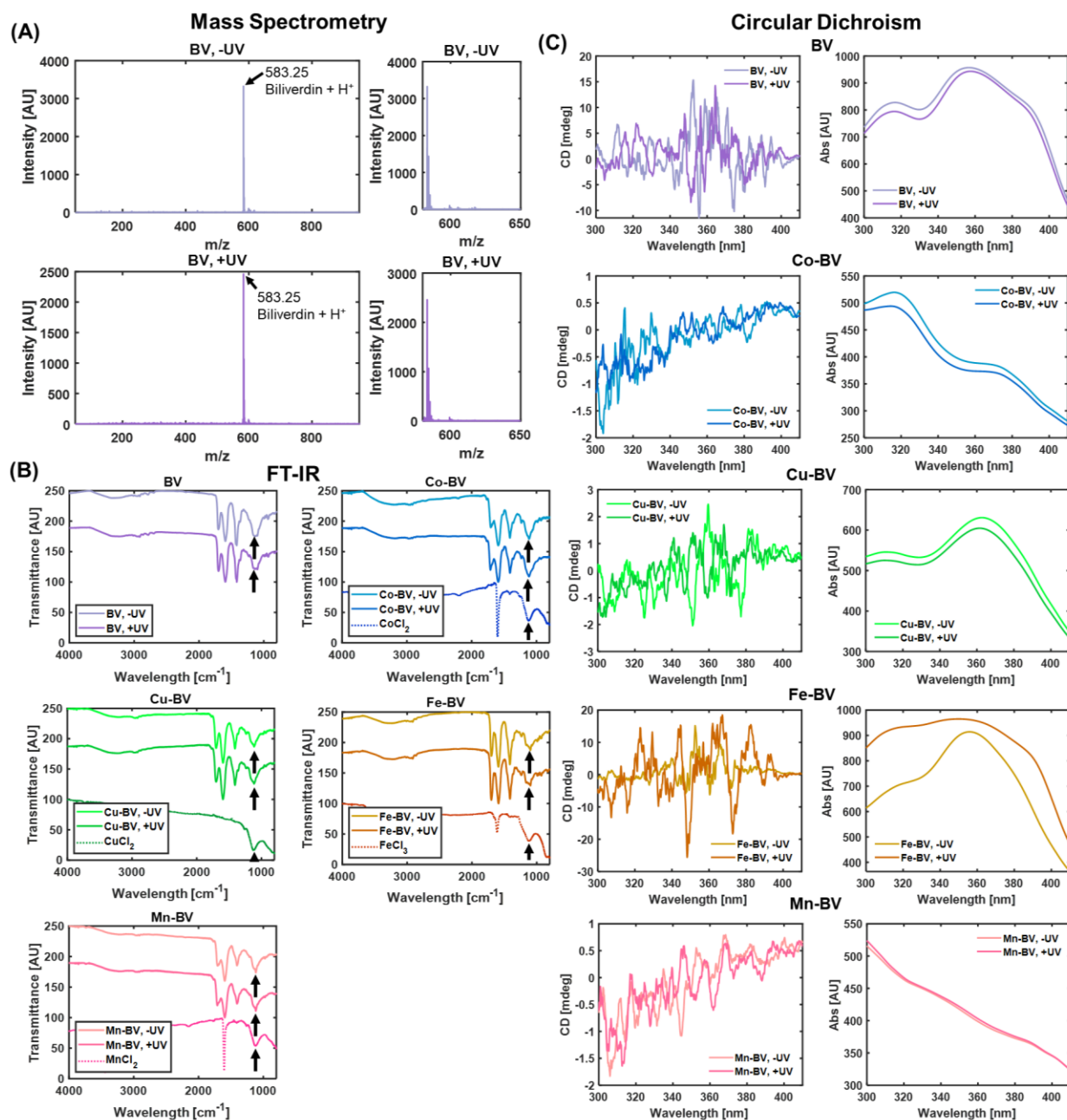
Figure 3.2. BV stability and conformational change. **(A)** Mass specta of BV without UV irradiation and after 72 h of UV irradiation. The presence of BV characteristic peak and lack of appearance of new peaks of smaller masses indicates BV is not degrading as a result of the UV irradiation. **(B)** FT-IR spectra of BV and BV metal chelates. Black arrows identify peaks that are altered as a result of metal chelation. There is no apparent change as a result of UV irradiation. **(C)** Circular dichroism spectra of BV and BV metal chelates. UV irradiation leads to flipping of circular dichroism peaks, which is especially apparent in BV, Cu-BV, and Fe-BV.

94

specifically leading to the flipping of peaks at approximately 315 nm, 330 nm, 350 nm, 360 nm, and 375 nm. Additionally, chelation of metals even without UV irradiation led to some peak shifting and flipping with respect to those of BV. Most notably, one or more of the peaks at approximately 350 nm, 360 nm, and 375 nm are flipped in Cu-BV, Fe-BV, and Mn-BV. Additionally, the magnitude of peaks in Co-BV and Mn-BV are much lower than those of BV alone. These spectra are different in shape from previously reported spectra because they were collected without complexation of biliverdin within a matrix, in contrast to some previous reports.[192]

3.3.3 Density Functional Theory (DFT) studies of metal-chelated BV structures

To further explore the effect of metal chelation on BV conformation and the resulting spectral properties, we performed density functional theoretical calculations. It can be said from the energy minimized geometries of the metal complexes that the metal coordination restricted the flexibility of the tetrapyrrole rings of BV (**Fig. 3.3A and Fig. E5**). This supports our observation that metal chelation attenuates the effects of UV irradiation on BV fluorescence intensity, which is likely a result of the restricted flexibility of metal-chelated BV. The electronic energy diagram and molecular orbital of the geometry optimized structures were then analyzed. It can be seen that HOMO is largely located on the carboxylic acid group whereas LUMO is largely located on the tetrapyrrole rings for BV. The energy gap (ΔE) between E_{HOMO} and E_{LUMO}, which is an important parameter to determine the charge transfer interaction and chemical stability of a molecule, was also calculated (**Fig. 3.3B**). The order of increasing ΔE from 1.31 eV for Mn-BV, 1.35 eV for Co-BV, 1.39 eV for Cu-BV, 1.43 eV for Fe-BV to 1.44 eV for BV closely corroborates with the NIR absorbance starting wavelength for the compounds (**Fig. 3.3B and Fig. E6**).
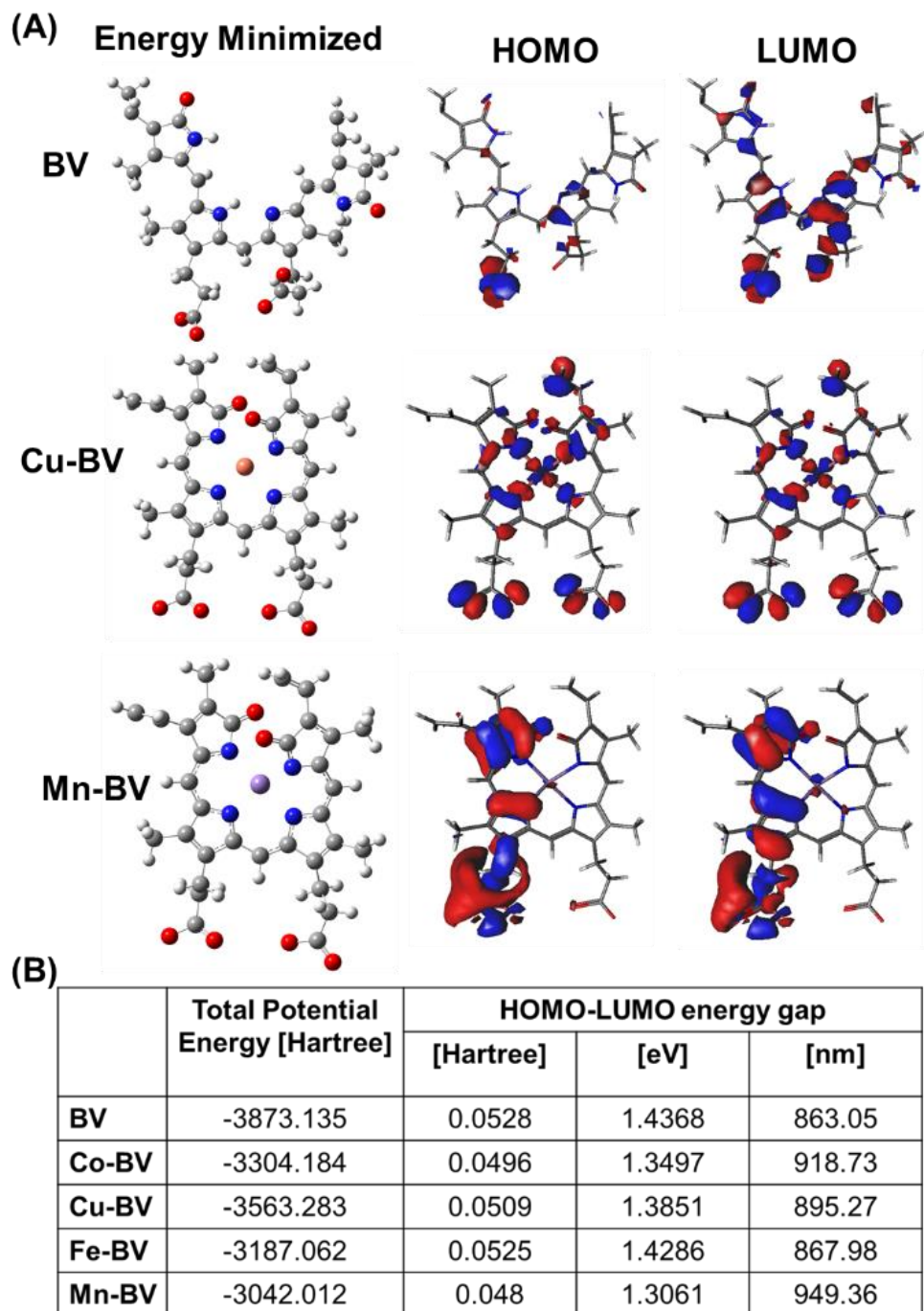
Figure 3.3. Density Functional Theory (DFT) results. **(A)** Energy minimized structures together with the HOMO-LUMO surface maps are shown for BV, Cu-BV, and Mn-BV. **(B)** Corresponding total potential energy and HOMO-LUMO energy gaps for BV, Co-BV, Cu-BV, Fe-BV, and Mn-BV.

3.3.4 Effects of metal chelation and UV irradiation on BVNP absorbance and fluorescence

BVNPs were exposed to either copper (II) chloride, or manganese (II) chloride. Copper and manganese were chosen for these experiments for two reasons. First, because Cu-BV and Mn-BV had the highest and lowest total potential energy magnitudes respectively, of all the metal-chelated BV combinations. Second, when combined with UV irradiation in the molecular BV experiments, Cu-BV and Mn-BV had the highest 365-nm fluorescence intensities of all tested metals. The color of BVNP samples under white light changed based on the chelated metal **(Fig. 3.4A)**. Similar to their molecular BV chelate counterparts, Cu-BVNPs and Mn-BVNPs had blue-green and olive-green hues respectively. As we observed with BV, there were no visible differences in BVNP sample color under white light for samples treated with UV irradiation and those not treated with UV irradiation.

Transmission electron microscopy (TEM) images of BVNPs and metal-chelated BVNPs before and after 72 h UV irradiation show no apparent changes in BVNP appearance **(Fig. 3.4B)**. This suggests that the particles are stable even under long-term UV exposure. UV-visible spectra **(Fig. 3.4C)** for chelated and unchelated BVNP samples exhibited a decrease in absorption as a result of chelation. The spectra shapes for Cu-BVNPs and Mn-BVNPs are consistent with the shapes of the spectra for Cu-BV and Mn-BV respectively. The BVNP Q band appears blue-shifted in Cu-BVNPs, and multiple Q band peaks are observed for Mn-BVNPs. UV irradiation did not appear to have as great of an impact on the absorption spectra. Ratios of final (after UV irradiation) to initial (without UV irradiation) 365 nm absorbance and 680 nm absorbance of BVNPs exhibited little to no change in absorbance as a result of UV irradiation **(Fig. E7)**. As in BV samples, the effects of metal chelation on BVNP absorbance ratios remained similar, regardless of whether or not the samples were exposed to UV irradiation.
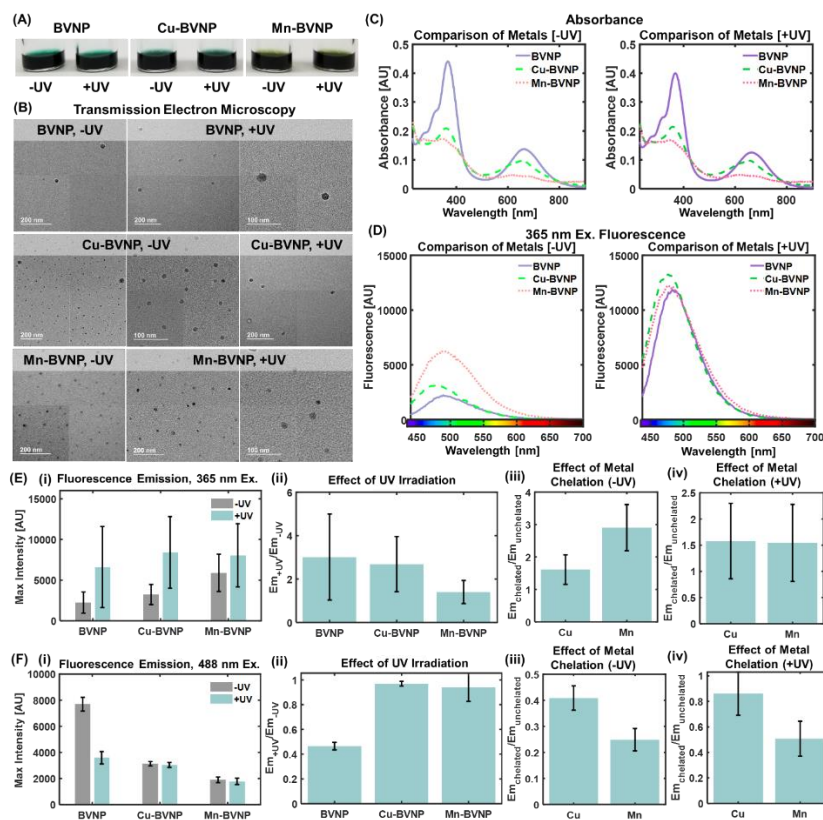
Figure 3.4. Absorbance and fluorescence behavior of BVNPs. **(A)** Appearance of samples with and without 72 h UV exposure, as well as with and without metal chelation. Samples are illuminated with ambient white light. The solution color differs based on the metal chelated. **(B)** Transmission electron microscopy images of BVNPs and metal-chelated BVNPs before and after 72 h of 365 nm UV irradiation. Presence of particles after UV irradiation indicates that particles have not degraded as a result of UV exposure. **(C)** UV-visible absorption spectra of BVNP samples without UV irradiation and after 72 h of UV irradiation. Metal chelation leads to attenuated absorbance similar to the effects of metal chelation on BV. **(D)** Fluorescence spectra of BVNP samples without UV irradiation and after 72 h of UV irradiation. UV irradiation enhances fluorescence intensity. An excitation wavelength of 365 nm and gain of 150 was used. **(E)** Average fluorescence intensity for 365 nm excitation. Error bars represent standard deviation across three trials. **(i)** Average fluorescence intensity for BVNPs with and without 72 h UV irradiation. **(ii)** Average ratio of fluorescence intensity with UV irradiation to fluorescence intensity without UV irradiation. **(iii)** Average ratio of fluorescence intensity with metal chelation to fluorescence intensity without metal chelation, in the absence of UV irradiation. **(iv)** Average ratio of fluorescence intensity with metal chelation to fluorescence intensity without metal chelation, after 72 h UV irradiation. **(F)** Average fluorescence intensity for 488 nm excitation. Error bars represent standard deviation across three trials. **(i)** Average fluorescence intensity for BVNPs with and without 72 h UV irradiation. **(ii)** Average ratio of fluorescence intensity with UV irradiation to fluorescence intensity without UV irradiation. **(iii)** Average ratio of fluorescence intensity with metal chelation to fluorescence intensity without metal chelation, in the absence of UV irradiation. **(iv)** Average ratio of fluorescence intensity with metal chelation to fluorescence intensity without metal chelation, after 72 h UV irradiation.

Representative BVNP fluorescence spectra for 365 nm excitation illustrate an increase in fluorescence after 72 h of UV irradiation **(Fig. 3.4D)**. There did not appear to be a shift in fluorescence emission as a result of metal chelation or UV irradiation **(Fig. E8)**. For 365 nm excitation, UV irradiation appeared to lead to an increase in fluorescence intensity **(Fig. 3.4E (i))**, although the standard deviations for average fluorescence intensity of the UV-irradiated samples overlapped with those of the non-irradiated samples. The ratio of fluorescence intensity with irradiation to fluorescence intensity without irradiation was also lower in BVNP samples compared to BV samples, with a less than 4-fold increase in fluorescence after 72 h of irradiation. This can be explained by restrictions in conformational changes of BV molecules that have been crosslinked into BVNPs. The self-assembly of cross-linked BVNPs likely leads to steric hindrance, which can limit the extent of deformation that individual biliverdin molecules within the BVNPs can undergo. This in turn would be reflected in the spectral properties of the particles. In addition, the lower initial fluorescence intensity of BVNPs compared to BV, even when utilizing a higher gain for BVNP spectra, reveals that BV molecules undergo fluorescence quenching when assembled into BVNPs. Without UV irradiation, chelation of Mn into BVNPs (Mn-BVNPs) led to an approximately 3-fold increase in fluorescence intensity, while chelation of Cu into BVNPs (Cu-BVNPs) led to an approximately 1.5-fold increase in fluorescence intensity **(Fig. 3.4E (iii))**. With UV irradiation, the effects of Cu chelation and Mn chelation are indistinguishable from each other, each having only a 1.5-fold increase in fluorescence intensity compared to BVNPs **(Fig. 3.4E (iv))**. Thus, it appears that in molecular BV, the effects of UV irradiation on fluorescence behavior are much more pronounced than those from metal chelation, while in BVNPs the individual contributions from UV irradiation and metal chelation are approximately equal. This is likely due to limited deformation of BV molecules within the crosslinked BVNP structure.

For 488 nm excitation, the fluorescence intensity was highest for BVNPs without UV irradiation or metal chelation **(Fig. 3.4F (i))**. UV irradiation led to a decrease in BVNP fluorescence intensity, but had no effect on the fluorescence intensities of Cu-BVNP and Mn-BVNP **(Fig. 3.4F (ii))**. Without UV irradiation, Cu-BVNP fluorescence was higher than that of Mn-BVNP fluorescence, although both had a lower fluorescence than that of BVNP alone **(Fig. 3.4F (iii))**. With UV irradiation, Cu-BVNP fluorescence was again higher than that of Mn-BVNP, although they were both closer to that of BVNP **(Fig. 3.4F (iv))**.

3.3.5 Evaluation of BVNP Stability and Conformational Changes

We conducted mass spectrometry on BVNP samples before and after UV irradiation **(Fig. E9A)**. In both cases, the characteristic peak at an m/z value of approximately 583 is observed, in addition to peaks at higher masses, corresponding to the formation of BVNPs from biliverdin. There are no new peaks that appear after 72 h of UV irradiation, which confirms that BVNPs are not being degraded. This is supported by observations from the TEM images discussed above. FT-IR studies were further utilized to confirm that BVNP composition is maintained even after UV irradiation and that metals are chelated within the BVNPs **(Fig. E9B)**. The FT-IR spectra exhibited little or no change as a result of UV irradiation. Additionally, the characteristic peak between 1050 cm^{-1} and 1200 cm^{-1} exhibited a sharpening which correlated with the peaks observed for the metal salt solutions, as we observed for BV. We also collected circular dichroism (CD) spectra for BVNPs **(Fig. E9C)**. The formation of BVNPs from BV did not lead to a change of peak sign, but led to an overall lower magnitude of the circular dichroism spectra. The effect of UV irradiation is less apparent in the BVNP CD spectra than it is in the BV CD spectra. However, this can be expected from the overall lower effect of UV irradiation on BVNPs compared to its effect on BV.

3.3.6 Single-particle analysis of BVNP brightness

Single-particle imaging of BVNPs was conducted with a total internal reflection fluorescence microscopy (TIRFM) system using a 488 nm laser. The average intensity of the particles was found to be higher for Cu-BVNPs than BVNPs or Mn-BVNPs **(Fig. E10A)**. This contrasts with well-plate measurements of the fluorescence emission of BVNPs **(Fig. 3.4F)**. We then determined the on-time duty cycle (defined as the percentage of each cycle for which the particle is in the "on" state), and examined the product of the on-time duty cycle and the average intensity of the particles **(Fig. E10B)**. Since bulk fluorescence intensity depends on the instantaneous intensity as well as the on-time duty cycle, their product is considered to be a more accurate reflection of bulk-state properties.[243] We found that the product of particle intensity and on-time duty cycle for BVNPs, Cu-BVNPs, and Mn-BVNPs was largely unaffected by the 72 h of UV irradiation, which matches the bulk-state BVNP fluorescence behavior for 488 nm excitation. Similar to bulk-state measurements, BVNP+UV appeared to have a slightly lower product of intensity and on-time duty cycle than BVNP-UV; however, these measurements were within experimental error. These findings further support our hypothesis that the 72 h UV irradiation at 365 nm may "train" the particles for an altered spectral response to only the 365 nm wavelength.

3.3.7 Single-particle analysis of BVNP photoblinking behavior

When excited by light, fluorescent nanoparticles cycle between an "on" state in which they are emitting fluorescence, and "off" state in which they are not emitting any fluorescence. This collective behavior is known as photoblinking. Additionally, when excited by light for long periods of time, nanoparticles can photobleach as other fluorophores do. To evaluate the effects of metal chelation and 72 h UV irradiation of BVNP photoblinking behavior, single-particle analysis was

carried out using a TIRFM system as described above. Log-log plots and power law fits of the time on and time off distributions **(Fig. 3.5A)** illustrate the effects of metal chelation and 72 h UV irradiation on the time on and time off distributions of the BVNPs. The slopes of the power law fits are provided in **Fig. 3.5B**, and the intercept and R^2 values are provided in **Figure D11**. For BVNP and Mn-BVNP, the magnitude of the time on power law slope decreased as a result of 72 h of UV irradiation, while for Cu-BVNP it slightly increased. The magnitude of the time off power law slope decreased for BVNP and Cu-BVNP as a result of 72 h of UV irradiation, but slightly increased for Mn-BVNP. Additionally, while Cu chelation in the absence of UV irradiation led to a decrease in BVNP time on slope magnitude, it led to an increase in time off slope magnitude. Mn chelation in the absence of UV irradiation led to an increase in magnitude for the time on slope, but had little to no impact on the time off slope. These findings indicate that the effects of metal chelation on time on and time off depends on the chelated metal, and that the time on and time off behavior do not follow the same trend. This suggests that some metals can increase the length of time for which BVNPs are in the "on" state, while others can decrease the time for which BVNPs are in the "on" state. When combined with the lack of a uniform effect from UV irradiation on the time on and time off slopes, this indicates that the BVNP single-particle response to 488 nm cannot be predicted from
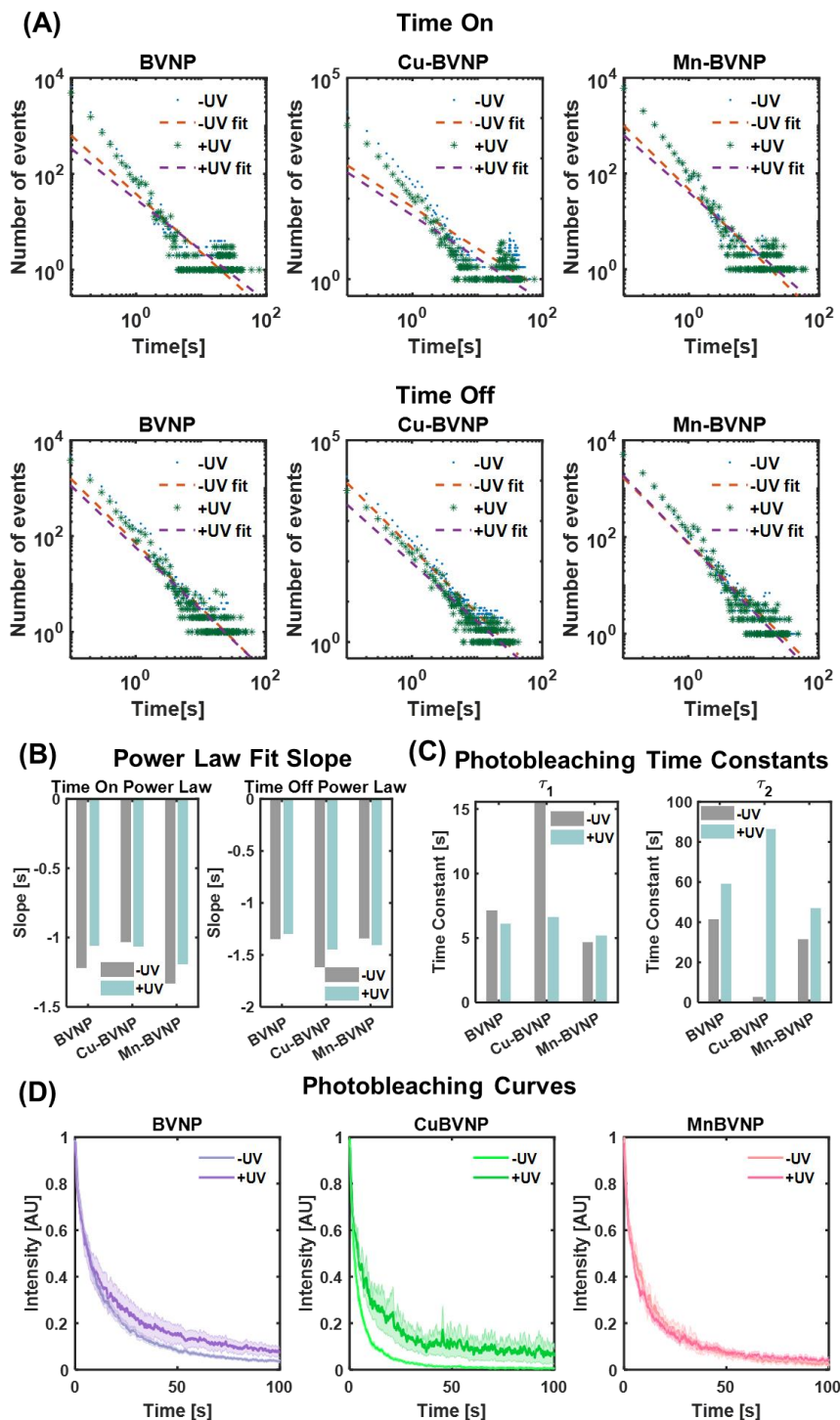
Figure 3.5. Single-particle photoblinking behavior. **(A)** Time on and time off curves and respective power law fits, displaying the number of instances of each on and off time (log-log scale). **(B)** Calculated slopes from time on and time off power law fits. **(C)** Time constants from single-particle photobleaching experiments. **(D)** Photobleaching curves for BVNP, Cu-BVNP, and Mn-BVNP. Envelopes represent standard error of the mean as measured across multiple individual particles.

bulk-state measurements. An alternative illustration of the time on data from Fig. 5A is provided in **Fig. E12** in the form of log-log histograms. These histograms reveal the apparent existence of two populations of particles, a majority population that has a low time on, and a much smaller population that has a higher time on. These multiple populations are present regardless of UV irradiation or metal chelation, suggesting that some aspect of BVNP synthesis leads to the formation of particles with multiple subpopulations, each with differing single-particle photoblinking behavior.

Photobleaching time constants **(Fig. 3.5C)** were calculated from second-order exponential fits of the time to photobleaching curves **(Fig. 3.5D)**. Without UV irradiation, copper chelation led to an increase in the first time constant and a decrease in the second time constant, while manganese chelation led to a decrease in both time constants. UV irradiation led to a decrease in the first time constant for BVNPs and Cu-BVNPs, and an increase in time constant for Mn-BVNPs. UV irradiation additionally led to an increase in the second time constant for BVNPs, Cu-BVNPs, and Mn-BVNPs.

We further calculated the single-particle blinking rate **(Fig. E13)**, finding that the particles had a blinking rate of approximately 0.6 to 0.8 Hz. This blinking rate matches closely with our previous reports of carbon dot blinking rates.[243] Regardless of UV irradiation, the blinking rates between BVNPs, Cu-BVNPs, and Mn-BVNPs had overlapping error bars, indicating that 365 nm UV irradiation and metal chelation had little to no effect on the rate of nanoparticle blinking, despite their effects on the nanoparticle time on and time off distributions. Thus, although the length of time for which particles were on or off may have been altered by metal chelation and UV irradiation, the frequency with which the particles would switch between the on and off states remained unaffected.

3.4 CONCLUSION

We have demonstrated that metal (Co, Cu, Fe, and Mn) chelation and or exposure to 72 h of 365 nm UV irradiation lead to conformational changes in biliverdin, which was determined using circular dichroism spectroscopy. UV irradiation was found to increase BV fluorescence emission for 365 nm excitation without leading to degradation, as confirmed by mass spectrometry. Metal chelation altered the shapes of BV absorbance spectra, and, in the absence of UV irradiation, led to BV fluorescence enhancement for an excitation wavelength of 365 nm. For 488 nm excitation, UV-irradiated metal-chelated BV had little to no change in fluorescence emission compared to metal-chelated BV. Unchelated BV, however, had reduced fluorescence emission for an excitation of 488 nm as a result of 72 h of 365 nm UV irradiation. We further explored the effects of metal (Cu, Mn) chelation and 72 h of 365 nm UV irradiation on biliverdin nanoparticle spectral properties. We found that similar to the effects of these stimuli on BV behavior, BVNPs exhibited altered absorbance and fluorescence spectra. However, the effects of metal chelation and UV irradiation were less drastic for BVNPs than they were in BV. This is likely due to the loss of conformational flexibility in the biliverdin molecules that have been crosslinked to form BVNPs. Using single-particle imaging, we found that the metal used governed the effects of metal chelation on BVNP photobleaching dynamics. Despite this, metal chelation and UV irradiation had no effects on single-particle brightness or photoblinking frequency, suggesting that the relationship between BVNP behavior at the single-particle and bulk-state levels is highly complicated and depends on a number of factors. Overall, this work suggests that conformational changes induced by metal chelation and UV irradiation can be taken advantage of in order to enhance the spectral properties of biliverdin and biliverdin nanoparticles. The dramatic enhancement of fluorescence emission (365 nm excitation) after 72 h of 365 nm UV irradiation suggests that the UV irradiation

wavelength may play a role in "training" biliverdin to respond to specific wavelengths. Further studies must be performed to determine whether other irradiation wavelengths also lead to selective enhancement of fluorescence emission for specific excitation wavelengths. However, the present study provides a detailed exploration of the effects of metal chelation and 365 nm UV irradiation on BV and BVNP behavior, as well as the first demonstration of single-particle imaging of tetrapyrrolic nanoparticles.

CHAPTER 4: BILIVERDIN NANOPARTICLES FOR CELLULAR PH SENSING

4.1 INTRODUCTION

During the initial BVNP synthesis experiments, it became apparent that the low pH of MES may be playing a role in the MES-BVNP behavior. In addition to fluorescing a yellow-green color, MES-BVNPs had lower absorbance than water-BVNPs and NaCl-BVNPs. MES-BVNPs also seemed to fall out of solution more easily. The absorbance behavior was especially interesting because it could potentially influence not just the fluorescence of the particles, but also their photoacoustic intensity. Thus, the idea of using BVNPs for pH sensing was born. Specifically, we expected that the increasing absorbance of BVNPs with increasing pH would lead to higher photoacoustic intensity, despite the lower fluorescence of water-BVNPs and NaCl-BVNPs compared to MES-BVNPs. Since nanoparticles have been used for a variety of intracellular pH sensing applications, we decided to explore the use of BVNPs in cellular pH sensing.

4.2 RESULTS AND DISCUSSION

In preliminary experiments, we conducted fluorescence spectroscopy studies using MES-BVNPs. In the first experiment, MES-BVNPs were diluted with water, the initial pH was measured, and the pH was sequentially lowered through the addition of HCl ("experiment 1-part 1"). Following this, the pH was sequentially increased through the addition of NaOH ("experiment 1-part 2"). We found that the color of the particles visibly changed as a result of pH, and that pH values of less than 6 led to precipitation of the particles (**Fig. 4.1**). Fluorescence spectra collected for each pH revealed that for an excitation of 365 nm in experiment 1-part 1, maximum fluorescence intensity decreased with an increase in pH (**Fig. 4.2**). For an excitation of 365 nm in

experiment 1-part 2, the maximum fluorescence intensity and most blue-shifted fluorescence peak both occur at a pH of ~6.

For 265 nm excitation, a decrease in maximum fluorescence intensity with decreasing pH is observed in experiment 1-part 1; there was no clear trend in the location of peak fluorescence emission **(Fig. 4.3)**. For 265 nm excitation experiment 1-part 2, there was an increase in fluorescence intensity with increase in pH until a pH of ~6. Afterwards, there was a decrease in maximum fluorescence intensity with further pH increase; the location of peak fluorescence emission red-shifted with an increase in pH. For 465 nm excitation, experiment 1-part 1, maximum fluorescence intensity decreased with a decrease in pH; there was no trend for the location of peak fluorescence emission. For 465 nm excitation, experiment 1-part 2, the maximum fluorescence intensity increased until a pH of ~6, and then decreased afterwards; there was again no trend for the location of peak fluorescence emission. The results for experiment 1 are summarized in **Table 4.1**.

Table 4.1. Summary of results from experiment 1.

		Maximum Fluorescence Intensity	Maximum Fluorescence Wavelength
365 nm	Decreasing pH (part 1)	Increased	Red-shifted
	Increasing pH (part 2)	Increased then decreased, peak pH ~6	Red-shifted then blue-shifted, trough pH ~6
265 nm	Decreasing pH (part 1)	Decreased	No trend
	Increasing pH (part 2)	Increased then decreased, peak pH ~6	Red-shifted
465 nm	Decreasing pH (part 1)	Decreased	No trend
	Increasing pH (part 2)	Increased then decreased, peak pH ~6	No trend

Before Precipitation

After Precipitation
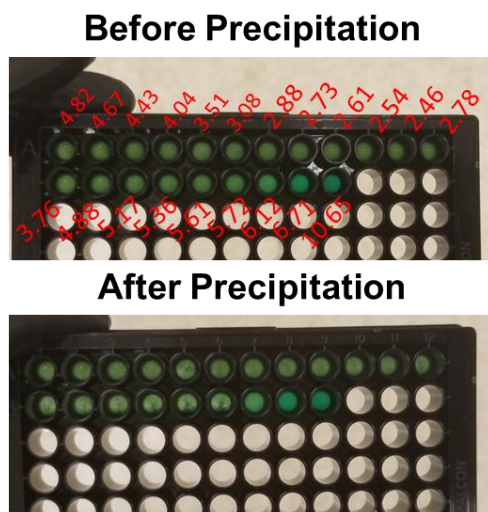
Figure 4.1. BVNPs from Experiment 1 in wellplate. pH of BVNPs was first decreased through addition of HCl and then increased through addition of NaOH. It is apparent that pH values below ~6 lead to nanoparticle precipitation. The color of BVNPs also changes with pH. A higher pH leads to a darker color.
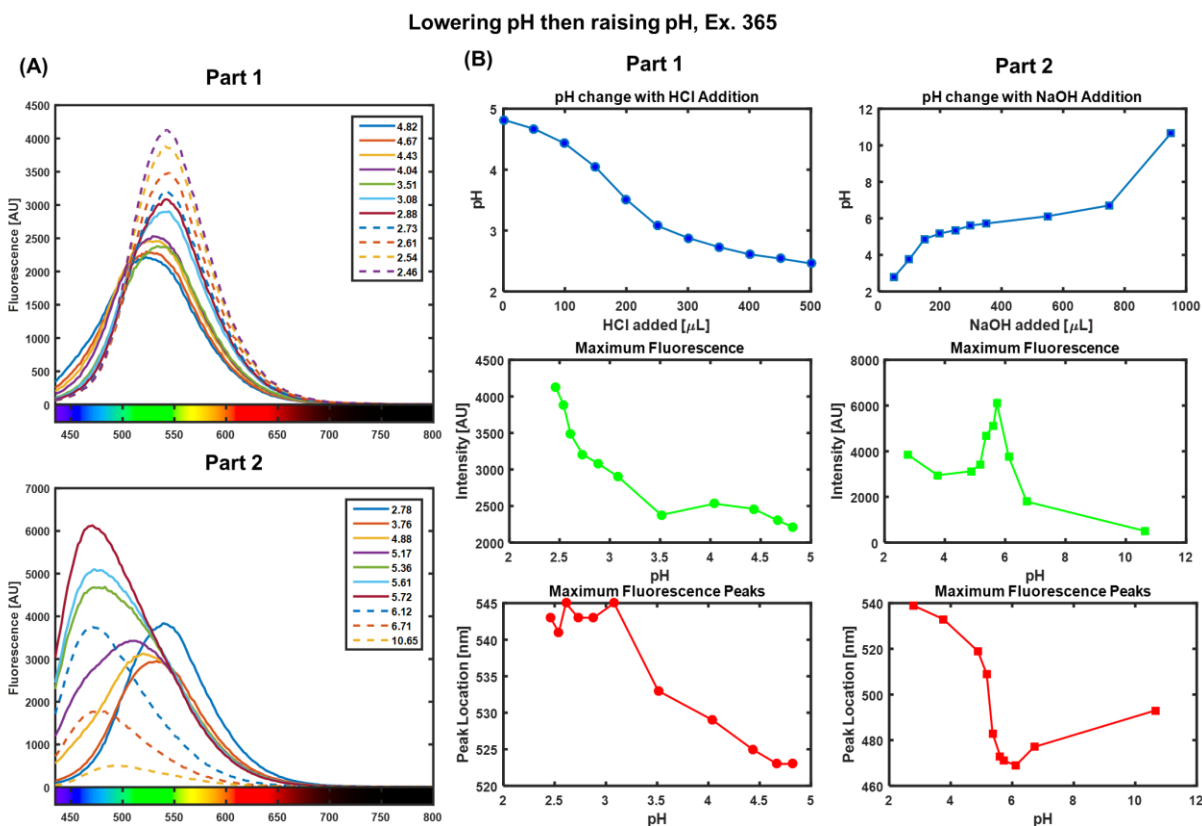
Figure 4.2. 365 nm excitation fluorescence of BVNPs in Experiment 1. **(A)** Fluorescence spectra of BVNPs during pH reduction (Part 1) and pH increase (Part 2). **(B)** Graphs of pH change with acid or base addition, maximum fluorescence intensity at each pH, and location of maximum fluorescence for each pH.

Figure 4.3. 265 nm excitation fluorescence of BVNPs in Experiment 1. **Left:** Fluorescence spectra of BVNPs during pH reduction (Part 1) and pH increase (Part 2). **Right:** Graphs of pH change with acid or base addition, maximum fluorescence intensity at each pH, and location of maximum fluorescence for each pH.

110

Figure 4.4. 465 nm excitation fluorescence of BVNPs in Experiment 1. **Left:** Fluorescence spectra of BVNPs during pH reduction (Part 1) and pH increase (Part 2). **Right:** Graphs of pH change with acid or base addition, maximum fluorescence intensity at each pH, and location of maximum fluorescence for each pH.

In the second experiment, MES-BVNPs were diluted with water, the initial pH was measured, and the pH was sequentially increased through the addition of NaOH ("experiment 2-

part 1"). Following this, the pH was sequentially decreased through the addition of HCl ("experiment 2-part 2"). We found that the color of the particles again visibly changed as a result of pH, as did the fluorescence observed under 254 nm and 365 nm excitation **(Fig. 4.5)**. Fluorescence spectra collected for each pH revealed that for an excitation of 365 nm in experiment 2-part 1, maximum fluorescence intensity increased as pH increased until a pH of ~6, after which it decreased **(Fig. 4.6)**. The wavelength of maximum fluorescence blue-shifted until a pH of ~6, after which it red-shifted with increasing pH. For an excitation of 365 nm in experiment 2-part 2, the maximum fluorescence intensity decreased with decreasing pH; there was no clear trend in the wavelength of maximum fluorescence.

For 465 nm excitation, experiment 2-part 1, maximum fluorescence intensity slightly increased until a pH of ~6, after which it decreased; there was no trend for the location of peak fluorescence emission **(Fig. 4.7)**. For 465 nm excitation, experiment 2-part 2, there was no clear trend in the maximum fluorescence intensity or the wavelength of maximum fluorescence. A summary of the experiment 2 results is provided in **Table 4.2**.

Table 4.2. Summary of results from experiment 2.

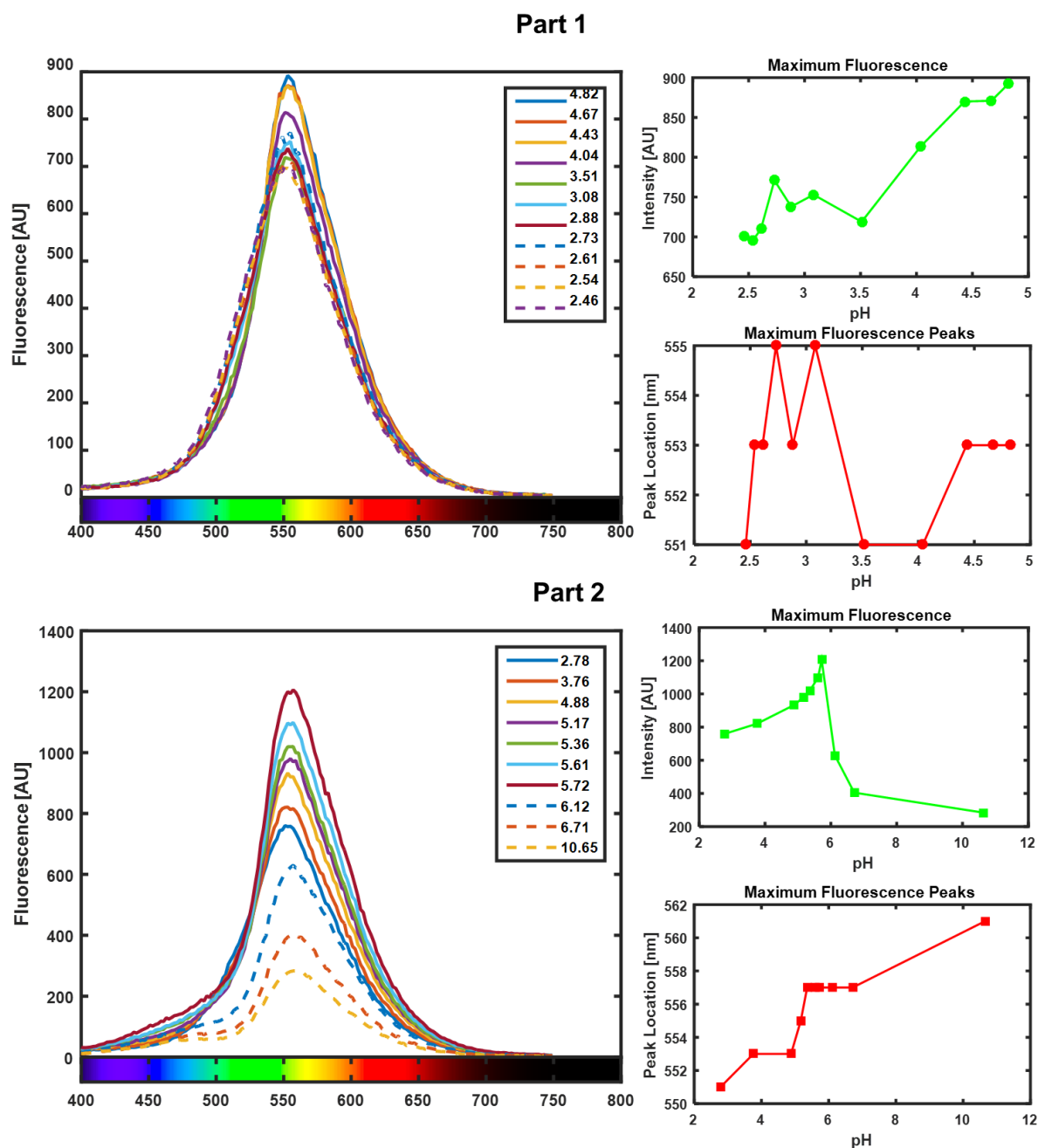|		Maximum Fluorescence Intensity	Maximum Fluorescence Wavelength
365 nm	Increasing pH (part 1)	Increased until pH ~6, then decreased	Blue-shifted until pH ~6, then red-shifted
	Decreasing pH (part 2)	Decreased	No clear trend
465 nm	Increasing pH (part 1)	Slightly increased until pH ~6, then decreased	No clear trend
	Decreasing pH (part 2)	No clear trend	No clear trend
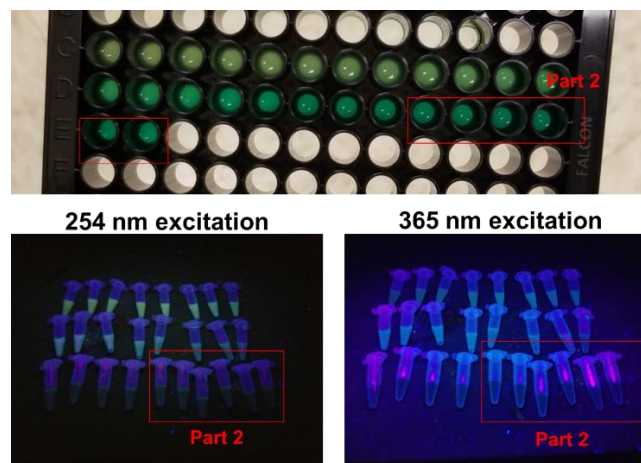
Figure 4.5. BVNPs from Experiment 2. pH of BVNPs was first increased through addition of NaOH and then decreased through addition of HCl. An increase in pH appears to lead to blue-shifted fluorescence, which is apparent in samples placed under 254 nm and 365 nm excitation UV lamps.

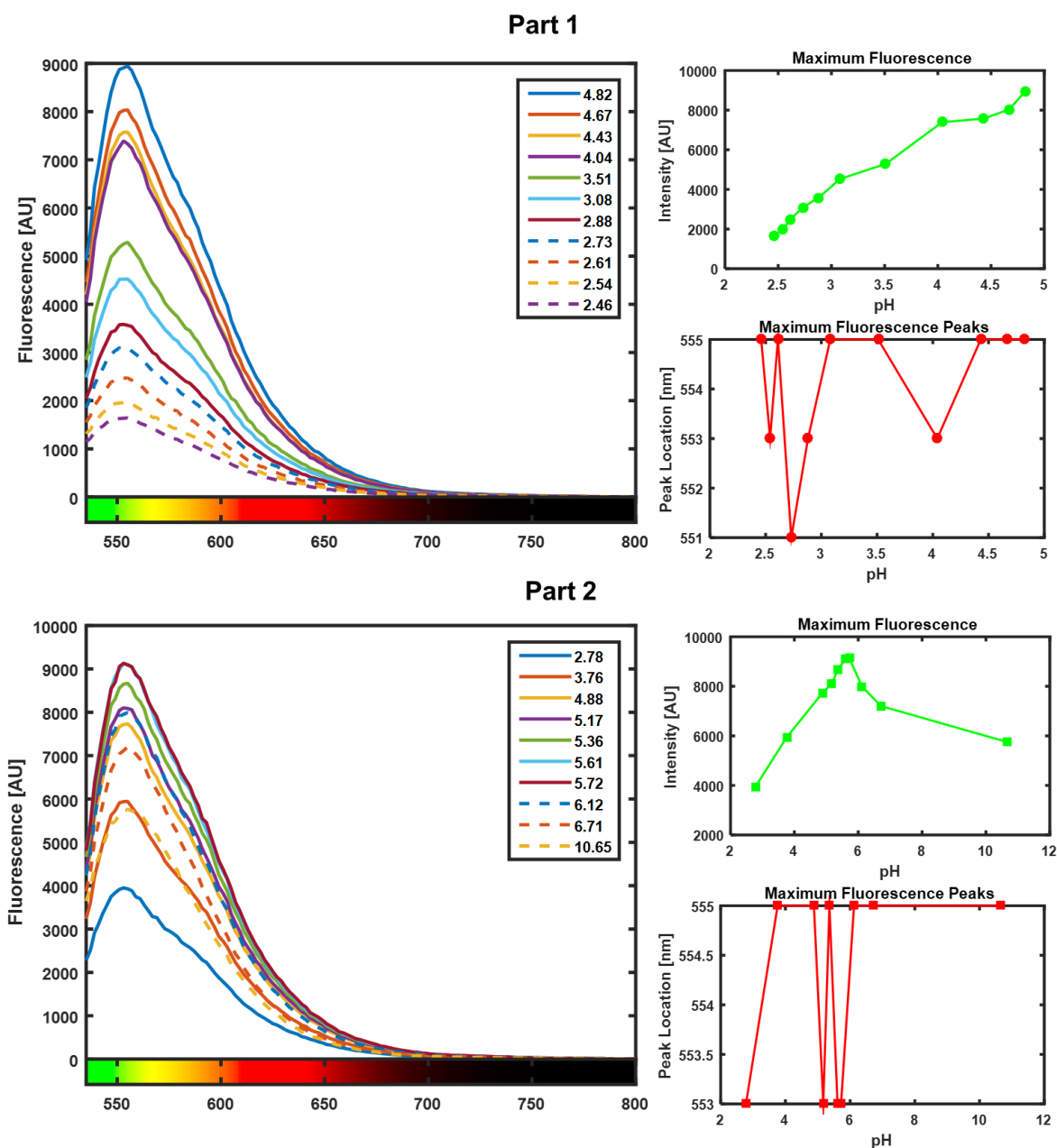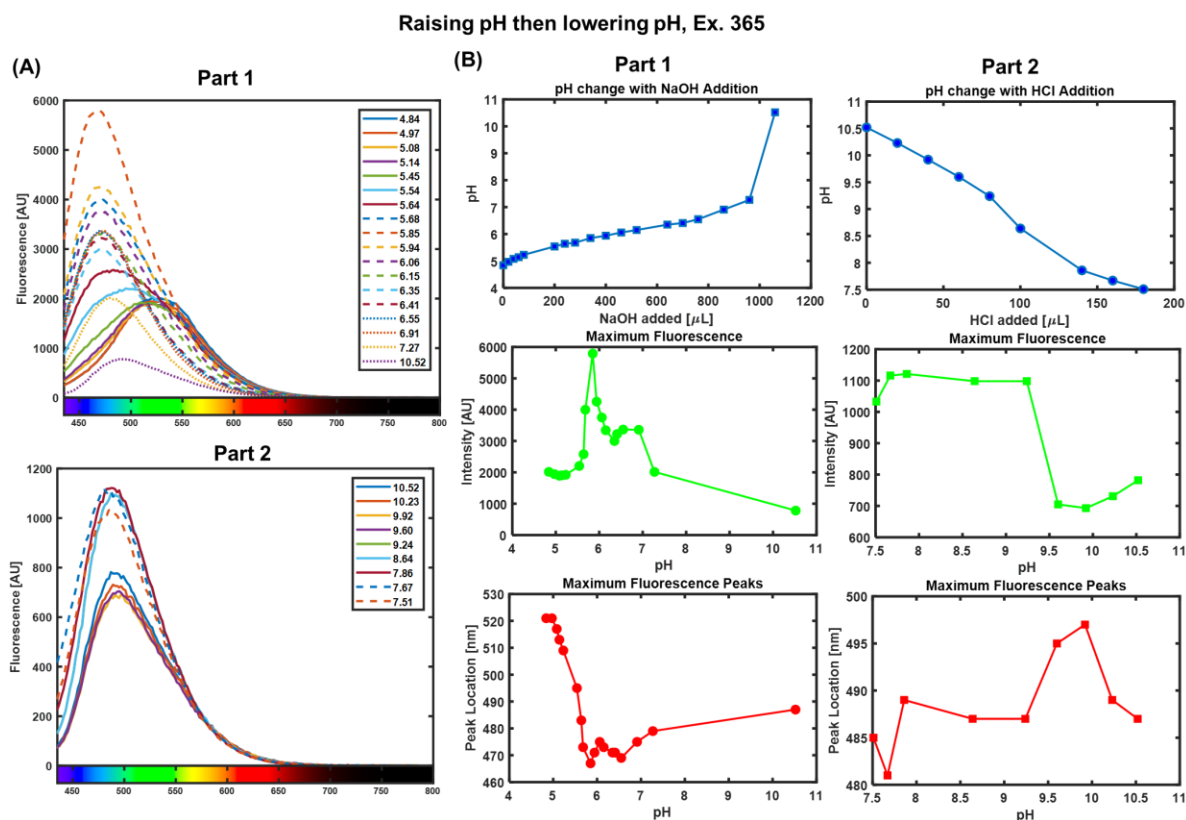**Figure 4.6.** 365 nm excitation fluorescence of BVNPs in Experiment 2. **(A)** Fluorescence spectra of BVNPs during pH increase (Part 1) and pH decrease (Part 2). **(B)** Graphs of pH change with base or acid addition, maximum fluorescence intensity at each pH, and location of maximum fluorescence for each pH.

113
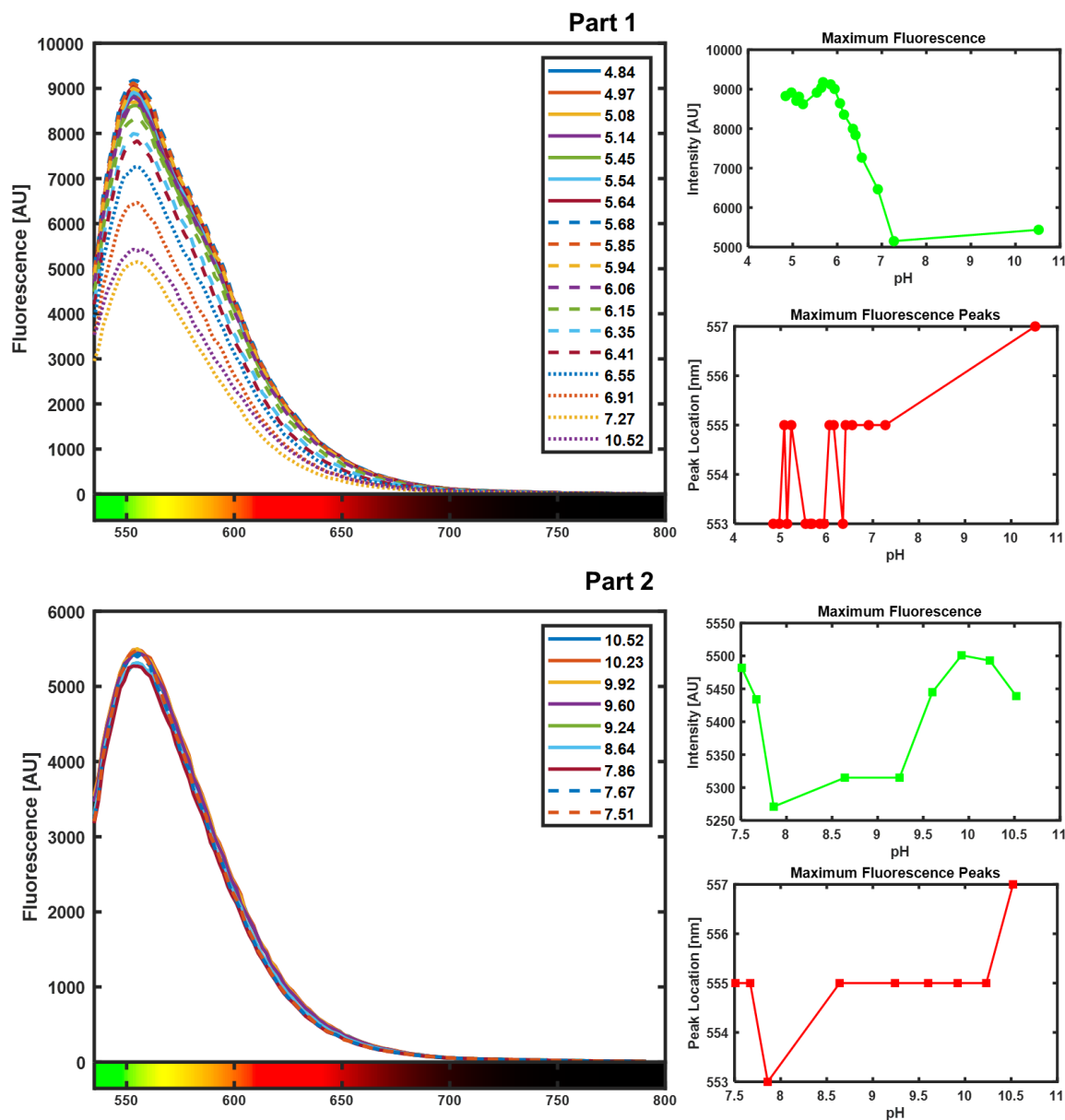
Figure 4.7. 465 nm excitation fluorescence of BVNPs in Experiment 2. **Left:** Fluorescence spectra of BVNPs during pH increase (Part 1) and pH decrease (Part 2). **Right:** Graphs of pH change with base or acid addition, maximum fluorescence intensity at each pH, and location of maximum fluorescence for each pH.

Following the fluorescence well-plate experiments, we decided to conduct in vitro photoacoustic imaging to determine whether the pH sensitivity of the BVNPs could be translated

to cellular pH sensing **(Fig. 4.8)**. MDA-MB-231 cells incubated with dialyzed 24 h NaCl-BVNPs for 24 h were imaged at two different pH values (pH 6.5, pH 7). We found that with an increase in pH, the measured PA signal from the cells increased. This confirmed our hypothesis that the increased absorbance of BVNPs at a higher pH would lead to increased PA contrast that could allow for cell-level pH sensing.
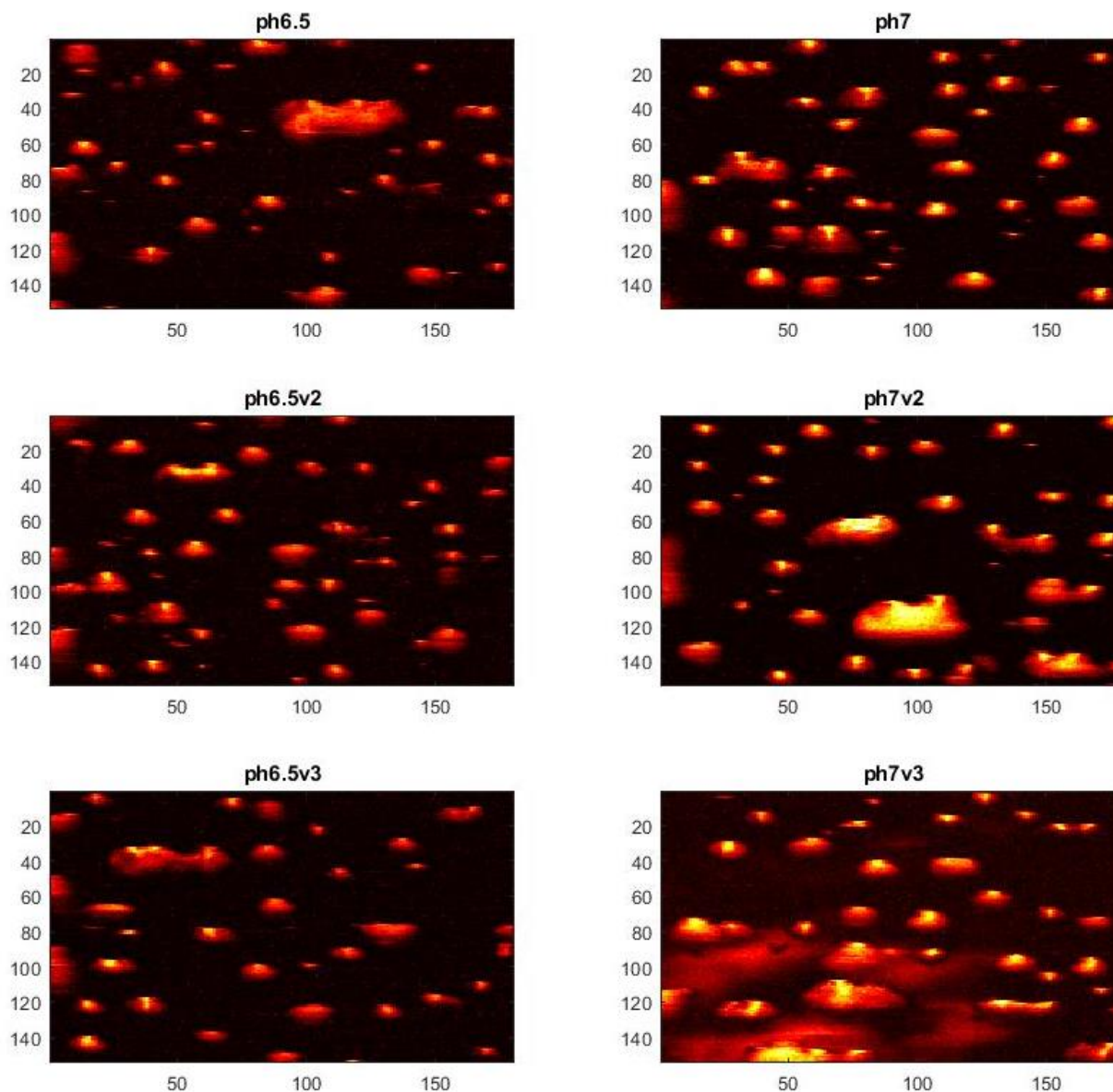
Figure 4.8. Cellular photoacoustic imaging of MDA-MB-231 cells incubated with 24 h NaCl-BVNPs. Images were taken with cell pH altered to 6.5 (left) and 7 (right).

4.3 CONCLUSIONS AND FUTURE WORK

We have demonstrated that the pH sensitivity of BVNPs leads to alterations in fluorescence and photoacoustic properties in response to small changes in pH. This can allow not only for well-plate pH sensing, but also pH sensing at the cellular level. Further experiments must be conducted to demonstrate cellular pH sensing using fluorescence microscopy.

4.4 METHODS

4.4.1 Experiment 1

24 hr MES-BVNPs were prepared as previously described. Approximately 6 mL of the MES-BVNPs were dialyzed against MES. 4.5 mL of the dialyzed sample was diluted to a final volume of 10 mL.

4.4.1.1 Part 1 of pH study: reducing pH. 0.1 N HCl was added to the sample in 50 µL increments, with pH recorded after each addition. For each pH value, 200 µL of the sample was aliquoted for fluorescence spectroscopy. The starting pH was 4.82, and the final pH was 2.46.

4.4.1.2 Part 2 of pH study: increasing pH. The sample from the end of part 1 of the pH study was used for part 2 of the experiment. 1% NaOH was added to the sample in 50-200 µL increments, with pH recorded after each addition. 200 µL of the sample was collected at each pH value and used for fluorescence spectroscopy. The measured starting pH was 2.46, and the final pH was 10.65.

Fluorescence spectra were collected for excitation wavelengths of 265, 365, and 465 nm.

4.4.2 Experiment 2

24 hr MES-BVNPs were prepared as previously described. Approximately 6 mL of the MES-BVNPs were dialyzed against MES. 4.5 mL of the dialyzed sample was diluted to a final volume of 10 mL.

4.4.2.1 Part 1 of pH study: increasing pH

1% NaOH was added to the sample and the pH was recorded after each addition. For each pH value, 200 μL of the sample was aliquoted for fluorescence spectroscopy. The starting pH was 4.84, and the final pH was 10.52.

4.4.2.2 Part 2 of pH study: decreasing pH

The sample from the end of part 1 of the pH study was used for part 2 of the experiment. 0.1 N HCl was added to the sample, with pH recorded after each addition. 200 μL of the sample was collected at each pH value and used for fluorescence spectroscopy. The measured starting pH was 10.52, and the final pH was 7.51.

Fluorescence spectra were collected for excitation wavelengths of 365 nm and 465 nm.

4.4.3 Cellular pH imaging

Cellular pH adjustments were made following previously published reports.[347]

4.4.3.1 Preparation of potassium buffer solution. The buffer was prepared by dissolving KCl (9.6947 g), NaCl (1.1781 g), $CaCl_2$ (55.9 mg), $MgCl_2$ (104.5 mg), and HEPES (2.3853 g) in 1 L millipure water.

4.4.3.2 Preparation of 5 M NaOH solution. 20 g NaOH was dissolved in 100 mL millipure water.

4.4.3.3 Preparation of 5N HCl solution. 50 mL of 10 N HCl solution was added to 50 mL of millipure water.

4.4.3.4 Adjusting pH of K buffer solution. The potassium buffer solution was aliquoted into 3 300-mL portions. Each 300 mL aliquot was separately pH-adjusted using 5 M NaOH and/or 5 N HCl solutions for final pH values of 6.85, 7.4, and 8.

4.4.3.5 Addition of ion transporters to K buffer solutions. 50 mL aliquots of each buffer solution (pH 6.85, 7.4, and 8) were collected in the biosafety cabinet. Without removal from the biosafety cabinet, 10 µL nigericin stock solution (stock concentration of 5 mg/mL) and 2.5 µL valinomycin stock solution (10 mg/mL stock concentration) were added to each 50 mL buffer aliquot. Regular buffer was stored at room temperature, while buffer with ion transporter was stored at 4 °C.

4.4.3.6 Nanoparticle incubation with cells. For each sample, 5 mL MDA-MB-231 cells (concentration 37.6 x 10^3 cells/mL) were plated in small petri dishes. Samples were incubated overnight. The medium was discarded the following day, and replaced with diluted 24 h NaCl-BVNP solution (2.5 mL DMEM, 0.5 mL as-prepared dialyzed NaCl-BVNPs). Samples were then incubated for a further 24 h.

4.4.3.7 pH adjustment and cell imaging. After 24 h of nanoparticle incubation, the medium was discarded and samples were washed twice with 5 mL of buffer solution at the desired pH. The liquid was then discarded and 5 mL of the desired pH buffer solution containing the ion transporter was added. Samples were incubated at room temperature for 5 min, and then cellular PA imaging was conducted.

CHAPTER 5: COBALT-CHELATED BILIVERDIN NANOPARTICLES FOR T2-WEIGHTED MAGNETIC RESONANCE IMAGING CONTRAST

5.1 INTRODUCTION

The use of biliverdin nanoparticles as contrast agents for common clinical imaging modalities would take advantage of BVNP biodegradability and provide an avenue for their direct translation to clinical use. MR imaging is of particular interest because it is commonly used for cancer diagnosis. In this project, we sought to employ biliverdin's ability to chelate metals in order to chelate cobalt ions for use in MRI contrast. An overview is provided in **Fig. 5.1**.
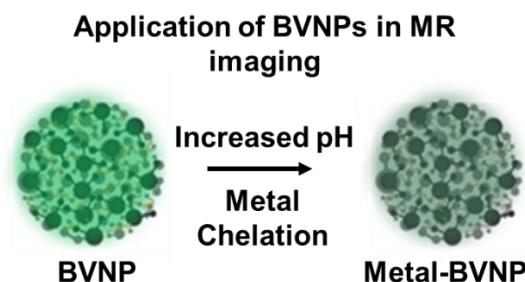
Figure 5.1. Overview of BVNP use for MR imaging.

5.2 METHODS, RESULTS AND DISCUSSION

5.2.1 Chelation of metal into BVNPs

We utilized 24 h NaCl-BVNPs (dialyzed against 0.9 % NaCl solution) and changed the solution pH in order to enable metal chelation to take place. We added a 20:1 molar ratio of metal salt:biliverdin, where the concentration of biliverdin was assumed to be its initial concentration of 10 mg/mL. The metal salts were added in the form of cobalt (II) chloride or iron (III) chloride to the nanoparticle solution and chelation was allowed to take place for 24 h under constant stirring. The particles were then dialyzed against solutions with the pH of interest, and the resulting particles were characterized. We conducted 3 series of experiments. In the first set of experiments,

we sought to determine the effect of chelation pH (10 vs 12) and the chosen metal (Co vs. Fe) on the MR contrast provided by the particles. In the second set of experiments, we sought to determine the effect of the dialysis pH (10 vs. 6) on the quantity of metal chelated within the particles.In the third set of experiments, we sought to determine the effect of the dialysis liquid (MES, 0.9% NaCl solution, or PBS) on the quantity of metal chelated within the particles. An overview of the conducted experiments is provided in **Table 5.1** below.

Table 5.1. Summary of various experiments conducted for this project

	Experiment ID	Details	ICP Results
First Set of Experiments	Co-BVNP 1	Chelation pH: unchanged from synthesis Dialysis pH: unchanged from synthesis	N/A
	Co-BVNP 2	Chelation pH: ~10 Dialysis pH: ~10	N/A
	Fe-BVNP 1	Chelation pH: ~10 Dialysis pH: ~10	1495 ppm Fe
	Co-BVNP 3	Chelation pH: ~12 Dialysis: 0.9% NaCl solution, pH ~10.8	1634 ppm Co
Second Set of Experiments	Co-BVNP 4	Chelation pH: ~12 Dialysis: molecular biology grade water, pH ~6	1374 ppm Co
Third Set of Experiments	Co-BVNP 5	Chelation pH: ~12 Dialysis: MES buffer	308 ppm Co
	Co-BVNP 6	Chelation pH: ~12 Dialysis: 0.9 % NaCl solution, pH ~7.4	1287 ppm Co
	Co-BVNP 7	Chelation pH: ~12 Dialysis: PBS	1348 ppm Co

5.2.2. First Set of Experiments

The chelation of metal into the BVNPs caused a visible change in color, with cobalt-chelated samples having a black color and iron-chelated samples having a dark brown color (**Fig. 5.2**). If the metal ions were chelated at a 1:1 ratio with biliverdin, and if all biliverdin present in the beginning of the synthesis was formed into nanoparticles, we would expect a final concentration of 90.8 ppm Co or 86 ppm Fe in the chelated particles. However, ICP results revealed 1495 ppm Fe in Fe-BVNP 1 and 1634 ppm Co in Co-BVNP 3, corresponding to more than 17 metal atoms chelated for each initial biliverdin molecule. This suggests that the metals may not only be chelated by the biliverdin molecules, but may also be absorbed into the

nanoparticles. We further observed that when the chelation experiment was conducted at low pH values (e.g. Co-BVNP 1) we were unable to obtain successful metal chelation. We conducted further characterization with UV-Visible spectroscopy and fluorescence spectroscopy. The absorbance of BVNPs exhibited a dramatic change with metal chelation **(Fig. 5.3)**. The fluorescence of Co-BVNP 3 was the highest of all samples for excitation wavelengths of 365 and 465 nm **(Fig. 5.4)**. Although we initially believed this can be attributed to a pH effect on the BVNP fluorescence, that is unlikely to be the case since BVNP fluorescence typically decreases with an increase in pH. Thus, it may be a result of interactions between cobalt and BVNPs.
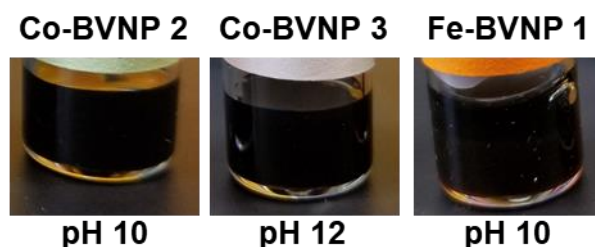
Figure 5.2. metal-chelated biliverdin nanoparticle samples.
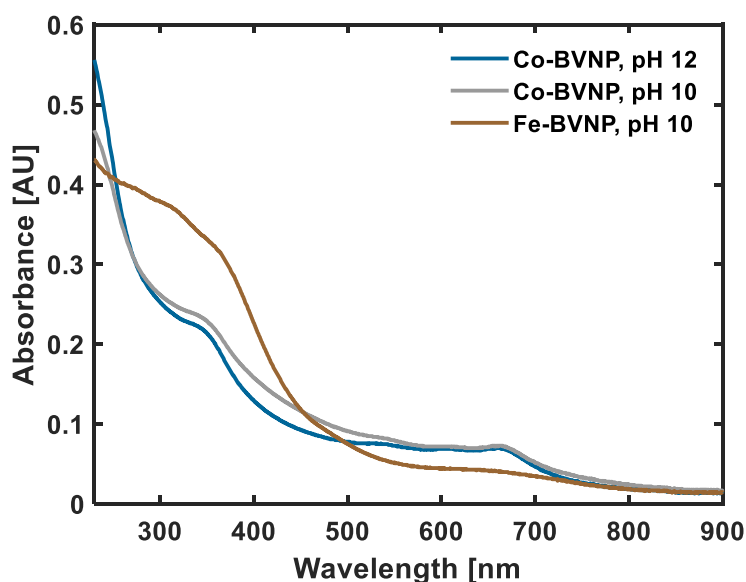
Figure 5.3. UV-visible spectra for Co-BVNP 2, Co-BVNP 3, and Fe-BVNP 1

121
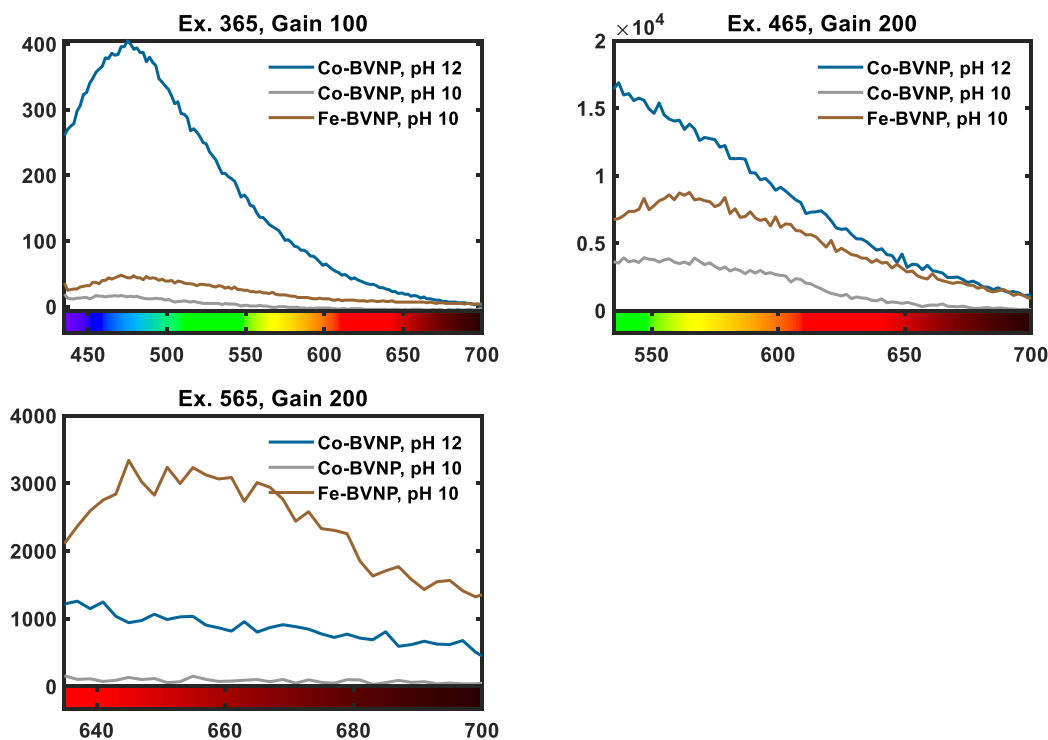
Figure 5.4. Fluorescence spectra for Co-BVNP 2, Co-BVNP 3, and Fe-BVNP 1 at excitation wavelengths of 365 nm, 465 nm, and 565 nm.

Since we were interested in using the metal-chelated BVNPs for MR imaging, we conducted MR imaging experiments in a tissue phantom. The samples were placed in sealed individual glass tubes and placed next to each other within a 50 mL conical tube. The conical tube was then filled with 0.9 % NaCl solution such that the samples were submerged within the solution. MR images were then acquired. The orientation of the samples within the tissue phantom are provided in **Fig. 5.5**. T2-weighted, T2*-weighted, and T1T2-weighted images are provided in **Fig. 5.6**, **Fig. 5.7**, and **Fig. 5.8** respectively. The intensity vs. time graphs are provided in **Fig. 5.9**, along with the exponential fit parameters. The time constants for the T2-weighted images were computed **(Table 5.2)**, finding that Co-BVNP 3 had the lowest time constant, with a shorter T2 time constant corresponding to darker contrast. These experiments demonstrated the potential for cobalt-chelated

BVNPs to be utilized as a T2-weighted MR contrast agent. Additionally, the chelation pH was demonstrated to play an important role in determining the T2 time constant, with a higher chelation pH correlating to a lower (more favorable) T2 time constant.
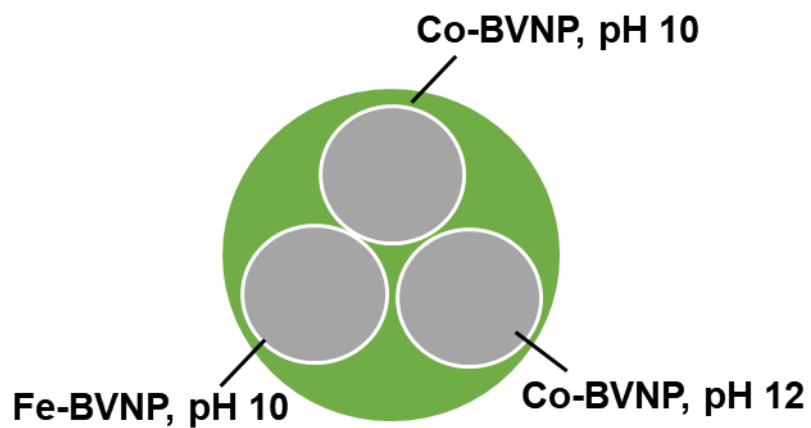
Figure 5.5. Layout of metal-chelated BVNP samples in tissue phantom.

Spin Echo T2
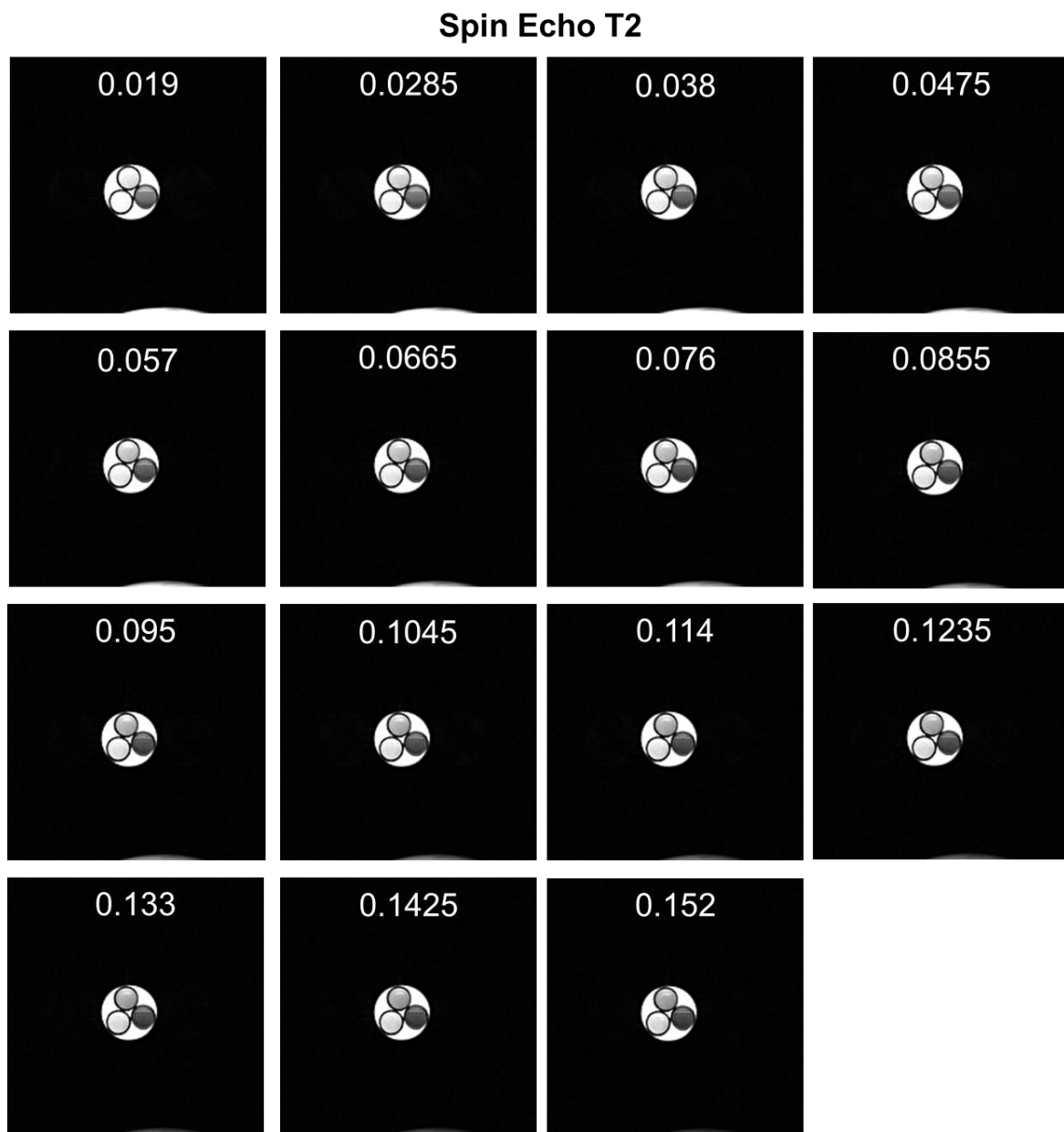
Figure 5.6. T2-weighted MR imaging of metal-chelated BVNPs. White numbers represent time in seconds for each image.

Gradient Echo T2*
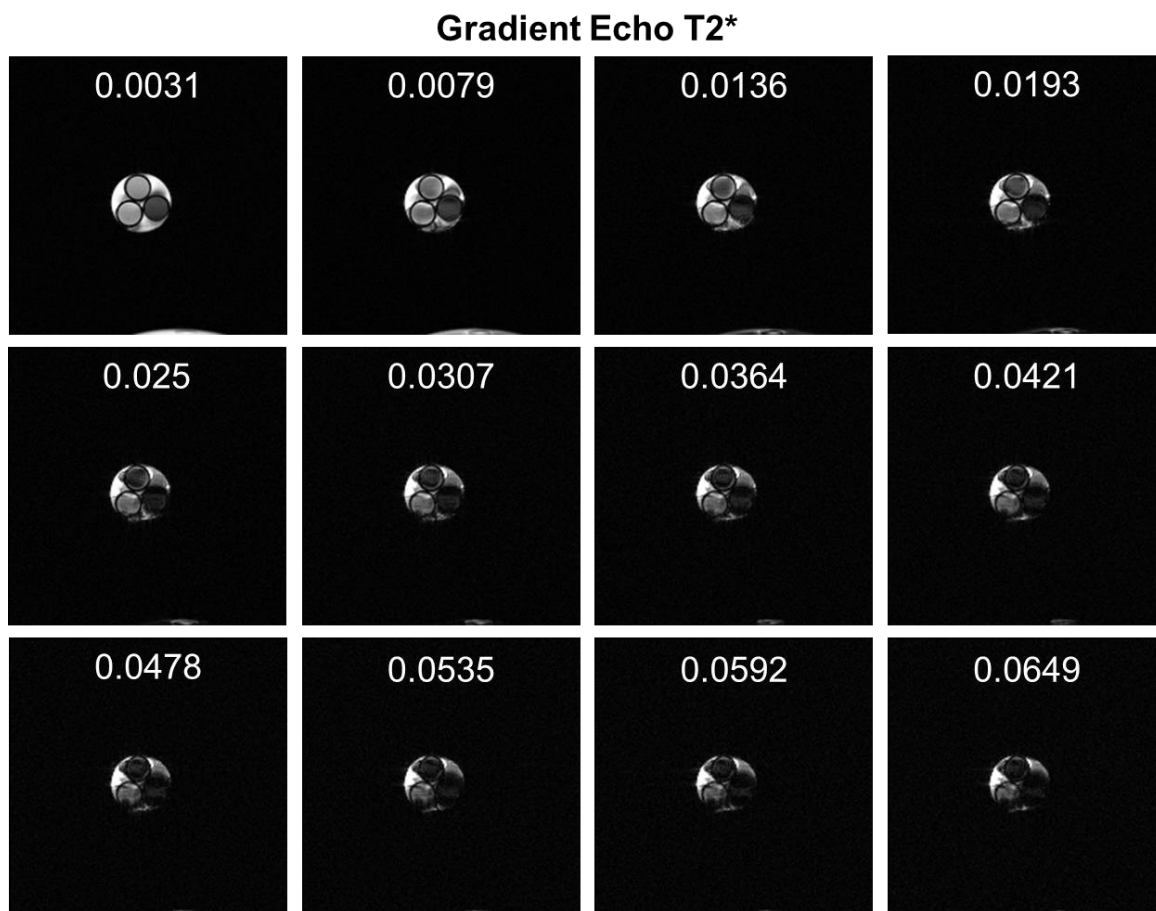
Figure 5.7. T2* MR imaging of metal-chelated BVNPs. White numbers represent time in seconds for each image.

Inversion Recovery T1T2
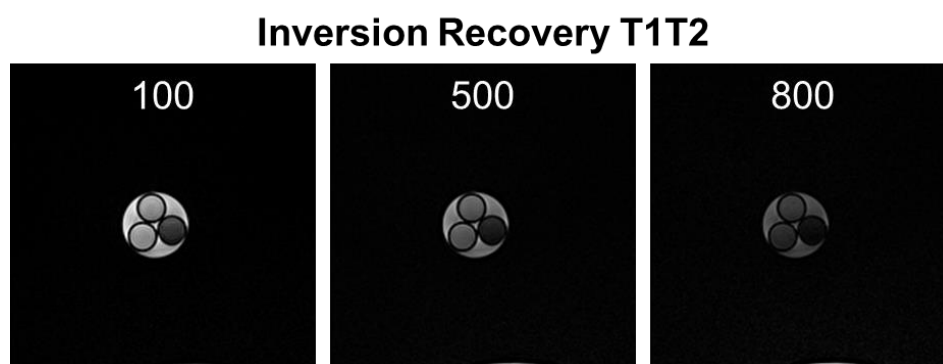
Figure 5.8. T1T2 MR imaging of metal-chelated BVNPs. White numbers represent time in milliseconds for each image.
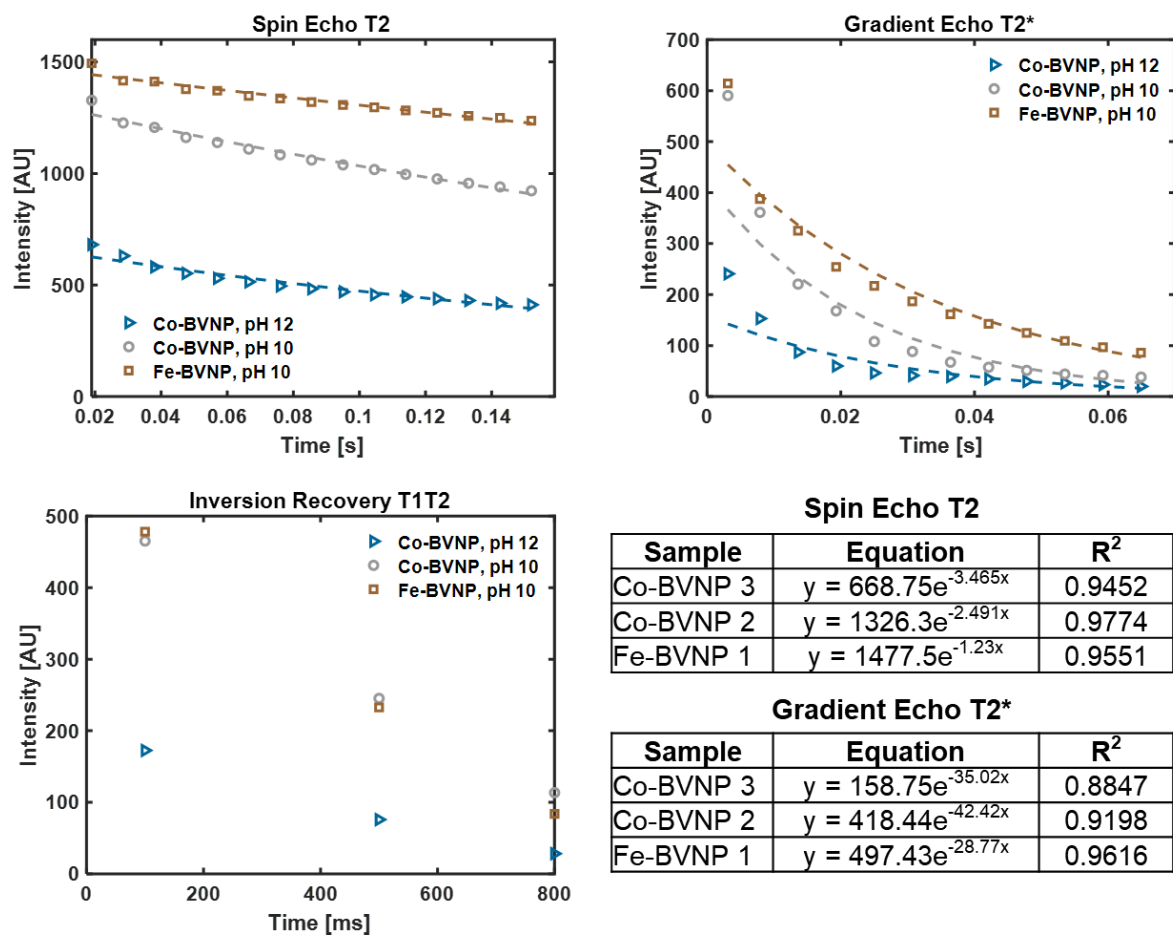
Figure 5.9. MR image quantification for metal-chelated BVNPs. Exponential fits for T2 and T2* images are provided in the tables.

Spin Echo T2

Sample	Equation	R^2
Co-BVNP 3	$y = 668.75e^{-3.465x}$	0.9452
Co-BVNP 2	$y = 1326.3e^{-2.491x}$	0.9774
Fe-BVNP 1	$y = 1477.5e^{-1.23x}$	0.9551

Gradient Echo T2*

Sample	Equation	R^2
Co-BVNP 3	$y = 158.75e^{-35.02x}$	0.8847
Co-BVNP 2	$y = 418.44e^{-42.42x}$	0.9198
Fe-BVNP 1	$y = 497.43e^{-28.77x}$	0.9616

Table 5.2. T2-weighted imaging time constants

Sample	τ (T2)
Co-BVNP 2	0.401
Co-BVNP 3	0.289
Fe-BVNP 1	0.813

To verify that Co-BVNPs retain the favorable photoacoustic contrast that BVNPs have, we conducted tissue phantom PA imaging experiments (**Fig. 5.10**). The samples still have high photoacoustic contrast even after metal chelation. Thus, these particles have strong potential for use as a multimodal PA and MRI contrast agent. We additionally confirmed the formation of

nanoparticles through TEM imaging of Co-BVNP 3 **(Fig. 5.11)**. The cobalt-chelated particles

exhibited higher contrast than unchelated particles, which serves as a further confirmation of the

successful incorporation of the metals within the nanoparticles.
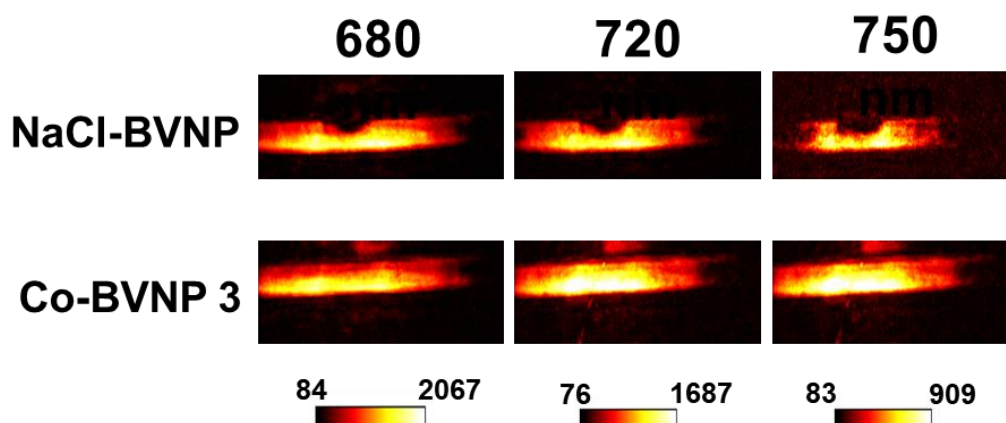
Figure 5.10. Photoacoustic image comparison of Co-BVNP 3 and NaCl-BVNPs.
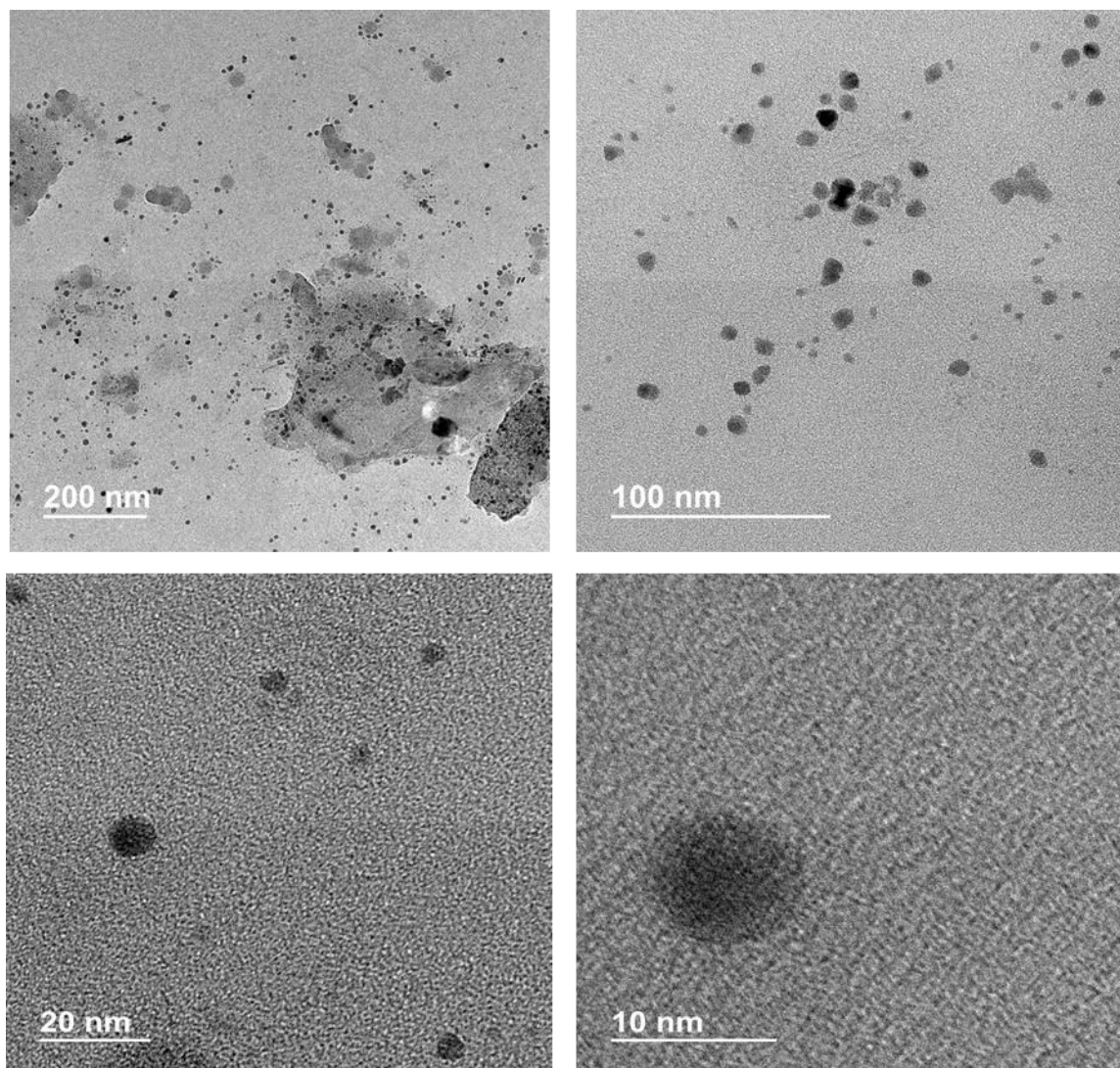
Figure 5.11. TEM images of Co-BVNP 3.

5.2.3 Second Set of Experiments

In the second phase of experimentation, we sought to determine whether the pH of the dialysis liquid would impact the amount of cobalt loaded within the nanoparticles (i.e. if a high pH is required for chelation to occur, would dialyzing the sample against a liquid with a lower pH then lead to the release of the cobalt ions?). Thus, we synthesized the Co-BVNP 4 batch of particles, which were dialyzed against water with a pH of ~6. We found that the Co-BVNP 4 batch had 1374 ppm Co, compared to 1634 ppm Co for the Co-BVNP 3 batch. Thus, there was a slight reduction

in the amount of cobalt within the nanoparticles. However, the cobalt content in Co-BVNP 4 was still many times what would be expected with a 1:1 chelation ratio with biliverdin, indicating that it would still be a potentially favorable option. Additionally, the exact amount of biliverdin remaining after nanoparticle synthesis must be taken into consideration to determine the exact chelation efficiency of the particles, as the amount of biliverdin incorporated into the particles may differ from one batch to another.

5.2.4 Third Set of Experiments

Having established that the chelation pH was more important than the dialysis pH, we then proceeded to determine what role the chelation solvent played on the retention of cobalt in the particles. We synthesized one batch of Co-BVNPs, then dialyzed one aliquot against MES buffer, a second aliquot from the same batch of particles against 0.9 % NaCl solution with pH ~7.4, and a third aliquot from the same batch of particles against PBS. Based on this, we determined that the particles dialyzed against PBS had the highest cobalt retention, while those dialyzed against MES had the lowest. This indicates that exposure MES may lead to a removal of cobalt from the nanoparticles, either due to the effect of pH or due to interactions between MES and biliverdin. Furthermore, the fluorescence intensity of MES-Co-BVNPs (Co-BVNP 5) was higher than that of the other particle types (**Fig. 5.12**), which aligns with our previous observations of the effect of pH and the presence of MES buffer on the fluorescence behavior of BVNPs. Importantly, the high Co content observed in NaCl-Co-BVNPs and PBS-Co-BVNPs at a pH of 7.4 indicates their potential for use in *in vivo* imaging experiments, whether strongly acidic or basic solutions may prove harmful to tissue.

We then conducted MTT assays to determine whether the particles would have a negative impact on cell viability **(Fig. 5.13)**. We found that at low concentrations, cells exposed to NaCl-Co-BVNPs, had high viability. Interestingly, although the MES-Co-BVNPs had the lowest amount of Co retained, they led to low cell viability, even at low concentrations. This is possibly due to the low pH of MES buffer itself. The favorable viability of NaCl-Co-BVNP and PBS-Co-BVNP further proves that these particles have strong potential for use in *in vivo* imaging.
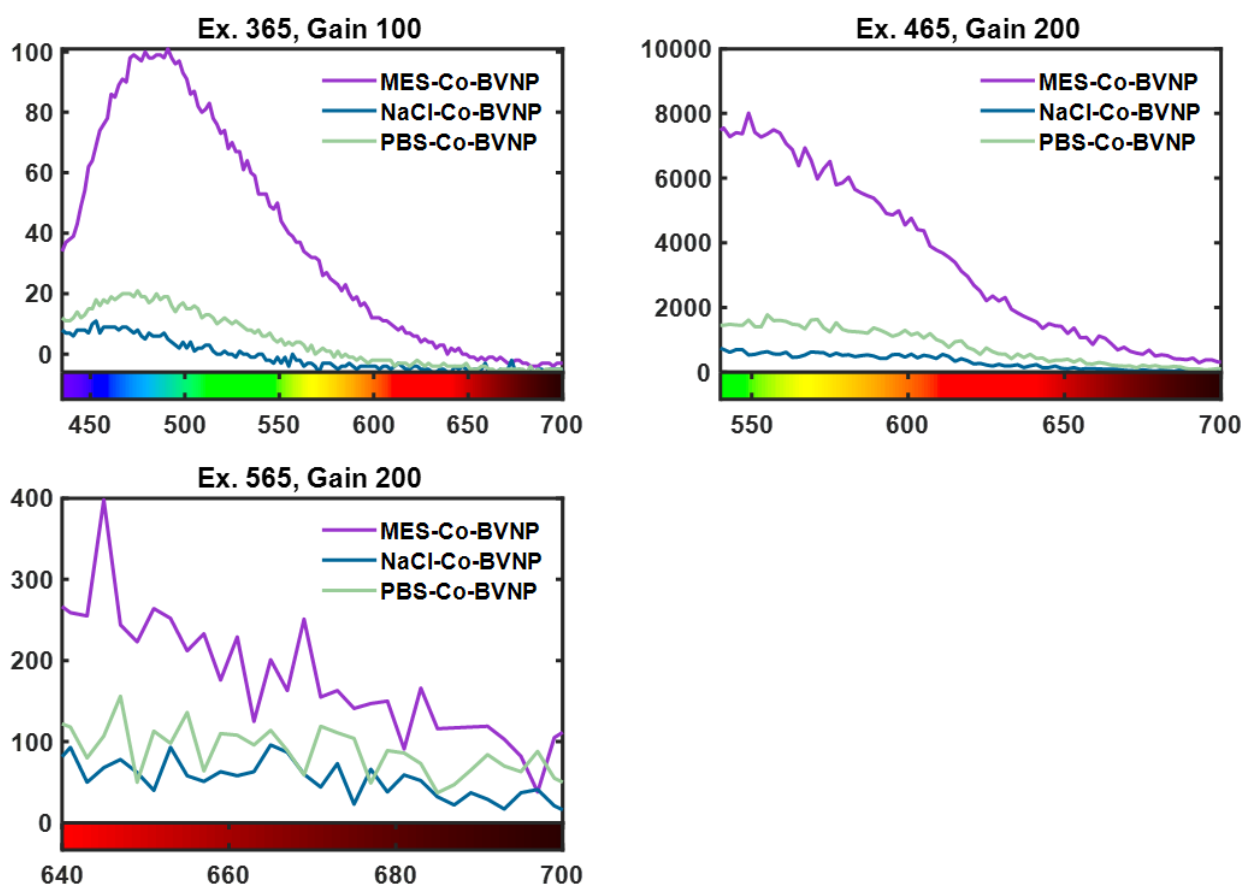
Figure 5.12. Fluorescence behavior of Co-BVNPs dialyzed with MES, NaCl, and PBS.
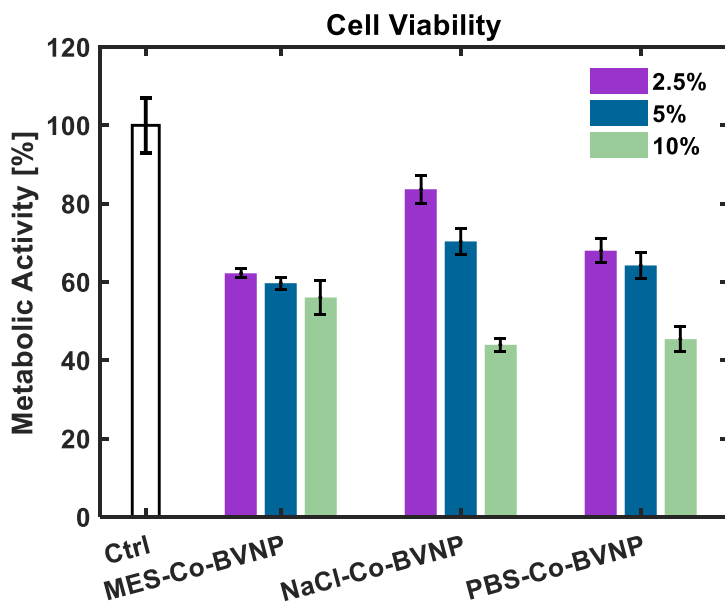
Figure 5.13. Viability of MCF-7 cells exposed to MES-Co-BVNPs, NaCl-Co-BVNPs, or PBS-Co-BVNPs at various volumetric concentrations.

5.3 CONCLUSION

We have demonstrated that cobalt can be chelated into BVNPs for use in multimodal MR and PA imaging. We conducted experiments to determine the effects of chelation pH and dialysis pH on retention of cobalt within the particles. Through these experiments, we demonstrated that a high amount of cobalt was retained in particles, even when dialyzed against solutions with a pH of 7.4. We further demonstrated that at low concentrations, these particles did not lead to unacceptable levels of cell death. In future experiments, the contrast generated by these particles should be compared to those generated by superparamagnetic iron oxide nanoparticles. In addition, the ability of Co-BVNPs to release cobalt in the pH environment of tumor cells should be explored, along with the potential for these particles to be used in photothermal therapy.

CHAPTER 6: BILIVERDIN-SILICA HYBRID NANOPARTICLES FOR NEAR-INFRARED II IMAGING

6.1 INTRODUCTION

Imaging in the near-infrared window allows for strong fluorescent contrast with minimal tissue interference. The goal of this project was to develop biliverdin-silica hybrid nanoparticles with potential for use in imaging in the near-infrared II window. We expected that the fluorescence behaviors of biliverdin and silica would interact with each other, potentially pushing the nanoparticles to fluoresce in the NIR-II region. To this end, we developed four different types of particles. In the first kind, BVISiNPs, biliverdin's carboxylic acid functional groups were reacted with (3-aminopropyl)triethoxysilane (henceforth referred to as "aminopropyl"), forming SiBVD. We then utilized (3-iodopropyl)trimethoxysilane (henceforth referred to as "iodopropyl") to form siloxane bonds between SiBVD molecules, leading to nanoparticle formation. In the second type of particle, SiBVD was reacted with an excess of tetraethyl orthosilicate (TEOS), forming SiBVNPs. In the third type of particle, an excess of iodopropyl was reacted with SiBVD, forming ISiBVNP. Finally, iodinated silica nanoparticles (ISiNPs) were formed by reacting aminopropyl with iodopropyl (**Fig. 6.1**).

6.2 METHODS, RESULTS, AND DISCUSSION

6.2.1 Synthesis of Si-BVD

The first step in these syntheses was the synthesis of Si-BVD, which is a biliverdin molecule reacted with aminopropyl, resulting in a biliverdin molecule with two triethoxysilane arms (**Fig. 6.2**). To achieve this, 11.5 mg biliverdin hydrochloride was dissolved in 5 mL DMF overnight on a stirplate. The following day, 14.7 mg EDC and 8.7 mg NHS were added and the solution was allowed to mix at 500 rpm for 10 min. Afterwards, 17.5 µL aminopropyl solution

was added, the stirplate was kept at 500 rpm, and the reaction was allowed to proceed for 24 h.

Mass spectrometry was conducted to confirm that the Si-BVD product was successfully formed

(Fig. 6.3, Fig. 6.4).
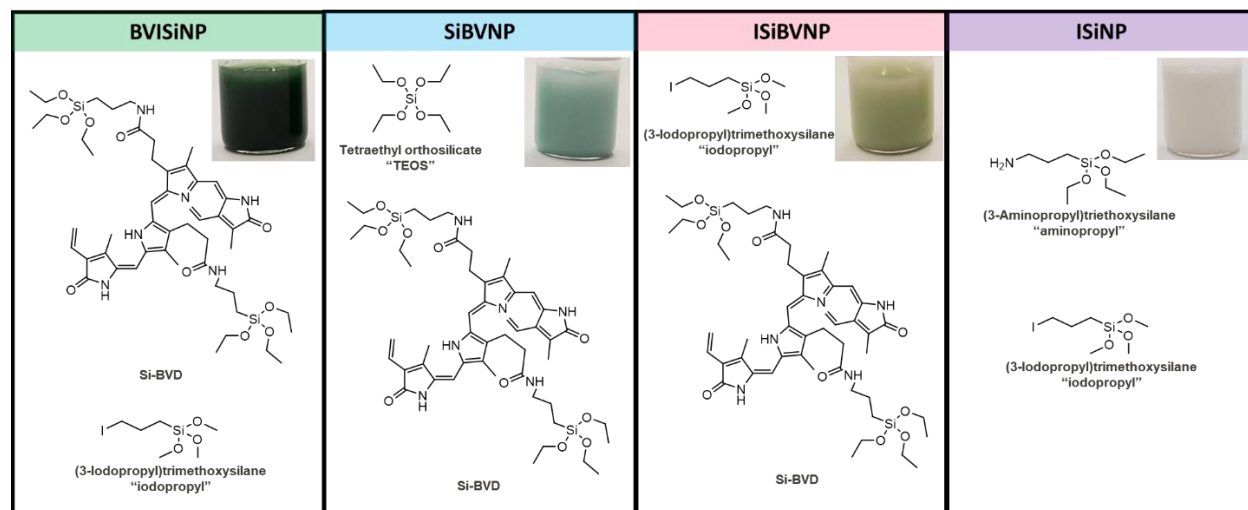
Figure 6.1. Four types of nanoparticles synthesized in the development of hybrid biliverdin-silica nanoparticles.
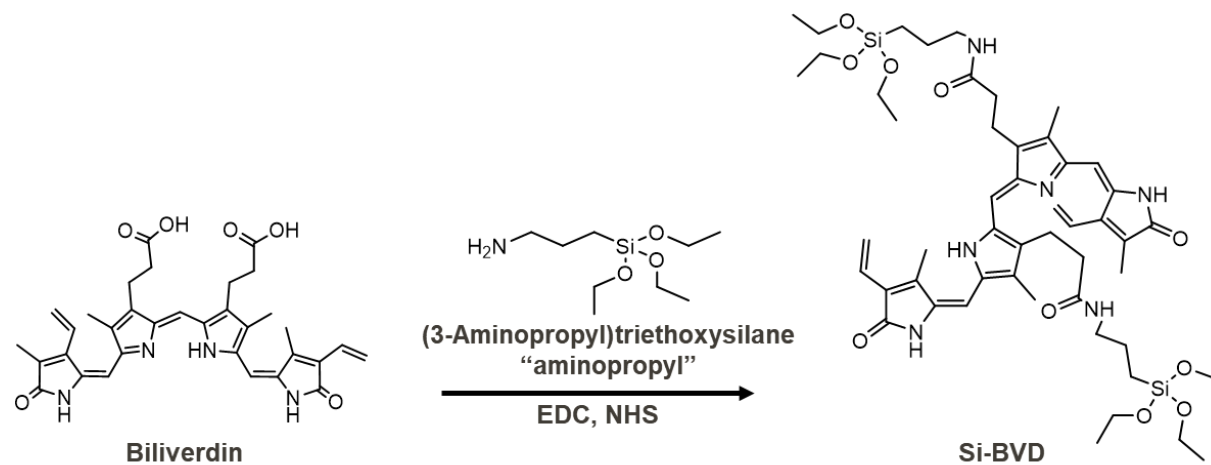
Figure 6.2. Reaction schematic for formation of Si-BVD.
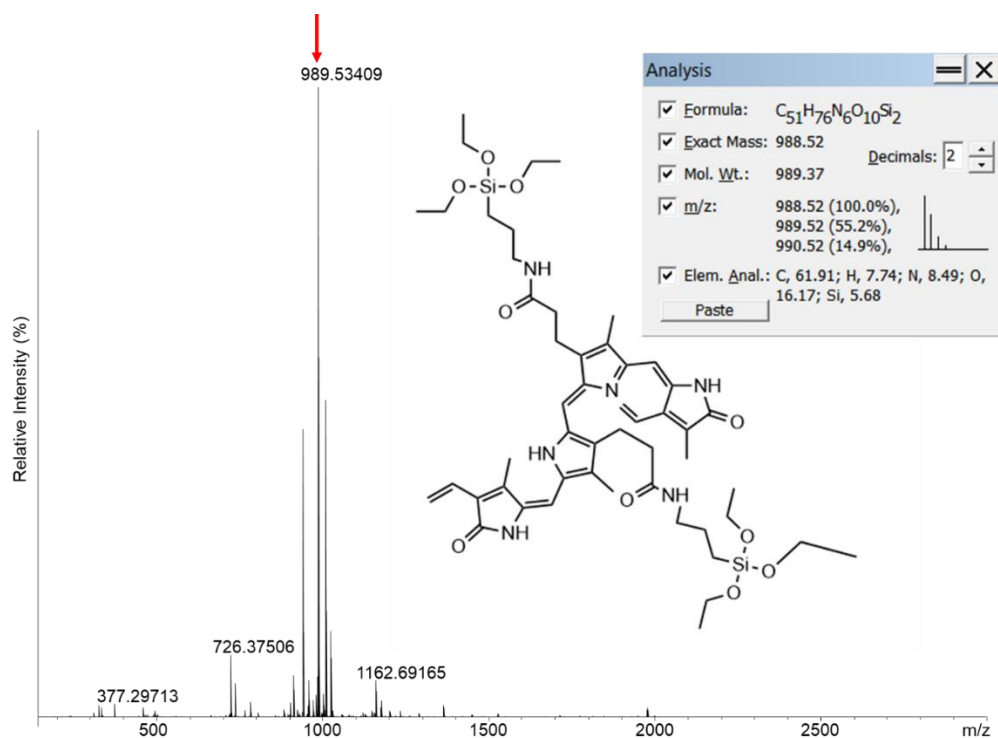
Figure 6.3. Mass spectrometry results for Si-BVD. Formation of Si-BVD molecule was confirmed due to the m/z peak at 989.5.
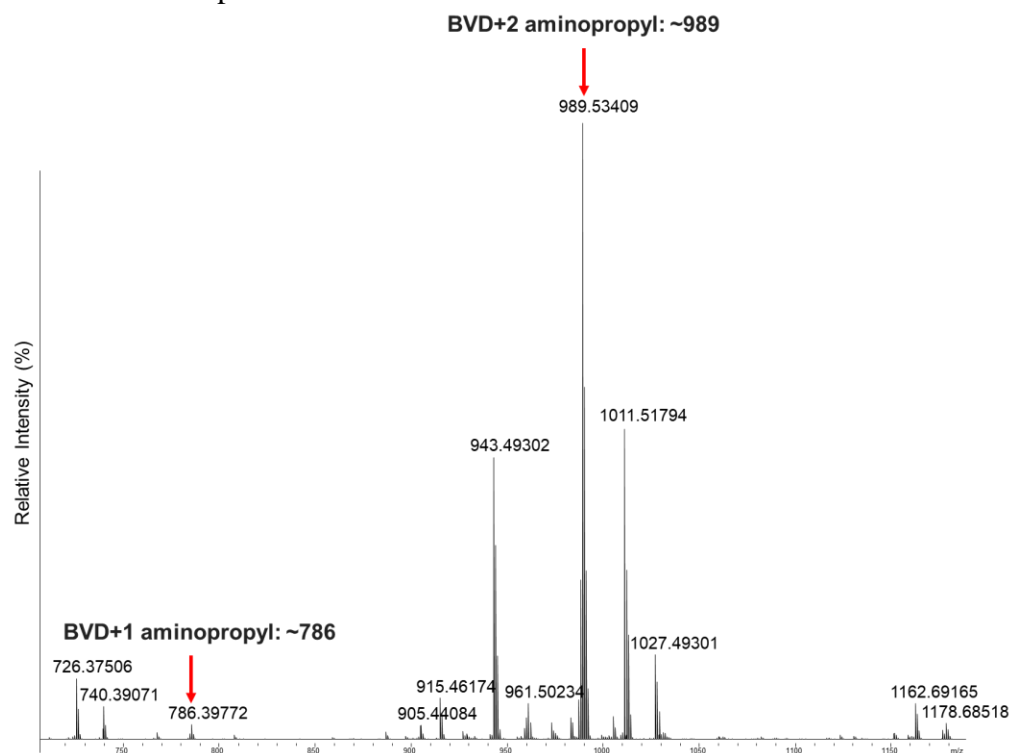
Figure 6.4. Higher-resolution mass spectrometry results for Si-BVD formation.

6.2.2 Synthesis of ISiBVNPs

The ISiBVNPs were the first type of particle synthesized for this project. For these particles, as-prepared Si-BVD was diluted in DMF for a total volume of approximately 1 mL. Iodopropyl was then added, and the particles were placed on a stirplate at room temperature and 500 rpm. The reaction was initiated by the addition of 0.8 mL of ammonium hydroxide, and allowed to continue for 24 h. The samples were then removed and centrifuged at 1500 rpm for 5 min. Samples were washed with water and centrifuged a further two to three times, and the final time each sample was resuspended in 2 mL of water. Synthesis volumes are provided in Table 4.B.1, and molar ratios are provided in Table 4.B.2. In these experiments, we varied the ratio of iodopropyl to aminopropyl, such that the 1X ISiBVNPs had approximately 140.6 iodopropyl molecules per Si-BVD molecule, while the 3X, 5X, and 7X ISiBVNPs had 3X, 5X, and 7X that amount of iodopropyl respectively. This essentially resulting in the synthesis of silica particles that were doped with biliverdin.

Table 6.1. Synthesis volumes for ISiBVNPs. Volumes are provided in μL.

	DMF	Si-BVD	Iodopropyl
ISiBVNP, 1X	956	44.3	46.8
ISiBVNP, 3X	956	44.3	140.4
ISiBVNP, 5X	956	44.3	234
ISiBVNP, 7X	956	44.3	327.6

Table 6.2. Molar ratios of Si-BVD and iodopropyl in ISiBVNPs.

	Si-BVD Used [μmoles]	Iodopropyl used [μmoles]	Molar ratio of Si-BVD:Iodopropyl	Molar ratio of iodopropyl:Si-BVD
ISiBVNP, 1X	1.7	239	0.007112971	140.588235
ISiBVNP, 3X	1.7	717	0.00237099	421.764706
ISiBVNP, 5X	1.7	1195	0.001422594	702.941176
ISiBVNP, 7X	1.7	1673	0.001016139	984.117647

Preliminary characterization conducted on 1X ISiBVNPs determined that the particles formed were large nanoparticles, with a size of approximately 400 nm **(Fig. 6.5)**. The particles

appeared uniform in size, although the presence of some smaller nanoparticles was noted during TEM imaging. UV-Visible spectroscopy revealed that the particles had high absorbance in the near-infrared region, with absorbance that appeared to continue well past 900 nm **(Fig. 6.6)**. This led us to explore the fluorescence behavior of the 1X ISiBVNPs. When placed under 365 nm UV irradiation, the particles appeared to fluoresce a yellow-orange color **(Fig. 6.7 A)**. W undiluted aminopropyl, undiluted iodopropyl, undiluted SiBVD, and undiluted ISiBVNPs were imaged under a gel imager **(Fig. 6.7 B)**. Iodopropyl appeared to have a fluorescence response to blue and green excitation, while neither iodopropyl nor Si-BVD had fluorescence emission for red excitation. On the other hand, ISiBVNPs had fluorescence emission for excitations in the blue, green, and red wavelengths. This indicated that the formation of the particles results in ISiBVNP fluorescence, even in wavelength ranges where the precursors did not fluoresce. This aligns well with the absorbance behavior observed for the particles, with the particles exhibiting a high absorbance across a broad spectrum of wavelengths. This was further examined through fluorescence spectroscopy, and ISiBVNPs were found to have favorable fluorescence, even for excitation wavelengths as high as 700 nm **(Fig. 6.7 C)**. Higher wavelengths were not tested due to limitations in the spectrophotometer operating range.
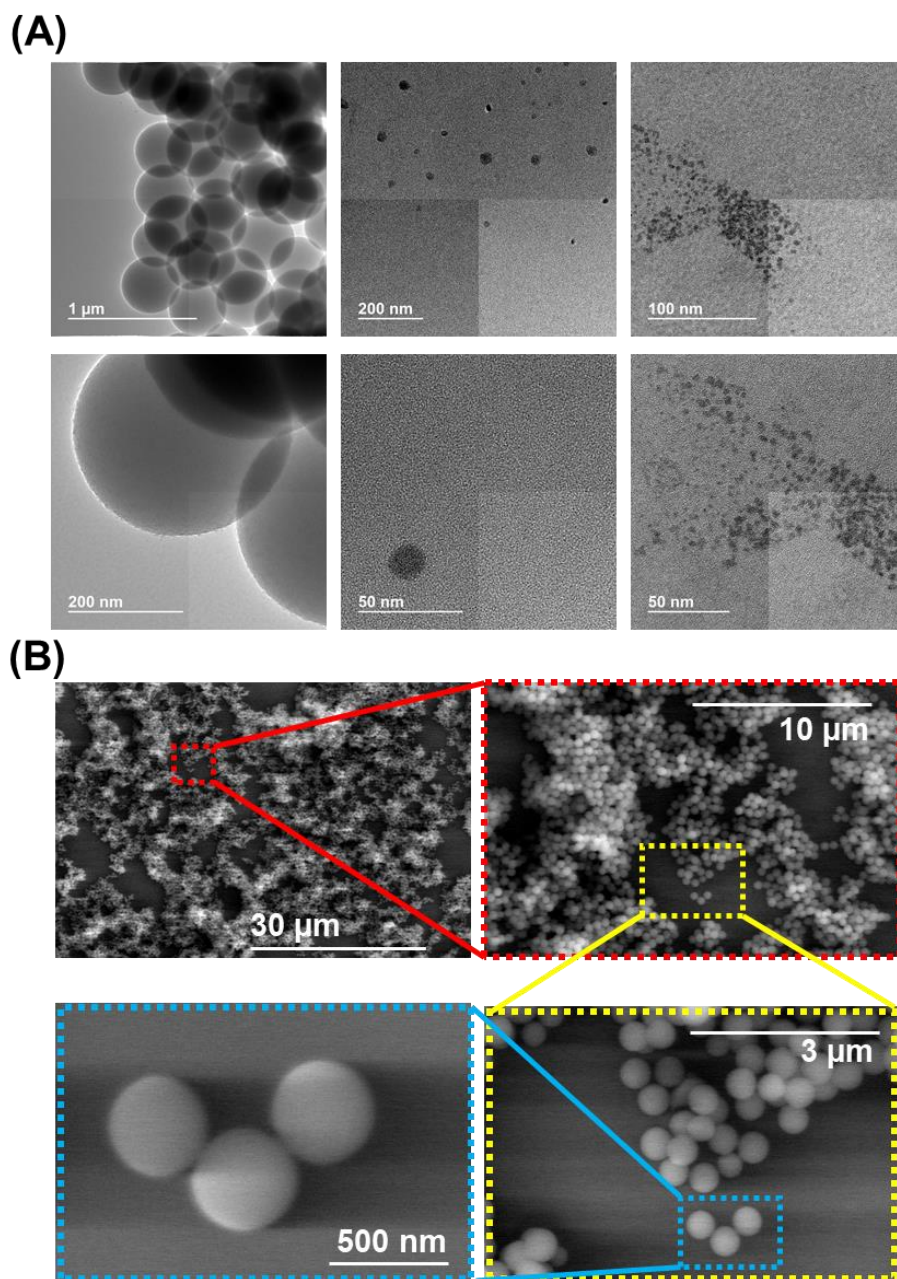
Figure 6.5. Microscopy of 1X ISiBVNPs. **(A)** Transmission electron microscopy images. **(B)** Scanning electron microscopy images. Particles appear monodisperse.
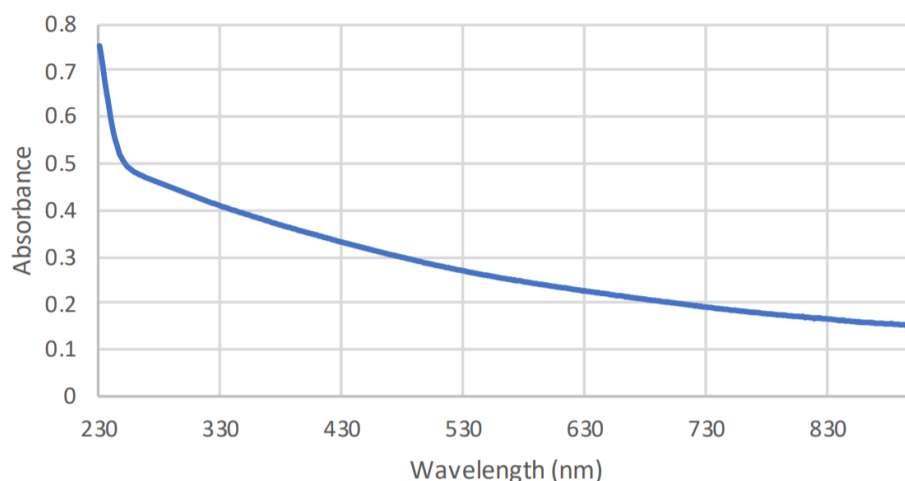
Figure 6.6. UV-visible absorbance spectra for 1X ISiBVNPs diluted in water.

In further experiments, we increased the ratio of iodopropyl:Si-BVD, forming 3X, 5X, and 7X ISiBVNPs. Scanning electron microscopy revealed that the increase in iodopropyl led to an increase in particle size, resulting in the formation of microparticles rather than nanoparticles **(Fig. 6.8)**. We observed that the 7X ISiBVNPs were highly unstable in solution and formed some chunks in addition to the microparticles. This was also apparent in SEM images. Since the particles were believed to have iodine incorporated due to the use of iodopropyl, we examined the X-ray contrast provided by these particles. We initially examined the contrast provided by the 1 X ISiBVNPs **(Fig. 6.9)**. We found that increasing the iodopropyl ratio to 3X, 5X, or 7X increased the contrast, but it was still not very favorable for use as an X-ray contrast agent **(Fig. 6.10)**.
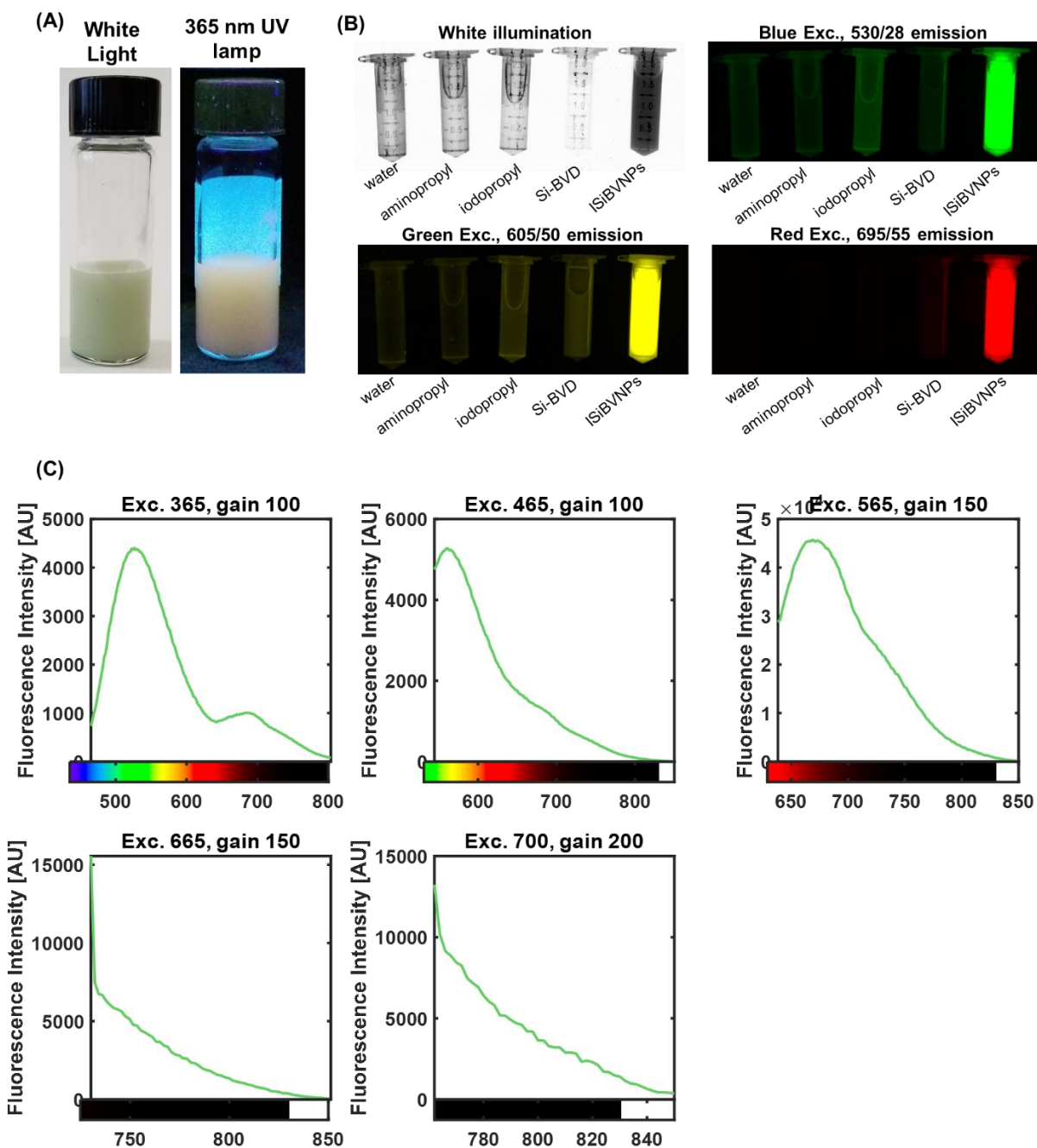
Figure 6.7. Fluorescence behavior of the 1X ISiBVNPs. **(A)** Particles placed under white light vs. 365 nm UV irradiation. **(B)** Water, undiluted aminopropyl, undiluted iodopropyl, undiluted SiBVD, and ISiBVNPs imaged under a gel imager. Iodopropyl appears to have a fluorescence response to blue and green excitation. Neither iodopropyl nor Si-BVD had fluorescence emission for red excitation, but ISiBVNPs did. **(C)** Fluorescence spectra of 1X ISiBVNPs for various excitations and gains.
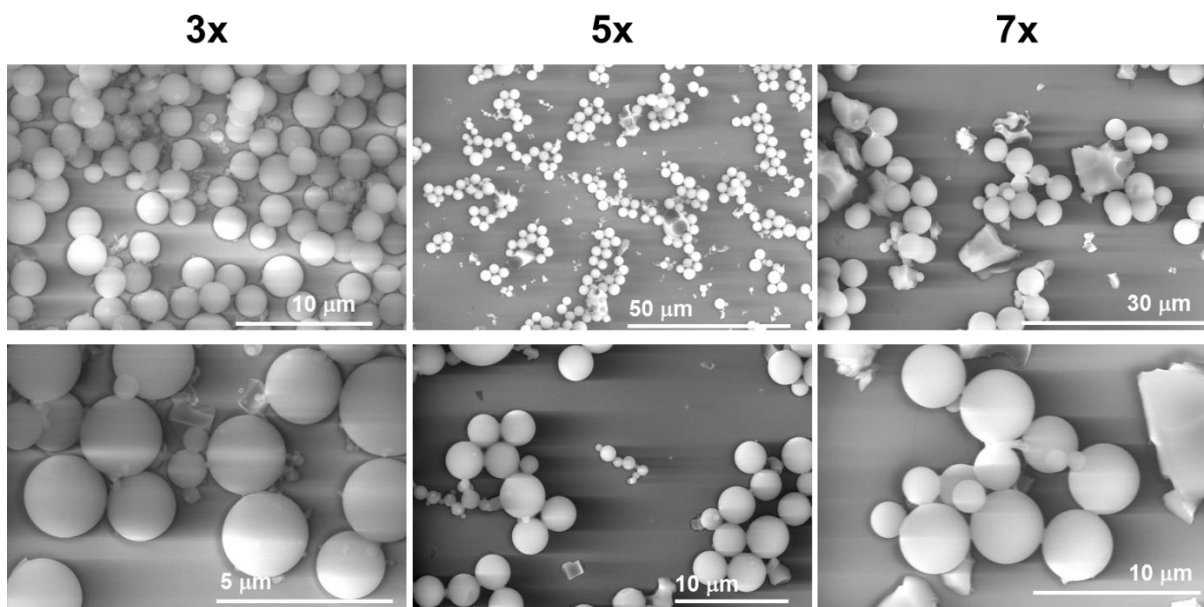
Figure 6.8. Scanning electron microscopy images of 3X, 5X, and 7X ISiBVNPs. The higher amount of iodopropyl in these particles led to the formation of microparticles rather than nanoparticles.
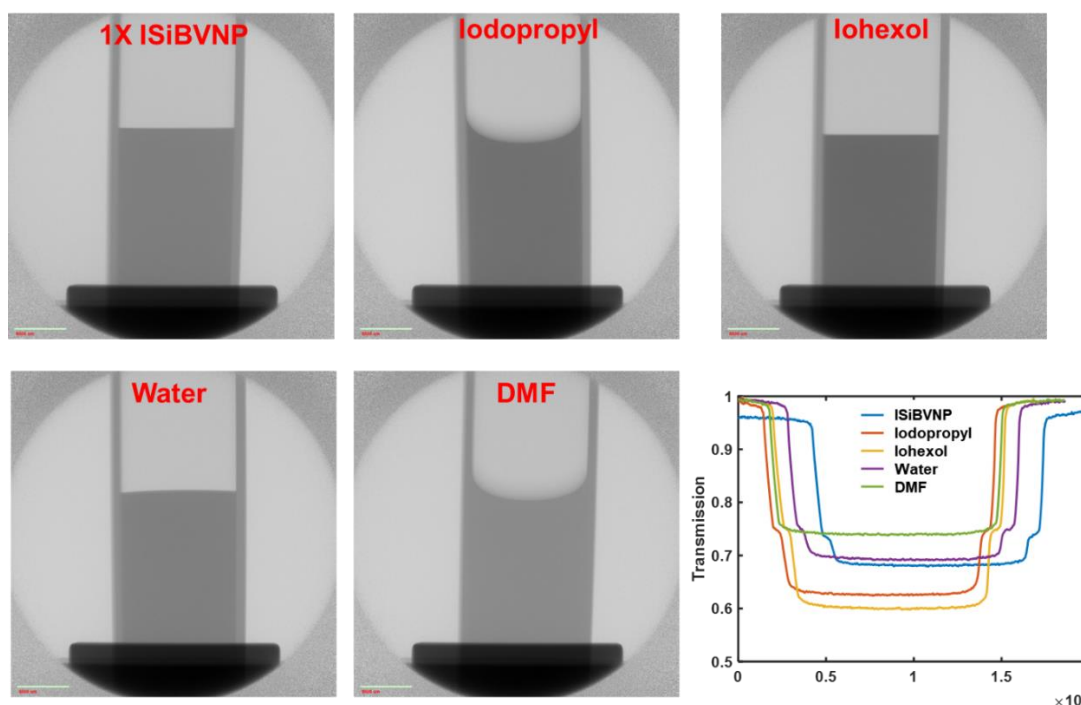
Figure 6.9. X-ray contrast for ISiBVNPs compared to iodopropyl (diluted in DMF to the iodopropyl concentration used for the synthesis), iohexol (dissolved in water at equivalent molar iodine concentration to that of the iodopropyl used in the reaction), water, and DMF. Quantitative analysis revealed that iodopropyl and iohexol provide slightly less transmission than water. The 1X ISiBVNPs provided similar transmission to water, indicating that they provided poor X-ray contrast.

140
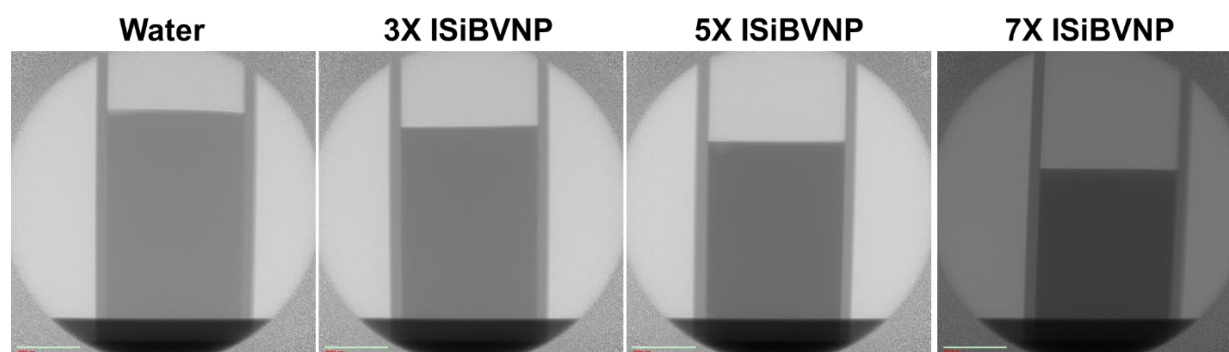
Figure 6.10. X-ray contrast for 3X, 5X, and 7X ISiBVNPs. An increase in iodopropyl content led to an increase in X-ray contrast. However, contrast was still very low compared to what would be useful for an X-ray contrast agent.

6.2.3 Synthesis of BVISiNPs, SiBVNPs, and ISiNPs

We next synthesized BVISiNPs, SiBVNPs, and ISiNPs using the synthesis parameters provided in **Table 6.3**, **Table 6.4**, and **Table 6.5**. We observed that the particle colors differed based on the ratios of precursors. We conducted absorbance measurements in the full range between 200 nm and 2000 nm, finding that the particles provide absorbance in the near-infrared II region **(Fig. 6.11)**. This proves promising for potential applications in NIR-II imaging.

Table 6.3. Synthesis volumes for BVISiNPs, SiBVNPs, and ISiNPs. Volumes are provided in μL.

	DMF	Si-BVD	Diluted Aminopropyl	Iodopropyl	TEOS
BVISiNP, reg	-	1000	-	46.8	-
BVISiNP, high	-	1000	-	225.6	-
SiBVNP, 1X	956	44.3	-	-	53.4
SiBVNP, 5X	956	44.3	-	-	267
ISiNP, 1X	956	-	44.3	46.8	-
ISiNP, 5X	956	-	44.3	234	-

Table 6.4. Synthesis quantities for BVISiNPs, SiBVNPs, and ISiNPs.

	Si-BVD Used [μmoles]	Iodopropyl used [μmoles]	TEOS used [μmoles]
BVISiNP, reg	38.4	239	-
BVISiNP, high	38.4	1152.103	-
SiBVNP, 1X	1.7	-	239
SiBVNP, 5X	1.7	-	1195
ISiNP, 1X	-	239	-
ISiNP, 5X	-	1195	-
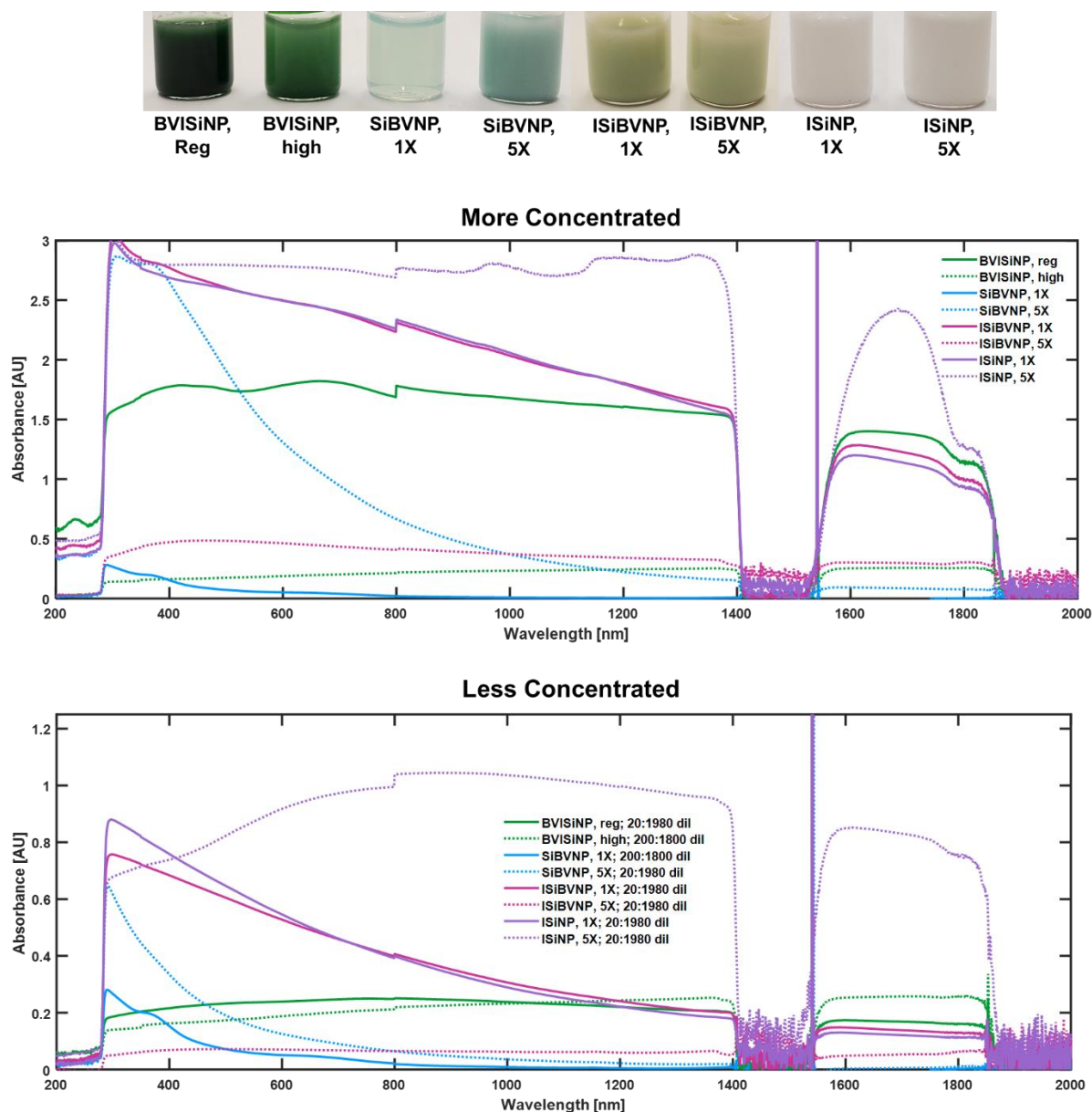
Figure 6.11. Nanoparticle suspensions and absorbance measurements in the full range from 200 nm to 2000 nm. The two expected absorbance peaks of biliverdin are clearly visible in the BV ISiNP, reg spectrum for the more concentrated samples. All samples appeared to have absorbance in the NIR-II region, although the SiBVNPs appear to have the least amount of absorbance. However, the concentrations of these particles are not directly comparable. The particles must be lyophilized and resuspended at equivalent masses for a better understanding of how their absorbance behaviors compare.

Table 6.5. Molar ratios for BVISiNPs, SiBVNPs, and ISiNPs.

	Molar ratio of Si-BVD:Iodopropyl	Molar ratio of iodopropyl:Si-BVD	Molar Ratio of Si-BVD: TEOS	Molar Ratio of TEOS:Si-BVD	Molar ratio of iodopropyl:aminopropyl
BVISiNP, reg	0.160669	6.223958	-	-	-
BVISiNP, high	0.03333	30.00267	-	-	-
SiBVNP, 1X	-	-	0.007112971	140.588235	-
SiBVNP, 5X	-	-	0.001422594	702.941176	-
ISiNP, 1X	-	-	-	-	360.7096
ISiNP, 5X	-	-	-	-	1803.548

6.3 CONCLUSIONS AND FUTURE WORK

We have demonstrated the synthesis of hybrid-biliverdin silica nanoparticles. Further characterization is required, including SEM and TEM imaging of the BVISiNPs, SiBVNPs, and ISiNPs. Preliminary experiments revealed absorbance in the near-infrared II region. This indicates that the synthesized hybrid particles may be useful as a NIR-II contrast agent. NIR-II microscopy experiments and in vivo studies should be conducted to demonstrate this capability of the nanoparticles. Other variations of the particles can also be synthesized with crosslinkers aside from iodopropyl (**Fig. 6.12**).
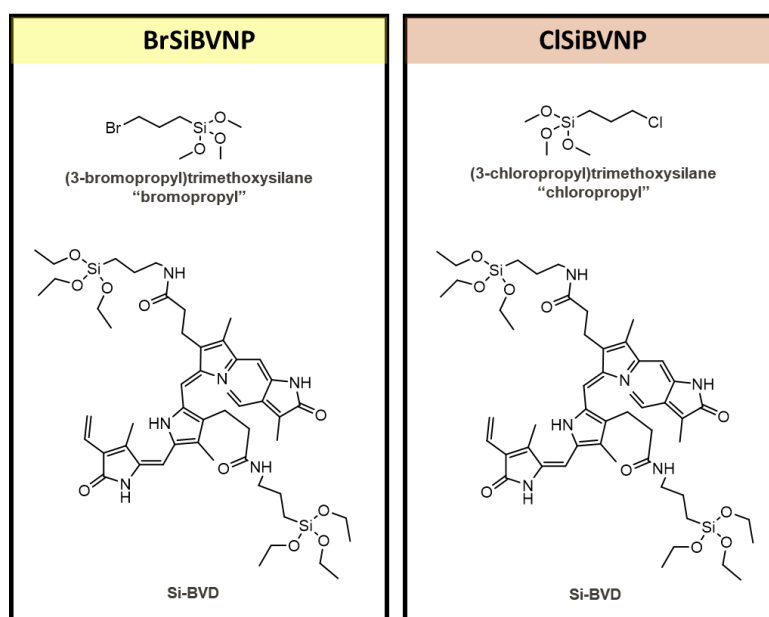
Figure 6.12. Other possible synthesis variations.

CHAPTER 7: THERAPEUTIC APPLICATIONS OF BILIVERDIN NANOPARTICLES

7.1 ABSTRACT

Recently, we reported the synthesis of biodegradable photoacoustic nanoparticles formed by nanoprecipitation of biliverdin, an endogenous chromophore. In further work, we have utilized these nanoparticles for targeted delivery of chemotherapeutic agents for treatment of triple-negative breast cancer. We have demonstrated that doxorubicin-loaded biliverdin nanoparticles (Dox-BVNPs) provide a platform for controlled release of doxorubicin, while also maintaining a high near-infrared absorbance, providing photoacoustic and fluorescent imaging contrast. The therapeutic efficacy of these nanoparticles was demonstrated in both MDA-MB-231 and 4T1 breast cancer cells, and their uptake mechanism was determined through inhibitor studies. Dox-BVNPs were extensively characterized with UV-visible spectroscopy, fluorescence spectroscopy, FT-IR spectroscopy, transmission electron microscopy, scanning electron microscopy, and zeta potential measurements. The use of Dox-BVNPs for *in vitro* and *in vivo* image-guided therapy was also explored.

7.2 INTRODUCTION

Breast cancer has the second-highest mortality among cancer types and accounts for 11.6% of cancer deaths[348]. For women, it is the most commonly diagnosed and leading cause of cancer-related death[348]. Breast cancer disproportionately affects racial minorities[349]. Of the different breast cancer subtypes, basal-like breast cancer, a particularly aggressive subtype, accounts for 11% of breast cancer cases in white women, and 22% of breast cancer cases in African American women[350]. Breast cancer subtypes affect the targeting mechanisms and efficacy of therapeutic interventions[351]. In aggressive subtypes such as triple-negative breast cancer, there is a lack of targeted therapeutics, leading to poor prognosis[352]. The goal of this work was to utilize biliverdin

nanoparticles for combined drug delivery and photothermal therapy of triple-negative breast cancer **(Fig. 7.1)**.
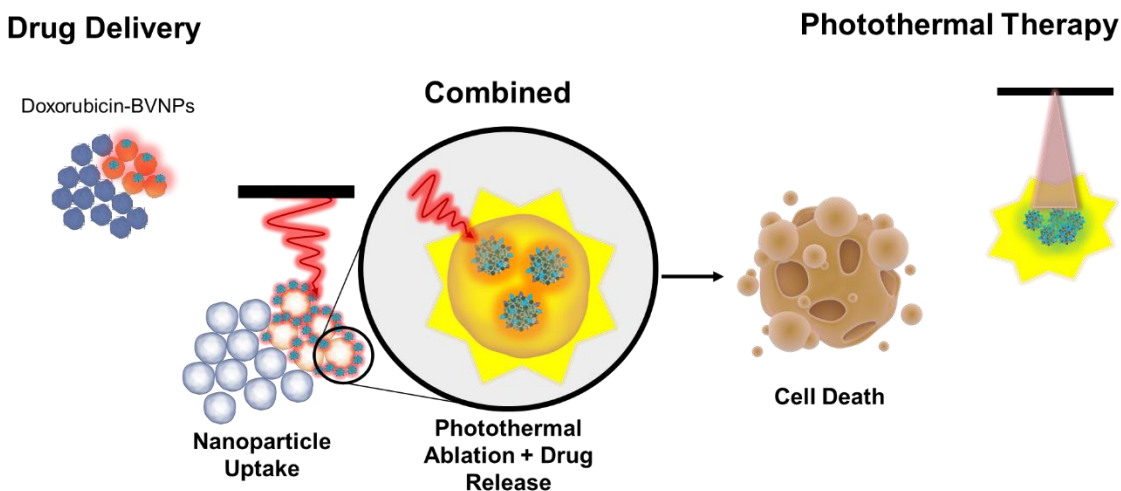
Figure 7.1. Proposed use of doxorubicin-loaded biliverdin nanoparticles for combined drug delivery and photothermal therapy.

7.3 RESULTS AND DISCUSSION

7.3.1 Electron Microscopy

Dox-BVNPs were obtained by EDC-NHS crosslinking **(Fig 7.2)**. Similar to the BVNP synthesis, Dox-BVNP synthesis was done at two time-scales: 10 min and 24 h. The resulting particle suspensions contained both microparticles and nanoparticles, which could be separated from each other via centrifugation. Transmission electron microscopy images of 10 min NaCl-BVNPs, 10 min Dox-BVNPs, and 24 h Dox-BVNPs reveal particles with sizes below 100 nm **(Fig. 7.3A)**. Interestingly, 24 h Dox-BVNPs possess crystalline structures that are characteristic of previously reported doxorubicin-loaded nanoparticles.[353] Scanning electron microscopy micrographs of 10 min and 24 h doxorubicin-loaded particles reveal the presence of microparticles (approximately 2-3 µm diameter) in the uncentrifuged particle suspensions **(Fig. 7.3B)**. Particles reacted for 10 min had more clearly distinguishable microparticles than those reacted for 24 h,

which appeared to have many microparticles fused together. The microparticles from the 10 min reacted particle population also exhibit a nonuniform surface that appears to be decorated with smaller particles. This is likely due to the presence of multiple particle populations that become linked as the EDC-NHS crosslinking process continues. From this point forward, the full particle population will be referred to as Dox-BVPs, while the nanoparticles separated by centrifugation will be referred to as Dox-BVNPs.
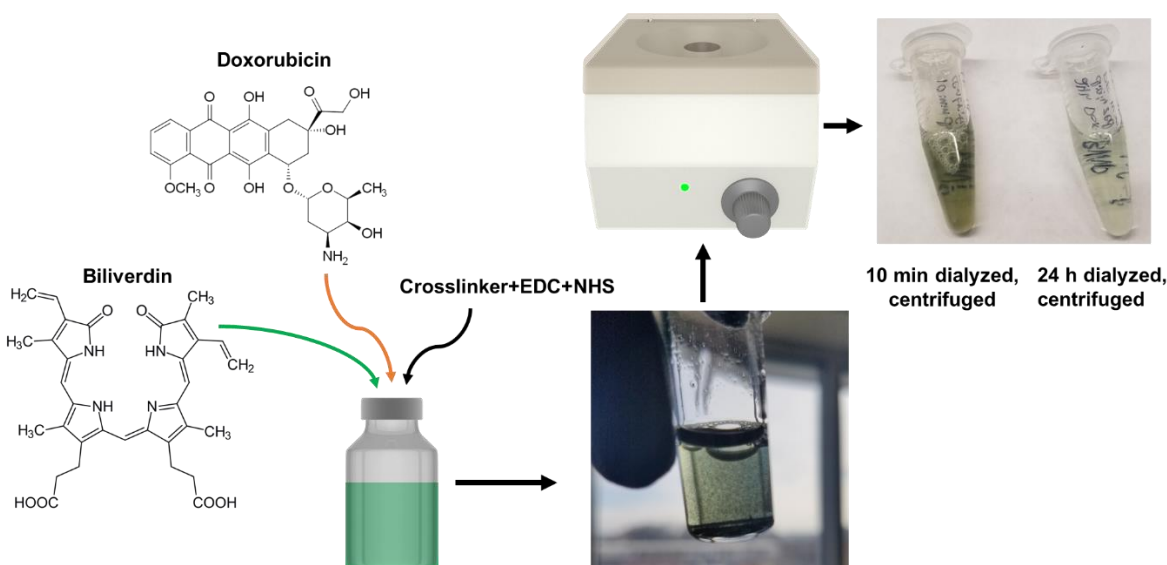
Figure 7.2. Synthesis of Dox-BVNPs. A solution of doxorubicin and biliverdin is formed, and nanoparticles are synthesized via EDC-NHS crosslinking. After dialysis, the resulting particle suspension includes both microparticles and nanoparticles. The nanoparticles can be separated from the microparticles via centrifugation.

7.3.2 Zeta Potential and FT-IR spectroscopy

Zeta potential measurements were conducted on the Dox-BVPs after dialysis and Dox-BVNPs after dialysis (**Fig. 7.4**). Dox-BVNPs had an overall greater magnitude of zeta potential compared to Dox-BVPs, indicating their greater stability. 10 min and 24 h Dox-BVNPs had zeta potentials of between -15 and -20 mV. FT-IR spectra of 10 min and 24 h Dox-BVPs after dialysis reveal many similarities to those of BVNPs and biliverdin. Collection of FT-IR spectra of doxorubicin alone should be conducted for further comparison.

(A)

10 min NaCl-BVNP   **10 min Dox-BVNP**

200 nm   200 nm   200 nm

24 h Dox-BVNP

0.2 μm   0.2 μm   100 nm

(B)   **10 min Dox-BVNP**

10 μm   5 μm   4 μm

24 h Dox-BVNP

20 μm   5 μm   5 μm
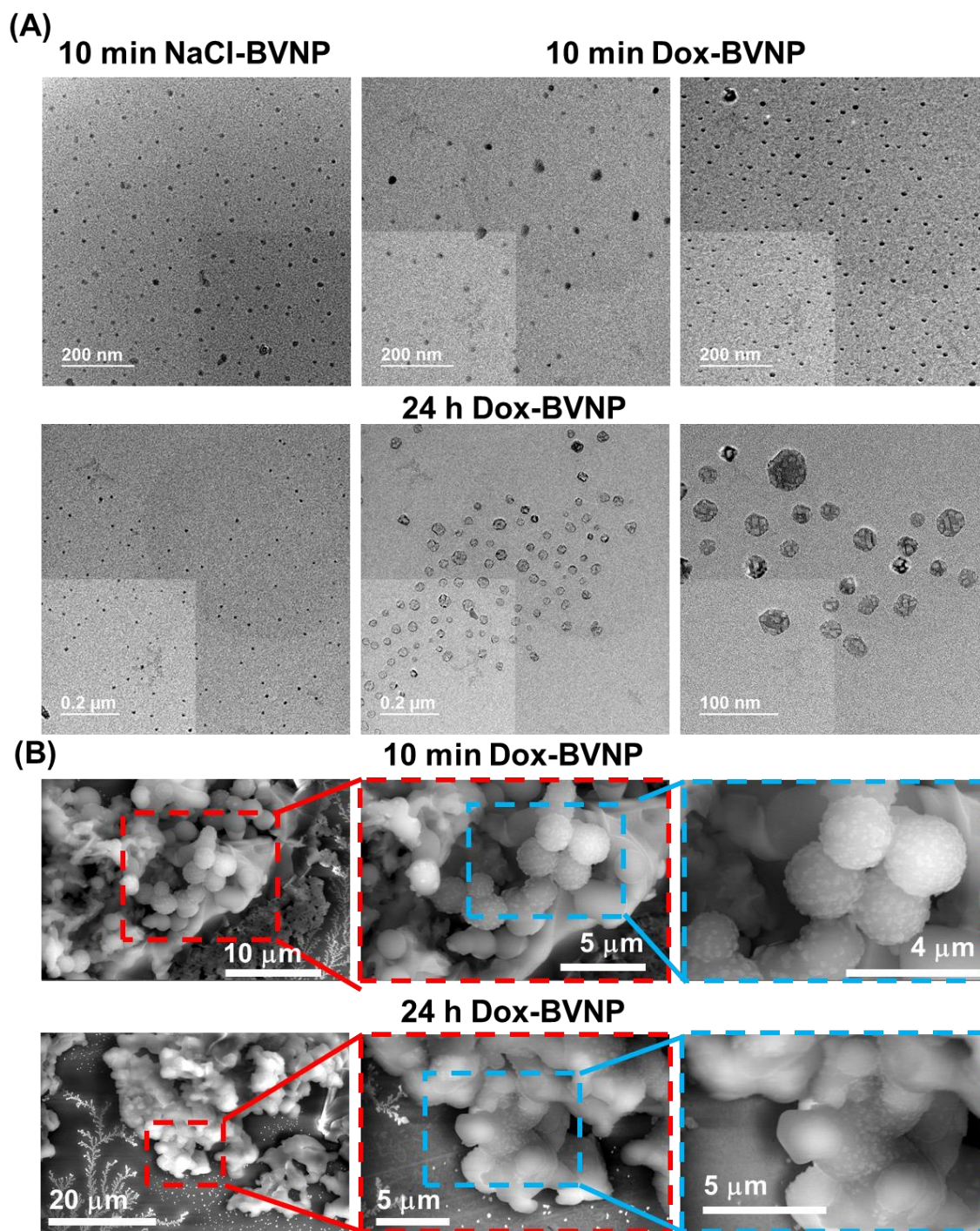
Figure 7.3. Electron microscopy on Dox-BVNPs and Dox-BVPs. (**A**) Transmission electron microscopy images of 10 min NaCl-BVNPs, 10 min Dox-BVNPs (after centrifugation), and 24 h Dox-BVNPs (after centrifugation). 10 min NaCl-BVNPs and 10 min Dox-BVNPs appear similar in size. 24 h Dox-BVNPs exhibit larger particle sizes as a result of the longer reaction time. (**B**) Scanning electron microscopy images of 10 min Dox-BVPs and 24 h Dox-BVPs without centrifugation. Presence of microparticles is apparent in SEM images.

147
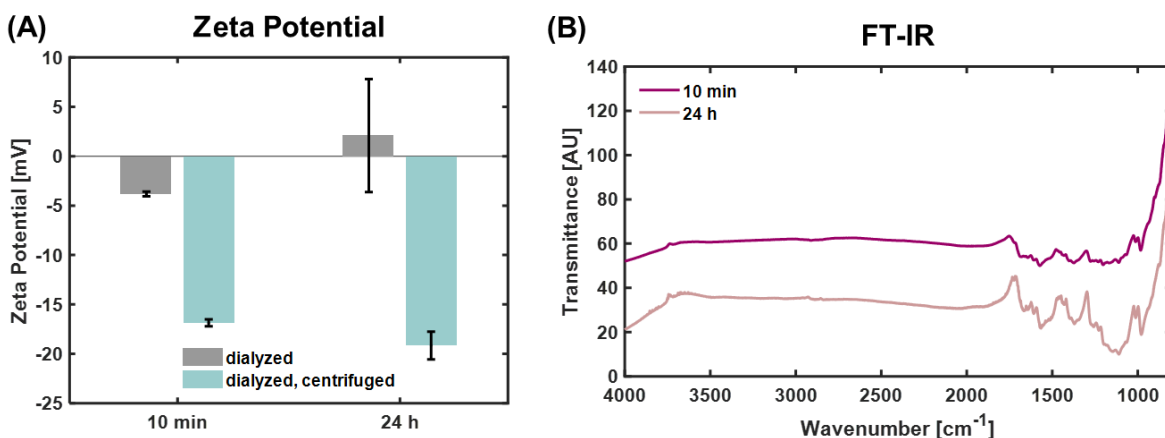
Figure 7.4. (A) Zeta potential measurements of the Dox-BVPs and Dox-BVNPs. **(B)** FT-IR spectra of the uncentrifuged Dox-BVNPs.

7.3.3 UV-Visible Spectroscopy and UV Lamp Imaging

UV-Visible spectroscopy was conducted to confirm the successful loading of doxorubicin within the nanoparticles. First, the absorbance spectra of various concentrations of doxorubicin (Dox) were collected to determine the location of the absorbance peak and determine the linearity of absorbance intensity with concentration. Doxorubicin was found to have an absorbance peak at approximately 480 nm **(Fig. 7.5A)**. We further found that doxorubicin had no absorbance between 600 and 900 nm. The linearity of doxorubicin's 480 nm absorbance allowed for the establishment of a linear calibration curve relating the concentration of doxorubicin to the 480 nm absorbance **(Fig. 7.5B)**. Next, the absorbance spectra of as-prepared dialyzed 10 min and 24 h NaCl-BVNPs and Dox-BVNPs were collected **(Fig. 7.6, Fig. 7.7)**. The nanoparticle absorbances at 365 nm, 480 nm, 670 nm, and 680 nm scaled approximately linearly with concentration, indicating that absorbance spectroscopy would be a reliable technique for determination of nanoparticle concentration. Through visual observation and absorbance spectroscopic measurements, it became apparent that there was an overall lower concentration of nanoparticles in the 24 h Dox-BVNPs than in the 10 min Dox-BVNPs. This was documented with images taken under white light, 365

nm UV light, and 254 nm UV light (**Fig. 7.8, Fig. 7.9**). 10 min and 24 h Dox-BVNPs were

calculated to have encapsulation efficiencies of 8.91 % and 2.52 % respectively; the encapsulation

efficiencies of 10 min and 24 h Dox-BVPs were found to be 29.38 % and 84.7 % respectively.

Thus, the loading of doxorubicin within the Dox-BVP population was highly efficient, but the

loading of doxorubicin within the Dox-BVNP population was lower in efficiency because the

majority of the doxorubicin was loaded within the microparticles.
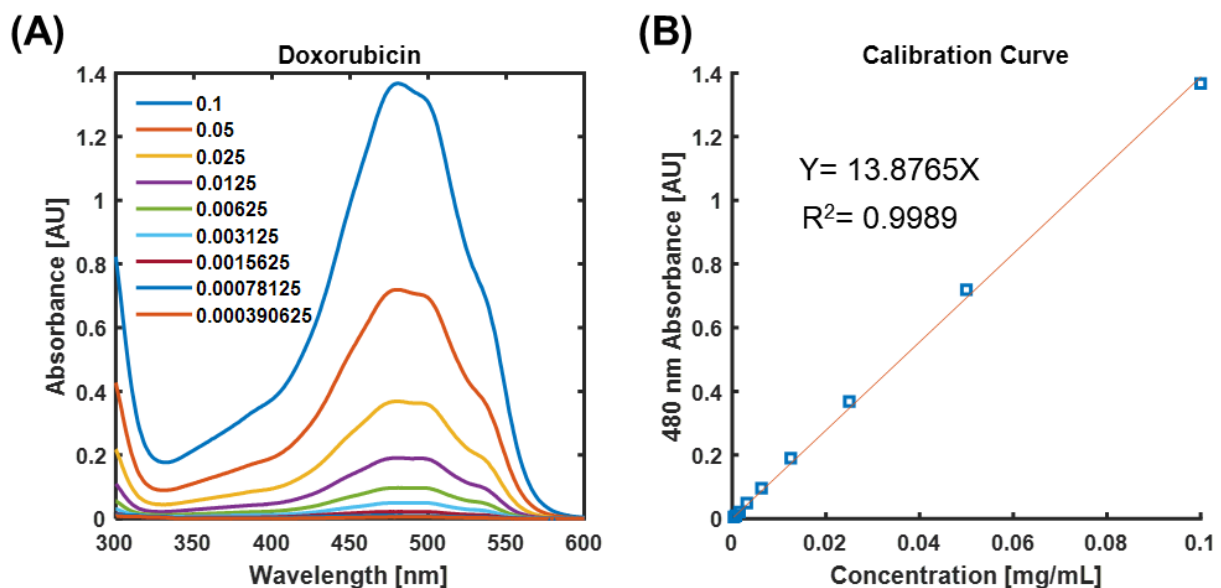
Figure 7.5. (A) UV-visible spectra of various concentrations (mg/mL) of doxorubicin in water.
(B) 480 nm absorbance was found to scale linearly with doxorubicin concentration.

(A)

(B)
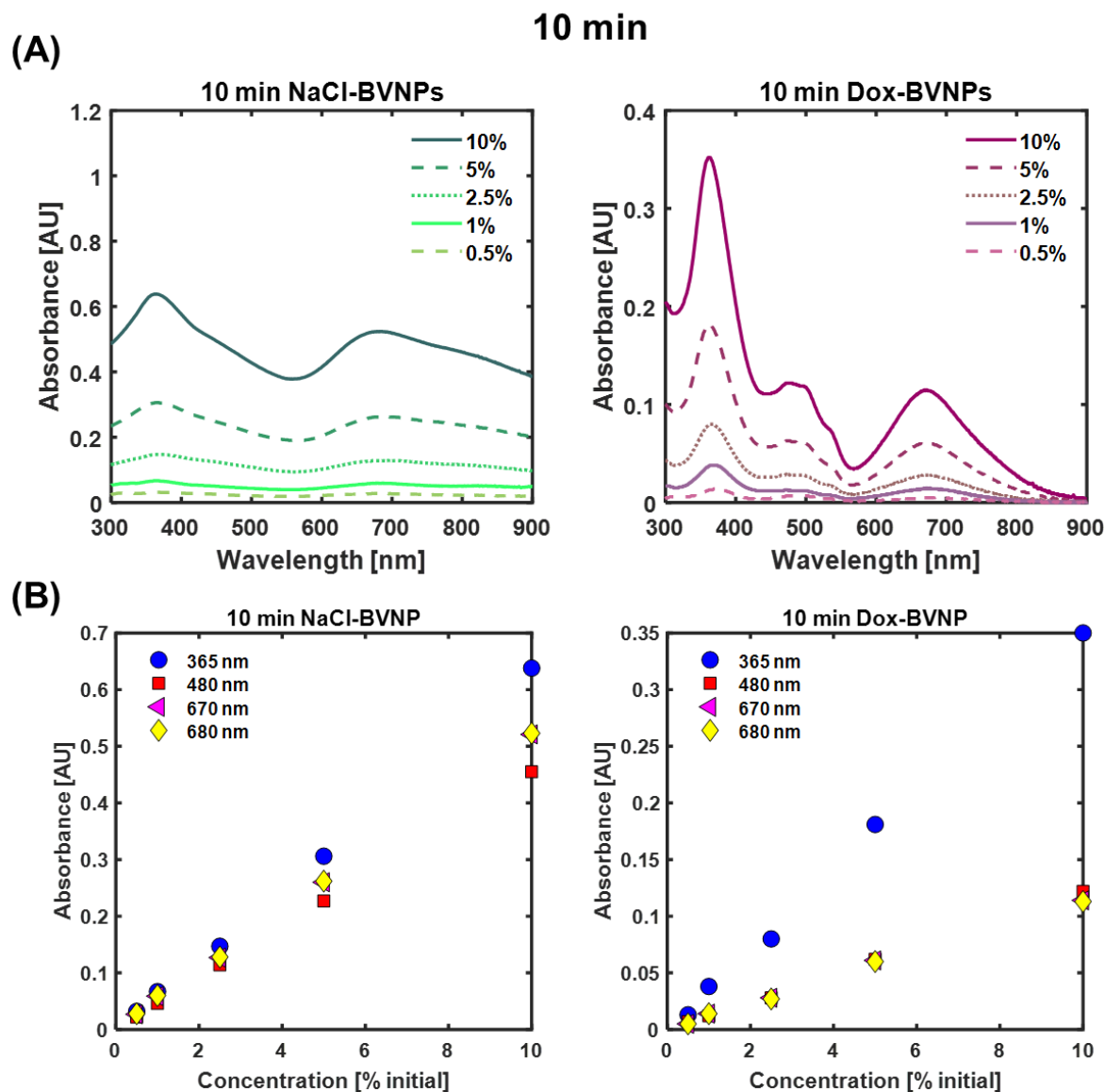
Figure 7.6. Absorbance of 10 min NaCl-BVNPs and 10 min Dox-BVNPs (after centrifugation) **(A)** absorbance spectra at various concentrations. Concentrations are expressed as a final volumetric ratio of the as-prepared undiluted dialyzed nanoparticle solutions. **(B)** Absorbance at 365 nm, 480 nm, 670 nm, and 680 nm. Absorbances appear approximately linear with concentration.
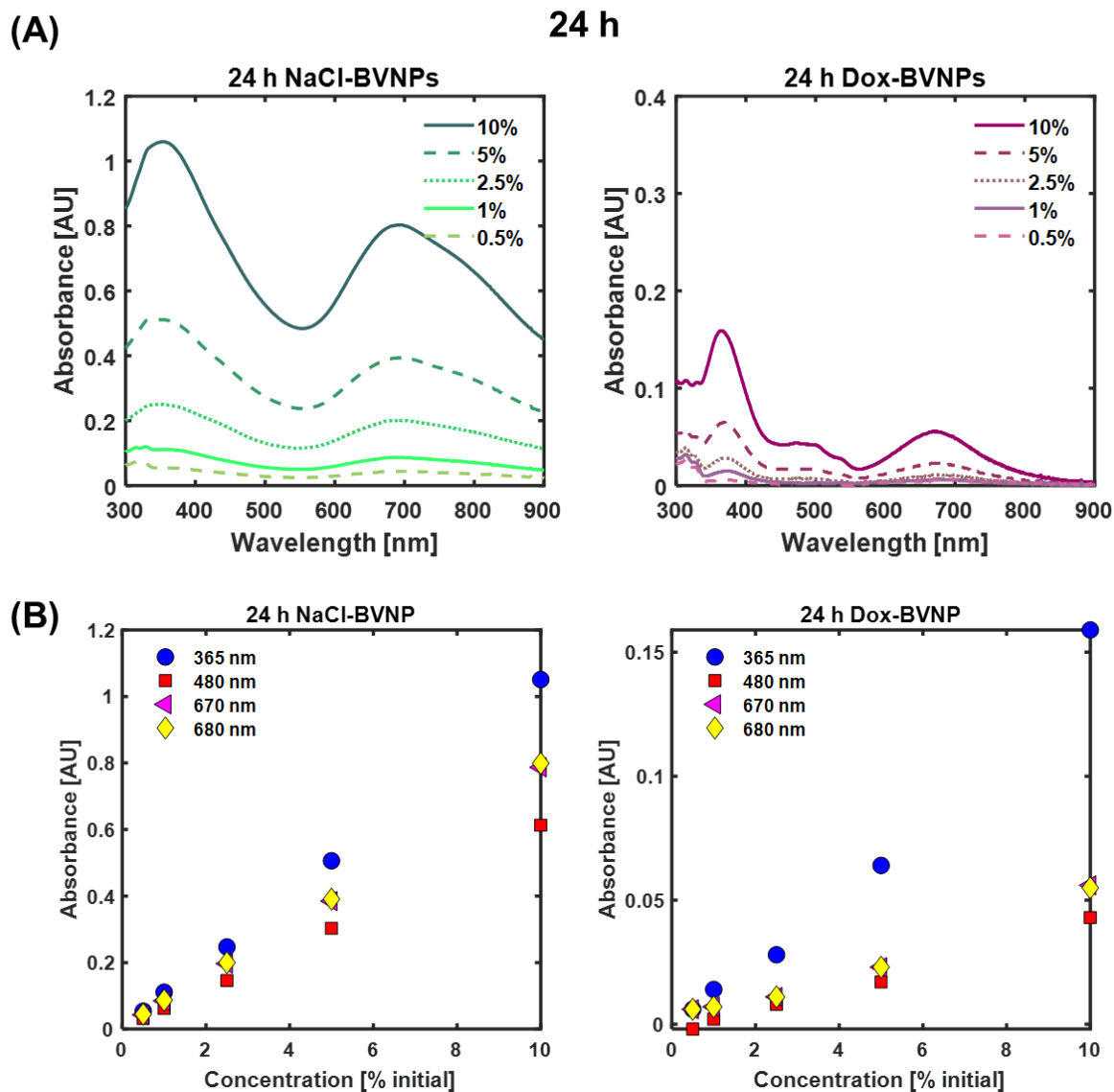
Figure 7.7. Absorbance of 24 h NaCl-BVNPs and 24 h Dox-BVNPs (after centrifugation) **(A)** absorbance spectra at various concentrations. Concentrations are expressed as a final volumetric ratio of the as-prepared undiluted dialyzed nanoparticle solutions. **(B)** Absorbance at 365 nm, 480 nm, 670 nm, and 680 nm. Absorbances appear approximately linear with concentration.
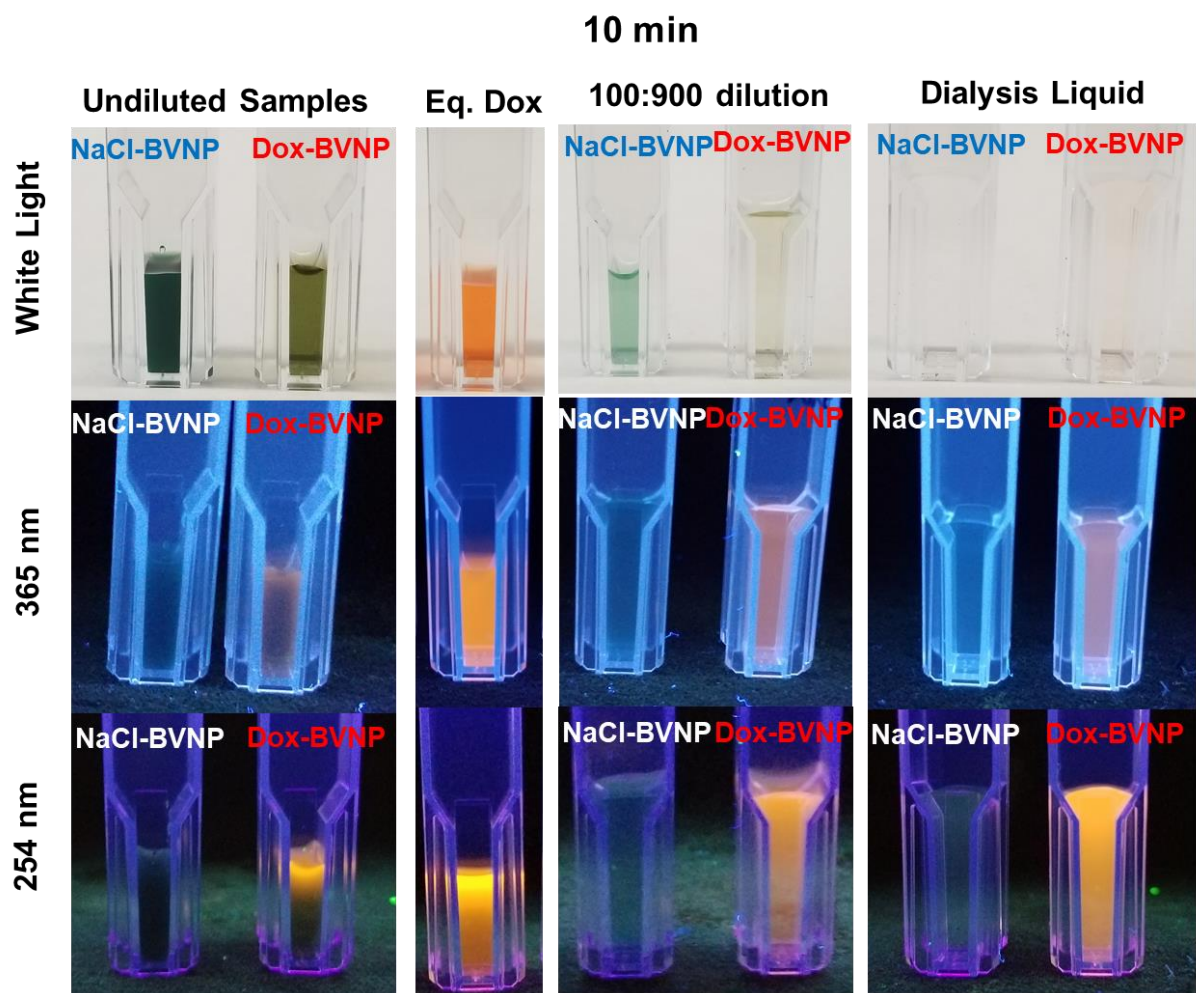
Figure 7.8. 10 min NaCl-BVNPs and 10 min Dox-BVNPs under white light, 365 nm UV light, and 254 nm UV light. Doxorubicin at an equivalent concentration to that loaded in the 10 min Dox-BVNPs is shown for comparison. The color of Dox-BVNP fluorescence is more apparent when diluted at a 100:900 dilution of particles to diluent. The dialysis liquid from Dox-BVNPs has the characteristic orange fluorescence of doxorubicin, indicating some of the drug was not loaded within the particles.
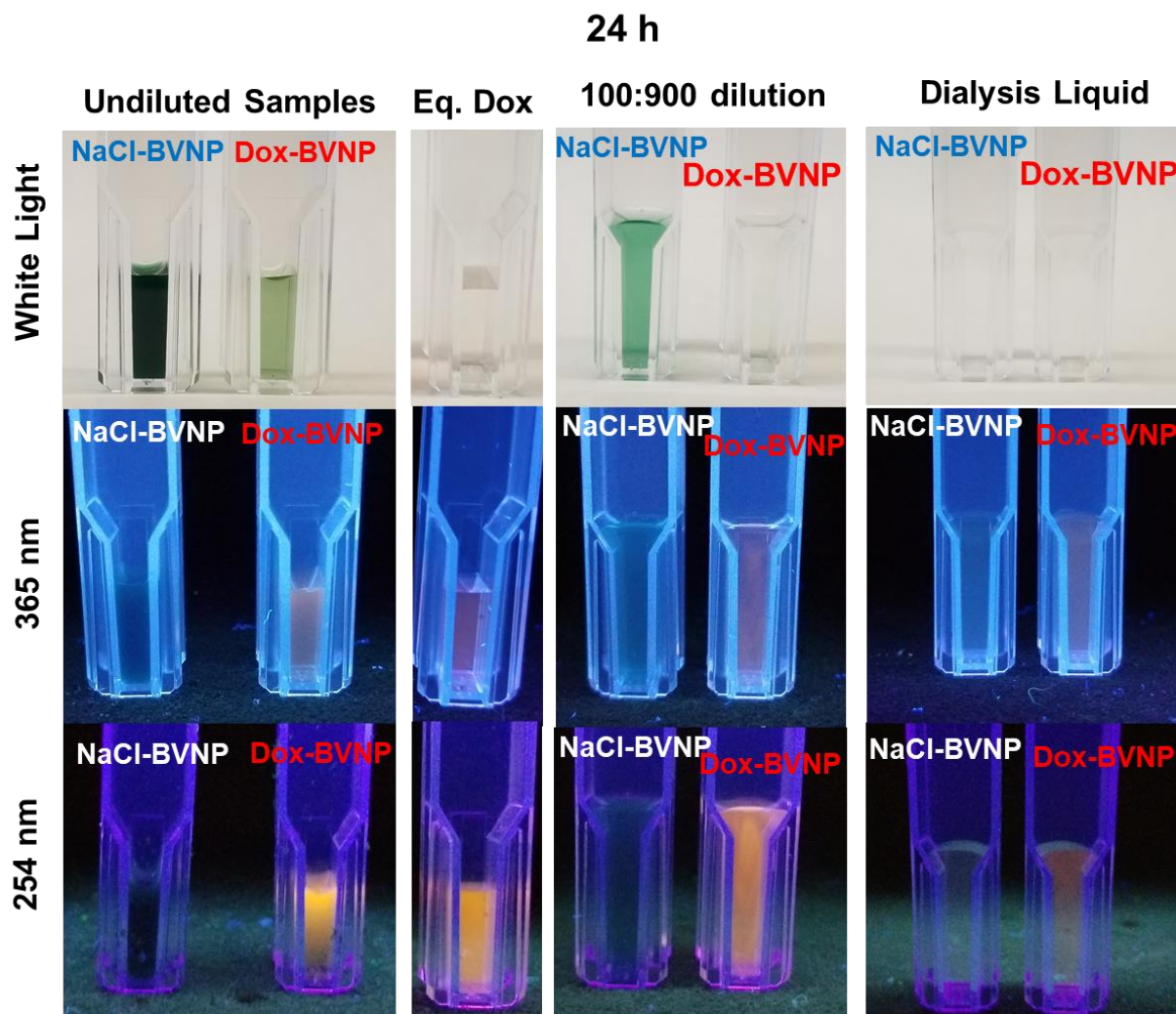
Figure 7.9. 24 h NaCl-BVNPs and 24 h Dox-BVNPs under white light, 365 nm UV light, and 254 nm UV light. Doxorubicin at an equivalent concentration to that loaded in the 10 min Dox-BVNPs is shown for comparison. The color of Dox-BVNP fluorescence is more apparent when diluted at a 100:900 dilution of particles to diluent. The dialysis liquid from Dox-BVNPs has the characteristic orange fluorescence of doxorubicin, indicating some of the drug was not loaded within the particles.

7.3.4 Fluorescence Spectroscopy

We then conducted fluorescence spectroscopy on the 10 min and 24 h NaCl-BVNPs and Dox-BVNPs. Fluorescence spectra of Dox-BVNPs contained two emission peaks, reflecting the emission peaks of both NaCl-BVNPs and doxorubicin **(Fig. 7.10A, Fig. 7.11A)**. For 365 nm excitation, lower concentrations of NaCl-BVNPs have higher fluorescence emission intensities than undiluted NaCl-BVNPs. This indicates that NaCl-BVNPs have a fluorescence quenching

effect upon themselves with increasing concentration. Additionally, for 365 nm excitation, lower concentrations of Dox-BVNPs have a higher fluorescence emission peak in the 400-500 nm range (i.e. fluorescence intensity and concentration have an inverse relationship in this emission range); higher concentrations of Dox-BVNPs have a higher fluorescence emission peak at approximately 600 nm **(Fig. 7.10A, Fig. 7.11A)** (i.e. fluorescence intensity and concentration have a direct relationship in this emission range). For 465 nm and 500 nm excitation, the fluorescence intensity of Dox-BVNPs and NaCl-BVNPs scales with the nanoparticle concentration **(Fig. 7.10 B-C, Fig. 7.11 B-C)**. For all excitation wavelengths, the maximum fluorescence intensity of 10 min Dox-BVNPs was lower than the maximum fluorescence intensity of an equivalent concentration of doxorubicin **(Fig. 7.10)**. This suggests that encapsulation of doxorubicin within NaCl-BVNPs can lead to a quenching of doxorubicin's fluorescence due to interactions between the fluorescence of biliverdin and doxorubicin. Furthermore, the amount of doxorubicin incorporated within the as-prepared dialyzed Dox-BVNPs was higher 10 min into the synthesis than 24 h into the synthesis. This was likely a result of a tendency towards the formation of microparticles rather than nanoparticles with increasing reaction time. Thus, 10 min NaCl-BVNPs and 10 min Dox-BVNPs were considered to be the most promising for further exploration.
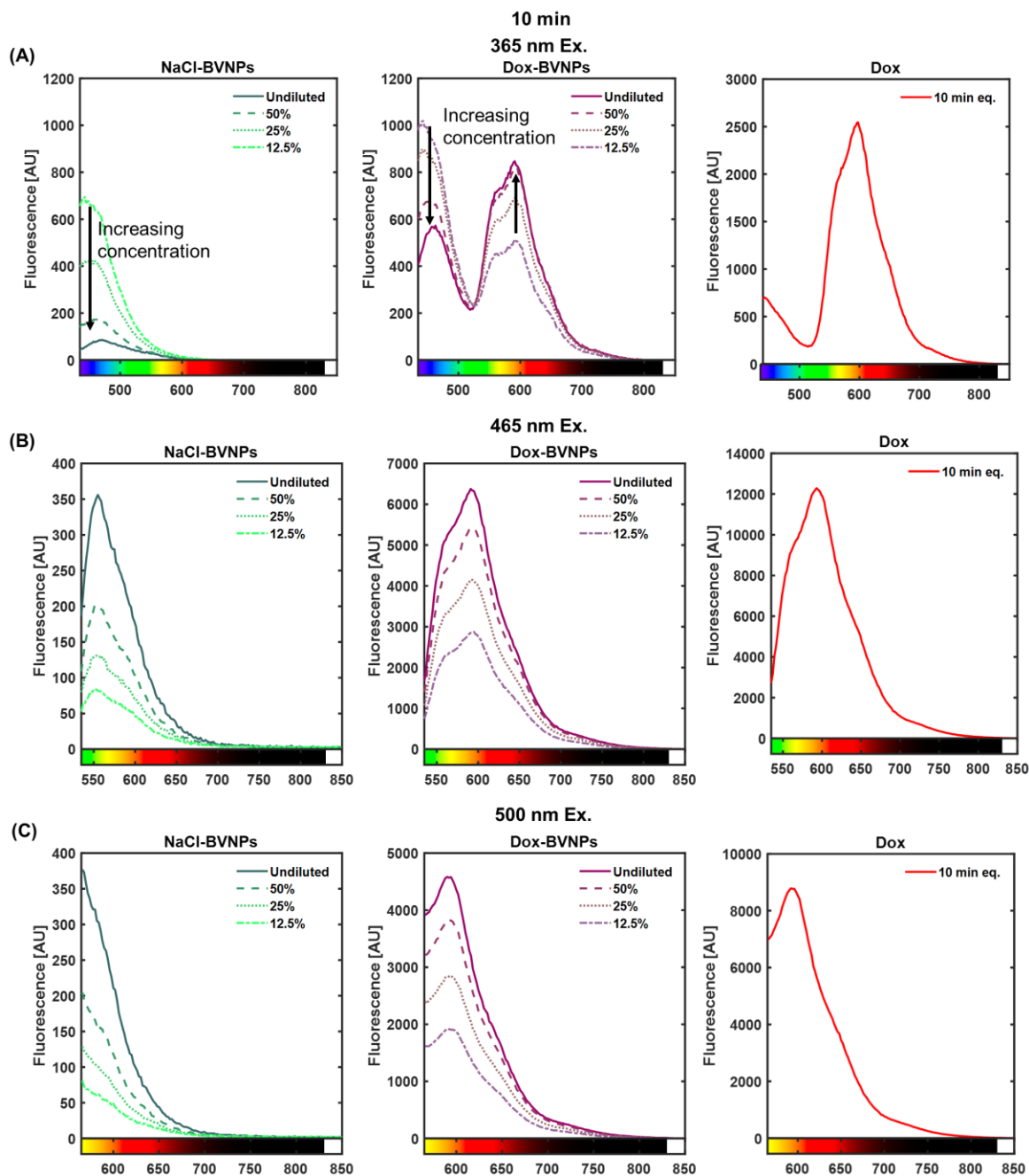
Figure 7.10. Fluorescence spectra of 10 min NaCl-BVNPs, 10 min Dox-BVNPs, and an equivalent concentration of doxorubicin. Particle concentrations are expressed as a % of their as-prepared dialyzed concentrations. **(A)** Fluorescence spectra for an excitation of 365 nm. NaCl-BVNPs experience fluorescence quenching with an increase in concentration. **(B)** Fluorescence spectra for an excitation wavelength of 465 nm. **(C)** Fluorescence spectra for an excitation wavelength of 500 nm.
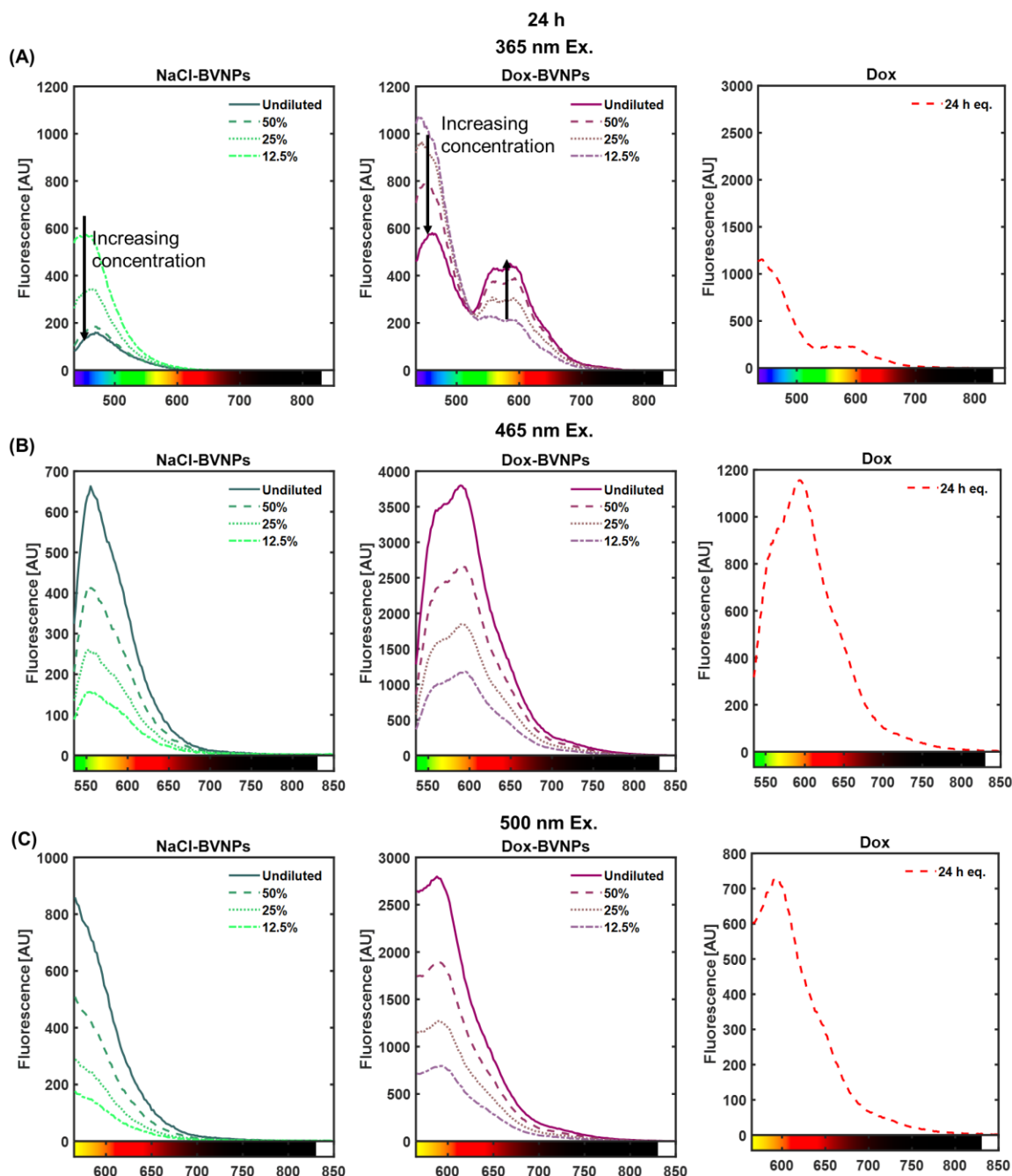
Figure 7.11. Fluorescence spectra of 24 h NaCl-BVNPs, 24 h Dox-BVNPs, and an equivalent concentration of doxorubicin. Particle concentrations are expressed as a % of their as-prepared dialyzed concentrations. **(A)** Fluorescence spectra for an excitation of 365 nm. NaCl-BVNPs experience fluorescence quenching with an increase in concentration. **(B)** Fluorescence spectra for an excitation wavelength of 465 nm. **(C)** Fluorescence spectra for an excitation wavelength of 500 nm.

7.3.5 Nanoparticle Uptake Inhibition Studies

To determine the uptake mechanism of the Dox-BVPs in cancer cells, inhibitor studies were conducted in two representative breast cancer cell lines: MCF-7 metastatic breast cancer cells and MDA-MB-231 triple-negative breast cancer cells following previously reported methods.[354] A list of inhibitors used for these experiments is provided in **Table 7.1**. The successful inhibition of Dox-BVP uptake would lead to cells exposed to Dox-BVPs and the inhibitor having a cell viability equivalent to that of cells exposed to the inhibitor alone. Experiments in MCF-7 cells demonstrated that the uptake mechanism of Dox-BVPs in MCF-7 cells is that of oxidative phosphorylation **(Fig. 7.12, Fig. 7.13)**. Experiments in MDA-MB-231 cells failed to identify an uptake mechanism for Dox-BVPs in these cells **(Fig. 7.14, Fig. 7.15)**, suggesting that the uptake mechanism for Dox-BVPs may differ from MCF-7 cells to MDA-MB-231 cells. This serves as a potential indication that the uptake mechanism of particles of interest must be evaluated in multiple cell lines in order to provide an accurate understanding of how particles can be internalized in various cell lines and models.

Table 7.1. Inhibitors used in nanoparticle uptake inhibition studies.

Inhibitor Number	Inhibitor Name	Pathway Inhibited
1	Sodium azide+2-deoxy-d-glucose	oxidative phosphorylation
2	chlorpromazine (CPM)	clathrin-mediated endocytosis
3	Sucrose	clathrin dependent entry, endosome to lysosome transport
4	Nystatin	caveolar endocytosis
5	Dynasore	dynamin-dependent endocytosis, clathrin & caveolae-mediated endocytosis
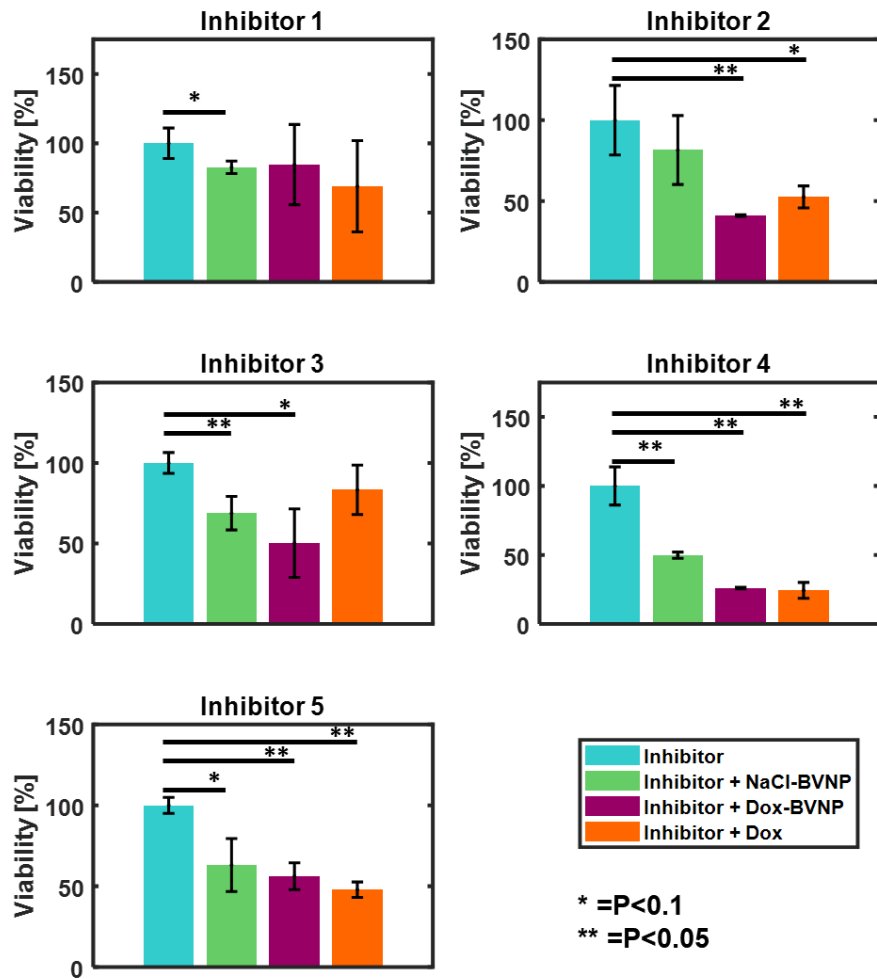
MCF-7, 10 min Dox-BVPs

Figure 7.12. Nanoparticle uptake inhibition results for 10 min Dox-BVPs in MCF-7 cells.
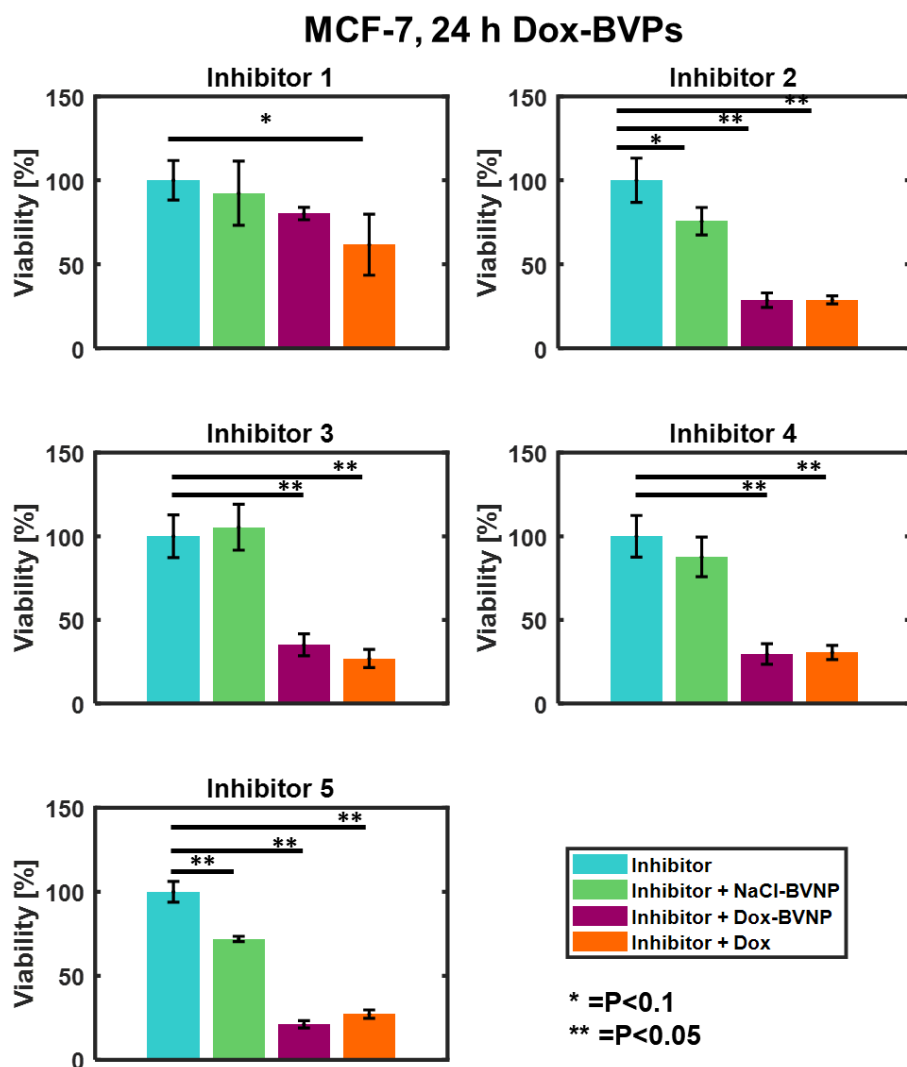
Inhibitors	Inhibited Pathway
1	**Oxidative phosphorylation**
2	Clathrin-mediated endocytosis
3	Clathrin-dependent entry Endosome to lysosome transport
4	Caveolar endocytosis
5	Dynamin-dependent endocytosis Clathrin & caveolae-mediated endocytosis

MCF-7, 24 h Dox-BVPs

Figure 7.13. Nanoparticle uptake inhibition results for 24 h Dox-BVPs in MCF-7 cells.

Inhibitors	Inhibited Pathway
1	**Oxidative phosphorylation**
2	Clathrin-mediated endocytosis
3	Clathrin-dependent entry Endosome to lysosome transport
4	Caveolar endocytosis
5	Dynamin-dependent endocytosis Clathrin & caveolae-mediated endocytosis

MDA-MB-231, 10 min Dox-BVPs
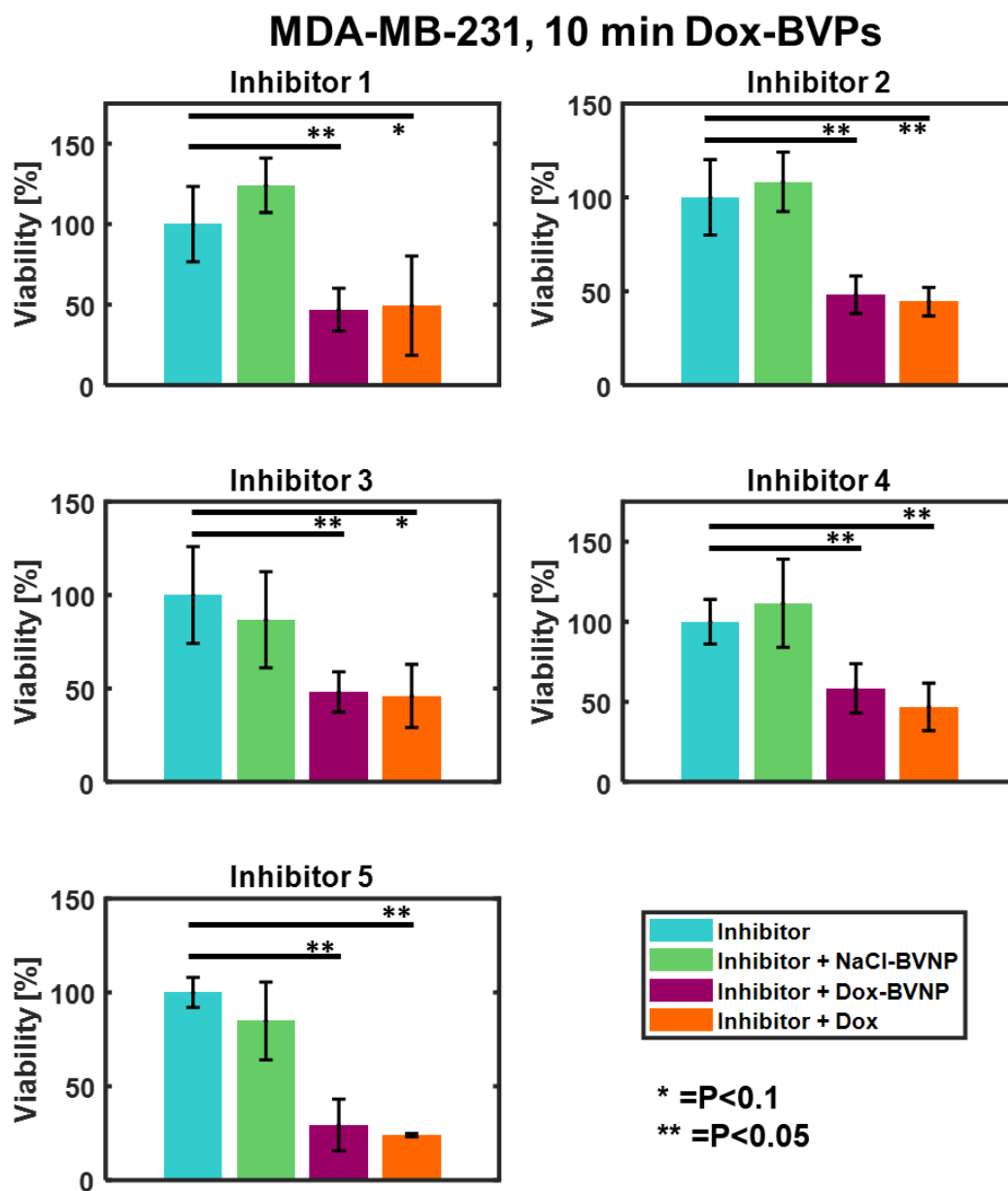
Figure 7.14. Nanoparticle uptake inhibition results for 10 min Dox-BVPs in MDA-MB-231 cells.
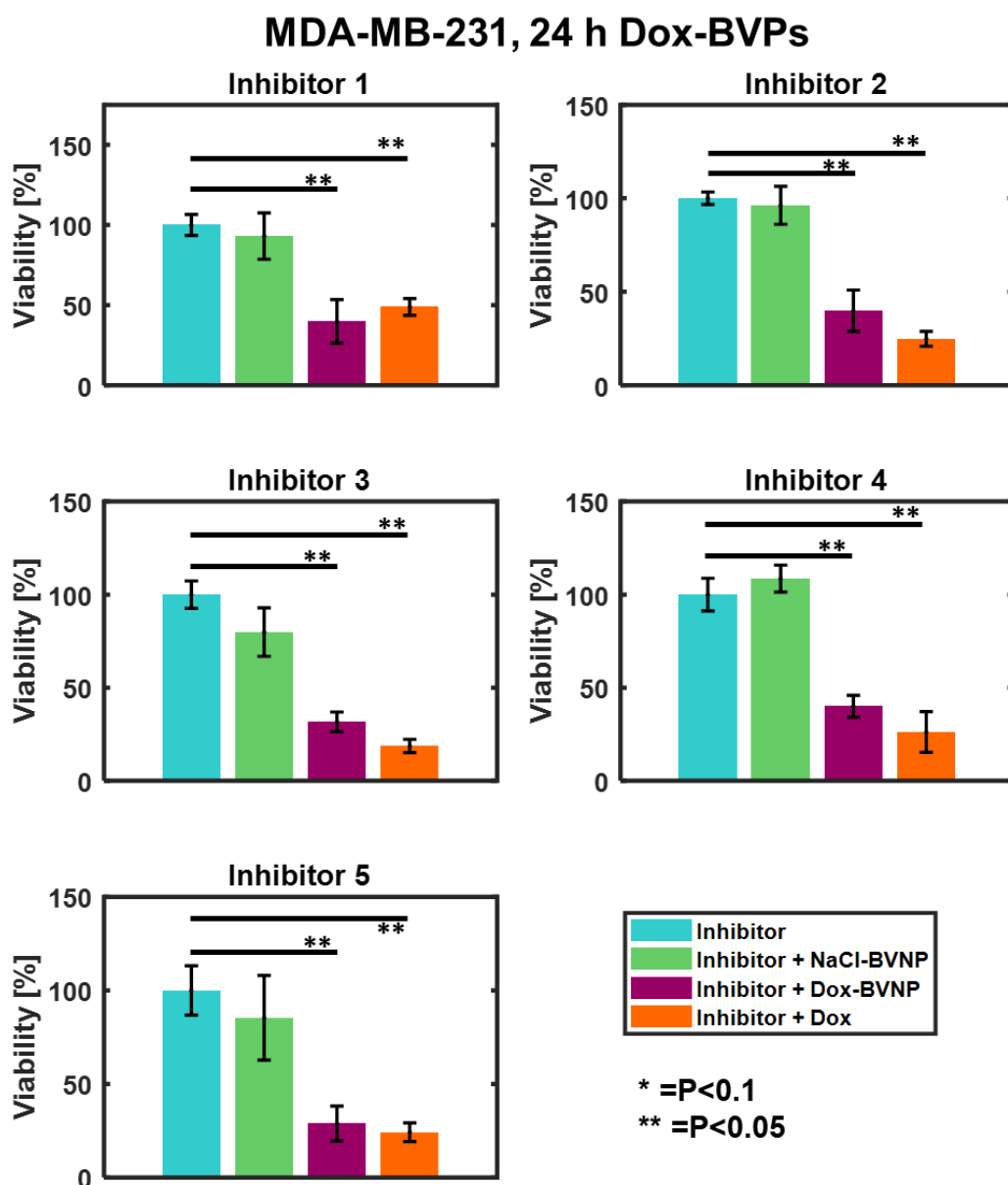
Figure 7.15. Nanoparticle uptake inhibition results for 24 h Dox-BVPs in MDA-MB-231 cells.

7.3.6 Preliminary MTT Experiments in MDA-MB-231 and 4T1 cells

In preliminary MTT experiments, cell viability was evaluated in MDA-MB-231 and 4T1 cells that were exposed to various dilutions of as-prepared dialyzed 10 min and 24 h NaCl-BVNPs and Dox-BVNPs **(Fig. 7.16)**. These two cell lines were selected because they are triple-negative breast cancer cell lines of human and murine origin respectively. These experiments demonstrated that after only 24 h of incubation, the NaCl-BVNPs had greater toxicity than the Dox-BVNPs. After 24 h of incubation, the 10 min Dox-BVNPs performed similarly to the equivalent doxorubicin concentration. Additionally, the particles were generally more toxic to 4T1 cells than to MDA-MB-231 cells. However, the low viability of cells exposed to NaCl-BVNPs suggests that the particles were either contaminated, or that the Dox-BVNPs and NaCl-BVNPs must be resuspended at equivalent biliverdin concentrations in order to allow for direct comparison of their toxicities.

7.3.7 MTT Experiments over a period of 72 h

In subsequent MTT experiments, we dialyzed the NaCl-BVNPs and Dox-BVNPs with water rather than NaCl solution, freeze-dried the particles, and resuspended them at an equivalent biliverdin concentration. This would allow for direct comparison of nanoparticle toxicity resulting from biliverdin and toxicity resulting from doxorubicin. MTT assays conducted over a period of 72 h demonstrate that Dox-BVNPs have comparable toxicity to the equivalent doxorubicin concentration **(Fig. 7.17)**. NaCl-BVNPs were again found to lower the metabolic activity of the cells, which suggests that the low cell viability observed in the previous experiment may have been the result of contaminants in the biliverdin nanoparticle synthesis. Interestingly however, cells treated with NaCl-BVNPs for 72 h appeared visually similar to untreated (control) cells, while

those treated with Dox-BVNPs or doxorubicin appeared to have experienced significant damage (**Fig. 7.18, Fig. 7.19**). This suggests that NaCl-BVNPs may be reducing cell metabolic activity without necessarily leading to high amounts of cell death.

7.3.8 Exploration of NaCl-BVNP toxicity

To evaluate the inherent toxicity of 10 min NaCl-BVNPs, the NaCl-BVNP synthesis was repeated under "semi-sterile" conditions. The viability of cells exposed to NaCl-BVNPs was then determined using both an MTT assay and an acridine orange/propidium iodide fluorescence assay (**Fig. 7.20**). We found that NaCl-BVNPs showed high viability in the acridine orange/propidium iodide fluorescence assay (**Fig. 7.20 A**). Quantification of cell viability based on this assay demonstrated that even cells treated with up to 20 % NaCl-BVNP solution showed viability similar to that of the control. In MTT assays, an increase in nanoparticle concentration was shown to lead to a decrease in cell viability (**Fig. 7.20 B**). However, the semi-sterile synthesis led to higher viability than what was previously observed, which suggests that a semi-sterile synthesis procedure is most favorable for further experimentation. Additionally, the differences in viability observed through acridine orange/propidium iodide staining and MTT assays indicate that NaCl-BVNPs may impact cell metabolic activity without necessarily leading to cell death.

24 h Incubation

48 h Incubation

Figure 7.16. Preliminary MTT experiments in MDA-MB-231 and 4T1 cells after 24 h and 48 h of exposure to as-prepared 10 min and 24 h NaCl-BVNPs and Dox-BVNPs

Figure 7.17. MTT results for cells treated with varying concentrations of 10 min Dox-BVNPs. Results expressed as % metabolic activity of the control. **(A)** MDA-MB-231 results. **(B)** 4T1 results.

MDA-MB-231, 72 h exposure

Control

Dox-BVNP   **NaCl-BVNP**   **Dox**

5 %

10 %

20 %
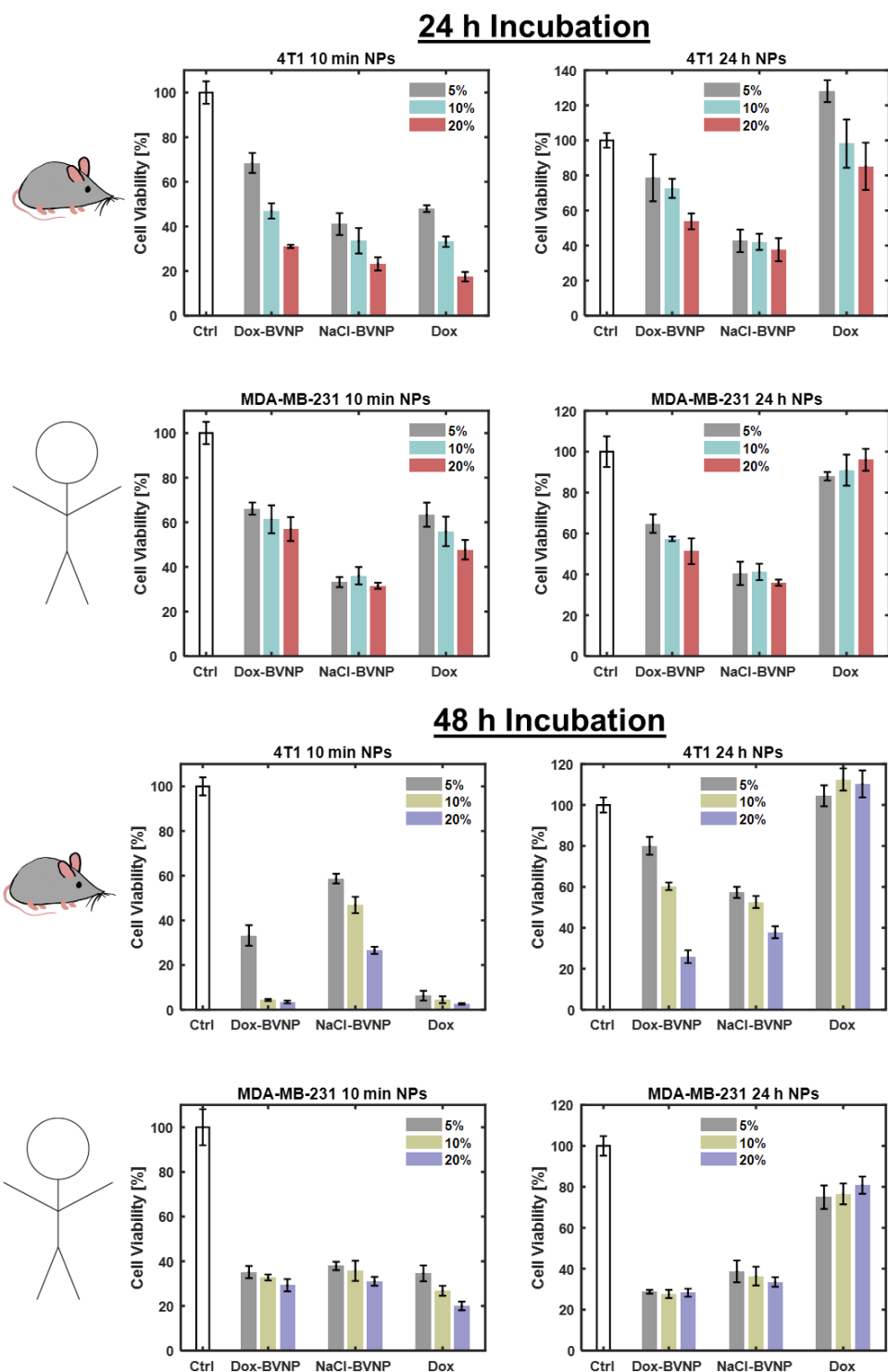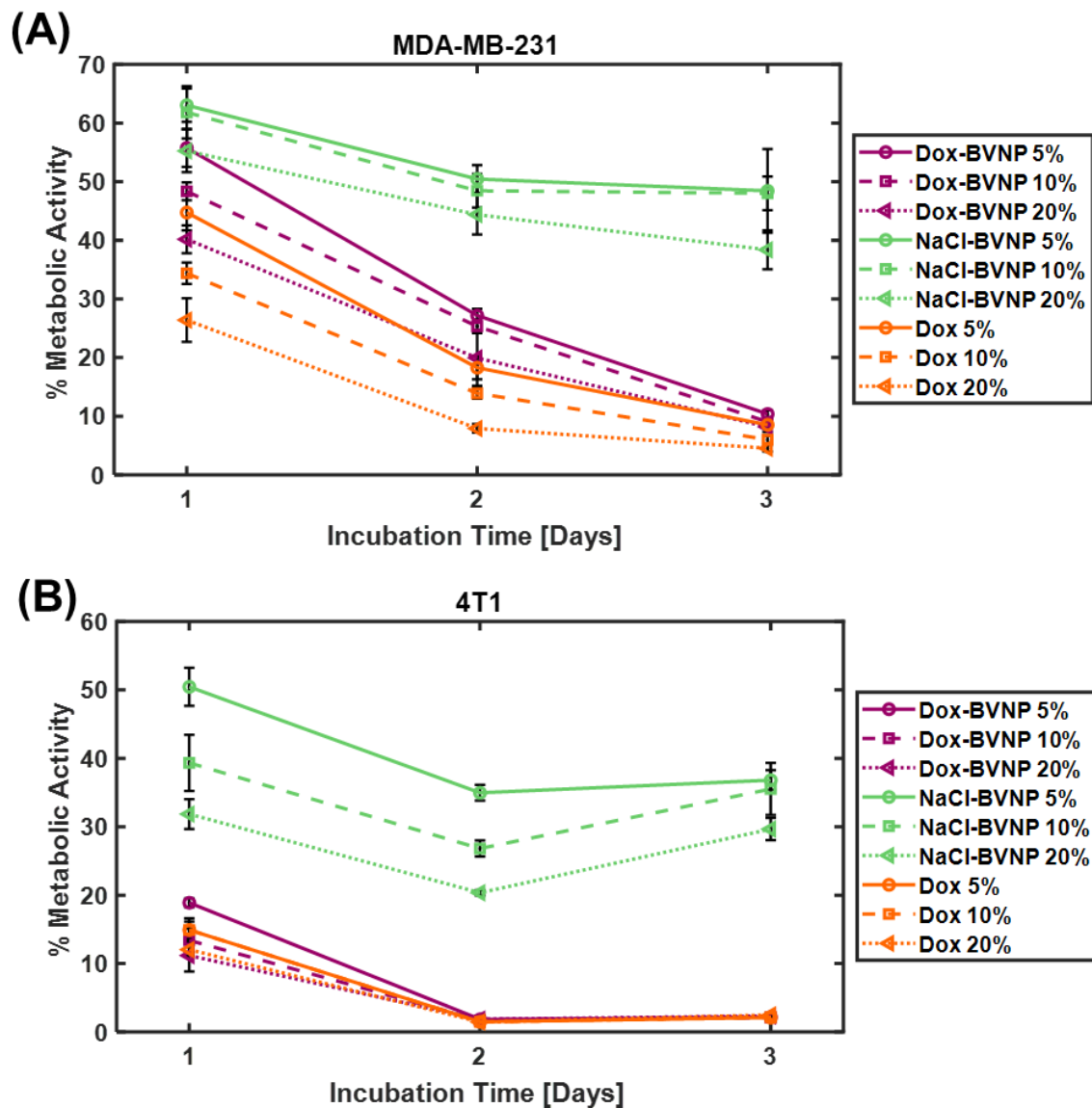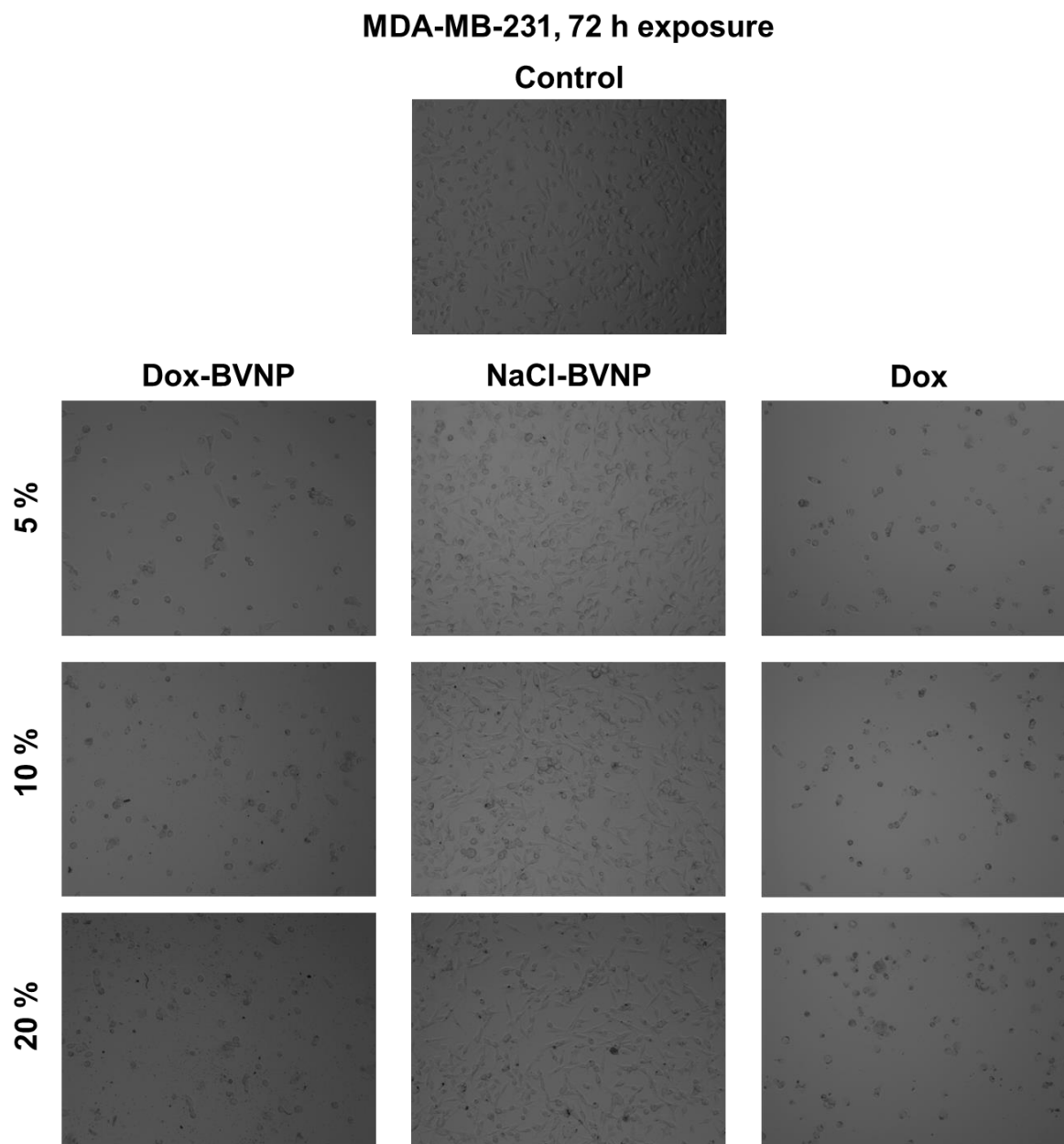
Figure 7.18. Bright-field microscopy of MDA-MB-231 cells exposed to Dox-BVNPs, NaCl-BVNPs, or doxorubicin for 72 h. Dox-BVNPs and doxorubicin lead to noticeable changes in cell morphology, while cells exposed to NaCl-BVNPs look similar to untreated control cells.

4T1, 72 h exposure

Control

Dox-BVNP　　　　**NaCl-BVNP**　　　　**Dox**
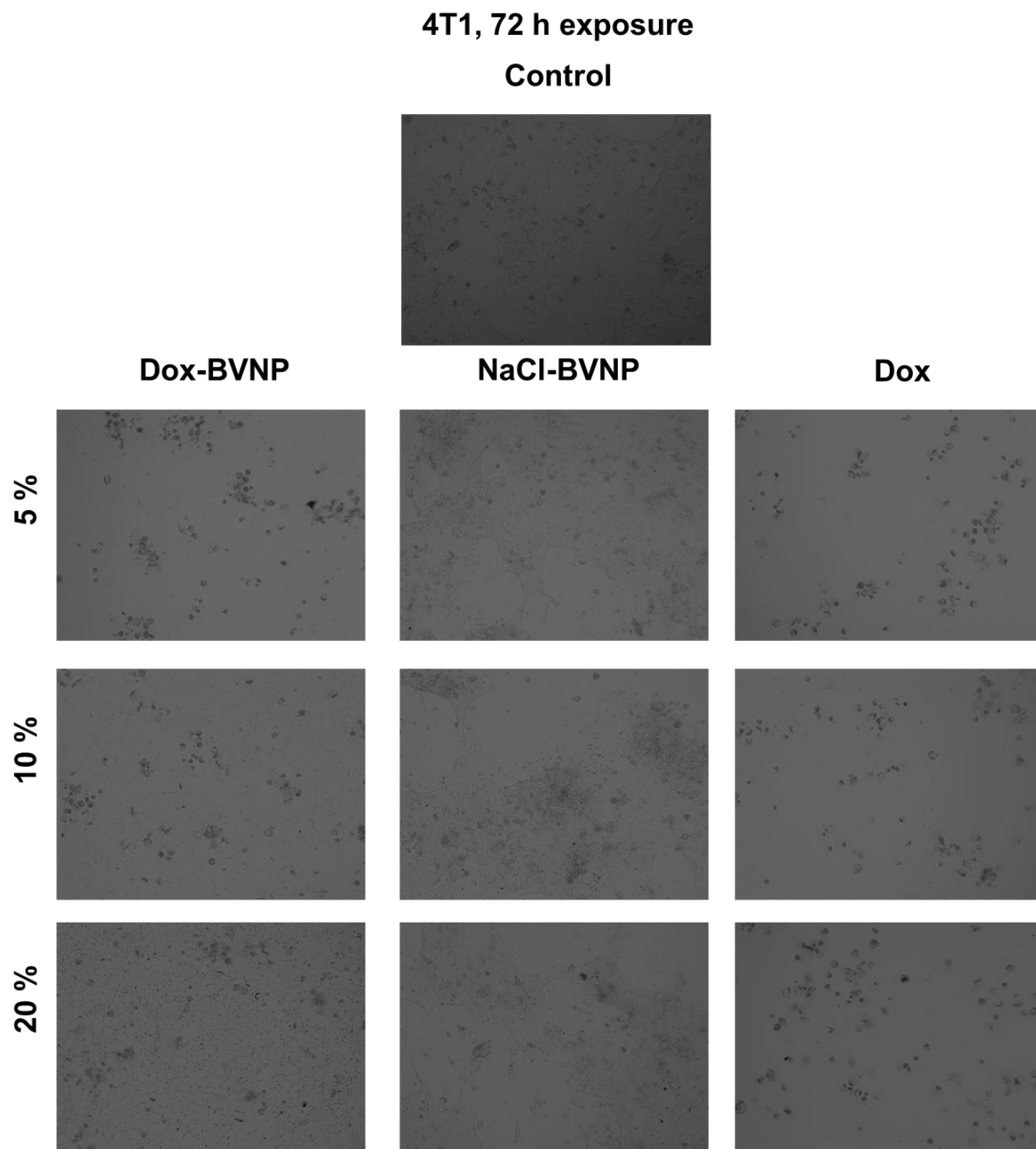
Figure 7.19. Bright-field microscopy of 4T1 cells exposed to Dox-BVNPs, NaCl-BVNPs, or doxorubicin for 72 h. Dox-BVNPs and doxorubicin lead to noticeable changes in cell morphology, while cells exposed to NaCl-BVNPs look similar to untreated control cells.
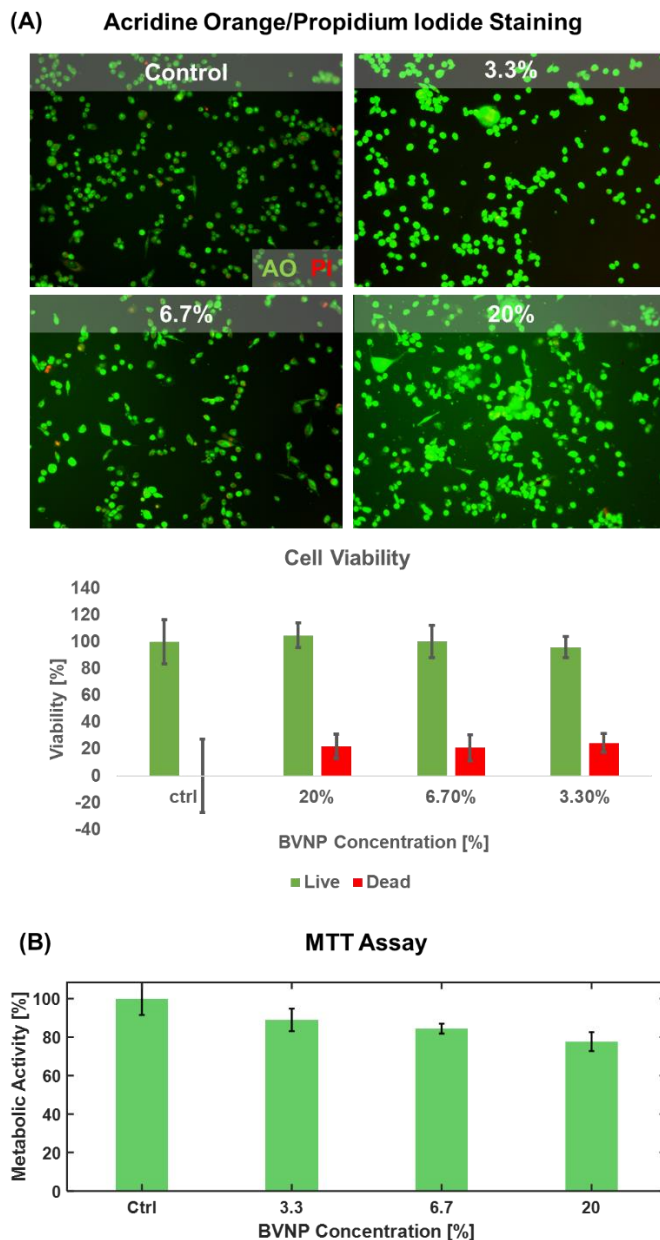
Figure 7.20. Viability of MDA-MB-231 cells after 24 h of exposure to NaCl-BVNPs synthesized with a semi-sterile synthesis. **(A)** Acridine orange/propidium iodide staining and quantification of live and dead percentage. **(B)** MTT assay for quantification of cell viability based on metabolic activity.

7.3.9 Preliminary Photothermal Therapy Experiments

Preliminary photothermal therapy experiments were conducted in MDA-MB-231 cells with a 635

nm laser **(Fig. 7.21)**. The results did not show the desired effect of laser irradiation on cell viability.

Additionally, although the same batch of NaCl-BVNPs was used as before, the viability of cells exposed only to the BVNPs without laser irradiation dramatically fell. This suggests that the BVNPs may not have remained in their "semi-sterile" state despite being opened only in the biosafety cabinet, or that the particles may otherwise become toxic over time. Additionally, the lack of effect from laser irradiation suggests that a higher concentration of BVNPs, longer irradiation time, or longer wavelength laser (670 nm) may be needed in order to achieve the desired photothermal effects.
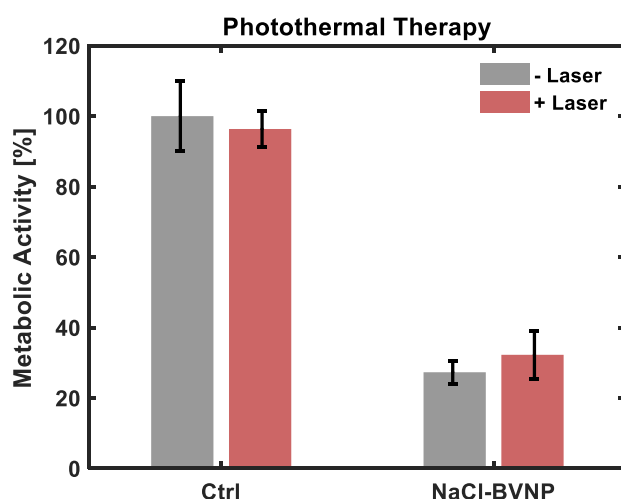
Figure 7.21. Preliminary photothermal therapy results for MDA-MB-231 cells incubated with 5 % NaCl-BVNPs for 24 h, and exposed to 635 nm laser for 5 min.

7.3.10 Tumor Uptake Studies

To establish the amount of time needed for the particles to reach the tumor, 10 min NaCl-BVNPs were systemically administered to 4T1 tumor-bearing mice. ROI analysis reveals significant uptake of particles within the tumor as early as 30 min post-injection **(Fig. 7.22)**. The small size of the 10 min nanoparticles appears to lead to their rapid uptake and clearance from the tumor site. Interestingly, just 2-3 hours after injection, the particles appear to move from the tumor site to becoming accumulated within the vessels near the tumor.
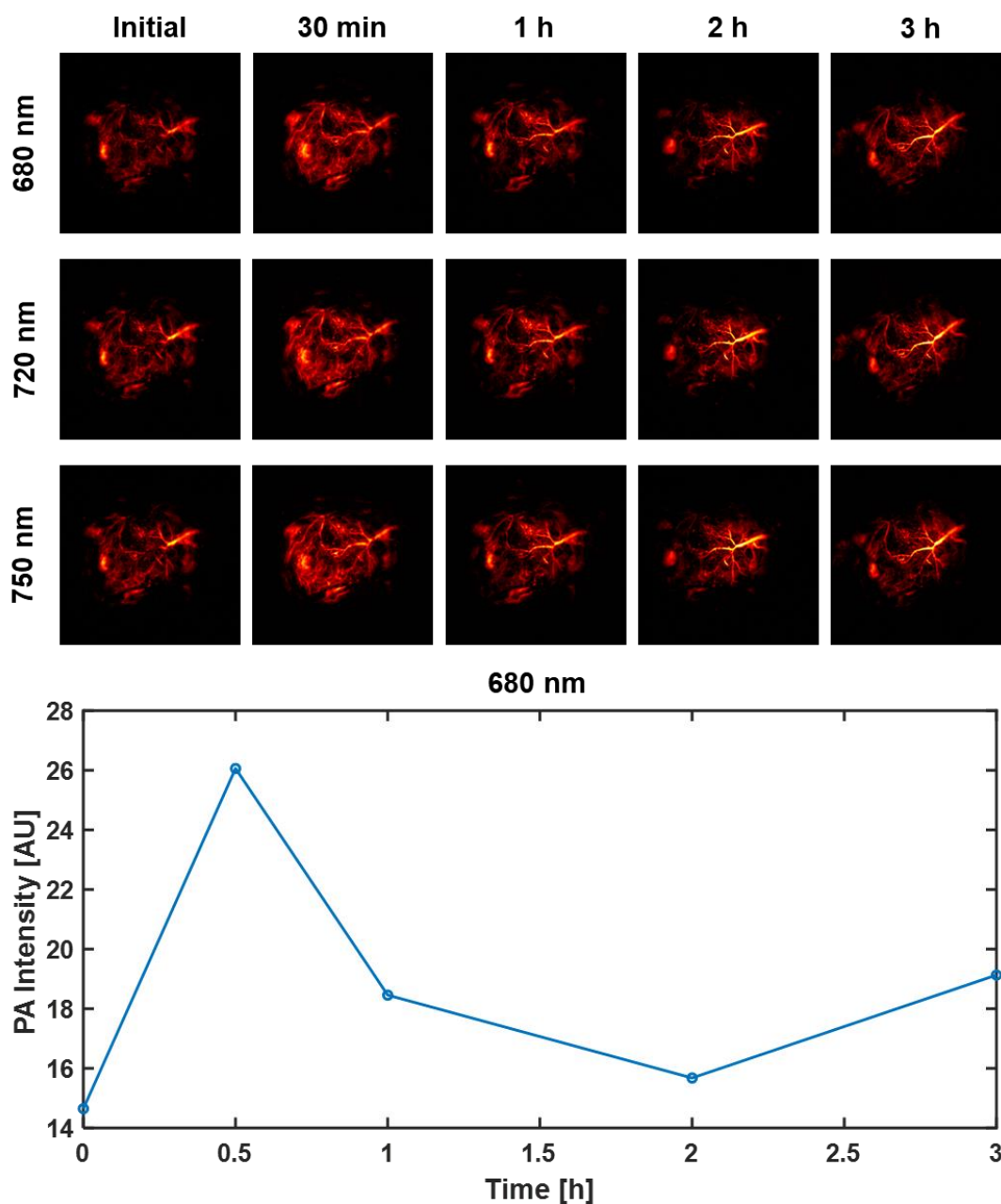
Figure 7.22. NaCl-BVNP tumor uptake in mouse bearing 4T1 tumor. ROI analysis illustrates increase in signal at 30 min post-injection as a result of uptake of NaCl-BVNPs within tumor.

7.4 CONCLUSIONS AND FUTURE WORK

Dox-BVNPs appear to show promise in treating triple-negative breast cancer. Unfortunately, the worldwide COVID-19 pandemic prevented us from conducting further experiments to examine the in vivo antitumor efficacy of Dox-BVNPs. After things return to normal, we plan to complete in vivo experiments to demonstrate the use of Dox-BVNPs in tumor

170

imaging and treatment. We will also utilize hyperspectral dark-field imaging to track doxorubicin release *in vitro*. One general consideration to keep in mind is that the hydroxy groups on doxorubicin may have allowed for its crosslinking into the biliverdin nanoparticle, thus providing us with dox-biliverdin hybrid nanoparticles rather than doxorubicin-loaded nanoparticles. This would potentially alter the release kinetics of the particles, and merits further exploration.

7.5 MATERIALS AND METHODS

7.5.1 Materials

Doxorubicin hydrochloride was purchased from Cayman chemicals. Biliverdin hydrochloride was purchased from Frontier Scientific.

7.5.2 Synthesis of Dox-BVNPs

10 mg biliverdin hydrochloride and 10 mg of doxorubicin hydrochloride were dissolved in 10 mL of 0.9 % NaCl solution at 500 rpm overnight. The following morning, approximately 7 mg EDC and 5 mg NHS were added to the solution and allowed to stir for 10 min. Afterwards 3.5 µL diamine was added to initiate the reaction. After the particles had reacted for 10 min or 24 h, samples were dialyzed against 0.9 % NaCl solution or pure water (molecular biology grade). For samples that were dialyzed in water, samples were subsequently freeze-dried and resuspended at appropriate concentrations in 0.9 % NaCl solution. For dialysis, 3 mL of nanoparticle solution was dialyzed against 500 mL of liquid. For larger volume dialysis, 10 mL of nanoparticle solution was dialyzed against 1 L of liquid. Dialysis was conducted for 24 h. To separate Dox-BVNPs from Dox-BVPs, 1 mL of Dox-BVP solution was centrifuged at 500 rpm for 5 min.

7.5.3 Synthesis of NaCl-BVNPs

10 mg biliverdin hydrochloride was dissolved in 10 mL of 0.9 % NaCl solution at 500 rpm overnight. The following morning, approximately 6.7 mg EDC and 4.0 mg NHS were added to the solution and allowed to stir for 10 min. Afterwards 3.5 µL diamine was added to initiate the reaction. After the particles had reacted for 10 min or 24 h, samples were dialyzed against 0.9 % NaCl solution or pure water (molecular biology grade). For samples that were dialyzed in water, samples were subsequently freeze-dried and resuspended at appropriate concentrations in 0.9 % NaCl solution. For dialysis, 3 mL of nanoparticle solution was dialyzed against approximately 500 mL of liquid. For larger volume dialysis, 10 mL of nanoparticle solution was dialyzed against approximately 1 L of liquid. Dialysis was conducted for 24 h.

7.5.4 TEM imaging

TEM grids were prepared by dropcasting 2.5 µL of diluted Dox-BVNP or NaCl-BVNP solution (10 µL particle solution: 90 µL water) on copper grids. Excess moisture was wicked away after 2 minutes. Samples were imaged on a JEOL Cryo 2100 TEM with an acceleration voltage of 200 keV.

7.5.5 Scanning Electron Microscopy

Dox-BVP solution was drop-casted onto glass microscope slides and dried under vacuum prior to imaging. Samples were imaged uncoated on a Field-Emission Environmental Scanning Electron Microscope (ESEM-FEG) with an acceleration voltage of 15 kV.

7.5.6 FT-IR spectroscopy

500 µL of as-prepared dialyzed 10 min and 24 h Dox-BVPs were deposited on Kevley MirrIR Corner Frosted FT-IR slides and dried under vacuum. FT-IR measurements were taken using a Thermo Nicolet Nexus 670 FT-IR with the smart refractor accessory.

7.5.7 Other characterization

Zeta potential was measured using a Malvern Zetasizer. Fluorescence spectra were collected on a TECAN infinite M200PRO. UV-Visible Spectroscopy was conducted using a Thermo Scientific Genesys 10S UV−Vis spectrophotometer.

7.5.8 Determination of doxorubicin loaded for fluorescence spectroscopy experiments and preliminary MTT experiments

The concentration of doxorubicin loaded with in Dox-BVNPs was determined by UV-visible spectroscopy. Dox-BVNPs were diluted to various concentrations of nanoparticle solution:0.9 % NaCl solution prepared in molecular biology grade water (100:900, 50:950, 25:975, 10:990, 5:995 particle solution:NaCl solution ratios). 480 nm absorbance was determined for each Dox-BVNP dilution, then used to calculate the amount of doxorubicin loaded within the particles based on the nanoparticle dilution and the previously collected calibration curves of doxorubicin 480 nm absorbance as a function of concentration. The calculated total doxorubicin per mL of nanoparticle solution was then averaged across multiple dilutions of the sample in order to provide a reliable estimate of the actual amount of doxorubicin loaded within the particles. It is important to note that the contribution from biliverdin's 480 nm absorbance was included in the 480 nm absorbance of Dox-BVNPs. Since there was no way to reliably separate the contribution of

doxorubicin itself from the contribution of biliverdin, the estimate of doxorubicin loaded within the nanoparticles may be slightly higher than the amount actually loaded within the particles. The as-prepared 10 min and 24 h Dox-BVNPs were calculated to have concentrations of 0.089071 mg/mL and 0.025222 mg/mL of doxorubicin respectively. Encapsulation efficiency of the as-prepared dialyzed Dox-BVNPs was calculated using the following equation:

$$Encapsulation\ Efficiency = \left(\frac{Drug\ Loaded}{Initial\ Drug\ Added}\right) \times\ 100\ \%$$

(Equation 7.1)

Since the initial concentration of doxorubicin used within the syntheses was 1 mg/mL, this represents encapsulation efficiencies of 8.91 % and 2.52 % for 10 min and 24 h Dox-BVNPs respectively. To determine the amount of doxorubicin loaded within the full Dox-BVP population, the amount of excess dox within the dialysis liquid was measured. Using the previously collected calibration curve, it was determined that the dialysis liquid (490 mL) of the 3 mL of dialyzed 10 min Dox-BVPs contained 2.1187 mg of the initial 3 mg of doxorubicin, while that of dialyzed 24 h Dox-BVPs contained only 0.459 mg of the initial 3 mg of doxorubicin. The encapsulation efficiency of the Dox-BVPs was then determined using Equation 7.1 and Equation 7.2:

$$Drug\ loaded = Initial\ Drug\ Added - Drug\ Removed\ During\ Dialysis$$

(Equation 7.2)

The encapsulation efficiency of 10 min and 24 h Dox-BVPs were found to be 29.38 % and 84.7 % respectively.

7.5.9 Nanoparticle uptake inhibition studies

Nanoparticle uptake inhibition studies were conducted following the previously published method.[354] Experimental groups included cells alone, cells treated with inhibitors and solutions of interest (24 h NaCl-BVNPs, 24 h Dox-BVNPs, or doxorubicin) or with only the solutions of interest (24 h NaCl-BVNPs, 24 h Dox-BVNPs, or doxorubicin). Cells were grown for 24 h, then incubated with the inhibitor for 1-2 hours. Afterwards, the media was replaced with treated media (1 % v/v as-prepared dialyzed nanoparticle solution in DMEM or doxorubicin alone in DMEM) for 48 h. A stock solution of 1 mg/mL doxorubicin was diluted for the doxorubicin-treated cells. An MTT assay was then conducted to determine the viability of cells exposed to the inhibitors and the particles. Successful inhibition of nanoparticle uptake would prevent the cytotoxic effects of Dox-BVNPs from leading to decreased cell viability compared to the control (cells treated with only the inhibitor, but no nanoparticles or doxorubicin).

7.5.10 Preliminary MTT studies on 4T1 and MDA-MB-231 cells

As-prepared dialyzed nanoparticles were used. Nanoparticle dilutions were made using medium (RPMI for 4T1 cells, DMEM for MDA-MB-231 cells) for final nanoparticle volumetric concentrations of 20 %, 10 %, or 5 %. 10 min and 24 h Dox-BVNPs and 10 min and 24 h NaCl-BVNPs were used for these experiments. Cell plating densities of 8000 cells/well and 10000 cells/well were used for MDA-MB-231 and 4T1 cells respectively. Cells were plated in the wells of 96-well plates, allowed to grow overnight, and then exposed to the nanoparticle solutions for 24 or 48 h. Afterwards, an MTT assay was conducted to determine cell viability. Cells exposed to a Dox-BVNP equivalent concentration of doxorubicin were used for comparison of Dox-BVNP toxicity with doxorubicin toxicity.

7.5.11 MTT Experiments over a period of 72 h

10 min Dox-BVNPs and 10 min NaCl-BVNPs were synthesized as described above. The particles were dialyzed against water and subsequently lyophilized. Lyophilized Dox-BVNPs were resuspended at a concentration of 1 mg/mL in 0.9% NaCl solution. Calibration curves were prepared of the 480 nm and 670 nm absorbance for various dilutions of Dox-BVNPs, NaCl-BVNPs, and doxorubicin using an absorbance plate reader. The Dox-BVNP 670 nm absorbance (due to biliverdin) was used to determine the concentration at which NaCl-BVNPs needed to be resuspended in order to obtain an equivalent 670 nm absorbance to that of the Dox-BVNPs **(Fig. 7.23)**. When Dox-BVNPs were suspended at a concentration of 1 mg/mL, NaCl-BVNPs at a concentration of 0.86393 mg/mL would give the equivalent 670 nm absorbance. The equivalent doxorubicin concentration was found by matching the 480 nm absorbance of the doxorubicin solution with the 480 nm absorbance of the Dox-BVNP solution. The doxorubicin concentration in 1 mg/mL 10 min Dox-BVNPs was found to be 0.2286 mg/mL. Thus, doxorubicin accounted for 22.86 % of the Dox-BVNP mass.

Figure 7.23. Absorbance plate reader calibration curves for biliverdin, NaCl-BVNP, Dox-BVNP, and doxorubicin.
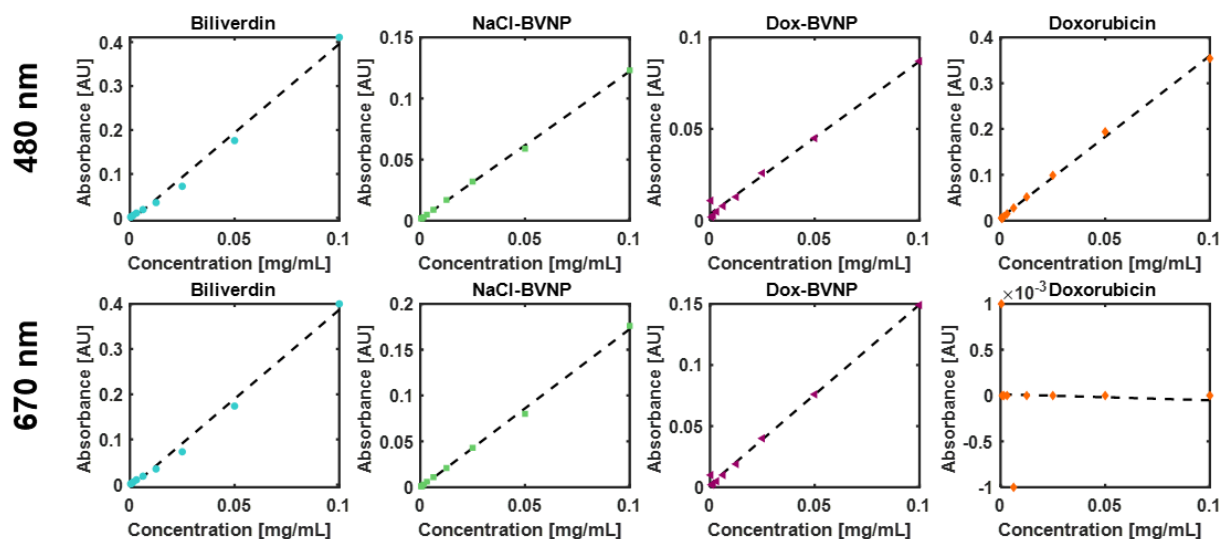
Curve Name	Curve Formula	A	B	R^2
Biliverdin, 480 nm	Y=A*X+B	4.04	-0.00799	0.991
Biliverdin, 670 nm	Y=A*X+B	3.94	-0.00706	0.993
Doxorubicin, 480 nm	Y=A*X+B	3.54	0.00606	0.998
Doxorubicin, 670 nm	Y=A*X+B	-0.00066	1.46E-05	0.00193
Dox-BVNP, 480 nm	Y=A*X+B	0.831	0.00379	0.99
Dox-BVNP, 670 nm	Y=A*X+B	1.47	0.00236	0.997
NaCl-BVNP, 480 nm	Y=A*X+B	1.21	0.00122	0.999
NaCl-BVNP, 670 nm	Y=A*X+B	1.73	-0.00046	0.998

MDA-MB-231 cells and 4T1 cells were plated at a density of 5000 cells per well in 96-well plates. Cells were grown overnight and then replaced with medium containing the nanoparticle solutions. Nanoparticle solutions were prepared as volumetric dilutions of their final resuspended concentrations. A sample size of 3 to 5 wells was used for each condition. Cells were incubated with the nanoparticle solutions for 24, 48, or 72 h, after which cell viability was determined using MTT assays.

7.5.12 Evaluation of NaCl-BVNP toxicity

NaCl-BVNPs were synthesized as described above, but under "semi-sterile" conditions. Although the doxorubicin and biliverdin were not sterile, they were weighed out in the biosafety cabinet. All steps of the synthesis were conducted in the biosafety cabinet, and all liquids used were sterilized prior to use. The beakers used for dialysis were also autoclaved prior to use. After dialysis against molecular biology grade water, 10 min NaCl-BVNPs were lyophilized and resuspended (in the biosafety cabinet) at a concentration of 0.86393 mg/mL in 0.9 % NaCl solution.

MDA-MB-231 cells were plated at a density of 5000 cells per well in a 96-well plate. Cells were allowed to grow overnight, after which they were incubated for 24 h with 20 %, 6.7 %, or 3.3 % v/v Dox-BVNP solution in DMEM. Following the incubation, the medium was discarded and MTT or acridine orange/propidium iodide (AO/PI) viability measurements were conducted. The protocol for AO/PI experiments was adapted from previous reports.[355] For the AO/PI experiments, 1 mg/mL stock solutions of dye in water or PBS were prepared. An AO/PI incubation solution was prepared by mixing 15 µL stock AO solution, 15 µL stock PI solution, and 2970 µL medium. After medium removal, 100 µL of AO/PI incubation solution was added to each well, and cells were incubated at room temperature for 10-15 min. Afterwards, the liquid was discarded and the cells were rinsed once with 100 µL of PBS. The PBS was then replaced with 100 µL fresh PBS and imaging was conducted using an inverted fluorescence microscope. Fluorescence quantification was completed using a plate reader. An excitation of 485/20 nm and emission of 590/35 nm was used to measure the fluorescence of acridine orange. An excitation of 530/25 nm and emission of 590/35 nm was used to measure the propidium iodide fluorescence. The cell viability and non-viability were determined using the following equations, where F_{AO} represents

178

the fluorescence intensity of the AO excitation-emission pair, and F_{PI} represents the fluorescence intensity of the PI excitation-emission pair:

$$\% \, Cell \, Viability = \frac{(F_{AO,test} - F_{AO,blank})}{(F_{AO,control} - F_{AO,blank})} \times 100 \, \%$$

(Equation 7.3)

$$\% \, Cell \, Nonviability = \frac{(F_{PI,test} - F_{PI,blank})}{(F_{PI,control} - F_{PI,blank})} \times 100 \, \%$$

(Equation 7.4)

7.5.13 Preliminary Photothermal Therapy Experiments

10 min NaCl-BVNPs from the batch used in the AO/PI experiments were used for photothermal therapy experiments (8 days after synthesis). MDA-MB-231 cells were plated at a final concentration of $0.1*10^6$ cells/mL, 1 mL per well of a 12-well plate. Cells were allowed to grow overnight, after which they were incubated with 5 % (v/v) of 10 min NaCl-BVNPs for 24 h. After incubation, cells were washed and replaced with fresh medium. Cells were irradiated with a 635 nm laser for 5 min, and incubated for a further four hours. An MTT assay was then conducted to determine cell viability.

7.5.14 NaCl-BVNP Tumor Uptake experiments

NaCl-BVNPs were prepared as described previously, and resuspended at a concentration of 0.86393 mg/mL in 0.9 % NaCl solution. Nanoparticles were administered to 4T1 tumor-bearing mice via retroorbital injection. Mice were imaged with photoacoustic tomography prior to nanoparticle administration, and 30 min, 1 h, 2 h, and 3 h after administration.

CHAPTER 8: A PUMPLESS MICROFLUIDIC LYMPHATIC VESSEL ON A CHIP TO EVALUATE THE EFFECTS OF SHEAR FLOW ON PRIMARY HUMAN LYMPHATIC ENDOTHELIAL CELLS

8.1 ABSTRACT

Lymph nodes comprise a complex organ system that is essential in regulating the development of host immune responses. Due to the complexity of lymph nodes and the lack of *in vitro* models that replicate lymphatic function, there is a need for a human-based lymphatic model that can provide a better understanding of the effects of flow parameters, therapeutics, and other stimuli on the lymphatic system. In this report, a fluidic device models the cyclical lymphatic flow under normal and diseased conditions. The device utilizes a pumpless design, operating with gravitational forces to simulate normal conditions with a shear of 0.092 Pa as well as disease conditions with increased shear (0.67 Pa). The cyclical pumping present in lymphatic vessels is replicated by applying shear stress for a period of ten seconds multiple times per minute. Primary human lymphatic endothelial cells (HLECs) cultured in the device for ten days produce less interleukin 8 (IL-8), and tumor necrosis factor alpha (TNF-α) per cell than cells cultured under static conditions. The results are consistent with previously published *in vivo* measurements, indicating that the fluidic device mimics conditions for IL-8 and TNF-α expression well. Data obtained with the devices also indicate that primary human lymphatic endothelial cells proliferate faster under high shear than under low shear conditions.

8.2 INTRODUCTION

The lymphatic system is designed to clear the body of toxins and foreign substances. It does so primarily through the circulation of lymph fluid that picks up immune cells in the lymph

nodes and distributes them throughout the body.[284] The lymph-mediated immune response can be an important tool when treating cancer,[356–358] but the presence of tumors close to lymph nodes can disturb lymphatic function. Tumors that grow nearby and drain into a node can metastasize there.[297–302] and increase the flow in lymphatic vessels. Metastatic tissue that already grows inside a lymph node can decrease lymphatic flow.[73] A tumor-related increase in flow causes heightened expression of ICAM-1, which can lead to additional metastatic growth,[68] and reduction of lymph flow due to a tumor causes increased expression of tumor necrosis factor alpha (TNF-α) and interleukin 6 (IL6),[303] two cytokines that are known to reduce contraction and pumping in the lymphatic system.[303]

Because the lymphatic system is intimately involved in the immune response, which in turn can be a vital part of treating cancer[356–358], human-based lymph node flow models will allow us to systematically probe the role of lymph flow on these processes. Current *in vitro* models of lymph nodes[75,315,316,359,360] primarily use 2D cultures, and the models often utilize human dermal lymphatic or microvascular endothelial cells[75,76,316] under low-shear conditions[68,75]. Microfluidic tissue-chip and organ-chip models have recently gained increasing interest as potential alternatives to traditional *in vitro* culture models, allowing for more accurate recapitulation of physiologically relevant flows[361–364]. Here, we have developed a microfluidic device that produces a pulsatile flow pattern as seen in lymphatic vessels, and with shears that mimic healthy conditions (low shear), or disease conditions (high shear or no shear). We have used our devices to culture primary human lymphatic endothelial cells (HLECs) for up to ten days, producing a healthy endothelium under low shear conditions, and an endothelium with elevated TNF-α and IL8 production under static conditions.

Flow in human and mammalian lymph nodes is unidirectional due to a complex valving system[293–296], ensuring that lymph travels only from the afferent to the efferent lymphatics. Lymph node shear values of up to 1.2 Pa (12 dyn/cm^2) have been reported in rodents[72], and computer simulations have predicted shears of up to 0.6 Pa (6 dyn/cm^2) in human lymph nodes[74]. Other studies have reported peak shear stresses of up to 0.8 Pa (8 dyn/cm^2) for rodent lymph nodes[365,366]. Under edemagenic conditions, shear stresses of up to 4 Pa (40 dyn/cm^2) have been reported in rat lymphatics[367]. Additionally, flow in the lymph nodes is not continuous, but rather is marked by contractile pumping. Lymphatic vessel pulsing frequencies in mice have been reported in the range of approximately five to eight contractions per minute[303].

The major factors considered for the development of our design were the use of gravity-driven flow, the ability to use the device for a wide range of shears, and the use of only unidirectional flow. The use of gravity-driven flow provides the ability to obtain the desired shear stresses without the need for an active pumping mechanism. This design allows for the simultaneous operation of multiple devices, thereby reducing the cost of adopting such tissue-on-a-chip technologies. We achieved gravity-driven flow by placing our devices on periodically-rotating platforms, which were developed in-house. The use of unidirectional flow serves as a physiologically accurate mimic of flow in the lymphatic system.

8.3 RESULTS AND DISCUSSION
8.3.1 Device Design

Our microfluidic device design utilizes two halves which are connected by hemispherical reservoirs for the addition and removal of culture medium (**Figure 8.1 A-B**). Each half of the device is composed of a larger channel to generate a high flowrate, followed by two smaller channels with reduced width and height to take advantage of conservation of mass to achieve

higher flow velocities. Channel heights of 750 µm and a width of 5.5 mm were utilized for the larger channels, and heights of 350 µm and widths of 1.75 mm were utilized for the smaller channels. Flow occurs only on one side of the device at a time, and only in one direction (**Figure 8.1 C**). When the device is rotated 180°, flow occurs on the other side of the device.

The shear generated within the device was calculated using:

$$\tau = \frac{6\eta u_{max}}{h}$$
(Equation 8.1)

Where u_{max} is the maximum velocity, η is the dynamic viscosity, and h is the channel height. The maximum velocity for the large and small channels was calculated using the volumetric flowrate measured when the device was placed at a 45° angle on the rotating platform. The average flowrate was determined to be 2.86 mL/min ± 0.14 mL/min for the devices, corresponding to an average flowrate of 1.43 mL/min in the small channels. When placed at an angle of 45° on the rotating platform, the device obtains shear stresses of up to 0.67 Pa (6.7 dyn/cm^2) in small channels and 0.092 Pa (0.92 dyn/cm^2) in larger channels. A dynamic viscosity of 1000 Pa*s was utilized for all calculations.

8.3.2 Rotating Platform and Device Fabrication

The rotating platforms (**Figure 8.1 D**) were 3D-printed and make use of an Arduino microcontroller and basic circuitry to rotate 180°, hold the position for 10 s, and then rotate another 180°. The platform base remains stationary, while the platform rotor position can be set to angles between 0° and 90° to control the flowrates and resulting shear stresses in the device. Devices were fabricated using three layers of PDMS (**Figure 8.1 E**). A detailed description of the fabrication process is provided in the experimental section.
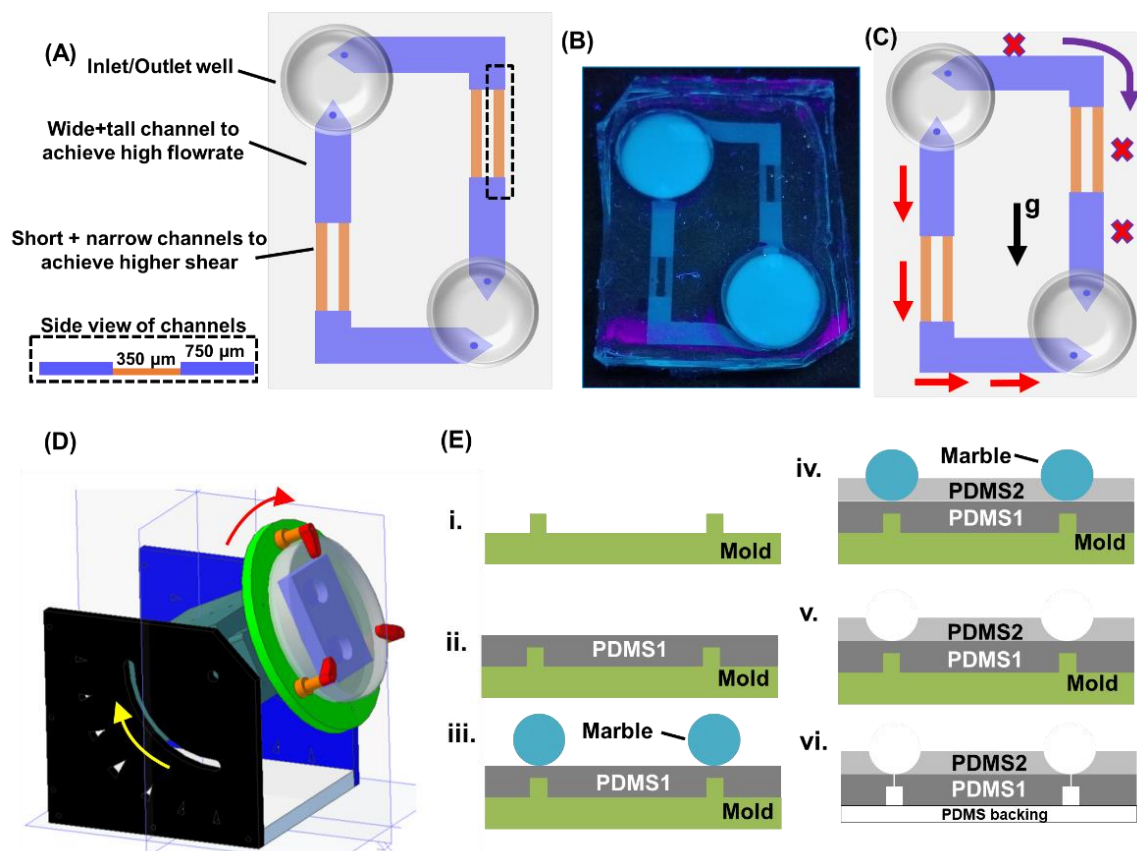
Figure 8.1. Device design. **(A)** A combined inlet/outlet well allows for liquid to flow from one side of the device into the other side of the device. Wide and tall channels allow the device to achieve a high flowrate and allow for the growth of cells under low-shear conditions. Shorter narrower channels allow for growth of cells under a higher shear condition. **(B)** Fabricated device filled with a solution of fluorescent molecule, visualized under a 365 nm ultraviolet lamp. **(C)** Red arrows and 'x' indicate presence and absence of flow respectively. Unidirectional flow is achieved by having flow on only one side of the device at a time. Purple arrow indicates direction of 180° rotation of platform to achieve flow on other side of device. *g* indicates gravity. **(D)** 3D model of rotating platform on which devices are placed. Yellow arrow indicates adjustable positioning of platform angle. Red arrow indicates direction of platform rotation. **(E)** Cross-section view of device fabrication. **i.** A 3D-printed mold is obtained. **ii.** A layer of PDMS is cured onto the mold. **iii.** Marbles are placed over the desired location of inlet and outlet wells. **iv.** A second layer of PDMS is added and cured onto the mold. **v.** The marbles are removed, retaining the well feature of the device. **vi.** The device is separated from the mold, holes are punched in the inlet and outlet wells, and the device is sealed with a PDMS backing.

8.3.3 Long-term culture of primary human lymphatic endothelial cells

Primary human lymphatic endothelial cells were grown in the microfluidic device for ten days. In the wider channel section, the cells experienced a shear of 0.092 Pa (0.92 dyn/cm^2), and in the narrow channel section, the cells experienced a shear of 0.67 Pa (6.7 dyn/cm^2). The lower shear

condition mimics flow conditions expected under healthy physiologic conditions,[74] and the higher shear condition mimics flow conditions present when non-metastatic tumors grow nearby[73]. Like in the human body, the shear created with our device also periodically increases and decreases. Lymphatic vessel pulsing frequencies in mice have been reported in the range of approximately five to eight contractions per minute,[303] and each side of our device undergoes three on-off cycles per minute (each 180 degree rotation takes approximately one second and is followed by a stationary ten seconds before the next rotation). This allows us to obtain six on cycles and six off cycles per device per minute.

We also cultured cells in devices under static conditions, where no shear was applied. Different to typical static cultures, however, our culture was done inside the microfluidic channel to mimic static conditions that exist in cases where the tumor growth burden at a lymph node is so large that lymphatic flow decreases below normal values as found by Proulx et al[73]. Different to typical static cultures, this condition also implies that nutrient and waste exchange in the microfluidic vessel occurs mostly via diffusion. A summary of the flow conditions is provided in **Figure 8.2**.
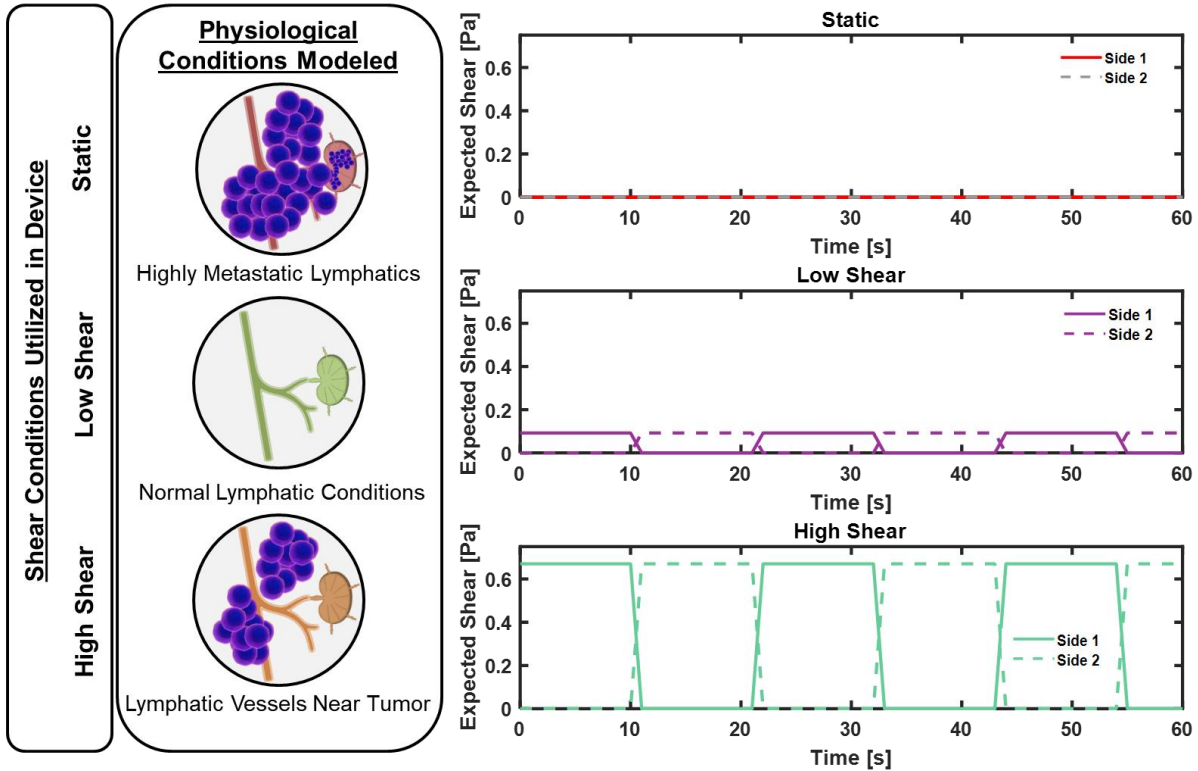
Figure 8.2. Conditions simulated within devices. The use of static, low shear, and high shear conditions allows for the simulation of both normal and diseased lymphatic conditions. Expected shear profiles depict the cyclic nature of shear exerted on the devices, with each side of each device experiencing multiple on-off cycles per minute.

Cells cultured both under static and dynamic conditions were imaged with bright-field and fluorescence microscopy after five and ten days of cell culture. Confluence of cells increased with time under all conditions (**Figure 8.3 A**), but cells under shear formed uniform monolayers without gaps between cells, while cells under static conditions did not appear to reach full confluence throughout all parts of the channels. Immunostaining of PECAM/CD31 adherens junctions (**Figure 8.3 B**) conducted on the cell cultures confirms this finding and illustrates the development of adherens junctions throughout the cell layer under low and high shear, and in all areas populated by cells under static conditions. The images also show that shear alters the cell shapes from a rounded shape to a more elongated shape which aligns with the direction of flow. This result is

consistent with what we and others have found with human umbilical vein endothelial cells grown under cyclical fluidic flow[368].
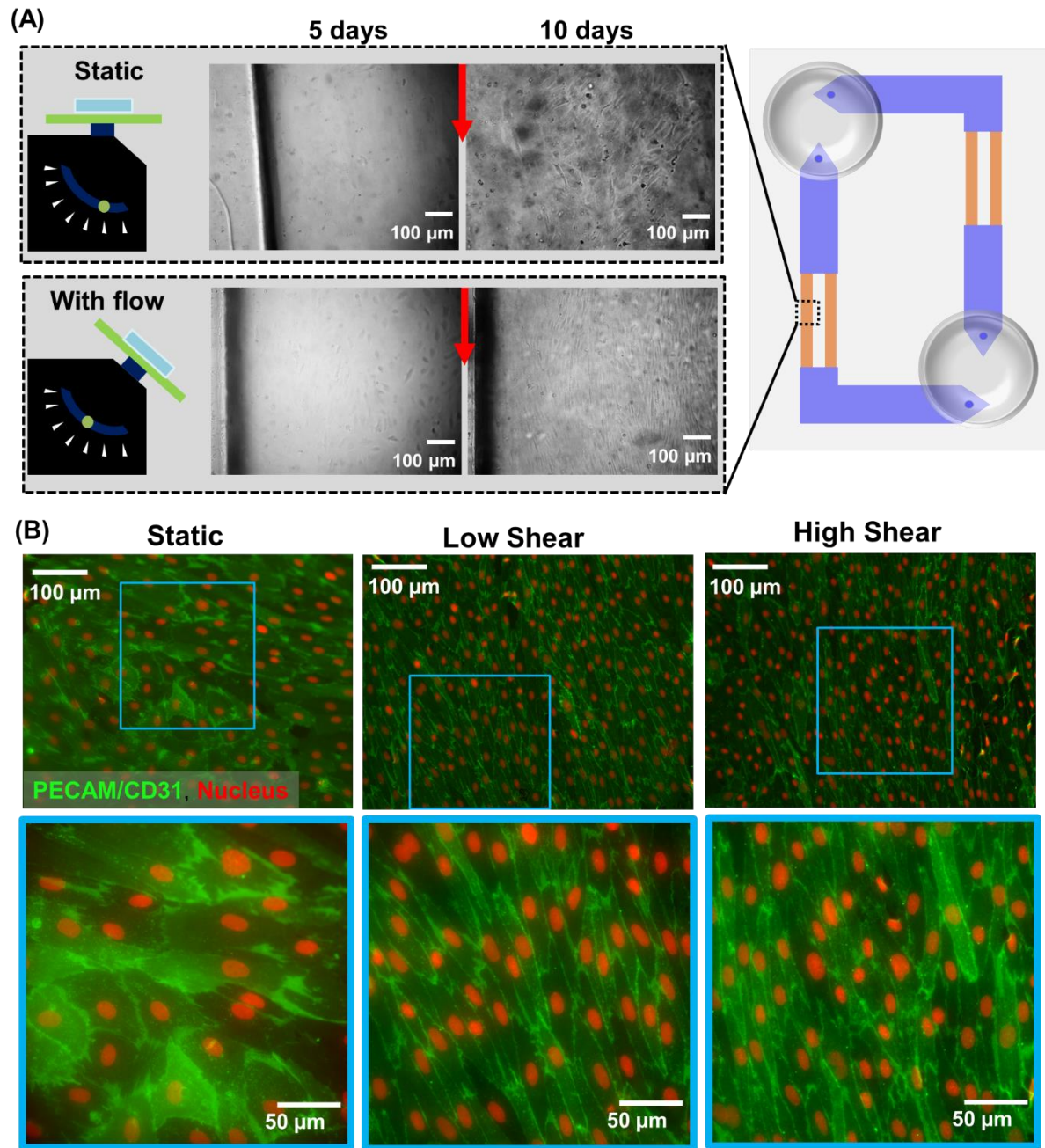
Figure 8.3. (A) Bright-field images 5 days and 10 days into cell culture experiment. Red arrows indicate direction of flow. Cells in static devices appear irregularly oriented, while cells in devices with flow appear to align with the direction of flow. **(B)** PECAM/CD31 adherens junction staining of cells grown in devices for 10 days. Cells grown under all conditions continue to express PECAM/CD31 on their surfaces, while those grown under shear flow align with the direction of flow. Green color represents PECAM/CD31, red color represents the nuclear counterstain.

8.3.4 Cells exposed to shear had higher viability than those grown under static conditions

Live-dead staining determined that cells grown in both the static and flow conditions had a viability of greater than 80 % **(Figure 8.4 A-B)**. However, cells grown under high shear had a significantly higher viability than those grown under static conditions **(Figure 8.4 B)**. There was no significant difference between viability of cells in the low-shear and high-shear conditions. This confirms that the presence of flow plays an important role in delivering nutrients and other factors such as intercellular signals to the cells.

8.3.5 Cell count increased and size decreased with shear

In addition to the changes in cell viability, the cell count per unit area increased with increases in shear **(Figure 8.4 C)**. The cell count was highest at 0.67 Pa, and lowest under static conditions. Under static conditions, the lower cell count can be partially attributed to gaps in the cell layer, but the difference in cell count between the low shear and high shear conditions was due to a difference in cell size. Indeed, under both high-shear and low-shear conditions, the monolayer was complete without uncovered surface area. In conjunction with this, cell major axis length distributions, cell minor axis length distributions, and cell area distributions were found to relate to the cell count **(Figure 8.4 D)**. The lower cell count in the static culture condition corresponded with longer major and minor axis lengths and a greater cell area, while the distribution of these measurements shifted towards lower values for each of the higher shear conditions. These findings indicate that the application of shear, as well as the magnitude of shear applied may influence the propagation of primary human lymphatic endothelial cells.
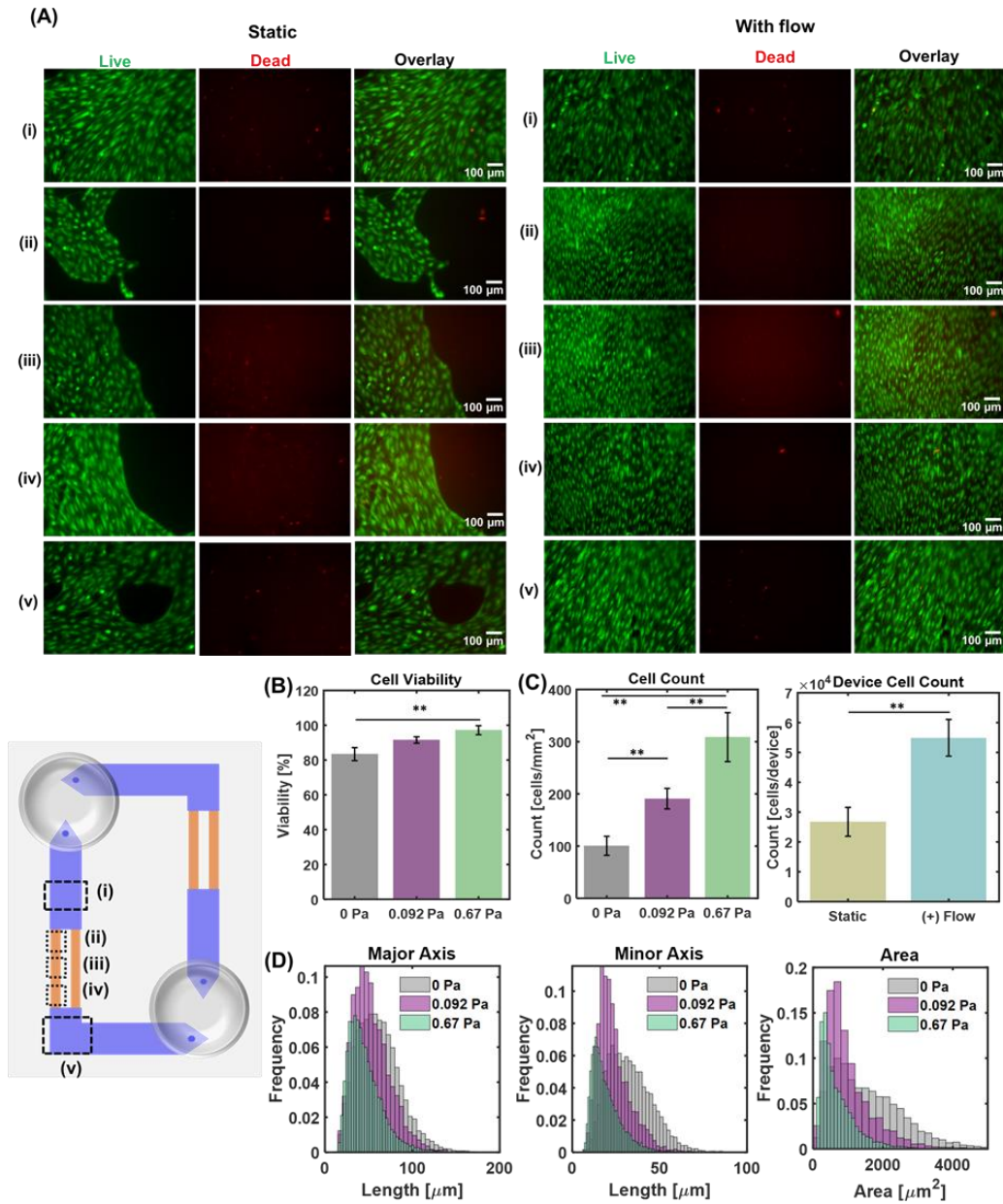
Figure 8.4. Live-dead images. (**A**) Representative live-dead fluorescence images of cells in devices under static conditions (left) and with flow (right). Images were taken at different positions (i-v) within the channels. The endothelial cell layer grown in devices without flow appears to be patchy, although cell viability is high. (**B**) Cell viability calculated for each flow condition. A shear of 0.67 Pa led to significantly higher cell viability than the no-shear condition. (**C**) Cell count per unit area for each flow condition (left) and calculated cells per device (right). An increase in shear led to a direct increase in cell count. Devices with flow had a higher cell count than static devices. (**D**) Histograms of major axis length, minor axis length, and cell area calculated for cells grown under each shear condition. Cell size parameters appeared to exhibit slight decreases with increases in shear. ** indicates statistical significance with $P < 0.05$.

189

8.3.6 Cells aligned with the direction of flow

When cell directionality was quantified **(Figure 8.5)**, the cells grown under low shear and high shear conditions were found to have an average directionality of approximately 80° to 90°, with 90° directionality indicating the cells have aligned with the direction of shear, and consequently vertically within the images. Cells grown under static conditions had an average directionality of approximately 40° to 60°, indicating that the cells had not aligned with the direction of fluidic flow. Previous studies on endothelial cell alignment with the direction of flow[369–373] have primarily focused on human umbilical vein endothelial cells, and the results obtained here with human lymphatic endothelial cells confirm a similar behavior for the *in vitro* lymphatic endothelium.
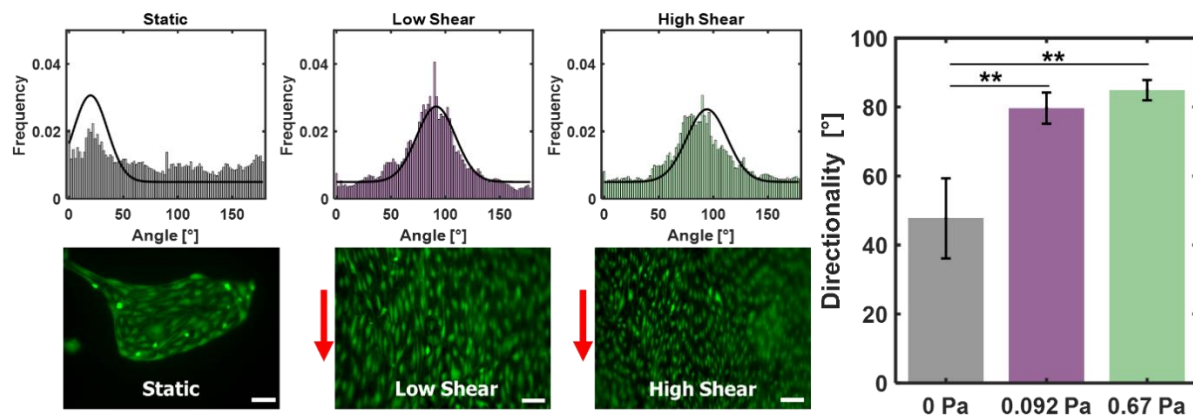
Figure 8.5. Cell alignment with shear flow. Red arrows indicate direction of flow. A directionality of 90° indicates complete vertical alignment. Cells grown under low or high shear were more aligned than those grown under static conditions. ** indicates statistical significance with P <0.025.

8.3.7 Static cultures had higher normalized TNF-α and IL-8 levels

Medium was collected from the cell cultures daily, and ELISA assays were used to determine the levels of TNF-α and IL-8 in the medium at days 2, 4, 6, 8, and 10 **(Figure 8.6, Figure F1)**. Taking into consideration the higher overall cell counts for devices with flow compared to static devices, normalized cytokine expression was calculated by dividing the cytokine concentrations by the

average cell count in each device **(Figure 8.6 A-B)**. This allowed us to isolate the effects of shear from the effects of overall cell density on cytokine expression. The analysis determined that the application of flow led to reduced production of IL-8 and TNF-α per endothelial cell. Using static experiments with permeable membranes, it has previously been reported that high TNF-α levels are related to high lymphatic vessel permeability[374,375], not unlike the disjointed endothelial cell layer of cells grown under static conditions in our device. In addition, high TNF-α expression has been linked to reduced contractility in mesenteric rat lymph nodes *in vivo*[376]. In breast cancer patients, lymph node metastases have been correlated with a higher expression of TNF-α, and a correlation between TNF-α and IL-8 levels has also been demonstrated.[70] Thus, our findings that static conditions within fluidic channels led to higher TNF-α levels demonstrate that our device provides a system that can be used to recapitulate the lymphatic vessel microenvironment in ways that are physiologically relatable to *in vivo* physiological conditions.
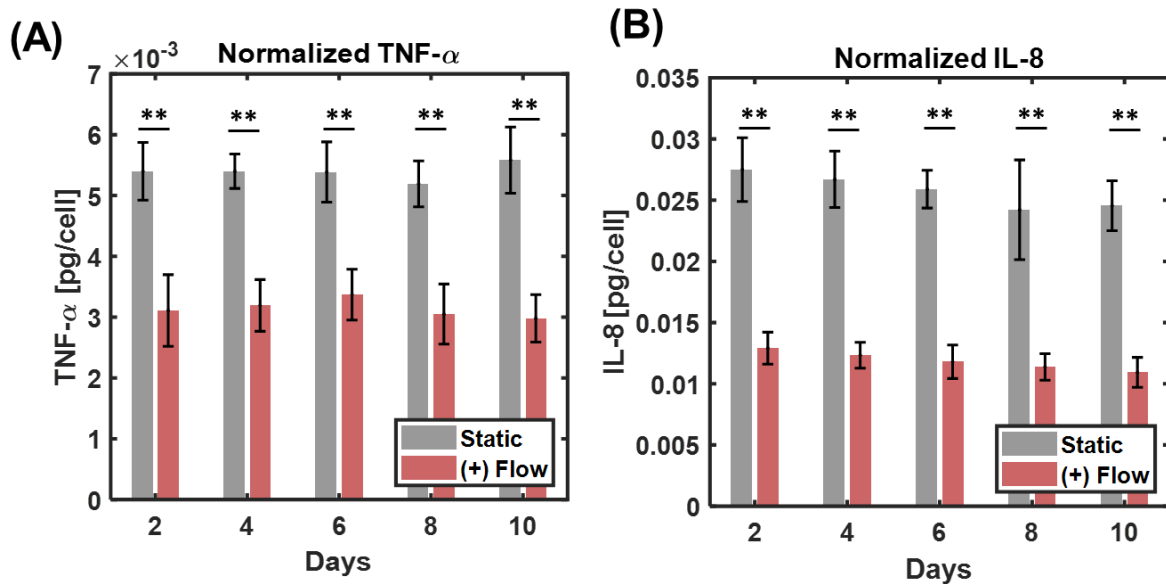
Figure 8.6. Cytokine expression over time. **(A)** TNF-α expression normalized by final cell count. Cells grown under static conditions had higher expression. **(B)** IL-8 expression normalized by final cell count. Cells grown under static conditions had higher expression. ** indicates statistical significance with $P < 0.001$

8.4. CONCLUSION

We have grown primary human lymphatic endothelial cells for ten days under fluidic flow conditions that mimic healthy and disease conditions in lymphatic vessels. Healthy conditions were simulated by applying cyclical shear of 0.092 Pa (0.92 dyn/cm^2) to the cells, mimicking the natural pulsatile flow in lymphatic vessels. Disease conditions were simulated by either removing all flow from the culture, or by applying cyclical high shear (0.67 Pa, 6.7 dyn/cm^2) to the cultures. Cells grown under both shear conditions formed uniform endothelial cell layers where cells developed adherens junctions and aligned with the direction of shear. Cells grown in devices under static conditions (no flow) were formed only disjointed endothelial cell layers. Cells grown under high shear had higher viability than those grown in static conditions, although viability was high (>80%) in all cases. The cell count per unit area increased with the application of shear flow, indicating that higher shear promotes cell proliferation. Static conditions led to higher TNF-α and IL-8 levels per cell, which aligns with previous reports of the effects of lymphatic flow on cytokine expression. Overall, our study demonstrates that the developed microfluidic device can model lymph node behaviour in both healthy and diseased states. To the best of our knowledge, this the first microfluidic model of lymphatic vessels. The developed device and rotating platform provide a versatile *in vitro* system for evaluation of lymphatic behavior under physiological shear flows.

8.5. EXPERIMENTAL SECTION
8.5.1 Materials

Devices were fabricated using polydimethylsiloxane (PDMS) (Sylgard 184) with a 10:1 base to curing agent mix ratio. Primary human lymphatic endothelial cells, endothelial cell medium, supplements, and Trypsin Neutralization solution were purchased from ScienCell Research Laboratories. Normocin was purchased from InvivoGen. The mold for device fabrication was generated 3D drawing software and exported in a file format for 3D-printing. Molds were 3D-

printed using an optically-clear material with a viscosity of approximately ~260 mPa s (260 cps) at 0 °C and a density of approximately 1.12 g/cm3 at 25 °C. A resolution of 50.8 μm was used. Fibronectin was purchased from Sigma-Aldrich. ELISA assays for IL-8 and TNF-α were purchased from RayBiotech. 200-μL pipette tips used for well inlets/outlets were purchased from VWR (product 10017-098). LIVE/DEAD Cell Imaging kits, CD31 (PECAM-1) Monoclonal Antibody (Gi18), and Rabbit anti-Mouse IgG (H+L) Cross-Adsorbed Secondary Antibody, Alexa Fluor 488 were purchased from ThermoFisher Scientific. Any mention of commercial products is for information only; it does not imply recommendation or endorsement by NIST.

8.5.2 Cell Culture

HLECs were cultured in Endothelial Cell Medium completed with fetal bovine serum, endothelial cell growth supplement, and penicillin/streptomycin as recommended by the manufacturer. Medium was additionally supplemented with Normocin at a concentration of 0.1 mg/mL. For all experiments, medium was warmed to room temperature, per manufacturer guidelines, prior to addition to cells. Prior to culture, flasks were coated overnight with 2 μg/cm^2 fibronectin. Cells were cultured in an incubator at 37 °C with a volume fraction of 5 % CO_2. For cell passaging, 5 mL Dulbecco's Phosphate Buffered Saline (DPBS) was used to rinse each T-25 flask, after which the DPBS was replaced with 1 mL of 0.25 % volume fraction trypsin, and cells were placed in the incubator for 2 min to 3 min. The trypsin was then neutralized with 1 mL trypsin neutralization solution, and cells were transferred to a centrifuge tube containing 5 mL fetal bovine serum (FBS). Cells were centrifuged at 6283 radians/min (1000 rpm) for 5 min and were resuspended in fresh medium. Each flask was split into 3 flasks during passaging.

8.5.3 Device Fabrication

The 3D-printed mold was first taped down to a large petri dish (diameter= 14 cm). This dish was completely filled with PDMS and then cured. After curing, a 5.5 cm by 7 cm cut was used to remove the PDMS from the part of the mold containing the channel features. This prepared mold was then used for device fabrication.

For the first layer, 15 g of PDMS were added to the mold and allowed to cure at 80°C for 22 min to 25 min. To achieve the hemispherical wells in the second layer, marbles (diameter=2.54 cm) were taped onto the regions in which the hemispherical indentation was desired. 25 g PDMS were then added to the mold, and cured for 35 min. The combined first and second layer of the device was then removed from the mold, and a 1 mm biopsy punch was used to punch one hole for each inlet/outlet (two holes total per hemispherical well). In order to keep the holes open, the tips of 200 µL pipette tips were cut to size and inserted into the 1 mm holes.

The thin bottom layer of the device was formed by partially curing 5 grams of PDMS in a 5.5 cm by 7 cm section of a 100 mm diameter petri dish. Devices were assembled immediately, and the edges of the interface between the first and third layers of the device were sealed using PDMS. Assembled devices were then cured to solidify the connections between layers. Cured devices were sterilized in an autoclave and cooled prior to use.

8.5.4 Device Preparation for Cell Seeding

8.5.4.1 Channel Priming. Autoclaved devices were used for all experiments. Devices were transferred to a biosafety cabinet and placed in individual sterile petri dishes. Devices were kept flat and 1 mL ethanol solution with a volume fraction of 70 % was pipetted into one of the hemispherical wells for each device. The ethanol was allowed to wick into the channels, after which 1 mL of ethanol solution with a volume fraction of 70 % was added to the other

hemispherical well for each device and allowed to wick into the channels. The wells and petri dish were then completely filled with ethanol solution with a volume fraction of 70 %. Devices were incubated at room temperature for 1 h.

8.5.4.2 Fibronectin Coating. Devices were then transferred to fresh sterile petri dishes, and the ethanol solution with a volume fraction of 70 % was replaced with DPBS three times on each side of each device while the device was tilted, after which 1 mL of diluted fibronectin solution (150 µL fibronectin, 5 mL DPBS) was added to each side of the channel and the outflowing liquid was discarded. Devices were then laid flat, their wells were filled with DPBS, and were placed in the incubator overnight. Two small segments of wet sterilized sponges were placed beside the device within each petri dish prior to device incubation. These sponges assisted in maintaining humidity to prevent solution evaporation, and were replaced every other day throughout long-term culture experiments.

8.5.5 Cell Seeding

Cells in passages 3 to 6 were used for all experiments in devices. Cells were allowed to grow to cover a fractional surface area of 90 % to 100 % (90 % to 100 % confluency), and were trypsinized and spun down as previously described. Each T-25 flask was resuspended in 4 mL of cell culture medium, and used for seeding one device. After overnight incubation with fibronectin, the liquid within each side of the device was replaced three times with cell culture medium while the device was tilted to allow for flow. Each side of each device was then seeded with 2 mL of the cell suspension, with the well output being saved and added back into the wells after the device was laid flat. Devices were then incubated for 2 h to allow HLECs to adhere to the channel surface. Following this, medium on each side of the device was replaced twice with fresh medium while the device was tilted. Devices were then placed horizontally, and medium in the wells were

195

replaced with a total of 800 µL medium per device. For experiments, devices were either placed horizontally in the incubator (no-flow condition) or at an angle of 45° on the rotating platform (with-flow condition).

8.5.6 Long-term Culture of Cells in Devices

8.5.6.1 Flow Experiments. The rotating platform angle was initially adjusted to 0°, and devices were stacked on the platform rotor, after which they were secured in place using 3D-printed fasteners built into the platform. Up to two devices at a time were placed on each platform. Platform rotation was started, and platform angle was then gently adjusted to 45°. Rotating platforms were then placed in the incubator. Experiments were conducted for 10 days, with medium collected each day and replaced with 800 µL fresh medium. Medium was stored frozen for use in ELISA assays.

8.5.6.2 No-flow Experiments. Experiments were conducted for 10 days, with medium collected each day and replaced with 800 µL fresh medium. Devices were tilted and medium was allowed to flow through the channels at least two times for each side of the device prior to medium collection. This procedure ensured that collected medium was well-mixed and that cytokines produced over the past day were evenly distributed within the device and collected medium. Similarly, after the addition of fresh medium each day, devices were tilted and medium was allowed to flow through the channels at least two times for each side of the device. This procedure ensured that the cells within channels had access to fresh medium and would not starve in nutrient-depleted medium. Media was stored frozen for use in ELISA assays.

8.5.6.3 Cell Viability Experiments. After 10 days of culture, live-dead fluorescent staining was conducted on 4 devices each for the flow and no-flow conditions. Culture medium was removed while devices were laid flat. Live and dead dye kit components were mixed and diluted in a 1:1

196

ratio with fresh culture medium, and added to devices while devices were tilted to allow for flow. After devices were laid flat, 1 mL of dye-medium solution was added to each side of each device, and devices were then incubated in the dark at room temperature for 15 min to 20 min. The dye-medium solution was then replaced with DPBS for fluorescence microscopy.

The number of live and dead cells were quantified in ImageJ using the "Find Maxima" Process, and the cell viability was defined by the following equation:

$$\% \, Viability = \left(\frac{number \, of \, live \, cells}{number \, of \, live \, cells + number \, of \, dead \, cells} \right) \times 100\%$$

(Equation 8.2)

8.5.6.4 Analysis for Devices with Flow. To determine the viability under high-shear conditions, 3 images (top, middle, and bottom) were collected for each small channel (12 images per device). The number of live cells and number of dead cells were summed across all 12 images for each device. 4 devices were used for this analysis, with averages and standard deviations calculated for these 4 devices.

To determine the viability under low-shear conditions, on each side of each device one image was taken in the portion of the large channel before the small channels, and one was taken in the portion of the large channel after the small channels (4 images per device). The number of live cells and number of dead cells were summed across all 4 images for each device. 4 devices were used for this analysis, with averages and standard deviations calculated for these 4 devices.

8.5.6.5 Analysis for Devices without Flow. To determine the viability under no-flow conditions, 3 images (top, middle, and bottom) were acquired for each small channel (12 images per device), and 2 images were collected for each large channel (4 images per device). The number of live cells and number of dead cells were summed separately for the small channels and large channels in

197

each device. The cell viability for the devices without flow was weighted based on the percentage of total channel area that was within each part of the device. This was done to prevent biasing of the results towards cell behaviour in the smaller channels, as those channels represented a smaller percentage of the total channel but a larger number of images taken. The smaller channels represented a 13.2 % fraction of total channel area, while the larger channels represented a 86.8 % fraction of total channel area. Thus, the viability of the cells in the small channels and large channels were weighted to 13.2 % and 86.8 % of the viability for each device respectively. 4 devices were used for this analysis, with averages and standard deviations calculated for these 4 devices.

8.5.7 Immunostaining

After 10 days of culture, cells were fixed and permeabilized, and were stained for PECAM/CD31 cell surface markers, with NucBlue used as the nuclear counterstain.

8.5.7.1 Fixation and Permeabilization. Cell fixation was conducted in multiple steps. Cells were first rinsed with DPBS 3 times. This was then replaced with 4 % by volume paraformaldehyde three times on each side of each device, and cells were fixed in this solution for 10 min. This was then replaced three times on each side of the device with 1 % by volume BSA in DPBS and cells were kept in this solution for 10 min. This solution was then replaced three times on each side of each device with 0.5 % by volume Triton-X solution, and cells were kept in this solution for 10 min. This was again replaced three times with 1 % by volume BSA in DPBS and cells were kept in this solution for 10 min. The wells were then filled with DPBS and devices were stored in the fridge until antibody staining was conducted.

8.5.7.2 Antibody Stain and Nuclear Counterstain. Prior to staining, devices with fixed and permeabilized cells were taken apart using a scalpel to separate the backing layer of PDMS from the top two layers of PDMS. Samples were then incubated with a solution of 98 µL 1% BSA in DPBS, 2 µL primary antibody for approximately one hour while protected from light. After this, samples were washed three times with 1% BSA in DPBS. Samples were then incubated with a solution of 95 µL 1% BSA in DPBS, 5 µL secondary antibody for approximately one hour while protected from light, followed by washing three times with 1% BSA in DPBS. NucBlue was diluted at a concentration of two drops per mL in 1% BSA solution, and applied to the samples for 15-20 minutes while protected from light. Samples were then imaged on an inverted fluorescence microscope using the appropriate filters.

8.5.8 Determination of Cell Count

8.5.8.1 Cell count per unit area. Final cell count after 10 days of culture in the devices was calculated using the live-dead fluorescence images acquired for cell viability experiments. Cell count in each image was defined as the number of live cells per image divided by the area of each image. For the cell count in devices without flow, the cell count was weighted with the percentage of total channel area that was within each part of the device (small channels vs. large channels).

8.5.8.2 Number of cells per device. The number of cells per device were calculated by multiplying the cell count per unit area for each device by the total channel area for the device. For comparison of flow and no-flow conditions, the cell count per unit area for the devices with flow was weighted by the percentage of total channel area that was within each part of the device (small channels vs. large channels).

8.5.9 Determination of Cell Area and Morphology

CellProfiler was utilized to determine the major axis length, minor axis length, and average area occupied by cells under the no-flow, low-shear, and high shear conditions. A modification of the "Human Cells" pipeline was used for this analysis, with a minimum diameter of 20 pixels and maximum diameter of 200 pixels. Average values were computed for each device, and averages were taken across four devices of each type (flow, no flow). Values were weighted as described above.

8.5.10 Determination of Cell Directionality

Cell directionality analysis was conducted on the same fluorescence images acquired during live-dead cell staining. Cell directionality was determined in ImageJ using the Directionality function with Fourier components and 90 bins following previous reports[368]. The average cell directionality within each device was computed by averaging the directionality values from the images for each device. Values were weighted as described above.

8.5.11 ELISA Assays

ELISA assays were conducted on medium collected 2, 4, 6, 8, and 10 days into the long-term device culture experiments using standard ELISA kit protocols. For IL-8 measurements, medium was diluted 1:1 with the provided assay diluent, and final IL-8 concentration was calculated with this dilution factor taken into consideration. A total of 150 µL culture medium was used in ELISA assays for each device. A sample size of 8 devices for the flow condition and 7 devices for the no-flow condition were used. To calculate the normalized cytokine expression, ELISA values for each

condition (with flow, without flow) were divided by the average calculated cell count per device for each condition.

8.5.12 Statistical Analysis

Statistical significance was determined using Student's t-tests assuming unequal variances. For cases in which more than one comparison was made, the Bonferroni correction was utilized to determine actual significance.

CHAPTER 9: TISSUE-CHIP EVALUATION OF EXOSOMAL CROSS-TALK BETWEEN CANCER CELLS, IMMUNE CELLS, AND LYMPHATIC ENDOTHELIAL CELLS

9.1 INTRODUCTION

The role of exosome transport between cancer cells, lymphatic cells, and immune cells is of great importance in shaping the lymphatic and tumor microenvironments.[377–380] To expand the applications of the lymphatic vessel on-a-chip, we sought to utilize it in exploring the exosomal and cell-level interactions between various cell types and lymphatic vessels. To this end, we chose two breast cancer cell lines (MCF-7 metastatic breast cancer, and MDA-MB-231 triple-negative metastatic breast cancer) and two T cell lines (JURKAT human blood leukemic T-cell lymphoblasts, and MOLT-4 human blood leukemic T-cell lymphoblasts) for exploration. The goal of these experiments was to transduce each of these cell lines to express red fluorescent protein (RFP) in secreted exosomes expressing CD63, a common exosomal marker. We sought to establish these RFP-expressing cell lines using pCT-CD63-RFP Cyto-Tracer (Systems Biosciences). After RFP transduction, the cells could individually be introduced to the lymphatic vessel chip, and the location of cells and their secreted exosomes could be tracked with fluorescence microscopy. By doing this, we hoped to illustrate the migration of cancer cells and T cells along the lymphatic vessel, in addition to uptake of breast cancer and T cell exosomes in the lymphatic vessel.

Additionally, we were interested in exploring the effects of shear flow on the expression of proteins and miRNA in the RFP-labelled exosomes. To do this, we planned to isolate exosomes from the media collected each day from the microfluidic devices. After quantifying the concentration of RFP-expressing exosomes (from the cancer or T cell lines) and non-RFP-expressing exosomes (CD63$^-$ exosomes from the cancer or T cell lines, or exosomes from the

HLECs), we planned to further isolate the RFP-expressing exosomes via flow cytometry. The exosomes would then be subjected to protein and miRNA extraction. Proteomic analysis and PCR would then be conducted to better understand the effects of cross-talk between lymphatic endothelial cells and other cell types on their exosome contents.

9.2 RESULTS AND DISCUSSION

To allow for separation of RFP-transduced cells from non-transduced cells, it was important to establish antibiotic kill curves for each cell line. Since the pCT-CD63-RFP transduction would result in cells with increased puromycin susceptibility, establishing the minimal concentration that would lead to cell death would allow for puromycin-based selection of transduced cell lines. In initial experiments, we exposed MDA-MB-231 and MCF7 cells to high concentrations of puromycin for 10 days. We found that even the lowest tested concentration led to no cell viability (**Figure 9.1**).
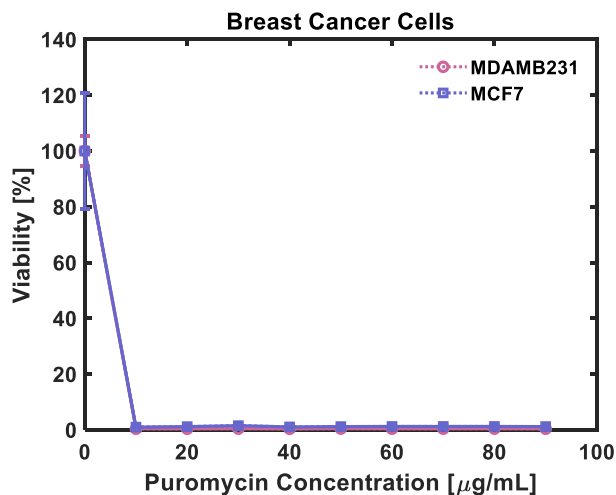
Figure 9.1. Antibiotic kill curve for MDA-MB-231 and MCF-7 cells exposed to 10-90 µg/mL puromycin for 10 days.

In further experiments, we exposed MDA-MB-231, MCF-7, Jurkat, and MOLT-4 cells to lower puromycin concentrations that were within reported ranges for antibiotic selection curves

for each of these cell types, and for a period of only seven days. Exposure to these lower concentrations of antibiotic did not lead to more favorable viability, however, and all cell lines had been completely killed by the end of the experiment **(Figure 9.2)**. Although these results do not agree with previously reported results, it is likely that other puromycin selection curves were established using cells that had undergone many passages and had mutated into more robust phenotypes. Since our experiments were conducted using cells in early passages, they may not be comparable to mutated cells that are more robust. Thus, the use of puromycin selection for our experiments does not appear promising, and isolation of RFP-expressing cells using flow cytometry would be a more favorable approach.
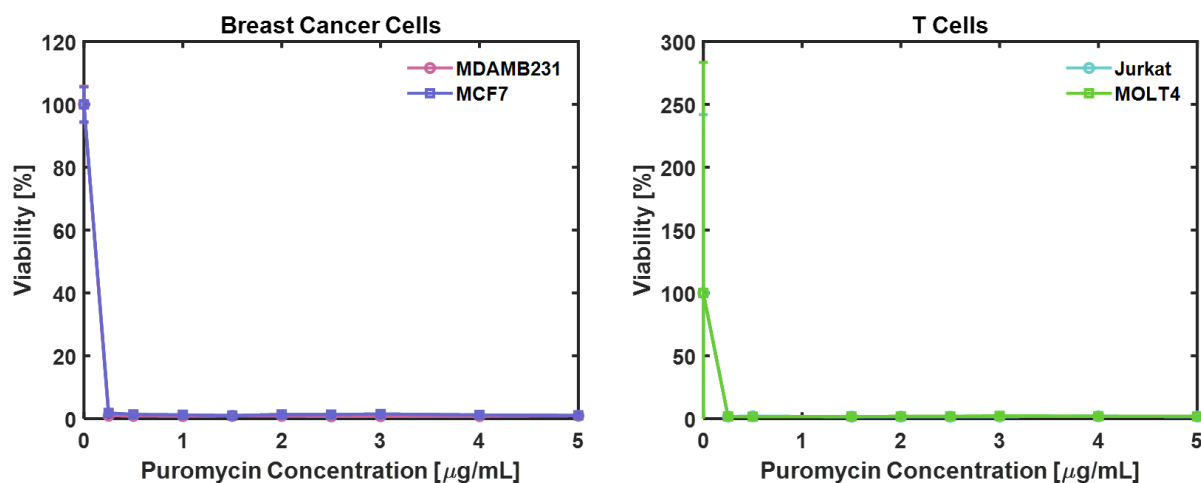
Figure 9.2. Antibiotic kill curve for MDA-MB-231, MCF-7, Jurkat, and MOLT-4 cells exposed to 0.25-5 µg/mL puromycin in for 7 days.

9.3 MATERIALS AND METHODS

9.3.1 Materials

Puromycin dihydrochloride from Streptomyces alboniger was purchased from Sigma. pCT-CD63-RFP Cyto-Tracer was purchased from Systems Biosciences.

9.3.2 Cell culture

MDA-MB-231 and MCF-7 cells were maintained in completed DMEM (with 1 % penicillin-streptomycin, 10 % fetal bovine serum). Jurkat and MOLT-4 cells were maintained in completed RPMI (with 1 % penicillin-streptomycin, 10 % fetal bovine serum).

9.3.3 Puromycin stock solutions

An initial puromycin stock solution was prepared by dissolving 25 mg puromycin in 2.5 mL DPBS (10 mg/mL stock). The stock solution was diluted to a concentration of 1 mg/mL in either completed DMEM or completed RPMI. Small volumes of the second stock solution were then further diluted in completed DMEM or completed RPMI to prepare the final desired puromycin concentrations. The recommended puromycin concentration range from Sigma was 10-100 µg/mL, while the recommended concentration from Thermofisher was 0.45-5 µg/mL.

9.3.4 Puromycin kill curves

Cells were plated in 96-well plates, with a concentration of 100,000 cells/mL, with 100 µL (10,000 cells) per well. Cells were allowed to grow overnight, after which their media was replaced with media containing antibiotic solution. Media was replaced every 2-3 days thereafter with fresh media containing antibiotic solution. Cell viability was determined using an MTT assay.

9.4 FUTURE WORK

Unfortunately, the COVID-19 situation prevented the completion of these experiments. Once stay-at-home orders are lifted, the RFP transduction protocol will be initiated, transduced cells will be separated via flow cytometry, and the other experiments will be completed as planned. We will demonstrate the attachment of cancer and T cells to the lymphatic vessel walls, and track exosomal cross-talk between these cells and primary human lymphatic endothelial cells.

CHAPTER 10: LYMPH NODES ON A CHIP

10.1 INTRODUCTION

Antigens are transported within lymph in lymphatic vessels, and cross the lymph node subcapsular sinus in order to enter the lymph nodules. On the other hand, immune cells can enter and exit the lymph nodules directly via the high endothelial venules. A majority of the lymph node's function occurs within the lymph nodules. In order to more accurately model the lymphatic system, it is necessary not only to model the lymphatic vessels, but also the lymph nodes themselves. The goal in this "2nd generation" lymph node chip was to incorporate the lymphatic vessels, subcapsular sinus, high endothelial venules, and lymph nodules within a single device. To achieve this, we designed a device with two halves, each of which has four chambers. One chamber would be used for the culture of cells in a 3D matrix; a second chamber would be used either for the static culture of other cell types, or as a media reservoir for the 3D matrix. The third and fourth chambers would be used for the culture of cells under shear flow, modelling the subcapsular sinus and high endothelial venules (**Fig. 10.1**). The joining of the two halves of the device would simulate the connection of two separate lymph nodes via the lymphatic vessels.

A 3D rendering of the two layers of the device is provided in **Fig. 10.2**. Assembly of the two layers of the device would involve the incorporation of a porous membrane that separates the top half of the device from the bottom half of the device. The subcapsular sinus channel would be lined with human lymphatic endothelial cells (HLECs), while the high endothelial venule channel would be lined with high endothelial venule endothelial cells (HEVECs). The bottom chamber would be used for 3D culture of immune cells and/or cancer cells.
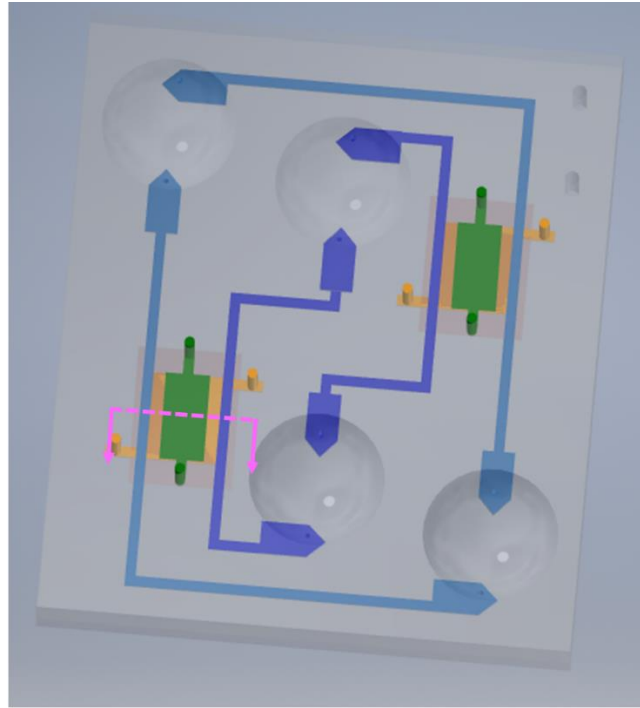
Lymph Nodes on-a-chip
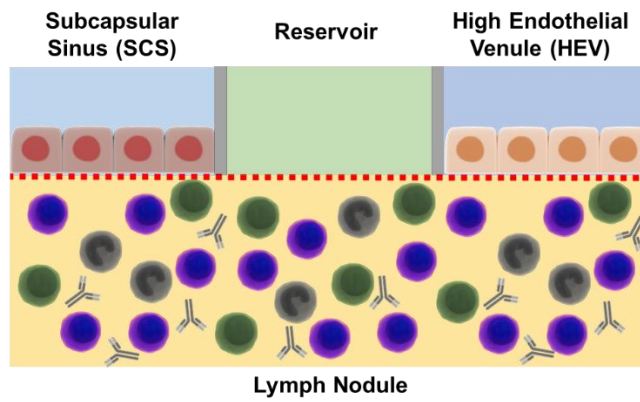
Figure 10.1. 3D rendering and cross-section view of the lymph nodes on-a-chip. The device incorporates four chambers on each half of the chip. The top half (comprising of the SCS, reservoir, and HEV) is separated from the bottom half of the device (lymph nodule) by a porous membrane.
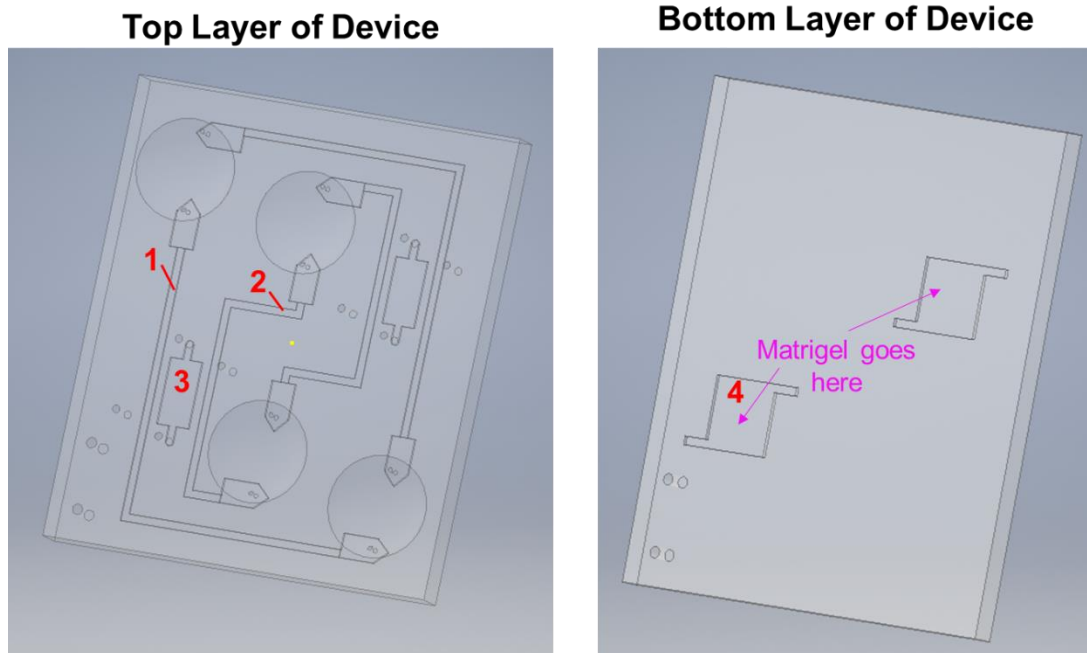
Figure 10.2. The two layers of the lymph nodes on-a-chip. The top layer of the device incorporates three chambers (labeled "1", "2", and "3") on each half of the device. The bottom layer incorporates one chamber (labeled "4") on each half of the device. The two halves of the device are connected via marble wells to allow for continuous unidirectional flow.
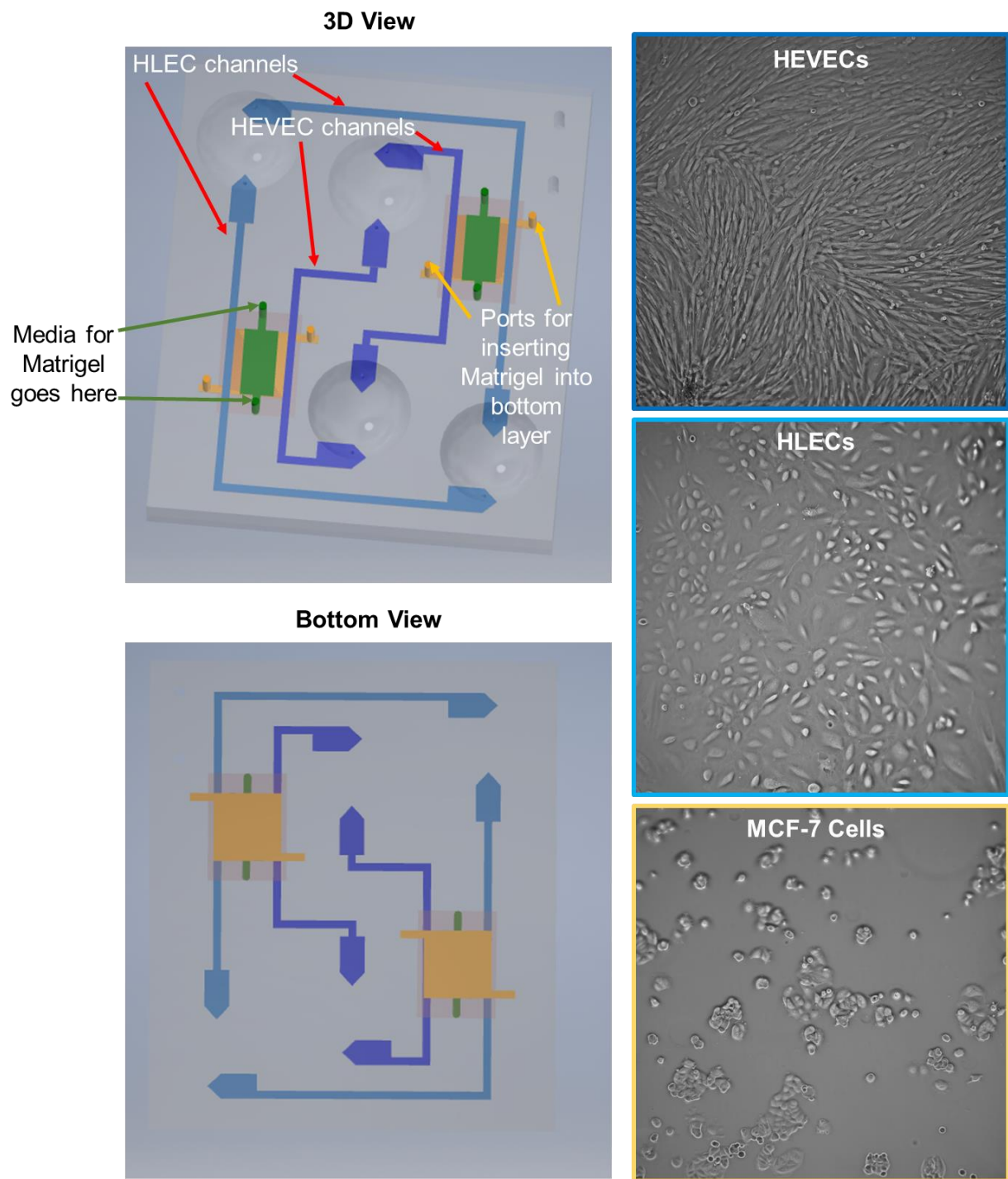
Figure 10.3. 3D renderings of chip design, along with images of cell types used within device.

10.2 METHODS, RESULTS, AND DISCUSSION

10.2.1 Device Design and Fabrication

The device was designed such that placing it at an angle of 45 ° on the rotating platform would allow for a maximum shear of 8.87 dyn/cm^2 in the HLEC channels and a maximum shear of 5.7 dyn/cm^2 in the HEVEC channels. As before, the shear level can be adjusted by adjusting the angle at which the rotating platform is kept. Device fabrication was done using PDMS cured on 3D-printed molds **(Fig. 10.4)**. Two separate molds were prepared for the top and bottom of the device. Media reservoirs were created using marbles as was done for the lymphatic vessel chip. The top and bottom layers of the device were separated by a membrane (1 µm or 10 µm pore size). 3D renderings and images of the 3D-printed molds are provided in **Fig. 10.5**. Molds were printed by Protolabs, using the Watershed material. Images of fabricated devices are provided in **Fig. 10.6**.

Preliminary tests were conducted to confirm that the devices could obtain flow within the channels. Since the porous membranes allow for transport of liquid between the top channels and bottom channels, we found that the best method for inserting Matrigel into the devices was to add the Matrigel within the Matrigel wells prior to adding any liquids. After incubating the device to allow for Matrigel solidification, liquid could then be added to other channels within the device.
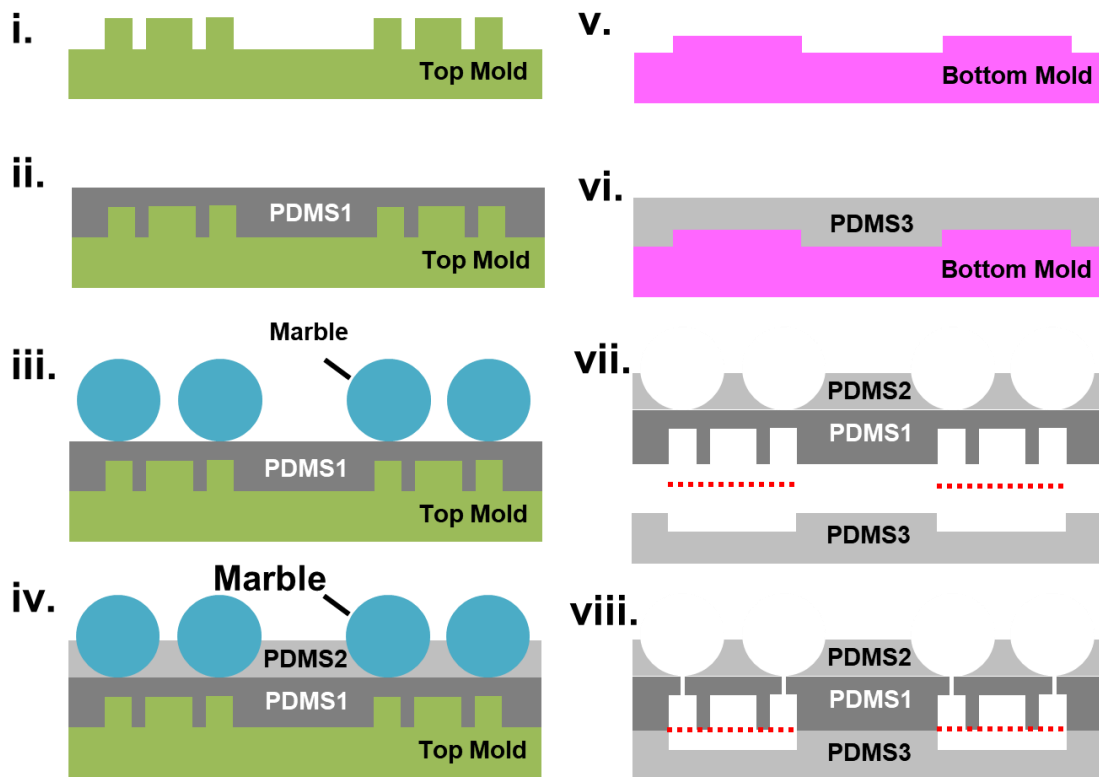
Figure 10.4. Device Fabrication. **(i)** A 3D-printed mold for the top channels is obtained. **(ii)** A layer of PDMS is cured to form the channels. **(iii)** Marbles are placed on top of the curved PDMS layer. **(iv)** A second layer of PDMS is cured to incorporate the marble wells. **(v)** A 3D-printed mold for the bottom of the device is obtained. **(vi)** A layer of PDMS is cured to form the bottom layer of device. **(vii)** The top half and bottom half of the device are separated from their molds. **(viii)** The top half and bottom half of the device are assembled, with a porous membrane separating the top and bottom channels.
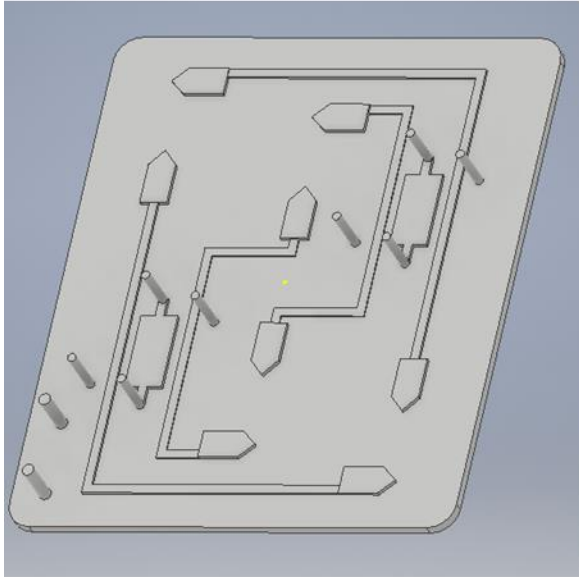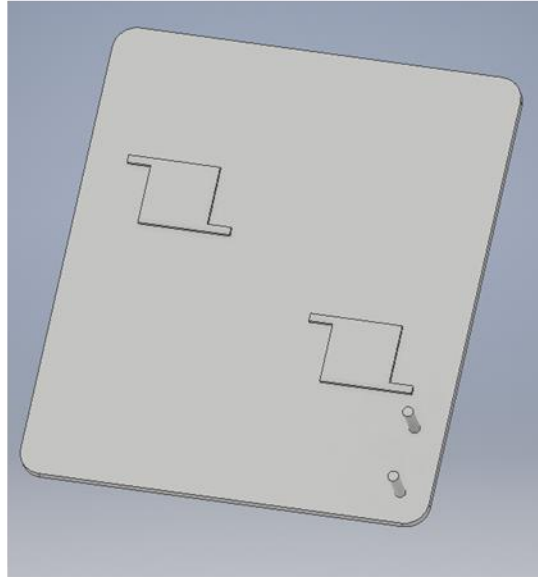
Figure 10.5. 3D models and 3D-printed channel molds for top and bottom layers of the device.

Figure 10.6. Fabricated devices without marble wells **(left)** and with marble wells **(right)**.

10.2.2 Isolation of HEVECs

HEVECs are typically isolated directly from human tonsils. The two markers that are used to identify HEVECs are MECA-79 and DARC. However, DARC expression has been shown to be rapidly down-regulated during ex vivo culture.[347] As a result, MECA-79 is the more reliable marker. Successful isolation of HEVECs from human tonsils using MECA-79 antibodies has been demonstrated previously.[381] To simplify the isolation process, we hypothesized that we could isolate HEVECs from purchased primary human tonsil endothelial cells (HTECs, ScienCell Research Laboratories).

We cultured HTECs in endothelial cell medium as recommended by the supplier. After a few days in culture, HTECs were trypsinized and spun down, after which they were resuspended in 1 mL immunomagnetic cell separation buffer (PBS with 0.5 % BSA, 2 mM EDTA). 10 µL MECA-79 antibody (mAb MECA-79 IgM Kappa Rat, Novus Biologicals) was added, and the sample was incubated at 4 °C for 15 min. 2 mL buffer was then added, and the sample was

centrifuged at 3000 x g for 10 min. The supernatant was discarded and cells were then resuspended in 80 µL buffer. 20 µL magnetic beads (Anti-Rat Kappa MicroBeads, Miltenyi Biotec) were added to the cell suspension. The suspension was mixed and then incubated at 4 °C for 15 min. 10 µL FITC-labeled secondary antibody (Mouse anti-Rat IgG1 Secondary Antibody, FITC, eBioscience) was then added to the suspension, and cells were incubated for a further 5 min 4 °C. 2 mL of the buffer was then mixed into the suspension, and cells were centrifuged at 200 x g for 10 min. Cells were resuspended in 500 µL buffer and the magnetic cell separation was performed using a miniMACS column and separator (Miltenyi Biotec) following manufacturer instructions. Isolated cells were then cultured following the same guidelines as those used for HTECs and HLECs. Bright-field microscopy images of HEVECs and HLECs are provided in **Fig. 10.7.** HEVECs are visibly different from HLECs.
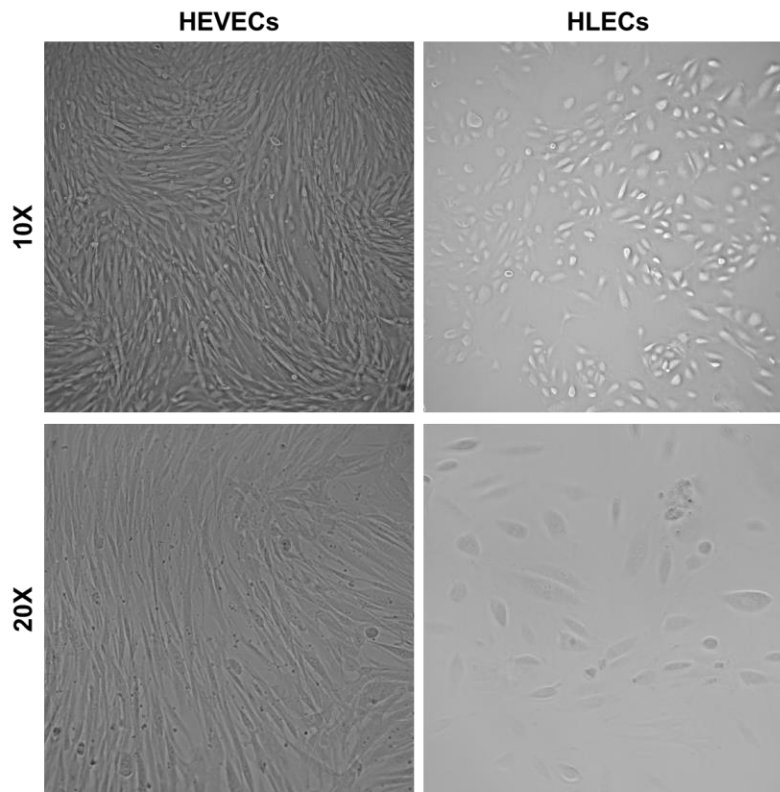
Figure 10.7. HEVECs and HLECs in culture.

10.3 CONCLUSIONS AND FUTURE WORK

Now that the device design has been established, the lymph node chip can be utilized in a variety of applications. To study cancer cell transport **(Fig. 10.8 A)**, fluorescently-labeled cancer cells can be introduced into the HLEC channel. Their transport across the subcapsular sinus and into the 3D matrix can then be measured. Cancer cells can alternatively be seeded directly into the 3D matrix, and their transport across the subcapsular sinus and high endothelial venules can be evaluated. The device can also be used to evaluate nanoparticle transport **(Fig. 10.8 B)**. BVNPs can be introduced to the HLEC channel and their transport across the subcapsular sinus and subsequent uptake in cancer cells can be evaluated. The transport of CD63-RFP-labelled exosomes from cancer cells into the subcapsular sinus or high endothelial venules can also be evaluated. Tumor spheroids can also be incorporated in the Matrigel layer **(Fig. 10.9)**. The spheroid-loaded devices can then be used to more accurately estimate nanoparticle and exosome transport between the various compartments of the device.

Incorporation of immune cells within the lymph node chip would provide opportunity for further evaluation of lymphatic behavior in this *in vitro* model **(Fig. 10.10)**. Migration of immune cells from the high endothelial venules or into the high endothelial venules could be examined. The transport of BVNPs into the nodule containing immune cells could be evaluated, along with subsequent immune cell activation. Transport of cancer cell exosomes into the nodule can also be examined, along with transport of immune cell exosomes from the nodules into the subcapsular sinus and high endothelial venules. Detailed descriptions of potential experiments are provided in **Table 10.1** and subsequent sections. An overview of relevant cell markers and cytokines are provided in **Tables 10.2 and 10.3**.

Furthermore, it is important to note that the device that we have designed is versatile and may be used for modelling a variety of scenarios, even outside of lymphatic modeling. With 4 chambers in which cells can be cultured under static or flow conditions, there are many different applications that the device may be used for. For example, human umbilical vein endothelial cells (HUVECs) can be cultured into both sets of blue channels, modelling veins. The larger channels for 3D culture can be utilized to represent the interstitial tissue, and transport between the vein channels and the interstitial tissue channels can be studied. Another application could involve the study of tissue oxygenation and deoxygenation. The inlets for one set of the channels can be plugged to minimize the introduction of oxygen to the cells within that channel. The transport of oxygen from the other channel within the oxygen-deprived channel can then be evaluated. The device can also be used in other applications such as evaluating transport across the blood-brain barrier. If desired for some applications, alginate can be incorporated as a 3D matrix in place of Matrigel. The alginate solution can be added where the Matrigel would normally be added, and calcium chloride solution could be added where the Matrigel media is usually added. After gelation of alginate, the calcium chloride solution can then be replaced with the desired media. Further details about some potential experiments are included in Appendix G.
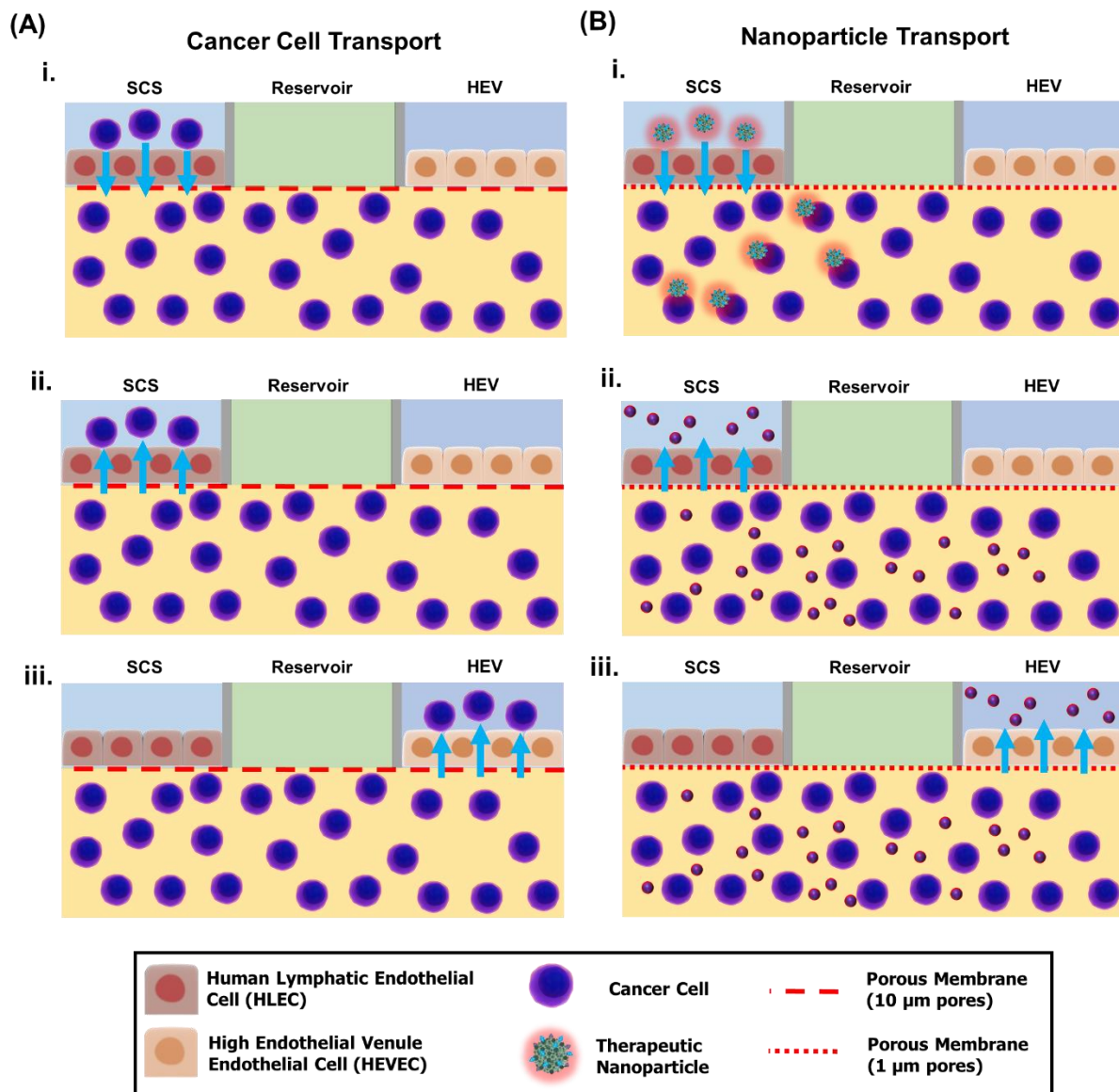
Figure 10.8. Incorporation of cancer cells in lymph node chip. **(A)** Cancer cell transport in the chip. Transport across subcapsular sinus and into nodule **(i.)**, transport from nodule into subcapsular sinus **(ii.)**, and transport from nodule into high endothelial venule **(iii.)**. **(B)** Nanoparticle transport in the chip. Transport of BVNPs from subcapsular sinus into nodule **(i.)**, transport of cancer exosomes from nodule across subcapsular sinus **(ii.)**, and transport of cancer exosomes from nodule into high endothelial venule **(iii.)**.

217
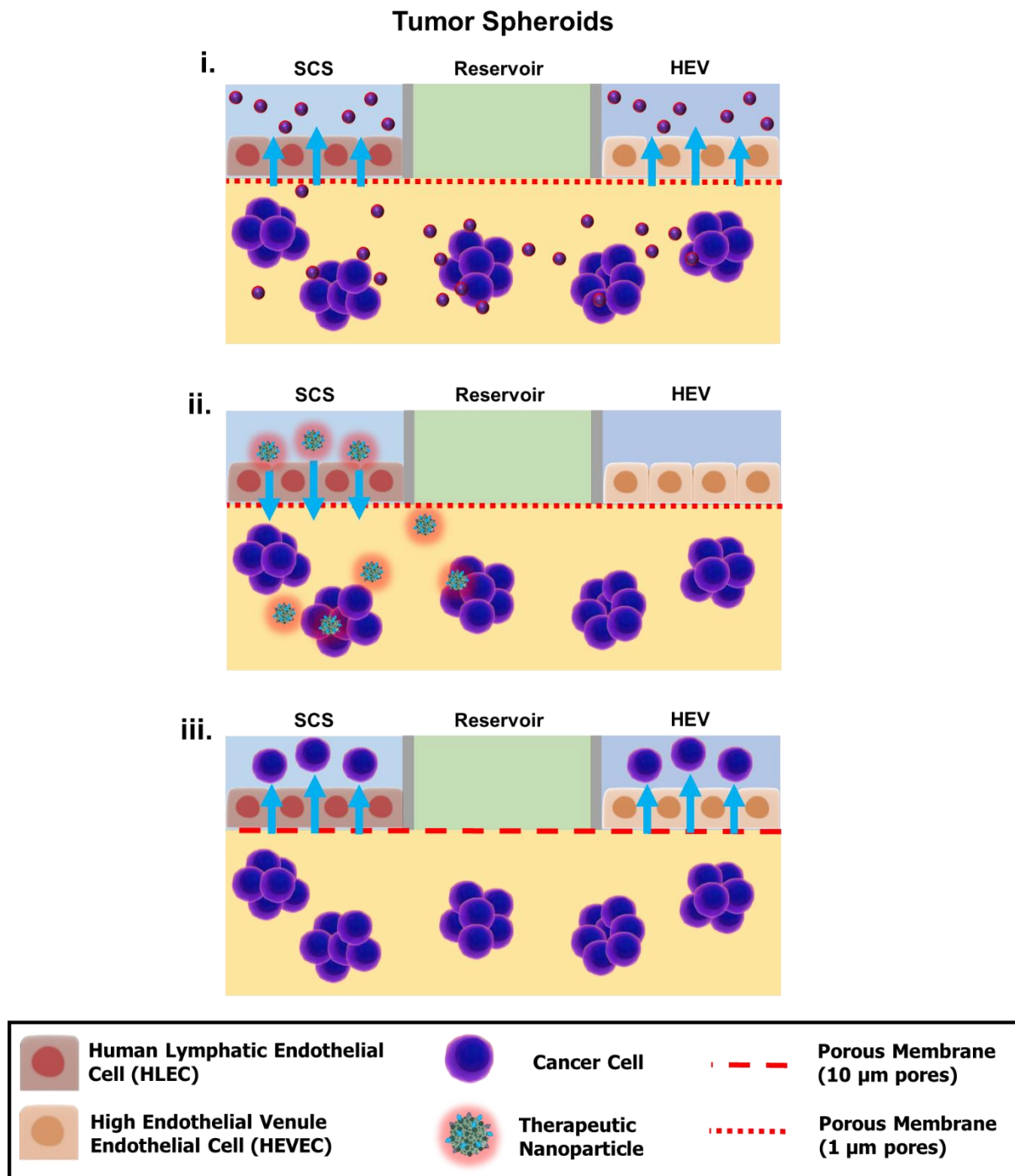
Figure 10.9. Incorporation of tumor spheroids in lymph node chip. Exosome secretion from the cancer cells and into the high endothelial venules or subcapsular sinus **(i.)**. Transport of BVNPs across subcapsular sinus, and subsequent uptake in tumor spheroids **(ii.)**. Extravasation of cancer cells from tumor spheroids and into the subcapsular sinus or high endothelial venule **(iii.)**.

Immune Cell Incorporation
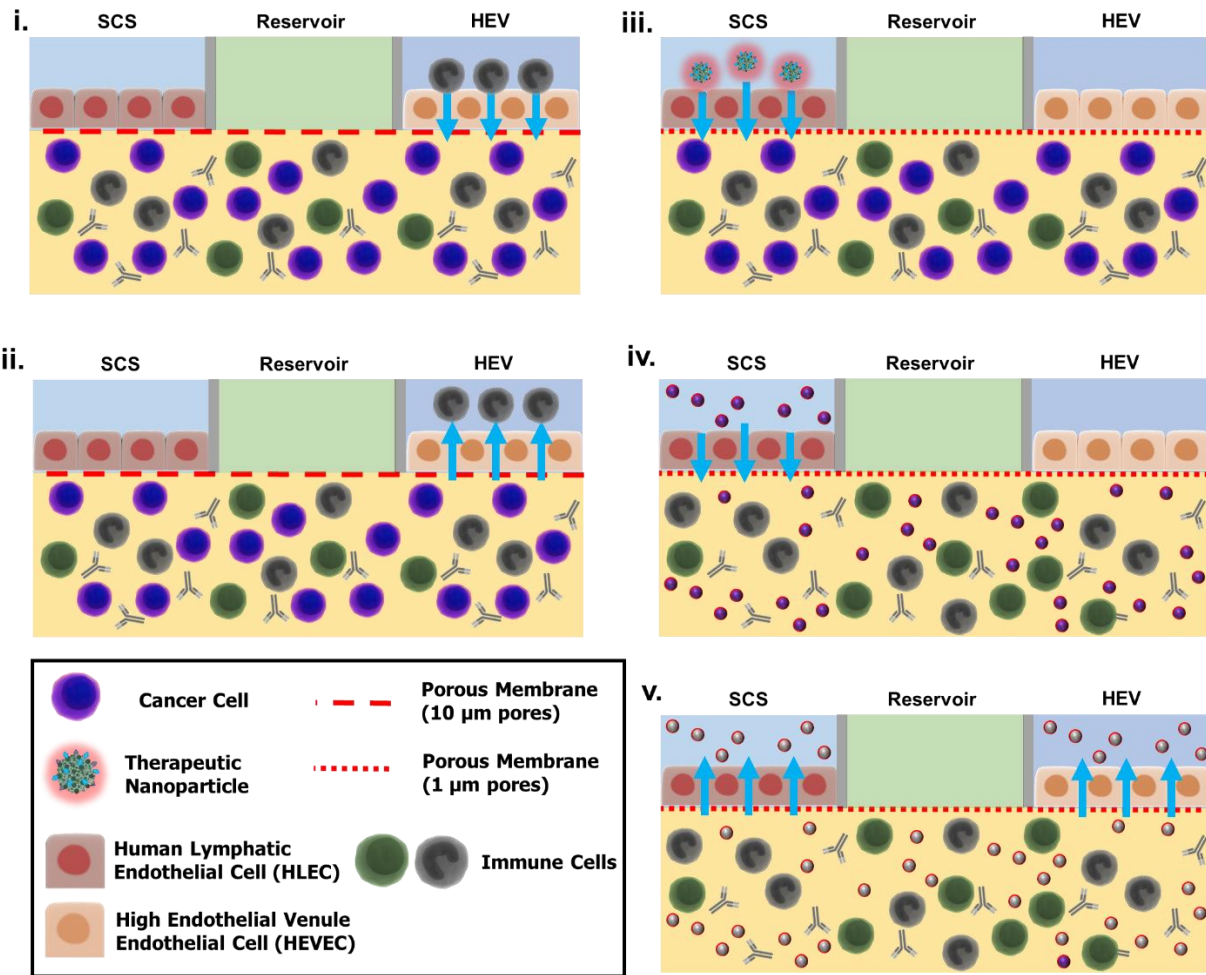
Figure 10.10. Incorporation of immune cells in the lymph node chip. Transport of immune cells from high endothelial venule into the lymph nodule (**i.**) and from the nodule into the high endothelial venule (**ii.**). Transport of nanoparticles into nodule and subsequent immune cell interactions (**iii.**). Transport of cancer cell exosomes from the subcapsular sinus into the lymph nodule (**iv.**). Transport of immune cell exosomes from lymph nodule into subcapsular sinus and high endothelial venule.

219

Table 7.1. Potential Experiments to be conducted with the lymph node chip**.**

#	Experiment	Cancer Cells?	Immune Cells?
I.	Confirming isolation of HEVECs from HTECs	No	No
II.	Establishing cocultures of HLECs and HEVECs in devices	No	No
III.	Establishing tricultures of HLECs, HEVECs, and cancer cells in devices	Yes	No
IV.	Invasion of cancer cells across subcapsular sinus and into Matrigel	Yes	No
V.	Extravasation of cells from Matrigel	Yes	No
VI.	Extravasation of cells from Matrigel and intravasation into the next node	Yes	No
VII.	Establish whether cancer cells will activate immune cells (transwell studies)	Yes	Yes
VIII	Establish whether immune cells can survive growing in Matrigel	No	Yes
IX.	Establish whether cancer cells will activate immune cells (contact studies)	Yes	Yes
X.	Coculture of immune cells, cancer cells, HLECs, and HEVECs in devices	Yes	Yes
XI.	Immune cell extravasation from high endothelial venules and intravasation across subcapsular sinus	No	Yes

Table 7.2. Cell markers of interest.

Marker	Cell Type				
	HLECs	**HEVECs**	**MDA-MB-231**	**MOLT-4**	**Jurkat**
PECAM/CD31	+	+			
LYVE-1	+	-?			
MECA-79	-?	+			
CD44			+		
CD24			-		
CD1 (49%), CD2 (35%), CD3 A (26%) B (33%) C (34%), CD4 (55%), CD5 (72%), CD6 (22%), CD7 (77%)				+ to all	
CD3					+

Table 7.3 Cytokines of interest for evaluation in lymph node chip.

Cytokine	Function
ELK3	Promotes breast cancer metastasis
CCL1	Promotes tumor cell entry into lymph node

CHAPTER 11: NEAR-INFRARED EMITTING DUAL-STIMULI-RESPONSIVE CARBON DOTS FROM ENDOGENOUS BILE PIGMENTS

11.1 ABSTRACT

Careful selection of carbon dot precursors and surface modification techniques has allowed for the development of carbon dots with strong near-infrared fluorescence emission. However, the rational selection of tetrapyrrolic carbon dot precursors to obtain stimuli-responsive behavior in addition to strong fluorescence contrast is unexplored. In this work, the first synthesis of carbon nanoparticles derived from endogenous bile pigments bilirubin (BR-CDots) and biliverdin (BV-CDots) is reported. The precursor choice lends BV-CDots and BR-CDots with enzymatically switchable or both enzymatically and photolytically switchable spectroscopic characteristics, respectively. Water-dispersible carbon dots with strong fluorescent contrast are obtained without the need for surface modifications post-synthesis. Interestingly, BV- and BR-CDots retain their stimuli-responsive behaviors intrinsic to their precursors post-synthesis. As demonstrated in the UV and fluorescence spectroscopic data, exposure to bilirubin oxidase or UV irradiation resulted in a shift in absorbance and fluorescence properties of BR-CDots, causing them to bear a resemblance to those of BV-CDots. Similarly, after exposure to biliverdin reductase, BV-CDots shift their UV and fluorescence spectral characteristics to become more similar to those of BR-CDots. BR-CDots are additionally found to provide strong near-infrared fluorescence contrast and high biocompatibility. This work demonstrates the use of rationally selected carbon sources for obtaining near-infrared fluorescence and stimuli-responsive switching behavior in carbon dots.

11.2 INTRODUCTION

Optical imaging using near-infrared wavelengths provides strong signals with minimal interference from tissue autofluorescence.[382–387] Carbon nanoparticles or carbon dots are a promising platform for near-infrared fluorescence imaging due to their relatively simple synthesis procedure, stable fluorescence that can be advantageous in studying naturally-occurring phytochromes, and known biocompatibility. Rational selection of precursors and reaction conditions has yielded carbon nanoparticles with high quantum yield,[243,388–390] high near-infrared emission,[391–394] and stimuli-responsive behavior[244,395], for *in vitro*, *in vivo*, and fundamental applications[396–403]. Despite these advantages, there have been few reports of tetrapyrrolic precursors for carbon dot synthesis and the effects of the use of these precursors on carbon dot behavior.[262–265] Recently, the use of nanoparticles made of bilirubin, a naturally-occurring fluorescent tetrapyrrolic pigment, has been reported.[199–204] The use of such pigments as nanoparticle precursors generates nanoparticles that provide contrast for biological imaging. Despite this observation, the use of bilirubin as a precursor for nanoparticles can prove challenging due to its limited solubility in water.[199,203] In this work, we sought to utilize tetrapyrrolic bilirubin and biliverdin, endogenous tetrapyrrole molecules found in bile, as carbon dot precursors to generate strong near-infrared fluorescence contrast and to exploit their stimuli-responsive behaviors.

Biliverdin, a green phytochrome, is the end product of a reaction between heme and heme oxygenase, which is further reduced into the yellow phytochrome bilirubin through the action of an enzyme, biliverdin reductase.[137] Bilirubin can be re-converted to biliverdin through the action of bilirubin oxidase,[404,405] or in response to ultraviolet (UV) irradiation.[343] Biliverdin and bilirubin can be distinguished from each other by biliverdin's high near-infrared absorbance peak at ca. 670

nm[62] and bilirubin's near-infrared fluorescence emission[406–409] respectively. Here we present the synthesis and characterization of carbon nanoparticles derived from biliverdin and bilirubin. Because of the interchangeable property of these fundamental molecules in heme metabolism, we sought to utilize these bile pigments as precursors for carbon nanoparticle synthesis with the end goal of exploiting their inherent properties and utilizing external stimuli to inter-switch the particle behaviors **(Figure 11.1)**.

Using a simple solvothermal synthesis, we created water-dispersible carbon dots from bilirubin and biliverdin. We found that the carbon dots retained many of the properties of their precursors, including their ability to respond to enzymatic exposure or UV irradiation. To the best of our knowledge, ours is the first demonstration of a carbon dot nanoparticle-based-system with precursor-derived alterable photophysical properties that can be stimulated by an external trigger. Additionally, we found that the bilirubin-derived carbon dots had high biocompatibility and provided strong contrast in *ex vivo* tissue-imaging experiments.
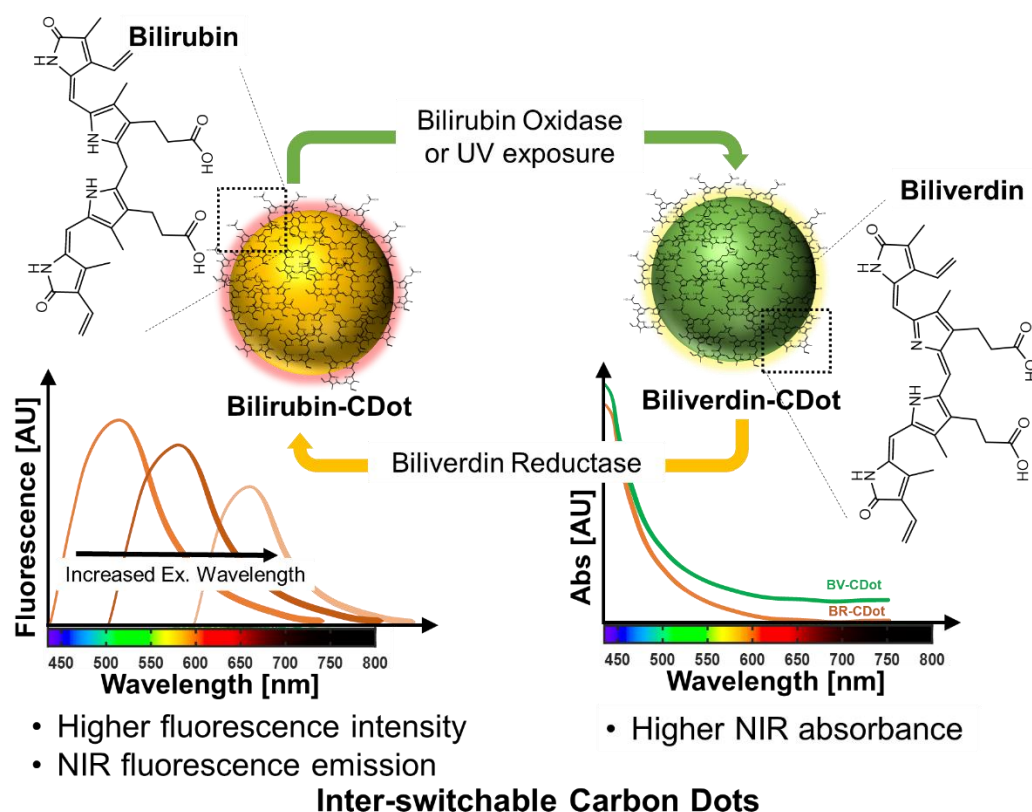
Figure 11.1. Schematic representation of stimuli-responsive inter-switchable CDots. Carbon dots derived from bilirubin and biliverdin posess photophysical behaviors that can be altered in response to exposure to specific enzymes or UV irradiation. Exposure of BR-CDots to UV irradiation or bilirubin oxidase causes their spectral properties to become more similar to those of BV-CDots. Exposure of BV-CDots to biliverdin reductase causes their spectral properties to become more similar to those of BR-CDots. Such behavior is characteristic of the precursor molecules (bilirubin and biliverdin), which were used to synthesize the carbon dots. The green trace is a schematic representation of BV-CDot absorbance behavior, while the orange traces are schematic representations of BR-CDot fluorescence and absorbance behavior.

11.3 RESULTS AND DISCUSSION

BR-CDots and BV-CDots were synthesized through solvothermal synthesis with precursor concentrations of 0.17 mol/L in a mixture of dimethylsulfoxide (DMSO) and water as co-solvents. Particles were filtered, then subjected to rotary evaporation and lyophilization, followed by resuspension at equivalent mass concentrations in water. Detailed experimental methods are described in the experimental section. The pH of the solution containing the CDots was raised to 8~9 in order to enable enzyme activity, and particles were then exposed to enzymes (with

cofactors) or UV irradiation. We reasoned that upon exposure to bilirubin oxidase or 365 nm UV irradiation, BR-CDots would be oxidized and exhibit spectral properties more like BV-CDots. Similarly, BV-CDots exposed to biliverdin reductase should be reduced and exhibit spectral properties more like BR-CDots.

The presence of carbon dots before and after exposure to enzymes or UV irradiation was confirmed with transmission electron microscopy (TEM) **(Figure 11.2A)**. CDot size was quantified **(Figure 11.2B, Table 11.1)** based on TEM images. BR-CDots had an average size of 9.1 nm ± 4.8 nm initially, and sizes of 15.2 nm ± 8.5 nm and 3.8 nm ± 1 nm after bilirubin oxidase exposure or UV irradiation respectively. BV-CDots had an initial average size of 1 nm ± 0.3 nm, and a size of 1.8 nm ± 0.8 nm after biliverdin reductase exposure. Enzyme-treated particles appeared to exhibit a trend of increased anhydrous particle size, possibly due to the accumulation of the enzyme and cofactor at the surface of the nanoparticles. Despite this, the overlapping standard deviations for untreated particles and enzyme-treated or UV-treated particles indicate that the observed changes in particle size are within measurement error. These results indicate that any inter-switching behaviors of the particles cannot be attributed purely to nanoparticle degradation, but rather to a change in photophysical properties in response to applied stimuli.

Table 11.1. CDot anhydrous size (mean diameter ± standard deviation) based on analysis from TEM images before and after exposure to stimuli. A minimum of 15 particles were used for each sample.

Particles	Before treatment [nm]	After enzyme treatment [nm]	After UV irradiation [nm]
BR-CDot	9.1 ± 4.8	15.2 ± 8.5	3.8 ± 1
BV-CDot	1 ± 0.3	1.8 ±0.8	N/A

High-resolution TEM imaging of BR-CDots revealed lattice fringes that are characteristic of previously reported carbon dots **(Figure 11.2C)**.[410–413] Lattice fringes measured at two different

locations within the BR-CDot had an average d-spacing of 0.3087 ± 0.0537 nm and 0.3266 ± 0.0658 nm. These values are in agreement with accepted d-spacing values for graphitic structures.[414,415] This confirms that the particles described in this work are carbon dots that are composed of graphitic carbon.

At the same mass concentration, BR-CDots initially had very low absorbance in the 600 nm to 700 nm range, while BV-CDots had higher absorbance, thus retaining the absorbance behaviors of their precursors. BR-CDots exposed to bilirubin oxidase had a steady increase in NIR absorbance over several days **(Figure 11.2D, Figure H1)**. BR-CDots exposed to 365 nm irradiation had an initial decrease in NIR absorbance, perhaps due to photobleaching. However, with continued UV exposure the BR-CDots steadily recovered their NIR absorbance **(Figure 11.2E, Figure H1)**, indicating switching from bilirubin-like behavior to biliverdin-like behavior. BV-CDots exposed to biliverdin reductase for a period of 6 days had a steady decrease in NIR absorbance with exposure time, suggesting that the BV-CDot behavior was switched from biliverdin-like to bilirubin-like **(Figure 11.2F, Figure H1)**. BV-CDots exposed to UV irradiation exhibited a decrease in absorbance due to photobleaching **(Figure 11.2G, Figure H1)**.

We sought to further explore whether this inter-switching ability extended to the particle fluorescence behaviors. BR-CDots had a higher initial fluorescence than BV-CDots **(Figure 11.3A)**. When exposed to bilirubin oxidase or UV irradiation, BR-CDot fluorescence decreased. The decrease after exposure to bilirubin oxidase can be attributed to a shift from bilirubin-like behavior to biliverdin-like behavior, while the decrease after UV exposure can be attributed to combined bilirubin to biliverdin switching and photobleaching. The differences in the shapes of
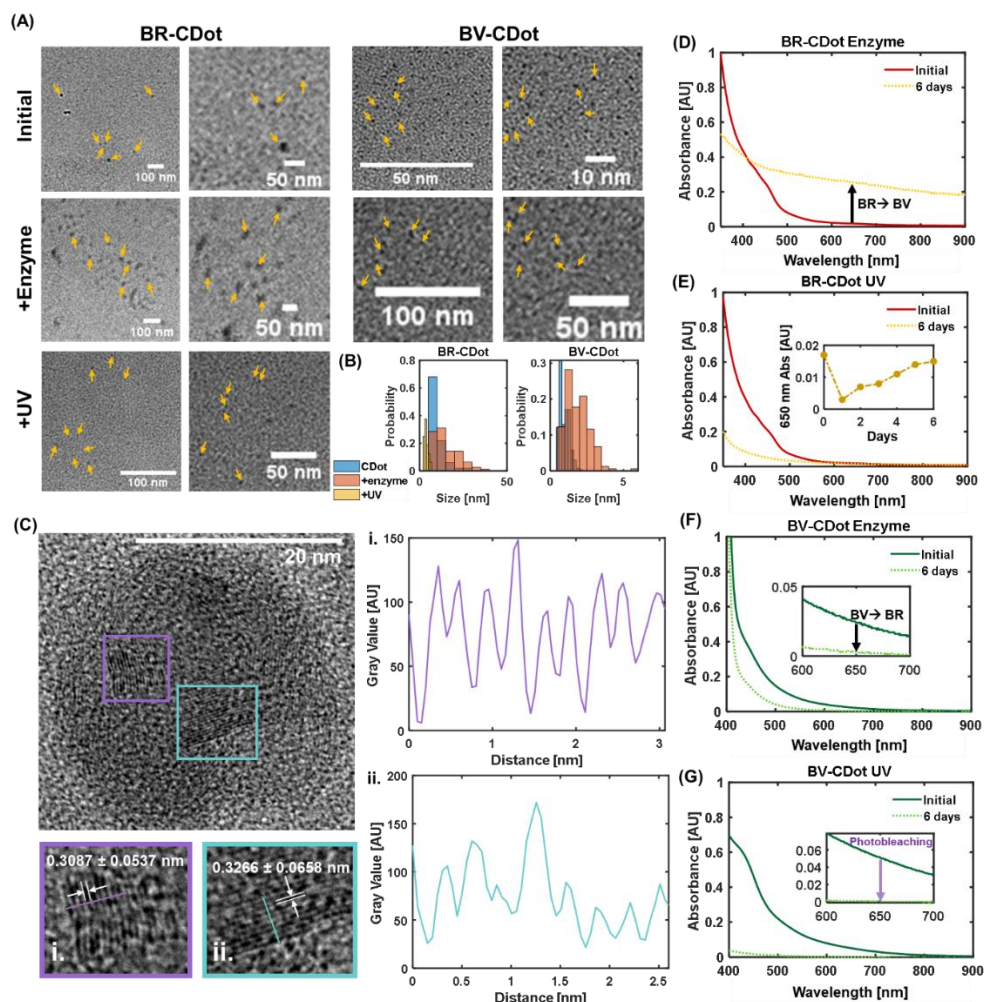
Figure 11.2. Morphology and absorbance behavior of bile pigment-derived CDots. **(A)** TEM images of BR-CDots before and after exposure to enzymes or UV irradiation confirm the presence of carbon nanoparticles before and after exposure to stimuli. Yellow arrows indicate some examples of nanoparticles. **(B)** Particle size distributions based on TEM images, confirming that these stimuli are not destroying the CDots. Distributions were calculated using all measured particles for each sample, with a minimum of 15 particles per sample. **(C)** High-resolution TEM image of a BR-CDot, demonstrating the presence of lattice fringes. Lattice fringe quantification was done using profile plots for purple inset **(i)** and blue inset **(ii)**. **(D)** BR-CDots have low initial NIR absorbance. When exposed to bilirubin oxidase, their NIR absorbance increases. "Initial" spectrum was collected immediately after enzyme addition, in order to account for any spectral changes that occur as a result of enzyme addition. **(E)** BR-CDots exposed to 365 nm UV irradiation have increased NIR absorbance with exposure time, after initial photobleaching. **(F)** BV-CDots have higher initial NIR absorbance than BR-CDots. When exposed to biliverdin reductase, their NIR absorbance decreases. "Initial" spectrum was collected immediately after enzyme and cofactor addition, in order to account for any spectral changes that occur as a result of their addition. **(G)** BV-CDots exposed to 365 nm UV irradiation experience a decrease in absorbance, presumably due to photobleaching.

fluorescence spectra of BV-CDots and final enzyme-treated BR-CDots can be attributed to some slight effects of pH on spectral behavior. BV-CDots exposed to biliverdin reductase had increased fluorescence intensity after 6 days of exposure, indicating inter-switching from biliverdin-like behavior to bilirubin-like behavior. BV-CDots exposed to UV irradiation had a decrease in fluorescence intensity resulting from photobleaching. These findings are supported by previous reports that UV irradiation converts bilirubin to biliverdin,[343] but that the reverse is not true.

Due to bilirubin's known NIR fluorescence emission [409], we further evaluated BR-CDot fluorescence behavior for higher excitation wavelengths. BR-CDots had high fluorescence emission intensities for excitation wavelengths of 465, 565, and 600 nm, with emissions in the NIR region **(Figure 11.3B, Figure H2)**. As observed for an excitation wavelength of 365 nm, fluorescence emission at these higher wavelengths fell as a result of inter-particle switching in response to exposure to bilirubin oxidase or UV irradiation **(Figure 11.3B, Figure H2)**.

Observation of BR-CDots and BV-CDots under a 365 nm lamp before and after 6 days of UV irradiation determined that BV-CDots indeed appeared less intense initially, and exhibited photobleached fluorescence with time **(Figure 11.3C)**. It is important to note that the enzymatic activity rates of bilirubin oxidase and biliverdin reductase differ from each other, which is why the magnitude of the absorbance and fluorescence behaviors of the inter-switched particles do not exactly match those of the particles they are being switched to.

To complement the conclusions drawn from high-resolution TEM imaging, we conducted Fourier transform infrared spectroscopy (FT-IR) experiments **(Figure H3)**. These experiments demonstrated that BR-CDots and BV-CDots retained many of the peaks from their respective precursors, indicating that the tetrapyrrolic behavior of the particles is not a result of a tetrapyrrolic core, but also some imidolic structures that were likely retained on the surface of the particles.

Additionally, it is unlikely that the particles are composed of a graphitic core and surface-functionalized with pure biliverdin or bilirubin. Due to bilirubin's poor solubility in water, if BR-
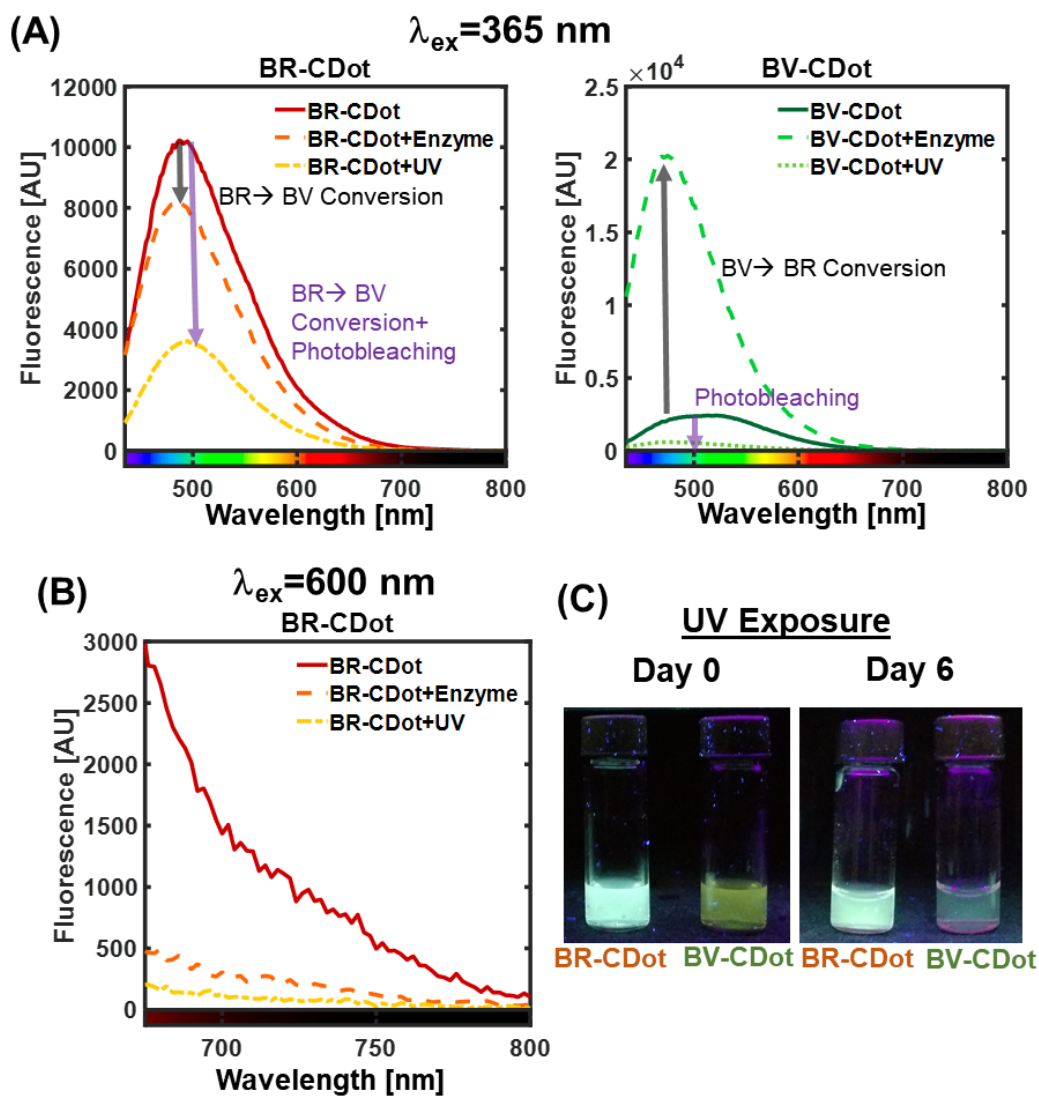
Figure 11.3. Fluorescence spectroscopic studies. (**A**) Fluorescence emission in response to 365 nm excitation. BR-CDots have higher fluorescence intensity than BV-CDots. Exposure of BR-CDots to bilirubin oxidase or 365 nm UV irradiation decreases fluorescence intensity. Exposure of BV-CDots to biliverdin reductase increases fluorescence intensity, while UV irradiation leads to photobleaching. (**B**) BR-CDot fluorescence spectra at 600 nm excitation. BR-CDots possess NIR emission. Exposure to bilirubin oxidase or UV irradiation reduces fluorescence intensity. (**C**) Fluorescence of BR-CDots and BV-CDots under 365 nm illumination before and after 6 days of continuous irradiation. BV-CDots exhibit extensive photobleaching, while BR-CDots do not.

CDots were coated in pure bilirubin, their suspension in water would have proved challenging. A number of studies have focused on elucidating the photophysical interactions between carbon dots that have been surface-modified with other molecules. [239,244,269,270,395,396,416] While the coating of carbon dots with tetrapyrroles would be a valuable direction for further exploration, that was not the goal of this work, and such explorations are beyond the scope of this study.

We further conducted X-ray photoelectron spectroscopy (XPS) **(Figure 11.4)** to elucidate the elemental composition of the surface of these particles. BR-CDots and BV-CDots retained C 1s, N 1s, and O 1s atoms from their precursors **(Figure 11.4A)**. The spectra for BR-CDots and BV-CDots appear quite similar due to the inherent similarities between bilirubin and biliverdin, the carbon dot precursors. In addition to identifying the presence of atoms that were within the precursor structures, we also identified the presence of S 2p, likely caused by the incorporation of sulfur atoms from DMSO during the solvothermal synthesis process. Exposure of BR-CDots and BV-CDots to enzymes for a period of six days led to some alterations in spectra, although these changes can be attributed to the presence of the enzymes rather than the inter-switching behaviors of the particles, as the initial spectra of BR-CDots and BV-CDots were quite similar to each other. The CDots were found to be primarily composed of C 1s and O 1s **(Figure 11.4B)**. Deconvolution of the C 1s peak revealed the presence of characteristic energies corresponding to the presence of carbon atoms in C-C/C=C, C-N/C-O, and COOH configurations **(Figure 11.4C)**. These findings serve to further confirm that the synthesized carbon dots successfully retained atoms from the precursor molecules upon the carbon dot surfaces.
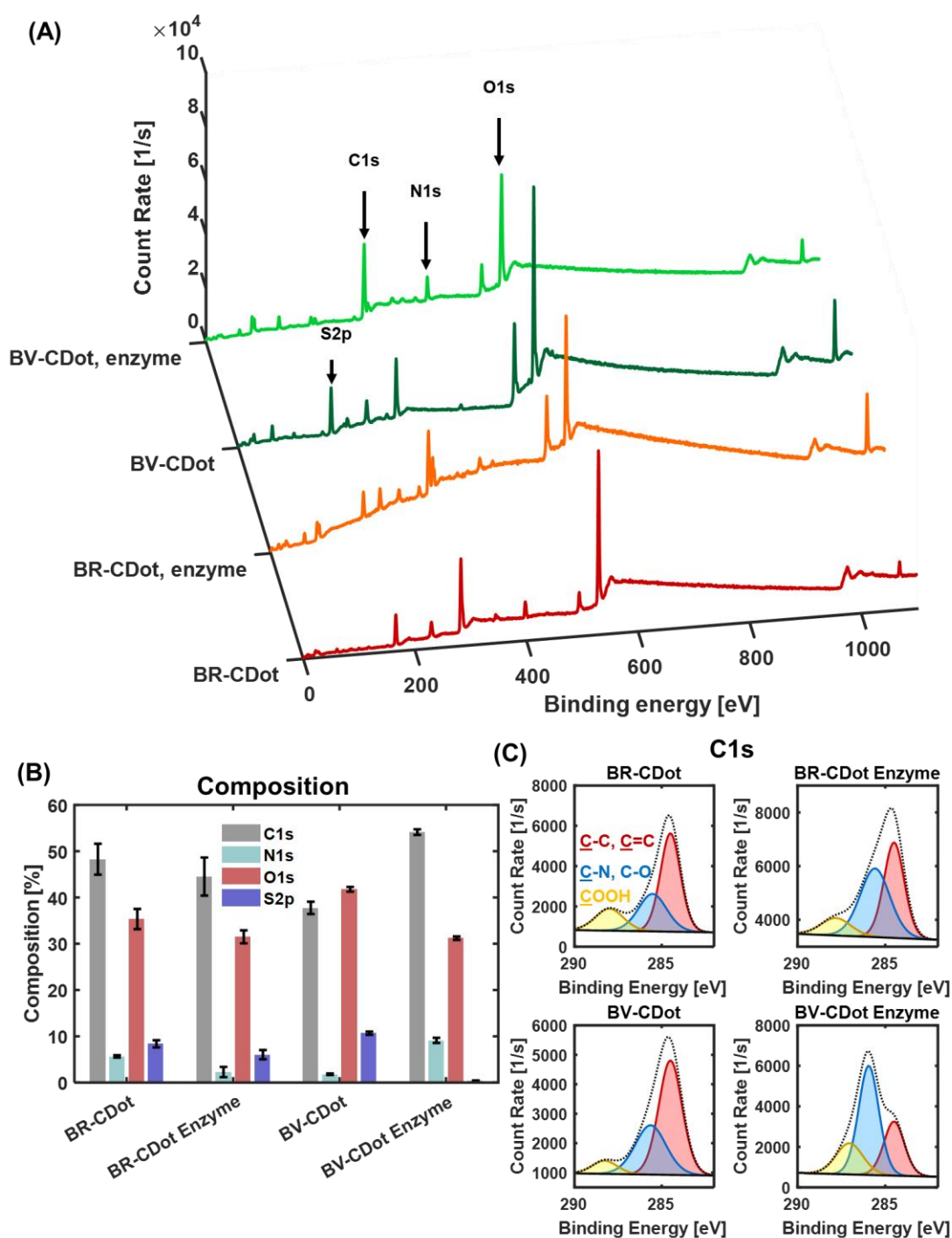
Figure 11.4. X-ray photoelectron spectroscopy studies. **(A)** XPS spectra of BR-CDots, BR-CDots treated with bilirubin oxidase, BV-CDots, and BV-CDots treated with biliverdin reductase. **(B)** XPS % composition analysis of C 1s, N 1s, O 1s, and S 2p atoms. The abundant presence of C 1s and O 1s atoms aligns with expectations based on bilirubin and biliverdin structures, as well as with typical carbon dot compositions. **(C)** Deconvolved C 1s XPS peaks. Deconvolution reveals the presence of C 1s atoms corresponding to C-C/C=C, C-N/C-O, and COOH.

To examine the biocompatibility of these particles, 3-(4,5dimethylthiazol-2-yl)-2,5-diphenyltetrazolium bromide (MTT) assays were conducted with MCF-7, MDA-MB-231, and Hep G2 cells **(Figure 11.5)**. These cell lines are metastatic breast cancer cells, triple-negative breast cancer cells, and liver cancer cells, respectively. All three cell lines exhibited high metabolic activity (>75%) when exposed to low concentrations of BR-CDots or BV-CDots. In fact, low concentrations of BR-CDots in some cases increased metabolic activity to higher than that of the control cells, while higher concentrations returned metabolic activity to normal levels. Due to pure bilirubin's poor solubility in water, comparisons between the metabolic activity of bilirubin-treated cells and BR-CDot-treated cells is not possible. High concentrations of BV-CDots decreased metabolic activity of the cells. However, this may have been due to increased uptake of BV-CDots as a result of their smaller size, as size has been found to play a role in nanoparticle uptake within cells.[417]
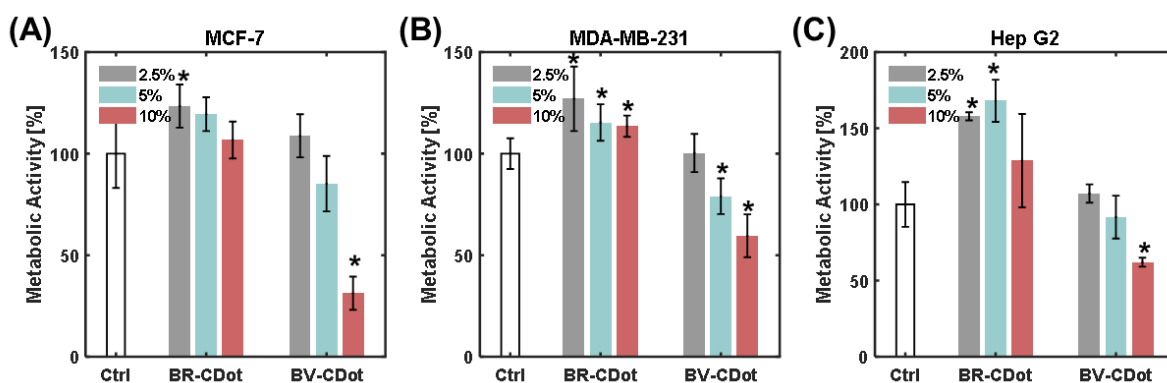
Figure 11.5. Metabolic activity of cells exposed to various concentrations of BR-CDots and BV-CDots. Particle concentrations are expressed as a % of initial concentration (1 mg/mL). **(A)** Metabolic activity of MCF-7 breast cancer cells. **(B)** Metabolic activity of MDA-MB-231 triple-negative breast cancer cells. **(C)** Metabolic activity of Hep G2 liver cancer cells. Error bars represent standard deviation. * represents statistical significance from control, with P<0.05. BR-CDots lead to high metabolic activity in all cell lines. High concentrations of BV-CDots lead to decreased metabolic activity in all cell lines.

Due to the favorable biocompatibility and fluorescence behavior of BR-CDots, we further evaluated their potential for use as a near-infrared imaging contrast agent in biological tissue. BR-CDots were injected just beneath the surface of chicken breast tissue, and imaged using a Spectrum In Vivo Imaging System (IVIS). Additional images were taken with another layer of chicken placed on top of the injection site, providing a depth of 8.5 mm for the BR-CDot fluorescence to penetrate. BR-CDots provided notable fluorescence contrast for a variety of excitation and near-infrared emission wavelengths, with representative images for excitation wavelengths of 605, 640, and 675 nm and emission at 840 nm shown in **Figure 11.6A**. Images for other excitation and emission pairs are provided in **Figure H4-H13**. Region of interest (ROI) analysis of images **(Figure 11.6B, Figure H14)** confirm that BR-CDots provide a high radiant efficiency over a range of excitation and emission wavelengths. Despite a loss of signal with increased tissue depth, the location of BR-CDots is still apparent (Figure 6A). ROI quantification for lower wavelengths is presented in **Figure H14**.

Further experiments were conducted in which BR-CDots were injected subcutaneously in the rear leg of a euthanized mouse. IVIS images obtained of the mouse under 605 nm excitation illustrate high radiant efficiency at the location of nanoparticle injection (Figure 11.7). ROI analysis of the injection site demonstrated the ability of these particles to provide strong near-infrared fluorescence emission within biological tissues, with strong emission in the range of 660 nm to 840 nm.
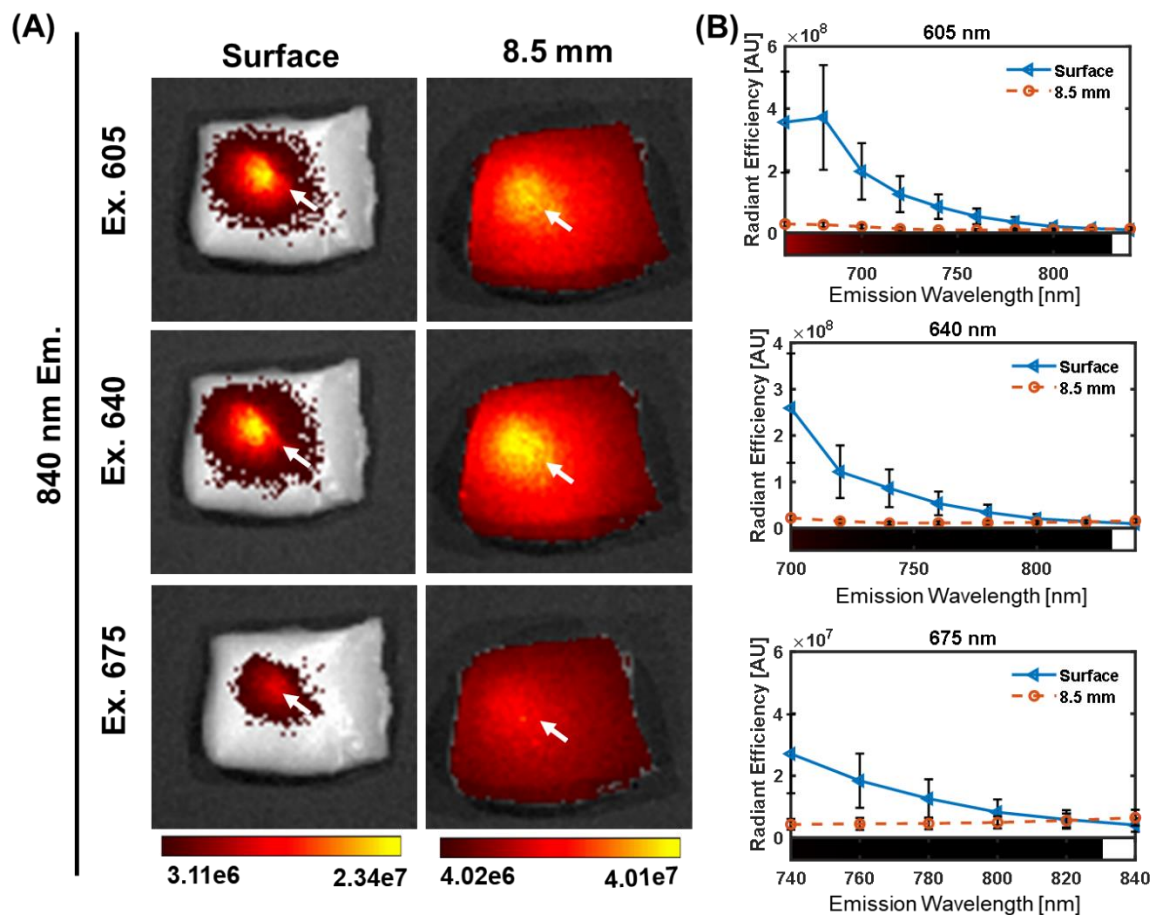
Figure 11.6. (A) Ex vivo fluorescence imaging of BR-CDots injected in a chicken breast tissue phantom. Images are presented for excitation wavelengths of 605 nm, 640 nm, and 675 nm, with emission measured at 840 nm. BR-CDots provide high signal in the near-infrared region, even under 8.5 mm of chicken tissue. White arrows indicate location of nanoparticles. **(B)** Background-subtracted radiant efficiency of BR-CDots for excitation wavelengths of 605 nm, 640 nm, and 675 nm. ROI background subtraction was conducted as described in the methods.
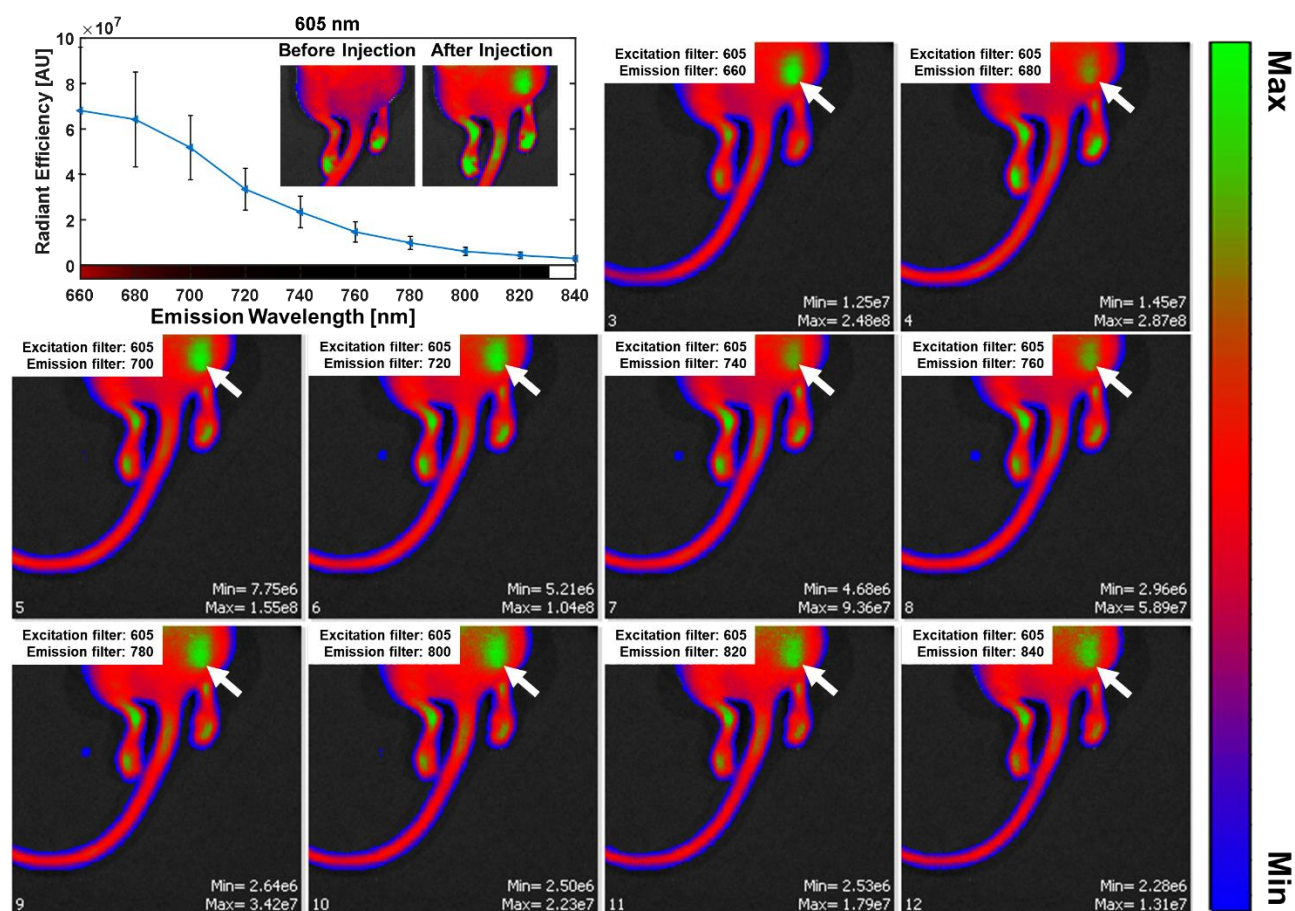
Figure 11.7. Ex vivo imaging of mouse injected with BR-CDots. Images were acquired for an excitation wavelength of 605 nm. White arrows indicate the location of nanoparticles. ROI analysis displays strong radiant efficiency in the near-infrared region. Calculated ROIs were background-subtracted as described in the methods.

11.4 CONCLUSION

To summarize, we have demonstrated the ability of stimuli-responsive carbon dots to be derived from endogenous bile pigments bilirubin and biliverdin. BR-CDots had lower NIR absorbance and higher fluorescence emission than BV-CDots. Exposure of BR-CDots to bilirubin oxidase or 365 nm UV irradiation for several days led to increased NIR absorbance and decreased fluorescence intensity, a "switch" from bilirubin-like behavior to biliverdin-like behavior. Exposure of BV-CDots to biliverdin reductase led to increased fluorescence intensity and decreased NIR absorbance. Further studies must be conducted to explore whether the stimuli-responsive behaviors of BR-CDots and BV-CDots are reversible after stimuli exposure, however,

such studies are way beyond the scope of this work. BR-CDots exhibited high NIR fluorescence emission for higher excitation wavelengths, and provided high radiant efficiency and strong contrast in *ex vivo* chicken tissue phantom imaging and *ex vivo* imaging in mice. This work is the first demonstration of rational selection of stimuli-responsive carbon dot precursors which lead to stimuli-responsive inter-switching of behaviors between two carbon nanoparticle types. This sets the foundation for the use of carbon nanoparticles synthesized from endogenous precursors to generate an inherently stimuli-responsive system with strong NIR fluorescence emission without the need for post-synthesis surface modification.

In recent years, research in carbon dots has grown rapidly and a variety of carbohydrate precursors have been used for synthesizing these particles. The selection of these molecules so far has been random and not clearly basing on a scientific rationale. However, as the field progresses, the importance of careful screening of precursors is being comprehended. Through this work, we highlight that precursor is a key determinant of carbon dot performance, yet in the current literature, very few studies seem to exist investigating the effect on their functional properties from using different precursor materials. Much of the current literature does not consider the raw precursors as an important parameter and ignores the importance of material characteristics which could be fundamentally exploited for optimization of carbon dot properties. Furthermore, the use of precursors that can be switchable by applying stimulus could produce stimuli-responsive nanoparticles that have a variety of biomedical applications. For example, they could be used for real-time monitoring of enzyme concentrations. Biliverdin reductase is an enzyme that is found in the liver and a variety of other organs, and thus monitoring its concentration in real-time could provide valuable information. However, the goal of this work was not to create nanoparticles to sense these specific enzymes, but rather to look at the impact of precursor on carbon dot behavior.

As such, the goal of this work is to provide a conceptual advancement of this field where application is deliberately underemphasized.

11.5. EXPERIMENTAL SECTION

11.5.1 Materials

Bilirubin and biliverdin hydrochloride were purchased from Frontier Scientific. Bilirubin Oxidase from Myrothecium Verrucaria, Biliverdin Reductase A Human, and NADPH disodium salt were purchased from Sigma Aldrich. Bilirubin oxidase was dissolved in water at a final concentration of 0.5 units/μL. Normocin was purchased from InvivoGen, and MTT was purchased from Biosynth.

11.5.2 Carbon Dot Synthesis

Bilirubin and biliverdin hydrochloride were each separately dissolved overnight at a concentration of 100 mg/mL in a solution of 500 μL water /500 μL DMSO. Each solution was placed in a separate, clean 50-mL PTFE-lined autoclave vessel. Samples were placed in the oven at 162.5 °C for 8 h, after which they were allowed to cool overnight. The following day, samples were removed from the vessels, and any excess liquid was removed through rotovapping and lyophilization. Dried samples were dissolved in 5 mL of water, and probe sonicated on a Qsonica Q700 probe sonicator for 30 min with an amplitude of 1, on time of 1 s, and off time of 2 s. Samples were then filtered using syringe filters with a pore size of 0.22 μm, lyophilized, and resuspended at a concentration of 1 mg/mL in water.

11.5.3 Enzymatic Inter-switching

11.5.3.1 BR-CDot. 1 milliliter of BR-CDot solution was placed in a capped 4-mL glass scintillation vial. 10 microliters to 25 microliters of 1 mol/L NaOH solution was added to increase the CDot solution pH to 8~9. Bilirubin oxidase solution (2 μL) was added to the CDot solution. Samples were shielded from light using foil, and were placed on a stir plate at 52.4 rad/s (500 rpm) and 40 °C. Sample absorbance was measured immediately after addition of NaOH and bilirubin oxidase, and every day subsequently.

11.5.3.2 BV-CDot. 1 milliliter of BV-CDot solution was placed in a capped 4-mL glass scintillation vial. 10 microliters to 25 microliters of 1 mol/L NaOH solution was added to increase the CDot solution pH to 8~9. NADPH (15.9 mg), a cofactor for biliverdin reductase, was added to the BV-CDot solution and allowed to mix for 10 min to 15 min, after which 2 μL biliverdin reductase was added. Samples were shielded from light using foil, and were placed on a stir plate at 52.4 rad/s (500 rpm) and 40 °C. Sample absorbance was measured immediately after addition of NaOH, NADPH, and biliverdin reductase, and every day subsequently.

11.5.4 UV Irradiation

1 milliliter each of BR-CDot or BV-CDot was placed in a capped 4-mL glass scintillation vial. The pH of each solution was raised to 8~9 using 1 mol/L NaOH as described above. Samples were then placed directly under a 365-nm UV lamp for six days. UV-visible absorption was measured immediately before placement under the UV lamp, and every day subsequently.

11.5.5 UV-Visible Spectroscopy

UV-visible spectra were collected for wavelengths ranging from 350 nm to 900 nm using a Thermo Scientific Genesys 10S UV−Vis spectrophotometer. CDot samples were not diluted for absorbance measurements. The baseline measurement was taken using 1 mL of water.

11.5.6 Transmission Electron Microscopy (TEM)

Microscopy samples were prepared on 300-mesh to 400-mesh carbon-coated copper TEM grids. Undiluted CDot samples (2.5 μL) were drop-cast onto each TEM grid and allowed to settle for 2 min, after which the excess liquid was wicked away with qualitative filter paper. Samples were then placed within centrifuge tubes and stored dry until the imaging session. TEM images were acquired with an acceleration voltage of 200 keV on a JEOL Cryo 2100 TEM.

11.5.7 Nanoparticle Sizing

Nanoparticle size was determined using ImageJ software. A global scale was assigned for each image using the scale bar embedded within the image. Images were converted to 8-bit format, and the threshold was adjusted so that only the particles were visible. Particle size was then determined using the "Analyze particles" tool, which provided the average particle area. This value was converted to a diameter using the following formula:

$$d = 2\sqrt{\left(\frac{A}{\pi}\right)}$$

(Equation 11.1)

A minimum of 15 particles were measured for each sample. Distributions, averages, and standard deviations were computed using all measured particles from each sample.

11.5.8 Quantification of d-spacing

Lattice fringe d-spacing was computed using ImageJ. A global scale was assigned for the image using the scale bar embedded within the image. A line was drawn perpendicular to the lattice fringes of interest. The intensity profile of the line was determined using the "Plot profile" tool, with a higher intensity corresponding to the brighter portions of the image. The distance between adjacent peaks (representing high intensity locations within the image) were computed and averaged.

11.5.9 Fluorescence Spectroscopy

Fluorescence spectra were acquired for undiluted 100 μL samples of each particle type. Excitation wavelengths of 365 nm, 465 nm, 565 nm, and 600 nm were used, with gains of 100, 100, 150, and 175 respectively. Fluorescence spectra were collected on a TECAN infinite M200PRO. Fluorescence spectra of BV-CDots were collected after pH adjustment.

11.5.10 Fourier Transform Infrared Spectroscopy

FT-IR samples were prepared by dropping the nanoparticle solution onto Kevley MirrIR corner frosted FT-IR slides, after which they were placed under vacuum until they had completely dried. FT-IR measurements were taken using a Thermo Nicolet Nexus 670 FT-IR with the smart refractor accessory.

11.5.11 X-ray Photoelectron Spectroscopy

Gold-coated silicon wafer sample substrates were cleaned with piranha cleaning solution. 5 microliters of each sample were placed on the cleaned gold-coated silicon substrate and allowed

to dry under vacuum, after which another 5 µL of each sample were deposited and allowed to dry again under vacuum. XPS measurements were performed on a Kratos Analytical Axis Ultra DLD instrument with a monochromated Al Kα X-ray source at 150 W (10 mA, 15 kV). X-rays were collected at a 0° angle from surface normal on an area of 300 µm × 700 µm. Low resolution survey scans (160 eV pass energy, 0.5 eV step size) and high resolution narrow scans (40 eV pass energy, 0.1 eV step size) of O 1s, N 1s, C 1s, and S 2p were obtained. Charge neutralization was used during measurements. The binding energy scale was calibrated to the C1s, C*- C aliphatic carbon peak at 284.5 eV. The CasaXPS program was utilized to analyze the spectra.

11.5.12 MTT Assays

3-(4,5dimethylthiazol-2-yl)-2,5-diphenyltetrazolium bromide (MTT) was dissolved at a concentration of 5 mg/mL in phosphate buffered saline (PBS). Cells were grown to 70 % to 80 % confluence in 25 cm^2 tissue culture flasks. Dulbecco's modified eagle medium (DMEM) supplemented with 10 % fetal bovine serum (FBS), 1 % Penicillin-Streptomycin solution, and 100 µg/mL Normocin was utilized for culture of all three cell lines (MCF-7, MDA-MB-231, and HepG2). Cells were plated at a concentration of 10,000 cells/well in 96-well plates and were incubated overnight under 37 °C under standard cell culture conditions. CDot solutions (1 mg/mL starting concentration) were diluted to volume fractions of 2.5 %, 5 %, or 10 % in medium, and 100 µL of CDot-containing medium was added to each well. The cells were incubated for 24 h at 37 °C under standard cell culture conditions. The medium from each well was then discarded and replaced with 100 µL diluted MTT solution (15 µL MTT solution in PBS, 85 µL completed medium) and cells were incubated for a further 4 h. Afterwards, the medium from each well was

discarded, and formazan crystals in each well were dissolved with 100 μL DMSO. The 650 nm and 570 nm absorbance of each well was measured, and viability was calculated by:

$$\% \, Viability = \left(\frac{Sample \, Abs_{570} - Sample \, Abs_{650}}{Control \, Abs_{570} - Control \, Abs_{650}} \right) * 100\%$$

(Equation 11.2)

Four or more wells were used for each condition, and results were reported as an average, with error bars representing standard deviation.

11.5.13 Tissue Phantom Imaging

100 microliters BR-CDots were injected directly beneath the surface of a chicken tissue sample. Fluorescence images were acquired on an IVIS imaging system for excitation wavelengths of 465 nm, 500 nm, 605 nm, 640 nm, and 675 nm. For images collected at an 8.5-mm depth, a second chicken tissue sample was placed on top chicken tissue into which BR-CDots were placed, and images were subsequently retaken.

11.5.14 Ex Vivo Mouse Imaging

100 microliters BR-CDots were injected subcutaneously in the right rear leg of a previously euthanized athymic mouse. IVIS images were acquired with an excitation wavelength of 605 nm.

11.5.15 ROI analysis

For each sample, one ROI measurement was taken at the nanoparticle injection site, and one ROI measurement was taken at a location not containing nanoparticles. The second ROI measurement was subtracted from the first, providing a measurement of the net average radiant efficiency. Sample ROIs for tissue phantom imaging and *ex vivo* mouse imaging are provided in **Figure H15** and **Figure H16** respectively.

CHAPTER 12: BULK-STATE AND SINGLE-PARTICLE IMAGING ARE CENTRAL TO UNDERSTANDING CARBON DOT PHOTO-PHYSICS AND ELUCIDATING THE EFFECTS OF PRECURSOR COMPOSITION AND REACTION TEMPERATURE

12.1 ABSTRACT

Carbon dots have garnered attention for their strong multi-color luminescence properties and unprecedented biocompatibility. Despite significant progress in the recent past, a fundamental understanding of their photoluminescence and structure-properties relationships, especially at the bulk vs. single-particle level, has not been well established. Here we present a comparative study of bulk- and single-particle properties as a function of precursor composition and reaction temperature. The synthesis and characterization of multicolored inherently functionalized carbon dots were achieved from a variety of carbon sources, and at synthesis temperatures of 150 °C and 200 °C. Solvothermal synthesis at 200 °C led to quantum yields as high as 86 %, smaller particle sizes, and a narrowed fluorescence emission, while synthesis at 150 °C resulted in a greater UV-visible absorbance, increase in nanoparticle stability, red-shifted fluorescence, and a greater resistance to bulk photobleaching. These results suggest the potential for synthesis temperature to be utilized as a simple tool for modulating carbon dot photophysical properties. Single-particle imaging resolves that particle brightness is determined by both the instantaneous intensity and the on-time duty cycle. Increasing the synthesis temperature causes an enhancement in blinking frequency, which leads to an increase in on-time duty cycle in three out of four precursors.

12.2 INTRODUCTION

Carbon dots (CDots) and carbon nanoparticles (CNPs) have generated interest due to their fluorescent properties and improved biocompatibility compared to other fluorescent nanoparticles

such as semiconductor quantum dots[418,419]. The fluorescent properties of these particles are believed to be caused by two properties: the sp^2 characteristic of the CDot/CNP core, and the surface state's extrinsic fluorescence[420]. Together, these two properties attribute to a bandgap, transitions within which lead to fluorescence[420]. CDot fluorescence has also been attributed to defects on the surface of these particles[421].

These nanoparticles have been used in a variety of applications in cellular and in-vivo biological imaging, biosensing, and drug and gene delivery[395,422–426]. Bioimaging applications have included in-vivo imaging of gliomas[422] and sentinel lymph node mapping in mice[423], as well carbon dots injected for other contrast applications[395,424–426]. Carbon dots have also been used in multicolor imaging[428], live-cell imaging[429], and intracellular tracking[396]. Sensing applications of carbon dots have included examples such as pH sensing[430] and the detection of metals and hormones[431–433]. Carbon dots have also been utilized in delivering cancer drugs[434], as well as in the non-viral delivery of DNA for therapeutic applications[435,436].

A variety of surface functionalization techniques have been explored in order to enhance carbon dot brightness and tune emission wavelengths for bioimaging applications. These include methods such as surface passivation with polymers and other molecules[437,438], and the incorporation of divalent cations and organic solvents during synthesis[439]. Other reports have demonstrated a relationship between the carbon source functional groups and nanoparticle surface functional groups[431,440,441]. Additionally, there has been much interest in producing carbon nanoparticles with high quantum yields[442–444]. as well as utilizing these nanoparticles in single-particle imaging applications[445–447].

While other particle types such as semiconductor quantum dots have been studied extensively at the single-particle scale[448–453], there is a need for a fundamental understanding of the effects of carbon nanoparticle composition and synthesis parameters on the photophysical properties of these nanoparticles, especially at the single-particle level. The goal of this work is to explore the effects of carbon source and synthesis temperature on the bulk and single-particle level photophysical properties **(Figure 12.1)**. To the best of our knowledge, there have been no previous reports that have explored this relationship. To this end, nanoparticles were synthesized using 4 different precursors and 2 synthesis temperatures. The precursors were chosen such that we evaluated both mono- and di-saccharides, as well as α and β isomers, in addition to phosphate and carboxylate anionic functionalities. The synthesis temperatures were chosen such that one temperature was higher than, and the other was lower than the boiling point of dimethylsulfoxide (DMSO).
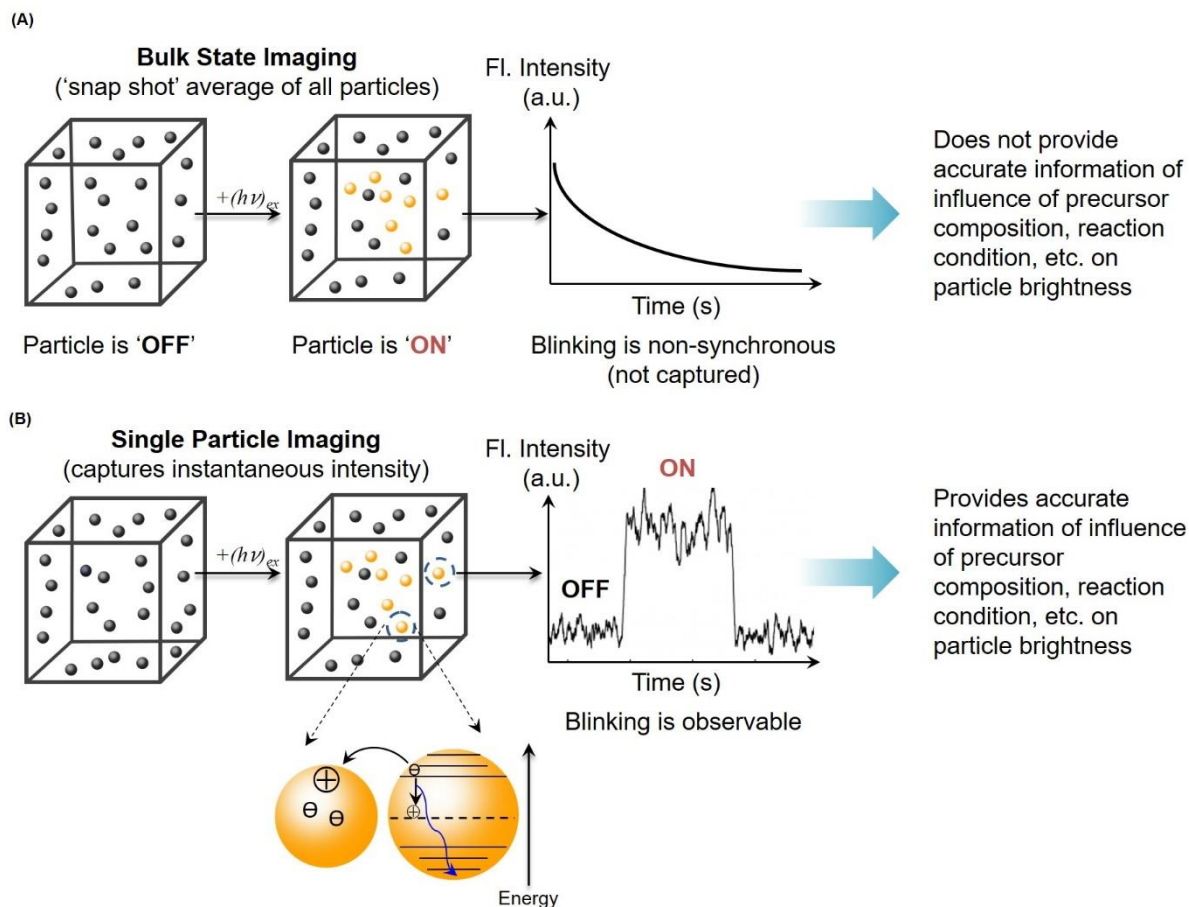
Figure 12.1. Bulk state vs. single particle imaging. **(A)** Bulk state imaging provides a snap shot average of all particles in the sample. The particle blinking in the bulk sample is non-synchronous, leading to a lack of information about the influence of temperature and composition on particle brightness. **(B)** Single particle imaging captures information about the instantaneous intensity of individual particles, allowing for evaluation of particle brightness based on individual particle "on" and "off" characteristics.

12.3 EXPERIMENTAL SECTION
12.3.1 Synthesis

CDots were synthesized using the solvothermal method. Although, the solvothermal method is commonly used for carbon dot synthesis [454–456], our synthesis differs in our selection of carbon sources and solvent ratio. α-D-Glucose 1-phosphate dipotassium salt hydrate, β-D-Glucosamine pentaacetate, D-glucuronic acid, and sucrose were separately utilized as the carbon sources. For each synthesis, 100 mg of the carbon source was mixed with 200 μL of DMSO and 800 μL of

water, and subsequently transferred to an autoclave holder. This ratio of DMSO to water was selected to aid in dissolution of the carbon sources while also allowing for the excess solvent to be evaporated during post-solvothermal processing. The holder was then placed in an oven at 200 °C or 150 °C for eight hours. The mixture was then removed, and the liquid was evaporated using a rotary evaporator. In some cases, the particles were placed under further vacuum after rotary evaporation to allow for the complete removal of the solvents. The CDots were then resuspended in 5 mL of water, and probe sonicated on for 30 minutes, with an amplitude of 1, on time of 2 s, and off time of 1 s. CDots were then filtered with a 0.22 μm filter, and were stored at 4 °C.

For all experiments except the microscopy, samples were lyophilized, after which they were resuspended in water at a concentration of 1 mg/100 μL.

12.3.2 Transmission Electron Microscopy (TEM) imaging

TEM grids were prepared by dropcasting 2.5 μL of the undiluted liquid CDot solution on copper grids, and excess moisture was wicked away after 2 minutes. An acceleration voltage of 20 keV was used.

Nanoparticle size analysis was conducted in ImageJ. Images were smoothed, and contrast was adjusted as necessary for separation of nanoparticles from the background. The images were then made binary and analyzed using the "analyze particles" tool.

12.3.3 UV-Visible (UV-Vis) and Fluorescence Spectroscopy

UV-Vis measurements were performed on samples. For these measurements, 2 μL of the nanoparticle solution was diluted with 998 μL of water. The UV-Vis spectra were collected over the 230 nm to 800 nm range. Fluorescence measurements were taken using an excitation

wavelength of 365 nm and a gain of 70, with a measured emission range of 385 nm to 850 nm. Sample volumes of 100 μL were used, and samples were not diluted for fluorescence measurements.

12.3.4 Quantum Yield Calculations

Quantum yield was calculated using the equation below, where Φ represents quantum yield, I corresponds to the integrated fluorescence intensity, A corresponds to the absorbance at 365 nm, and η corresponds to the refractive index of the solvent. Quinine Sulfate (QS, Φ_{QS}=0.54) in H_2SO_4 (η=1.33) was used as the reference for quantum yield calculations. Absorbance and integrated fluorescence intensity values are given in Tables S.2 and S.3.

$$\Phi_{CNP} = \Phi_{QS} * \left(\frac{I_{CNP}}{I_{QS}}\right) * \left(\frac{1 - 10^{-A_{QS}}}{1 - 10^{-A_{CNP}}}\right) * \left(\frac{\eta_{CNP}}{\eta_{QS}}\right)$$

(Equation 12.1)

For α-D-gluc and β-D-gluc CDots at 200 °C, UV-vis spectra were recollected at a higher concentration (980 µL water: 20 µL CDots) due to their low absorbances, and quantum yield calculations were conducted using quinine sulfate at the same higher concentration as the reference.

12.3.5 Fourier Transform Infrared Spectroscopy (FT-IR)

Aqueous suspension of the nanoparticles was dried onto IR-reflective glass slides. For each measurement $100\,\mu m \times 100\,\mu m$ images were collected at $1\ cm^{-1}$ spectral resolution with 64 scans per pixel and a $25\,\mu m \times 25\,\mu m$ pixel size. Individual spectra were corrected for atmospheric contributions.

12.3.6 X-ray Photoelectron Spectroscopy (XPS)

XPS samples were prepared by drop-casting 50 µL of CDots, on approximately 0.5 cm by 0.5 cm glass slides, allowing them to dry in a vacuum oven overnight, and then repeating the process until 2 layers had been drop-casted. XPS spectra were collected with Al Kα (1486.6 eV) radiation and were analyzed using CasaXPS software.

12.3.7 Zeta Potential Measurements

50 µL of CDots were diluted with 950 µL water for zeta potential measurements. Measurements were repeated 3 times for each nanoparticle type, with 10 or more runs conducted for each measurement.

12.3.8 Bulk Photobleaching Experiments

Samples were prepared by drying 0.2 µL of CDot solutions on clean glass coverslips. Individual particles were detected as bright diffraction-limited spots. The sample was diluted in water so that 200 particles were detected within an 80 µm × 80 µm field of view. A home-built, objective-based total internal reflection fluorescence microscopy (TIRFM) was used for single-particle imaging. An inverted microscope was equipped with a 100× oil immersion objective (100X, N.A. 1.49, oil immersion). A 488-nm continuous wavelength laser was used as the light source and the power was set at 1.5 mW at the back aperture of the objective. The incident light was directed through the objective via an exciter and a dual-band dichroic filter. The luminescence photons from individual CDots were collected by the same objective, passing an emitter and captured by an Electron Multiplying Charge Coupled Device (EMCCD) camera. A total of 8 min trajectory was acquired for each field of view. At least four replicates were measured for each sample. A home-

written script was used to extract the number of particles for each frame. The bleaching curve was generated by plotting the normalized number of particles versus time. The curve was then fitted with a two-component exponential function. The photobleaching lifetime was extracted from the fitted values.

12.3.9 Single-Particle Photobleaching

A droplet of 0.2 µL of CDot samples was applied to a clean coverslip. The coverslip was then kept in a clean biosafety cabinet for 10 min to allow the droplet to dry. Concentrations of each CDot sample were adjusted so that a layer formed on the surface. To measure the photostability of CDots, the coverslip was placed on a home-built TIRF microscope and the boundary of the dried smear of CDots was localized[457].

An inverted microscope equipped with a 100x oil immersion objective was used. The laser beam was then expanded, collimated to about 35 mm, and directed into the microscope by a lens (focal length = 400 mm). The incident light was directed through the objective via an exciter and a dual-band dichroic filter. The mean excitation power before the objective is 1.5 mW/cm^2.

For each field of view, 2400 time-stamped images were taken with the exposure time of 200 ms per frame, which accounts for a total of 8 min of trajectory. The CDot signal (inside the boundary) and background (outside the boundary) were extracted by averaging a total of 100×100 pixels in the corresponding area. The net signal of CDots was calculated by subtracting the background from the gross CDot signal for each frame. The emission decaying curve was generated by normalizing the maximum net CDot signal to 1.0. A script was used to fit the normalized emission decaying curve with a two-component exponential function. The photobleaching lifetime was extracted from the fitted values.

12.3.10 Data Analysis for Single-particle Photobleaching

A MATLAB (Version R2016a) code was generated from the built-in "Curve Fitting Tool" to fit the single-particle photobleaching trajectories. A two-component exponential function

$$f(t) = ae^{(\frac{1}{\tau_1})t} + ce^{(\frac{1}{\tau_2})t}$$

(Equation 12.2)

gave the best fit, which generated two time constants, τ_1 and τ_2, as well as their respective weights and the goodness of fit (R^2). Because the variance of the data is larger at the longer timescale than at the shorter timescale, the "Weighted Least Square" fit option was used and each data point was weighted by its variance.

12.3.11 Single-Particle Photoblinking analysis

Single-particle trajectories were segmented to define the "on" and "off" states based on the changepoint analysis[458,459]. The intensity threshold was defined as the mean of the segment with the lowest intensity plus three times the standard deviation of that segment (Mean + 3 σ). A segment of the trajectory whose intensity was above this threshold is defined as an "ON" state and its duration as t_{on}. An "OFF" state refers to any segment whose intensity was below the threshold and its duration as t_{off}. An array of t_{on} and t_{off} was collected from each trajectory and pooled for the same type of particle. The power-law distribution of t_{on} and t_{off} were generated by plotting the histogram of pooled data.

12.4. RESULTS AND DISCUSSION

12.4.1. Synthesis, Particle Size, and Photophysical Properties

CDots were obtained through the solvothermal synthesis method at 200 °C and 150 °C using α-D-glucose 1-phosphate dipotassium salt hydrate, β-D-glucosamine pentaacetate, D-glucuronic acid, and sucrose as the carbon sources, and a solution of DMSO and water as the liquid phase. After particle formation and evaporation of the liquid phase, the particles were resuspended in water. Further details are provided in the Materials and Methods section. These nanoparticles will henceforth be referred to as α-D-gluc, β-D-gluc, D-glucuronic acid or D-gluc, and Sucrose nanoparticles respectively. TEM images **(Figure 12.2A)** revealed a slight decrease in nanoparticle size **(Table 12.1)** as the synthesis temperature increased. α-D-gluc CDots had a size (average ± standard deviation) of 5 nm ± 3 nm at 200 °C and a size of 11 nm ± 2 nm at 150 °C, β-D-gluc CDots had sizes of 8 nm ± 4 nm and 10 nm ± 4 nm respectively, D-gluc CDots had sizes of 4 nm ± 1 nm and 22 nm ± 19 nm respectively, and Sucrose CDots had sizes of 8 nm ± 3 nm and 16 nm ± 11 nm respectively. Thus, synthesis at 200 °C typically resulted in nanoparticles small enough to be considered carbon dots, while the syntheses at 150 °C yielded some CDots in the below 10 nm range, and some particles that were slightly larger. The dependence of nanoparticle size on the synthesis temperature may have been caused by the boiling points of the solvents in the liquid phase. Water and DMSO do not form an azetrope, and DMSO has a boiling temperature of 189 °C. Thus, a synthesis temperature of 150 °C allows for only water to reach its boiling point, while a synthesis temperature of 200 °C allows both water and DMSO to reach their boiling points. Particles were formed in both cases due to water reaching its boiling point, but the boiling of both water and DMSO led to hindered growth, causing smaller nanoparticles to form at 200 °C.
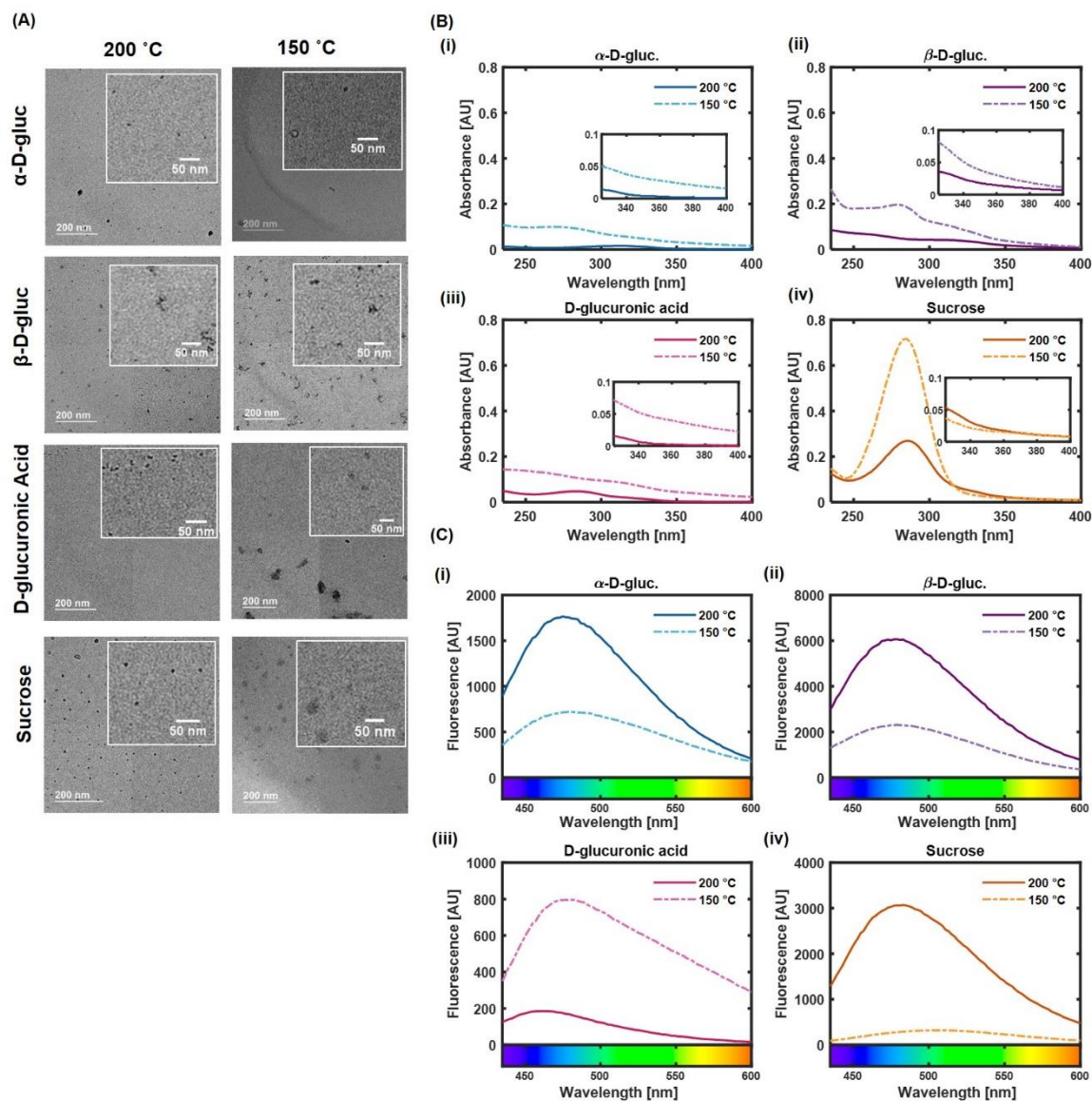
Figure 12.2. (A) TEM micrographs of CDots for each composition and synthesis temperature. Particles synthesized at 150 °C appear visually larger than those synthesized at 200 °C. Scale bar represents 200 nm. **(B)** UV-Vis spectra for CDots of each carbon source (i) α-D-gluc, (ii) β-D-gluc, (iii) D-glucuronic acid, and (iv) sucrose, at each synthesis temperature. A lower synthesis temperature led to higher absorbance. **(C)** Fluorescence spectra for CDots of each carbon source (i) α-D-gluc, (ii) β-D-gluc, (iii) D-glucuronic acid, and (iv) sucrose, at each synthesis temperature. An excitation wavelength of 365 nm was used. α-D-gluc, β-D-gluc, and Sucrose CDots had an increase in fluorescence intensity with an increase in synthesis temperature.

254

Table 12.1. Nanoparticle size (average ± standard deviation) as determined by analysis of TEM images

Carbon Source	Synthesis Temperature	
	200 °C	150 °C
α-D-gluc	5 nm ± 3 nm	11 nm ± 2 nm
β-D-gluc	8 nm ± 4 nm	10 nm ± 4 nm
D-gluc	4 nm ± 1 nm	22 nm ± 19 nm
Sucrose	8 nm ± 3 nm	16 nm ± 11 nm

UV-Vis spectra collected for the CDots showed that those synthesized at 150 °C had higher absorbance than those synthesized at 200 °C for most carbon sources (**Figure 12.2B**). This may have been caused by the larger size of the particles synthesized at 150 °C, which in turn led to a larger surface area over which absorbance could occur. When excited at 365 nm, α-D-gluc, β-D-gluc, and Sucrose CDots synthesized at 200 °C had a higher fluorescence intensity than their counterparts synthesized at 150 °C (**Figure 12.2C**). This trend did not hold true for D-gluc CDots. However, quantum yield calculations showed a uniform trend across all carbon sources, with all carbon sources having a higher quantum yield when synthesized at 200 °C than when synthesized at 150 °C (**Figure 12.3A**). α-D-gluc nanoparticles synthesized at 200 °C exhibited the highest quantum yield at 86 %, one of the highest reported values for carbon dots [445–447]. β-D-gluc CDots synthesized at 200 °C had the next highest quantum yield at 48 %, followed by D-glucuronic acid CDots at 45 %, and Sucrose CDots at 22 %. Quantum yield values for the CDots synthesized at 150 °C were much lower, ranging from 3 % to 10 %. Although the fluorescence intensity of D-gluc CDots synthesized at 150 °C is much higher than that of D-gluc CDots synthesized at 200 °C, the quantum yield of the higher temperature synthesis was found to be significantly higher than the low temperature product. This observation was presumably caused by the very high absorbance of the 150 C D-gluc CDots compared to that of the 200C D-gluc CDots resulting in a discrepancy
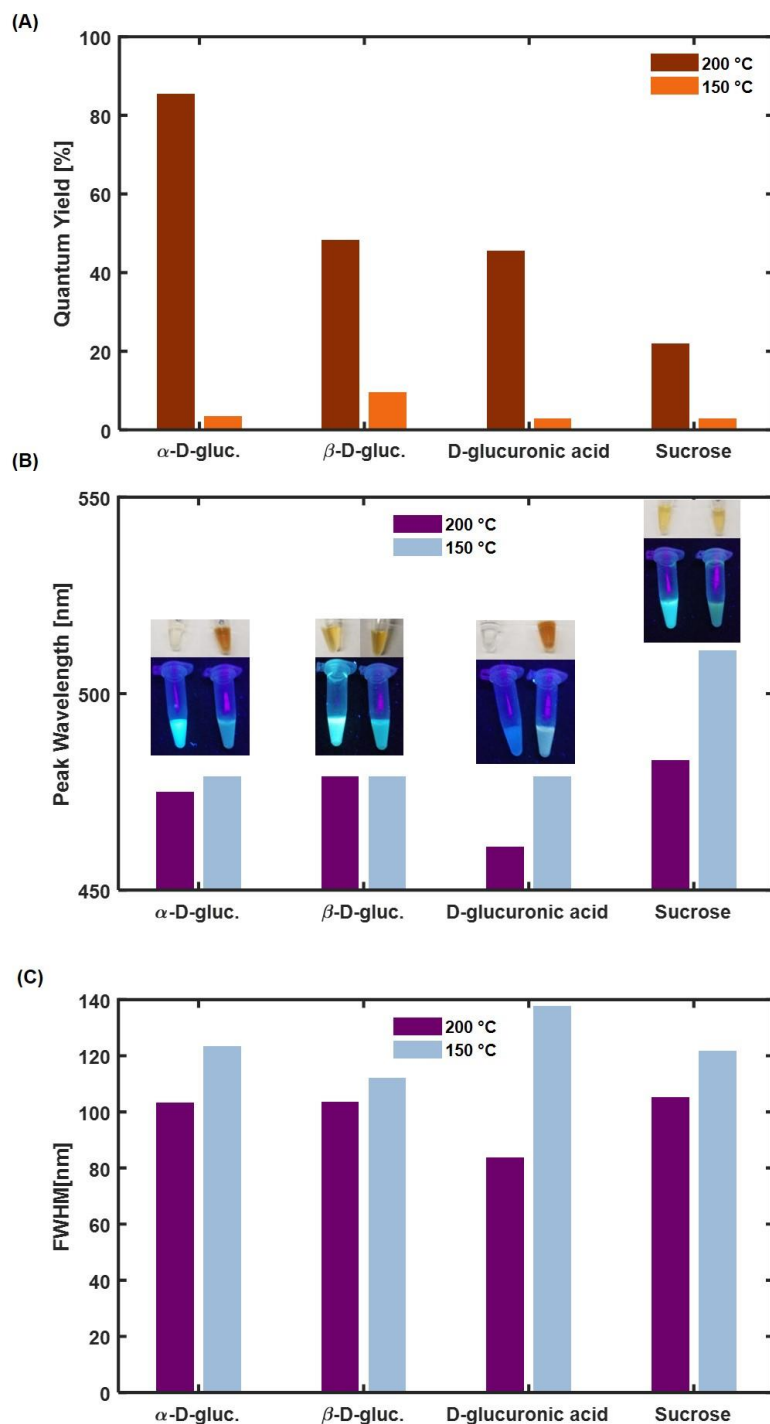
Figure 12.3. **(A)** Quantum yield for CDots at each synthesis temperature. Quantum yield was determined using quinine sulfate as a reference dye. A higher synthesis temperature was found to lead to higher quantum yields for all carbon sources evaluated. **(B)** Location of fluorescence peak for CDots at an excitation wavelength of 365 nm. α-D-gluc, D-gluc, and Sucrose CDots exhibit a red-shifted fluorescence for the lower synthesis temperature. **(C)** Full width at half maximum values calculated for fluorescence spectra collected at an excitation wavelength of 365 nm. A higher temperature leads to narrower fluorescence emission peaks.

of the quantum yield measurements. Quantum yield depends on both the integrated fluorescence intensity (I) and the absorbance (A) as defined in Equation 12.1.

The increase in quantum yield is a step change with respect to the boiling temperature of the solvent mixture. We anticipate that our future studies will focus on the effects of smaller temperature changes on CDot properties, but it is likely that the "optimized" temperature for each synthesis may depend not only on the solvent but also on the individual carbon source. We believe that the present work is adequate in providing a basis for studying CDot photophysical properties with respect to varying precursor composition. All quantum yields reported in this manuscript are from individual batches of nanoparticles, as is common in the literature [442,443].

The relationship between carbon dot quantum yield and temperature may have also been caused by differences in nanoparticle size. Greater nanoparticle size led to increased absorption due to higher surface area. However, this would also lead to a larger distance for absorbed light to travel from the core of the nanoparticle to its surface for emission, causing a reduced efficiency in emission of light. Quantum yield is defined as the ratio of photons emitted to the photos absorbed. The ability of larger particles to absorb light was enhanced, and their ability to emit light was reduced. Thus, the higher temperature synthesis conditions which led to the formation of smaller particles also led to them having a higher yield compared to particles of the same composition with a larger size.

Further analysis of the fluorescence spectra determined that a lower synthesis temperature led to a slightly red-shifted fluorescence for α-D-gluc, D-glucuronic acid, and Sucrose CDots **(Figure 12.3B)**. Synthesis temperature did not appear to have a large impact on β-D-gluc CDot peak emission wavelength. The full width at half maximum (FWHM) value for all CDots was found to decrease with a higher synthesis temperature, indicating narrower fluorescence emission

peaks for CDots synthesized at 200 °C compared to those synthesized at 150 °C **(Figure 12.3C)**. This suggests that synthesis at 150 °C may be leading to the formation of multiple nanoparticle populations due to greater nanoparticle growth, forming a broad emission peak, while the synthesis at 200 °C leads to the formation of fewer or a single nanoparticle population with a narrower blue-shifted fluorescence emission due to the hindered nanoparticle growth caused by the presence of boiling DMSO during the synthesis.

12.4.2. Chemical Characterization

XPS confirmed the presence of carbon source functional groups on the surface of CDots **(Figure 12.4, Table I1)**. α-D-gluc CDots at both synthesis temperatures had an approximately 3 % P 2p composition, while α-D-gluc CDots synthesized at 200 °C had an approximately 15 % K 2p composition. β-D-gluc CDots for both synthesis temperatures had a 2 to 3 % N 1s composition. All CDots had some S 2p in their composition even after evaporation of the DMSO-water phase and resuspension of nanoparticles in water alone, indicating the incorporation of sulfur from DMSO into the nanoparticles during the synthesis process. The DMSO content was comparable for particles of both the high and low synthesis temperature, which indicates that the removal of residual DMSO after nanoparticle formation was not affected by the synthesis temperature. Thus, the observations made about particle photophysical characteristics were not caused by the presence of DMSO in the final nanoparticle solution, but rather by the role of DMSO during the synthesis process. Inductively coupled plasma (ICP) analysis was conducted to determine whether the small amount of K that was present in the XPS spectra for β-D-gluc 200 °C, D-gluc 200 °C, and D-gluc

(A)
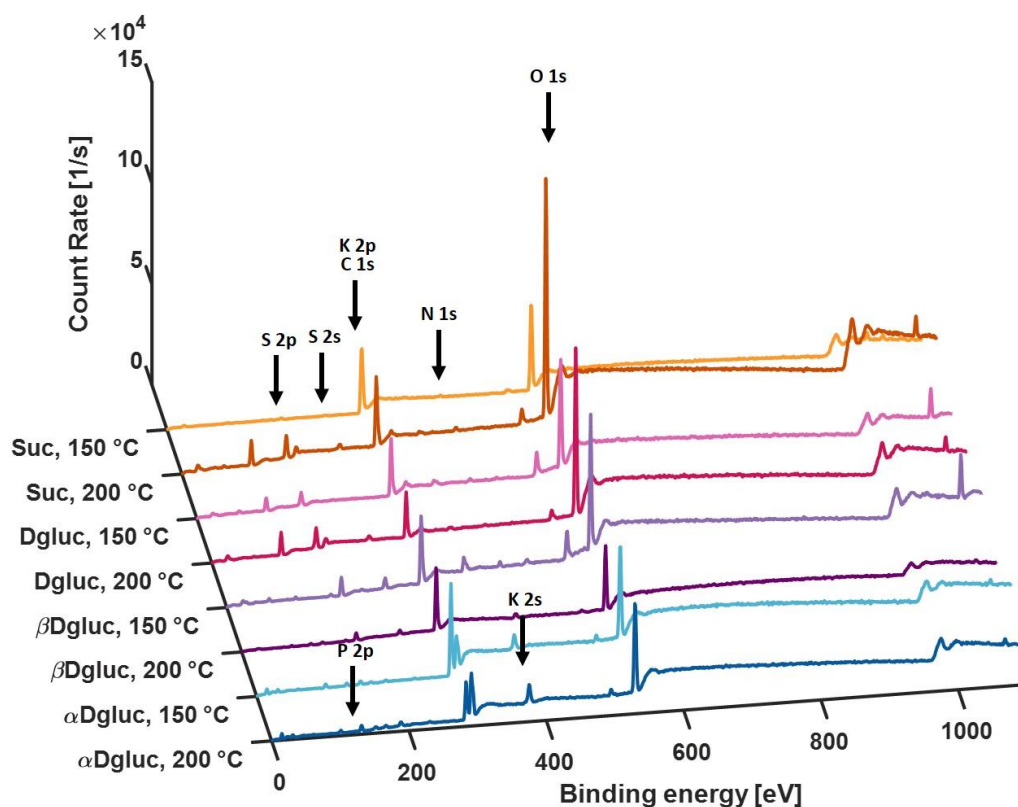
(B)
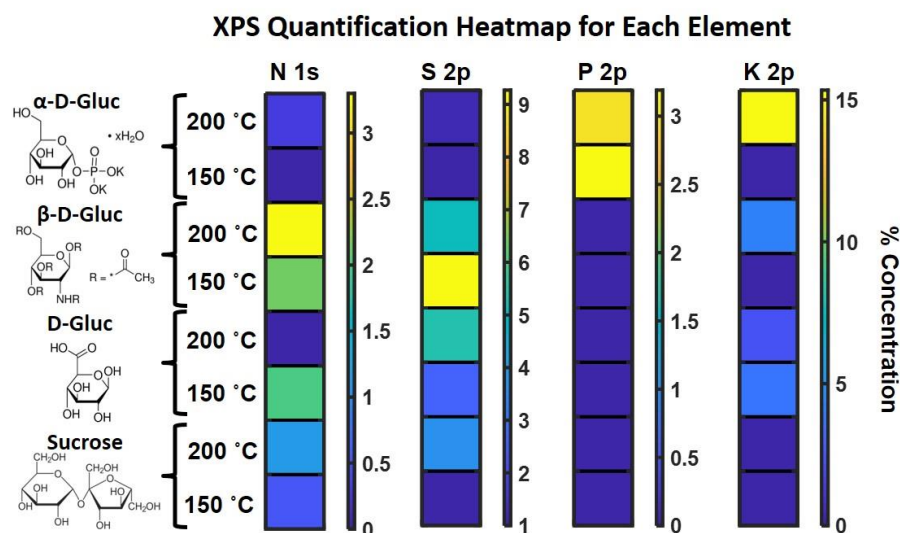
Figure 12.4. (A) XPS Spectra for CDots at each composition and synthesis temperature. **(B)** Heatmap representation of percent concentration of each element. N 1s was present in high concentrations in β-D-gluc CDots, while K 2p and P 2p were present in high concentrations in α-D-gluc CDots. S 2p was present in many of the nanoparticle compositions, indicating possible incorporation of sulfur from DMSO in CDots.

150 °C was indeed present within the samples. This found a K content of only 1.54%, 1.13%, and 1.93% respectively. This indicates that the identification of K in these XPS signals was likely due to background signal rather than the presence of K in the particles.

Deconvolution of the C1s peak **(Figure 12.5)** confirmed the presence of C-C/C=C, C-O, COOH, and C-K peaks in the α-D-gluc CDots. While C-C/C=O and C-O occur naturally in the carbon source, the presence of COOH peaks and C-K peaks indicate the formation of these bonds as a result of the synthesis process. Deconvolution also confirmed the presence of C-C/C=C, C-O/C-N, and COOH peaks for β-D-gluc CDots, D-gluc CDots, and sucrose CDots. The percent composition of each bond type did not appear to follow a trend based on synthesis temperature or carbon source.

FT-IR studies **(Figure I1)** were performed to determine the successful incorporation of functional groups from the carbon sources onto the CDot surfaces. Irrespective of the temperature used for synthesis, CDots were shown to possess hydrophilic groups such as O-H, N-H and C=O on their surface ensuring their dispersion in aqueous media[395,427,434,460]. Aside from this, CDots also gave signature peaks which corresponded to the precursor source (PO_4^{3-} in **Figure I1 A**).

Zeta potential measurements led to the observation of a higher zeta potential magnitude for CDots synthesized at 150 °C than those synthesized at 200 °C **(Figure I2)**, indicating higher nanoparticle stability for lower synthesis temperatures. Additionally, α-D-gluc CDots had the greatest stability (as indicated by zeta potential magnitude) for a synthesis temperature of 150 °C, followed by Sucrose, β-D-gluc, and D-glucuronic acid CDots. For the synthesis temperature of 200 °C, α-D-gluc CDots had the greatest stability, while β-D-gluc and Sucrose CDots have zeta
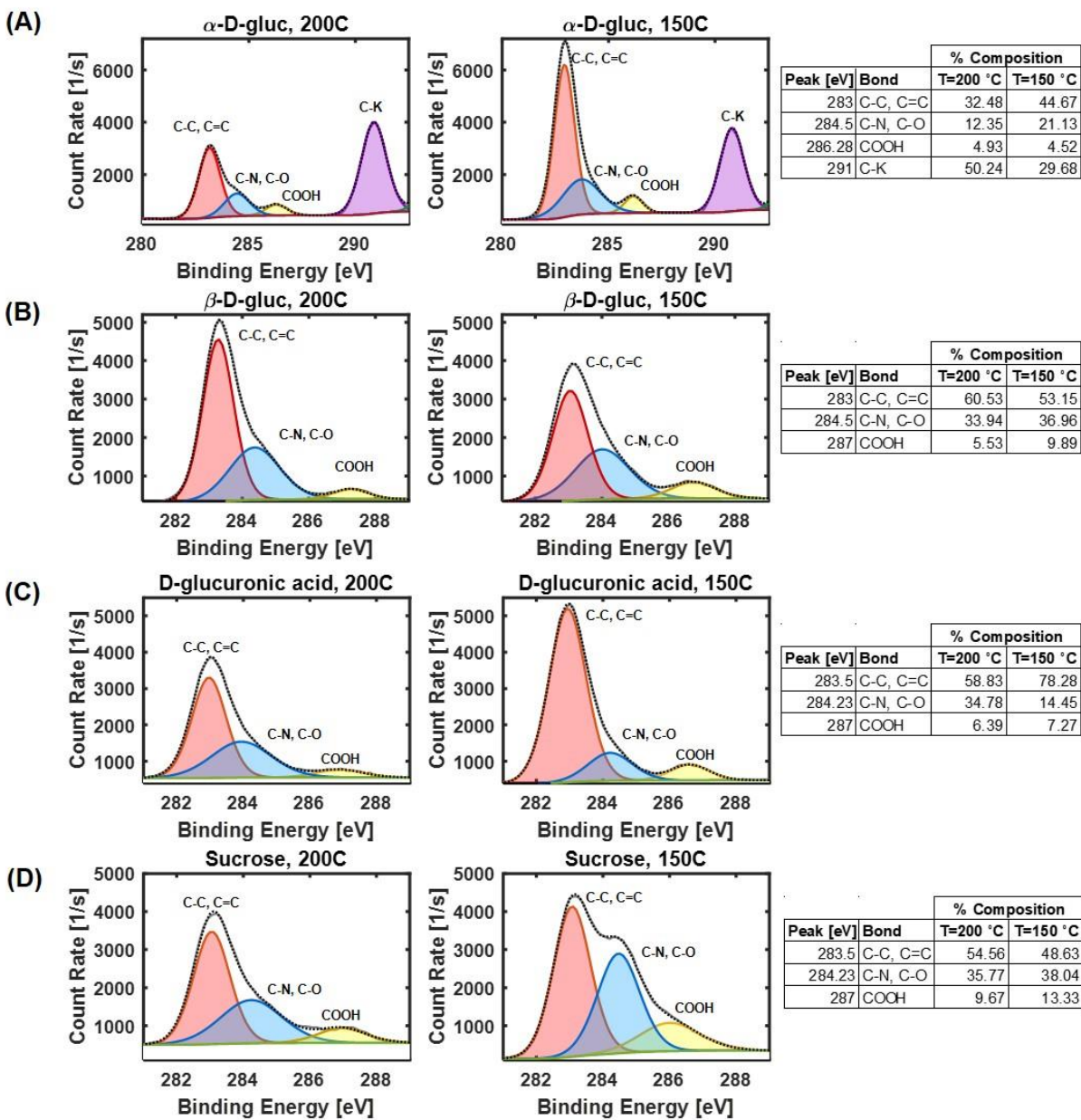
Figure 12.5. Deconvolved XPS C1s peak for CDots of each composition and synthesis temperature. **(A)** α-D-gluc CDots have peaks for C-C, C=C, C-O, COOH, and C-K. **(B)** β-D-gluc CDots have peaks for C-C, C=C, C-O, C-N, and COOH. **(C-D)** D-gluc, and sucrose C1s deconvolution resulted in peaks for C-C, C=C, C-O, and COOH.

potentials with a similar magnitude to each other. These observations indicate that the hindering of nanoparticle growth during the synthesis process may have also hindered the growth of the nanoparticle surface charge layer.

12.4.3 Interpreting particle brightness by single-particle imaging analysis

Bulk measurements of each type of CDots showed that they display a wide range of particle brightness. To better understand their photophysics, we proceeded to analyze single-particle imaging data. By employing a changepoint data analysis algorithm[458,459], we parsed individual trajectories of each type of particle into "on" and "off" segments. The "on" segment was defined by intensity thresholding with the mean value of the darkest segment plus three times the standard deviation of that segment.

We first determined if different precursor materials and temperatures affect particle brightness. There are two parameters that can be used to quantify particle brightness: 1) the instantaneous brightness, which is the mean value of intensity in all the "on" segments, and 2) the on-time duty cycle, which determines the probability of a particle staying in the emissive state during the data acquisition time. We first calculated the instantaneous particle intensity **(Figure 6A)**. Although different particles showed different instantaneous intensities, their variation is much less than those measured in bulk. This result indicates that, before photobleaching, each type of particle has a comparable capacity in emitting photons, an observation that seems to contradict the bulk fluorescence measurement.

We then further determined the on-time duty cycle of each type of particle. Different particles displayed a variety of on-time duty cycles, with the largest duty cycle (20 %, β-D-gluc at 200 °C) almost doubling the smallest one (9 %, D-glucuronic acid, 200 °C). We reason that

fluorescence intensity measured by bulk measurement is determined by both the instantaneous intensity and the on-time duty cycle. Indeed, if both factors are considered, the product of instantaneous intensity and on-time duty cycle (**Figure 6B**) much better resembles the bulk fluorescence measurement.
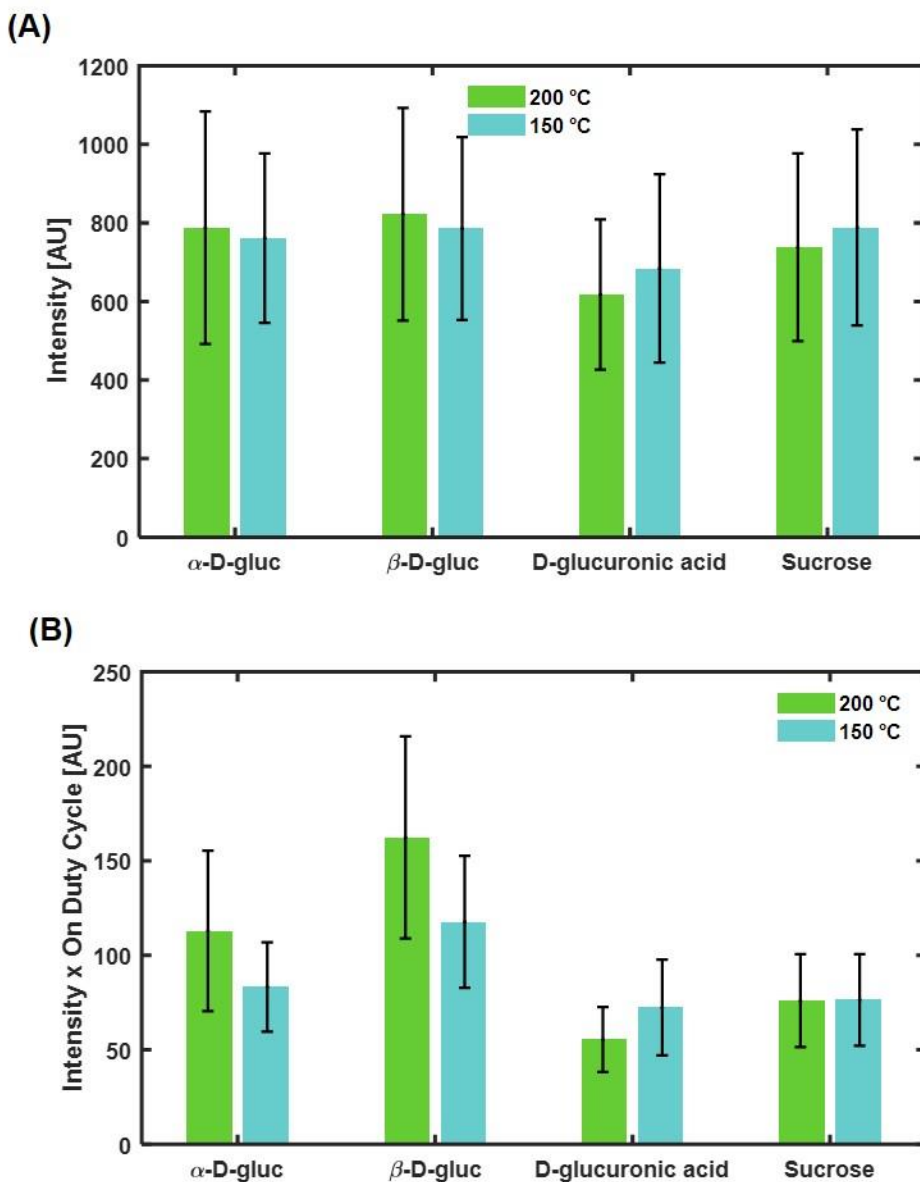
Figure 12.6. Single particle analysis of particle brightness. **(A)** Average particle intensity. All particle types have comparable intensities. **(B)** The product of average intensity and t_{on} duty cycle. This appears more comparable to the bulk results than just examining intensity alone.

Consideration of both the instantaneous intensity and on-time duty cycle helped us better understand the photophysics of different types of particles. For instance, β-D-gluc 200 °C displayed the largest instantaneous intensity, as well as the largest on-time duty cycle, therefore standing out as the brightest type of particle, consistent with the bulk measurement. On the other hand, although sucrose 150 °C, β-D-gluc 150 °C, and α-D-gluc 200 °C CDots show a similar instantaneous intensity, the on-time duty cycle of Su150 is only 9%, much less than that of β-D-gluc 150 °C (15%) or α-D-gluc 200 °C (14%). Consequently, sucrose 150 °C CDots are dimmer than β-D-gluc 150 °C or α-D-gluc 200 °C CDots. Thus, single-particle imaging allows for delineation of photophysical mechanisms underlying carbon dot emission. In general, the intensity at different synthesis temperatures within the same precursor remains comparable, whereas the intensity difference is more significant between different precursor materials.

12.4.4 Comparing the photobleaching kinetics between bulk and single-particle measurements

Bulk photobleaching experiments determined that the photobleaching curves **(Figure I3 A)** could be best fit with a second order exponential (Equation 12.2), implying that there may be more than one nanoparticle population present for each composition and temperature. This led to obtaining two time constants for each nanoparticle **(Figure I3 B)**.

For all nanoparticle compositions, the second time constant was greater in the low temperature synthesis than in the higher temperature synthesis. This trend held true for the first time constant for α-D-gluc, β-D-gluc, and D-glucuronic acid CDots as well, indicating an overall decrease in resistance to photobleaching with an increase in synthesis temperature.

In single-particle photobleaching experiments **(Figure 12.7A)**, the photobleaching curves **(Figure 12.7B)** were again best fit with second order exponential functions. All fit results were tabulated
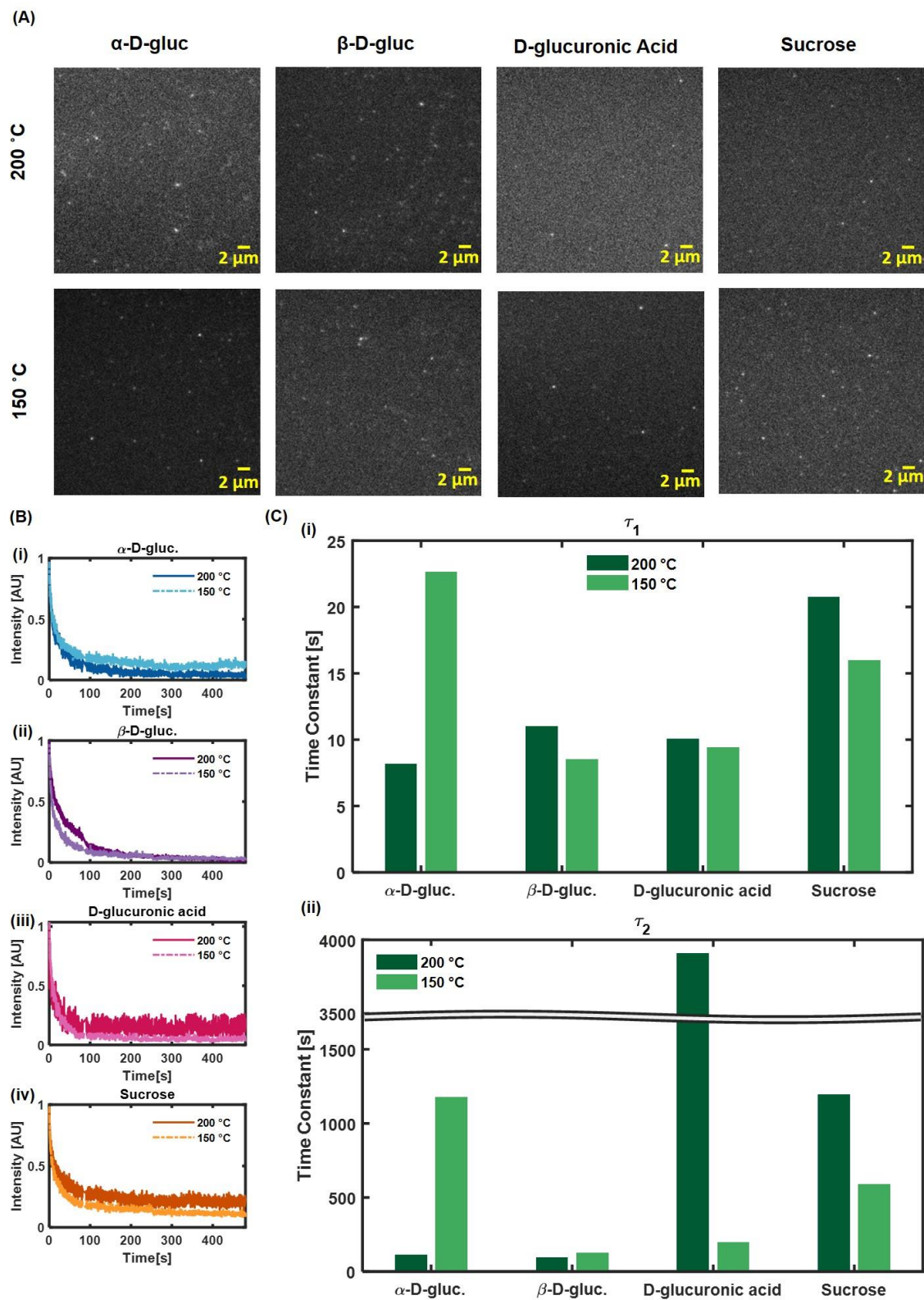
Figure 12.7. Single-particle photobleaching. **(A)** Single-particle images. **(B)** Time to photobleaching curves for single particles (n=4 for each type). **(C)** Time constants determined form a second order exponential fit of the time to photobleaching curves.

in Table I5. However, the single particle time constants **(Figure 12.7C)** displayed a trend that was different than that of the bulk photobleaching experiments. α-D-gluc and Sucrose CDots had a higher first time constant for nanoparticles synthesized at 200 °C than those synthesized at 150 °C, while the first time constant for β-D-gluc was lower for nanoparticles synthesized at 200 °C than those synthesized at 150 °C. The first time constant did not change very much from one synthesis temperature to another for D-glucuronic acid CDots. The second time constant was found to decrease with a decrease in synthesis temperature for α-D-gluc and β-D-gluc CDots but increased with a decrease in temperature for D-glucuronic acid and sucrose CDots. We note that the bulk blinking lifetime is subjected to the "intensity-dependent" artifact. Indeed, densely packed particles can modify the local emission properties via e.g. secondary absorption of the emitted light. Thus, we focus on quantification of the photophysical properties of CDots at the single-particle level.

12.4.5 Quantification of CDot Photoblinking

The double exponential components in the bleaching lifetime motivates us to pay closer attention to particle photophysics. A detailed examination of single-particle trajectories revealed two types of photophysical behaviors: 1) a single-step photobleaching and 2) a multiple-step photoblinking. Although the emission mechanism underlying these two distinct photophysics remains to be elucidated, these two types of optical behaviors may correspond to two types of nanoparticles with distinct photobleaching characteristics. In particular, the single-step bleaching should contribute primarily to the fast decay constant, whereas the multiple-step photoblinking may account for the prolonged decay constant.

To better understand the photoblinking of single CDots, we proceeded to analyze their distribution of time on (t_{on}) and time off (t_{off}). It has been shown that carbon nanoparticles, like

other types of nanosized emitters such as quantum dots, display a power-law distribution of t_{on} and t_{off}. Indeed, by using a changepoint algorithm to identify bright and dark state, we assigned each segment of the single-particle trajectories to either an "on" or "off" state. Consistent with previous studies[461], both t_{on} and t_{off} of nanoparticles showed a linear line in the log-log plot of probability vs. durations of t_{on} and t_{off} **(Figure 12.8 A-B)**. We observed that the slopes of t_{on} and t_{off} do not vary significantly over temperature or precursor material **(Figure 12.8 C-D, Figure I4, Tables I6-I7)**. At first sight, this result seems to be contradictory to the observation that the on-time duty cycle between each type of particles significantly varies (e.g. from 9% to 20%) because a similar t_{on} slope implies that the probability distribution of each on-time duration remains the same. In fact, we can estimate the mean duration of on-time by a weighted average from each t_{on} power-law plot. The resulted mean values between each particle were indeed very consistent within a small range of 0.42 to 0.65 seconds, with the maximum value occurring for D-glucuronic acid 150 °C CDots, whose on-time duty cycle is at the lower end of 10 %.

This discrepancy can be explained by considering that the on-time duty cycle not only depends on the probability distribution of on-time duration but also depends on the blinking frequency. Indeed, when we calculated the average blinking frequency for each type of particle, which is defined as the number of blinking events per unit time, we observed a significantly different range across all samples, ranging from 0.11 Hz (D-glucuronic acid 150 °C CDots) to 0.26 Hz (β-D-gluc 200 °C) **(Figure 12.8E)**. The transition rate of each type of particle quantitatively determines the capacity of a particle to recover from an off state to an on state. Thus, for particles with similar instantaneous intensity (e.g. α-D-gluc 200 °C, β-D-gluc 150 °C, and sucrose 150 °C), the increase of particle brightness, which primarily arises from an increase of on-time duty cycle, arises from an increase of blinking frequency rather than a change in the distribution of on-time
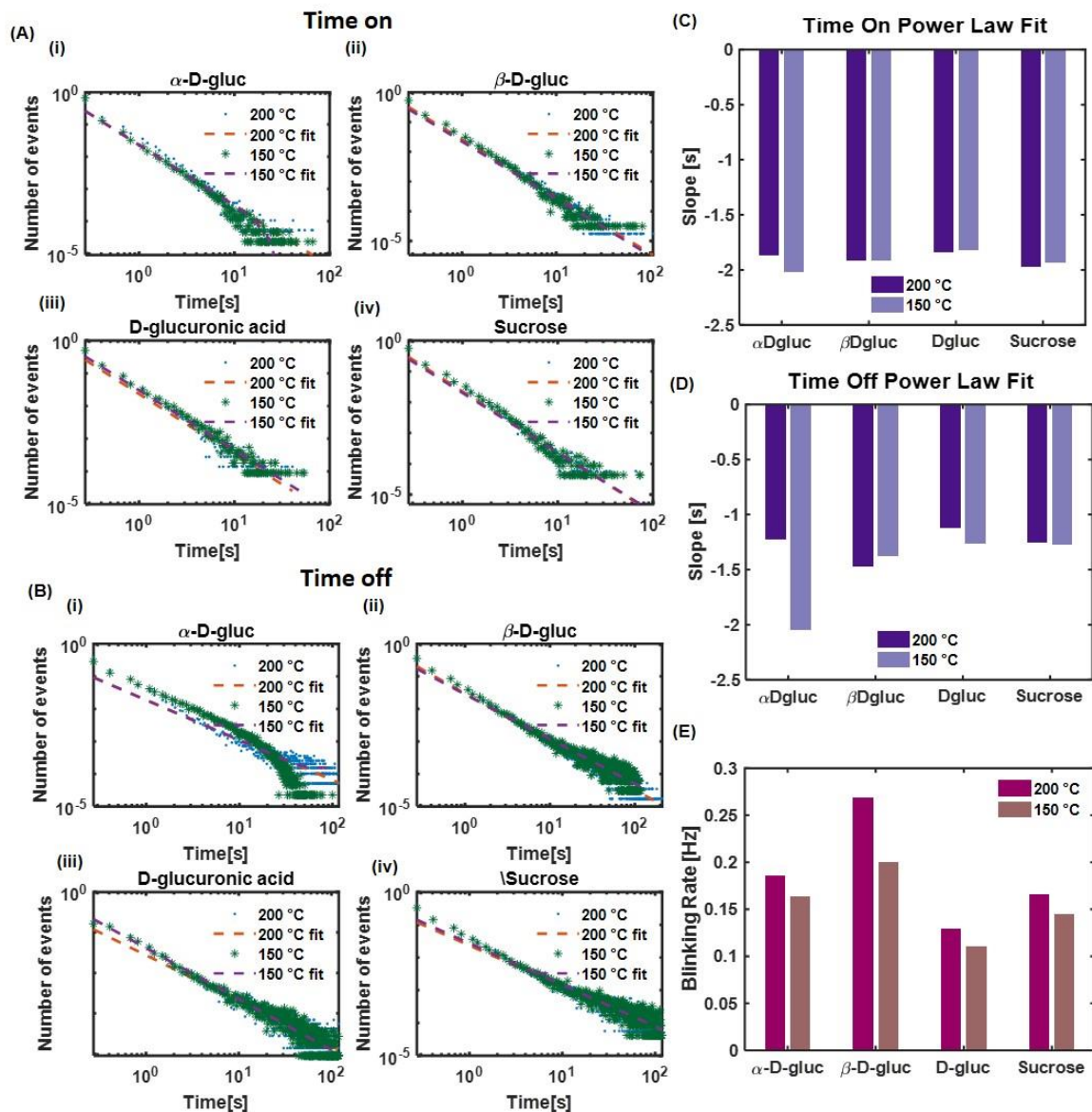
Figure 12.8. t_{on} and t_{off} photoblinking data based on many single-particle trajectories. Data was fit with a power law distribution. **(A)** Time on distributions for each carbon source and synthesis temperature. **(B)** Time off distributions for each carbon source and synthesis temperature. **(C)** Slopes of time on power law fits. **(D)** Slopes of time off power law fits. **(E)** Blinking rate (transition rate) for each particle type and synthesis temperature

duration. Within all four precursor materials, an increase of the synthesis temperature leads to a slight increase of the blinking frequency. A summary of all results is provided in **Figure 12.9**.

(A)

Higher Temperature = Blue-shifted Fluorescence

Higher Temperature = Smaller FWHM

Higher Temperature = Higher Quantum Yield

Understanding Bulk Behavior

(B)

Higher Temperature = Greater Photo-blinking Frequency

≠

Understanding Single-Particle Behavior

(C)

Single-Particle Brightness

Particle type	Instantaneous intensity [1/s]	Standard deviation [1/s]	Number of particles	On-time duty cycle [%]	Average on time [s]	Blinking frequency [Hz]
α-D-gluc, 200 °C	788.10	296.00	876	14.33	0.53	0.19
α-D-gluc, 150 °C	761.10	215.60	1223	10.94	0.46	0.16
β-D-gluc, 200 °C	822.30	270.60	1775	19.76	0.59	0.27
β-D-gluc, 150 °C	786.00	232.90	1351	14.98	0.51	0.20
D-glucuronic acid, 200 °C	617.90	191.40	619	8.97	0.47	0.13
D-glucuronic acid, 150 °C	684.10	239.50	985	10.58	0.65	0.11
Sucrose, 200 °C	738.00	238.90	871	10.30	0.42	0.17
Sucrose, 150 °C	788.50	249.50	1351	9.69	0.45	0.14

Figure 12.9. Summary of Results. **(A)** At the bulk level, a higher synthesis temperature was found to lead to a blue-shifted fluorescence, a smaller fluorescence full-width at half maximum (FWHM), and a higher quantum yield. **(B)** At the single-particle level, a higher temperature was found to lead to a greater photo-blinking frequency, which led to brighter signals from particles. **(C)** Evaluation at the single-particle level elucidates the effects of precursor and synthesis temperature on particle brightness.

We note that the on- and off-time power-law distribution curves down at the timescale of 10-100 sec. The downward curving of the power-law distribution may indicate competing physical processes that interrupt power-law blinking at this timescale. Indeed, this phenomenon has also

been reported in early studies of quantum dots [462] and nanowires[463]. A slight better fit can be achieved with a "truncated power law". Because such modification does not change the conceptual description of photoblinking behaviors in this work, we chose to use the ordinary power-law distribution.

12.5 CONCLUSION

α-D-gluc, β-D-gluc, D-glucuronic acid, and Sucrose CDots with inherent surface-abundant functional groups were obtained through a single-step synthesis method. A higher synthesis temperature was found to lead to a higher quantum yield, smaller particle size, blue-shifted and narrower fluorescence emission, and lower magnitude zeta potential. A lower synthesis temperature was found to lead to a greater UV-visible absorbance, an increase in nanoparticle stability as determined by zeta potential measurements, red-shifted fluorescence, and a greater resistance to bulk photobleaching. Overall, carbon source and synthesis temperature in relation to the solvent boiling temperatures were found to play a large role in modulating the photophysical properties of CDots. These findings suggest that a higher synthesis temperature may be more desirable for applications such as sensing or intracellular imaging, in which a blue-shifted fluorescence would be acceptable as long as a high quantum yield can be obtained. On the other hand, low synthesis temperatures may be more desirable for carbon dots that will be used for in-vivo bioimaging applications, where a red-shifted fluorescence may be more desirable. This lower synthesis temperature may also be applicable for situations in which chromatographic separation of carbon dots of a single carbon source into multiple colors is desired, as the broader range of fluorescence emission will allow for separation of varied colors. At the single-particle level, an increase in synthesis temperature was found to lead to an increase in photoblinking frequency, which in turn contributed to increased particle brightness. This further suggests the utility of high

synthesis temperatures for in-vitro and single-particle imaging applications. Thus, the end application is of utmost importance in selection of CDot synthesis temperature.

CHAPTER 13: IN-SITU SURFACE-DIRECTED ASSEMBLY OF 2D METAL NANOARCHITECTURES FOR DRUG-FREE TREATMENT OF ANTIBIOTIC-RESISTANT BACTERIA

13.1 INTRODUCTION

This project came about from the observation that when the BVNP synthesis was conducted without the use of EDC or NHS, and the sample was quenched with 2N HCl at the end of the reaction, the TEM images revealed the formation of very nice 2D hexagonal nanostructures. After much experimentation and many attempts to reproduce these structures, it became apparent that the structures had nothing to do with biliverdin at all. In fact, the structures looked the same even in the absence of biliverdin. This led to further experiments that demonstrated that the particles were resulting from an interaction between HCl, the diamine crosslinker, and copper on the TEM grids, which resulted in the formation of copper chloride crystals on the copper surface, as well as other metal chloride crystals on other metal surfaces. We then explored the use of the copper chloride crystals as an antibacterial surface (**Fig. 13.1**)
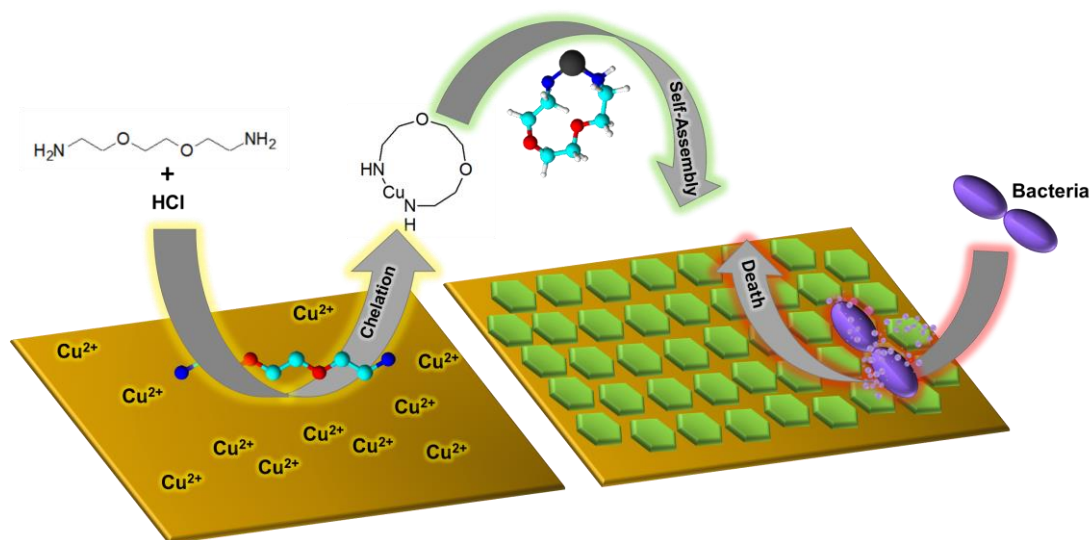
Figure 13.1 Schematic overview of nanoplatelets project. The diamine crosslinker may play a role as a metal chelator in these experiments, potentially aiding in the formation of the copper chloride crystals.

13.2 METHODS, RESULTS, AND DISCUSSION

13.2.1 Synthesis of copper chloride nanoplatelets on various copper surfaces

Synthesis with HCl was conducted by adding 50 µL 2N HCl to 1 mL water, then depositing 2.5-3.5 µL of the resulting solution onto a copper surface. The resulting samples formed on the copper surface are referred to as the "HCl" nanoplatelets. For samples that were formed on a TEM grid, samples were deposited on the copper side of a carbon-coated copper mesh TEM grid. Excess moisture was wicked away 2 min after the solution was deposited onto the grid. For samples synthesized with both HCl and diamine (referred to as the "diamine" nanoplatelets), diamine was first diluted in water (3.5 µL diamine, 10 mL water). 50 µL 2N HCl was then added to 1 mL of the diluted diamine solution. The remainder of the procedure was the same as the procedure that was followed for the formation of the HCl nanoplatelets. TEM and SEM images of nanoplatelets formed directly on a carbon-coated copper mesh TEM grid are provided in **Fig. 13.2**. The diamine nanoplatelets were larger and more well-defined than those formed by HCl alone. The presence of rod-like structures in the diamine nanoplatelet TEM image can be attributed to nanoplatelets that are vertical rather than laying horizontally on the carbon coating. SEM images of HCl nanoplatelets formed on a TEM grid are provided in **Fig. 13.3**. The presence of these was less well-defined than those that were formed with the combined diamine and HCl solution.
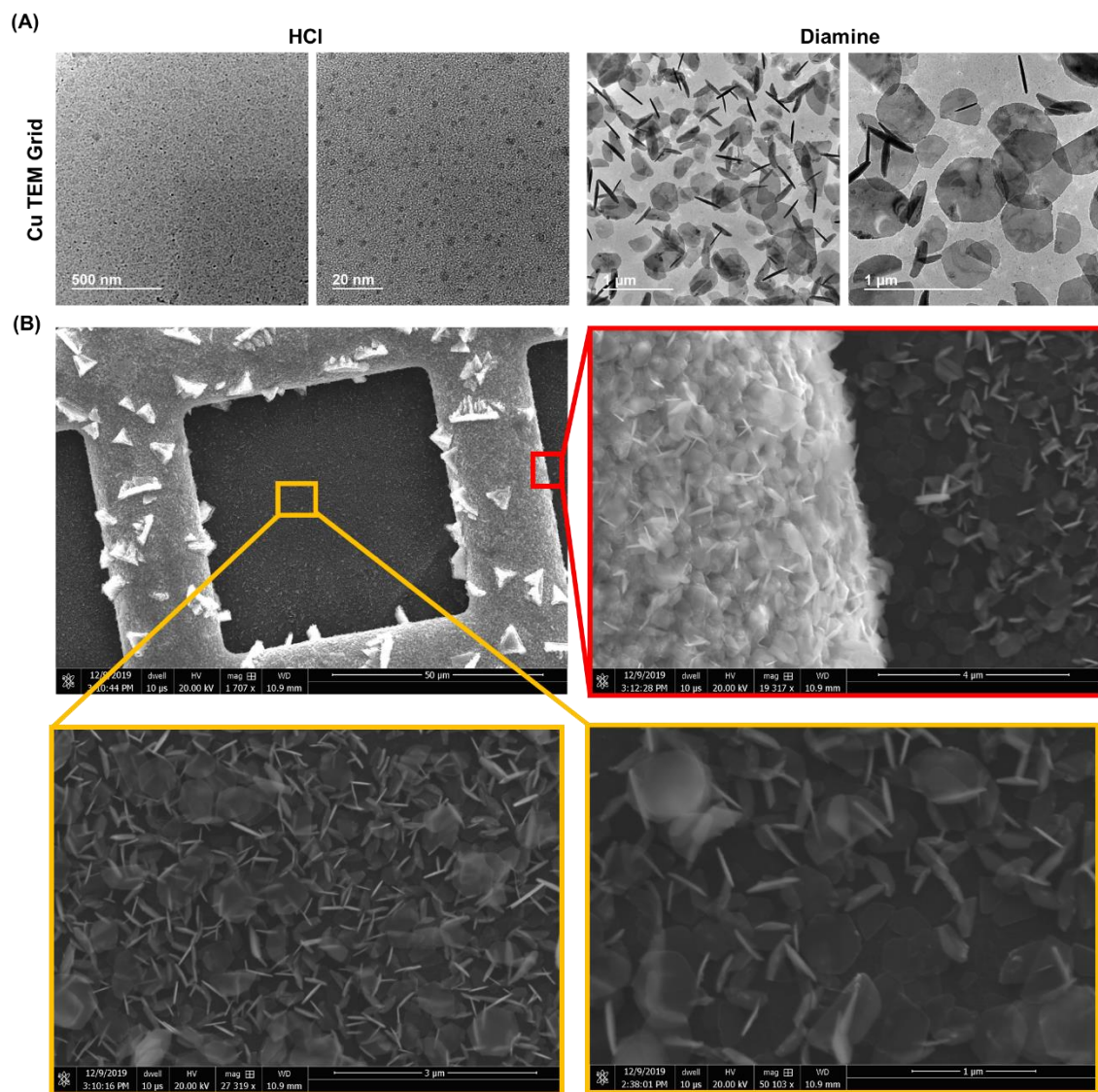
Figure 13.2. Copper Chloride nanoplatelets formed on copper TEM grids. **(A)** TEM images of nanoplatelets formed directly on TEM grids using the HCl solution (left) or the HCl and diamine solution (right). Nanostructures formed using the HCl solution include small nanoplatelets and nanoparticles, while the HCl and diamine solution results in the formation of hexagonal nanoplatelets. Rod-like structures are nanoplatelets that are oriented vertically rather than horizontally **(B)** SEM image of copper grid containing nanoplatelets formed from the HCl and diamine solution. Nanoplatelets are found both on the copper portion of the grid and on the carbon portion of the grid.
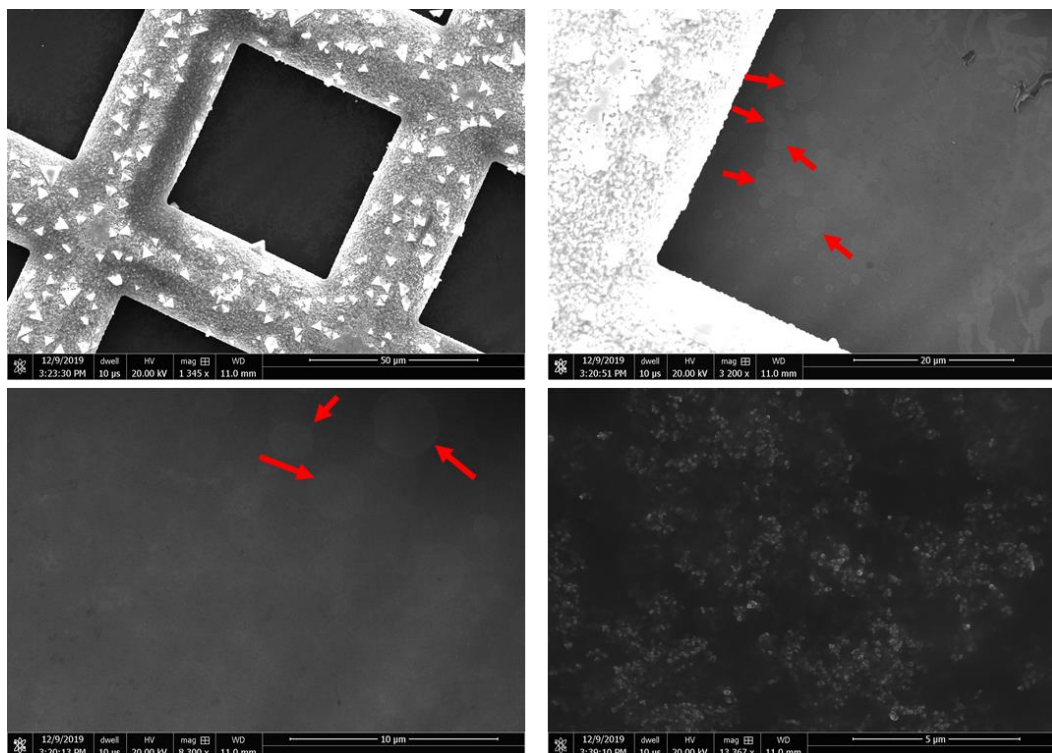
Figure 13.3. SEM images of copper chloride nanoplatelets formed by depositing the HCl solution on copper TEM grids. Arrows point to examples of nanoplatelets.

EDS measurements conducted on diamine nanoplatelets located on multiple parts of the TEM grid confirm that the particles contain copper **(Fig. 13.4)**. These measurements were taken from the sections of the grid that contained the carbon coating, in order to ensure that the copper from the copper mesh would not result in a background signal. We also demonstrated the formation of these particles on other copper surfaces, including a copper electrode and copper granule **(Fig. 13.5)**. We additionally demonstrated that these nanoplatelets could also be formed directly on copper tape surfaces, such as those used for prototyping circuits **(Fig. 13.6 A)**. The HCl nanoplatelets appeared smaller in size than the diamine nanoplatelets, and also appeared to be trapezoidal in shape, in contrast to the hexagonal shapes observed for the diamine nanoplatelets. XRD spectra revealed the appearance of some new peaks to the Cu tape spectra as a result of the formation of the nanoplatelets **(Fig. 13.6 B)**. Some of these peaks match those found in the spectra

275

of copper (II) chloride. FT-IR spectra for nanoplatelets formed on a Cu tape surface were different from the Cu tape itself **(Fig. 13.6 C)**. We also conducted scanning electron microscopy on copper (II) chloride powder to ensure that the morphologies observed were not commonly observed in copper chloride **(Fig. 13.7)**.

Top-left table:

Element	Weight %	Atomic %	Error %	Net Int.	K Ratio	Z	A	F
C K	75.63	82.86	5.46	893.07	0.4724	1.0197	0.6125	1
O K	19.41	15.97	13.09	111.92	0.0252	0.9746	0.1332	1
Cl K	0.85	0.31	10.19	42.21	0.0071	0.8232	1.0038	1.0171
Cu K	4.11	0.85	8.4	45.39	0.034	0.7107	1.0189	1.1402

Top-right table:

Element	Weight %	Atomic %	Error %	Net Int.	K Ratio	Z	A	F
C K	74.09	81.82	5.73	819.74	0.4457	1.0216	0.5888	1
O K	20.33	16.86	12.69	116.24	0.0269	0.9764	0.1356	1
Cl K	0.97	0.36	10.86	47.14	0.0082	0.825	1.0006	1.0165
Cu K	4.6	0.96	8.87	49.01	0.0377	0.7123	1.0196	1.1277

Bottom-left table:

Element	Weight %	Atomic %	Error %	Net Int.	K Ratio	Z	A	F
C K	76.5	83.01	5.12	1167.25	0.4964	1.017	0.6381	1
O K	19.75	16.09	12.84	140.18	0.0254	0.9718	0.1323	1
Cl K	0.79	0.29	9.85	49.23	0.0067	0.8206	1.0091	1.018
Cu K	2.97	0.61	11.96	42.06	0.0253	0.7082	1.0204	1.1803

Figure 13.4. EDS measurements at different locations on the copper grid treated with the HCl and diamine solution. The detection of copper on the carbon coating of the grids indicates that the nanoplatelets indeed contain copper.

276

HCl
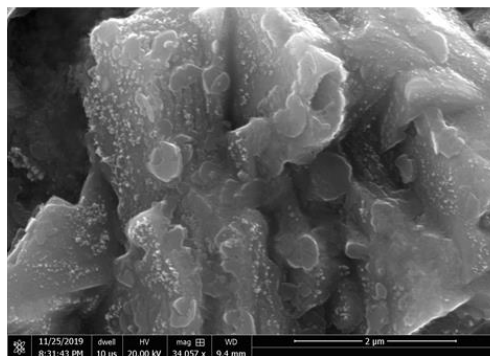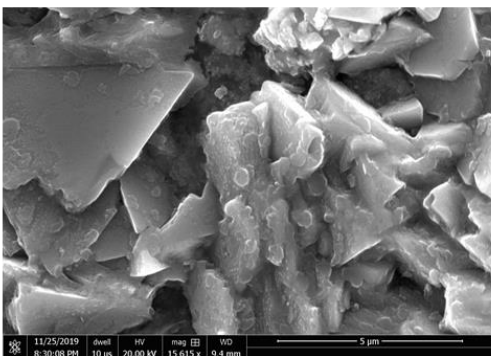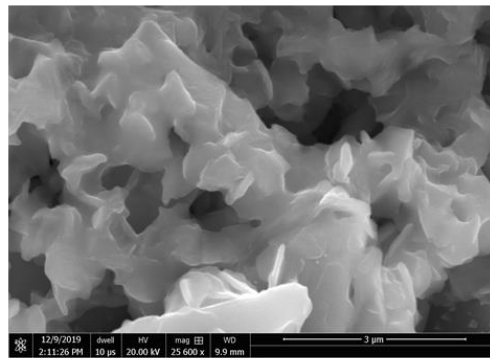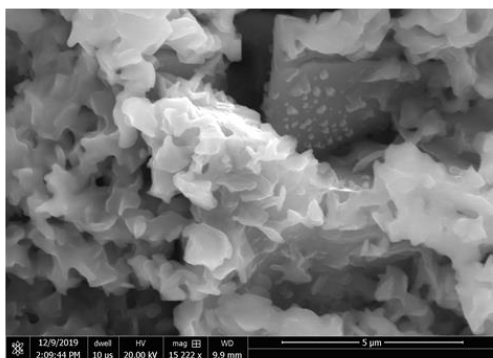
Diamine
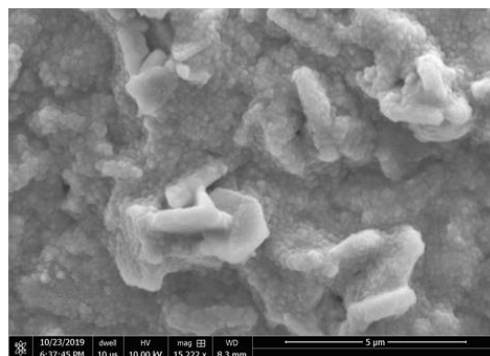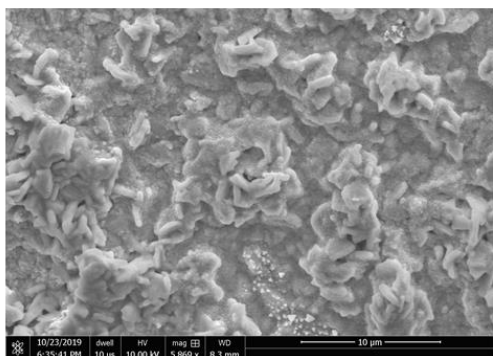
Figure 13.5. Nanoplatelets formed on a copper electrode surface and copper granule surface.

277

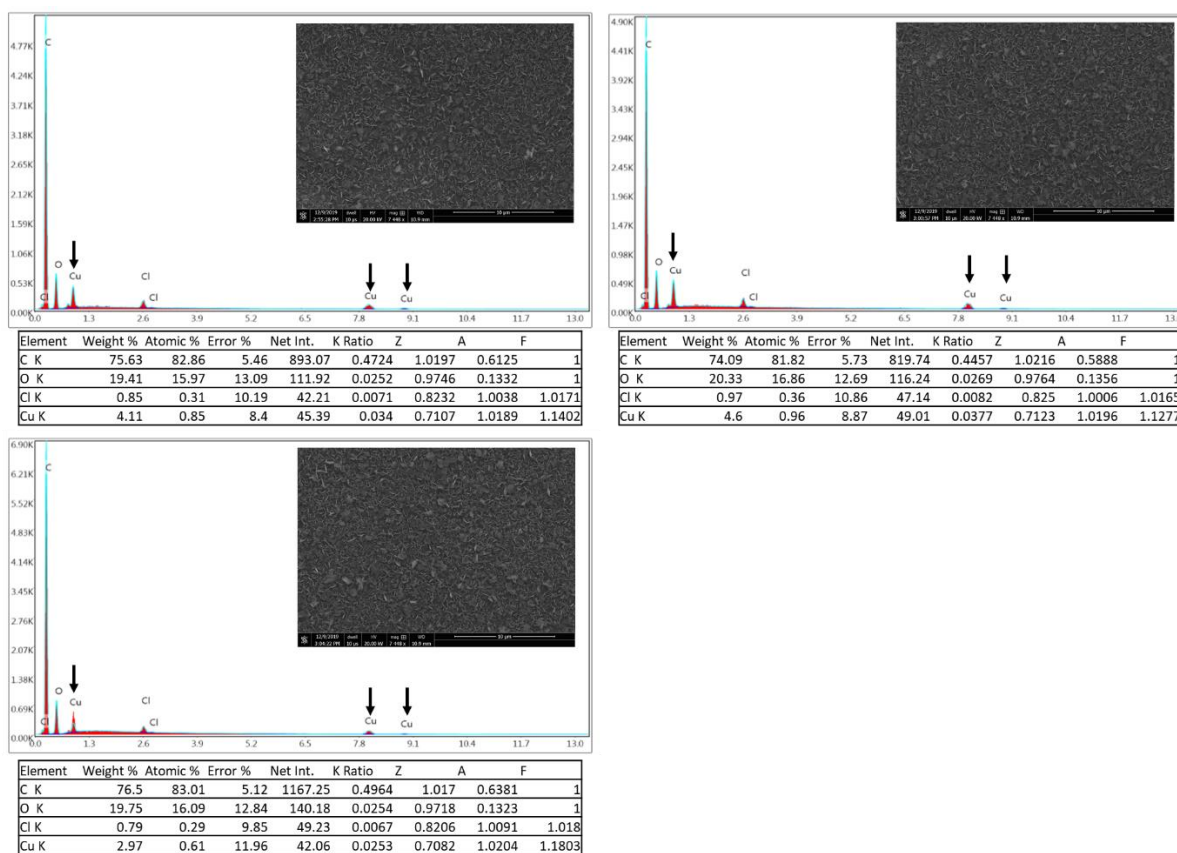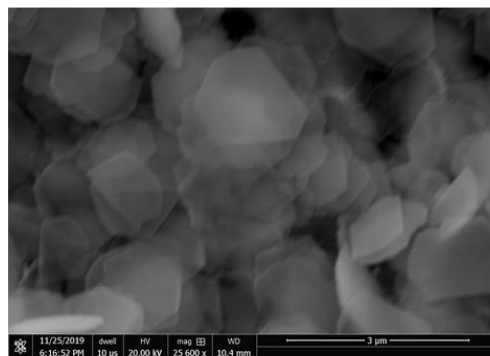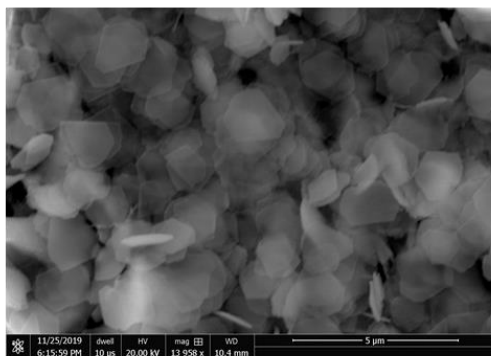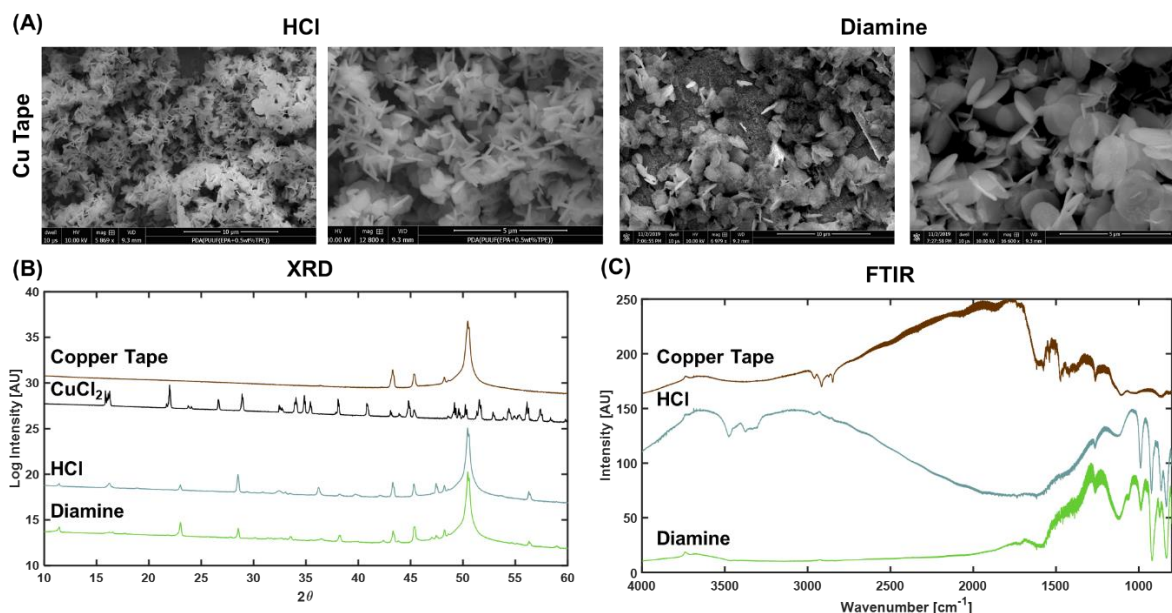**Figure 13.6.** Characterization of copper chloride nanoplatelets formed on copper tape. **(A)** SEM images of nanoplatelets formed directly on copper tape using the HCl solution (left) or the HCl and diamine solution (right). **(B)** XRD spectra of copper tape, copper (II) chloride crystals, nanoplatelets formed directly on copper tape using the HCl solution, and nanoplatelets formed directly on copper tape using the HCl and diamine solution. **(C)** FTIR spectra of copper tape, nanoplatelets formed directly on copper tape using the HCl solution, and nanoplatelets formed directly on copper tape using the HCl and diamine solution.
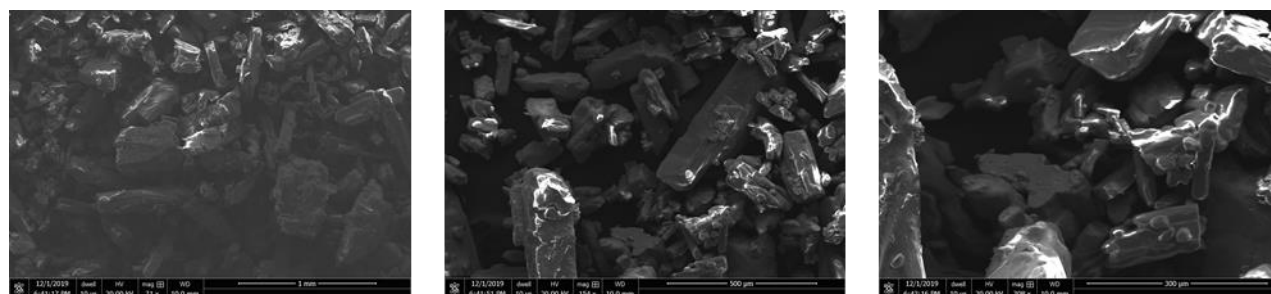
Figure 13.7. SEM images of copper (II) chloride crystals.

13.2.2 Use of Nanoplatelets to Treat S. Mutans

Since copper surfaces are known to have antibacterial properties, we next sought to determine the use of nanoplatelets assembled directly on copper tape as an antibacterial surface. We found that diamine nanoplatelets had a more vibrant green color than the HCl nanoplatelets **(Fig. 13.8 A)**. When exposed to the bacteria, nanoplatelets quickly dissolved into the solution, altering the solution color. We determined that the nanoplatelets dissolved into bacterial broth even

in the absence of bacteria. The dissolution of the copper chloride crystals into the broth was demonstrated with UV-visible spectroscopy **(Fig. 13.8 B)**. We also conducted experiments in which we attempted to dissolve the nanoplatelets in water, but found that they could not be dissolved (data not shown). This indicates that these nanoplatelets may in fact be composed of copper (I) chloride, which is not water soluble, rather than copper (II) chloride. Exposure of S. Mutans to the nanoplatelets resulted in a reduction of bacterial growth **(Fig. 13.8 C-F)**. The HCl nanoplatelets led to a much greater attenuation of bacterial growth than did the diamine nanoplatelets, as demonstrated by the final fold change in bacterial density which was determined by measuring the OD600 values. For the bacterial experiments, the copper tape backing was removed, and the adhesive side of the tape was glued to the wells of a 24-well plate using a waterproof adhesive sealant. An example of the experimental setup is provided in **Fig. 13.9**. Additionally, there was an apparent color change in nanoplatelet samples exposed to bacteria **(Fig. 13.10)**.
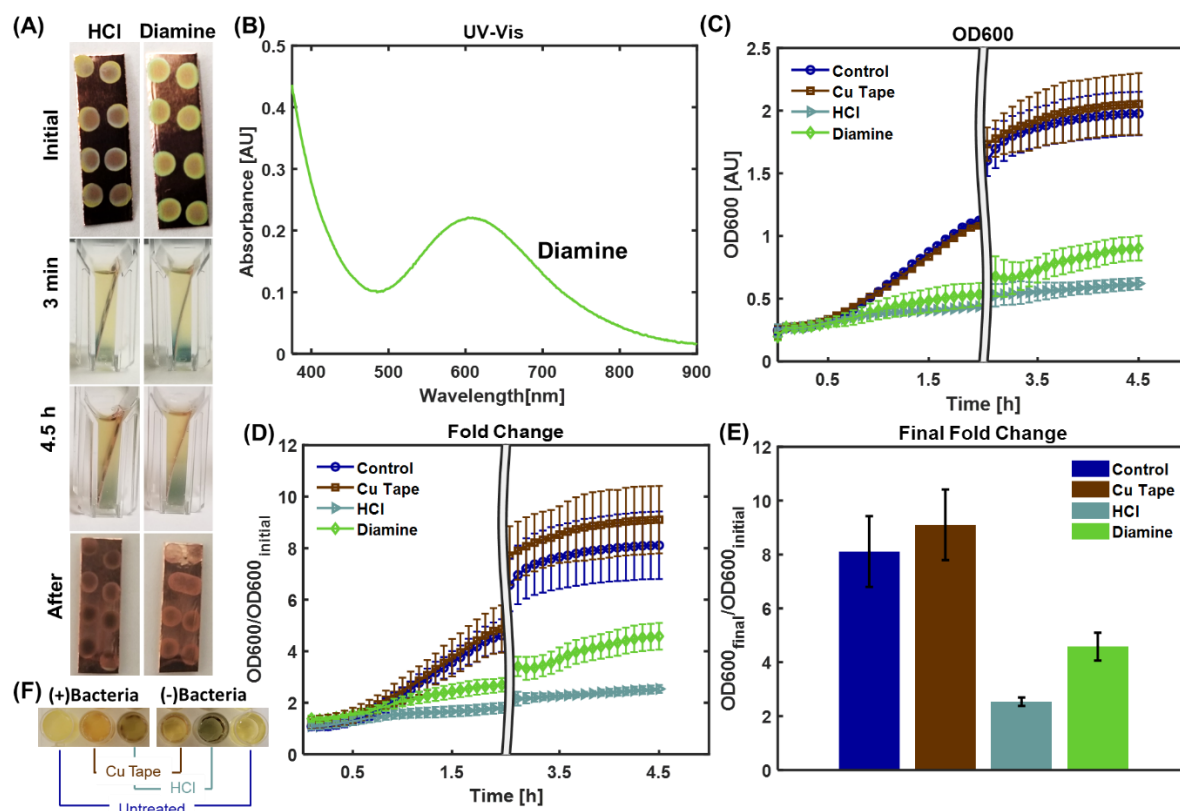
Figure 13.8. Nanoplatelet release from samples, and use in treating S. Mutans. **(A)** Nanoplatelet copper tape samples before and after exposure to S. Mutans bacteria. A visible color change occurs as a result of nanoplatelet dissolution into the media. **(B)** UV-visible absorbance spectra of nanoplatelets formed by HCl and diamine on copper tape, and dissolved into bacterial growth medium for 4.5 hours. A peak at 600 nm indicates the release of copper chloride from nanoplatelets into the medium. **(C)** Optical density at 600 nm (OD600) for untreated S. Mutans, copper tape-treated S. Mutans, and nanoplatelet copper tape-treated S. Mutans samples. OD600 values were adjusted to account for the contributions from dissolution of copper from tape samples into the medium. **(D)** Fold change in OD600 compared to initial OD600 values. **(E)** Fold change in OD600 at 4.5 hours compared to initial OD600 values. **(F)** Colors of bacteria and broth treated with copper tape or HCl nanoplatelets on copper tape for 4.5 hours.
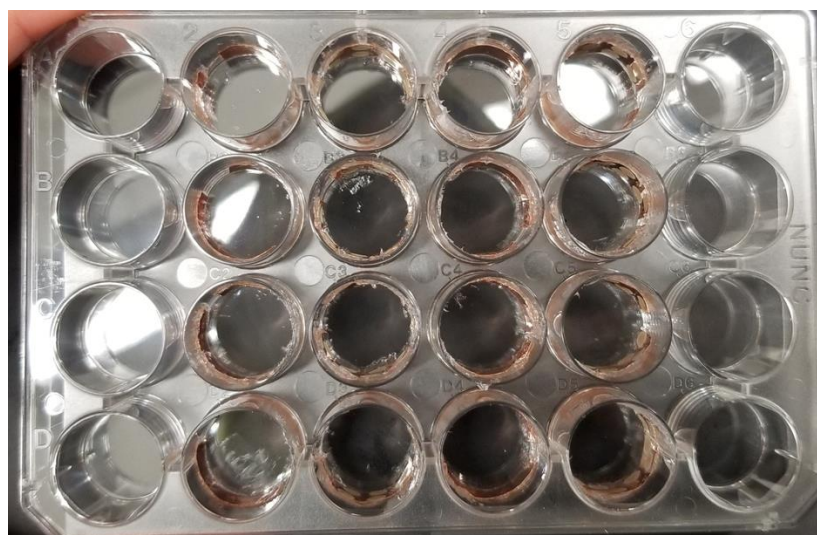
Cu Tape   **Nanohex on**   **Cu Tape**   **Nanohex on**
            Cu Tape   **Cu Tape**
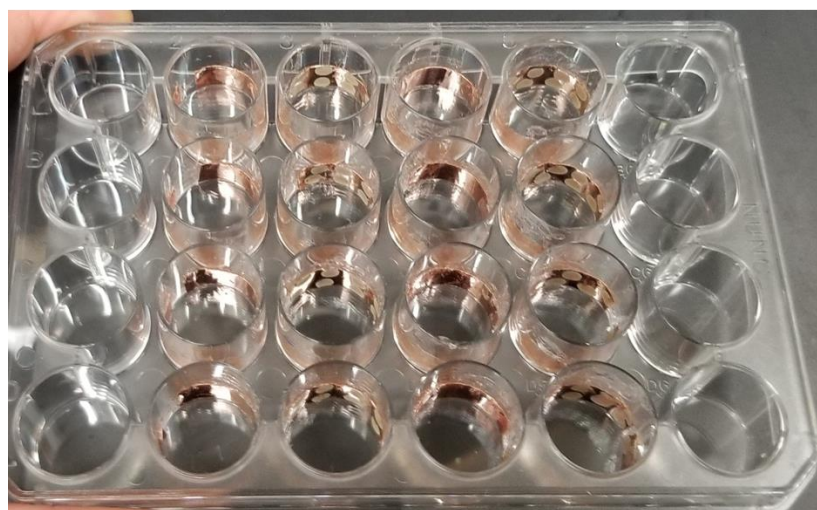
Cu Tape   **Nanohex on**   **Cu Tape**   **Nanohex on**
            Cu Tape   **Cu Tape**

Figure 13.9. Sample experimental setup for nanoplatelet bacterial experiments.
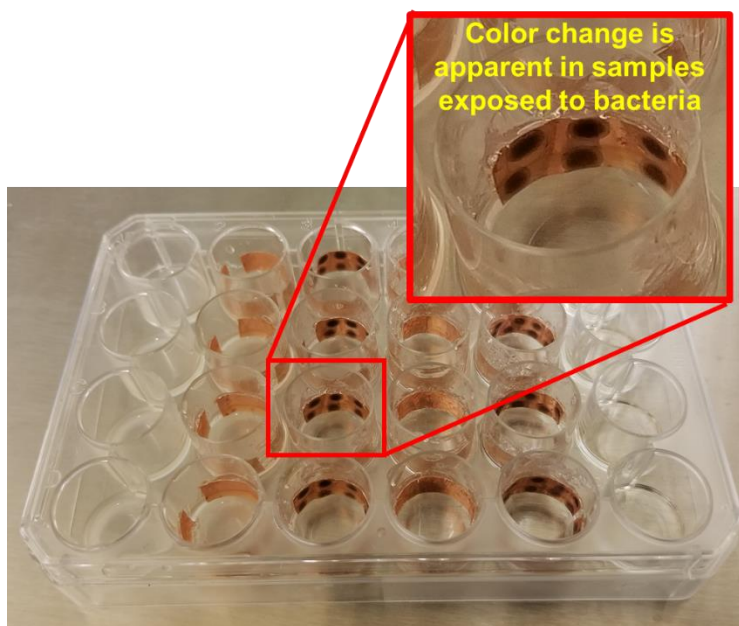
Figure 13.10. Color change in nanoplatelet samples that were exposed to bacteria.

Scanning electron microscopy images of bacteria treated with the diamine nanoplatelets revealed damaged bacteria throughout the sample **(Fig. 13.11)**. Additionally, EDS measurements conducted on bacteria treated with the nanoplatelets revealed the presence of copper in the samples **(Fig. 13.12)**, suggesting that the copper chloride may have dissolved into the broth and been internalized by the bacteria. We also conducted scanning electron microscopy on the nanoplatelet copper tape samples after they were used to treat bacteria. Damaged bacteria can be observed at the locations where the nanoplatelets had been deposited, while the locations that did not have nanoplatelets deposited on them exhibit signs of bacterial attachment **(Fig. 13.13)**.
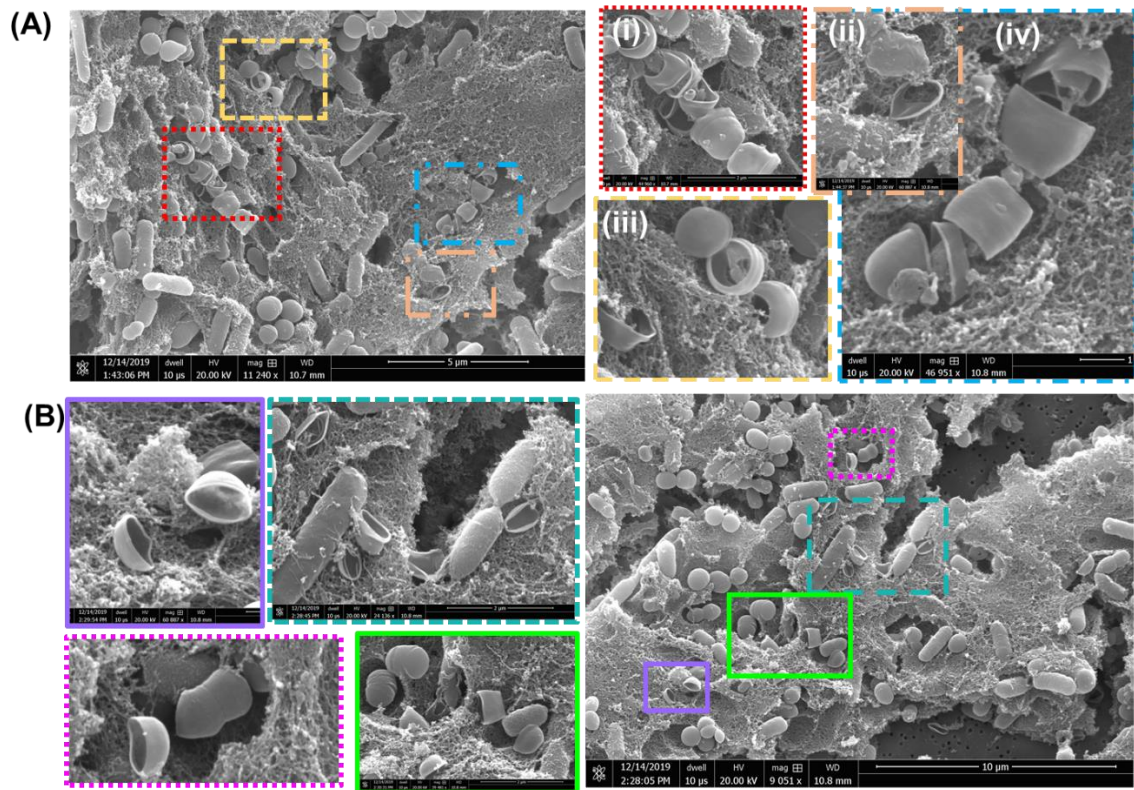
Figure 13.11. Microscopy of bacteria treated with nanoplatelets formed by solution of HCl and diamine on copper time. **(A-B)** SEM images of bacteria treated with copper nanoplatelets from HCl and diamine for 4.5 hours. Insets depict damaged bacteria.

Element	Weight %	Atomic %	Error %	Net Int.	K Ratio	Z	A	F
O K	24.01	56.21	15.4	89.36	0.0685	1.2707	0.2244	1
Na K	10.07	16.4	14.06	58.63	0.0313	1.1622	0.2675	1.0003
P K	4.41	5.33	11.06	65.72	0.0341	1.1263	0.6839	1.0044
Cl K	3.88	4.09	14.11	48.69	0.0279	1.0963	0.6486	1.0107
Pd L	13.93	4.9	12.88	85.56	0.0963	0.8794	0.7857	1.0005
Cu K	11.9	7.01	12.71	51.7	0.1313	0.9733	0.975	1.1627
Au L	31.81	6.05	27.47	26.71	0.2255	0.6949	1.0219	0.9981

Element	Weight %	Atomic %	Error %	Net Int.	K Ratio	Z	A	F
O K	24.34	57.15	15.53	92.77	0.07	1.2728	0.226	1
Na K	9.81	16.03	14.21	57.75	0.0304	1.1642	0.2659	1.0003
P K	3.86	4.68	11.25	58.44	0.0299	1.1282	0.6829	1.0043
Cl K	3.78	4	14.27	48.12	0.0271	1.0982	0.6467	1.0106
Pd L	13.61	4.81	12.42	84.83	0.094	0.8809	0.7834	1.0005
Cu K	12.05	7.13	11.04	53.37	0.1334	0.9753	0.9748	1.1646
Au L	32.56	6.21	26.98	27.82	0.2313	0.6966	1.0217	0.998

Figure 13.12. EDS on bacteria samples after 4.5 h of exposure to nanoplatelets of HCl and diamine. The presence of copper in these samples after filtration indicates that copper was absorbed by the bacteria as a result of treatment. Au and Pd presence is due to the Au-Pd conductive coating.

284
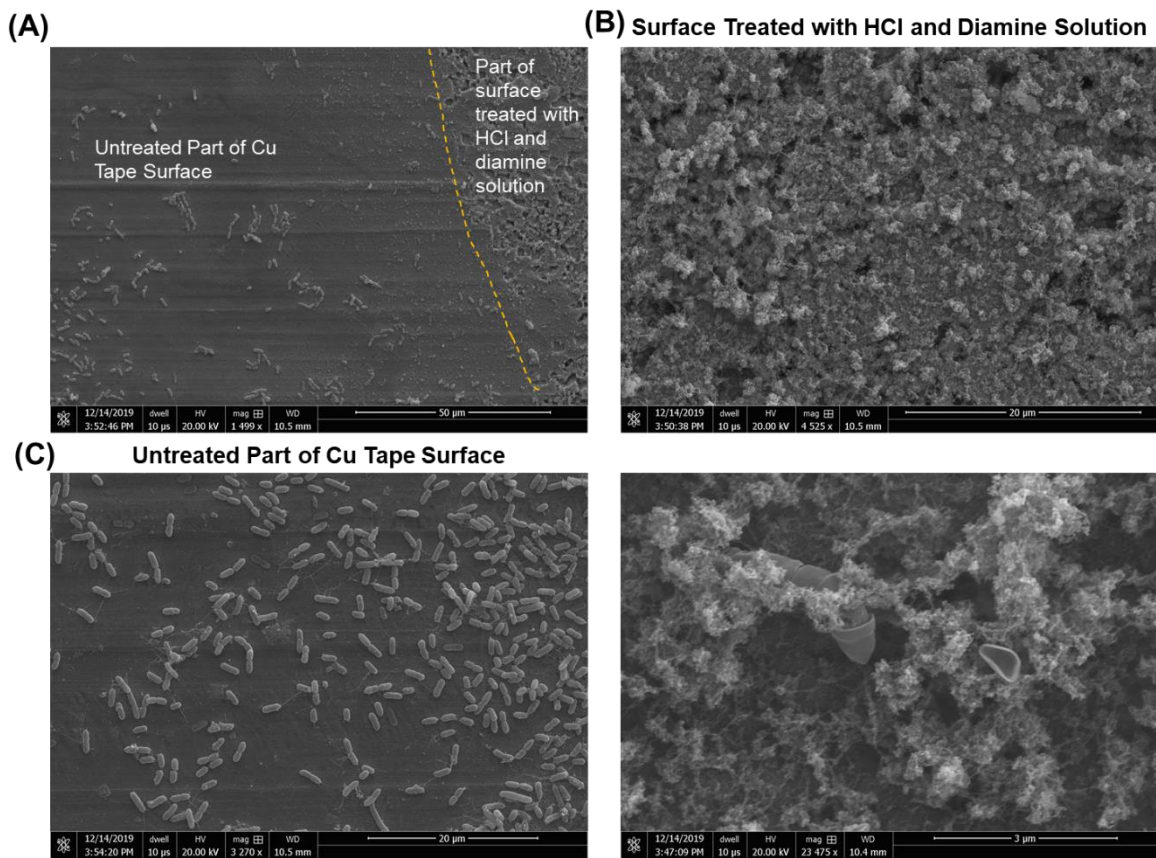
Figure 13.13. Tape surface after 4.5 hours of exposure to bacteria. Bacteria adhere to the portion of the tape surface which is untreated. Little bacterial adhesion is observed in the portion of the tape surface on which the HCl and diamine solution was deposited, forming the nanoplatelets.

13.2.3 Formation of Nanostructures on Other Metal Surfaces

In addition to forming the copper chloride crystals on copper surfaces, we sought to explore whether such nanostructures would spontaneously assemble on other metal surfaces. As such, we deposited the HCl and diamine solutions on a tin strip, a zinc strip, a zinc electrode, and a cobalt granule (**Fig. 13.14 and Fig. 13.15**). The diamine solution in particular appeared to lead to the formation of very well-defined structures compared to those formed by HCl alone.

HCl
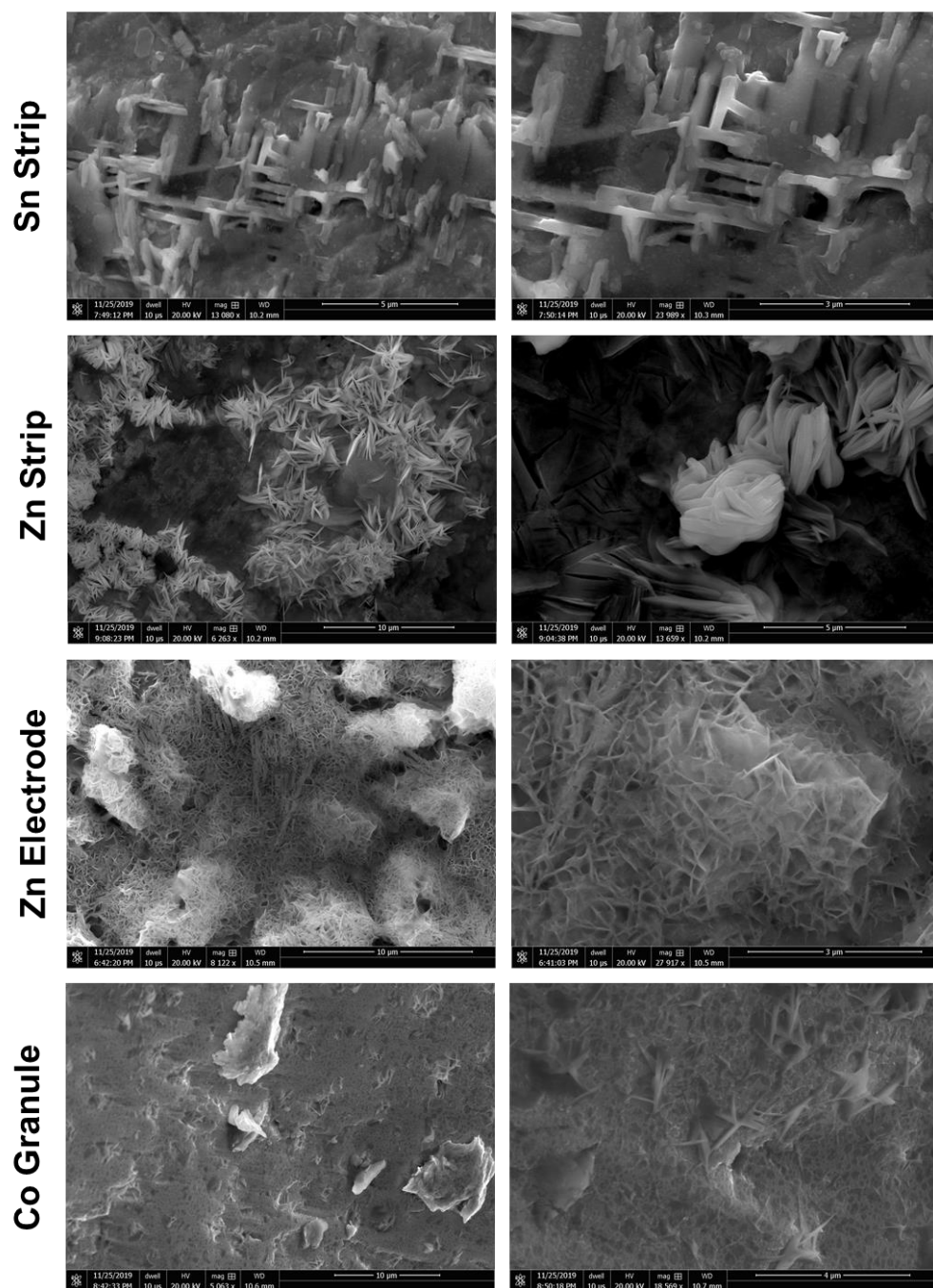
Figure 13.14. HCl nanostructures formed on Sn, Sn, and Co surfaces.
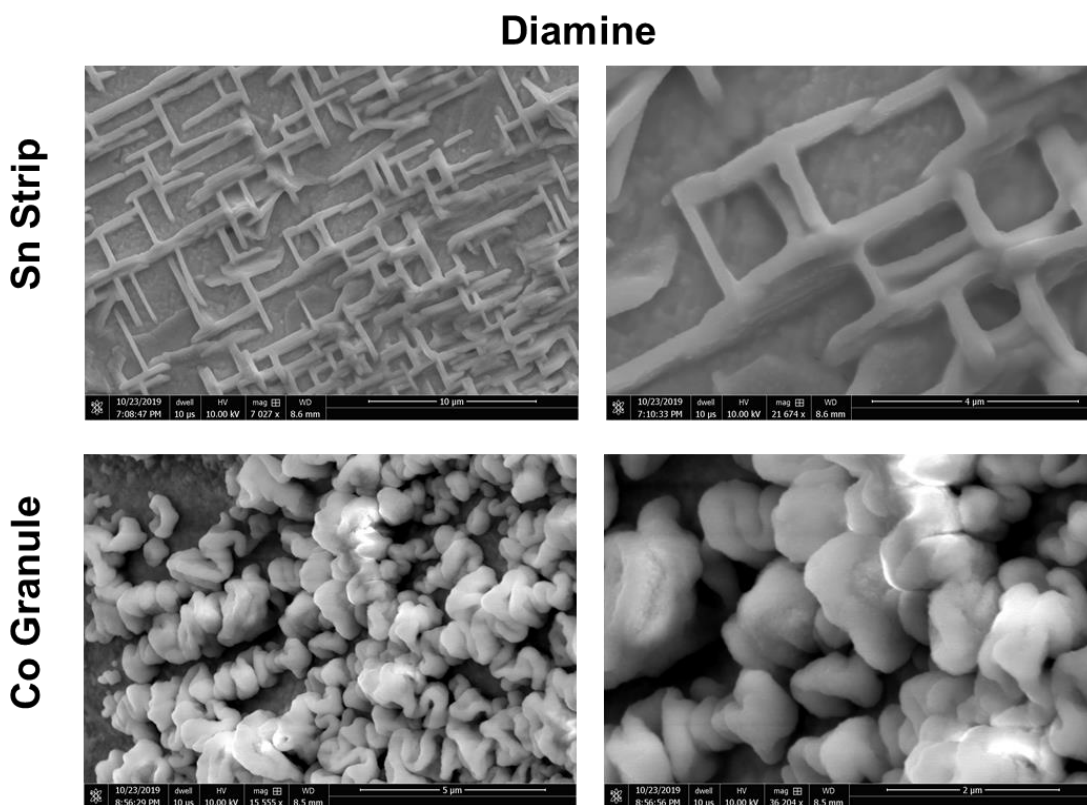
Figure 13.15. Diamine nanostructures formed on Sn, Sn, and Co surfaces.

13.2.4 Use of Nanoplatelets to Treat E. Coli and Multi-drug-resistant (MDR) E. Coli

Due the rising concern about antibiotic-resistant bacteria, we were next interested in determining whether the nanoplatelets could be utilized to treat multi-drug-resistant E. Coli. We found that both E. Coli and MDR E. Coli experienced very little growth when exposed to the HCl or diamine nanoplatelets **(Fig. 13.16)**. This indicates the strong potential for using these nanoplatelets as antibacterial surfaces. We then sought to determine the mechanism by which the nanoplatelets prevented growth of the bacteria. TUNEL assays revealed that the diamine and HCl nanoplatelets both induced dramatic damage at the DNA level in MDR E. Coli **(Fig. 13.17)**. The same DNA damage was not apparent in regular E. Coli, suggesting that the mechanism by which the nanoplatelets prevent bacterial division may differ from one type of bacteria to another. We also utilized live-dead staining assays to quantify the percentage of live cells for the treated

287

bacteria. The nanoplatelets appeared to lead to decreased bacterial cell viability for the MDR E. Coli, although the results were less logical in the case of regular E. Coli (**Fig. 13.18**).
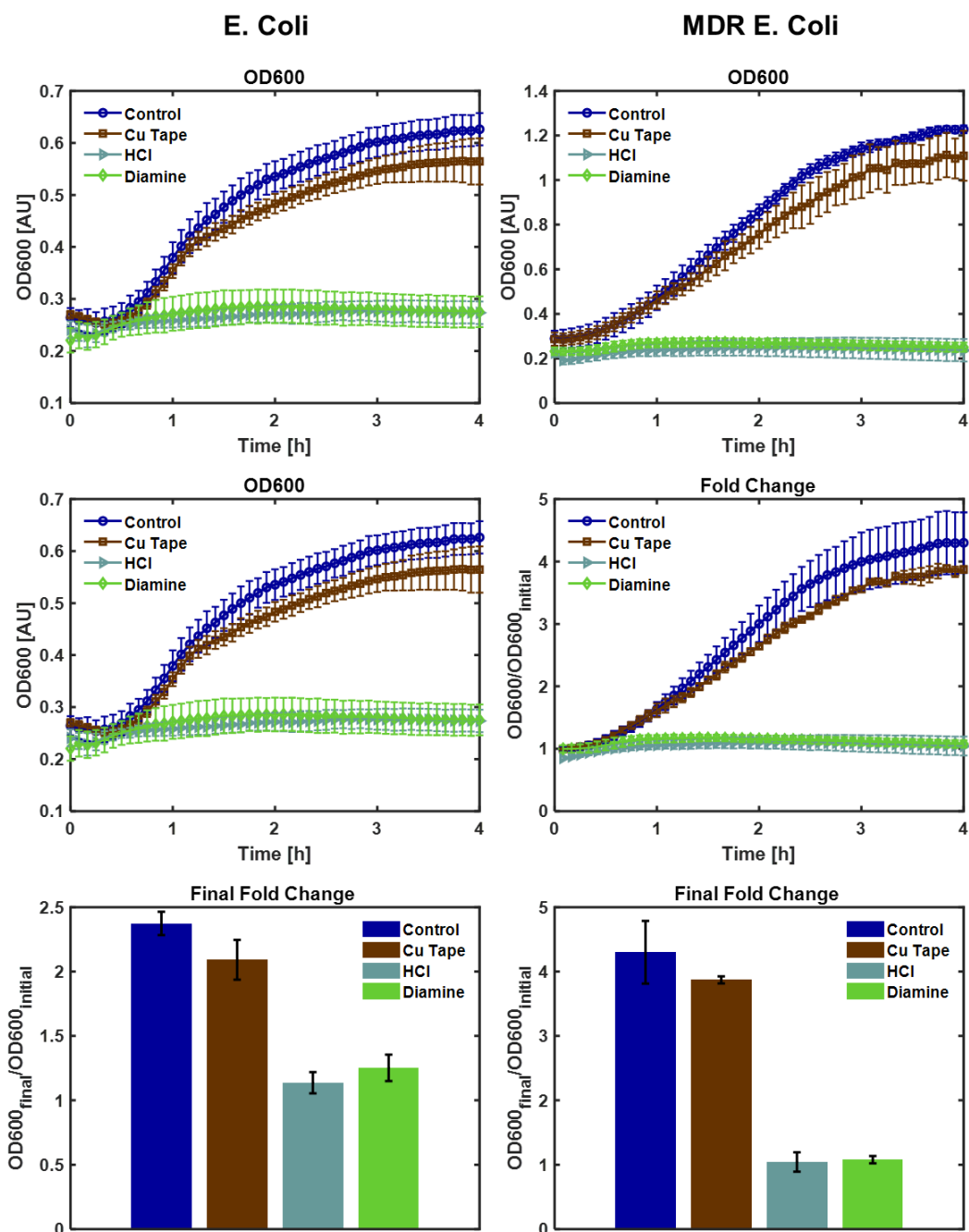
Figure 13.16. E. Coli and MDR E. Coli growth when exposed to the nanoplatelets. The samples experienced little to no growth in the presence of the nanoplatelets.
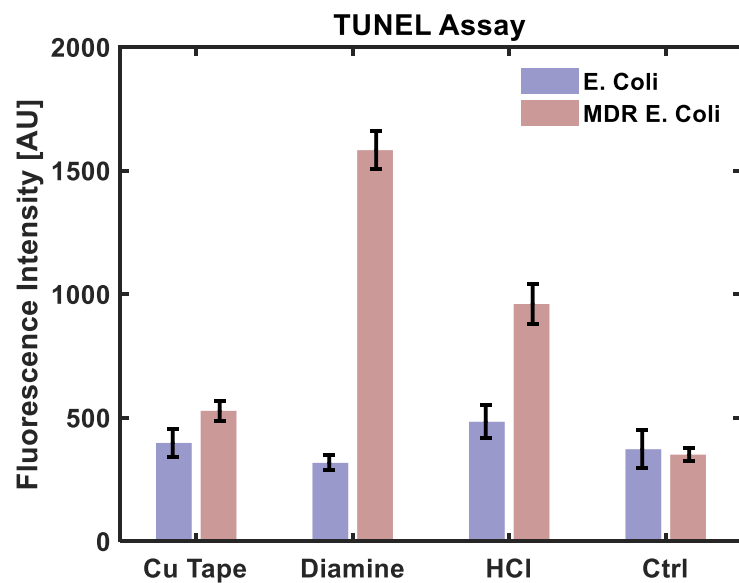
Figure 13.17. TUNEL staining results for E. Coli and MDR E. Coli treated with nanoplatelets.
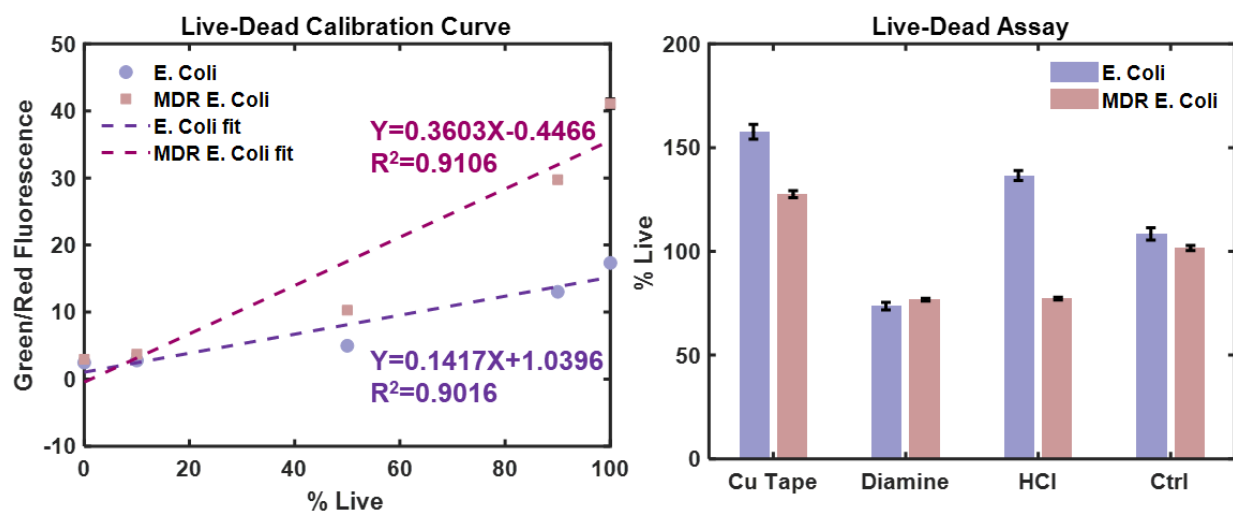
Figure 13.18. Live-dead staining of bacteria treated with the nanoplatelets.

13.3 CONCLUSIONS AND FUTURE WORK

We have demonstrated the spontaneous formation of copper chloride crystals on copper surfaces. We utilized these particles in treatment of multi-drug-resistant bacteria. Further work must be conducted to better understand the mechanisms by which these particles prevent bacterial growth. This will include experiments to determine the effect of nanoplatelet exposure on bacterial protein expression. Overall, these particles have proven to be a simple yet effective means of protecting against bacterial growth.

CHAPTER 14: METHYLENE-BLUE-DERIVED CARBON DOTS

The goal of this work was to develop carbon dots by hydrothermal synthesis using methylene blue. 100 mg methylene blue was dissolved in 2 mL water. The solution was heated in an autoclave holder at 150C for 8 h, after which excess liquid was removed through rotovapping. The sample was then probe sonicated and filtered with a 0.22 µm filter. The sample was dialyzed against 500 mL water for 24 h in a 10,000 MW cutoff dialysis cassette, with the dialysate replaced with fresh water multiple times throughout the 24 h. UV-visible spectra were collected, with methylene blue dye at a concentration of 1 mg/mL in water used for comparison **(Fig. 14.1)**. The hydrothermal synthesis led to carbon dots with a broadened absorbance peak compared to the narrow peak observed for methylene blue. However, the retention of high absorbance in the near-infrared region indicates potential for use of these particles in near-infrared imaging.
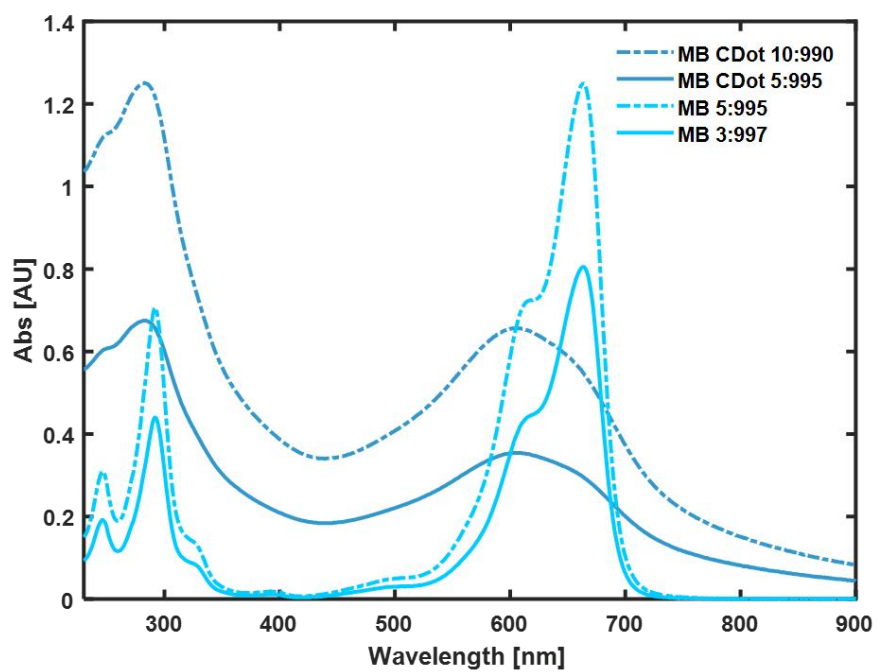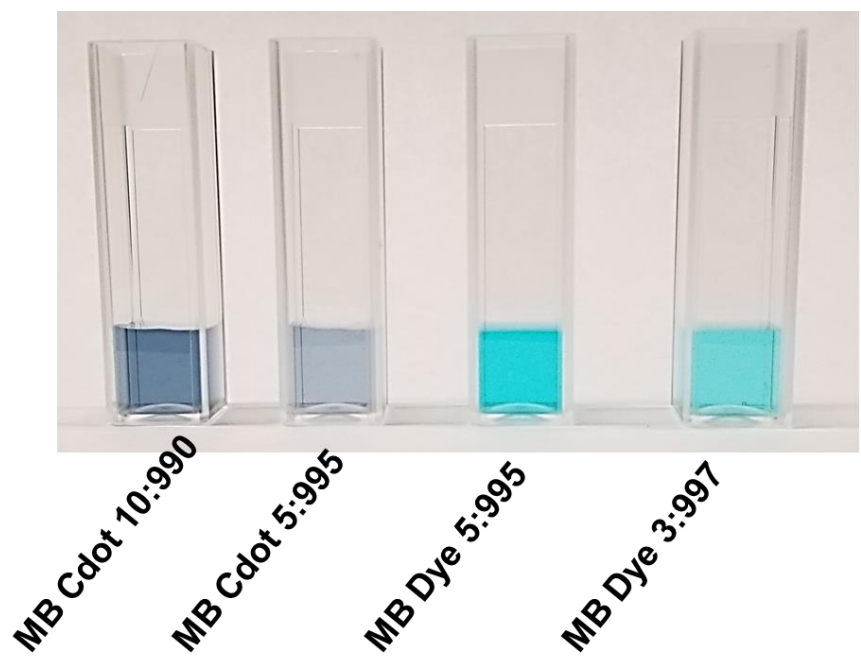
Figure 14.1. Appearance and absorbance behavior of methylene-blue-derived carbon dots (MB CDots) compared to pure methylene blue (MB dye).

REFERENCES

(1)   Seyfried, T. N.; Huysentruyt, L. C. On the Origin of Cancer Metastasis. *Crit. Rev. Oncog.* **2013**, *18* (1–2), 43–73.

(2)   Weigelt, B.; Peterse, J. L.; Veer, L. J. Van. BREAST CANCER METASTASIS: MARKERS AND MODELS. *Nat. Rev. Cancer* **2005**, *5* (August), 591–603.

(3)   Kim, T.; Giuliano, A. E.; Lyman, G. H. Lymphatic Mapping and Sentinel Lymph Node Biopsy in Early-Stage Breast Carcinoma: A Metaanalysis. *Cancer* **2006**, *106* (1), 4–16.

(4)   Ahmed, M.; Purushotham, A. D.; Douek, M. Novel Techniques for Sentinel Lymph Node Biopsy in Breast Cancer: A Systematic Review. *Lancet Oncol.* **2014**, *15* (8), e351–e362.

(5)   Uren, R. F.; Howman-Giles, R.; Chung, D.; Thompson, J. F. Imaging Sentinel Lymph Nodes. *Cancer J.* **2015**, *21* (1), 25–32.

(6)   Kang, J.; Chang, J. H.; Kim, S. M.; Lee, H. J.; Kim, H.; Wilson, B. C.; Song, T.-K. Real-Time Sentinel Lymph Node Biopsy Guidance Using Combined Ultrasound, Photoacoustic, Fluorescence Imaging: In Vivo Proof-of-Principle and Validation with Nodal Obstruction. *Sci. Rep.* **2017**, *7* (February), 45008.

(7)   Lyman, G. H.; Giuliano, A. E.; Somerfield, M. R.; Benson, A. B.; Bodurka, D. C.; Burstein, H. J.; Cochran, A. J.; Cody, H. S.; Edge, S. B.; Galper, S.; et al. American Society of Clinical Oncology Guideline Recommendations for Sentinel Lymph Node Biopsy in Early-Stage Breast Cancer. *J. Clin. Oncol.* **2005**, *23* (30), 7703–7720.

(8)   Krag, D.; Weaver, D.; Shikaga, T.; Moffat, F.; Klimberg, Suzanne, V.; Shriver, C.; Feldman, S.; Kusminsky, R.; Gadd, M.; Kuhn, J.; et al. THE SENTINEL NODE IN BREAST CANCER. *N. Engl. J. Med.* **2002**, *346* (15), 1105–1112.

(9)   McMasters, K.; Tuttle, T.; Carlson, D.; Brown, C.; Noyes, R.; Glaser, R.; Vennekotter, D.;

Turk, P.; Tate, P.; Sardi, A.; et al. Sentinel Lymph Node Biopsy for Breast Cancer: A Suitable Alternative to Routine Axillary Dissection in Multi-Institutional Practice When Optimal Technique Is Used. *J. Clin. Oncol.* **2000**, *18* (13), 2560–2566.

(10) Ung, O. A. Australasian Experience and Trials in Sentinel Lymph Node Biopsy: The RACS SNAC Trial. *Asian J. Surg.* **2004**, *27* (4), 284–290.

(11) Bobrow, L.; Klevesath, M. B.; Upponi, S.; Millar, K.; Duffy, S. W.; Myles, J. P.; Purushotham, A. D. Morbidity After Sentinel Lymph Node Biopsy in Primary Breast Cancer: Results From a Randomized Controlled Trial. *J. Clin. Oncol.* **2005**, *23* (19), 4312–4321.

(12) Cardoso-Coelho, L. P.; Borges, R. S.; Alencar, A. P.; Cardoso-Campos-Verdes, L. M.; Da Silva-Sampaio, J. P.; Borges, U. S.; Gebrim, L. H.; Dasilva, B. B. Comparative Study between Ultrasound-Guided Fine Needle Aspiration Cytology of Axillary Lymph Nodes and Sentinel Lymph Node Histopathology in Early-Stage Breast Cancer. *Oncol. Lett.* **2017**, *13* (5), 3299–3302.

(13) Akinci, M.; Bulut, S. P.; Erözgen, F.; Gürbüzel, M.; Gülşen, G.; Kocakuşak, A.; Gülen, M.; Kaplan, R. Predictive Value of Fine Needle Aspiration Biopsy of Axillary Lymph Nodes in Preoperative Breast Cancer Staging. *Turkish J. Surg.* **2016**, *32* (3), 191–196.

(14) Johnson, L.; Charles-Edwards, G.; Douek, M. Nanoparticles in Sentinel Lymph Node Assessment in Breast Cancer. *Cancers (Basel).* **2010**, *2* (4), 1884–1894.

(15) Mcgregor, A.; Pavri, S. N.; Tsay, C.; Kim, S. Use of Indocyanine Green for Sentinel Lymph Node Biopsy : Case Series and Methods Comparison. 1–4.

(16) Shen, S. Comparison of Sentinel Lymph Node Biopsy Guided by Blue Dye with or without Indocyanine Green in Early Breast Cancer. **2018**, No. March, 1841–1847.

(17) Liu, J.; Huang, L.; Wang, N.; Chen, P. Indocyanine Green Detects Sentinel Lymph Nodes in Early Breast Cancer. **2017**.

(18) Guo, J.; Yang, H.; Wang, S.; Cao, Y.; Liu, M.; Xie, F.; Liu, P.; Zhou, B.; Tong, F.; Cheng, L.; et al. Comparison of Sentinel Lymph Node Biopsy Guided by Indocyanine Green , Blue Dye , and Their Combination in Breast Cancer Patients : A Prospective Cohort Study. **2017**, No. 11, 1–8.

(19) Xie, X.; Ku, G.; Wang, X.; Wang, L. V.; Stoica, G. Noninvasive Imaging of Hemoglobin Concentration and Oxygenation in the Rat Brain Using High-Resolution Photoacoustic Tomography. *J. Biomed. Opt.* **2006**, *11* (2), 024015.

(20) van Adrichem, L. N. A.; van Neck, J. W.; Kolkman, R. G. M.; Siphanto, R. I.; Steenbergen, W.; van Leeuwen, T. G.; de Mul, F. F. M.; Thumma, K. K. Serial Noninvasive Photoacoustic Imaging of Neovascularization in Tumor Angiogenesis. *Opt. Express* **2005**, *13* (1), 89.

(21) Wang, L. V. Photoacoustic Tomography: Omniscale Imaging from Organelles to Patient. **2017**, No. March, T5A.1.

(22) Pramanik, M.; Ku, G.; Li, C.; Wang, L. V. Design and Evaluation of a Novel Breast Cancer Detection System Combining Both Thermoacoustic (TA) and Photoacoustic (PA) Tomography. *Med. Phys.* **2008**, *35* (6), 2218–2223.

(23) Li, C.; Wang, L. V. Photoacoustic Tomography and Sensing in Biomedicine. *Phys. Med. Biol.* **2009**, *54* (19).

(24) Servais, E. L.; Colovos, C.; Bograd, A. J.; White, J.; Sadelain, M.; Adusumilli, P. S. Animal Models and Molecular Imaging Tools to Investigate Lymph Node Metastases. *J. Mol. Med.* **2011**, *89* (8), 753–769.

(25)   Cekanova, M.; Rathore, K. Animal Models and Therapeutic Molecular Targets of Cancer: Utility and Limitations. *Drug Des. Devel. Ther.* **2014**, *8*, 1911–1922.

(26)   Cavo, M.; Fato, M.; Peñuela, L.; Beltrame, F.; Raiteri, R.; Scaglione, S. Microenvironment Complexity and Matrix Stiffness Regulate Breast Cancer Cell Activity in a 3D in Vitro Model. *Sci. Rep.* **2016**, *6* (September), 1–13.

(27)   Nagaraju, S.; Truong, D.; Mouneimne, G.; Nikkhah, M. Microfluidic Tumor–Vascular Model to Study Breast Cancer Cell Invasion and Intravasation. *Adv. Healthc. Mater.* **2018**, *7* (9), 1–12.

(28)   Saliba, J.; Daou, A.; Damiati, S.; Saliba, J.; El-Sabban, M.; Mhanna, R. Development of Microplatforms to Mimic the in Vivo Architecture of CNS and PNS Physiology and Their Diseases. *Genes (Basel).* **2018**, *9* (6), 1–29.

(29)   Song, H. H. G.; Park, K. M.; Gerecht, S. Hydrogels to Model 3D in Vitro Microenvironment of Tumor Vascularization. *Adv. Drug Deliv. Rev.* **2014**, *79*, 19–29.

(30)   Rejniak, K. A. *Systems Biology of Tumor Microenvironment: Quantitative Modeling and Simulations*; 2016; Vol. 936.

(31)   Zhang, Y.; Wang, L.; Liu, L.; Lin, L.; Liu, F.; Xie, Z.; Tian, H.; Chen, X. Engineering Metal Organic Frameworks for Photoacoustic Imaging Guided Chemo/Photothermal Combinational Tumor Therapy. *ACS Appl. Mater. Interfaces* **2018**, *10*, 41035−41045.

(32)   Qiao, Y.; Gumin, J.; Maclellan, C. J.; Gao, F.; Bouchard, R.; Lang, F. F.; Stafford, R. J.; Melancon, M. P. Magnetic Resonance and Photoacoustic Imaging of Brain Tumor Mediated by Mesenchymal Stem Cell Labeled with Multifunctional Nanoparticle Introduced via Carotid Artery Injection. *Nanotechnology* **2018**, *29* (16), 1–11.

(33)   Kwon, H. J.; Shin, K.; Soh, M.; Chang, H.; Kim, J.; Lee, J.; Ko, G.; Kim, B. H.; Kim, D.;

Hyeon, T. Large-Scale Synthesis and Medical Applications of Uniform-Sized Metal Oxide Nanoparticles. *Adv. Mater.* **2018**, *30* (42), 1–24.

(34)   Köker, T.; Tang, N.; Tian, C.; Zhang, W.; Wang, X.; Martel, R.; Pinaud, F. Cellular Imaging by Targeted Assembly of Hot-Spot SERS and Photoacoustic Nanoprobes Using Split-Fluorescent Protein Scaffolds. *Nat. Commun.* **2018**, *9* (1), 607.

(35)   Kim, T.; Zhang, Q.; Li, J.; Zhang, L.; Jokerst, J. V. A Gold/Silver Hybrid Nanoparticle for Treatment and Photoacoustic Imaging of Bacterial Infection. *ACS Nano* **2018**, *12* (6), 5615–5625.

(36)   Kang, J.; Kim, D.; Wang, J.; Han, Y.; Zuidema, J. M.; Hariri, A.; Park, J. H.; Jokerst, J. V.; Sailor, M. J. Enhanced Performance of a Molecular Photoacoustic Imaging Agent by Encapsulation in Mesoporous Silicon Nanoparticles. *Adv. Mater.* **2018**, *30* (27), 1–8.

(37)   Huang, Y.; Li, F.; Ma, G.; Yang, W.; Zhang, X.; Lin, J.; Luo, Y.; Huang, P. Aggregation Induced Photoacoustic Detection of Mercury (II) Ions Using Quaternary Ammonium Group-Capped Gold Nanorods. *Talanta* **2018**, *187* (April), 65–72.

(38)   Hanske, C.; Sanz-Ortiz, M. N.; Liz-Marzán, L. M. Silica-Coated Plasmonic Metal Nanoparticles in Action. *Adv. Mater.* **2018**, *30* (27), 1–28.

(39)   Hajfathalian, M.; Amirshaghaghi, A.; Naha, P. C.; Chhour, P.; Hsu, J. C.; Douglas, K.; Dong, Y.; Sehgal, C. M.; Tsourkas, A.; Neretina, S.; et al. Wulff in a Cage Gold Nanoparticles as Contrast Agents for Computed Tomography and Photoacoustic Imaging. *Nanoscale* **2018**, *10* (39), 18749–18757.

(40)   Tang, W.; Yang, Z.; Wang, S.; Wang, Z.; Song, J.; Yu, G.; Fan, W.; Dai, Y.; Wang, J.; Shan, L.; et al. Organic Semiconducting Photoacoustic Nanodroplets for Laser-Activatable Ultrasound Imaging and Combinational Cancer Therapy. *ACS Nano* **2018**, *12*

(3), 2610–2622.

(41) Yin, C.; Wen, G.; Liu, C.; Yang, B.; Lin, S.; Huang, J.; Zhao, P.; Wong, S. H. D.; Zhang,
K.; Chen, X.; et al. Organic Semiconducting Polymer Nanoparticles for Photoacoustic
Labelling and Tracking of Stem Cells in the Second Near-Infrared Window. *ACS Nano*
2018, *12*, 12201–12211.

(42) Guo, B.; Sheng, Z.; Hu, D.; Liu, C.; Zheng, H.; Liu, B. Through Scalp and Skull NIR-II
Photothermal Therapy of Deep Orthotopic Brain Tumors with Precise Photoacoustic
Imaging Guidance. *Adv. Mater.* **2018**, *30* (35), 1–8.

(43) Qin, X.; Chen, H.; Yang, H.; Wu, H.; Zhao, X.; Wang, H.; Chour, T.; Neofytou, E.; Ding,
D.; Daldrup-Link, H.; et al. Photoacoustic Imaging of Embryonic Stem Cell-Derived
Cardiomyocytes in Living Hearts with Ultrasensitive Semiconducting Polymer
Nanoparticles. *Adv. Funct. Mater.* **2018**, *28* (1), 1–12.

(44) Jung, E.; Kang, C.; Lee, J.; Yoo, D.; Hwang, D. W.; Kim, D.; Park, S. C.; Lim, S. K.;
Song, C.; Lee, D. Molecularly Engineered Theranostic Nanoparticles for Thrombosed
Vessels: H2O2-Activatable Contrast-Enhanced Photoacoustic Imaging and
Antithrombotic Therapy. *ACS Nano* **2018**, *12* (1), 392–401.

(45) Pan, D.; Pramanik, M.; Senpan, A.; Ghosh, S.; Wickline, S. a.; Wang, L. V.; Lanza, G. M.
Near Infrared Photoacoustic Detection of Sentinel Lymph Nodes with Gold Nanobeacons.
Biomaterials **2010**, *31* (14), 4088–4093.

(46) Pan, D.; Cai, X.; Yalaz, C.; Senpan, A.; Omanakuttan, K.; Wickline, S. a.; Wang, L. V.;
Lanza, G. M. Photoacoustic Sentinel Lymph Node Imaging with Self-Assembled Copper
Neodecanoate Nanoparticles. *ACS Nano* **2012**, *6* (2), 1260–1267.

(47) Pan, D.; Cai, X.; Kim, B.; Stacy, A. J.; Wang, L. V.; Lanza, G. M. Rapid Synthesis of near

Infrared Polymeric Micelles for Real-Time Sentinel Lymph Node Imaging. *Adv. Healthc. Mater.* **2012**, *1* (5), 582–589.

(48)   Song, K. H.; Kim, C.; Cobley, C. M.; Xia, Y.; Wang, L. V. Noninvasive Photoacoustic Sentinel Lymph Node Mapping Using Au Nanocages as a Lymph Node Tracer in a Rat Model. **2009**, *9* (1), 183–188.

(49)   Kobayashi, H.; Kawamoto, S.; Bernardo, M.; Brechbiel, M. W.; Knopp, M. V.; Choyke, P. L. Delivery of Gadolinium-Labeled Nanoparticles to the Sentinel Lymph Node: Comparison of the Sentinel Node Visualization and Estimations of Intra-Nodal Gadolinium Concentration by the Magnetic Resonance Imaging. *J. Control. Release* **2006**, *111* (3), 343–351.

(50)   Akers, W. J.; Kim, C.; Berezin, M.; Guo, K.; Fuhrhop, R.; Lanza, G. M.; Fischer, G. M.; Daltrozzo, E.; Zumbusch, A.; Cai, X.; et al. Noninvasive Photoacoustic and Fluorescence Sentinel Lymph Node Identification Using Dye-Loaded Perfluorocarbon Nanoparticles. *ACS Nano* **2011**, *5* (1), 173–182.

(51)   Zhang, Y. N.; Poon, W.; Tavares, A. J.; McGilvray, I. D.; Chan, W. C. W. Nanoparticle–Liver Interactions: Cellular Uptake and Hepatobiliary Elimination. *J. Control. Release* **2016**, *240*, 332–348.

(52)   Piao, M. J.; Kang, K. A.; Lee, I. K.; Kim, H. S.; Kim, S.; Choi, J. Y.; Choi, J.; Hyun, J. W. Silver Nanoparticles Induce Oxidative Cell Damage in Human Liver Cells through Inhibition of Reduced Glutathione and Induction of Mitochondria-Involved Apoptosis. *Toxicol. Lett.* **2011**, *201* (1), 92–100.

(53)   Sharma, V.; Anderson, D.; Dhawan, A. Zinc Oxide Nanoparticles Induce Oxidative DNA Damage and ROS-Triggered Mitochondria Mediated Apoptosis in Human Liver Cells

(HepG2). *Apoptosis* **2012**, *17* (8), 852–870.

(54) Bhattacharya, R.; Mukherjee, P. Biological Properties of "Naked" Metal Nanoparticles. *Adv. Drug Deliv. Rev.* **2008**, *60* (11), 1289–1306.

(55) Hussain, S. M.; Hess, K. L.; Gearhart, J. M.; Geiss, K. T.; Schlager, J. J. In Vitro Toxicity of Nanoparticles in BRL 3A Rat Liver Cells. *Toxicol. Vitr.* **2005**, *19* (7), 975–983.

(56) Chen, Y. S.; Hung, Y. C.; Liau, I.; Huang, G. S. Assessment of the In Vivo Toxicity of Gold Nanoparticles. *Nanoscale Res. Lett.* **2009**, *4* (8), 858–864.

(57) Schrand, A. M.; Rahman, M. F.; Hussain, S. M.; Schlager, J. J.; Smith, D. A.; Syed, A. F. Metal-Based Nanoparticles and Their Toxicity Assessment. *Wiley Interdiscip. Rev. Nanomedicine Nanobiotechnology* **2010**, *2* (5), 544–568.

(58) Jeng, H. A.; Swanson, J. Toxicity of Metal Oxide Nanoparticles in Mammalian Cells. *J. Environ. Sci. Heal. - Part A Toxic/Hazardous Subst. Environ. Eng.* **2006**, *41* (12), 2699–2711.

(59) Takeda, T.; Mu, A.; Tai, T. T.; Kitajima, S.; Taketani, S. Continuous de Novo Biosynthesis of Haem and Its Rapid Turnover to Bilirubin Are Necessary for Cytoprotection against Cell Damage. *Sci. Rep.* **2015**, *5* (October 2014), 1–12.

(60) Wegiel, B.; Otterbein, L. E. Go Green: The Anti-Inflammatory Effects of Biliverdin Reductase. *Front. Pharmacol.* **2012**, *3* (47), 1–8.

(61) Öllinger, R.; Yamashita, K.; Bilban, M.; Erat, A.; Kogler, P.; Thomas, M.; Csizmadia, E.; Usheva, A.; Margreiter, R.; Bach, F. H. Bilirubin and Biliverdin Treatment of Atherosclerotic Diseases. *Cell Cycle* **2007**, *6* (1), 39–43.

(62) Singleton, J. W.; Laster, L. Biliverdin Reductase of Guinea Pig Liver. *J. Biol. Chem.* **1966**, *240* (23), 5518–5525.

(63) Shu, X.; Royant, A.; Lin, M. Z.; Aguilera, T. a; Lev-ram, V.; Steinbach, A.; Tsien, R. Y. Mammalian Expression of Infrared Fluorescent Proteins Engineered from a Bacterial Phytochrome. *Science.* **2009**, *324* (5928), 804–807.

(64) Cho, K.; Wang, X.; Nie, S.; Chen, Z.; Shin, D. M. Therapeutic Nanoparticles for Drug Delivery in Cancer. *Clin. Cancer Res.* **2008**, *14* (5), 1310–1316.

(65) Singh, R.; Lillard, J. W. Nanoparticle-Based Targeted Drug Delivery. *Exp. Mol. Pathol.* **2009**, *86* (3), 215–223.

(66) Rizvi, S. A. A.; Saleh, A. M. Applications of Nanoparticle Systems in Drug Delivery Technology. *Saudi Pharm. J.* **2018**, *26* (1), 64–70.

(67) Sinha, R. Nanotechnology in Cancer Therapeutics: Bioconjugated Nanoparticles for Drug Delivery. *Mol. Cancer Ther.* **2006**, *5* (8), 1909–1917.

(68) Kawai, Y.; Kaidoh, M.; Yokoyama, Y.; Ohhashi, T. Pivotal Roles of Shear Stress in the Microenvironmental Changes That Occur within Sentinel Lymph Nodes. *Cancer Sci.* **2012**, *103* (7), 1245–1252.

(69) Matsumoto, Y.; Kawai, Y.; Watanabe, K.; Sakai, K.; Murata, M.; Handa, M.; Nakamura, S.; Ikeda, Y. Fluid Shear Stress Attenuates Tumor Necrosis Factor-Alpha-Induced Tissue Factor Expression in Cultured Human Endothelial Cells. *Blood* **1998**, *91* (11), 4164–4172.

(70) Xu, J.; Ji, Y.-H.; Dai, Z.-J.; Ma, Y.; Ren, Y.; Wu, C.-J. IL-6, IL-8 and TNF-α Levels Correlate with Disease Stage in Breast Cancer Patients. *Adv. Clin. Exp. Med.* **2017**, *26* (3), 421–426.

(71) Lee, E.; Pandey, N. B.; Popel, A. S. Lymphatic Endothelial Cells Support Tumor Growth in Breast Cancer. *Sci. Rep.* **2014**, *4*, 1–11.

(72) Zawieja, D. C.; Greiner, S. T.; Dixon, J. B.; Moore, J. E.; Cote, G. L.; Gashev, A. A.

Lymph Flow, Shear Stress, and Lymphocyte Velocity in Rat Mesenteric Prenodal Lymphatics. *Microcirculation* **2006**, *13* (7), 597–610.

(73) Proulx, S. T.; Luciani, P.; Derzsi, S.; Rinderknecht, M.; Mumprecht, V.; Leroux, J.-C.; Detmar, M. Quantitative Imaging of Lymphatic Function with Liposomal Indocyanine Green. *Cancer Res.* **2010**, *70* (18), 7053–7062.

(74) Jafarnejad, M.; Woodruff, M. C.; Zawieja, D. C.; Carroll, M. C.; Moore, J. E. Modeling Lymph Flow and Fluid Exchange with Blood Vessels in Lymph Nodes. *Lymphat. Res. Biol.* **2015**, *13* (4), 234–247.

(75) Pisano, M.; Triacca, V.; Barbee, K. A.; Swartz, M. A. An in Vitro Model of the Tumor-Lymphatic Microenvironment with Simultaneous Transendothelial and Luminal Flows Reveals Mechanisms of Flow Enhanced Invasion. *Integr. Biol. (United Kingdom)* **2015**, *7* (5), 525–533.

(76) Jafarnejad, M.; Cromer, W. E.; Kaunas, R. R.; Zhang, S. L.; Zawieja, D. C.; Moore, J. E. Measurement of Shear Stress-Mediated Intracellular Calcium Dynamics in Human Dermal Lymphatic Endothelial Cells. *Am. J. Physiol. Circ. Physiol.* **2015**, *308* (7), H697–H706.

(77) Sinha, S. H.; Owens, E. A.; Feng, Y.; Yang, Y.; Xie, Y.; Tu, Y.; Henary, M.; Zheng, Y. G. Synthesis and Evaluation of Carbocyanine Dyes as PRMT Inhibitors and Imaging Agents. *Eur. J. Med. Chem.* **2012**, *54*, 647–659.

(78) Bhardwaj, V.; Gumber, D.; Abbot, V.; Dhiman, S.; Sharma, P. Pyrrole: A Resourceful Small Molecule in Key Medicinal Hetero-Aromatics. *RSC Adv.* **2015**, *5* (20), 15233–15266.

(79) Martins, P.; Jesus, J.; Santos, S.; Raposo, L. R.; Roma-Rodrigues, C.; Baptista, P. V.;

Fernandes, A. R. Heterocyclic Anticancer Compounds: Recent Advances and the Paradigm Shift towards the Use of Nanomedicine's Tool Box. *Molecules* **2015**, *20* (9), 16852–16891.

(80)   Krall, N.; Pretto, F.; Decurtins, W.; Bernardes, G. J. L.; Supuran, C. T.; Neri, D. A Small-Molecule Drug Conjugate for the Treatment of Carbonic Anhydrase IX Expressing Tumors. *Angew. Chemie - Int. Ed.* **2014**, *53* (16), 4231–4235.

(81)   Schaafsma, B. E.; Mieog, J. S. D.; Hutteman, M.; Van Der Vorst, J. R.; Kuppen, P. J. K.; Löwik, C. W. G. M.; Frangioni, J. V.; Van De Velde, C. J. H.; Vahrmeijer, A. L. The Clinical Use of Indocyanine Green as a Near-Infrared Fluorescent Contrast Agent for Image-Guided Oncologic Surgery. *J. Surg. Oncol.* **2011**, *104* (3), 323–332.

(82)   Carr, J. A.; Franke, D.; Caram, J. R.; Perkinson, C. F.; Saif, M.; Askoxylakis, V.; Datta, M.; Fukumura, D.; Jain, R. K.; Bawendi, M. G.; et al. Shortwave Infrared Fluorescence Imaging with the Clinically Approved Near-Infrared Dye Indocyanine Green. *Proc. Natl. Acad. Sci. U. S. A.* **2018**, *115* (17), 4465–4470.

(83)   Varghese, P.; Abdel-Rahman, A. T.; Akberali, S.; Mostafa, A.; Gattuso, J. M.; Carpenter, R. Methylene Blue Dye - A Safe and Effective Alternative for Sentinel Lymph Node Localization. *Breast J.* **2008**, *14* (1), 61–67.

(84)   Simmons, R.; Thevarajah, S.; Brennan, M. B.; Christos, P.; Osborne, M. Methylene Blue Dye as an Alternative to Isosulfan Blue Dye for Sentinel Lymph Node Localization. *Ann. Surg. Oncol.* **2003**, *10* (3), 242–247.

(85)   Ji, Y. B.; Lee, K. J.; Park, Y. S.; Hong, S. M.; Paik, S. S.; Tae, K. Clinical Efficacy of Sentinel Lymph Node Biopsy Using Methylene Blue Dye in Clinically Node-Negative Papillary Thyroid Carcinoma. *Ann. Surg. Oncol.* **2012**, *19* (6), 1868–1873.

(86)   Mrsa, C. LookingT Oward Basic Science for Potential Drug DiscoveryTargets Against. *Med. Res. Rev.* **2009**, *30* (1), 1–22.

(87)   Alander, J. T.; Kaartinen, I.; Laakso, A.; Pätilä, T.; Spillmann, T.; Tuchin, V. V.; Venermo, M.; Välisuo, P. A Review of Indocyanine Green Fluorescent Imaging in Surgery. *Int. J. Biomed. Imaging* **2012**, *2012*.

(88)   Thevarajah, S.; Huston, T. L.; Simmons, R. M. A Comparison of the Adverse Reactions Associated with Isosulfan Blue versus Methylene Blue Dye in Sentinel Lymph Node Biopsy for Breast Cancer. *Am. J. Surg.* **2005**, *189* (2), 236–239.

(89)   Blamire, A. M.; Ogawa, S.; Ugurbil, K.; Rothman, D.; McCarthy, G.; Ellermann, J. M.; Hyder, F.; Rattner, Z.; Shulman, R. G. Dynamic Mapping of the Human Visual Cortex by High-Speed Magnetic Resonance Imaging. *Proc. Natl. Acad. Sci. U. S. A.* **1992**, *89* (22), 11069–11073.

(90)   Yang, W.; Zhu, G.; Wang, S.; Yu, G.; Yang, Z.; Lin, L.; Zhou, Z.; Liu, Y.; Dai, Y.; Zhang, F.; et al. In Situ Dendritic Cell Vaccine for Effective Cancer Immunotherapy. *ACS Nano* **2019**, *13* (3), 3083–3094.

(91)   Dobrucki, L.; Pan, D.; Smith, A. Multiscale Imaging of Nanoparticle Drug Delivery. *Curr Drug Targets* **2015**, *16* (6), 560–570.

(92)   Pan, D.; Pramanik, M.; Wickline, S. A.; Wang, L. V.; Lanza, G. M. Recent Advances in Colloidal Gold Nanobeacons for Molecular Photoacoustic Imaging. *Contrast Media Mol. Imaging* **2011**, *6* (5), 378–388.

(93)   Pan, D.; Schirra, C. O.; Wickline, S. A.; Lanza, G. M. Multicolor Computed Tomographic Molecular Imaging with Noncrystalline High-Metal-Density Nanobeacons. *Contrast Media Mol. Imaging* **2014**, *9* (1), 13–25.

(94)   Pan, D.; Pham, C. T. N.; Weilbaecher, K. N.; Tomasson, M. H.; Wickline, S. A.; Lanza, G. M. Contact-Facilitated Drug Delivery with Sn2 Lipase Labile Prodrugs Optimize Targeted Lipid Nanoparticle Drug Delivery. *Wiley Interdiscip. Rev. Nanomedicine Nanobiotechnology* **2016**, *8* (1), 85–106.

(95)   Pan, D.; Kim, B.; Wang, L. V.; Lanza, G. M. A Brief Account of Nanoparticle Contrast Agents for Photoacoustic Imaging. *Wiley Interdiscip. Rev. Nanomedicine Nanobiotechnology* **2013**, *5* (6), 517–543.

(96)   Zhou, W.; Shao, J.; Jin, Q.; Wei, Q.; Tang, J.; Ji, J. Zwitterionic Phosphorylcholine as a Better Ligand for Gold Nanorods Cell Uptake and Selective Photothermal Ablation of Cancer Cells. *Chem. Commun.* **2010**, *46* (9), 1479–1481.

(97)   Jose, S.; Cinu, T. A.; Sebastian, R.; Shoja, M. H.; Aleykutty, N. A.; Durazzo, A.; Lucarini, M.; Santini, A.; Souto, E. B. Transferrin-Conjugated Docetaxel–PLGA Nanoparticles for Tumor Targeting: Influence on MCF-7 Cell Cycle. *Polymers (Basel).* **2019**, *11*.

(98)   Wu, P. H.; Opadele, A. E.; Onodera, Y.; Nam, J. M. Targeting Integrins in Cancer Nanomedicine: Applications in Cancer Diagnosis and Therapy. *Cancers (Basel).* **2019**, *11* (11), 1–24.

(99)   Martín-Rapun, R.; De Matteis, L.; Ambrosone, A.; Garcia-Embid, S.; Gutierrez, L.; de la Fuente, J. M. Targeted Nanoparticles for the Treatment of Alzheimer's Disease. *Curr. Pharm. Des.* **2017**, *23* (13), 1927–1952.

(100) Garbuzenko, O. B.; Kuzmov, A.; Taratula, O.; Pine, S. R.; Minko, T. Strategy to Enhance Lung Cancer Treatment by Five Essential Elements: Inhalation Delivery, Nanotechnology, Tumor-Receptor Targeting, Chemo- and Gene Therapy. *Theranostics* **2019**, *9* (26), 8362–8376.

(101) Dupont, D.; Brullot, W.; Bloemen, M.; Verbiest, T.; Binnemans, K. Selective Uptake of Rare Earths from Aqueous Solutions by EDTA-Functionalized Magnetic and Nonmagnetic Nanoparticles. *ACS Appl. Mater. Interfaces* **2014**, *6* (7), 4980–4988.

(102) Piao, X.; Yin, H.; Guo, S.; Wang, H.; Guo, P. RNA Nanotechnology to Solubilize Hydrophobic Antitumor Drug for Targeted Delivery. *Adv. Sci.* **2019**, *1900951*, 1–7.

(103) Taschauer, A.; Polzer, W.; Alioglu, F.; Billerhart, M.; Decker, S.; Kittelmann, T.; Geppl, E.; Elmenofi, S.; Zehl, M.; Urban, E.; et al. Peptide-Targeted Polyplexes for Aerosol-Mediated Gene Delivery to CD49f-Overexpressing Tumor Lesions in Lung. *Mol. Ther. - Nucleic Acids* **2019**, *18* (December), 774–786.

(104) Wang, Z.; Zhang, F.; Shao, D.; Chang, Z.; Wang, L.; Hu, H.; Zheng, X.; Li, X.; Chen, F.; Tu, Z.; et al. Janus Nanobullets Combine Photodynamic Therapy and Magnetic Hyperthermia to Potentiate Synergetic Anti-Metastatic Immunotherapy. *Adv. Sci.* **2019**.

(105) Pereira, I.; Sousa, F.; Kennedy, P.; Sarmento, B. Carcinoembryonic Antigen-Targeted Nanoparticles Potentiate the Delivery of Anticancer Drugs to Colorectal Cancer Cells. *Int. J. Pharm.* **2018**, *549* (1–2), 397–403.

(106) Harris, J. C.; Scully, M. A.; Day, E. S. Cancer Cell Membrane-Coated Nanoparticles for Cancer Management. *Cancers (Basel).* **2019**, *11* (12), 1–19.

(107) Deng, H.; Dong, A.; Song, J.; Chen, X. Injectable Thermosensitive Hydrogel Systems Based on Functional PEG/PCL Block Polymer for Local Drug Delivery. *J. Control. Release* **2019**, *297* (October 2018), 60–70.

(108) Liu, Y.; Gong, C. S.; Dai, Y.; Yang, Z.; Yu, G.; Liu, Y.; Zhang, M.; Lin, L.; Tang, W.; Zhou, Z.; et al. In Situ Polymerization on Nanoscale Metal-Organic Frameworks for Enhanced Physiological Stability and Stimulus-Responsive Intracellular Drug Delivery.

Biomaterials **2019**, *218* (June), 119365.

(109) Deng, H.; Lin, L.; Wang, S.; Yu, G.; Zhou, Z.; Liu, Y.; Niu, G.; Song, J.; Chen, X. X-Ray-Controlled Bilayer Permeability of Bionic Nanocapsules Stabilized by Nucleobase Pairing Interactions for Pulsatile Drug Delivery. *Adv. Mater.* **2019**, *31* (37), 1–8.

(110) Yu, G.; Zhu, B.; Shao, L.; Zhou, J.; Saha, M. L.; Shi, B.; Zhang, Z.; Hong, T.; Li, S.; Chen, X.; et al. Host−guest Complexation-Mediated Codelivery of Anticancer Drug and Photosensitizer for Cancer Photochemotherapy. *Proc. Natl. Acad. Sci. U. S. A.* **2019**, *116* (14), 6618–6623.

(111) Fan, W.; Yung, B. C.; Chen, X. Stimuli-Responsive NO Release for On-Demand Gas-Sensitized Synergistic Cancer Therapy. *Angew. Chemie - Int. Ed.* **2018**, *57* (28), 8383–8394.

(112) Yang, Z.; Song, J.; Tang, W.; Fan, W.; Dai, Y.; Shen, Z.; Lin, L.; Cheng, S.; Liu, Y.; Niu, G.; et al. Stimuli-Responsive Nanotheranostics for Real-Time Monitoring Drug Release by Photoacoustic Imaging. *Theranostics* **2019**, *9* (2), 526–536.

(113) Huang, P.; Wang, G.; Su, Y.; Zhou, Y.; Huang, W.; Zhang, R.; Yan, D. Stimuli-Responsive Nanodrug Self-Assembled from Amphiphilic Drug-Inhibitor Conjugate for Overcoming Multidrug Resistance in Cancer Treatment. *Theranostics* **2019**, *9* (20), 5755–5768.

(114) Huang, X.; Deng, G.; Han, Y.; Yang, G.; Zou, R.; Zhang, Z.; Sun, S.; Hu, J. Right Cu2−xS@MnS Core–Shell Nanoparticles as a Photo/H2O2-Responsive Platform for Effective Cancer Theranostics. *Adv. Sci.* **2019**, *6* (20).

(115) Guo, F.; Li, G.; Ma, S.; Zhou, H.; Chen, X. Multi-Responsive Nanocarriers Based on β-CD-PNIPAM Star Polymer Coated MSN-SS-Fc Composite Particles. *Polymers (Basel).*

2019.

(116) Liu, Y.; Gong, C. S.; Dai, Y.; Yang, Z.; Yu, G.; Liu, Y.; Zhang, M.; Lin, L.; Tang, W.; Zhou, Z.; et al. In Situ Polymerization on Nanoscale Metal-Organic Frameworks for Enhanced Physiological Stability and Stimulus-Responsive Intracellular Drug Delivery. *Biomaterials* **2019**, *218* (July), 119365.

(117) Mir, M.; Ahmed, N.; Permana, A. D.; Rodgers, A. M.; Donnelly, R. F.; Rehman, A. Enhancement in Site-Specific Delivery of Carvacrol against Methicillin Resistant Staphylococcus Aureus Induced Skin Infections Using Enzyme Responsive Nanoparticles : A Proof of Concept Study. *Pharmaceutics* **2019**.

(118) Xu, C.; Gao, F.; Wu, J.; Niu, S.; Li, F.; Jin, L.; Shi, Q.; Du, L. Biodegradable Nanotheranostics with Hyperthermia-Induced Bubble Ability for Ultrasound Imaging–Guided Chemo-Photothermal Therapy. *Int. J. Nanomedicine* **2019**, *14*, 7141–7153.

(119) Datta, S.; Misra, S. K.; Saha, M. L.; Lahiri, N.; Louie, J.; Pan, D.; Stang, P. J. Orthogonal Self-Assembly of an Organoplatinum(II) Metallacycle and Cucurbit[8]Uril That Delivers Curcumin to Cancer Cells. *Proc. Natl. Acad. Sci. U. S. A.* **2018**, *115* (32), 8087–8092.

(120) Pan, D. Theranostic Nanomedicine with Functional Nanoarchitecture. *Mol. Pharm.* **2013**, *10* (3), 781–782.

(121) Pan, D. Next Generation Gene Delivery Approaches: Recent Progress and Hurdles. *Mol. Pharm.* **2015**, *12* (2), 299–300.

(122) Fathi, P.; Capron, G.; Tripathi, I.; Misra, S.; Ostadhossein, F.; Selmic, L.; Rowitz, B.; Pan, D. Computed Tomography-Guided Additive Manufacturing of Personalized Absorbable Gastrointestinal Stents for Intestinal Fistulae and Perforations. *Biomaterials* **2020**, *228* (June 2019), 119542.

(123) Schirra, C. O.; Roessl, E.; Koehler, T.; Brendel, B.; Thran, A.; Pan, D.; Anastasio, M. A.; Proksa, R. Statistical Reconstruction of Material Decomposed Data in Spectral CT. *IEEE Trans. Med. Imaging* **2013**, *32* (7), 1249–1257.

(124) Schirra, C. O.; Senpan, A.; Roessl, E.; Thran, A.; Stacy, A. J.; Wu, L.; Proska, R.; Pan, D. Second Generation Gold Nanobeacons for Robust K-Edge Imaging with Multi-Energy CT. *J Mater Chem* **2012**, *22* (43), 23071–23077.

(125) Pan, D.; Schirra, C. O.; Senpan, A.; Schmieder, A. H.; Stacy, A. J.; Roessl, E.; Thran, A.; Wickline, S. A.; Proska, R.; Lanza, G. M. An Early Investigation of Ytterbium Nanocolloids for Selective and Quantitative "Multicolor" Spectral CT Imaging. *ACS Nano* **2012**, *6* (4), 3364–3370.

(126) Pan, D.; Roessl, E.; Schlomka, J. P.; Caruthers, S. D.; Senpan, A.; Scott, M. J.; Allen, J. S.; Zhang, H.; Hu, G.; Gaffney, P. J.; et al. Computed Tomography in Color: Nanok-Enhanced Spectral CT Molecular Imaging. *Angew. Chemie - Int. Ed.* **2010**, *49* (50), 9635–9639.

(127) Pan, D.; Williams, T. A.; Senpan, A.; Allen, J. S.; Scott, M. J.; Gaffney, P. J.; Wickline, S. A.; Lanza, G. M. Detecting Vascular Biosignatures with a Colloidal, Radio-Opaque Polymeric Nanoparticle. *J. Am. Chem. Soc.* **2009**, *131* (42), 15522–15527.

(128) Pan, D.; Caruthers, S. D.; Senpan, A.; Yalaz, C.; Stacy, A. J.; Hu, G.; Marsh, J. N.; Gaffney, P. J.; Wickline, S. A.; Lanza, G. M. Synthesis of NanoQ, a Copper-Based Contrast Agent for High-Resolution Magnetic Resonance Imaging Characterization of Human Thrombus. *J. Am. Chem. Soc.* **2011**, *133* (24), 9168–9171.

(129) Kim, B.; Schmieder, A. H.; Stacy, A. J.; Williams, T. A.; Pan, D. Sensitive Biological Detection with a Soluble and Stable Polymeric Paramagnetic Nanocluster. *J. Am. Chem.*

Soc. **2012**, *134* (25), 10377–10380.

(130) Jin, R.; Lin, B.; Li, D.; Ai, H. Superparamagnetic Iron Oxide Nanoparticles for MR Imaging and Therapy: Design Considerations and Clinical Applications. *Curr. Opin. Pharmacol.* **2014**, *18*, 18–27.

(131) Vallabani, N. V. S.; Singh, S. Recent Advances and Future Prospects of Iron Oxide Nanoparticles in Biomedicine and Diagnostics. *3 Biotech* **2018**, *8* (6).

(132) Zanganeh, S.; Hutter, G.; Spitler, R.; Lenkov, O.; Mahmoudi, M.; Shaw, A.; Pajarinen, J. S.; Nejadnik, H.; Goodman, S.; Moseley, M.; et al. Iron Oxide Nanoparticles Inhibit Tumour Growth by Inducing Pro-Inflammatory Macrophage Polarization in Tumour Tissues. *Nat. Nanotechnol.* **2016**, *11* (11), 986–994.

(133) Thiesen, B.; Jordan, A. Clinical Applications of Magnetic Nanoparticles for Hyperthermia. *Int. J. Hyperth.* **2008**, *24* (6), 467–474.

(134) Im, J.; Lawrence, J.; Seelig, D.; Nho, R. S. FoxM1-Dependent RAD51 and BRCA2 Signaling Protects Idiopathic Pulmonary Fibrosis Fibroblasts from Radiation-Induced Cell Death Article. *Cell Death Dis.* **2018**, *9* (6).

(135) Song, K. H.; Jung, S. Y.; Park, J. I.; Ahn, J.; Park, J. K.; Um, H. D.; Park, I. C.; Hwang, S. G.; Ha, H.; Song, J. Y. Inhibition of Karyopherin-A2 Augments Radiation-Induced Cell Death by Perturbing BRCA1-Mediated DNA Repair. *Int. J. Mol. Sci.* **2019**, *20* (11).

(136) Bladen, C. L.; Flowers, M. A.; Miyake, K.; Podolsky, R. H.; Barrett, J. T.; Kozlowski, D. J.; Dynan, W. S. Quantification of Ionizing Radiation-Induced Cell Death In Situ in a Vertebrate Embryo . *Radiat. Res.* **2007**, *168* (2), 149–157.

(137) Fathi, P.; Knox, H. J.; Sar, D.; Tripathi, I.; Misra, S. K.; Ostadhossein, F.; Esch, M. B.; Chan, J.; Pan, D. Biodegradable Biliverdin Nanoparticles for Efficient Photoacoustic

Imaging. *ACS Nano* **2019**, acsnano.9b01201.

(138) Wu, L.; Cai, X.; Nelson, K.; Xing, W.; Xia, J.; Zhang, R.; Stacy, A. J.; Luderer, M.; Lanza, G. M.; Wang, L. V.; et al. A Green Synthesis of Carbon Nanoparticles from Honey and Their Use in Real-Time Photoacoustic Imaging. *Nano Res.* **2013**, *6* (5), 312–325.

(139) Pan, D.; Pramanik, M.; Senpan, A.; Wickline, S. A.; Wang, L. V.; Lanza, G. M. A Facile Synthesis of Novel Self-Assembled Gold Nanorods Designed for Near-Infrared Imaging. *J. Nanosci. Nanotechnol.* **2010**, 8118–8123.

(140) Pan, D.; Pramanik, M.; Senpan, A.; Allen, J. S.; Zhang, H.; Wickline, S. A.; Wang, L. V.; Lanza, G. M. Molecular Photoacoustic Imaging of Angiogenesis with Integrin-Targeted Gold Nanobeacons. *FASEB J.* **2011**, *25* (3), 875–882.

(141) Pan, D.; Pramanik, M.; Senpan, A.; Yang, X.; Song, K. H.; Scott, M. J.; Zhang, H.; Gaffney, P. J.; Wickline, S. A.; Wang, L. V.; et al. Molecular Photoacoustic Tomography with Colloidal Nanobeacons. *Angew. Chemie - Int. Ed.* **2009**, *48* (23), 4170–4173.

(142) Whittington, N. C.; Wray, S. Suppression of Red Blood Cell Autofluorescence for Immunocytochemistry on Fixed Embryonic Mouse Tissue. *Curr. Protoc. Neurosci.* **2017**, *81*, 2.28.1-2.28.12.

(143) Zhao, J.; Zhong, D.; Zhou, S. NIR-I-to-NIR-II Fluorescent Nanomaterials for Biomedical Imaging and Cancer Therapy. *J. Mater. Chem. B* **2018**, *6* (3), 349–365.

(144) Li, J. Bin; Liu, H. W.; Fu, T.; Wang, R.; Zhang, X. B.; Tan, W. Recent Progress in Small-Molecule Near-IR Probes for Bioimaging. *Trends Chem.* **2019**, *1* (2), 224–234.

(145) Kim, C.; Erpelding, T. N.; Jankovic, L.; Pashley, M. D.; Wang, L. V. Deeply Penetrating in Vivo Photoacoustic Imaging Using a Clinical Ultrasound Array System. *Biomed. Opt. Express* **2010**, *1* (1), 278.

(146) Zhang, H. F.; Maslov, K.; Stoica, G.; Wang, L. V. Functional Photoacoustic Microscopy for High-Resolution and Noninvasive in Vivo Imaging. *Nat. Biotechnol.* **2006**, *24* (7), 848–851.

(147) Mallidi, S.; Luke, G. P.; Emelianov, S. Photoacoustic Imaging in Cancer Detection, Diagnosis, and Treatment Guidance. *Trends Biotechnol.* **2011**, *29* (5), 213–221.

(148) Gutierrez-Juarez, G.; Gupta, S. K.; Al-Shaer, M.; Polo-Parada, L.; Dale, P. S.; Papageorgio, C.; Viator, J. A. Detection of Melanoma Cells in Vitro Using an Optical Detector of Photoacoustic Waves. *Lasers Surg. Med.* **2010**, *42* (3), 274–281.

(149) Wang, X.; Xie, X.; Ku, G.; Wang, L. V.; Stoica, G. Noninvasive Imaging of Hemoglobin Concentration and Oxygenation in the Rat Brain Using High-Resolution Photoacoustic Tomography. *J. Biomed. Opt.* **2006**, *11* (2), 024015.

(150) Kruger, R. A.; Kuzmiak, C. M.; Lam, R. B.; Reinecke, D. R.; Del Rio, S. P.; Steed, D. Dedicated 3D Photoacoustic Breast Imaging. *Med. Phys.* **2013**, *40* (11), 1–8.

(151) Wang, L. V.; Hu, S. Photoacoustic Tomography: In Vivo Imaging from Organelles to Organs. *Science (80-.).* **2012**, *335* (6075), 1458–1462.

(152) Guggenheim, J. A.; Allen, T. J.; Plumb, A.; Zhang, E. Z.; Rodriguez-Justo, M.; Punwani, S.; Beard, P. C. Photoacoustic Imaging of Human Lymph Nodes with Endogenous Lipid and Hemoglobin Contrast. *J. Biomed. Opt.* **2015**, *20* (5), 050504.

(153) Weight, R. M.; Dale, P. S.; Viator, J. A. Detection of Circulating Melanoma Cells in Human Blood Using Photoacoustic Flowmetry. *Proc. 31st Annu. Int. Conf. IEEE Eng. Med. Biol. Soc. Eng. Futur. Biomed. EMBC 2009* **2009**, 106–109.

(154) Galanzha, E. I.; Shashkov, E. V.; Spring, P. M.; Suen, J. Y.; Zharov, V. P. In Vivo, Noninvasive, Label-Free Detection and Eradication of Circulating Metastatic Melanoma

Cells Using Two-Color Photoacoustic Flow Cytometry with a Diode Laser. *Cancer Res.* **2009**, *69* (20), 7926–7934.

(155) Longo, D. L.; Stefania, R.; Aime, S.; Oraevsky, A. Melanin-Based Contrast Agents for Biomedical Optoacoustic Imaging and Theranostic Applications. *Int. J. Mol. Sci.* **2017**, *18* (8).

(156) Chitgupi, U.; Nyayapathi, N.; Kim, J.; Wang, D.; Sun, B.; Li, C.; Carter, K.; Huang, W. C.; Kim, C.; Xia, J.; et al. Surfactant-Stripped Micelles for NIR-II Photoacoustic Imaging through 12 Cm of Breast Tissue and Whole Human Breasts. *Adv. Mater.* **2019**, *31* (40), 1–10.

(157) Liu, G.; Zhu, J.; Guo, H.; Sun, A.; Chen, P.; Xi, L.; Huang, W.; Song, X.; Dong, X. Mo2C-Derived Polyoxometalate for NIR-II Photoacoustic Imaging-Guided Chemodynamic/Photothermal Synergistic Therapy. *Angew. Chemie - Int. Ed.* **2019**, 2–8.

(158) Guo, B.; Chen, J.; Chen, N.; Middha, E.; Xu, S.; Pan, Y.; Wu, M.; Li, K.; Liu, C.; Liu, B. High-Resolution 3D NIR-II Photoacoustic Imaging of Cerebral and Tumor Vasculatures Using Conjugated Polymer Nanoparticles as Contrast Agent. *Adv. Mater.* **2019**, *31* (25), 1–9.

(159) Jiang, Y.; Li, J.; Zhen, X.; Xie, C.; Pu, K. Dual-Peak Absorbing Semiconducting Copolymer Nanoparticles for First and Second Near-Infrared Window Photothermal Therapy: A Comparative Study. *Adv. Mater.* **2018**, *30* (14), 1–7.

(160) Zou, L.; Wang, H.; He, B.; Zeng, L.; Tan, T.; Cao, H.; He, X.; Zhang, Z.; Guo, S.; Li, Y. Current Approaches of Photothermal Therapy in Treating Cancer Metastasis with Nanotherapeutics. *Theranostics* **2016**, *6* (6), 762–772.

(161) Riley, R. S.; Day, E. S. Gold Nanoparticle-Mediated Photothermal Therapy: Applications

and Opportunities for Multimodal Cancer Treatment. *Wiley Interdiscip. Rev. Nanomedicine Nanobiotechnology* **2017**, *9* (4).

(162) Song, X.; Liang, C.; Gong, H.; Chen, Q.; Wang, C.; Liu, Z. Photosensitizer-Conjugated Albumin-Polypyrrole Nanoparticles for Imaging-Guided in Vivo Photodynamic/Photothermal Therapy. *Small* **2015**, *11* (32), 3932–3941.

(163) Hyochol Ahn, PhD, Michael Weaver, PhD, Debra Lyon, PhD, Eunyoung Choi, RN, and Roger B. Fillingim, P. New Photosensitizers for Photodynamic Therapy. *Biochem J.* **2017**.

(164) Tokura, Y.; Moriwaki, S. I. Photodynamic Therapy. *Ther. Ski. Dis. A Worldw. Perspect. Ther. Approaches Their Mol. Basis* **2010**, *90* (12), 105–111.

(165) Espinosa, A.; Di Corato, R.; Kolosnjaj-Tabi, J.; Flaud, P.; Pellegrino, T.; Wilhelm, C. Duality of Iron Oxide Nanoparticles in Cancer Therapy: Amplification of Heating Efficiency by Magnetic Hyperthermia and Photothermal Bimodal Treatment. *ACS Nano* **2016**, *10* (2), 2436–2446.

(166) Li, M.; Bu, W.; Ren, J.; Li, J.; Deng, L.; Gao, M.; Gao, X.; Wang, P. Enhanced Synergism of Thermo-Chemotherapy for Liver Cancer with Magnetothermally Responsive Nanocarriers. *Theranostics* **2018**, *8* (3), 693–709.

(167) Lin, I. C.; Fang, J. H.; Lin, C. T.; Sung, S. Y.; Su, Y. L.; Hu, S. H. Enhanced Targeted Delivery of Cyclodextrin-Based Supermolecules by Core–Shell Nanocapsules for Magnetothermal Chemotherapy. *Macromol. Biosci.* **2016**, 1273–1286.

(168) Yoon, H. Y.; Selvan, S. T.; Yang, Y.; Kim, M. J.; Yi, D. K.; Kwon, I. C.; Kim, K. Engineering Nanoparticle Strategies for Effective Cancer Immunotherapy. *Biomaterials* **2018**, *178*, 597–607.

(169) Chu, D.; Zhao, Q.; Yu, J.; Zhang, F.; Zhang, H.; Wang, Z. Nanoparticle Targeting of

Neutrophils for Improved Cancer Immunotherapy. *Adv. Healthc. Mater.* **2016**, *5* (9), 1088–1093.

(170) Mi, Y.; Smith, C. C.; Yang, F.; Qi, Y.; Roche, K. C.; Serody, J. S.; Vincent, B. G.; Wang, A. Z. A Dual Immunotherapy Nanoparticle Improves T-Cell Activation and Cancer Immunotherapy. *Adv. Mater.* **2018**, *30* (25), 1–9.

(171) Hasegawa, Y.; Nakamura, Y.; Choyke, P. L.; Sato, N.; Sato, K.; Nagaya, T.; Kobayashi, H.; Xu, B. Spatially Selective Depletion of Tumor-Associated Regulatory T Cells with near-Infrared Photoimmunotherapy. *Sci. Transl. Med.* **2016**, *8* (352), 352ra110-352ra110.

(172) Luo, L.; Liu, C.; He, T.; Zeng, L.; Xing, J.; Xia, Y.; Pan, Y.; Gong, C.; Wu, A. Engineered Fluorescent Carbon Dots as Promising Immune Adjuvants to Efficiently Enhance Cancer Immunotherapy. *Nanoscale* **2018**, *10* (46), 22035–22043.

(173) Seybold, P. G.; Gouterman, M. Porphyrins. XIII: Fluorescence Spectra and Quantum Yields. *J. Mol. Spectrosc.* **1969**, *31* (1–13), 1–13.

(174) Kongshaug, M. Distribution of Tetrapyrrole Photosensitizers among Human Plasma Proteins. *Int. J. Biochem.* **1992**, *24* (8), 1239–1265.

(175) Zurlo, J.; Rudacille, D.; Goldberg, A. M. *Animals and Alternatives in Testing: History, Science, and Ethics*; 1994.

(176) Overchuk, M.; Zheng, M.; Rajora, M. A.; Charron, D. M.; Chen, J.; Zheng, G. Tailoring Porphyrin Conjugation for Nanoassembly-Driven Phototheranostic Properties. *ACS Nano* **2019**, *13* (4), 4560–4571.

(177) Tanaka, T.; Osuka, A. Conjugated Porphyrin Arrays: Synthesis, Properties and Applications for Functional Materials. *Chem. Soc. Rev.* **2015**, *44* (4), 943–969.

(178) Uttamlal, M.; Sheila Holmes-Smith, A. The Excitation Wavelength Dependent

Fluorescence of Porphyrins. *Chem. Phys. Lett.* **2008**, *454* (4–6), 223–228.

(179) Dayer, M.; Moosavi-Movahedi, A.; Dayer, M. Band Assignment in Hemoglobin Porphyrin Ring Spectrum: Using Four-Orbital Model of Gouterman. *Protein Pept. Lett.* **2010**, *17* (4), 473–479.

(180) Kou, J.; Dou, D.; Yang, L. Porphyrin Photosensitizers in Photodynamic Therapy and Its Applications. *Oncotarget* **2017**, *8* (46), 81591–81603.

(181) Roeder, B. Tetrapyrroles: A Chemical Class of Potent Photosensitizers for the Photodynamic Treatment of Tumours. *Lasers Med. Sci.* **1990**, *5* (2), 99–106.

(182) Fiel, R. J.; Musser, D. A.; Mark, E. H.; Mazurchuk, R.; Alletto, J. J. A Comparative Study of Manganese Meso-Sulfonatophenyl Porphyrins: Contrast-Enhancing Agents for Tumors. *Magn. Reson. Imaging* **1990**, *8* (3), 255–259.

(183) Place, D. A.; Faustino, P. J.; Berghmans, K. K.; van Zijl, P. C. M.; Chesnick, A. S.; Cohen, J. S. MRI Contrast-Dose Relationship of Manganese(III)Tetra(4-Sulfonatophenyl) Porphyrin with Human Xenograft Tumors in Nude Mice at 2.0 T. *Magn. Reson. Imaging* **1992**, *10* (6), 919–928.

(184) Fawwaz, R. A.; Winchell, H. S.; Frye, F.; Hephill, W.; Lawrence, J. H. Localization of 58Co and 65Zn-Hematoporphyrin Complexes in Canine Lymph Nodes. *J. Nucl. Med.* **1969**, *10* (9), 581–585.

(185) Fawwaz, R. A.; Hemphill, W.; Winchell, H. S. Potential Use of 109Pd-Porphyrin Complexes for Selective Lymphatic Ablation. *J. Nucl. Med.* **1972**, *12* (5), 231–236.

(186) Takehara, Y.; Sakahara, H.; Masunaga, H.; Isogai, S.; Kodaira, N.; Takeda, H.; Saga, T.; Nakajima, S.; Sakata, I. Tumour Enhancement with Newly Developed Mn-Metalloporphyrin (HOP-9P) in Magnetic Resonance Imaging of Mice. *Br. J. Cancer*

316

2001, *84* (12), 1681–1685.

(187) Fujimori, H.; Matsumura, A.; Yamamoto, T.; Shibata, Y.; Yoshizawa, T.; Nakagawa, K.; Yoshii, Y.; Nose, T.; Sakata, I.; Nakajima, S. Tumor Specific Contrast Enhancement Study of Mn-Metalloporphyrin (ATN-10)--Comparison of Rat Brain Tumor Model, Cytotoxic and Vasogenic Edema Models. *Acta Neurochir* **1997**, *70*, 167–169.

(188) UP, S.; JA, N.; DH, R.; A, M.; F, S.; T, F.; W, E.; G, S.-G. Pharmaceutical Properties, Biodistribution, and Imaging Characteristics of Manganese-Mesoporphyrin: A Potential Hepatobiliary Contrast Agent for Magnetic Resonance Imaging. *Invest. Radiol.* **1993**, 925–932.

(189) Takehara, Y.; Sakahara, H.; Masunaga, H.; Isogai, S.; Kodaira, N.; Sugiyama, M.; Takeda, H.; Saga, T.; Nakajima, S.; Sakata, I. Assessment of a Potential Tumor-Seeking Manganese Metalloporphyrin Contrast Agent in a Mouse Model. *Magn. Reson. Med.* **2002**, *47* (3), 549–553.

(190) Li, C.; Kräutler, B. Transition Metal Complexes of Phyllobilins - a New Realm of Bioinorganic Chemistry. *Dalt. Trans.* **2015**, *44* (22), 10116–10127.

(191) Dimitrijević, M. S.; Bogdanović Pristov, J.; Žižić, M.; Stanković, D. M.; Bajuk-Bogdanović, D.; Stanić, M.; Spasić, S.; Hagen, W.; Spasojević, I. Biliverdin-Copper Complex at Physiological PH. *Dalt. Trans.* **2019**, *48* (18), 6061–6070.

(192) Goncharova, I.; Urbanová, M. Vibrational and Electronic Circular Dichroism Study of Bile Pigments: Complexes of Bilirubin and Biliverdin with Metals. *Anal. Biochem.* **2009**, *392* (1), 28–36.

(193) Zhou, Y.; Liang, X.; Dai, Z. Porphyrin-Loaded Nanoparticles for Cancer Theranostics. *Nanoscale* **2016**, *8* (25), 12394–12405.

(194) Wang, M. Emerging Multifunctional NIR Photothermal Therapy Systems Based on Polypyrrole Nanoparticles. *Polymers (Basel).* **2016**, *8* (10).

(195) Cai, Y.; Si, W.; Huang, W.; Chen, P.; Shao, J.; Dong, X. Organic Dye Based Nanoparticles for Cancer Phototheranostics. *Small* **2018**, *14* (25), 1–17.

(196) Menon, R. B.; Lakshmi, V. S.; Aiswarya, M. U.; Keerthana, R.; Nair, S. C. Porphysomes-a Paradigm Shift in Targeted Drug Delivery. *Int. J. Appl. Pharm.* **2018**, *10* (2), 1–6.

(197) Huynh, E.; Zheng, G. Porphysome Nanotechnology: A Paradigm Shift in Lipid-Based Supramolecular Structures. *Nano Today* **2014**, *9* (2), 212–222.

(198) Huynh, E.; Zheng, G. Organic Biophotonic Nanoparticles: Porphysomes and Beyond. *IEEE J. Sel. Top. Quantum Electron.* **2014**, *20* (3), 27–34.

(199) Lee, Y.; Kim, H.; Kang, S.; Lee, J.; Park, J.; Jon, S. Bilirubin Nanoparticles as a Nanomedicine for Anti-Inflammation Therapy. *Angew. Chemie - Int. Ed.* **2016**, *55* (26), 7460–7463.

(200) Lee, Y.; Lee, S.; Lee, D. Y.; Yu, B.; Miao, W.; Jon, S. Multistimuli-Responsive Bilirubin Nanoparticles for Anticancer Therapy. *Angew. Chemie - Int. Ed.* **2016**, *55* (36), 10676–10680.

(201) Kim, J. Y.; Lee, D. Y.; Kang, S.; Miao, W.; Kim, H.; Lee, Y.; Jon, S. Bilirubin Nanoparticle Preconditioning Protects against Hepatic Ischemia-Reperfusion Injury. *Biomaterials* **2017**, *133*, 1–10.

(202) Kim, M. J.; Lee, Y.; Jon, S.; Lee, D. Y. PEGylated Bilirubin Nanoparticle as an Anti-Oxidative and Anti-Inflammatory Demulcent in Pancreatic Islet Xenotransplantation. *Biomaterials* **2017**, *133*, 242–252.

(203) Kim, D. E.; Lee, Y.; Kim, M. G.; Lee, S.; Jon, S.; Lee, S. H. Bilirubin Nanoparticles

Ameliorate Allergic Lung Inflammation in a Mouse Model of Asthma. *Biomaterials* **2017**, *140*, 37–44.

(204) Lee, D. Y.; Kim, J. Y.; Lee, Y.; Lee, S.; Miao, W.; Kim, H. S.; Min, J. J.; Jon, S. Black Pigment Gallstone Inspired Platinum-Chelated Bilirubin Nanoparticles for Combined Photoacoustic Imaging and Photothermal Therapy of Cancers. *Angew. Chemie - Int. Ed.* **2017**, *56* (44), 13684–13688.

(205) Xing, R.; Zou, Q.; Yuan, C.; Zhao, L.; Chang, R.; Yan, X. Self-Assembling Endogenous Biliverdin as a Versatile Near-Infrared Photothermal Nanoagent for Cancer Theranostics. *Adv. Mater.* **2019**, *31* (16), 1–8.

(206) Yang, J.; Xiong, L.; Li, M.; Xiao, J.; Geng, X.; Wang, B.; Sun, Q. Preparation and Characterization of Tadpole- and Sphere-Shaped Hemin Nanoparticles for Enhanced Solubility. *Nanoscale Res. Lett.* **2019**, *14*.

(207) Liu, Q.; Wang, H.; Shi, X.; Wang, Z. G.; Ding, B. Self-Assembled DNA/Peptide-Based Nanoparticle Exhibiting Synergistic Enzymatic Activity. *ACS Nano* **2017**, *11* (7), 7251–7258.

(208) Hayashi, K.; Nakamura, M.; Miki, H.; Ozaki, S.; Abe, M.; Matsumoto, T.; Ishimura, K. Near-Infrared Fluorescent Silica/Porphyrin Hybrid Nanorings for in Vivo Cancer Imaging. *Adv. Funct. Mater.* **2012**, *22* (17), 3539–3546.

(209) Hayashi, K.; Nakamura, M.; Miki, H.; Ozaki, S.; Abe, M.; Matsumoto, T.; Kori, T.; Ishimura, K. Photostable Iodinated Silica/Porphyrin Hybrid Nanoparticles with Heavy-Atom Effect for Wide-Field Photodynamic/Photothermal Therapy Using Single Light Source. *Adv. Funct. Mater.* **2014**, *24* (4), 503–513.

(210) Hayashi, K.; Wataru, S.; Yogo, T. Iodinated Silica/Porphyrin Hybrid Nanoparticles for X-

Ray Computed Tomography/Fluorescence Dual-Modal Imaging of Tumors. *J. Asian Ceram. Soc.* **2014**, *2* (4), 429–434.

(211) Ohulchanskyy, T. Y.; Roy, I.; Goswami, L. N.; Chen, Y.; Bergey, E. J.; Pandey, R. K.; Oseroff, A. R.; Prasad, P. N. Organically Modified Silica Nanoparticles with Covalently Incorporated Photosensitizer for Photodynamic Therapy of Cancer. *Nano Lett.* **2007**, *7* (9), 2835–2842.

(212) Qiu, H.; Xie, J.; Che, S. Formation of Chiral Mesostructured Porphyrin-Silica Hybrids. *Chem. Commun.* **2011**, *47* (9), 2607–2609.

(213) Hayashi, K.; Nakamura, M.; Ishimura, K. Silica-Porphyrin Hybrid Nanotubes for in Vivo Cell Tracking by near-Infrared Fluorescence Imaging. *Chem. Commun.* **2012**, *48* (32), 3830–3832.

(214) Lovell, J. F.; Jin, C. S.; Huynh, E.; Jin, H.; Kim, C.; Rubinstein, J. L.; Chan, W. C. W.; Cao, W.; Wang, L. V.; Zheng, G. Porphysome Nanovesicles Generated by Porphyrin Bilayers for Use as Multimodal Biophotonic Contrast Agents. *Nat. Mater.* **2011**, *10* (4), 324–332.

(215) Liu, T. W.; MacDonald, T. D.; Shi, J.; Wilson, B. C.; Zheng, G. Intrinsically Copper-64-Labeled Organic Nanoparticles as Radiotracers. *Angew. Chemie - Int. Ed.* **2012**, *51* (52), 13128–13131.

(216) Liu, T. W.; MacDonald, T. D.; Jin, C. S.; Gold, J. M.; Bristow, R. G.; Wilson, B. C.; Zheng, G. Inherently Multimodal Nanoparticle-Driven Tracking and Real-Time Delineation of Orthotopic Prostate Tumors and Micrometastases. *ACS Nano* **2013**, *7* (5), 4221–4232.

(217) Jin, C. S.; Lovell, J. F.; Chen, J.; Zheng, G. Ablation of Hypoxic Tumors with Dose-

Equivalent Photothermal, but Not Photodynamic, Therapy Using a Nanostructured Porphyrin Assembly. *ACS Nano* **2013**, *7* (3), 2541–2550.

(218) MacLaughlin, C. M.; Ding, L.; Jin, C.; Cao, P.; Siddiqui, I.; Hwang, D. M.; Chen, J.; Wilson, B. C.; Zheng, G.; Hedley, D. W. Porphyrin Lipid Nanoparticles for Enhanced Photothermal Therapy in a Patient-Derived Orthotopic Pancreas Xenograft Cancer Model. *Mol. Surg. Mol. Devices, Appl. II* **2016**, *9696* (8), 96960F.

(219) Macdonald, T. D.; Liu, T. W.; Zheng, G. An MRI-Sensitive, Non-Photobleachable Porphysome Photothermal Agent. *Angew. Chemie - Int. Ed.* **2014**, *53* (27), 6956–6959.

(220) Ng, K. K.; Takada, M.; Jin, C. C. S.; Zheng, G. Self-Sensing Porphysomes for Fluorescence-Guided Photothermal Therapy. *Bioconjug. Chem.* **2015**, *26* (2), 345–351.

(221) Muhanna, N.; Macdonald, T. D.; Chan, H.; Jin, C. S.; Burgess, L.; Cui, L.; Chen, J.; Irish, J. C.; Zheng, G. Multimodal Nanoparticle for Primary Tumor Delineation and Lymphatic Metastasis Mapping in a Head-and-Neck Cancer Rabbit Model. *Adv. Healthc. Mater.* **2015**, *4* (14), 2164–2169.

(222) Jin, C. S.; Overchuk, M.; Cui, L.; Wilson, B. C.; Bristow, R. G.; Chen, J.; Zheng, G. Nanoparticle-Enabled Selective Destruction of Prostate Tumor Using MRI-Guided Focal Photothermal Therapy. *Prostate* **2016**, *76* (13), 1169–1181.

(223) Ng, K. K.; Takada, M.; Harmatys, K.; Chen, J.; Zheng, G. Chlorosome-Inspired Synthesis of Templated Metallochlorin-Lipid Nanoassemblies for Biomedical Applications. *ACS Nano* **2016**, *10* (4), 4092–4101.

(224) Philp, L.; Chan, H.; Rouzbahman, M.; Overchuk, M.; Chen, J.; Zheng, G.; Bernardini, M. Q. Use of Porphysomes to Detect Primary Tumour, Lymph Node Metastases, Intra-Abdominal Metastases and as a Tool for Image-Guided Lymphadenectomy: Proof of

Concept in Endometrial Cancer. *Theranostics* **2019**, *9* (9), 2727–2738.

(225) Liu, D.; Chen, B.; Mo, Y.; Wang, Z.; Qi, T.; Zhang, Q.; Wang, Y. Redox-Activated Porphyrin-Based Liposome Remote-Loaded with Indoleamine 2,3-Dioxygenase (IDO) Inhibitor for Synergistic Photoimmunotherapy through Induction of Immunogenic Cell Death and Blockage of IDO Pathway. *Nano Lett.* **2019**, *19* (10), 6964–6976.

(226) Jin, R.; Aida, T.; Inoue, S. 'Caged' Porphyrin: The First Dendritic Molecule Having a Core Photochemical Functionality. *J. CHEM. SOC., CHEM. COMMUN* **1993**, *2* (1260), 1260–1262.

(227) Cheng, L.; Wang, C.; Feng, L.; Yang, K.; Liu, Z. Functional Nanomaterials for Phototherapies of Cancer. *Chem. Rev.* **2014**, *114* (21), 10869–10939.

(228) Moquin, A.; Hanna, R.; Liang, T.; Erguven, H.; Gran, E. R.; Arndtsen, B. A.; Maysinger, D.; Kakkar, A. PEG-Conjugated Pyrrole-Based Polymers: One-Pot Multicomponent Synthesis and Self-Assembly into Soft Nanoparticles for Drug Delivery. *Chem. Commun.* **2019**, *55* (66), 9829–9832.

(229) Alizadeh, N.; Akbarinejad, A. Soluble Fluorescent Polymeric Nanoparticles Based on Pyrrole Derivatives: Synthesis, Characterization and Their Structure Dependent Sensing Properties. *J. Mater. Chem. C* **2015**, *3* (38), 9910–9920.

(230) Pan, D.; Caruthers, S. D.; Hu, G.; Senpan, A.; Scott, M. J.; Gaffney, P. J.; Wickline, S. A.; Lanza, G. M. Ligand-Directed Nanobialys as Theranostic Agent for Drug Delivery and Manganese-Based Magnetic Resonance Imaging of Vascular Targets. *J. Am. Chem. Soc.* **2008**, *130* (29).

(231) Wu, F.; Chen, L.; Yue, L.; Wang, K.; Cheng, K.; Chen, J.; Luo, X.; Zhang, T. Small-Molecule Porphyrin-Based Organic Nanoparticles with Remarkable Photothermal

Conversion Efficiency for in Vivo Photoacoustic Imaging and Photothermal Therapy. *ACS Appl. Mater. Interfaces* **2019**, *11*, 21408–21416.

(232) Yang, L.; Li, H.; Liu, D.; Su, H.; Wang, K.; Liu, G.; Luo, X.; Wu, F. Organic Small Molecular Nanoparticles Based on Self-Assembly of Amphiphilic Fl Uoroporphyrins for Photodynamic and Photothermal Synergistic Cancer Therapy. *Colloids Surfaces B Biointerfaces* **2019**, *182* (April), 110345.

(233) Wang, D.; Niu, L.; Qiao, Z.; Cheng, D.; Wang, J.; Zhong, Y.; Bai, F.; Wang, H.; Fan, H. Synthesis of Self-Assembled Porphyrin Nanoparticle Photosensitizers. *ACS Nano* **2018**, 6–13.

(234) Wang, D.; Zhang, Z.; Lin, L.; Liu, F.; Wang, Y.; Guo, Z.; Li, Y.; Tian, H.; Chen, X. Porphyrin-Based Covalent Organic Framework Nanoparticles for Photoacoustic Imaging-Guided Photodynamic and Photothermal Combination Cancer Therapy. *Biomaterials* **2019**, *223* (July), 119459.

(235) Pan, D.; Liang, P.; Zhong, X.; Wang, D.; Cao, H.; Wang, W.; He, W.; Yang, Z.; Dong, X. Self-Assembled Porphyrin-Based Nanoparticles with Enhanced Near-Infrared Absorbance for Fluorescence Imaging and Cancer Photodynamic Therapy. *ACS Appl. Bio Mater.* **2019**, *2* (3), 999–1005.

(236) Tam, N. C. M.; McVeigh, P. Z.; MacDonald, T. D.; Farhadi, A.; Wilson, B. C.; Zheng, G. Porphyrin-Lipid Stabilized Gold Nanoparticles for Surface Enhanced Raman Scattering Based Imaging. *Bioconjug. Chem.* **2012**, *23* (9), 1726–1730.

(237) Ng, K. K.; Lovell, J. F.; Vedadi, A.; Hajian, T.; Zheng, G. Self-Assembled Porphyrin Nanodiscs with Structure-Dependent Activation for Phototherapy and Photodiagnostic Applications. *ACS Nano* **2013**, *7* (4), 3484–3490.

(238) Trapani, M.; Castriciano, M. A.; Romeo, A.; Luca, G. De; Machado, N.; Howes, B. D.; Smulevich, G.; Mons, L. Nanohybrid Assemblies of Porphyrin and Au 10 Cluster Nanoparticles. **2019**, 1–13.

(239) Summerfield, A.; Baldoni, M.; Kondratuk, D. V; Anderson, H. L.; Whitelam, S.; Garrahan, J. P.; Besley, E.; Beton, P. H. Ordering, Flexibility and Frustration in Arrays of Porphyrin Nanorings. *Nat. Commun.* No. 2019, 1–7.

(240) Ghosal, K.; Ghosh, A. Carbon Dots: The next Generation Platform for Biomedical Applications. *Mater. Sci. Eng. C* **2019**, *96* (July 2018), 887–903.

(241) Wang, J.; Qiu, J. A Review of Carbon Dots in Biological Applications. *J. Mater. Sci.* **2016**, *51* (10), 4728–4738.

(242) Liu, M. L.; Chen, B. Bin; Li, C. M.; Huang, C. Z. Carbon Dots: Synthesis, Formation Mechanism, Fluorescence Origin and Sensing Applications. *Green Chem.* **2019**, *21* (3), 449–471.

(243) Fathi, P.; Khamo, J. S.; Huang, X.; Srivastava, I.; Esch, M. B.; Zhang, K.; Pan, D. Bulk-State and Single-Particle Imaging Are Central to Understanding Carbon Dot Photo-Physics and Elucidating the Effects of Precursor Composition and Reaction Temperature. *Carbon N. Y.* **2019**, *145*, 572–585.

(244) Srivastava, I.; Khamo, J. S.; Pandit, S.; Fathi, P.; Huang, X.; Cao, A.; Haasch, R. T.; Nie, S.; Zhang, K.; Pan, D. Influence of Electron Acceptor and Electron Donor on the Photophysical Properties of Carbon Dots: A Comparative Investigation at the Bulk-State and Single-Particle Level. *Adv. Funct. Mater.* **2019**, *1902466*, 1902466.

(245) Ge, J.; Jia, Q.; Liu, W.; Guo, L.; Liu, Q.; Lan, M.; Zhang, H.; Meng, X.; Wang, P. Red-Emissive Carbon Dots for Fluorescent, Photoacoustic, and Thermal Theranostics in Living

Mice. *Adv. Mater.* **2015**, *27* (28), 4169–4177.

(246) Lee, C.; Kwon, W.; Beack, S.; Lee, D.; Park, Y.; Kim, H.; Hahn, S. K.; Rhee, S. W.; Kim, C. Biodegradable Nitrogen-Doped Carbon Nanodots for Non-Invasive Photoacoustic Imaging and Photothermal Therapy. *Theranostics* **2016**, *6* (12), 2196–2208.

(247) Lu, S.; Sui, L.; Liu, J.; Zhu, S.; Chen, A.; Jin, M.; Yang, B. Near-Infrared Photoluminescent Polymer–Carbon Nanodots with Two-Photon Fluorescence. *Adv. Mater.* **2017**, *29* (15), 1–6.

(248) Parvin, N.; Mandal, T. K. Dually Emissive P,N-Co-Doped Carbon Dots for Fluorescent and Photoacoustic Tissue Imaging in Living Mice. *Microchim. Acta* **2017**, *184* (4), 1117–1125.

(249) Bourlinos, A. B.; Bakandritsos, A.; Kouloumpis, A.; Gournis, D.; Krysmann, M.; Giannelis, E. P.; Polakova, K.; Safarova, K.; Hola, K.; Zboril, R. Gd(III)-Doped Carbon Dots as a Dual Fluorescent-MRI Probe. *J. Mater. Chem.* **2012**, *22* (44), 23327–23330.

(250) Du, F.; Zhang, M.; Ju, H.; Zhang, L.; Sun, M.; Zhou, Z.; Dai, Z.; Zhang, L.; Gong, A.; Wu, C. Engineering Iodine-Doped Carbon Dots as Dual-Modal Probes for Fluorescence and X-Ray CT Imaging. *Int. J. Nanomedicine* **2015**, 6943.

(251) Ren, X.; Liu, L.; Li, Y.; Dai, Q.; Zhang, M.; Jing, X. Facile Preparation of Gadolinium(Iii) Chelates Functionalized Carbon Quantum Dot-Based Contrast Agent for Magnetic Resonance/Fluorescence Multimodal Imaging. *J. Mater. Chem. B* **2014**, *2* (34), 5541–5549.

(252) Su, H.; Liao, Y.; Wu, F.; Sun, X.; Liu, H.; Wang, K.; Zhu, X. Cetuximab-Conjugated Iodine Doped Carbon Dots as a Dual Fluorescent/CT Probe for Targeted Imaging of Lung Cancer Cells. *Colloids Surfaces B Biointerfaces* **2018**, *170* (March), 194–200.

(253) Tang, J.; Kong, B.; Wu, H.; Xu, M.; Wang, Y.; Wang, Y.; Zhao, D.; Zheng, G. Carbon Nanodots Featuring Efficient FRET for Real-Time Monitoring of Drug Delivery and Two-Photon Imaging. *Adv. Mater.* **2013**, *25* (45), 6569–6574.

(254) Feng, T.; Ai, X.; An, G.; Yang, P.; Zhao, Y. Charge-Convertible Carbon Dots for Imaging-Guided Drug Delivery with Enhanced in Vivo Cancer Therapeutic Efficiency. *ACS Nano* **2016**, *10* (4), 4410–4420.

(255) Gong, X.; Zhang, Q.; Gao, Y.; Shuang, S.; Choi, M. M. F.; Dong, C. Phosphorus and Nitrogen Dual-Doped Hollow Carbon Dot as a Nanocarrier for Doxorubicin Delivery and Biological Imaging. *ACS Appl. Mater. Interfaces* **2016**, *8* (18), 11288–11297.

(256) Liu, C.; Zhang, P.; Zhai, X.; Tian, F.; Li, W.; Yang, J.; Liu, Y.; Wang, H.; Wang, W.; Liu, W. Nano-Carrier for Gene Delivery and Bioimaging Based on Carbon Dots with PEI-Passivation Enhanced Fluorescence. *Biomaterials* **2012**, *33* (13), 3604–3613.

(257) Pierrat, P.; Wang, R.; Kereselidze, D.; Lux, M.; Didier, P.; Kichler, A.; Pons, F.; Lebeau, L. Efficient Invitro and Invivo Pulmonary Delivery of Nucleic Acid by Carbon Dot-Based Nanocarriers. *Biomaterials* **2015**, *51*, 290–302.

(258) Wang, L.; Wang, X.; Bhirde, A.; Cao, J.; Zeng, Y.; Huang, X.; Sun, Y.; Liu, G.; Chen, X. Carbon-Dot-Based Two-Photon Visible Nanocarriers for Safe and Highly Efficient Delivery of SiRNA and DNA. *Adv. Healthc. Mater.* **2014**, *3* (8), 1203–1209.

(259) Lan, M.; Zhao, S.; Zhang, Z.; Yan, L.; Guo, L.; Niu, G.; Zhang, J.; Zhao, J.; Zhang, H.; Wang, P.; et al. Two-Photon-Excited near-Infrared Emissive Carbon Dots as Multifunctional Agents for Fluorescence Imaging and Photothermal Therapy. *Nano Res.* **2017**, *10* (9), 3113–3123.

(260) Zheng, M.; Li, Y.; Liu, S.; Wang, W.; Xie, Z.; Jing, X. One-Pot to Synthesize

Multifunctional Carbon Dots for Near Infrared Fluorescence Imaging and Photothermal Cancer Therapy. *ACS Appl. Mater. Interfaces* **2016**, *8* (36), 23533–23541.

(261) Ge, J.; Jia, Q.; Liu, W.; Lan, M.; Zhou, B.; Guo, L.; Zhou, H.; Zhang, H.; Wang, Y.; Gu, Y.; et al. Carbon Dots with Intrinsic Theranostic Properties for Bioimaging, Red-Light-Triggered Photodynamic/Photothermal Simultaneous Therapy In Vitro and In Vivo. *Adv. Healthc. Mater.* **2016**, *5* (6), 665–675.

(262) Wen, Y.; Jia, Q.; Nan, F.; Zheng, X.; Liu, W.; Wu, J.; Ren, H.; Ge, J.; Wang, P. Pheophytin Derived Near-Infrared-Light Responsive Carbon Dot Assembly as a New Phototheranotic Agent for Bioimaging and Photodynamic Therapy. *Chem. - An Asian J.* **2019**, *14* (12), 2162–2168.

(263) Wu, F.; Su, H.; Wang, K.; Wong, W. K.; Zhu, X. Facile Synthesis of N-Rich Carbon Quantum Dots from Porphyrins as Efficient Probes for Bioimaging and Biosensing in Living Cells. *Int. J. Nanomedicine* **2017**, *12*, 7375–7391.

(264) Li, Y.; Zheng, X.; Zhang, X.; Liu, S.; Pei, Q.; Zheng, M.; Xie, Z. Porphyrin-Based Carbon Dots for Photodynamic Therapy of Hepatoma. *Adv. Healthc. Mater.* **2017**, *6* (1), 1–6.

(265) Wu, F.; Su, H.; Cai, Y.; Wong, W. K.; Jiang, W.; Zhu, X. Porphyrin-Implanted Carbon Nanodots for Photoacoustic Imaging and in Vivo Breast Cancer Ablation. *ACS Appl. Bio Mater.* **2018**, *1* (1), 110–117.

(266) Zhao, J.; Huang, M.; Zhang, L.; Zou, M.; Chen, D.; Huang, Y.; Zhao, S. Unique Approach to Develop Carbon Dot-Based Nanohybrid Near-Infrared Ratiometric Fluorescent Sensor for the Detection of Mercury Ions. *Anal. Chem.* **2017**, *89* (15), 8044–8049.

(267) Li, X. G.; Li, A.; Huang, M. R.; Liao, Y.; Lu, Y. G. Efficient and Scalable Synthesis of Pure Polypyrrole Nanoparticles Applicable for Advanced Nanocomposites and Carbon

Nanoparticles. *J. Phys. Chem. C* **2010**, *114* (45), 19244–19255.

(268) Wang, X.; Qu, K.; Xu, B.; Ren, J.; Qu, X. Multicolor Luminescent Carbon Nanoparticles : Synthesis , Supramolecular Assembly with Porphyrin , Intrinsic Peroxidase-Like Catalytic Activity and Applications. *Nano Res.* **2011**, *4* (9), 908–920.

(269) Arcudi, F.; Dordevic, L.; Prato, M. Synthesis , Separation , and Characterization of Small and Highly Fluorescent Nitrogen-Doped Carbon NanoDots Angewandte. *Angew. Chemie* **2016**, 2107–2112.

(270) Huang, P.; Lin, J.; Wang, X.; Wang, Z.; Zhang, C.; He, M.; Wang, K.; Chen, F.; Li, Z.; Shen, G.; et al. Light-Triggered Theranostics Based on Photosensitizer- Conjugated Carbon Dots for Simultaneous Enhanced- Fluorescence Imaging and Photodynamic Therapy. *Adv. Mater.* **2012**, 5104–5110.

(271) Shan, L.; Fan, W.; Wang, W.; Tang, W.; Yang, Z.; Wang, Z.; Liu, Y.; Shen, Z.; Dai, Y.; Cheng, S.; et al. Organosilica-Based Hollow Mesoporous Bilirubin Nanoparticles for Antioxidation- Activated Self-Protection and Tumor-Speci Fi c Deoxygenation-Driven Synergistic Therapy. *ACS Nano* **2019**.

(272) Yang, X.; Lu, Y. Preparation of Polypyrrole-Coated Silver Nanoparticles by One-Step UV-Induced Polymerization. *Mater. Lett.* **2005**, *59* (19–20), 2484–2487.

(273) Takahashi, Y.; Furukawa, Y.; Ishida, T.; Yamada, S. Site-Selective Nanoscale-Polymerization of Pyrrole on Gold Nanoparticles via Plasmon Induced Charge Separation. *Nanoscale* **2016**, *8* (16), 8520–8524.

(274) Zotti, G.; Vercelli, B.; Berlin, A. Gold Nanoparticles Linked by Pyrrole- And Thiophene-Based Thiols. Electrochemical, Optical, and Conductive Properties. *Chem. Mater.* **2008**, *20* (2), 397–412.

(275) Ujiie, H.; Ding, L.; Fan, R.; Kato, T.; Lee, D.; Fujino, K.; Kinoshita, T.; Lee, C. Y.; Waddell, T. K.; Keshavjee, S.; et al. Porphyrin–High-Density Lipoprotein: A Novel Photosensitizing Nanoparticle for Lung Cancer Therapy. *Ann. Thorac. Surg.* **2019**, *107* (2), 369–377.

(276) Kamkaew, A.; Lim, S. H.; Lee, H. B.; Kiew, L. V.; Chung, L. Y.; Burgess, K. BODIPY Dyes in Photodynamic Therapy. *Chem. Soc. Rev.* **2013**, *42* (1), 77–88.

(277) Wu, F.; Chen, L.; Yue, L.; Wang, K.; Cheng, K.; Chen, J.; Luo, X.; Zhang, T. Small-Molecule Porphyrin-Based Organic Nanoparticles with Remarkable Photothermal Conversion Efficiency for in Vivo Photoacoustic Imaging and Photothermal Therapy. *ACS Appl. Mater. Interfaces* **2019**, *11* (24), 21408–21416.

(278) Cui, L.; Lin, Q.; Jin, C. S.; Jiang, W.; Huang, H.; Ding, L.; Muhanna, N.; Irish, J. C.; Wang, F.; Chen, J.; et al. A PEGylation-Free Biomimetic Porphyrin Nanoplatform for Personalized Cancer Theranostics. *ACS Nano* **2015**, *9* (4), 4484–4495.

(279) Freitas, R. A. Nanomedicine, Volume I: Basic Capabilities. **1999**.

(280) Roozendaal, R.; Mempel, T. R.; Pitcher, L. a.; Gonzalez, S. F.; Verschoor, A.; Mebius, R. E.; von Andrian, U. H.; Carroll, M. C. Conduits Mediate Transport of Low-Molecular-Weight Antigen to Lymph Node Follicles. *Immunity* **2009**, *30* (2), 264–276.

(281) Rantakari, P.; Auvinen, K.; Jäppinen, N.; Kapraali, M.; Valtonen, J.; Karikoski, M.; Gerke, H.; Iftakhar-E-Khuda, I.; Keuschnigg, J.; Umemoto, E.; et al. The Endothelial Protein PLVAP in Lymphatics Controls the Entry of Lymphocytes and Antigens into Lymph Nodes. *Nat. Immunol.* **2015**, *16* (4), 386–396.

(282) Hons, M.; Sixt, M. The Lymph Node Filter Revealed. *Nat. Publ. Gr.* **2015**, *16* (88), 397–405.

(283) Overview of the lymphoid immune system http://www.dartmouth.edu/~nlevy/pln3.html.

(284) Von Andrian, U. H.; Mempel, T. R. Homing and Cellular Traffic in Lymph Nodes. *Nat. Rev. Immunol.* **2003**, *3* (11), 867–878.

(285) Mondore, I.; Baratin, M.; Lagueyrie, M.; Kastenmuller, W.; Jiang, J. X.; Bajenoff, M. Lymphatic Endothelial Cells Are Essential Components of the Subcapsular Sinus Macrophage Niche. *Immunity* **2019**, *50*, 1–14.

(286) Sixt, M.; Kanazawa, N.; Selg, M.; Samson, T.; Roos, G.; Reinhardt, D. P.; Pabst, R.; Lutz, M. B.; Sorokin, L. The Conduit System Transports Soluble Antigens from the Afferent Lymph to Resident Dendritic Cells in the T Cell Area of the Lymph Node. *Immunity* **2005**, *22* (1), 19–29.

(287) Roozendaal, R.; Mebius, R. E.; Kraal, G. The Conduit System of the Lymph Node. *Int. Immunol.* **2008**, *20* (12), 1483–1487.

(288) Carrasco, Y. R.; Batista, F. D. B Cells Acquire Particulate Antigen in a Macrophage-Rich Area at the Boundary between the Follicle and the Subcapsular Sinus of the Lymph Node. *Immunity* **2007**, *27* (1), 160–171.

(289) Phan, T. G.; Grigorova, I.; Okada, T.; Cyster, J. G. Subcapsular Encounter and Complement-Dependent Transport of Immune Complexes by Lymph Node B Cells. *Nat. Immunol.* **2007**, *8* (9), 992–1000.

(290) Coombes, J. L.; Han, S. J.; van Rooijen, N.; Raulet, D. H.; Robey, E. A. Infection-Induced Regulation of Natural Killer Cells by Macrophages and Collagen at the Lymph Node Subcapsular Sinus. *Cell Rep.* **2012**, *2* (1), 124–135.

(291) Junt, T.; Moseman, E. A.; Iannacone, M.; Massberg, S.; Lang, P. A.; Boes, M.; Fink, K.; Henrickson, S. E.; Shayakhmetov, D. M.; Di Paolo, N. C.; et al. Subcapsular Sinus

Macrophages in Lymph Nodes Clear Lymph-Borne Viruses and Present Them to Antiviral B Cells. *Nature* **2007**, *450* (7166), 110–114.

(292) Triacca, V.; Güç, E.; Kilarski, W. W.; Pisano, M.; Swartz, M. A. Transcellular Pathways in Lymphatic Endothelial Cells Regulate Changes in Solute Transport by Fluid Stress. *Circ. Res.* **2017**, *120* (9), 1440–1452.

(293) Breslin, J. W. Mechanical Forces and Lymphatic Transport. *Microvasc. Res.* **2014**, *96*, 46–54.

(294) SCHMID-SCHÖNBEIN, G. W. The Second Valve System in Lymphatics. *Lymphat. Res. Biol.* **2003**, *1* (1).

(295) Von Der Weid, P. Y.; Zawieja, D. C. Lymphatic Smooth Muscle: The Motor Unit of Lymph Drainage. *Int. J. Biochem. Cell Biol.* **2004**, *36* (7), 1147–1153.

(296) Weber, E.; Sozio, F.; Gabbrielli, E.; Rossi, A. Lymphatic Vessels in Health and Disease. *Transl. Vasc. Med. Pathog. Diagnosis, Treat.* **2013**, *5* (February), 137–150.

(297) Harisinghani, M. G.; Barentsz, J.; Hahn, P. F.; Deserno, W. M.; Tabatabaei, S.; Kaa, C. H. van de; Rosette, J. de la; Weissleder, R. Noninvasive Detection of Clinically Occult Lymph-Node Metastases in Prostate Cancer. *New Engl J. Med* **2003**, *348* (25), 2491–2499.

(298) Maruyama, K.; Gunven, P.; Okabayashi, K.; Sasako, M.; Kinoshita, T. Lymph Node Metastases of Gastric Cancer. General Pattern in 1931 Patients. *Ann. Surg.* **1989**, *210* (5), 596–602.

(299) Gotoda, T.; Yanagisawa, A.; Sasako, M.; Ono, H.; Nakanishi, Y.; Shimoda, T.; Kato, Y. Incidence of Lymph Node Metastasis from Early Gastric Cancer: Estimation with a Large Number of Cases at Two Large Centers. *Gastric Cancer* **2000**, *3* (4), 219–225.

(300) Kosaka, Y.; Minatani, N.; Tanaka, Y.; Shida, A.; Kikuchi, M.; Nishimiya, H.; Waraya, M.; Katoh, H.; Sato, T.; Sengoku, N.; et al. Lymph Node Metastasis and High Serum CEA Are Important Prognostic Factors in Hormone Receptor Positive and HER2 Negative Breast Cancer. *Mol. Clin. Oncol.* **2018**, 566–574.

(301) Chai, R.; Ma, H.; Xu, M.; Arefan, D.; Cui, X.; Liu, Y.; Zhang, L.; Wu, S.; Xu, K. Differentiating Axillary Lymph Node Metastasis in Invasive Breast Cancer Patients: A Comparison of Radiomic Signatures from Multiparametric Breast MR Sequences. *J. Magn. Reson. Imaging* **2019**, 1–8.

(302) de Lima Vazquez, V.; Sachetto, T.; Perpetuo, N. M.; Carvalho, A. L. Prognostic Factors for Lymph Node Metastasis from Advanced Squamous Cell Carcinoma of the Skin of the Trunk and Extremities. *World J. Surg. Oncol.* **2008**, *6*, 1–6.

(303) Aldrich, M. B.; Sevick-Muraca, E. M. Cytokines Are Systemic Effectors of Lymphatic Function in Acute Inflammation. *Cytokine* **2013**, *64* (1), 362–369.

(304) Brown, M.; Assen, F. P.; Leithner, A.; Abe, J.; Schachner, H.; Asfour, G.; Bago-Horvath, Z.; Stein, J. V.; Uhrin, P.; Sixt, M.; et al. Lymph Node Blood Vessels Provide Exit Routes for Metastatic Tumor Cell Dissemination in Mice. *Science (80-.).* **2018**, *359* (6382), 1408–1411.

(305) Kimura, H.; Sakai, Y.; Fujii, T. Organ/Body-on-a-Chip Based on Microfluidic Technology for Drug Discovery. *Drug Metab. Pharmacokinet.* **2018**, *33* (1), 43–48.

(306) Wang, Z.; Samanipour, R.; Koo, K. I.; Kim, K. Organ-on-a-Chip Platforms for Drug Delivery and Cell Characterization: A Review. *Sensors Mater.* **2015**, *27* (6), 487–506.

(307) Bhise, N. S.; Ribas, J.; Manoharan, V.; Zhang, Y. S.; Polini, A.; Massa, S.; Dokmeci, M. R.; Khademhosseini, A. Organ-on-a-Chip Platforms for Studying Drug Delivery Systems.

J. Control. Release **2014**, *190*, 82–93.

(308) Zheng, F.; Fu, F.; Cheng, Y.; Wang, C.; Zhao, Y.; Gu, Z. Organ-on-a-Chip Systems: Microengineering to Biomimic Living Systems. *Small* **2016**, *12* (17), 2253–2282.

(309) Greenlee, J. D.; King, M. R. Engineered Fluidic Systems to Understand Lymphatic Cancer Metastasis. *Biomicrofluidics* **2020**, *14* (1).

(310) Shanti, A.; Teo, J.; Stefanini, C. In Vitro Immune Organs-on-Chip for Drug Development: A Review. *Pharmaceutics* **2018**, *10* (4).

(311) Kim, S.; Shah, S. B.; Graney, P. L.; Singh, A. Multiscale Engineering of Immune Cells and Lymphoid Organs. *Nat. Rev. Mater.* **2019**, *4* (6), 355–378.

(312) Sun, W.; Luo, Z.; Lee, J.; Kim, H.-J.; Lee, K.; Tebon, P.; Feng, Y.; Dokmeci, M.; Sengupta, S.; Khademhosseini, A. Organ-on-a-Chip for Cancer and Immune Organs Modeling. *Adv Heal. Mater.* **2019**, *8* (4).

(313) Henderson, A. R.; Choi, H.; Lee, E. Blood and Lymphatic Vasculatures On-Chip Platforms and Their Applications for Organ-Specific in Vitro Modeling. *Micromachines* **2020**, *11* (2).

(314) Mitra, B.; Jindal, R.; Lee, S.; Dong, D. X.; Li, L.; Sharma, N.; Maguire, T.; Schloss, R.; Yarmush, M. L. Microdevice Integrating Innate and Adaptive Immune Responses Associated with Antigen Presentation by Dendritic Cells. *RSC Adv.* **2013**, *3* (36), 16002–16010.

(315) Gopalakrishnan, N.; Hannam, R.; Casoni, G. P.; Barriet, D.; Ribe, J. M.; Haug, M.; Halaas. Infection and Immunity on a Chip: A Compartmentalised Microfluidic Platform to Monitor Immune Cell Behaviour in Real Time. *Lab Chip* **2015**, *15* (6), 1481–1487.

(316) Sato, M.; Sasaki, N.; Ato, M.; Hirakawa, S.; Sato, K.; Sato, K. Microcirculation-on-a-

Chip: A Microfluidic Platform for Assaying Blood-and Lymphatic-Vessel Permeability. *PLoS One* **2015**, *10* (9), 1–19.

(317) Ayuso, J. M.; Gong, M. M.; Skala, M. C.; Harari, P. M.; Beebe, D. J. Human Tumor-Lymphatic Microfluidic Model Reveals Differential Conditioning of Lymphatic Vessels by Breast Cancer Cells. *Adv. Healthc. Mater.* **2020**, *9* (3), 1–8.

(318) Shim, S.; Belanger, M. C.; Harris, A. R.; Munson, J. M.; Pompano, R. R. Two-Way Communication between Ex Vivo Tissues on a Microfluidic Chip: Application to Tumor-Lymph Node Interaction. *Lab Chip* **2019**, *19* (6), 1013–1026.

(319) Goyal, G.; Bausk, B.; Prabhala, P.; Xie, L.; Curran, D.; Long, J.; Cohen, L.; Levy, O.; Prantil-Baun, R.; Walt, D. R.; et al. Lymph Node Follicle Formation and Vaccination Responses Reconstituted in Vitro in a Human Organ Chip. *bioRxiv* **2019**, 806505.

(320) Yang, Y.; Fathi, P.; Holland, G.; Pan, D.; Wang, N. S.; Esch, M. B. Pumpless Microfluidic Devices for Generating Healthy and Diseased Endothelia. *Lab Chip* **2019**, *19* (19), 3212–3219.

(321) Knox, H. J.; Chan, J. Acoustogenic Probes: A New Frontier in Photoacoustic Imaging. *Acc. Chem. Res.* **2018**, *51* (11), 2897–2905.

(322) Anselmo, A. C.; Mitragotri, S. A Review of Clinical Translation of Inorganic Nanoparticles. *AAPS J.* **2015**, *17* (5), 1041–1054.

(323) Ehlerding, E. B.; Chen, F.; Cai, W. Biodegradable and Renal Clearable Inorganic Nanoparticles. *Adv. Sci.* **2015**, *3* (2), 1–8.

(324) Phillips, E.; Penate-Medina, O.; Zanzonico, P. B.; Carvajal, R. D.; Mohan, P.; Ye, Y.; Humm, J.; Gönen, M.; Kalaigian, H.; Schöder, H.; et al. Clinical Translation of an Ultrasmall Inorganic Optical-PET Imaging Nanoparticle Probe. *Sci. Transl. Med.* **2014**, *6*

(260), 1–9.

(325) Lin, M. M.; Kim, D. K.; El Haj, A. J.; Dobson, J. Development of Superparamagnetic Iron Oxide Nanoparticles (SPIONS) for Translation to Clinical Applications. *IEEE Trans. Nanobioscience* **2008**, *7* (4), 298–305.

(326) Liu, G.; Gao, J.; Ai, H.; Chen, X. Applications and Potential Toxicity of Magnetic Iron Oxide Nanoparticles. *Small* **2013**, *9* (9–10), 1533–1545.

(327) Choi, H. S.; Frangioni, J. V. Nanoparticles for Biomedical Imaging: Fundamentals of Clinical Translation. *Mol. Imaging* **2010**, *9* (6), 291–310.

(328) Lee, D. Y.; Kim, J. Y.; Lee, Y.; Lee, S.; Miao, W.; Kim, H. S.; Min, J. J.; Jon, S. Black Pigment Gallstone-Inspired Platinum-Chelated Bilirubin Nanoparticles for Combined Photoacoustic Imaging and Photothermal Therapy of Cancers. *Angew. Chemie - Int. Ed.* **2017**, *56*, 13684–13688.

(329) Maines, M. D. New Insights into Biliverdin Reductase Functions: Linking Heme Metabolism to Cell Signaling. *Physiology* **2005**, *20* (6), 382–389.

(330) Keating, C. S.; McClure, B. a.; Rack, J. J.; Rubtsov, I. V. Sulfoxide Stretching Mode as a Structural Reporter via Dual-Frequency Two-Dimensional Infrared Spectroscopy. *J. Chem. Phys.* **2010**, *133* (144513), 1–14.

(331) Knox, H. J.; Kim, T. W.; Zhu, Z.; Chan, J. Photophysical Tuning of N-Oxide-Based Probes Enables Ratiometric Photoacoustic Imaging of Tumor Hypoxia. *ACS Chem. Biol.* **2018**, *13* (7), 1838–1843.

(332) Marshall, M. V; Rasmussen, J. C.; Tan, I.; Aldrich, M. B.; Kristen, E.; Wang, X.; Fife, C. E.; Maus, E. A.; Smith, L. A.; Eva, M. Near-Infrared Fluorescence Imaging in Humans with Indocyanine Green: A Review and Update. *Open Surg Oncol J.* **2012**, *2* (2), 12–25.

(333) Su, Z.; Ye, P.; Teng, Y.; Zhang, L.; Shu, X. Adverse Reaction in Patients with Drug Allergy History After Simultaneous Intravenous Fundus Fluorescein. *J. Ocul. Pharmacol. Ther.* **2012**, *28* (4), 410–413.

(334) Hartman, K.; Ma, T.-J.; Levi, J.; Gambhir, S. S.; Kothapalli, S. R.; Khuri-Yakub, B. T. Design, Synthesis, and Imaging of an Activatable Photoacoustic Probe. *J. Am. Chem. Soc.* **2010**, No. 14.

(335) Buschmann, V.; Weston, K. D.; Sauer, M. Spectroscopic Study and Evaluation of Red-Absorbing Fluorescent Dyes. *Bioconjug. Chem.* **2003**, *14* (1), 195–204.

(336) Boguta, A.; Wróbel, D. Fluorescein and Phenolphthalein - Correlation of Fluorescence and Photoelectric Properties. *J. Fluoresc.* **2001**, *11* (2), 129–137.

(337) Kim, J.; Park, S.; Choi, W.; Park, G. B.; Jeong, U.; Kim, C. Contrast-Enhanced Photoacoustic Imaging with an Optical Wavelength of 1064 Nm. *Photons Plus Ultrasound Imaging Sens. 2018* **2018**, *10494* (104944I), 1–5.

(338) Koo, J.; Jeon, M.; Oh, Y.; Kang, H. W.; Kim, J.; Kim, C.; Oh, J. In Vivo Non-Ionizing Photoacoustic Mapping of Sentinel Lymph Nodes and Bladders with ICG-Enhanced Carbon Nanotubes. *Phys. Med. Biol.* **2012**, *57* (23), 7853–7862.

(339) Kim, C.; Song, K. H.; Gao, F.; Wang, L. V. Sentinel Lymph Nodes and Lymphatic Vessels : Noninvasive Dual-Modality In Vivo Mapping by Using Indocyanine Green in Rats — Volumetric Spectroscopic Photoacoustic Imaging and Planar Fluorescence Imaging. *Radiology* **2010**, *255* (2), 442–450.

(340) Zhang, X.; Zhang, X.; Tao, L.; Chi, Z.; Xu, J.; Wei, Y. Aggregation Induced Emission-Based Fluorescent Nanoparticles: Fabrication Methodologies and Biomedical Applications. *J. Mater. Chem. B* **2014**, *2* (28), 4398–4414.

(341) Hong, Y.; Lam, J. W. Y.; Tang, B. Z. Aggregation-Induced Emission. *Chem. Soc. Rev.* **2011**, *40* (11), 5361–5388.

(342) Wagnière, G.; Blauer, G. Calculations of Optical Properties of Biliverdin in Various Conformations. *J. Am. Chem. Soc.* **1976**, *98* (24), 7806–7810.

(343) Ostrow, J. D.; Branham, R. V. Photodecomposition of Bilirubin and Biliverdin in Vitro. *Gastroenterology* **1970**, *58* (1), 15–25.

(344) Rück, A.; Hildebrandt, C.; Köllner, T.; Schneckenburger, H.; Steiner, R. Competition between Photobleaching and Fluorescence Increase of Photosensitizing Porphyrins and Tetrasulphonated Chloro-Aluminiumphthalocyanine. *J. Photochem. Photobiol. B Biol.* **1990**, *5* (3–4), 311–319.

(345) Rotomskis, R.; Bagdonas, S.; Streckyte, G. Spectroscopic Studies of Photobleaching and Photoproduct Formation of Porphyrins Used in Tumour Therapy. *J. Photochem. Photobiol. B Biol.* **1996**, *33* (1), 61–67.

(346) Pan, L.; Wang, X.; Yang, S.; Wu, X.; Lee, I.; Zhang, X.; Rupp, R. A.; Xu, J. Ultraviolet Irradiation-Dependent Fluorescence Enhancement of Hemoglobin Catalyzed by Reactive Oxygen Species. *PLoS One* **2012**, *7* (8), 1–6.

(347) Zhang, X.-X.; Wang, Z.; Yue, X.; Ma, Y.; Kiesewetter, D. O.; Chen1, X. PH-Sensitive Fluorescent Dyes: Are They Really PH-Sensitive in Cells? *Mol Pharm.* **2013**, *10* (5), 1910–1917.

(348) Bray, F.; Ferlay, J.; Soerjomataram, I.; Siegel, R. L.; Torre, L. A.; Jemal, A. Global Cancer Statistics 2018: GLOBOCAN Estimates of Incidence and Mortality Worldwide for 36 Cancers in 185 Countries. *CA. Cancer J. Clin.* **2018**, *68* (6), 394–424.

(349) DeSantis, C. E.; Ma, J.; Goding Sauer, A.; Newman, L. A.; Jemal, A. Breast Cancer

Statistics, 2017, Racial Disparity in Mortality by State. *CA. Cancer J. Clin.* **2017**, *67* (6), 439–448.

(350) O'Brien, K. M.; Cole, S. R.; Tse, C. K.; Perou, C. M.; Carey, L. A.; Foulkes, W. D.; Dressler, L. G.; Geradts, J.; Millikan, R. C. Intrinsic Breast Tumor Subtypes, Race, and Long-Term Survival in the Carolina Breast Cancer Study. *Clin. Cancer Res.* **2010**, *16* (24), 6100–6110.

(351) Rouzier, R.; Perou, C. M.; Symmans, W. F.; Ibrahim, N.; Cristofanilli, M.; Anderson, K.; Hess, K. R.; Stec, J.; Ayers, M.; Wagner, P.; et al. Breast Cancer Molecular Subtypes Respond Differently to Preoperative Chemotherapy. *Clin. Cancer Res.* **2005**, *11* (16), 5678–5685.

(352) Bianchini, G.; Balko, J. M.; Mayer, I. A.; Sanders, M. E. Triple-Negative Breast Cancer : Challenges and Opportunities of a Heterogeneous Disease. *Nat. Publ. Gr.* **2016**, *13* (11), 674–690.

(353) Andriyanov, A. V.; Koren, E.; Barenholz, Y.; Goldberg, S. N. Therapeutic Efficacy of Combining PEGylated Liposomal Doxorubicin and Radiofrequency (RF) Ablation: Comparison between Slow-Drug-Releasing, Non-Thermosensitive and Fast-Drug-Releasing, Thermosensitive Nano-Liposomes. *PLoS One* **2014**, *9* (5).

(354) Misra, S. K.; Ostadhossein, F.; Daza, E.; Johnson, E. V.; Pan, D. Hyperspectral Imaging Offers Visual and Quantitative Evidence of Drug Release from Zwitterionic-Phospholipid-Nanocarbon When Concurrently Tracked in 3D Intracellular Space. *Adv. Funct. Mater.* **2016**, *26* (44), 8031–8041.

(355) Hussain, H.; L., S. R.; Ahmad, S.; Abd. Razak, M. F.; Wan Mohamud, W. N.; Bakar, J.; Ghazali, H. M. Determination of Cell Viability Using Acridine Orange/Propidium Iodide

Dual-Spectrofluorometry Assay. *Cogent Food Agric.* **2019**, *5* (1), 1–9.

(356) De Visser, K. E.; Eichten, A.; Coussens, L. M. Paradoxical Roles of the Immune System during Cancer Development. *Nat. Rev. Cancer* **2006**, *6* (1), 24–37.

(357) Finn, O. J. Immuno-Oncology: Understanding the Function and Dysfunction of the Immune System in Cancer. *Ann. Oncol.* **2012**, *23* (SUPPL.8), 8–11.

(358) Anderson, K. S.; LaBaer, J. The Sentinel within: Exploiting the Immune System for Cancer Biomarkers. *J. Proteome Res.* **2005**, *4* (4), 1123–1133.

(359) Moura Rosa, P.; Gopalakrishnan, N.; Ibrahim, H.; Haug, M.; Halaas, Ø. The Intercell Dynamics of T Cells and Dendritic Cells in a Lymph Node-on-a-Chip Flow Device. *Lab Chip* **2016**, *16* (19), 3728–3740.

(360) Ross, A. E.; Belanger, M. C.; Woodroof, J. F.; Pompano, R. R. Spatially Resolved Microfluidic Stimulation of Lymphoid Tissue: Ex Vivo. *Analyst* **2017**, *142* (4), 649–659.

(361) Nie, J.; Gao, Q.; Wang, Y.; Zeng, J.; Zhao, H.; Sun, Y.; Shen, J.; Ramezani, H.; Fu, Z.; Liu, Z.; et al. Vessel-on-a-Chip with Hydrogel-Based Microfluidics. *Small* **2018**, *14* (45), 1–14.

(362) Hao, S.; Ha, L.; Cheng, G.; Wan, Y.; Xia, Y.; Sosnoski, D. M.; Mastro, A. M.; Zheng, S. Y. A Spontaneous 3D Bone-On-a-Chip for Bone Metastasis Study of Breast Cancer Cells. *Small* **2018**, *14* (12), 1–10.

(363) Oliveira, M. B.; Salgado, C. L.; Song, W.; Mano, J. F. Combinatorial On-Chip Study of Miniaturized 3D Porous Scaffolds Using a Patterned Superhydrophobic Platform. *Small* **2013**, *9* (5), 768–778.

(364) Ribas, J.; Zhang, Y. S.; Pitrez, P. R.; Leijten, J.; Miscuglio, M.; Rouwkema, J.; Dokmeci, M. R.; Nissan, X.; Ferreira, L.; Khademhosseini, A. Biomechanical Strain Exacerbates

Inflammation on a Progeria-on-a-Chip Model. *Small* **2017**, *13* (15), 1–13.

(365) Mukherjee, A.; Hooks, J.; Nepiyushchikh, Z.; Dixon, J. B. Entrainment of Lymphatic Contraction to Oscillatory Flow. *Sci. Rep.* **2019**, *9* (1), 1–14.

(366) Dixon, J. B.; Greiner, S. T.; Gashev, A. A.; Cote, G. L.; Moore, J. E.; Zawieja, D. C. Lymph Flow, Shear Stress, and Lymphocyte Velocity in Rat Mesenteric Prenodal Lymphatics. *Microcirculation* **2006**, *13* (7), 597–610.

(367) Rahbar, E.; Akl, T.; Coté, G. L.; Moore, J. E.; Zawieja, D. C. Lymph Transport in Rat Mesenteric Lymphatics Experiencing Edemagenic Stress. *Microcirculation* **2014**, *21* (5), 359–367.

(368) Yang, Y.; Fathi, P.; Holland, G.; Pan, D.; Wang, N. S.; Esch, M. B. Pumpless Microfluidic Devices for Generating Healthy and Diseased Endothelia. *Lab Chip* **2019**.

(369) Sinha, R.; Gac, S. Le; Verdonschot, N.; Berg, A. Van Den; Koopman, B. Endothelial Cell Alignment as a Result of Anisotropic Strain and Flow Induced Shear Stress Combinations. *Nat. Publ. Gr.* **2016**, No. June, 1–12.

(370) Eskin, S. G.; Ives, C. L.; McIntire, L. V.; Navarro, L. T. Response of Cultured Endothelial Cells to Steady Flow. *Microvasc. Res.* **1984**, *94*, 87–94.

(371) Wang, C.; Lu, H.; Alexander, M. A Novel in Vitro Flow System for Changing Flow Direction on Endothelial Cells. *J. Biomech.* **2012**, *45* (7), 1212–1218.

(372) Kroon, J.; Heemskerk, N.; Kalsbeek, M. J. T.; Waard, V. De; Rijssel, J. Van; Théry, M.; Louis, H. Saint. Flow-Induced Endothelial Cell Alignment Requires the RhoGEF Trio as a Scaffold Protein to Polarize Active Rac1 Distribution. *Mol. Biol. Cell* **2017**, *28*, 1745–1753.

(373) Ping Ng, C.; Helm, C. E.; Swartz, M. A. Interstitial Flow Differentially Stimulates Blood

and Lymphatic Endothelial Cell Morphogenesis in Vitro. *Microvasc. Res.* **2004**, *68*, 258–264.

(374) Cromer, W. E.; Zawieja, S. D.; Tharakan, B.; Childs, E. W.; Newell, M. K.; Zawieja, D. C. The Effects of Inflammatory Cytokines on Lymphatic Endothelial Barrier Function. *Angiogenesis* **2014**, *17* (2), 395–406.

(375) Kawai, Y.; Kaidoh, M.; Yokoyama, Y.; Ohhashi, T. Pivotal Roles of Lymphatic Endothelial Cell Layers in the Permeability to Hydrophilic Substances through Collecting Lymph Vessel Walls: Effects of Inflammatory Cytokines. *Lymphat. Res. Biol.* **2014**, *12* (3), 124–135.

(376) Chen, Y.; Rehal, S.; Roizes, S.; Zhu, H.-L.; William, C. C.; Weid, P.-Y. von der. The Pro-Inflammatory Cytokine TNF-α Inhibits Lymphatic Pumping via Activation of the NF-KB - INOS Signaling Pathway. *Microcirculation* **2017**, *24* (3).

(377) Park, R. J.; Hong, Y. J.; Wu, Y.; Kim, P. M.; Hong, Y. K. Exosomes as a Communication Tool between the Lymphatic System and Bladder Cancer. *Int. Neurourol. J.* **2018**, *22* (3), 220–224.

(378) Kim, K. S.; Park, J. I.; Oh, N.; Cho, H. J.; Park, J. H.; Park, K. S. ELK3 Expressed in Lymphatic Endothelial Cells Promotes Breast Cancer Progression and Metastasis through Exosomal MiRNAs. *Sci. Rep.* **2019**, *9* (1), 1–10.

(379) Fiskaa, T.; Knutsen, E.; Nikolaisen, M. A.; Jørgensen, T. E.; Johansen, S. D.; Perander, M.; Seternes, O. M. Distinct Small RNA Signatures in Extracellular Vesicles Derived from Breast Cancer Cell Lines. *PLoS One* **2016**, *11* (8).

(380) McCann, J. V.; Liu, A.; Musante, L.; Erdbrügger, U.; Lannigan, J.; Dudley, A. C. A MiRNA Signature in Endothelial Cell-Derived Extracellular Vesicles in Tumor-Bearing

Mice. *Sci. Rep.* **2019**, *9* (1), 1–8.

(381) Baekkevold, E.; Jahnsen, F.; Johansen, F.; Bakke, O.; Gaudernack, G.; Brandtzaeg, P.; Haraldsen, G. Culture Characterization of Differentiated High Endothelial Venule Cells from Human Tonsils. *Lab Invest* **1999**, *79* (3), 327–336.

(382) Wu, W.; Yang, Y.; Yang, Y.; Yang, Y.; Zhang, K.; Guo, L.; Ge, H.; Chen, X.; Liu, J.; Feng, H. Molecular Engineering of an Organic NIR-II Fluorophore with Aggregation-Induced Emission Characteristics for In Vivo Imaging. *Small* **2019**, *15* (20), 1–10.

(383) Liu, X.; Lai, H.; Peng, J.; Cheng, D.; Zhang, X.; Yuan, L. Chromophore-Modified Highly Selective Ratiometric Upconversion Nanoprobes for Detection of ONOO − -Related Hepatotoxicity In Vivo . *Small* **2019**, *1902737*, 1902737.

(384) Shi, X.; Meng, H.; Sun, Y.; Qu, L.; Lin, Y.; Li, Z.; Du, D. Far-Red to Near-Infrared Carbon Dots: Preparation and Applications in Biotechnology. *Small* **2019**, *1901507*, 1–17.

(385) Zhang, Q.; Zhou, H.; Chen, H.; Zhang, X.; He, S.; Ma, L.; Qu, C.; Fang, W.; Han, Y.; Wang, D.; et al. Hierarchically Nanostructured Hybrid Platform for Tumor Delineation and Image-Guided Surgery via NIR-II Fluorescence and PET Bimodal Imaging. *Small* **2019**, *1903382*, 1903382.

(386) Lu, H.; Li, W.; Dong, H.; Wei, M. Graphene Quantum Dots for Optical Bioimaging. *Small* **2019**, *15* (36), 1902136.

(387) Zhu, S.; Tian, R.; Antaris, A. L.; Chen, X.; Dai, H. Near-Infrared-II Molecular Dyes for Cancer Imaging and Surgery. *Adv. Mater.* **2019**, *31* (24), 1–25.

(388) Wu, Z. L.; Gao, M. X.; Wang, T. T.; Wan, X. Y.; Zheng, L. L.; Huang, C. Z. A General Quantitative PH Sensor Developed with Dicyandiamide N-Doped High Quantum Yield Graphene Quantum Dots. *Nanoscale* **2014**, *6* (7), 3868–3874.

(389) Dong, Y.; Pang, H.; Yang, H. Bin; Guo, C.; Shao, J.; Chi, Y.; Li, C. M.; Yu, T. Carbon-Based Dots Co-Doped with Nitrogen and Sulfur for High Quantum Yield and Excitation-Independent Emission. *Angew. Chemie - Int. Ed.* **2013**, *52* (30), 7800–7804.

(390) Hu, L.; Sun, Y.; Li, S.; Wang, X.; Hu, K.; Wang, L.; Liang, X. J.; Wu, Y. Multifunctional Carbon Dots with High Quantum Yield for Imaging and Gene Delivery. *Carbon N. Y.* **2014**, *67*, 508–513.

(391) Bao, X.; Yuan, Y.; Chen, J.; Zhang, B.; Li, D.; Zhou, D.; Jing, P.; Xu, G.; Wang, Y.; Holá, K.; et al. In Vivo Theranostics with Near-Infrared-Emitting Carbon Dots—Highly Efficient Photothermal Therapy Based on Passive Targeting after Intravenous Administration. *Light Sci. Appl.* **2018**, *7* (1), 1–11.

(392) Li, H.; He, X.; Liu, Y.; Huang, H.; Lian, S.; Lee, S. T.; Kang, Z. One-Step Ultrasonic Synthesis of Water-Soluble Carbon Nanoparticles with Excellent Photoluminescent Properties. *Carbon N. Y.* **2011**, *49* (2), 605–609.

(393) Li, D.; Jing, P.; Sun, L.; An, Y.; Shan, X.; Lu, X.; Zhou, D.; Han, D.; Shen, D.; Zhai, Y.; et al. Near-Infrared Excitation/Emission and Multiphoton-Induced Fluorescence of Carbon Dots. *Adv. Mater.* **2018**, *30* (13), 1–8.

(394) Li, L.; Zhang, R.; Lu, C.; Sun, J.; Wang, L.; Qu, B.; Li, T.; Liu, Y.; Li, S. In Situ Synthesis of NIR-Light Emitting Carbon Dots Derived from Spinach for Bio-Imaging Applications. *J. Mater. Chem. B* **2017**, *5* (35), 7328–7334.

(395) Srivastava, I.; Misra, S. K.; Tripathi, I.; Schwartz-duval, A. In Situ Time-Dependent and Progressive Oxidation of Reduced State Functionalities at the Nanoscale of Carbon Nanoparticles for Polarity-Driven Multiscale Near-Infrared Imaging. *Adv. Biosyst.* **2018**, *1800009*, 1–11.

(396) Misra, S. K.; Srivastava, I.; Tripathi, I.; Daza, E.; Ostadhossein, F.; Pan, D. Macromolecularly Caged Carbon Nanoparticles for Intracellular Trafficking via Switchable Photoluminescence. *J. Am. Chem. Soc.* **2017**, *139* (5), 1746–1749.

(397) Sun, Y. P.; Zhou, B.; Lin, Y.; Wang, W.; Fernando, K. A. S.; Pathak, P.; Meziani, M. J.; Harruff, B. A.; Wang, X.; Wang, H.; et al. Quantum-Sized Carbon Dots for Bright and Colorful Photoluminescence. *J. Am. Chem. Soc.* **2006**, *128* (24), 7756–7757.

(398) Chan, K. M.; Xu, W.; Kwon, H.; Kietrys, A. M.; Kool, E. T. Luminescent Carbon Dot Mimics Assembled on DNA. *J. Am. Chem. Soc.* **2017**, *139* (37), 13147–13155.

(399) Wu, H.; Chen, Y.; Dai, X.; Li, P.; Stoddart, J. F.; Liu, Y. In Situ Photoconversion of Multicolor Luminescence and Pure White Light Emission Based on Carbon Dot-Supported Supramolecular Assembly. *J. Am. Chem. Soc.* **2019**, *141* (16), 6583–6591.

(400) Shin, D. H.; Lee, J. S.; Jun, J.; Kim, S. G.; Jang, J. Detection of Hazardous Gas Using Multidemensional Porous Iron Oxide Nanorods-Decorated Carbon Nanoparticles. *ACS Appl. Mater. Interfaces* **2015**, *7* (3), 1746–1751.

(401) Yang, P.; Tian, Y.; Men, Y.; Guo, R.; Peng, H.; Jiang, Q.; Yang, W. Metal-Organic Frameworks-Derived Carbon Nanoparticles for Photoacoustic Imaging-Guided Photothermal/Photodynamic Combined Therapy. *ACS Appl. Mater. Interfaces* **2018**, *10* (49), 42039–42049.

(402) Ali, H.; Bhunia, S. K.; Dalal, C.; Jana, N. R. Red Fluorescent Carbon Nanoparticle-Based Cell Imaging Probe. *ACS Appl. Mater. Interfaces* **2016**, *8* (14), 9305–9313.

(403) Zhou, L.; Qu, X.; Zheng, D.; Tang, H.; Liu, D.; Qu, D.; Xie, Z.; Li, J.; Qu, D. Electrochemical Hydrogen Storage in Facile Synthesized Co@N-Doped Carbon Nanoparticle Composites. *ACS Appl. Mater. Interfaces* **2017**, *9* (47), 41332–41338.

344

(404) Sakurai, T.; Kataoka, K. Basic and Applied Features of Multicopper Oxidases, Cueo, Bilirubin Oxidase, and Laccase. *Chem. Rec.* **2007**, *7* (4), 220–229.

(405) Murao, S.; Tanaka, N. A New Enzyme "Bilirubin Oxidase" Produced by Myrothecium Verrucaria MT-1. *Agric. Biol. Chem.* **1981**, *45* (10), 2383–2384.

(406) Alexander, C.; Bellah, G. G.; Lightner, D. A. On the Fluorescence of Bilirubin. *J. Am. Chem. Soc.* **1975**, *97* (9), 2579–2580.

(407) Lamola, A. A.; Eisinger, J.; Blumberg, W. E.; Patel, S. C.; Flores, J. Fluorometric Study of the Partition of Bilirubin among Blood Components: Basis for Rapid Microassays of Bilirubin and Bilirubin Binding Capacity in Whole Blood. *Anal. Biochem.* **1979**, *100* (1), 25–42.

(408) Shen, Y. F.; Tsai, M. R.; Chen, S. C.; Leung, Y. S.; Hsieh, C. T.; Chen, Y. S.; Huang, F. L.; Obena, R. P.; Zwulueta, M. M. L.; Huang, H. Y.; et al. Imaging Endogenous Bilirubins with Two-Photon Fluorescence of Bilirubin Dimers. *Anal. Chem.* **2015**, *87* (15), 7575–7582.

(409) Htun, N. M.; Chen, Y. C.; Lim, B.; Schiller, T.; Maghzal, G. J.; Huang, A. L.; Elgass, K. D.; Rivera, J.; Schneider, H. G.; Wood, B. R.; et al. Near-Infrared Autofluorescence Induced by Intraplaque Hemorrhage and Heme Degradation as Marker for High-Risk Atherosclerotic Plaques. *Nat. Commun.* **2017**, *8* (1), 1–16.

(410) Souza, S. K. B. A. D.; Suhail, B. Blue Light - Emitting Carbon Dots (CDs) from a Milk Protein and Their Interaction with Spinacia Oleracea Leaf Cells. *Int. Nano Lett.* **2019**, *9* (3), 203–212.

(411) Guner, T.; Yuce, H.; Tascioglu, D.; Simsek, E.; Savaci, U.; Genc, A.; Turan, S.; Demir, M. M. Optimization and Performance of Nitrogen-Doped Carbon Dots as a Color

Conversion Layer for White-LED Applications. *Beilstein J. Nanotechnol.* **2019**, *10*, 2004–2013.

(412) He, M.; Zhang, J.; Wang, H.; Kong, Y.; Xiao, Y.; Xu, W. Material and Optical Properties of Fluorescent Carbon Quantum Dots Fabricated from Lemon Juice via Hydrothermal Reaction. *Nanoscale Res. Lett.* **2018**, *13* (175).

(413) Liu, H.; Zhao, X.; Wang, F.; Wang, Y.; Guo, L.; Mei, J.; Tian, C. High-Efficient Excitation-Independent Blue Luminescent Carbon Dots. *Nanoscale Res. Lett.* **2017**, *12* (399).

(414) Fina, F.; Callear, S. K.; Carins, G. M.; Irvine, J. T. S. Structural Investigation of Graphitic Carbon Nitride via XRD and Neutron Diffraction. *Chem. Mater.* **2015**, *27*, 2612–2618.

(415) Wang, X.; Maeda, K.; Thomas, A.; Takanabe, K.; Xin, G.; Carlsson, J. M.; Domen, K.; Antonietti, M. A Metal-Free Polymeric Photocatalyst for Hydrogen Production from Water under Visible Light. *Nat. Mater.* **2008**, *8* (1), 76–80.

(416) Xia, C.; Zhu, S.; Feng, T.; Yang, M.; Yang, B. Evolution and Synthesis of Carbon Dots : From Carbon Dots to Carbonized Polymer Dots. **2019**, *1901316*.

(417) Fröhlich, E. The Role of Surface Charge in Cellular Uptake and Cytotoxicity of Medical Nanoparticles. *Int. J. Nanomedicine* **2012**, *7*, 5577–5591.

(418) Jaleel, J. A.; Pramod, K. Artful and Multifaceted Applications of Carbon Dot in Biomedicine. *J. Control. Release* **2018**, *269* (November 2017), 302–321.

(419) Zhang, Z.; Yan, K.; Yang, Q.; Liu, Y.; Yan, Z.; Chen, J. One-Pot Synthesis of Fluorescent Nitrogen-Doped Carbon Dots with Good Biocompatibility for Cell Labeling. *Luminescence* **2017**, *32* (8), 1488–1493.

(420) Zhu, S.; Song, Y.; Zhao, X.; Shao, J.; Zhang, J.; Yang, B. The Photoluminescence

Mechanism in Carbon Dots (Graphene Quantum Dots, Carbon Nanodots, and Polymer Dots): Current State and Future Perspective. *Nano Res.* **2015**, *8* (2), 355–381.

(421) Wang, X.; Cao, L.; Yang, S. T.; Lu, F.; Meziani, M. J.; Tian, L.; Sun, K. W.; Bloodgood, M. A.; Sun, Y. P. Bandgap-like Strong Fluorescence in Functionalized Carbon Nanoparticles. *Angew. Chemie - Int. Ed.* **2010**, *49* (31), 5310–5314.

(422) Ruan, S.; Qian, J.; Shen, S.; Zhu, J.; Jiang, X.; He, Q.; Gao, H. A Simple One-Step Method to Prepare Fluorescent Carbon Dots and Their Potential Application in Non-Invasive Glioma Imaging. *Nanoscale* **2014**, *6* (17), 10040–10047.

(423) Wu, L.; Luderer, M.; Yang, X.; Swain, C.; Zhang, H.; Nelson, K.; Stacy, A. J.; Shen, B.; Lanza, G. M.; Pan, D. Surface Passivation of Carbon Nanoparticles with Branched Macromolecules Influences near Infrared Bioimaging. *Theranostics* **2013**, *3* (9), 677–686.

(424) Kuo, T. R.; Sung, S. Y.; Hsu, C. W.; Chang, C. J.; Chiu, T. C.; Hu, C. C. One-Pot Green Hydrothermal Synthesis of Fluorescent Nitrogen-Doped Carbon Nanodots for in Vivo Bioimaging. *Anal. Bioanal. Chem.* **2016**, *408* (1), 77–82.

(425) Yang, Shengtao; Cao, Li; Luo, Pengju G; Lu, Fushen; Wang, xin; Wang, Haifeng; Meziani, Mohammed J.; Liu, Yuanfang, Qi, Gang; Sun, Y. Carbon Dots for Optical Imaging in Vivo. *J. Am. Chem. Soc.* **2009**, *131* (32), 11308–11309.

(426) Huang, P.; Lin, J.; Wang, X.; Wang, Z.; Zhang, C.; He, M.; Wang, K.; Chen, F.; Li, Z.; Shen, G.; et al. Light-Triggered Theranostics Based on Photosensitizer-Conjugated Carbon Dots for Simultaneous Enhanced-Fluorescence Imaging and Photodynamic Therapy. *Adv. Mater.* **2012**, *24* (37), 5104–5110.

(427) Ostadhossein, F.; Benig, L.; Tripathi, I.; Misra, S. K.; Pan, D. Fluorescence Detection of Bone Microcracks Using Monophosphonated Carbon Dots. *ACS Appl. Mater. Interfaces*

2018, *10*, 19408–19415.

(428) Jiang, K.; Sun, S.; Zhang, L.; Lu, Y.; Wu, A.; Cai, C.; Lin, H. Red, Green, and Blue Luminescence by Carbon Dots: Full-Color Emission Tuning and Multicolor Cellular Imaging. *Angew. Chemie - Int. Ed.* **2015**, *54* (18), 5360–5363.

(429) Zhi, B.; Cui, Y.; Wang, S.; Frank, B. P.; Williams, D. N.; Brown, R. P.; Melby, E. S.; Hamers, R. J.; Rosenzweig, Z.; Fairbrother, D. H.; et al. Malic Acid Carbon Dots : From Super-. *ACS Nano* **2018**, *12*, 5741–5752.

(430) Kong, B.; Zhu, A.; Ding, C.; Zhao, X.; Li, B.; Tian, Y. Carbon Dot-Based Inorganic-Organic Nanosystem for Two-Photon Imaging and Biosensing of PH Variation in Living Cells and Tissues. *Adv. Mater.* **2012**, *24* (43), 5844–5848.

(431) Zhang, Y.; Chan, K. F.; Wang, B.; Chiu, P. W. Y.; Zhang, L. Spore-Derived Color-Tunable Multi-Doped Carbon Nanodots as Sensitive Nanosensors and Intracellular Imaging Agents. *Sensors Actuators, B Chem.* **2018**, *271* (May), 128–136.

(432) Luo, M.; Hua, Y.; Liang, Y.; Han, J.; Liu, D.; Zhao, W.; Wang, P. Synthesis of Novel β-Cyclodextrin Functionalized S, N Codoped Carbon Dots for Selective Detection of Testosterone. *Biosens. Bioelectron.* **2017**, *98* (June), 195–201.

(433) Han, M.; Wang, L.; Li, S.; Bai, L.; Zhou, Y.; Sun, Y.; Huang, H.; Li, H.; Liu, Y.; Kang, Z. High-Bright Fluorescent Carbon Dot as Versatile Sensing Platform. *Talanta* **2017**, *174* (May), 265–273.

(434) Kampert, T.; Misra, S. K.; Srivastava, I.; Tripathi, I.; Pan, D. Phenotypically Screened Carbon Nanoparticles for Enhanced Combinatorial Therapy in Triple Negative Breast Cancer. *Cell. Mol. Bioeng.* **2017**, *10* (5), 371–386.

(435) Cao, X.; Wang, J.; Deng, W.; Chen, J.; Wang, Y.; Zhou, J.; Du, P.; Xu, W.; Wang, Q.;

Wang, Q.; et al. Photoluminescent Cationic Carbon Dots as Efficient Non-Viral Delivery of Plasmid SOX9 and Chondrogenesis of Fibroblasts. *Sci. Rep.* **2018**, *8* (1), 1–11.

(436) Zhao, H.; Duan, J.; Xiao, Y.; Tang, G.; Wu, C.; Zhang, Y.; Liu, Z.; Xue, W. Microenvironment-Driven Cascaded Responsive Hybrid Carbon Dots as a Multifunctional Theranostic Nanoplatform for Imaging-Traceable Gene Precise Delivery. *Chem. Mater.* **2018**, *30* (10), 3438–3453.

(437) Liu, C.; Zhang, P.; Tian, F.; Li, W.; Li, F.; Liu, W. One-Step Synthesis of Surface Passivated Carbon Nanodots by Microwave Assisted Pyrolysis for Enhanced Multicolor Photoluminescence and Bioimaging. *J. Mater. Chem.* **2011**, *21* (35), 13163–13167.

(438) Sun, Y. P.; Zhou, B.; Lin, Y.; Wang, W.; Fernando, K. A. S.; Pathak, P.; Meziani, M. J.; Harruff, B. A.; Wang, X.; Wang, H.; et al. Quantum-Sized Carbon Dots for Bright and Colorful Photoluminescence. *J. Am. Chem. Soc.* **2006**, *128* (24), 7756–7757.

(439) Chandra, S.; Pathan, S. H.; Mitra, S.; Modha, B. H.; Goswami, A.; Pramanik, P. Tuning of Photoluminescence on Different Surface Functionalized Carbon Quantum Dots. *RSC Adv.* **2012**, *2* (9), 3602–3606.

(440) Shen, C.; Yao, W.; Lu, Y. One-Step Synthesis of Intrinsically Functionalized Fluorescent Carbon Nanoparticles by Hydrothermal Carbonization from Different Carbon Sources. *J. Nanoparticle Res.* **2013**, *15* (10).

(441) Shen, P.; Xia, Y. Synthesis-Modification Integration: One-Step Fabrication of Boronic Acid Functionalized Carbon Dots for Fluorescent Blood Sugar Sensing. *Anal. Chem.* **2014**, *86* (11), 5323–5329.

(442) Hu, L.; Sun, Y.; Li, S.; Wang, X.; Hu, K.; Wang, L.; Liang, X. J.; Wu, Y. Multifunctional Carbon Dots with High Quantum Yield for Imaging and Gene Delivery. *Carbon N. Y.*

349

2014, *67*, 508–513.

(443) Yang, M.; Meng, X.; Li, B.; Ge, S.; Lu, Y. N, S Co-Doped Carbon Dots with High Quantum Yield: Tunable Fluorescence in Liquid/Solid and Extensible Applications. *J. Nanoparticle Res.* **2017**, *19* (6).

(444) Liu, H.; Li, Z.; Sun, Y.; Geng, X.; Hu, Y.; Meng, H.; Ge, J.; Qu, L. Synthesis of Luminescent Carbon Dots with Ultrahigh Quantum Yield and Inherent Folate Receptor-Positive Cancer Cell Targetability. *Sci. Rep.* **2018**, *8* (1), 1–8.

(445) Das, S. K.; Liu, Y.; Yeom, S.; Kim, D. Y.; Richards, C. I. Single-Particle Fluorescence Intensity Fluctuations of Carbon Nanodots. *Nano Lett.* **2014**, *14* (2), 620–625.

(446) Yang, Q.; Wei, L.; Zheng, X.; Xiao, L. Single Particle Dynamic Imaging and Fe3+ Sensing with Bright Carbon Dots Derived from Bovine Serum Albumin Proteins. *Sci. Rep.* **2015**, *5* (December), 1–12.

(447) Verma, N. C.; Khan, S.; Nandi, C. K. Single-Molecule Analysis of Fluorescent Carbon Dots towards Localization-Based Super-Resolution Microscopy. *Methods Appl. Fluoresc.* **2016**, *4* (4), 044006.

(448) Grecco, H. E.; Lidke, K. A.; Heintzmann, R.; Lidke, D. S.; Spagnuolo, C.; Martinez, O. E.; Jares-Erijman, E. A.; Jovin, T. M. Ensemble and Single Particle Photophysical Properties (Two-Photon Excitation, Anisotropy, FRET, Lifetime, Spectral Conversion) of Commercial Quantum Dots in Solution and in Live Cells. *Microsc. Res. Tech.* **2004**, *65* (4–5), 169–179.

(449) Chan, W. C. W.; Maxwell, D. J.; Gao, X.; Bailey, R. E.; Han, M.; Nie, S. Luminescent Quantum Dots for Multiplexed Biological Detection and Imaging. *Curr. Opin. Biotechnol.* **2002**, *13* (1), 40–46.

(450) Gao, X.; Chan, W. C. W.; Nie, S. Quantum-Dot Nanocrystals for Ultrasensitive Biological Labeling and Multicolor Optical Encoding. *J. Biomed. Opt.* **2002**, *7* (4), 532.

(451) Chan, W. C. W.; Nie, S.; Chan, W. C. W.; Nie, S. Quantum Dot Bioconjugates for Ultrasensitive Nonisotopic Detection Published by : American Association for the Advancement of Science Stable URL : Http://Www.Jstor.Org/Stable/2895734 Linked References Are Available on JSTOR for This Article : Quantum Dot. *Science (80-.).* **1998**, *281* (5385), 2016–2018.

(452) Howarth, M.; Takao, K.; Hayashi, Y.; Ting, A. Y.; Stephen, J.; Howarth, M.; Takaot, K.; Hayashit, Y.; Ting, A. Y. Targeting Quantum Dots to Surface Proteins in Living Cells with Biotin Ligase. *PNAS* **2005**, *102* (21), 7583–7588.

(453) Courty, S.; Luccardini, C.; Bellaiche, Y.; Cappello, G.; Dahan, M. Tracking Individual Kinesin Motors in Living Cells Using Single Quantum-Dot Imaging. *Nano Lett.* **2006**, *6* (7), 1491–1495.

(454) Yang, Z.; Li, Z.; Xu, M.; Zhang, L.; Zhang, J.; Su, Y.; Gao, F.; Wei, H. Controllable Synthesis of Fluorescent Carbon Dots and Their Detection Application as Nanoprobes. *Micro Nano Lett.* **2013**, *5* (4), 247–259.

(455) Zhang, Y. Q.; Ma, D. K.; Zhuang, Y.; Zhang, X.; Chen, W.; Hong, L. L.; Yan, Q. X.; Yu, K.; Huang, S. M. One-Pot Synthesis of N-Doped Carbon Dots with Tunable Luminescence Properties. *J. Mater. Chem.* **2012**, *22* (33), 16714–16718.

(456) Li, H.; Kang, Z.; Liu, Y.; Lee, S. T. Carbon Nanodots: Synthesis, Properties and Applications. *J. Mater. Chem.* **2012**, *22* (46), 24230–24253.

(457) Misra, S. K. K.; Srivastava, I.; Khamo, J. S.; Krishnamurthy, V. V; Sar, D.; Schwartz-Duval, A.; Soares, J.; Zhang, K.; Pan, D. Carbon Dots with Induced Surface Oxidation

Permits Imaging at Single-Particle Level for Intracellular Studies. *Nanoscale* **2018**.

(458) Watkins, L. P.; Yang, H. Detection of Intensity Change Points in Time-Resolved Single-Molecule Measurements. *J. Phys. Chem. B* **2005**, *109* (1), 617–628.

(459) Montiel, D.; Cang, H.; Yang, H. Quantitative Characterization of Changes in Dynamical Behavior for Single-Particle Tracking Studies [†]. *J. Phys. Chem. B* **2006**, *110* (40), 19763–19770.

(460) Srivastava, I.; Misra, S. K.; Ostadhossein, F.; Daza, E.; Singh, J.; Pan, D. Surface Chemistry of Carbon Nanoparticles Functionally Select Their Uptake in Various Stages of Cancer Cells. *Nano Res.* **2017**, *10* (10), 3269–3284.

(461) Khan, S.; Li, W.; Karedla, N.; Thiart, J.; Gregor, I.; Chizhik, A. M.; Enderlein, J.; Nandi, C. K.; Chizhik, A. I. Charge-Driven Fluorescence Blinking in Carbon Nanodots. *J. Phys. Chem. Lett.* **2017**, *8* (23), 5751–5757.

(462) Shimizu, K. T.; Neuhauser, R. G.; Leatherdale, C. A.; Empedocles, S. A.; Woo, W. K.; Bawendi, M. G. Blinking Statistics in Single Semiconductor Nanocrystal Quantum Dots. *Phys. Rev. B - Condens. Matter Mater. Phys.* **2001**, *63* (20), 1–5.

(463) FRANTSUZOV, P.; KUNO, M.; JANK´O, B. A.; MARCUS, R. A. Universal Emission Intermittency in Quantum Dots , Nanorods and Nanowires. *Nat. Phys.* **2008**, *4*, 519–522.

(464) Schmidt, M. W.; Baldridge, K. K.; Boatz, J. A.; Elbert, S. T.; Gordon, M. S.; Jensen, J. H.; Koseki, S.; Matsunaga, N.; Nguyen, K. A.; Su, S.; et al. General Atomic and Molecular Electronic Structure System. *J. Comput. Chem.* **1993**, *14* (11), 1347–1363.

(465) Camp, T.; Mehta, K.; Sligar, S. G.; Zhang, K. Molecular Orientation Determination in Nanodiscs at the Single-Molecule Level. *Anal. Chem.* **2020**, *92* (2), 2229–2236.

(466) Watkins, L. P.; Yang, H. Detection of Intensity Change Points in Time-Resolved Single-

Molecule Measurements. *J. Phys. Chem. B* **2005**, *109* (1), 617–628.

(467) Montiel, D.; Cang, H.; Yang, H. Quantitative Characterization of Changes in Dynamical

Behavior for Single-Particle Tracking Studies. *J. Phys. Chem. B* **2006**, *110* (40), 19763–

19770.

APPENDIX A: IMAGE ANALYSIS IN IMAGEJ

Image analysis using ImageJ played an important role in a number of analyses used in these projects. I utilized readily-available ImageJ plugins, as well as macros that I recorded or programmed myself, in order to carry out these analyses. Macros can be recorded using "Plugins" → "Macros" → "Record". For the macros that I utilized in this work, I would copy and paste the code from the recording window into the Startup Macros window ("Plugins" → "Macros" → "Startup Macros") and make changes as necessary. After adding a new macro to the Startup Macros, I would then restart ImageJ and install the Startup Macros again ("Plugins" → "Macros" →"Install"→ select the correct file) before proceeding with the analyses.

A.1 ANALYSIS OF PHOTOACOUSTIC IMAGES

Loading a sequence of photoacoustic images (dicom files):

`macro "macroimport[6]"{`	Name the Macro "macroimport" and set its shortcut to "Fn+6"
`run("Image Sequence...");`	Open an image sequence
`}`	

Creating a maximum intensity projection, determining the minimum and maximum intensity values for the projected image, applying a lookup table to the projected image, and saving it as a tiff file:

`macro "Parinazmacro [0]" {`	Name the Macro "Parinazmacro" and set its shortcut to "Fn+0"
`run("Z Project...", "projection=[Max Intensity]");`	Do a maximum intensity projection
`run("Red Hot");`	Apply the "Red Hot" lookup table
`getMinAndMax(min, max)`	Find the min and max intensity values in the current image
`print(getTitle+": "+min+"-"+max);`	Print those values into a table
`run("RGB Color");`	Change the image type to "RGB color"
`saveAs("Tiff...");`	Save the image as a tiff file

```
}
```

Creating a maximum intensity projection, applying a lookup table to the projected image, adjusting the minimum and maximum displayed contrast values as desired, and saving the resulting image as a tiff file:

`macro"macro_080918_160[9]"{`	Name the Macro "macro_080918_160" and set its shortcut to "Fn+9"
`run("Z Project...", "projection=[Max Intensity]");`	Do a maximum intensity projection
`run("Red Hot");`	Apply the "Red Hot" lookup table
`run("Brightness/Contrast...");`	Set the minimum and maximum display intensity values to 70 and 3000 respectively
`setMinAndMax(70, 3000);`	(these numbers can be replaced with whatever intensities are desired)
`//run("Close");`	
`run("RGB Color");`	Change the image type to "RGB color"
`saveAs("Tiff...");`	Save the image as a tiff file
`}`	

A.2 ANALYSIS OF CELL IMAGES

Generating the RGB image of the live cells

`macro "livecells[l]"{`	Name the Macro "livecells" and set its shortcut to "Fn+l"
`run("Green");`	Apply the "Green" lookup table
`run("RGB Color");`	Change the image type to RGB color
`saveAs("Tiff...");`	Save the image as a tiff file
`}`	

Generating the RGB image of the dead cells

`macro "deadcells[d]"{`	Name the Macro "deadcells" and set its shortcut to "Fn+d"
`run("Red");`	Apply the "Red" lookup table
`run("RGB Color");`	Change the image type to RGB color
`saveAs("Tiff...");`	Save the image as a tiff file

```
}
```

Generating the merged RGB image of the live and dead cells

`macro "livedeadmerge[m]"{`	Name the Macro "livedeadmerge" and set its shortcut to "Fn+m"
`run("Merge Channels...");`	Merge the color channels
`run("RGB Color");`	Change the image type to RGB color
`saveAs("Tiff...");`	Save the image as a tiff file
`}`	

Determining the directionality of cells in an image

`macro "directionalitymacro1[y]"{`	Name the Macro "directionalitymacro1" and set its shortcut to "Fn+y"
`run("8-bit");`	Set the image type to 8 bit
`run("Directionality", "method=[Fourier components] nbins=90 histogram=0 display_table");`	Use the directionality tool with the fourier components method and 90 bins, displaying the results in a table
`}`	

APPENDIX B: GENERAL CELL CULTURE PROTOCOLS

B.1 CULTURING HUMAN LYMPHATIC ENDOTHELIAL CELLS

Cell Lot Number (used at NIST): 19394 from Sciencell

Media to use: Endothelial Cell medium *(Sciencell* 1001)

Other Materials Needed: DPBS *(Sciencell 0303)*, Trypsin-EDTA *(Sciencell 0103)*, Trypsin Neutralization Solution (TNS- *Sciencell 0113*), Bovine plasma fibronectin *(Sciencell 8248 or Sigma F1141)*

Note: All media and solutions should be equilibrated at room temperature (not warmed up to 37 C)

Coating cell culture flasks

1. Mix 50 µL bovine plasma fibronectin with 1.67 mL of DPBS for each 25 cm^2 flask

2. Pipette the fibronectin-DPBS solution into the flask and move flask to gently spread the solution on the surface upon which cells will be cultured

3. Incubate the flask overnight

4. Remove the fibronectin-DPBS solution. It can be used two more times

Thawing vial

1. After already having the cell culture flasks coated with fibronectin, add 5 mL culture media into each flask

2. Defrost the vial in the water bath, and quickly add to the flask (*** do not centrifuge ***)

3. Incubate at 37C

4. Replace media a day after thawing the vial

Changing media (every 3 days until 70% confluency, then every 2 days)

1. Pipette out old media

2. Replace with 5 mL fresh media

Splitting cells (subculture at 90% confluency, split each flask into 2-3 new flasks)

1. Prepare a conical tube with 1.66 mL FBS for each 25 cm^2 flask

2. Rinse cells with 5 mL DPBS

3. Add 1 mL trypsin/EDTA to each 25 cm^2 flask

4. Incubate flasks at 37 C for 1-2 minutes

5. Check under microscope and tap on flask to make sure cells have dislodged. If they haven't, but back in incubator for another 1-2 minutes. If not all of the cells have detached yet, proceed to step 6-7 then repeat steps 2-6

6. Add 1 mL trypsin neutralizing solution (TNS) to the flask

7. Pipette the liquid into the conical tube with the FBS

8. Check flask under microscope to make sure most cells (≥95%) have been removed

9. Centrifuge at 1000 rpm for 5 min

10. Discard the supernatant and resuspend cells in 5 mL of new media for each new flask

Freezing cells

1. Remove cells and spin down as described for splitting cells

2. After discarding supernatant, resuspend in growth medium with 10% DMSO

3. Immediately place in freezing container and put in -80 C freezer

Table B1. DMSO calculations.

# of vials to freeze	Amount of Media	Amount of DMSO (μL)
1	900 μL	100
2	1.800 mL	200
3	2.700 mL	300
4	3.600 mL	400
5	4.500 mL	500
6	5.400 mL	600

B.2 CULTURING MCF-7 BREAST CANCER CELLS

Cell Details: Metastatic Breast Cancer, Immortalized Cell Line

Cell Lot Number (used at NIST): 64125078 from ATCC

Media to use: DMEM (Corning 10-017-CV) + 10% (final volume) FBS *(Sciencell 0500).*

Other Materials Needed: DPBS *(Sciencell 0303)*, Trypsin-EDTA *(Sciencell 0103)*, Trypsin

Neutralization Solution (TNS- *Sciencell 0113*)

Thawing vial

1. Prepare conical tube with 3 mL media for each vial that will be thawed

2. Thaw vial in water bath and immediately add to the conical tube

3. Centrifuge at 125 xg for 10 min (1000 rpm for 5 min also works just fine)

4. Discard supernatant

5. Tap tube to break cell pellet

6. Resuspend pellet in 5 mL media for each vial that was thawed

7. Pipette 5 mL of cell suspension into each 25 cm^2 flask

8. Incubate

Changing media (2-3 times a week)

1. Pipette out old media

2. Replace with 5 mL fresh media

Splitting cells (subculture at ~90% confluency, split each flask into 3-4 new flasks)

1. Rinse cells with 5 mL DPBS

2. Add 1 mL trypsin/EDTA to each 25 cm^2 flask

3. Keep flasks at room temperature for about 1 minute

4. Check under microscope and tap on flask to make sure cells have dislodged. If they haven't, wait 1 more minute

5. Add 1 mL trypsin neutralizing solution (TNS) to the flask

6. Add 3 mL media for each flask of cells that are being split

7. Centrifuge at 125 xg for 10 min (1000 rpm for 5 min also works just fine)

8. Discard supernatant

9. Tap tube to break cell pellet

10. Add 5 mL media for each new flask and resuspend cells

11. Aliquot suspension into new flasks

12. Incubate at 37 C

Freezing cells

1. Prepare conical tube with 3 mL media for each flask

2. Trypsinize cells as described for splitting cells

3. Add cell suspension into conical tube containing media

4. Centrifuge at 125 xg for 5-7 min

5. After discarding supernatant, resuspend in growth medium with 5% DMSO

6. Immediately place in freezing container and put in -80 C freezer

Table B2. DMSO calculations.

# of vials to freeze	Amount of Media	Amount of DMSO (μL)
1	950 μL	50
2	1.900 mL	100
3	2.850 mL	150
4	3.800 mL	200
5	4.750 mL	250
6	5.700 mL	300

B.3. CULTURING MDA-MB-231 BREAST CANCER CELLS

Cell Details: Triple Negative Breast Cancer, Immortalized Cell Line

Cell Lot Number: 70000792 from ATCC

Media to use: DMEM (Corning 10-017-CV) + 10% (final volume) FBS *(Sciencell 0500).*

Other Materials Needed: DPBS *(Sciencell 0303)*, Trypsin-EDTA *(Sciencell 0103)*, Trypsin

Neutralization Solution (TNS- *Sciencell 0113*)

Thawing vial

1. Prepare conical tube with 3 mL media for each vial that will be thawed

2. Thaw vial in water bath and immediately add to the conical tube

3. Centrifuge at 125 xg for 5-7 min (1000 rpm for 5 min also works just fine)

4. Discard supernatant

5. Resuspend pellet in 5 mL media for each vial that was thawed

6. Pipette 5 mL of cell suspension into each 25 cm^2 flask

7. Incubate

Changing media (3 times a week)

1. Pipette out old media

2. Replace with 5 mL fresh media

Splitting cells (subculture at 90% confluency, split each flask into 3-4 new flasks)

1. Rinse cells with 5 mL DPBS

2. Add 1 mL trypsin/EDTA to each 25 cm^2 flask

3. Keep flasks at room temperature for about 1 minute

4. Check under microscope and tap on flask to make sure cells have dislodged. If they

   haven't, wait 1 more minute

5. Add 1 mL trypsin neutralizing solution (TNS) to the flask

6. Add 5 mL media for each new flask

7. Aliquot suspension into new flasks

8. Incubate at 37 C

Freezing cells

1. Prepare conical tube with 3 mL media for each flask

2. Trypsinize cells as described for splitting cells

3. Add cell suspension into conical tube containing media

4. Centrifuge at 125 xg for 5-7 min (1000 rpm for 5 min also works just fine)

5. After discarding supernatant, resuspend in growth medium with 5% DMSO

6. Immediately place in freezing container and put in -80 C freezer

Table B3. DMSO calculations.

# of vials to freeze	Amount of Media	Amount of DMSO (μL)
1	950 μL	50
2	1.900 mL	100
3	2.850 mL	150
4	3.800 mL	200
5	4.750 mL	250
6	5.700 mL	300

B.4 CULTURING MCF-10A MAMMARY EPITHELIAL CELLS

Cell Details: Non-cancerous mammary epithelial cells, Immortalized Cell Line

Cell Lot Number (used at NIST): 70007818 from ATCC

Media to use: MEGM (Lonza CC-3150) without GA-1000 (gentamycin-amphotericin B mix), +
100 ng/mL cholera toxin (Sigma C8052)

Other Materials Needed: DPBS *(Sciencell 0303)*, Trypsin-EDTA *(Sciencell 0103)*, Trypsin
Neutralization Solution (TNS- *Sciencell 0113*)

Thawing vial

1. Prepare conical tube with 3 mL media for each vial that will be thawed

2. Thaw vial in water bath and immediately add to the conical tube

3. Centrifuge at 125 xg for 5-10 min (1000 rpm for 5 min also works just fine)

4. Discard supernatant

5. Resuspend pellet in 5 mL media for each vial that was thawed

6. Pipette 5 mL of cell suspension into each 25 cm^2 flask

7. Incubate

Changing media (3 times a week)

1. Pipette out old media

2. Replace with 5 mL fresh media

Splitting cells (subculture at 90% confluency, split each flask into 3-4 new flasks)

1. Rinse cells with 5 mL DPBS

2. Add 1 mL trypsin/EDTA to each 25 cm^2 flask

3. Put flask in incubator for 10 minutes

4. Check under microscope and tap on flask to make sure cells have dislodged. If they haven't, put back in incubator. Sometimes it can take up to 25 minutes for the cells to completely dislodge

5. Add 1 mL trypsin neutralizing solution (TNS) to the flask

6. Add 5 mL media for each new flask

7. Aliquot suspension into new flasks

8. Incubate at 37 C

Freezing cells

1. Prepare conical tube with 3 mL media for each flask

2. Trypsinize cells as described for splitting cells

3. Add cell suspension into conical tube containing media

4. Centrifuge at 125 xg for 5-10 min (1000 rpm for 5 min also works just fine)

5. After discarding supernatant, resuspend in growth medium with 7.5% DMSO

6. Immediately place in freezing container and put in -80 C freezer

Table B4. DMSO calculations.

# of vials to freeze	Amount of Media	Amount of DMSO (μL)
1	925 μL	75
2	1.85 mL	150
3	2.775 mL	225
4	3.7 mL	300
5	4.625 mL	375
6	5.55 mL	450

B.5 CULTURING HUMAN TONSIL ENDOTHELIAL CELLS

Media to use: Endothelial Cell medium *(Sciencell* 1001)

Other Materials Needed: DPBS *(Sciencell 0303)*, Trypsin-EDTA *(Sciencell 0103)*, Trypsin

Neutralization Solution (TNS- *Sciencell 0113*), Bovine plasma fibronectin *(Sciencell 8248 or*

Sigma F1141)

Note: All media and solutions should be equilibrated at room temperature (not warmed up to 37

C)

Coating cell culture flasks

1. Mix 50 µL bovine plasma fibronectin with 1.67 mL of DPBS for each 25 cm^2 flask

2. Pipette the fibronectin-DPBS solution into the flask and move flask to gently spread the

   solution on the surface upon which cells will be cultured

3. Incubate the flask overnight

4. Remove the fibronectin-DPBS solution. It can be used two more times

Thawing vial

1. After already having the cell culture flasks coated with fibronectin, add 5 mL culture

   media into each flask

2. Defrost the vial in the water bath, and quickly add to the flask (*** do not centrifuge ***)

3. Incubate at 37C

4. Replace media a day after thawing the vial

Changing media (every 3 days until 70% confluency, then every 2 days)

1. Pipette out old media

2. Replace with 5 mL fresh media

Splitting cells (subculture at 90% confluency, split each flask into 2-3 new flasks)

1. Prepare a conical tube with 1.66 mL FBS for each 25 cm^2 flask

2. Rinse cells with 5 mL DPBS

3. Add 1 mL trypsin/EDTA to each 25 cm^2 flask

4. Incubate flasks at 37 C for 1-2 minutes

5. Check under microscope and tap on flask to make sure cells have dislodged. If they haven't, but back in incubator for another 1-2 minutes. If not all of the cells have detached yet, proceed to step 6-7 then repeat steps 2-6

6. Add 1 mL trypsin neutralizing solution (TNS) to the flask

7. Pipette the liquid into the conical tube with the FBS

8. Check flask under microscope to make sure most cells (≥95%) have been removed

9. Centrifuge at 1000 rpm for 5 min

10. Discard the supernatant and resuspend cells in 5 mL of new media for each new flask

Freezing cells

1. Remove cells and spin down as described for splitting cells

2. After discarding supernatant, resuspend in growth medium with 10% DMSO

3. Immediately place in freezing container and put in -80 C freezer

Table B5. DMSO calculations.

# of vials to freeze	Amount of Media	Amount of DMSO (μL)
1	900 μL	100
2	1.800 mL	200
3	2.700 mL	300
4	3.600 mL	400
5	4.500 mL	500
6	5.400 mL	600

B.6 CULTURING HIGH ENDOTHELIAL VENULE ENDOTHELIAL CELLS

(ISOLATED FROM HTECS)

Media to use: Endothelial Cell medium *(Sciencell* 1001)

Other Materials Needed: DPBS *(Sciencell 0303)*, Trypsin-EDTA *(Sciencell 0103)*, Trypsin

Neutralization Solution (TNS- *Sciencell 0113*), Bovine plasma fibronectin *(Sciencell 8248 or*

Sigma F1141)

Note: All media and solutions should be equilibrated at room temperature (not warmed up to 37

C)

Coating cell culture flasks

1. Mix 50 µL bovine plasma fibronectin with 1.67 mL of DPBS for each 25 cm^2 flask

2. Pipette the fibronectin-DPBS solution into the flask and move flask to gently spread the
   solution on the surface upon which cells will be cultured

3. Incubate the flask overnight

4. Remove the fibronectin-DPBS solution. It can be used two more times

Thawing vial

1. After already having the cell culture flasks coated with fibronectin, add 5 mL culture
   media into each flask

2. Defrost the vial in the water bath, and quickly add to the flask (*** do not centrifuge ***)

3. Incubate at 37C

4. Replace media a day after thawing the vial

Changing media (every 3 days until 70% confluency, then every 2 days)

1. Pipette out old media

2. Replace with 5 mL fresh media

Splitting cells (subculture at 90% confluency, split each flask into 2-3 new flasks)

1. Prepare a conical tube with 1.66 mL FBS for each 25 cm^2 flask

2. Rinse cells with 5 mL DPBS

3. Add 1 mL trypsin/EDTA to each 25 cm^2 flask

4. Incubate flasks at 37 C for 1-2 minutes

5. Check under microscope and tap on flask to make sure cells have dislodged. If they haven't, but back in incubator for another 1-2 minutes. If not all of the cells have detached yet, proceed to step 6-7 then repeat steps 2-6

6. Add 1 mL trypsin neutralizing solution (TNS) to the flask

7. Pipette the liquid into the conical tube with the FBS

8. Check flask under microscope to make sure most cells (≥95%) have been removed

9. Centrifuge at 1000 rpm for 5 min

10. Discard the supernatant and resuspend cells in 5 mL of new media for each new flask

Freezing cells

1. Remove cells and spin down as described for splitting cells

2. After discarding supernatant, resuspend in growth medium with 10% DMSO

3. Immediately place in freezing container and put in -80 C freezer

Table B6. DMSO calculations.

# of vials to freeze	Amount of Media	Amount of DMSO (μL)
1	900 μL	100
2	1.800 mL	200
3	2.700 mL	300
4	3.600 mL	400
5	4.500 mL	500
6	5.400 mL	600

B.7 CULTURING HEPG2 CELLS

Culture of HepG2 cells follows the same protocol as culturing MDA-MB-231 cells and MCF-7 cells.

B.8 CULTURING 4T1 CELLS

4T1 cells can be cultured following a similar protocol as for MDA-MB-231 cells and MCF-7 cells, with the exception of using RPMI medium rather than DMEM

APPENDIX C: GENERAL SYNTHESIS PROCEDURES

Biliverdin Nanoparticle (BVNP) Synthesis

Materials

Fume hood

Biliverdin hydrochloride

1-Ethyl-3-(3-dimethylaminopropyl)carbodiimide (EDC)

N-hydroxysuccinimide (NHS)

2,2' ethylenedioxybisethylamine (abbreviated "diamine")

Water, 0.9% NaCl solution, or 2-(N-morpholino)ethanesulfonic acid (MES) buffer

Dialysis cassettes (10K MW cutoff, samples size of 1-3 mL or 15 mL)

Cobalt(II) chloride (optional)

Doxorubicin hydrochloride (optional)

Sodium hydroxide solution (optional)

pH meter (optional)

Safety Equipment to be used at all times

Lab coat

Disposable gloves

Safety goggles

Procedure

1. In the fume hood, add 10 mg of biliverdin hydrochloride to 10 mL water or 10 mL 0.9%

    NaCl solution or 10 mL MES buffer in a 20 mL scintillation vial

a. Place on stirplate at 500 rpm at room temperature

b. Cover bottle with foil

c. Allow to dissolve overnight

2. Add 6.7 mg EDC and 4.0 mg NHS

a. Keep sample covered with foil

b. Allow to dissolve for 10 minutes

3. Add 3.5 µL diamine

a. Keep sample covered with foil

b. Allow reaction to proceed for 10 minutes to 24 h

4. Dialyze sample against the same type of liquid used for the synthesis (water, 0.9% NaCl solution, or MES buffer)

a. First hydrate the dialysis cassettes by placing them in the liquid for 2 minutes

b. Pipette the sample into the dialysis cassette

c. Cover beaker with foil

d. Place on stirplate for 24 h

e. Parameters to keep in mind

i. For 3 mL of nanoparticle sample: use 500 mL dialysis liquid, 500 mL beaker, stir speed of 100 rpm

ii. For 10 mL of nanoparticle sample: use 1 L dialysis liquid, 1000 mL beaker, stir speed of 200 rpm

5. Discard dialysis supernatant in appropriate waste container

6. Utilize nanoparticles for the desired applications

<u>Variations</u>

BVNPs loaded with doxorubicin (for drug delivery applications)

- In step 1, add 10 mg doxorubicin hydrochloride to the liquid at the same time as the 10

  mg biliverdin hydrochloride

BVNPs chelated with cobalt (for MR contrast applications)

- After step 5, use NaOH solution to raise the pH of the nanoparticle solution to a pH of 12

- Add desired concentration of cobalt chloride

- Stir at 500 rpm overnight

- Dialyze the particles for 24 h as before
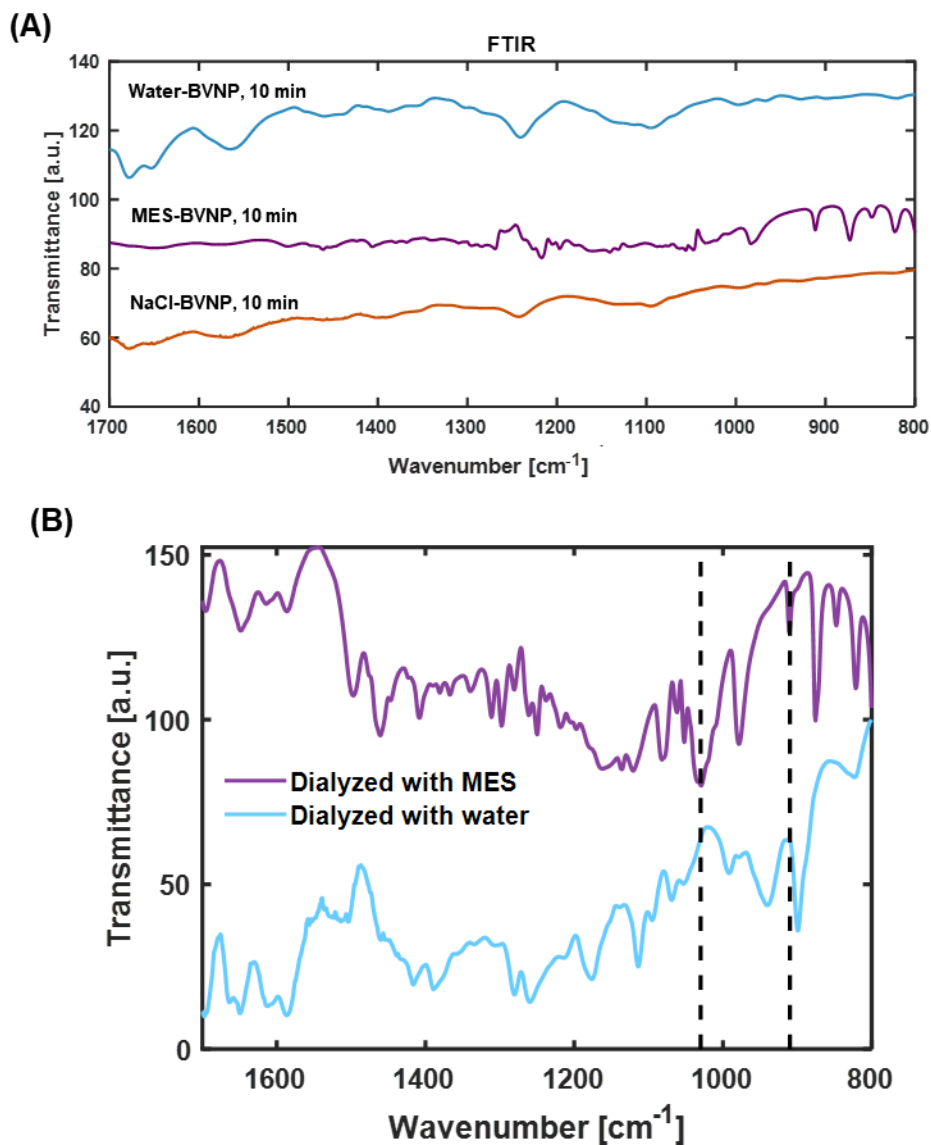
Figure D1. (A) FT-IR spectra for 10 min water-BVNPs, MES-BVNPs, and NaCl-BVNPs. **(B)** FT-IR spectra for 24 h MES-BVNPs dialyzed with MES and with water.
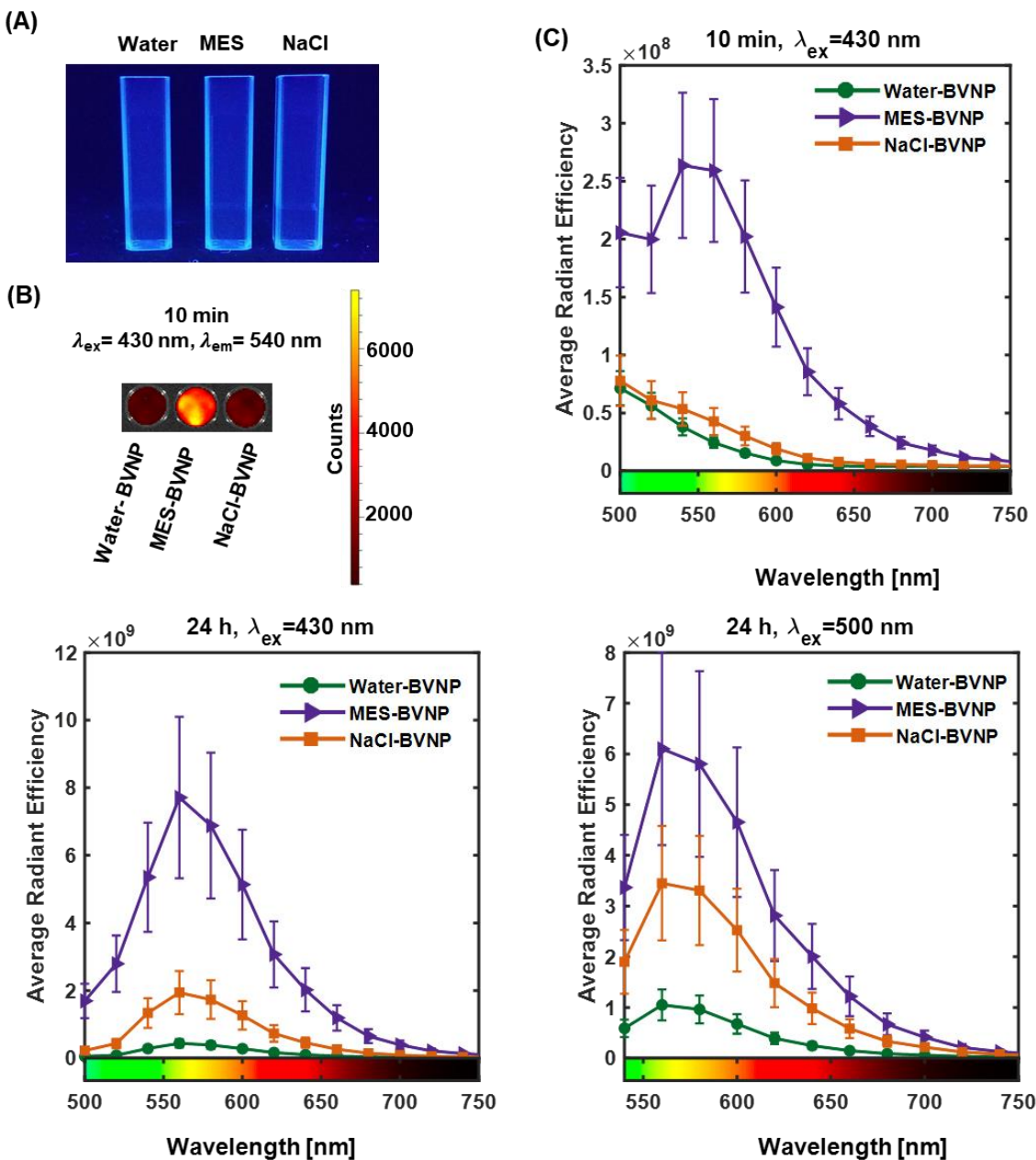
Figure D2. (A) Water, MES, and NaCl under a 365 nm UV lamp, showing no inherent fluorescence. (B) IVIS image of 10-minute BVNPs for an excitation wavelength of 430 nm and an emission wavelength of 540 nm. (C) Average radiant efficiency as a function of emission wavelength for a variety of excitation wavelengths, nanoparticle compositions, and dilutions. At the 10-minute timepoint, MES-BVNPs display the most red-shifted spectra. In all cases, the MES-BVNPs exhibited higher radiant efficiency than the other NP compositions

374
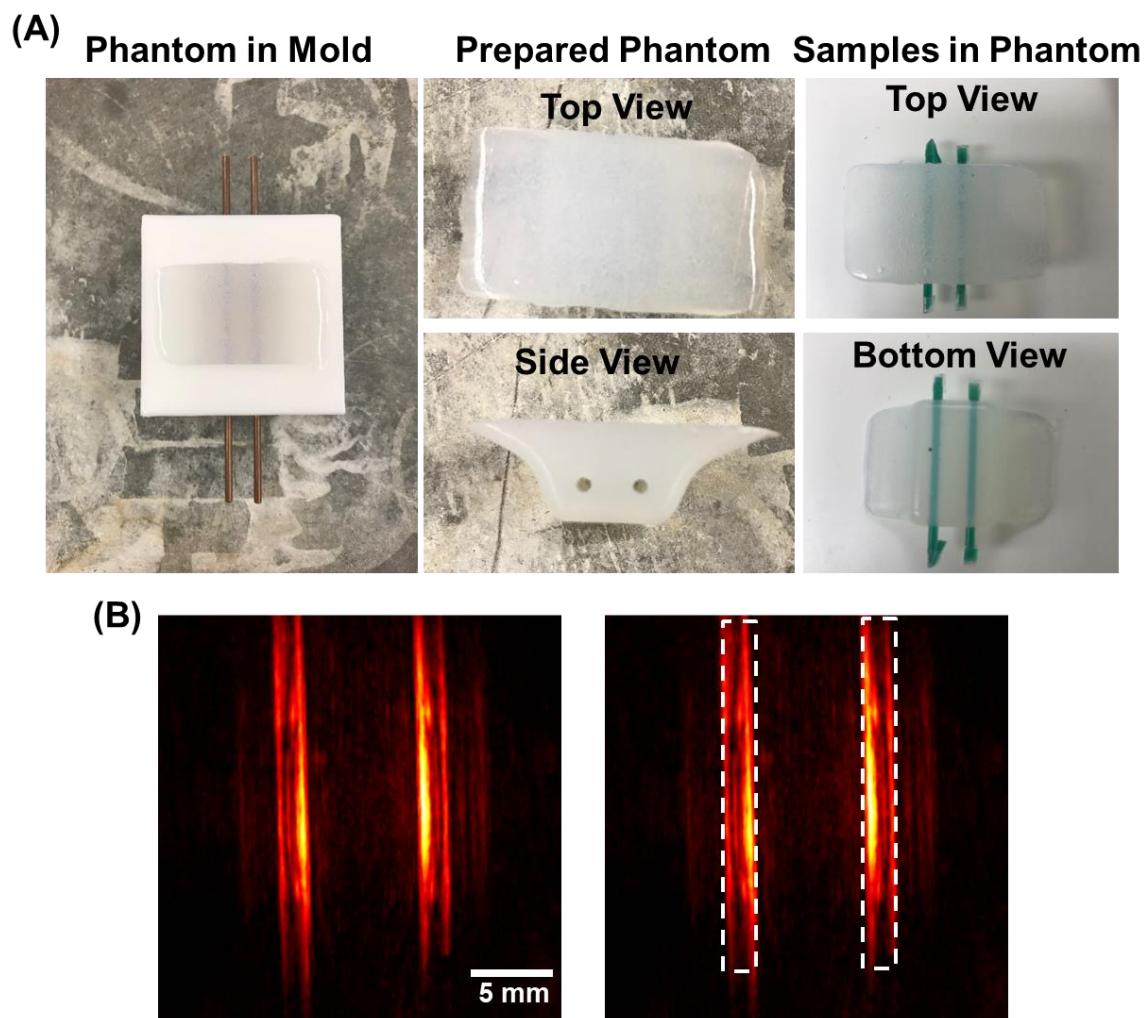
Figure D3. Photoacoustic imaging in tissue phantoms. **(A)** Phantom preparation process and loading of nanoparticle samples in tissue phantom. Agarose solution is poured into a custom Teflon mold. Hypodermic steel tubing is used to obtain holes in which samples can be placed. Samples are pipetted into fluorinated ethylene propylene tubing, which is then inserted into the agarose phantom for imaging experiments. **(B)** Sample photoacoustic images and regions of interest (white dashed boxes) for individual sample tubes.
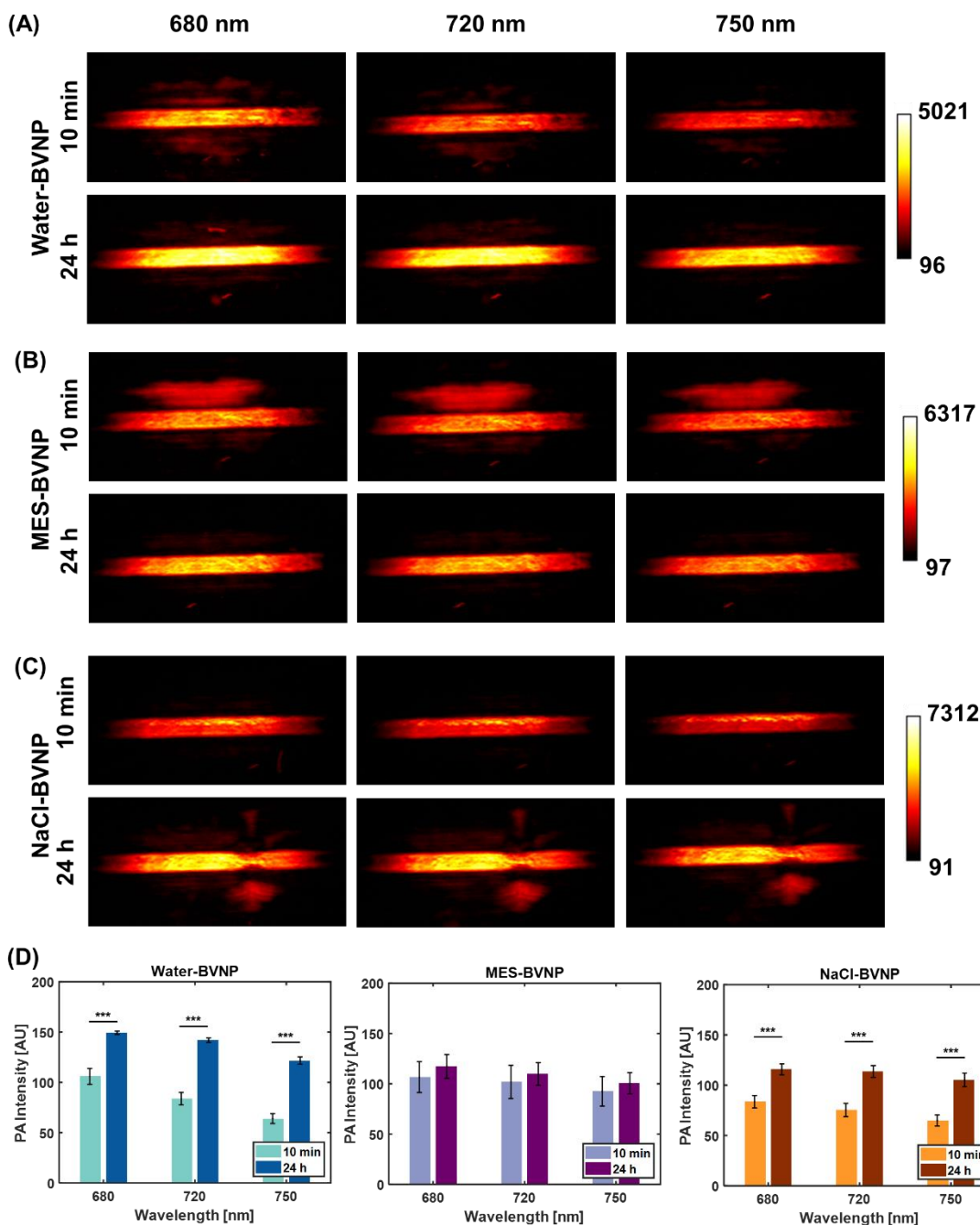
Figure D4. Photoacoustic imaging of 10 min and 24 h BVNPs. (**A**) PA images of 10 min and 24 h water-BVNPs. PA signal is brighter for 24 h water-BVNPs. (**B**) PA images of 10 min and 24 h MES-BVNPs. PA signal intensity does not change significantly with time for MES-BVNPs. (**C**) PA images of 10 min and 24 h NaCl-BVNPs. PA signal is brighter for 24 h NaCl-BVNPs. (**D**) ROI quantification. Water-BVNP and NaCl-BVNP intensities are higher at 24 h than at 10 min. PA intensity does not significantly change with time for MES-BVNPs.
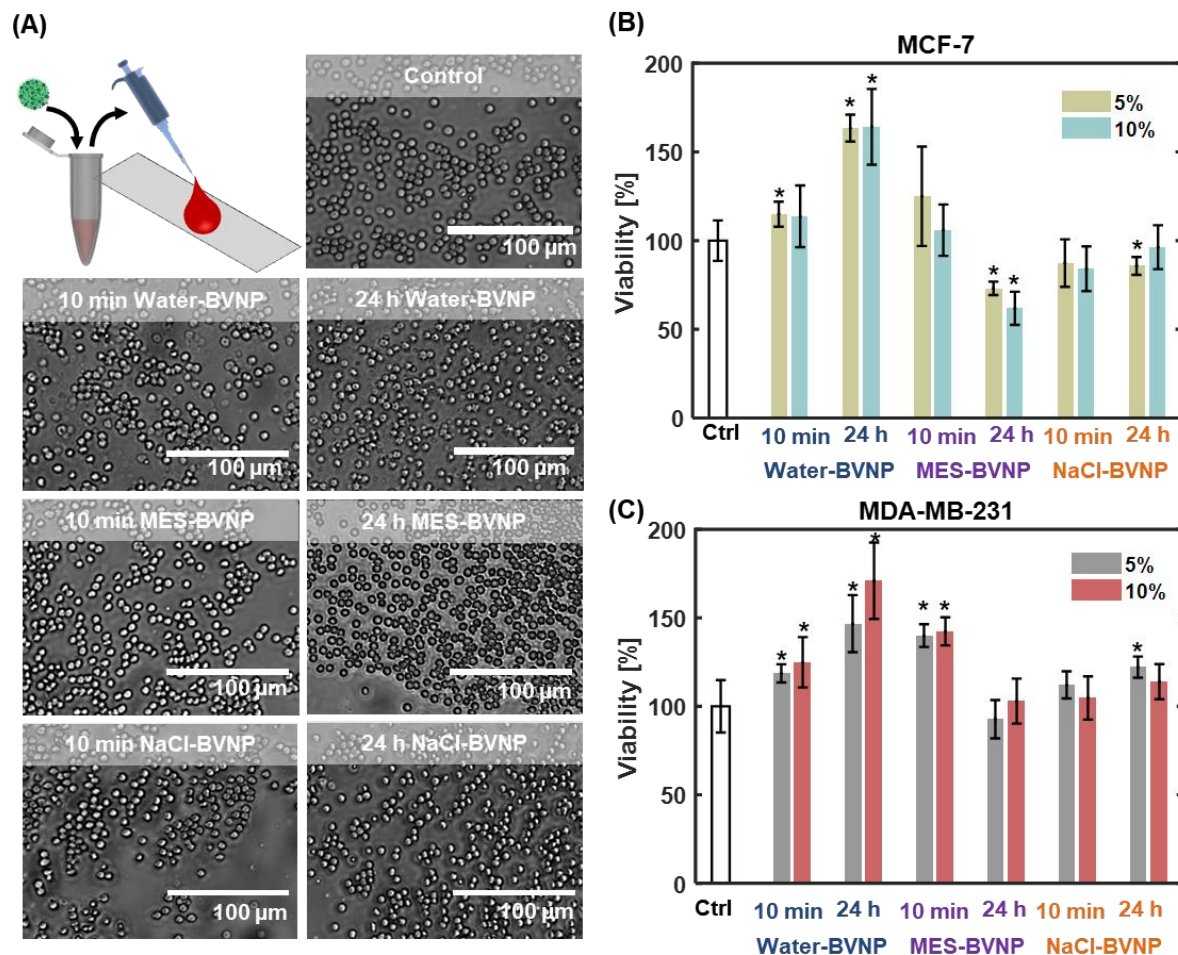
Figure D5. *In vitro* biocompatibility. **(A)** Blood smear images for blood exposed to BVNPs. Blood cells did not exhibit significant morphological changes after exposure to BVNPs, indicating a lack of adverse effects from BVNP exposure. **(B)** MTT results for MCF-7 cells exposed to BVNPs. Cells treated with BVNPs typically showed comparable or greater viability than the untreated control cells. **(C)** MTT results for MDA-MB-231 cells exposed to BVNPs. Cells treated with BVNPs showed comparable or greater viability than the untreated control cells.
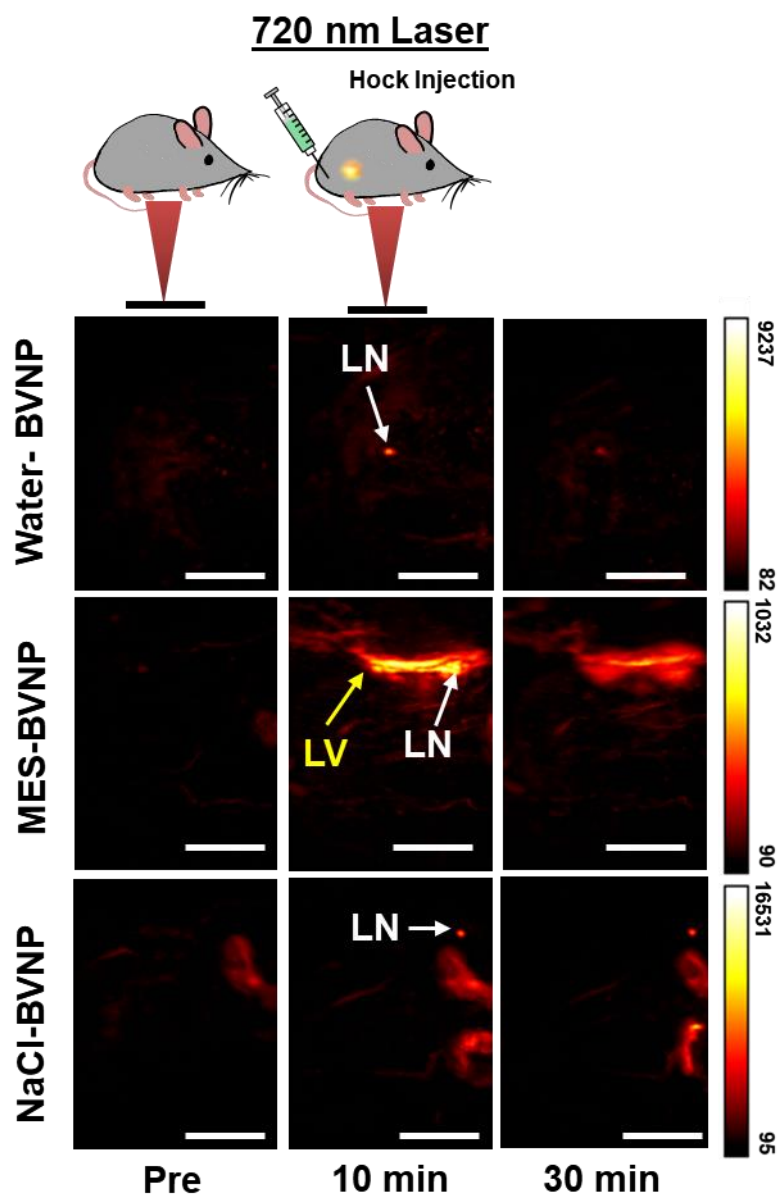
Figure D6. Photoacoustic Imaging of sentinel lymph nodes using BVNPs. 720 nm wavelength photoacoustic images of mice before nanoparticle injection, 10 min after injection, and 30 min after injection. An increase in PA signal intensity is observed post-injection, and nonspecific accumulation of BVNPs can be observed in lymph nodes. White scale bars represent 5 mm.
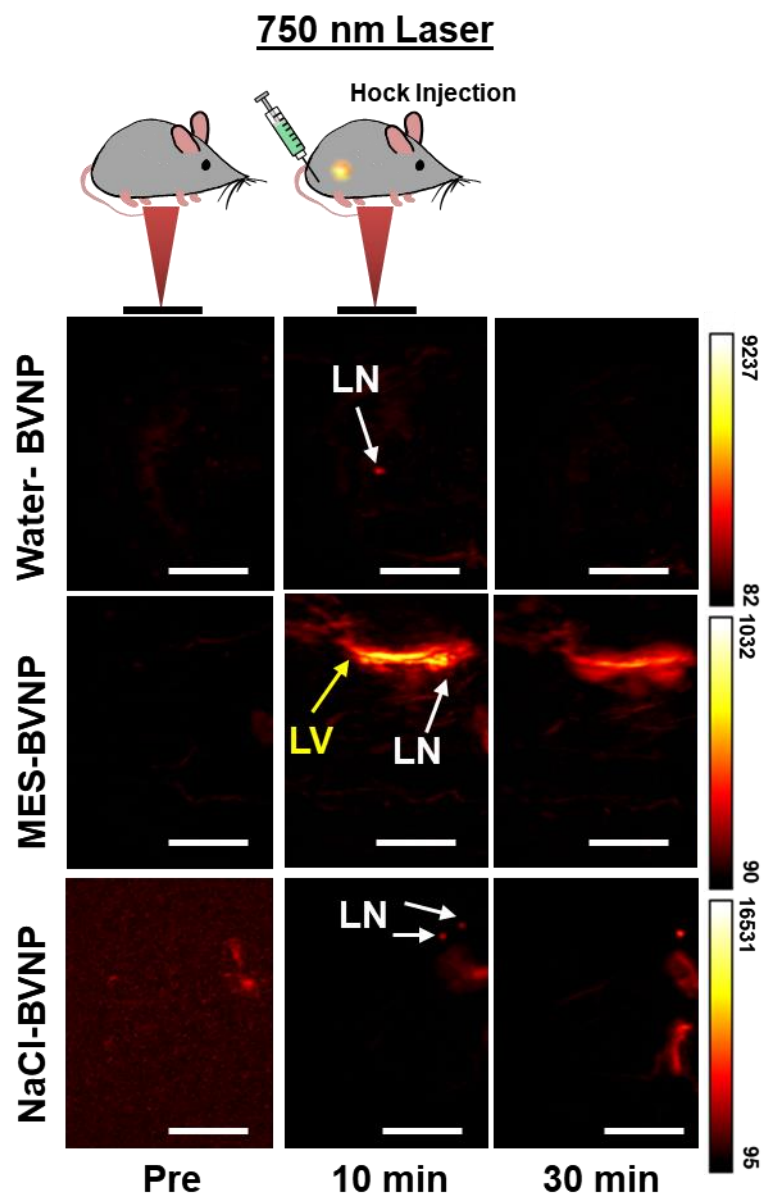
Figure D7. Photoacoustic Imaging of sentinel lymph nodes using BVNPs. 750 nm wavelength photoacoustic images of mice before nanoparticle injection, 10 min after injection, and 30 min after injection. An increase in PA signal intensity is observed post-injection, and nonspecific accumulation of BVNPs can be observed in lymph nodes. White scale bars represent 5 mm.
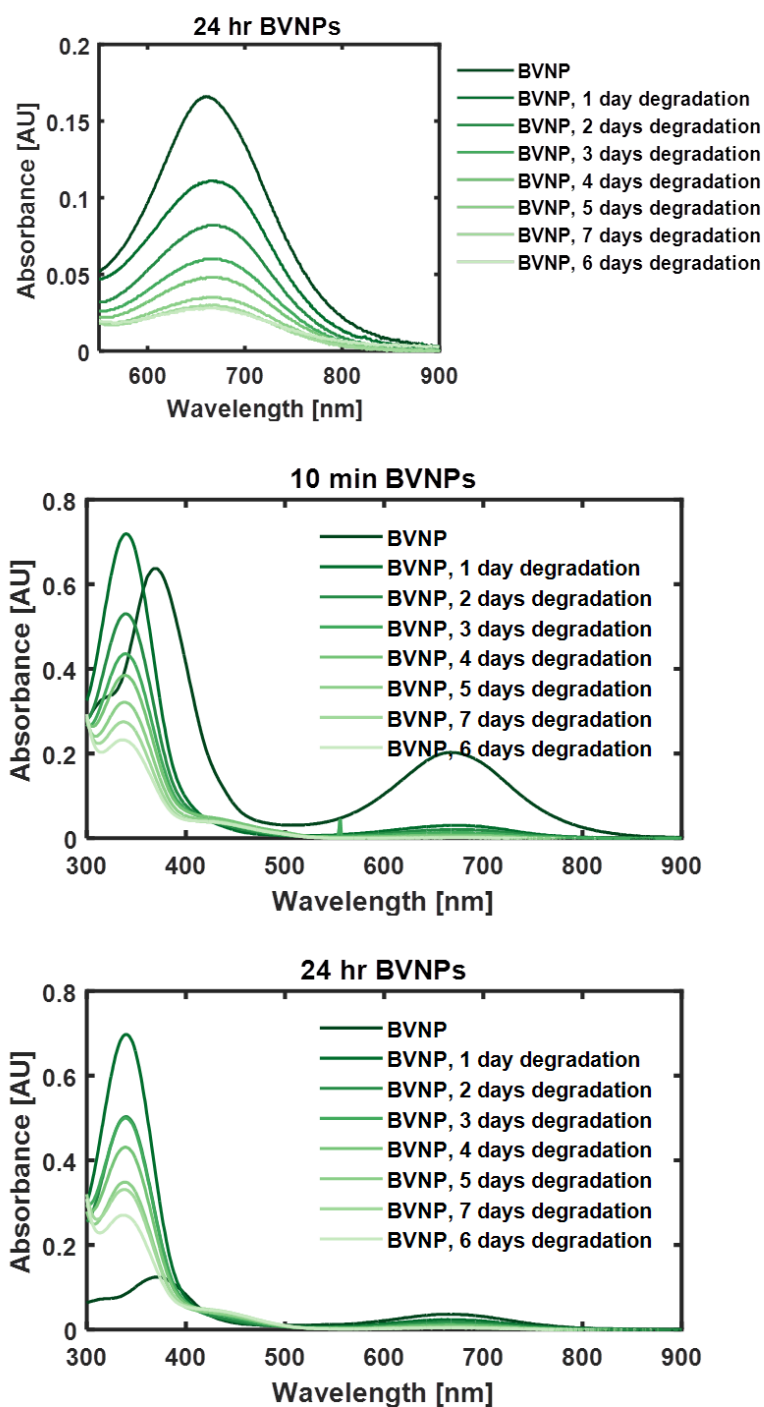
Figure D8. UV-Vis spectra for degradation study on 10-min and 24-hour water-BVNPs
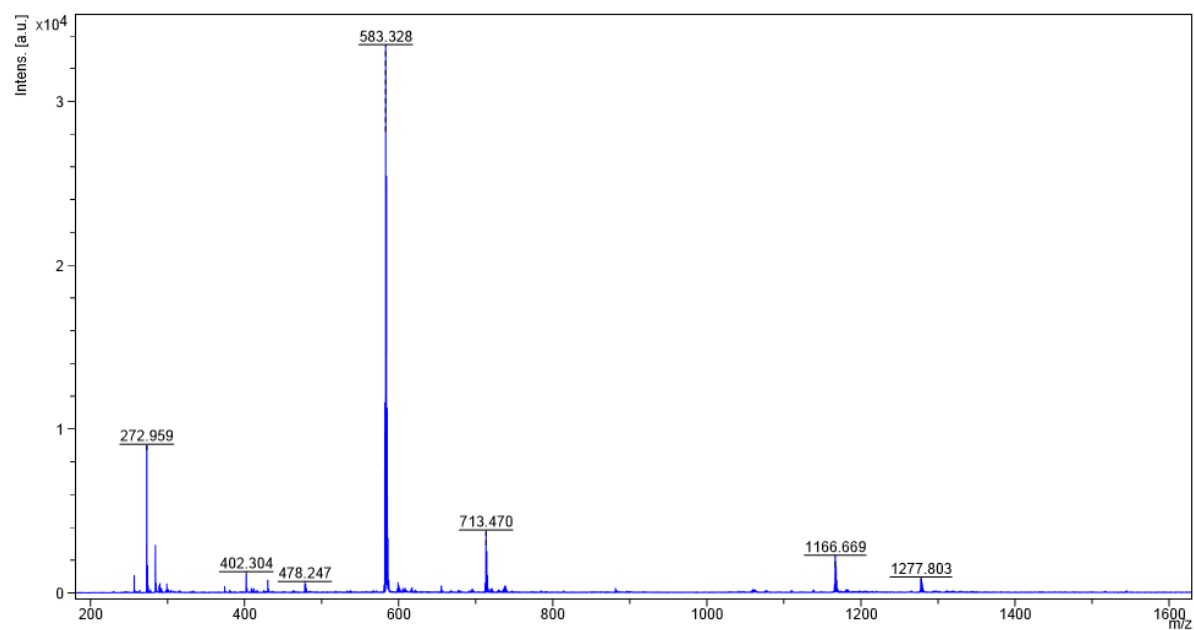
Figure D9. Mass spectrometry results for 10 min Water-BVNPs
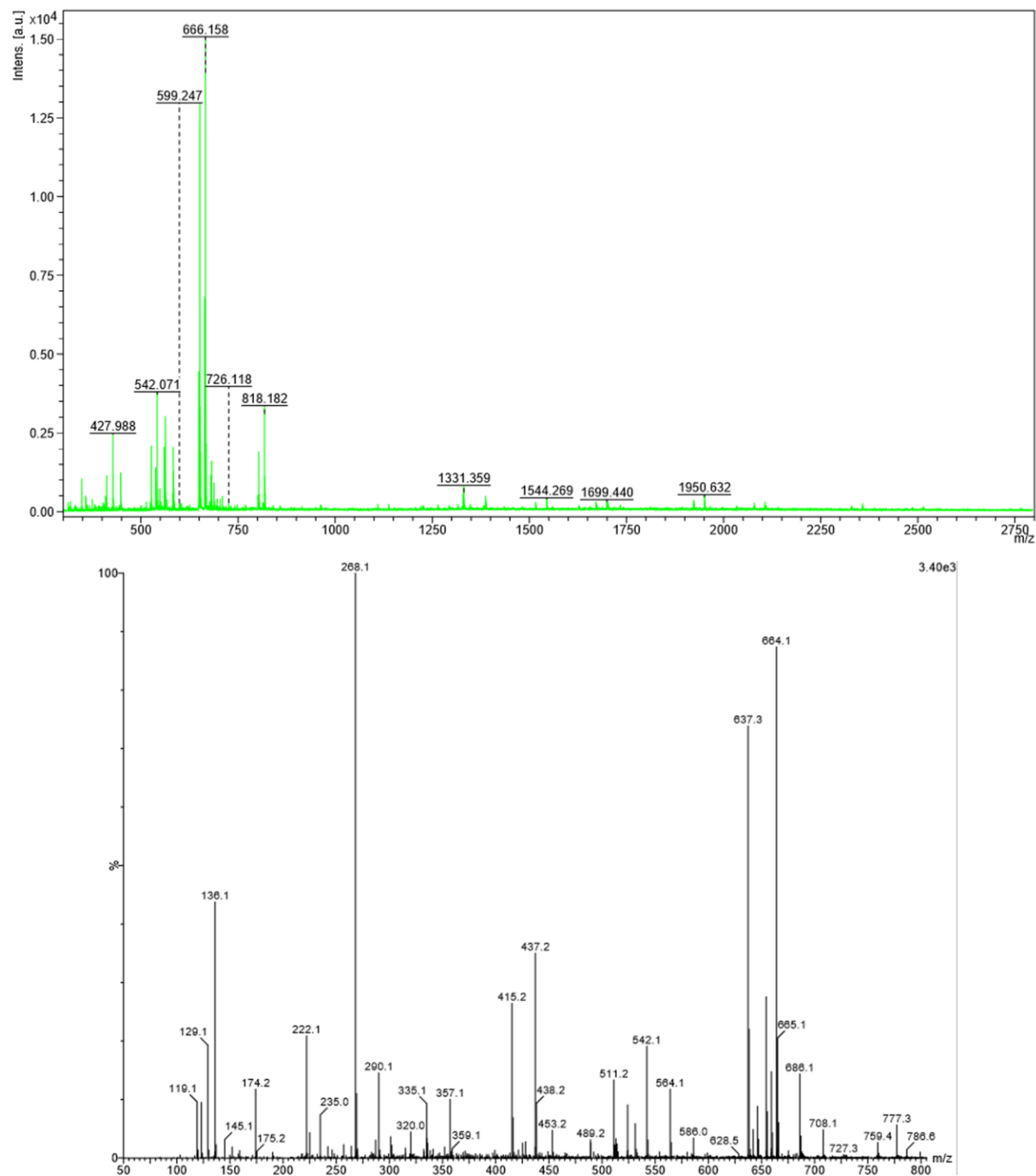
Figure D10. Mass Spectrometry results for 10 min Water-BVNPs after 5 days of degradation. Bottom spectra shows data for lower m/z range
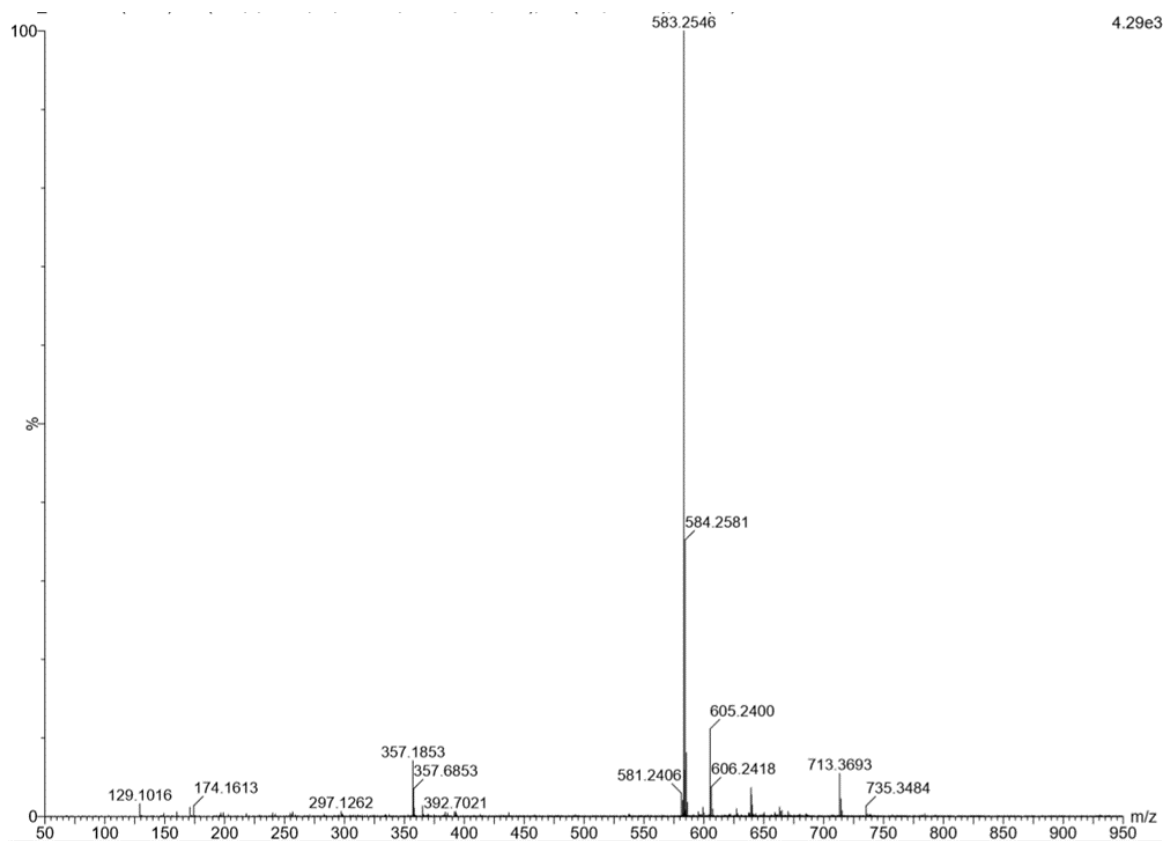
Figure D11. Mass Spectrometry results for 10 min NaCl-BVNPs prior to degradation.
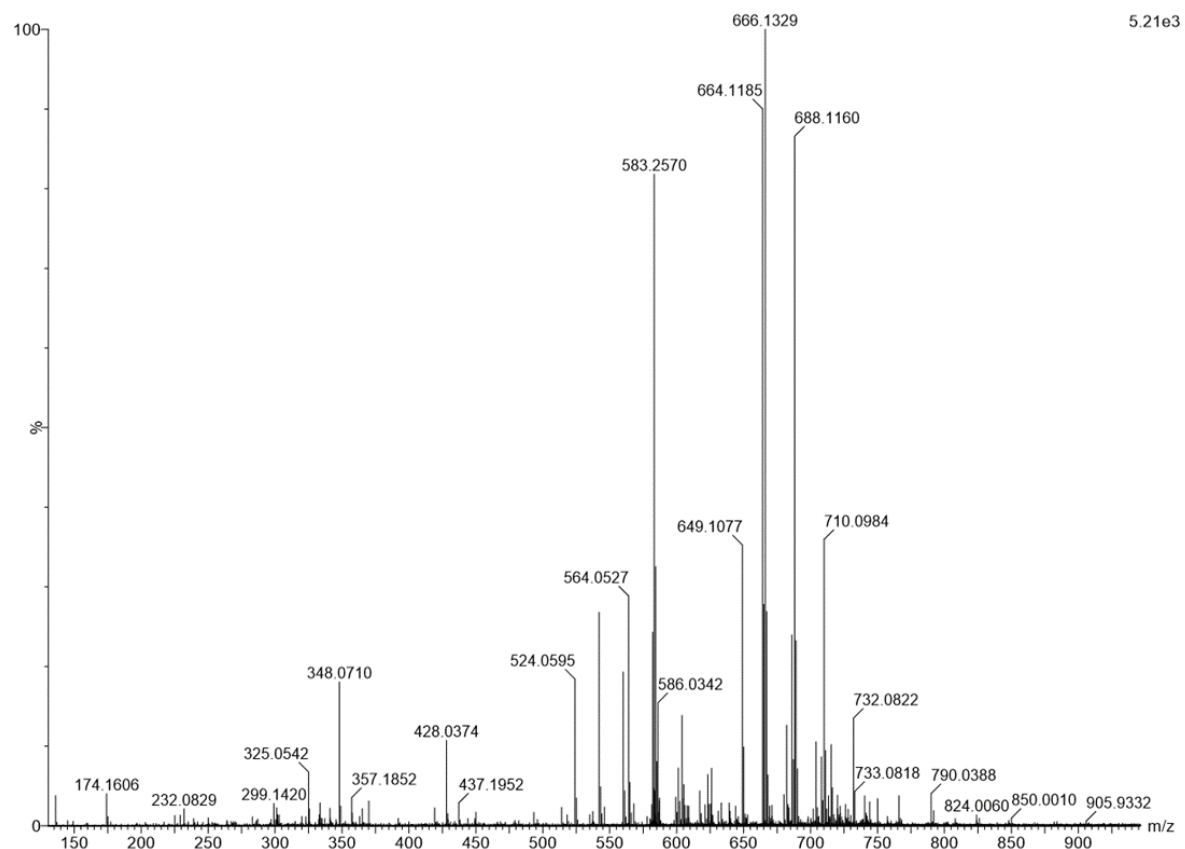
Figure D12. Mass Spectrometry results for 10 min NaCl-BVNPs after 5 days of degradation.
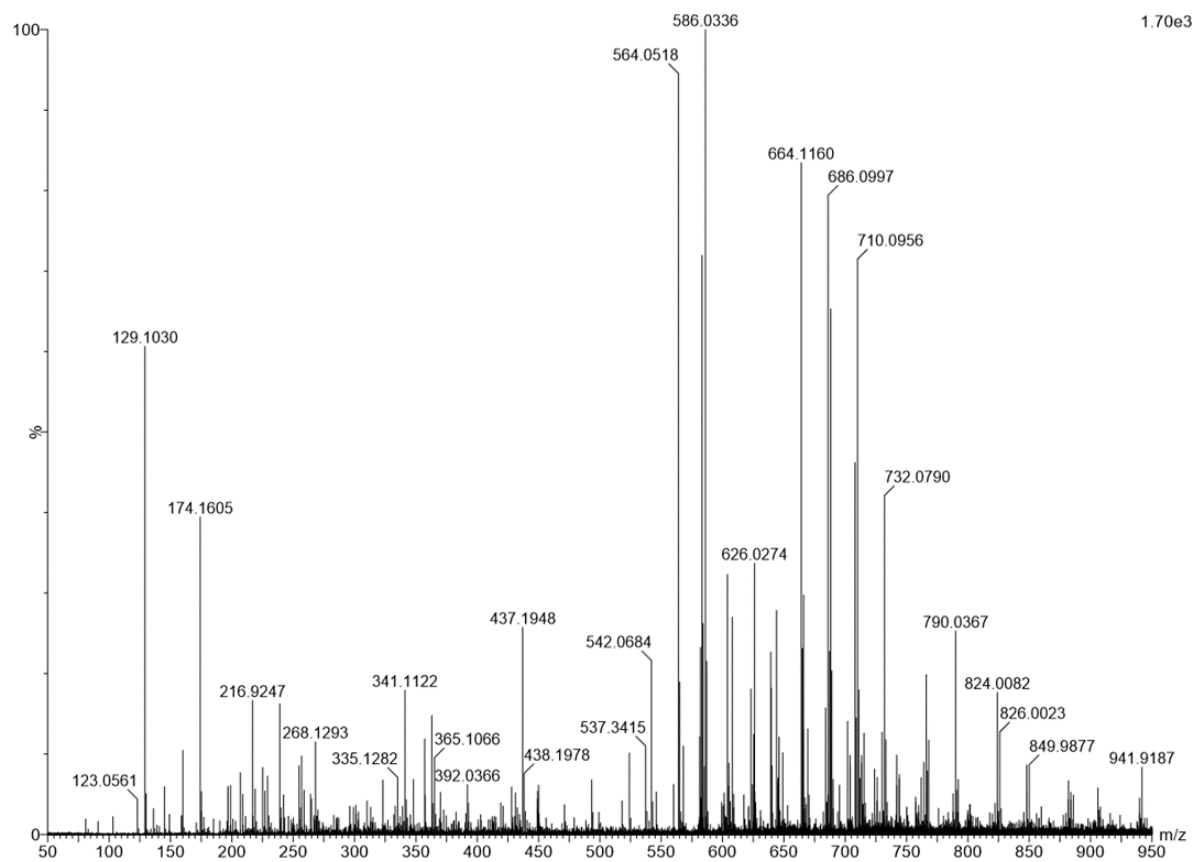
Figure D13. Mass Spectrometry results for 24 h NaCl-BVNPs after 5 days of degradation
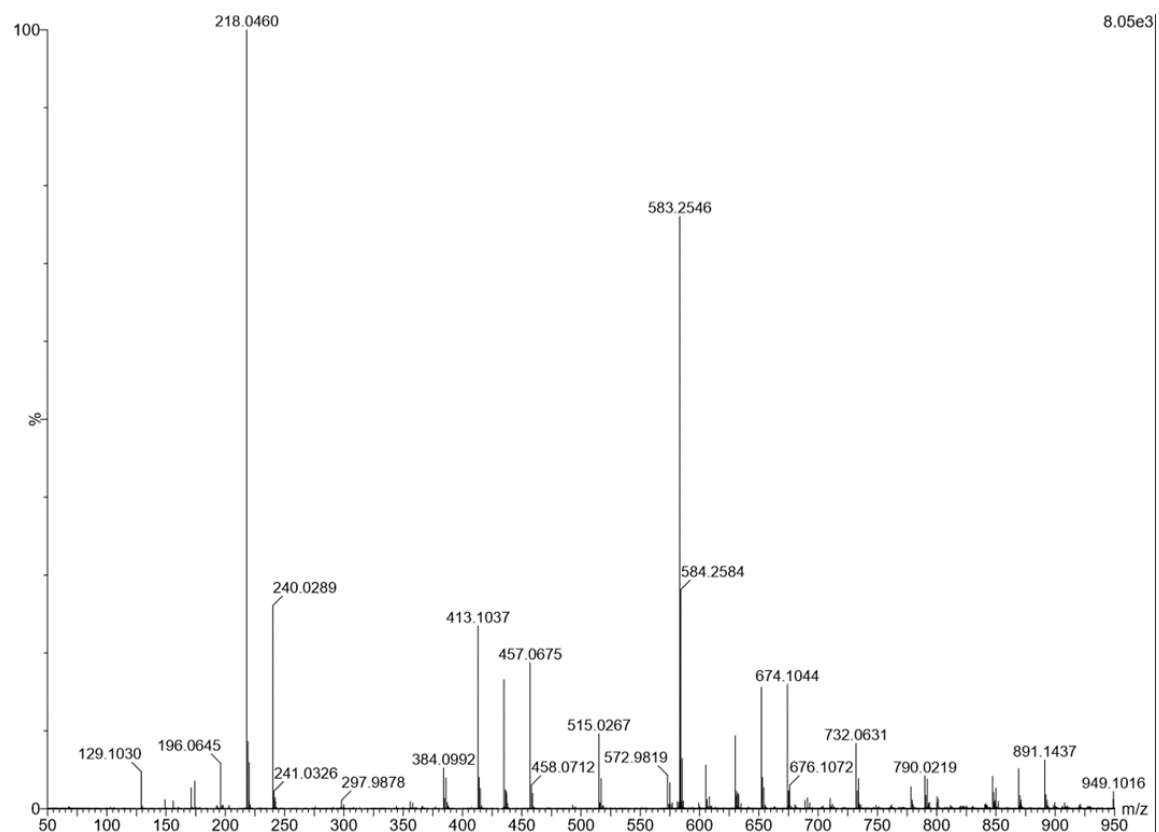
Figure D14. 10 min MES-BVNPs before degradation
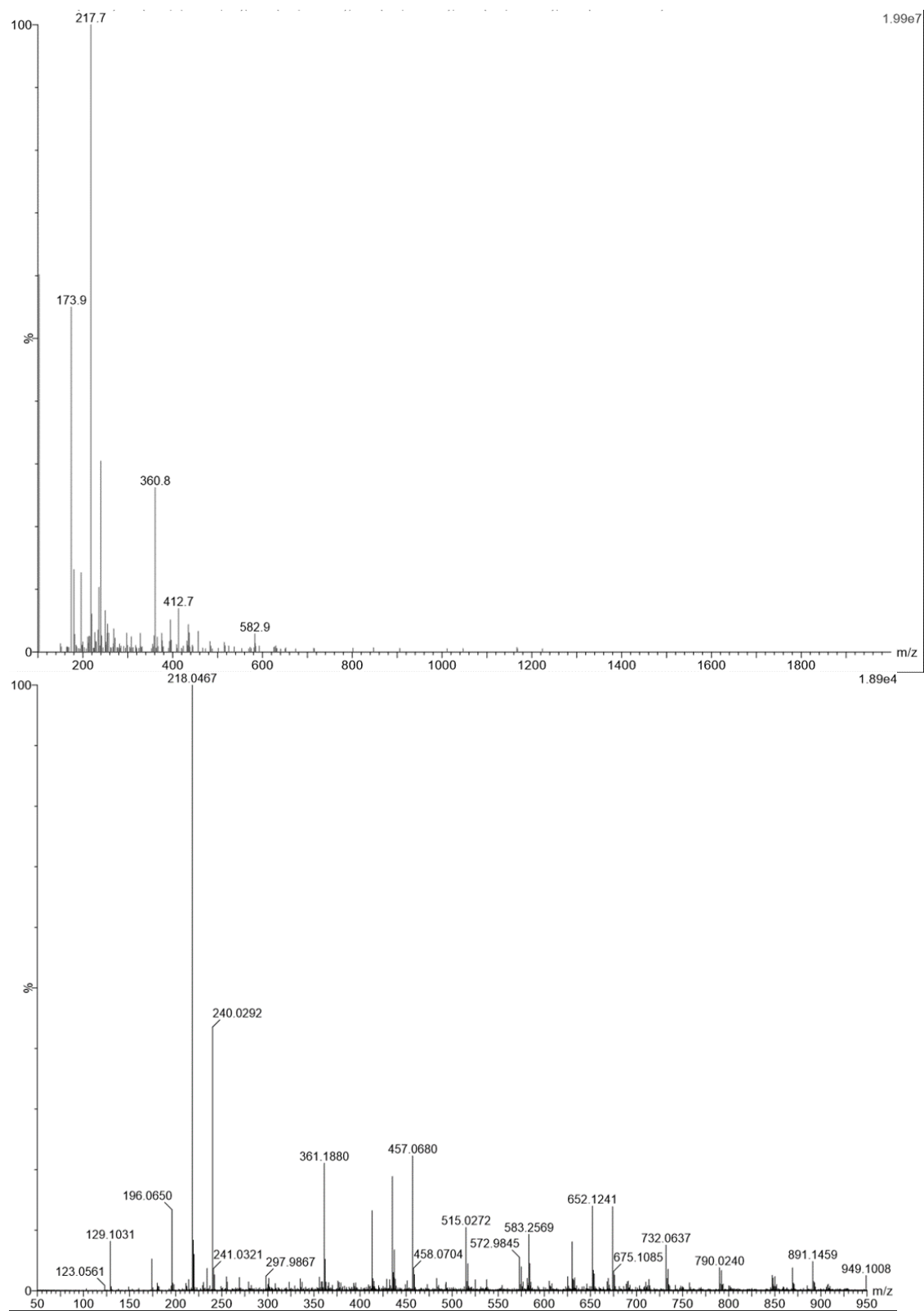
Figure D15. 10 min MES-BVNPs after 13 days degradation. Bottom spectra shows lower m/z range.
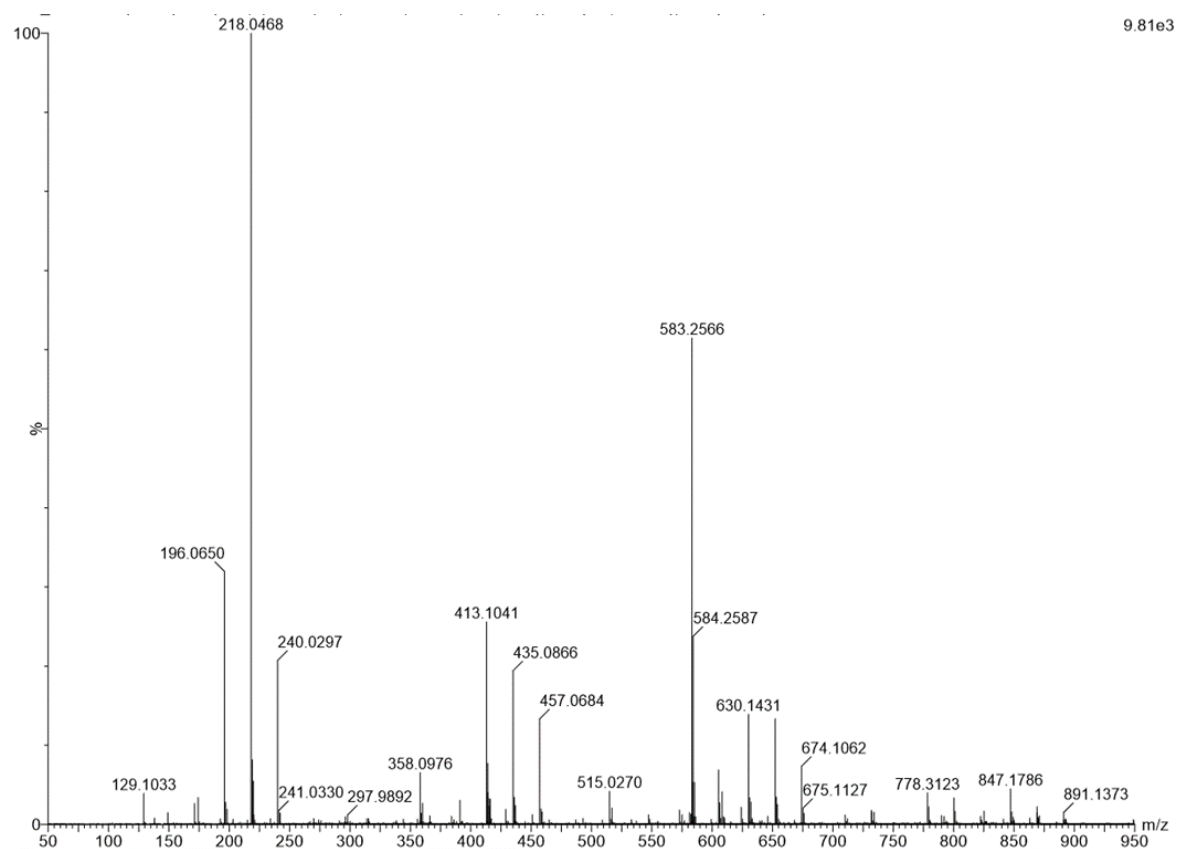
Figure D16. 24 h MES-BVNPs before degradation
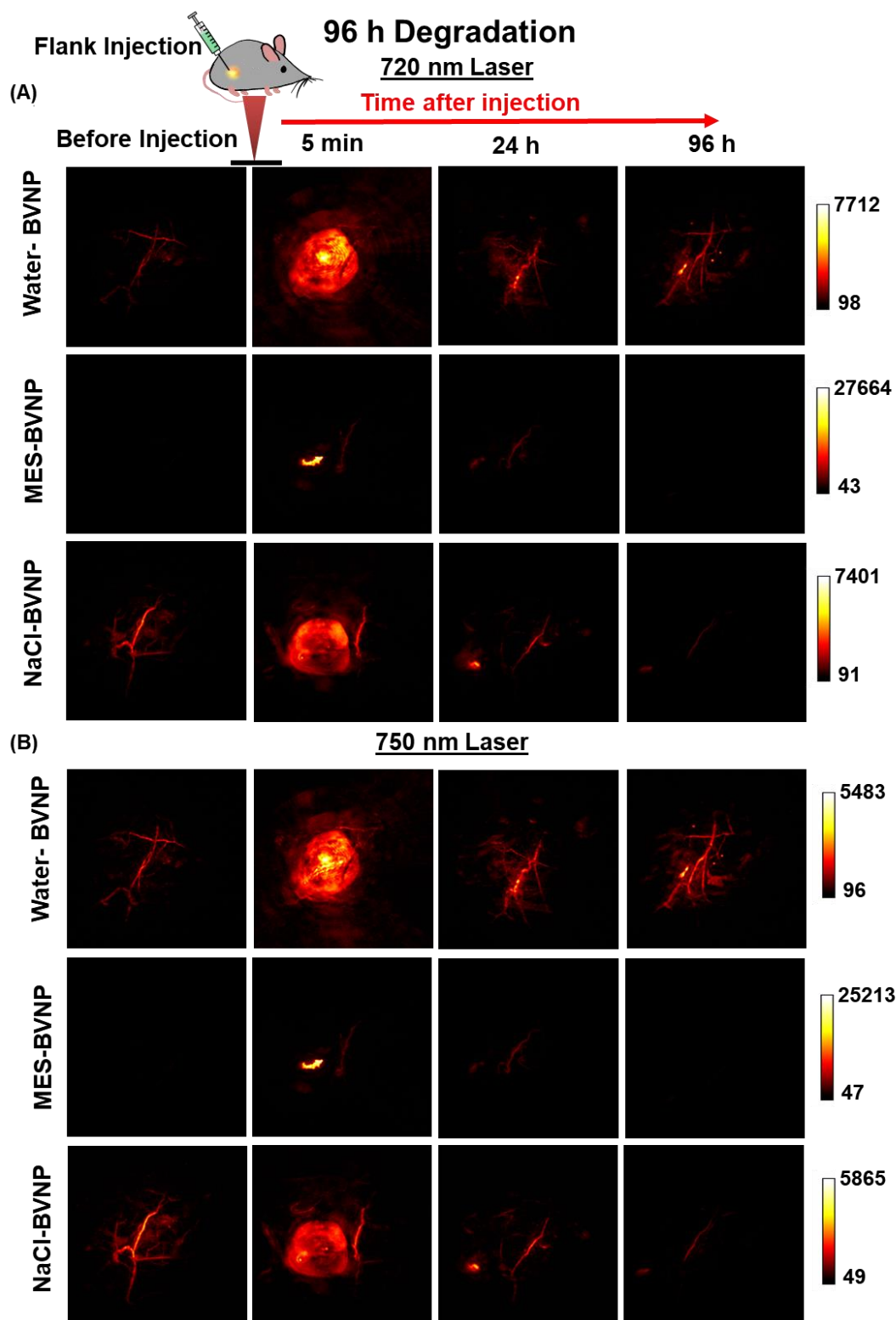
Figure D17. 96 h *in vivo* degradation at higher wavelengths. (**A**) PA images acquired at 720 nm. (**B**) PA images acquired at 750 nm.
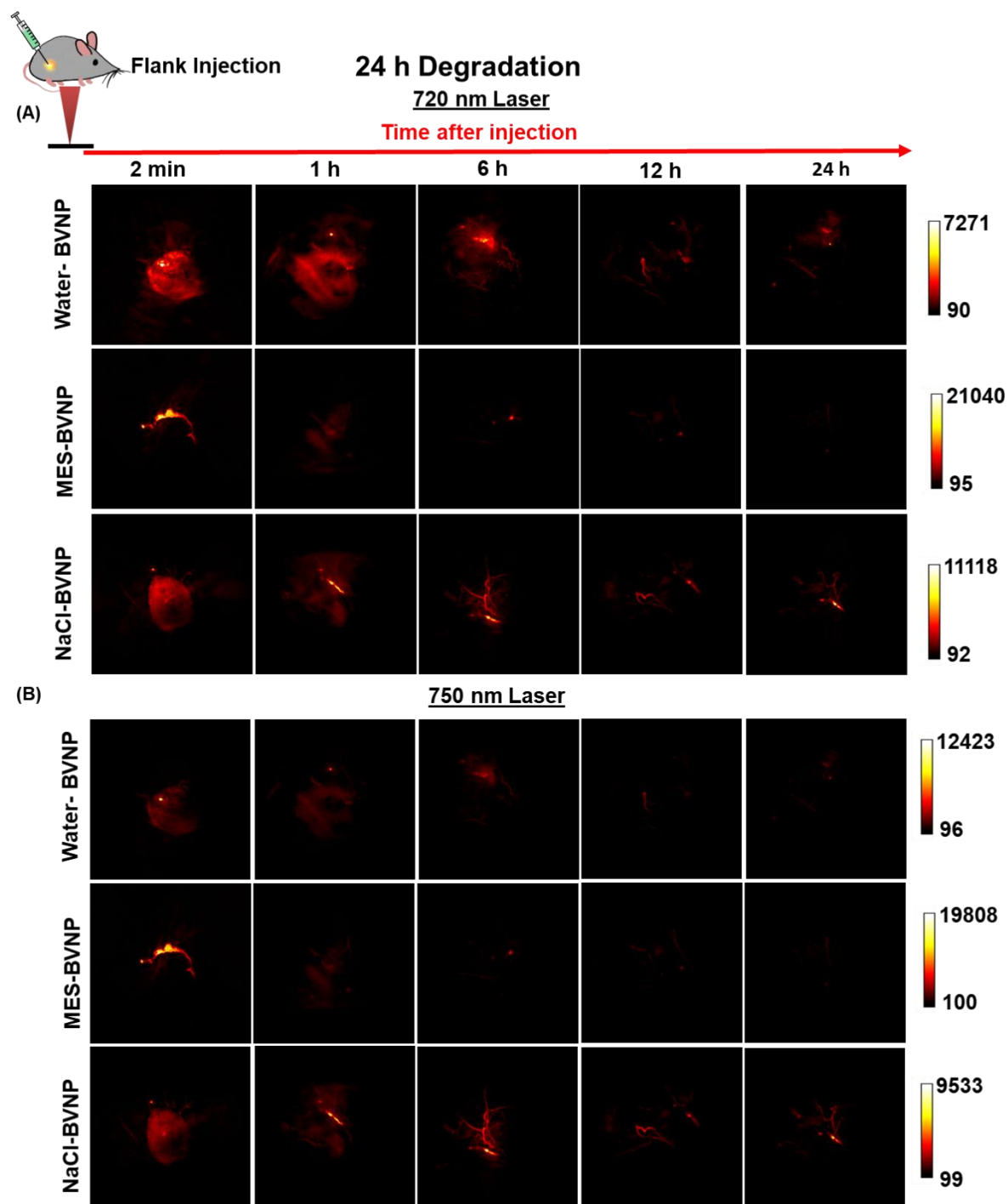
Figure D18. 24 h *in vivo* degradation at higher wavelengths. **(A)** PA images acquired at 720 nm. **(B)** PA images acquired at 750 nm.

Mass Spectrometry Calculations
10-min water-BVNPs after 5 days degradation
$(135 \times 3) + Na^+ = 428$
$(135 \times 4) + 2H^+ = 542$
$178 + 177 + 135 + 137 + K^+ = 666$
$(177 \times 3) + (135 \times 2) + NH_4^+ = 819$
$(177 \times 5) + 137 + (135 \times 2) + K^+ = 1331$
$(177 \times 3) + (135 \times 5) + 178 + 137 + Na^+ = 1544$
$(178 \times 8) + (137 \times 2) + H^+ = 1699$
$(177 \times 4) + (135 \times 7) + (137 \times 2) + Na^+ = 1950$

24-hour water-BVNPs after 5 days degradation
$(177 \times 2) + 178 + NH_4^+ = 550$
$177 + 178 + 135 + 137 + K^+ = 666$
$(178 \times 3) + (135 \times 2) + H^+ = 805$

10 min NaCl-BVNPs after 5 days degradation
$(135 \times 3) + Na^+ = 428$
$(137 \times 3) + 135 + Na^+ = 564$
$(177 \times 2) + 137 + 135 + Na^+ = 649$
$178 + 177 + (135 \times 2) + K^+ = 664$
$178 + 177 + 135 + 137 + K^+ = 666$
$177 + (178 \times 2) + 137 + NH4^+ = 688$
$(177 \times 3) + 178 + H^+ = 710$
$(177 \times 3) + 178 + Na^+ = 732$

24 h NaCl-BVNPs after 5 days degradation
$(135 \times 4) + 2H^+ = 542$
$(137 \times 3) + 135 + Na^+ = 564$
$178 + (135 \times 2) + 137 = 586$
$(137 \times 2) + 177 + 135 + NH4^+ = 604$
$178 + 177 + (135 \times 2) + H^+ = 626$
$178 + 177 + (135 \times 2) + K^+ = 664$
$177 + (178 \times 2) + 135 + NH4^+ = 686$
$(177 \times 4) = 708$
$(177 \times 3) + 178 + H^+ = 710$
$(177 \times 3) + 178 + Na^+ = 732$
$(178 \times 2) + (137 \times 3) + Na^+ = 790$
$(178 \times 3) + 137 + 135 + NH4^+ = 824$

10 min MES-BVNPs after 13 days degradation

(calculations for full mass range)
$(178 \times 2) + 4H^+ = 360$
$(177 \times 2) + 137 + Na^+ = 514$
$(177 \times 2) + (137 \times 2) + H^+ = 629$

(calculations for lower mass range)
178 + (137 x 2) + 5H+ = 457
178 + 177 + 137 + Na+ = 515
178 + 177 + (137 x 2) + H+ = 630
(137 x 2) + 178 + 177 + Na+ = 652
(137 x 3) + (178 x 2) + Na+ = 790

24 h MES-BVNPs after 13 days degradation
(178 x 2) + 5H+ = 361
178 + (137 x 2) + 5H+ = 457
178 + 177 + 137 + Na+ = 515
178 + 177 + (137 x 2) + H+ = 630
(137 x 2) + 178 + 177 + Na+ = 652
(178 x 3) + 137 + 3H+ = 674
(137 x 3) + (178 x 2) + Na+ = 790

Materials

Biliverdin hydrochloride was purchased from Frontier Scientific. Cobalt (II) chloride was purchased from Alfa Aesar. Copper (II) chloride, iron (III) chloride, and manganese (II) chloride were purchased from Sigma Aldrich.

Methods

Biliverdin chelation and UV irradiation experiments

Biliverdin hydrochloride was dissolved overnight in 10 mL of water at a concentration of 1 mg/mL. Samples were protected from light unless otherwise noted. Prior to metal chelation, the pH of the biliverdin solution was raised to a pH of 10 using 1.0 M NaOH. 500 µL of pH-adjusted biliverdin solution was placed in each 4-mL scintillation vial, and 50 µL of the corresponding metal chloride solution was added to each scintillation vial. Vials were shaken, after which the samples were either protected from light and placed under ambient conditions (-UV), or placed beneath a 365 nm UV lamp (VWR UV-AC Hand Lamp, Cat. # 89131-492, 115V-60Hz, 0.16 Amps) for 72 hours.

Metal chloride solutions

Metal chloride solutions were prepared by dissolving each metal salt for a final concentration of 2.306 mmol/liter.

Biliverdin nanoparticle synthesis

Biliverdin hydrochloride was dissolved overnight in 10 mL of NaCl solution (0.154 moles/Liter) at a concentration of 1 mg/mL. Samples were protected from light unless otherwise noted. 6.7 mg of 1-Ethyl-3-(3-dimethylaminopropyl)carbodiimide (EDC) and 4.0 mg of N-Hydroxysuccinimide (NHS) were then added and allowed to stir for 10 minutes. 3.5 µL 2 2'-(ethylenedioxy)bis(ethylamine) was then added to the solution to begin the reaction. BVNPs were

allowed for form for 24 hours, after which they were dialyzed for a further 24 hours against 500 mL of NaCl solution (0.154 moles/Liter) in dialysis cassettes with a molecular weight cutoff (MWCO) of 10,000 kDa.

Biliverdin nanoparticle chelation and UV irradiation experiments

Metal chloride solutions for BVNPs were prepared as described above. Prior to metal chelation, the pH of the BVNP solution was raised to a pH of 10 using 1.0 M NaOH. 500 µL of BVNP solution was placed in each 4-mL scintillation vial, and 50 µL of the corresponding metal chloride solution was added to each scintillation vial. Vials were shaken, after which the samples were either protected from light and placed under ambient conditions (-UV), or placed beneath a 365 nm UV lamp (VWR UV-AC Hand Lamp, Cat. # 89131-492, 115V-60Hz, 0.16 Amps) for 72 hours.

UV-Visible Spectroscopy

UV-visible spectra were collected for wavelengths ranging from 230 nm to 900 nm using a Thermo Scientific Genesys 10S UV−Vis spectrophotometer. The baseline measurement was taken using 1 mL of water for BV samples, and 1 mL of NaCl solution (0.154 moles/Liter) for BVNP samples. Data was collected for a dilution of 10 µL of sample to 900 µL of diluent for BV samples, and 10 µL of sample to 900 µL of diluent for BVNP samples.

Fluorescence Spectroscopy

Fluorescence spectra were acquired for undiluted 100 µL samples of each type. Excitation wavelengths of 365 nm and 488 nm were used. Fluorescence spectra were collected on a TECAN infinite M200PRO.

Fourier Transform Infrared Spectroscopy

FT-IR measurements were taken using the smart refractor accessory on a Thermo Nicolet Nexus 670 FT-IR. Samples were prepared by depositing the BV or BVNP solutions on Kevley MirrIR corner frosted FT-IR slides. Samples were dried under vacuum prior to collection of spectra.

Mass Spectrometry

Mass spectra were acquired using electrospray ionization (ESI) for m/z of 50 to 950 for BV samples, and 400 to 1500 for BVNP samples.

Circular Dichroism

Circular dichroism spectra were collected on a Jasco 710 CD spectrometer using a 2 mm quartz cuvette. Samples were diluted in water for these measurements, and multiple spectra were collected per sample.

Transmission Electron Microscopy

TEM images were acquired with an acceleration voltage of 200 keV on a JEOL Cryo 2100 TEM. Microscopy samples were prepared on 300-mesh to 400-mesh carbon-coated copper TEM grids. Samples were diluted (10 µL BVNP solution, 40 µL to 90 µL water). 2.5 µL of diluted solution was drop-cast onto each TEM grid and allowed to settle for 2 min, after which the excess liquid was wicked away with qualitative filter paper. Samples were then placed within centrifuge tubes and stored dry until the imaging session.

Density Functional Theory

The chemical structures were initially energy optimized and the HOMO-LUMO surfaces were then calculated from their energy minimized geometries using a general ab initio quantum chemistry package, General Atomic and Molecular Electronic Structure System (GAMESS) program.[464] We used B3LYP functional while performing the density functional theoretical (DFT)

calculations with 6-31G(d) as the basis set. Pople N31 was used for the polar groups. The highest occupied molecular orbital energy (E_{HOMO}), the lowest unoccupied molecular orbital energy (E_{LUMO}) and the energy gap between E_{LUMO} and E_{HOMO} was also calculated and represented as ΔE.

Single-particle Experiments and Analysis

Samples were prepared by drying 0.3 µL of diluted BVNP solutions on clean glass coverslips cleaned as done previously.[465] The coverslip was then kept in a clean biosafety cabinet for 10 min to allow the droplet to dry. All dilutions were made in degas-MiliQ water such that there were about 200 particles in single field of view. [243,457] A home-built, objective-based total internal reflection fluorescence microscopy (TIRFM) system was used for imaging single BV particles. A 100X oil immersion objective (100X, N.A. 1.49, oil immersion) was assembled on an inverted microscope. A 488-nm continuous wavelength laser was used as the light source and the power was set at 1.5mW at the back aperture of the objective. A neutral density filter of value 1 was placed in the path of light to control the amount of light going into the microscope. The incident light was directed through the objective via an exciter and a dual-band dichroic filter. Individual particles were seen as bright diffraction limited spots. The luminescence photons from individual BVNPs were collected by the same objective, passing an emitter and captured by an Electron Multiplying Charge Coupled Device (EMCCD) camera. A total of 1000 frames trajectory were acquired for each field of view with an integration time of 100 ms. At least four replicates were measured for each sample and was repeated for another batch of BVNPs.

A home-written script was used to extract the number of particles for each frame. The bleaching curve was generated by plotting the normalized number of particles versus time. The curve was then fitted with a two-component exponential function. The photobleaching lifetime

was extracted from the fitted values. The BV signal (inside the boundary) and background (outside the boundary) were extracted by averaging a total of 100 by 100 pixels in the corresponding area. The net signal of BVs was calculated by subtracting the background from the gross BV signal for each frame. The emission decaying curve was generated by normalizing the maximum net BV signal to 1.0. A script was used to fit the normalized emission decaying curve with a two-component exponential function. The photobleaching lifetime was extracted from the fitted values ($\tau 1$ and $\tau 2$). The two time constants $\tau 1$ and $\tau 2$, as well as their respective weights and the goodness of fit (R2) were calculated using the following equation:

$$f(t) = ae^{\left(\frac{1}{r1}\right)\tau 1} + be^{\left(\frac{1}{r2}\right)\tau 2}$$

(Equation E.1)

Because the variance of the data is larger at the longer timescale than at the shorter timescale, the "Weighted Least Square" fit option was used and each data point was weighted by its variance. Single-particle trajectories were segmented to define the "on" and "off" states based on changepoint analysis.[466,467] The intensity threshold was defined as the mean of the segment with the lowest intensity plus three times the standard deviation of that segment. A segment of the trajectory whose intensity was above this threshold is defined as an "ON" state and its duration as t_{on}. An "OFF" state refers to any segment whose intensity was below the threshold and its duration as t_{off}. An array of t_{on} and t_{off} was collected from each trajectory and pooled for the same type of particle. The power-law distribution of t_{on} and t_{off} were generated by plotting the histogram of pooled data.

Figures
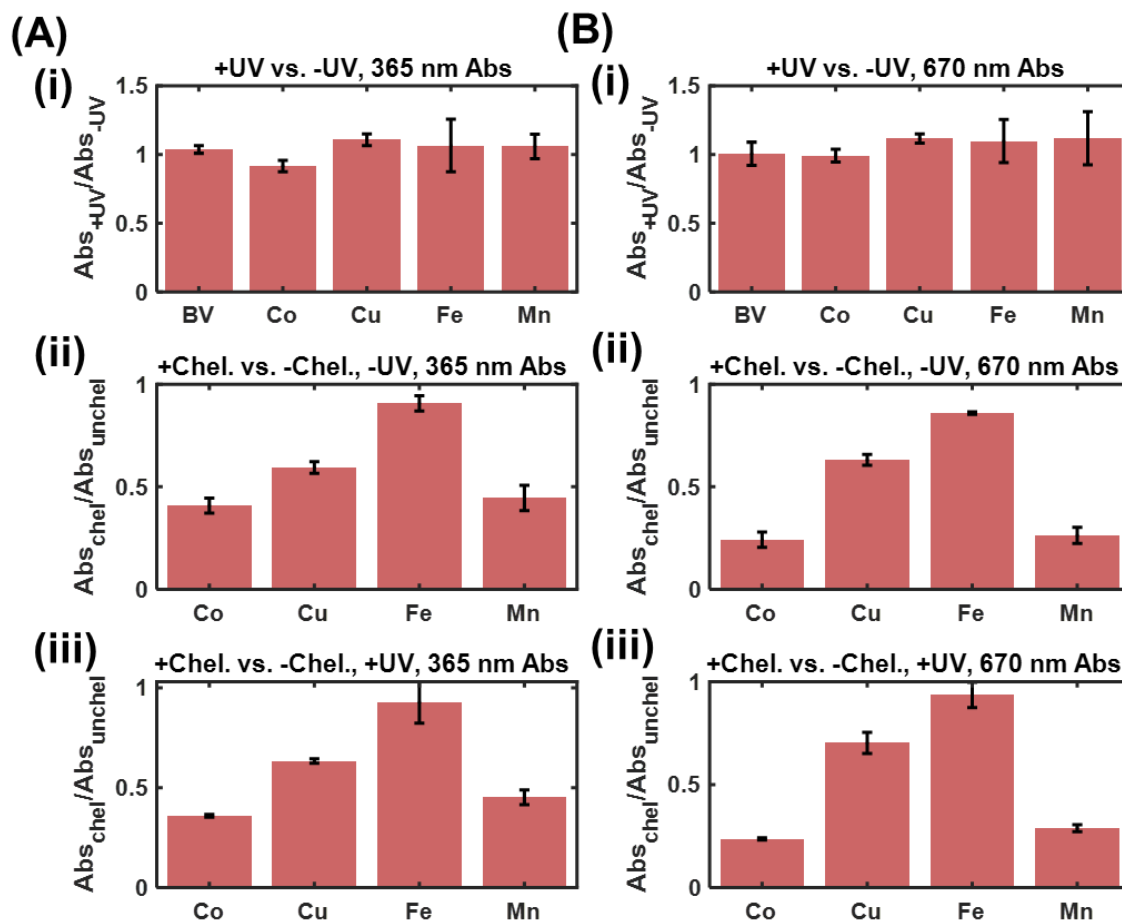

Figure E1. Absorbance ratios for BV. Error bars represent standard deviation across two separate experiments. **(A)** Ratio of 365 nm absorbance for samples **(i)** with and without UV irradiation, **(ii)** with and without metal chelation when no UV irradiation was used, and **(iii)** with and without metal chelation when UV irradiation was used. **(B)** Ratio of 680 nm absorbance for samples **(i)** with and without UV irradiation, **(ii)** with and without metal chelation when no UV irradiation was used, and **(iii)** with and without metal chelation when UV irradiation was used.

398
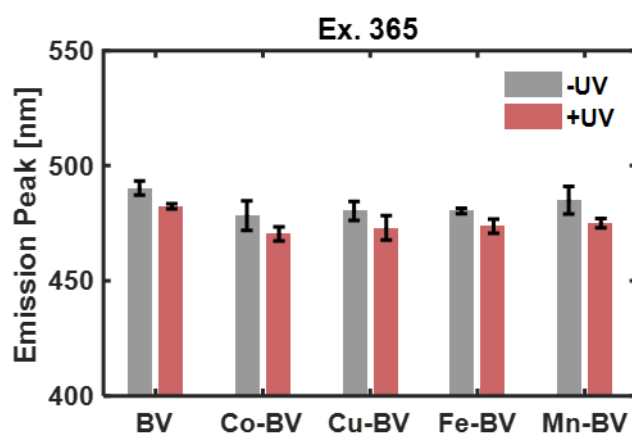
Figure E2. Wavelength of maximum fluorescence (ex. 365 nm) for BV samples before and after UV irradiation. Error bars represent standard deviation obtained with three separate experiments.
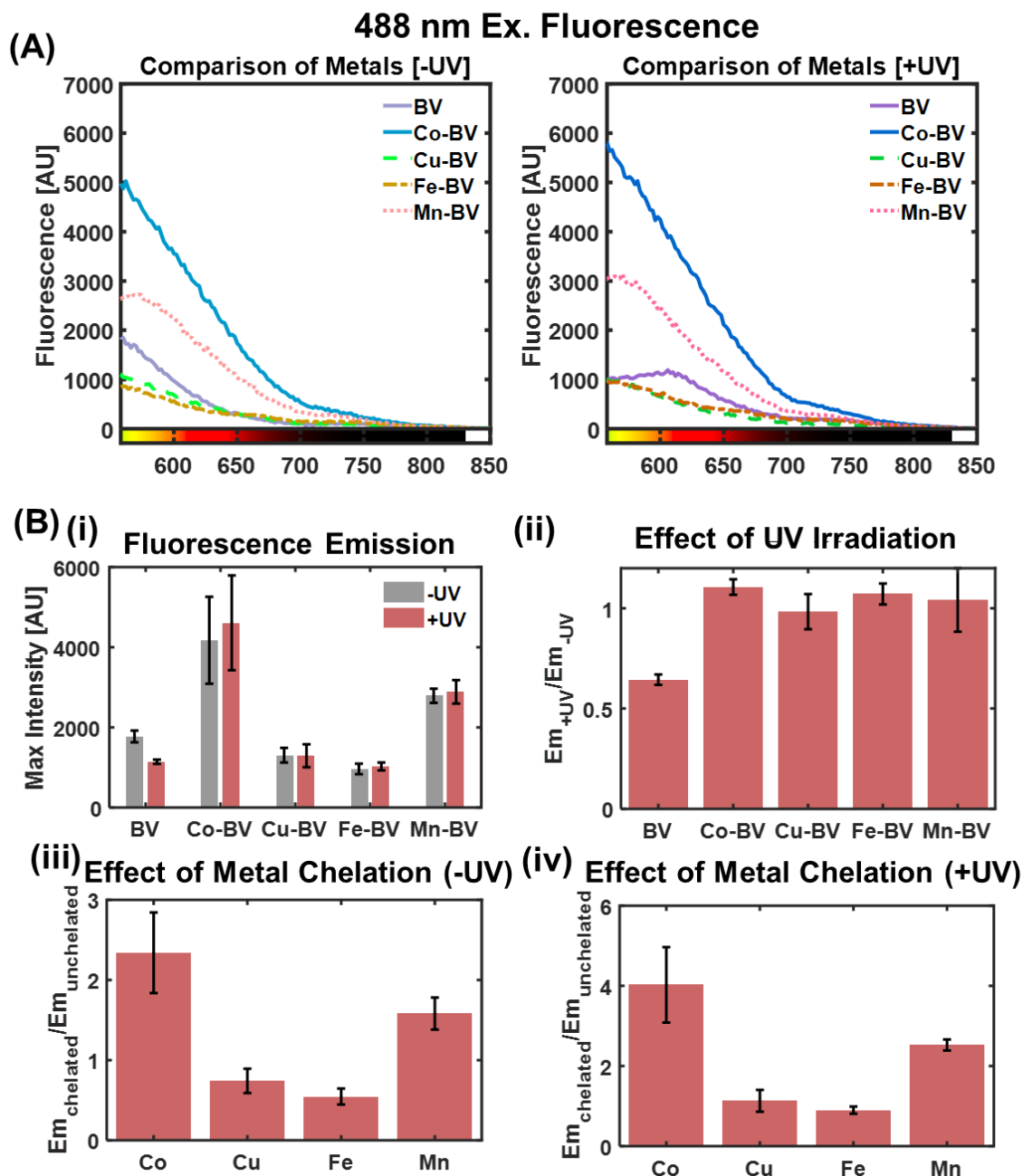
Figure E3. Fluorescence behavior of BV for 488 nm excitation. (**A**) Fluorescence spectra of BV samples without UV irradiation and after 72 h of UV irradiation. An excitation wavelength of 488 nm and gain of 150 was used. (**B**) Average fluorescence for 488 nm excitation. Error bars represent standard deviation across three separate experiments. (**i**) Average fluorescence intensity for BV with and without 72 h UV irradiation. (**ii**) Average ratio of fluorescence intensity with UV irradiation to fluorescence intensity without UV irradiation. (**iii**) Average ratio of fluorescence intensity with metal chelation to fluorescence intensity without metal chelation, in the absence of UV irradiation. (**iv**) Average ratio of fluorescence intensity with metal chelation to fluorescence intensity without metal chelation, after 72 h UV irradiation.
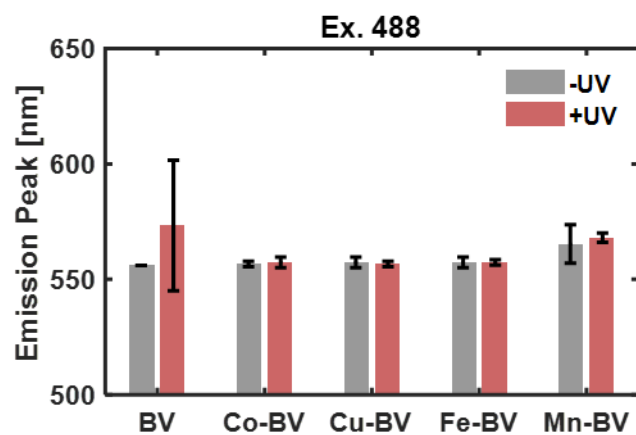
Figure E4. Wavelength of maximum fluorescence (ex. 488 nm) for BV samples before and after UV irradiation. Error bars represent standard deviation obtained with three separate experiments.
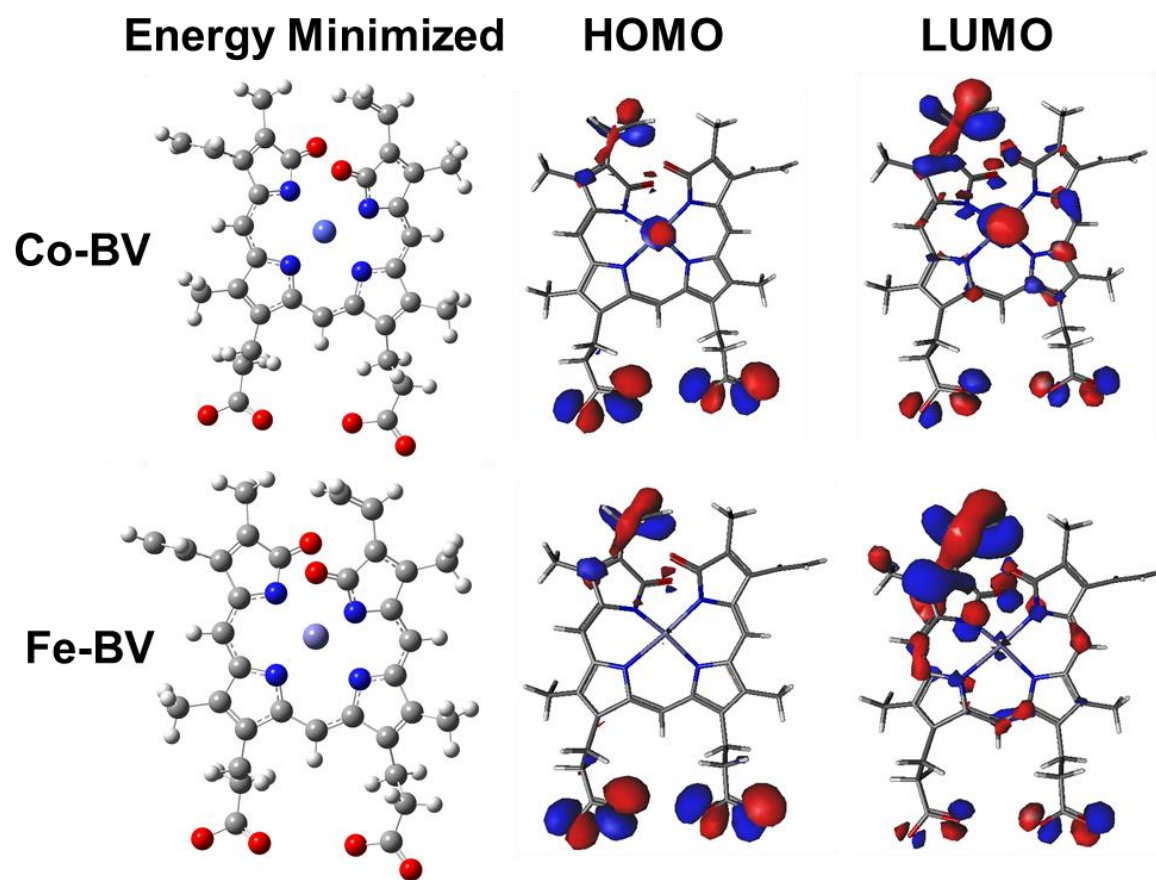
Figure E5. Energy minimized structures and HOMO LUMO surface maps for Co-BV and Fe-BV.
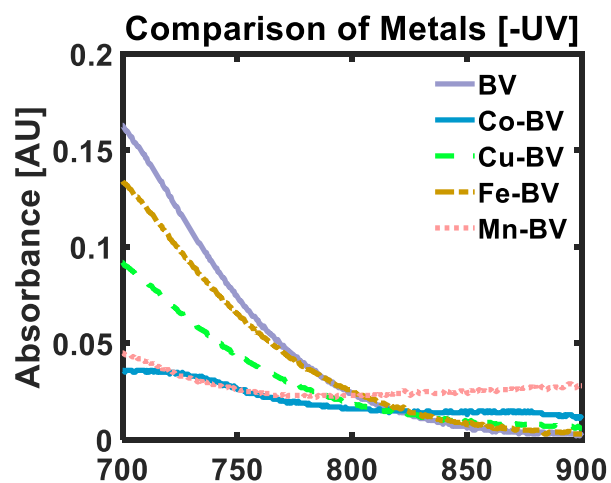
Figure E6. UV-Visible spectra of metal-chelated BV (in comparison to BV) without UV irradiation, in the range of 700 to 900 nm.
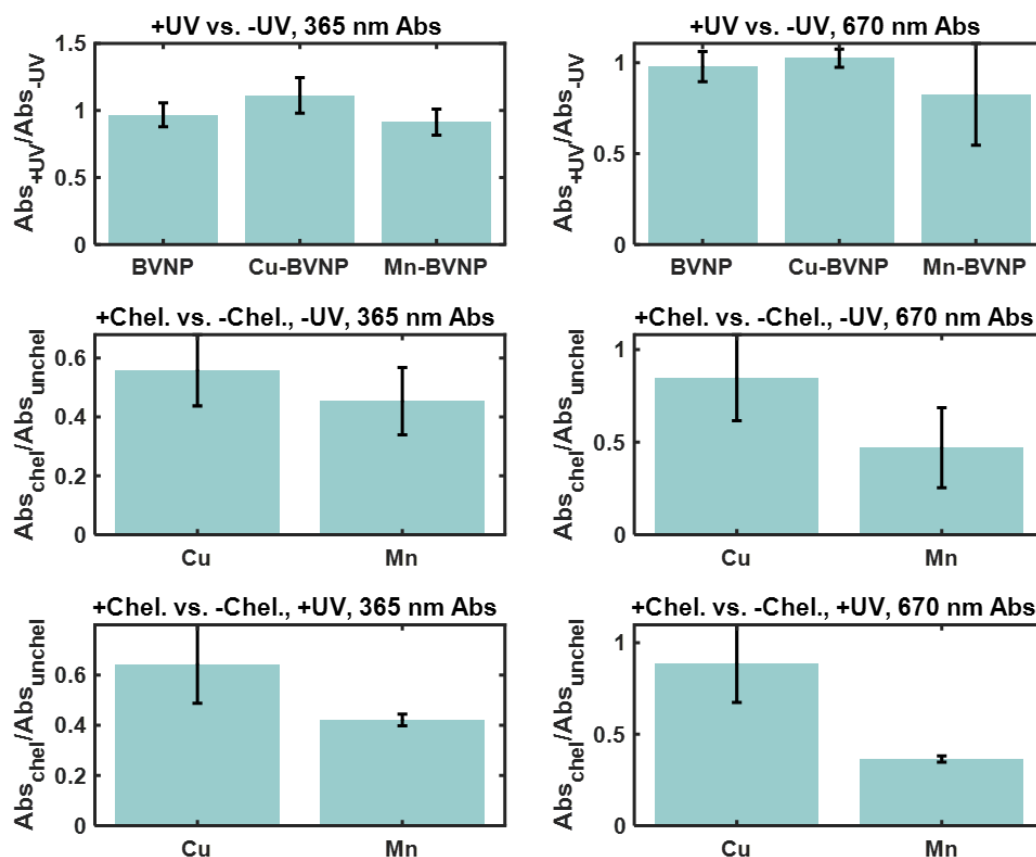
Figure E7. Absorbance ratios for BVNPs. Error bars represent standard deviation across two separate experiments. **(A)** Ratio of 365 nm absorbance for samples **(i)** with and without UV irradiation, **(ii)** with and without metal chelation when no UV irradiation was used, and **(iii)** with and without metal chelation when UV irradiation was used. **(B)** Ratio of 680 nm absorbance for samples **(i)** with and without UV irradiation, **(ii)** with and without metal chelation when no UV irradiation was used, and **(iii)** with and without metal chelation when UV irradiation was used.
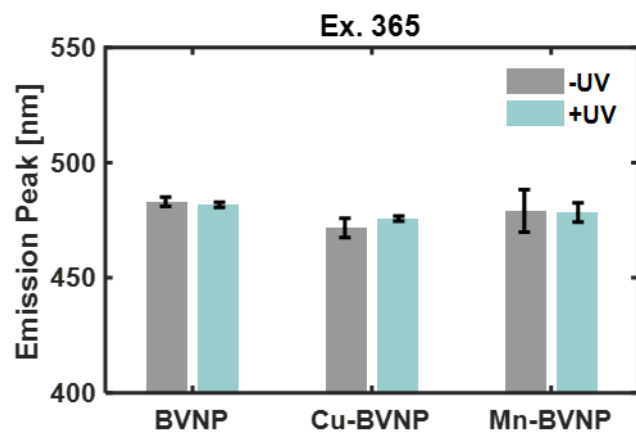
Figure E8. Wavelength of maximum fluorescence (ex. 365 nm) for BVNP samples before and after UV irradiation. Error bars represent standard deviation obtained with three separate experiments.
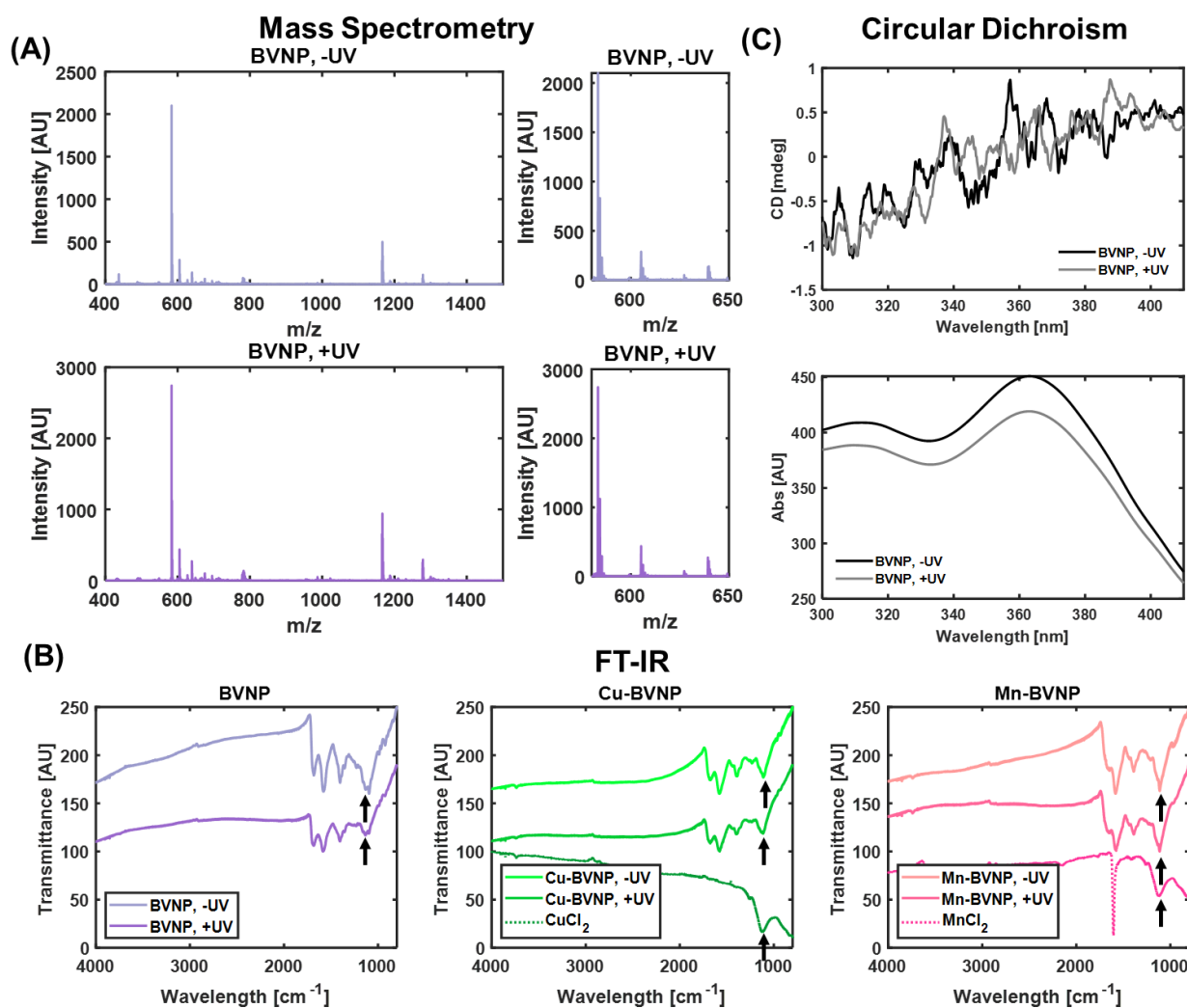
Figure E9. BVNP stability and conformational change. **(A)** Mass spectra of BVNP without UV irradiation and after 72 h of UV irradiation. The presence of expected characteristic peaks and lack of appearance of new peaks of smaller masses indicates BVNPs are not degrading as a result of the UV irradiation. **(B)** FT-IR spectra of BVNP and BVNP metal chelates. Black arrows identify peaks that are altered as a result of metal chelation. There is no apparent change as a result of UV irradiation. **(C)** Circular dichroism spectra of UV irradiation does not appear to have a noticable effect on the CD spectra. The magnitude of BVNP CD spectra is lower than that of BV.
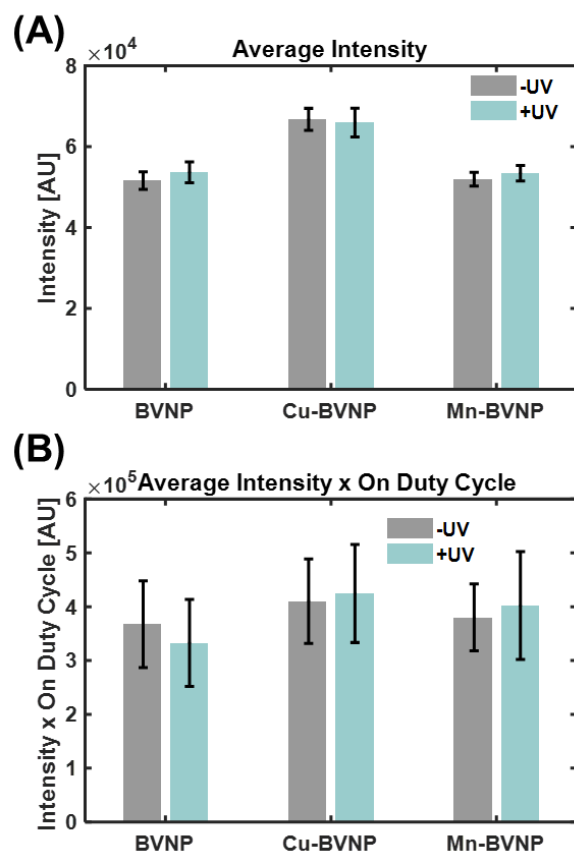
Figure E10. Single-particle brightness of BVNPs. Error bars represent standard deviation of measurements from multiple individual particles. **(A)** Average single-particle intensity of BVNP, Cu-BVNP, and Mn-BVNP, with and without UV irradiation. **(B)** Product of average single-particle intensity and on-time duty cycle for BVNP, Cu-BVNP, and Mn-BVNP.
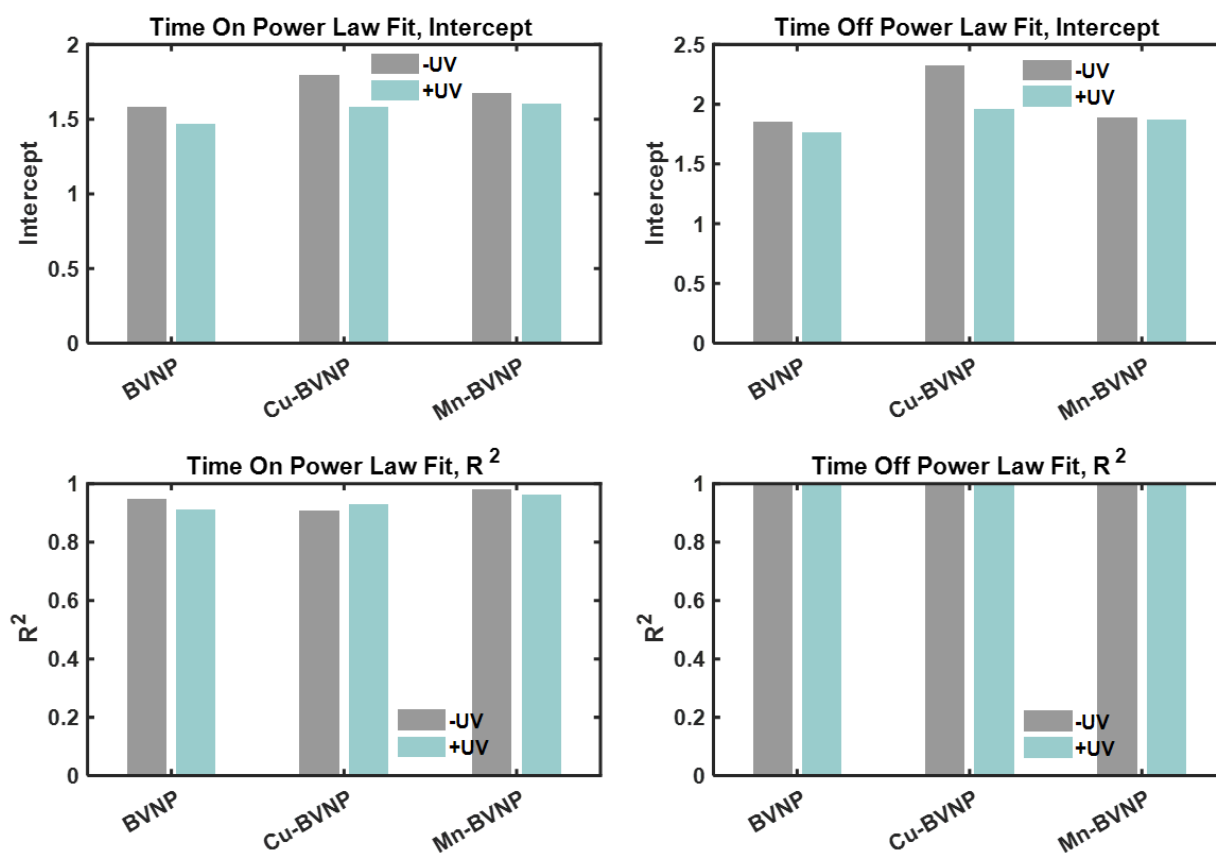
Figure E11. Time on and time off power law fit intercepts and R^2 values.
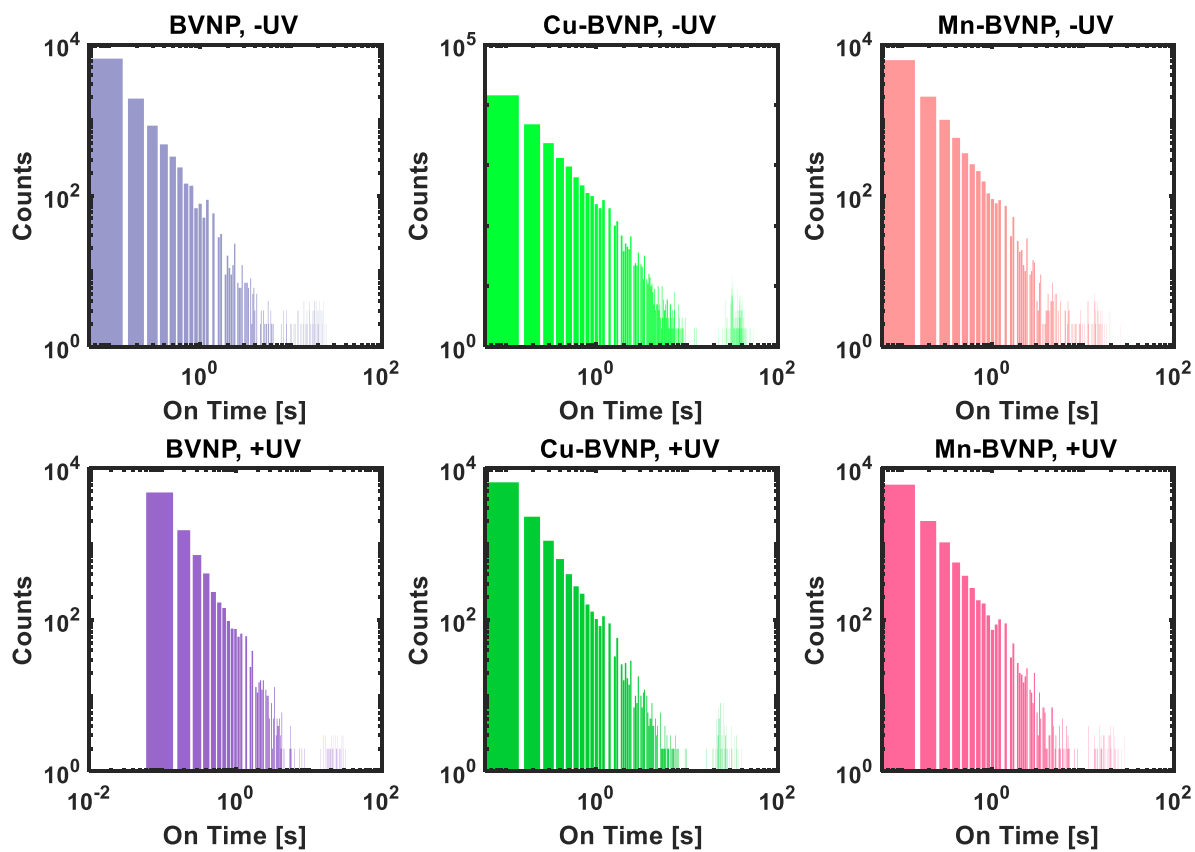
Figure E12. Log-log histograms of counts as a function of on time.
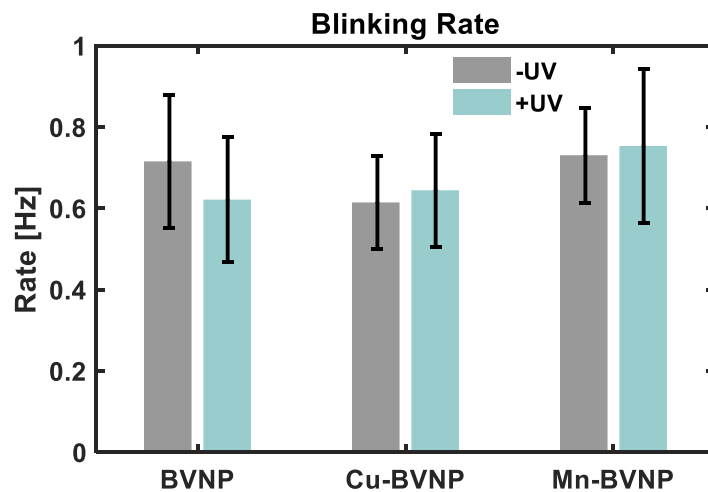
Figure E13. Single-particle blinking rate. Error bars represent standard deviation of measurements from multiple individual particles.

Figure F1. Non-normalized cytokine expression. (A)TNF-α expression, indicating no significant differences in devices with flow and without flow. (B) IL-8 expression, indicating no significant differences in devices with flow and without flow.

APPENDIX G: SUPPORTING INFORMATION FOR CHAPTER 10

I. CONFIRMING ISOLATION OF HEVECS FROM HTECS

Experiment Prep
1. Grow HEVECs

Special Considerations
N/A
Potential for optimization
- May need to conduct further immunomagnetic cell separations if the majority of the cell population isn't found to be HEVECs

Characterization
- Immunostaining for MECA-79 and fluorescence microscopy of cells
- Flow cytometry to isolate and quantify MECA-79+ cells

Questions to answer
1. Did we successfully isolate HEVECs from HTECs?
2. What % of the cell population is MECA-79+ (HEVEC vs. HTEC)? Is this good enough?

II. ESTABLISHING COCULTURES OF HLECS AND HEVECS IN DEVICES

Experiment Prep
1. Add Matrigel into Matrigel wells (no cells)
   a. Allow to solidify
2. Seed HLEC and HEVEC cells in their respective channels
3. Start flow and allow confluent cell layers to form

Special considerations
- Need to use EV-depleted FBS if doing EV analysis
- It would be best to do these experiments using membranes with a **small** pore size (prevent endothelial cell migration into the Matrigel)
- Maybe the amount of time each device spends at each position should be reduced to better match pumping speed of lymphatics
- Can either choose one angle to set platforms to, or test multiple angles (i.e. multiple shear values)
- The device angle may affect the amount of transport across the membrane purely due to gravity

Potential for optimization
- Cell seeding density
- Device angle for shear
- Number of days cells should remain in devices for

Characterization
- Take videos of devices and calculate shear values in HLEC and HEVEC channels
- Brightfield microscopy each day to track cell growth
- Measure dextran transport across endothelial cell layers and into Matrigel well to determine permeability
- Live-dead staining on final day to measure cell viability
- Daily media collection and storage
  - ELISAs for ELK3, CCL1, TNF-alpha, and IL-8 or IL-6
  - EV analysis
    - Gels, western blotting, TEM, nanoparticle tracking analysis (size and concentration), miRNA/RNA analysis
- Fixation and immunostaining of cells on membrane (or even in channels) at end of experiment
- Flow cytometry on Matrigel to determine if endothelial cells travelled across the membrane

Questions to answer
1. Are the shear values we are obtaining appropriate for our application?
2. Does the Matrigel remain solid for however many days of flow it takes to get the cell layers to become confluent?
3. How many days do we need to let the cells grow to get confluent layers?

4. What is the permeability of the cell layers?
5. Do any of the endothelial cells end up migrating into the Matrigel?

III. ESTABLISHING TRICULTURES OF HLECS, HEVECS, AND CANCER CELLS IN DEVICES

Experiment Prep
1. Add Matrigel+cancer cells into Matrigel wells
   a. Allow to solidify
2. Seed HLEC and HEVEC cells in their respective channels
3. Start flow and allow confluent cell layers to form

Special considerations
- Need to use EV-depleted FBS if doing EV analysis
- For initial experiments it may be best to do these experiments using membranes with a **small** pore size (prevent endothelial cell migration into the Matrigel and prevent cancer cells from migrating out)
- It might make things easier if we use fluorescently labelled cancer cells
- MDA-MB-231 cells may be best option because they are highly invasive and because that is also what I'm using to study the Dox-BVNPs

Potential for optimization
- Cancer cell seeding density in matrigel
- Number of days cells should remain in devices for

Characterization
- Brightfield microscopy each day to track cell growth
- Live-dead staining on final day to measure cell viability
- Fluorescence microscopy of Matrigel to see if cancer cells have formed 3D structures
- Daily media collection (including Matrigel media) and storage
  - ELISAs for ELK3, CCL1, TNF-alpha and IL-8 or IL-6
  - EV analysis
    - Gels, western blotting, TEM, nanoparticle tracking analysis (size and concentration), miRNA/RNA analysis
- Fixation and immunostaining of cells on membrane (or even in channels) at end of experiment
- Flow cytometry on Matrigel to determine number of live cancer cells

Questions to answer
1. Does the Matrigel remain solid for however many days of flow it takes to get the cell layers to become confluent, even when there are cancer cells in it?
2. Are we getting EVs transported between the endothelial cells and the Matrigel?
3. Are the contents of endothelial cell EVs being changed due to the presence of cancer cells?
4. Does the presence of cancer cells affect the viability of the endothelial cells in any way?
5. Does the presence of cancer cells affect the cytokine expression of the endothelial cells in any way?

IV. INVASION OF CANCER CELLS ACROSS SUBCAPSULAR SINUS AND INTO MATRIGEL

Experiment Prep
1. Add Matrigel into Matrigel wells (no cells)
   a. Allow to solidify
2. Seed HLEC and HEVEC cells in their respective channels
3. Start flow and allow confluent cell layers to form
4. Add cancer cells in suspension to the HLEC channel

Special considerations
- It would be best to do these experiments using membranes with a **larger** pore size to allow for cell migration, but we would need to make sure we don't accidentally get all of the HLECs and HEVECs to migrate into the Matrigel
- In cell invasion assays, cells typically migrate from with-serum media to without-serum media. Matrigel is supposed to be diluted in media without serum. That means that we will be trying to get our cells to go from a with-serum location (channels) to a without-serum location (matrigel). One possible way of dealing with this is to have serum in the media compartment for the Matrigel, but not in the Matrigel itself
- We can potentially add a chemoattractant to the Matrigel to get the cells to invade into it
- Would be best if we use fluorescently labelled cells
- MDA-MB-231 probably the best option to use

Potential for optimization
- Number of cancer cells to add into device
- How long devices are kept static between when cancer cells are added and flow is begun

Characterization
- Fluorescence microscopy to track position of cancer cells
- Live-dead staining on endothelial cells to determine their viability
- Media collection (spin down to remove free cells)
  o ELISAs for ELK3, CCL1, TNF-alpha, and IL-8 or IL-6
- Flow cytometry on Matrigel to quantify number of cancer cells that travelled across the membrane, and to quantify their viability

Questions to answer
1. How fast do the cancer cells migrate into the Matrigel? How long do we need to let the experiment run?
2. What effect does the presence of cancer cells have on the HLECS and HEVECs?

V. EXTRAVASATION OF CELLS FROM MATRIGEL

Experiment Prep
1. Add Matrigel+cancer cells into Matrigel wells
   a. Allow to solidify
2. Seed HLEC and HEVEC cells in their respective channels
3. Start flow and allow confluent cell layers to form

Special considerations
- May need to add fresh Matrigel+cancer cells later if we see that too many HLECS and HEVECS are entering the Matrigel during the seeding process
- It would be best to do these experiments using membranes with a **larger** pore size to allow for cell migration, but we would need to make sure we don't accidentally get all of the HLECs and HEVECs to migrate into the Matrigel
- We can potentially add a chemoattractant to the HLEC media to improve the chances of extravasation
- Would be best if we use fluorescently labelled cells
- MDA-MB-231 probably the best option to use

Potential for optimization
- Cancer cell seeding density in matrigel
- Number of days cells should remain in devices for

Characterization
- Fluorescence microscopy to track position of cancer cells
- Live-dead staining on endothelial cells to determine their viability
- Media collection (spin down to remove free cells)
  - ELISAs for ELK3, CCL1, TNF-alpha, and IL-8 or IL-6
- Flow cytometry on cells spun down from HLEC media to quantify number and viability of cancer cells that have extravasated from the matrigel

Questions to answer
1. How fast do the cancer cells migrate out of the Matrigel? How long do we need to let the experiment run?
2. What effect does the presence of cancer cells have on the HLECS and HEVECs?

VI. EXTRAVASATION OF CELLS FROM MATRIGEL AND INTRAVASATION INTO THE NEXT NODE

Experiment Prep
1. Add Matrigel+cancer cells into **one of** Matrigel wells, and just Matrigel into the other well
   a. Allow to solidify
2. Seed HLEC and HEVEC cells in their respective channels
3. Start flow and allow confluent cell layers to form

Special considerations
- May need to add fresh Matrigel+cancer cells later if we see that too many HLECS and HEVECS are entering the Matrigel during the seeding process
- It would be best to do these experiments using membranes with a **larger** pore size to allow for cell migration, but we would need to make sure we don't accidentally get all of the HLECs and HEVECs to migrate into the Matrigel
- We can potentially add a chemoattractant to the HLEC media **or into the cell-less Matrigel well** to improve the chances of extravasation/intravasation
- Would be best if we use fluorescently labelled cells
- MDA-MB-231 probably the best option to use

Potential for optimization
- Cancer cell seeding density in matrigel
- Number of days cells should remain in devices for

Characterization
- Fluorescence microscopy to track position of cancer cells
- Live-dead staining on endothelial cells to determine their viability
- Media collection (spin down to remove free cells)
  o ELISAs for ELK3, CCL1, TNF-alpha, and IL-8 or IL-6
- Flow cytometry on Matrigel that was initially cell-less to quantify number of cancer cells that travelled from one Matrigel well to another, and to quantify their viability

Questions to answer
1. How long does it take for the cells to migrate from one well to another?
2. What effect does the presence of cancer cells have on the HLECS and HEVECs?

VII. ESTABLISH WHETHER CANCER CELLS WILL ACTIVATE IMMUNE CELLS (TRANSWELL STUDIES)

Experiment Prep
1. Add cancer cells in top of transwell
2. Add immune cells (3 separate groups: PBMCs, Jurkat, MOLT-4) to bottom of transwell wellplate

Special considerations
N/A

Potential for optimization
- Number of cells per transwell and well

Characterization
- Media collection
  - ELISAs for IL-2 to determine if immune cells have become activated

Questions to answer
1. Will the presence of cancer cells activate the immune cells?

VIII.   ESTABLISH WHETHER IMMUNE CELLS CAN SURVIVE GROWING IN MATRIGEL

Experiment Prep
1. Add immune cells (3 separate groups: PBMCs, Jurkat, MOLT-4) in matrigel
2. Let cells proliferate for a few days

Special considerations
- Immune cells are typically grown in suspension

Potential for optimization
- Can try different concentrations of cells in matrigel

Characterization
   o MTT assay to confirm cell viability
   o Flow cytometry if needed for further confirmation of cell viability and cell type that is alive (specifically for PBMCs since those contain a lot of different cell types

Questions to answer
1. Will the immune cells proliferate in Matrigel?

IX. ESTABLISH WHETHER CANCER CELLS WILL ACTIVATE IMMUNE CELLS (CONTACT STUDIES)

Experiment Prep
1. Add immune cells (3 separate groups: PBMCs, Jurkat, MOLT-4) and cancer cells together in matrigel
2. Let them grow

Special considerations
N/A

Potential for optimization
- Ratios of immune cells to cancer cells

Characterization
- Media collection
  - ELISAs for IL-2 to determine if immune cells have become activated
- Flow cytometry to determine which cell types have survived

Questions to answer
1. Will the cancer cells and immune cells be able to coexist peacefully?

X. COCULTURE OF IMMUNE CELLS, CANCER CELLS, HLECS, AND HEVECS IN DEVICES

Experiment Prep
1. Add Matrigel+cancer cells+immune cells into Matrigel wells
    a. Allow to solidify
2. Seed HLEC and HEVEC cells in their respective channels
3. Start flow and allow confluent cell layers to form

Special considerations
- Need to use EV-depleted FBS if doing EV analysis
- For initial experiments it may be best to do these experiments using membranes with a **small** pore size (prevent endothelial cell migration into the Matrigel and prevent cancer/immune cells from migrating out)
- It might make things easier if we use fluorescently labelled cancer cells

Potential for optimization
- Cancer and immune cell seeding density in matrigel
- Number of days cells should remain in devices for

Characterization
- Brightfield microscopy each day to track cell growth
- Live-dead staining on final day to measure cell viability
- Fluorescence microscopy of Matrigel to see if cancer cells have formed 3D structures
- Measure dextran transport across endothelial cell layers and into Matrigel well to determine permeability
- Daily media collection (including Matrigel media) and storage
    - ELISAs for ELK3, CCL1, TNF-alpha and IL-8 or IL-6
    - EV analysis
        - Gels, western blotting, TEM, nanoparticle tracking analysis (size and concentration), miRNA/RNA analysis
- Fixation and immunostaining of cells on membrane (or even in channels) at end of experiment
- Flow cytometry on Matrigel to determine number of live cancer cells and immune cells and their types

Questions to answer
1. Does the Matrigel remain solid for however many days of flow it takes to get the cell layers to become confluent, even when there are cancer cells **and** immune cells in it?
2. Are we getting EVs transported between the endothelial cells and the Matrigel?
3. Are the contents of endothelial cell EVs being changed due to the presence of cancer cells and immune cells?
4. Does the presence of cancer cells and immune cells affect the viability of the endothelial cells in any way?

5. Does the presence of cancer cells and immune cells affect the cytokine expression of the endothelial cells in any way?
6. Do the cancer cells proliferate despite the presence of immune cells?

XI. IMMUNE CELL EXTRAVASATION FROM HIGH ENDOTHELIAL VENULES AND INTRAVASATION ACROSS SUBCAPSULAR SINUS

Experiment Prep
1. Add Matrigel (no cells) into Matrigel wells
   a. Allow to solidify
2. Seed HLEC and HEVEC cells in their respective channels
3. Start flow and allow confluent cell layers to form
4. Add immune cells in suspension into HEVEC channels

Special considerations
- Need to use EV-depleted FBS if doing EV analysis
- Need to use **large** pore size to allow for migration

Potential for optimization
- Number of immune cells to add into device
- How long devices are kept static between when immune cells are added and flow is begun

Characterization
- Live-dead staining on endothelial cells to determine their viability
- Media collection (spin down to remove free cells)
  o ELISAs for ELK3, CCL1, TNF-alpha, IL-2, and IL-8 or IL-6
- Flow cytometry on Matrigel to quantify number of immune cells that travelled across the membrane, and to quantify their viability
- Flow cytometry on collected media (spun down) to determine whether immune cells made their way into the HLEC channel

Questions to answer
1. How fast do the immune cells migrate into the Matrigel? How long do we need to let the experiment run for them to migrate out?
2. What effect does the presence of immune cells have on the HLECS and HEVECs?
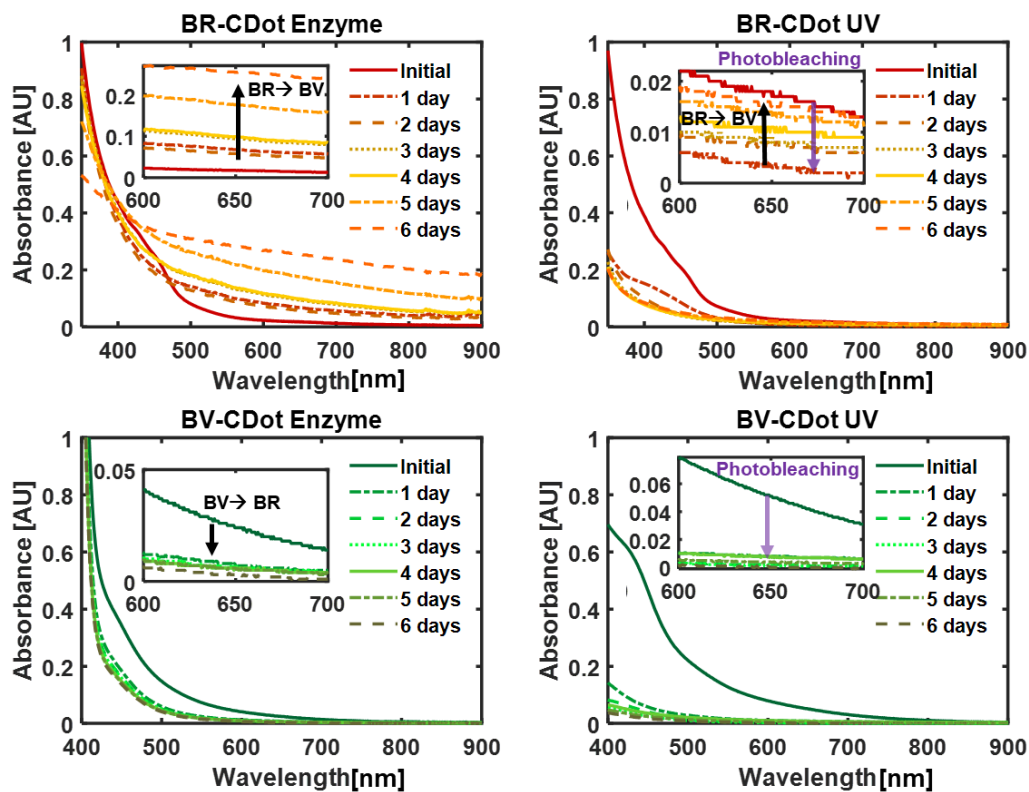
Figure H1. Absorbance behavior of bile pigment-derived CDots over a period of 6 days.
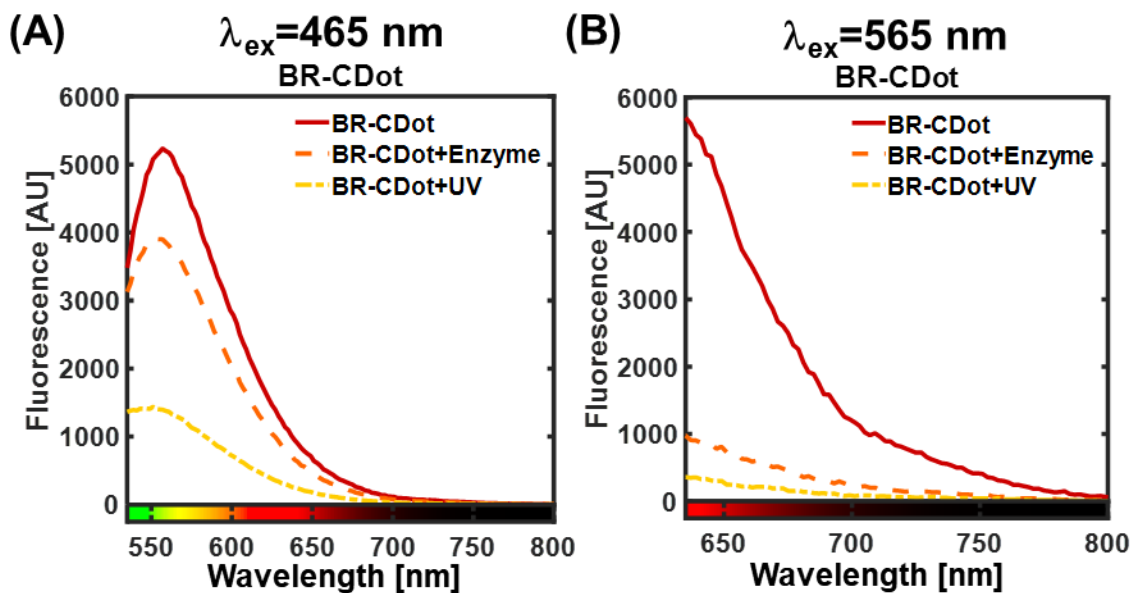
Figure H2. Fluorescence spectra of BR-CDots for excitation wavelengths of 465 nm (**A**) and 565 nm (**B**).
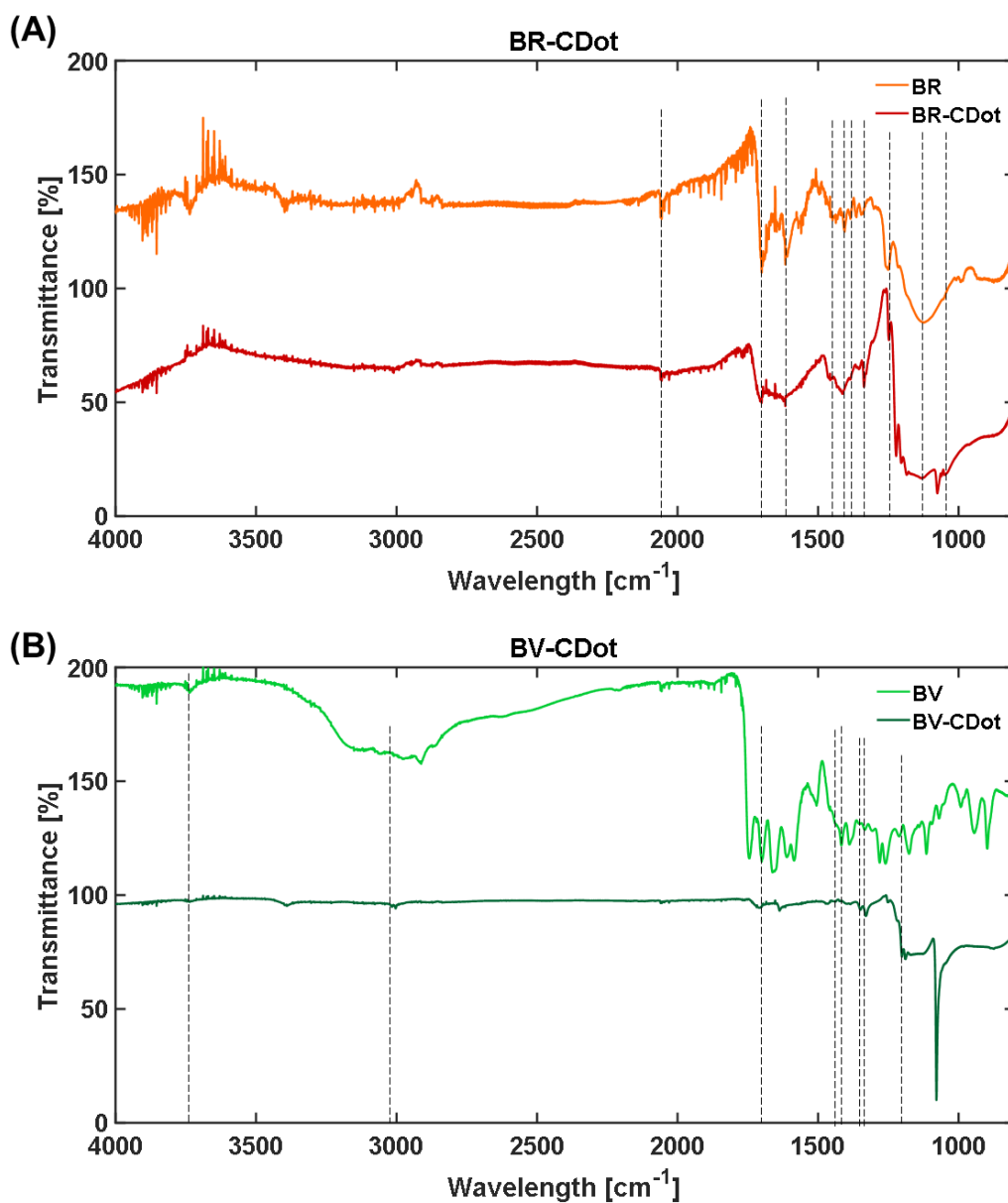
Figure H3. FT-IR Spectra of (A) Bilirubin (BR) and BR-CDot and (B) Biliverdin (BV) and BV-CDot. Dashed lines depict peaks that are seen in both the precursor and the nanoparticle. Retention of some FT-IR peaks in the carbon dots suggests that these functional groups are also present on the surface of the particles and not just within their core.
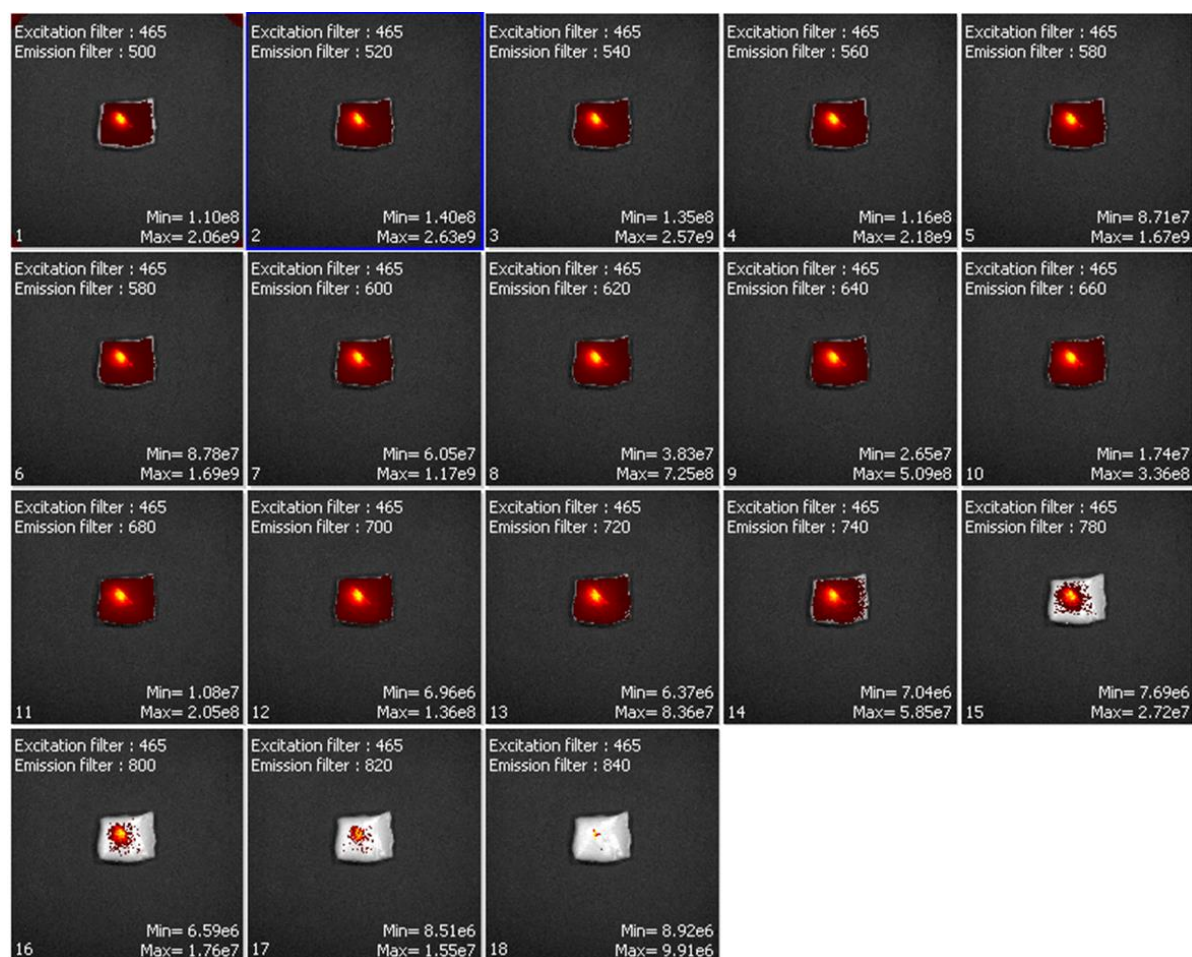
Figure H4. IVIS tissue phantom images of surface-injected BR-CDots for excitation wavelength of 465 nm and emissions in the range of 500 nm-840 nm.
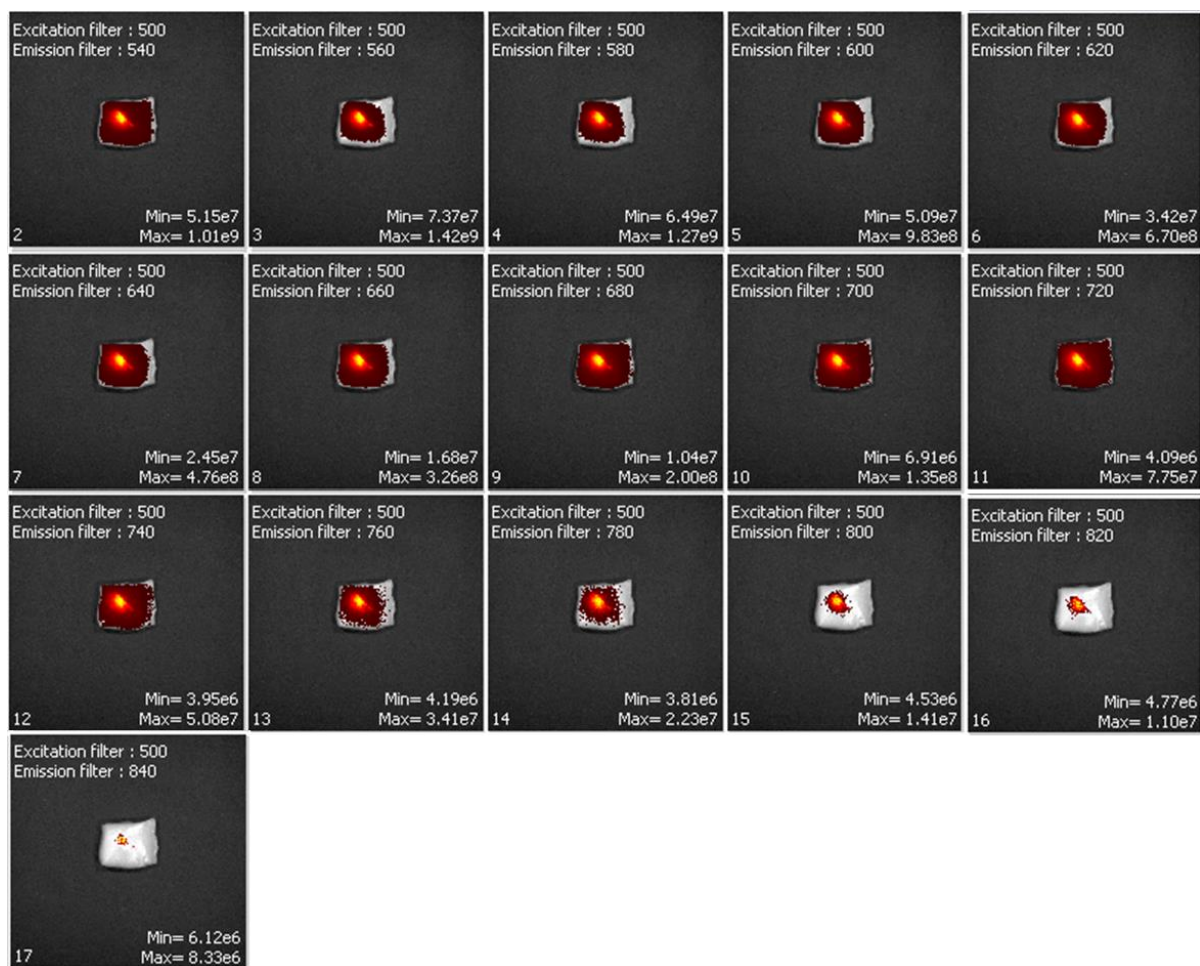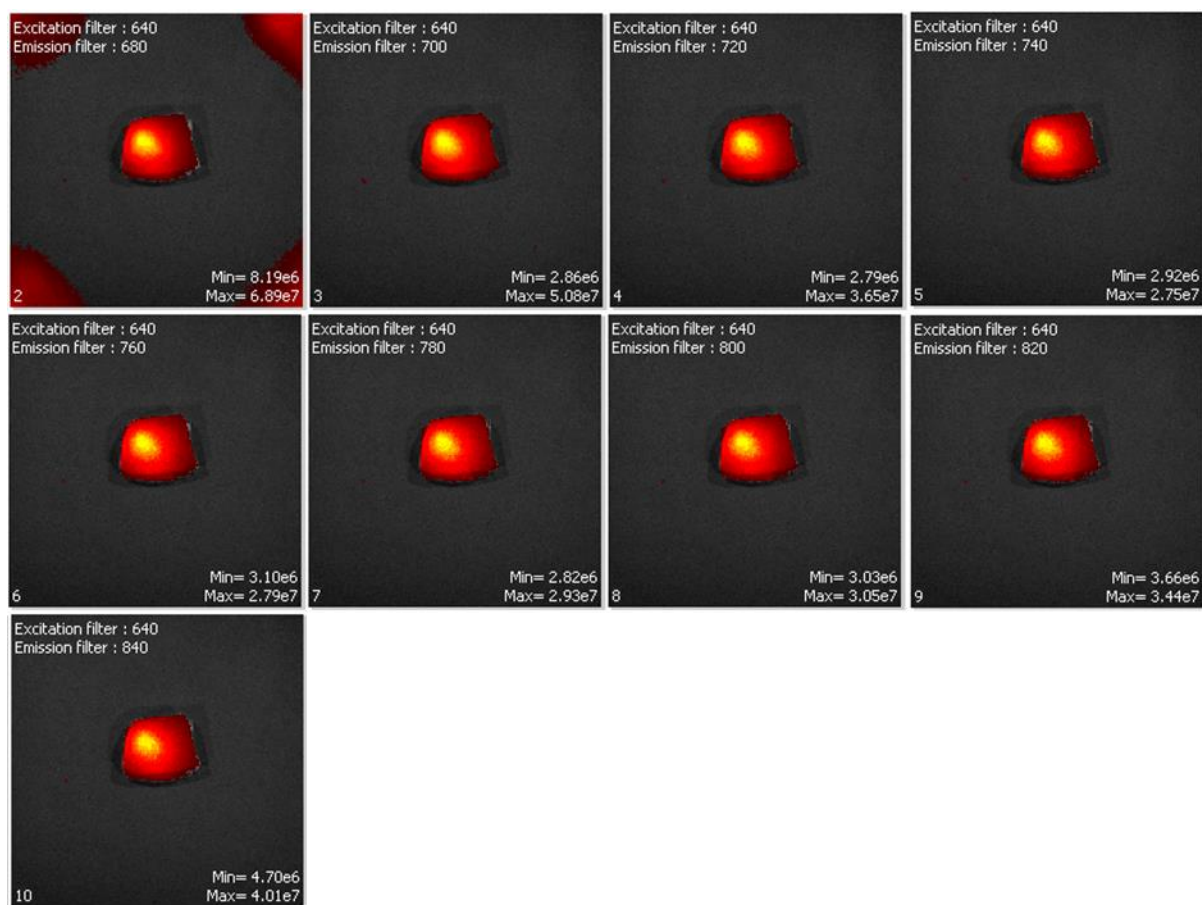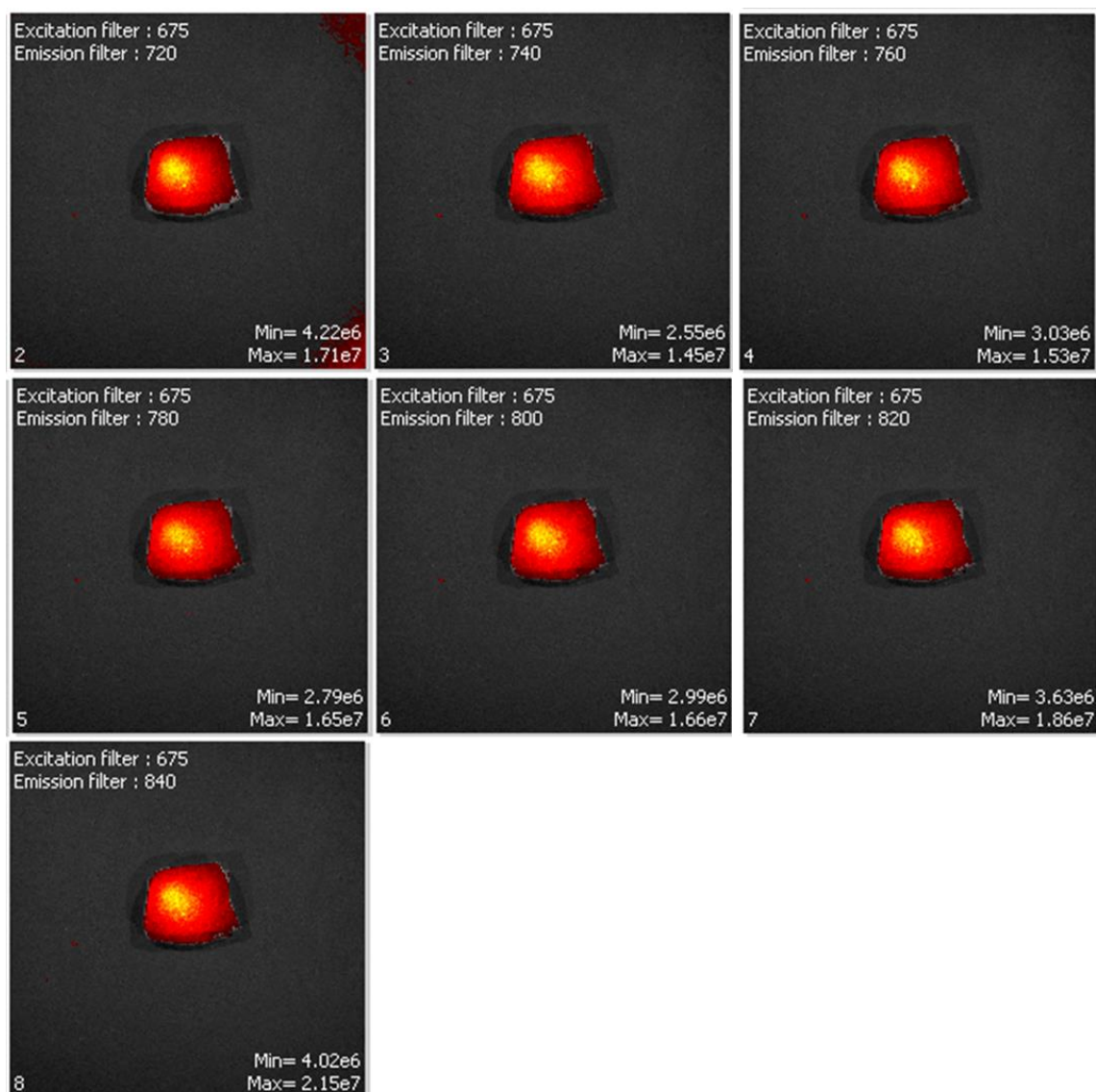
Figure H5. IVIS tissue phantom images of surface-injected BR-CDots for excitation wavelength of 500 nm and emissions in the range of 540 nm-840 nm.
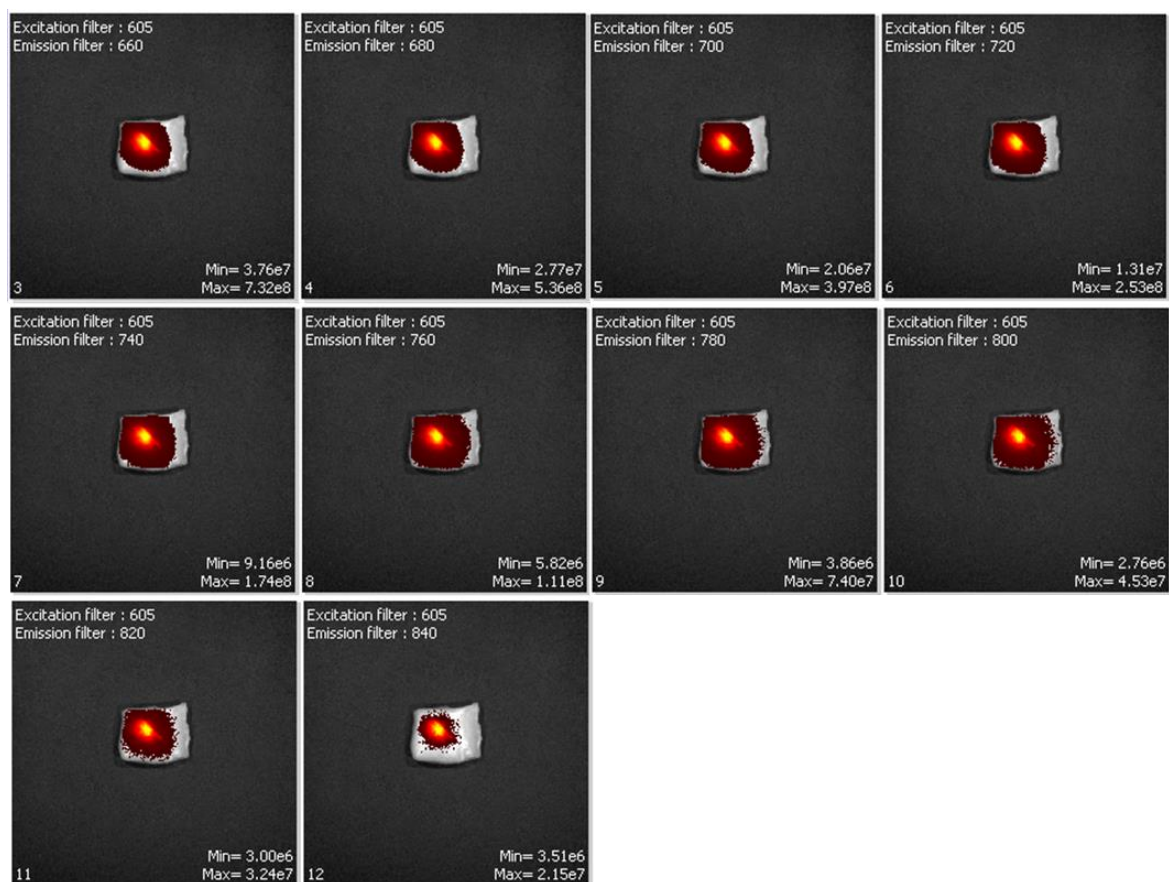
Figure H6. IVIS tissue phantom images of surface-injected BR-CDots for excitation wavelength of 605 nm and emission wavelengths in the range of 660 nm-840 nm.
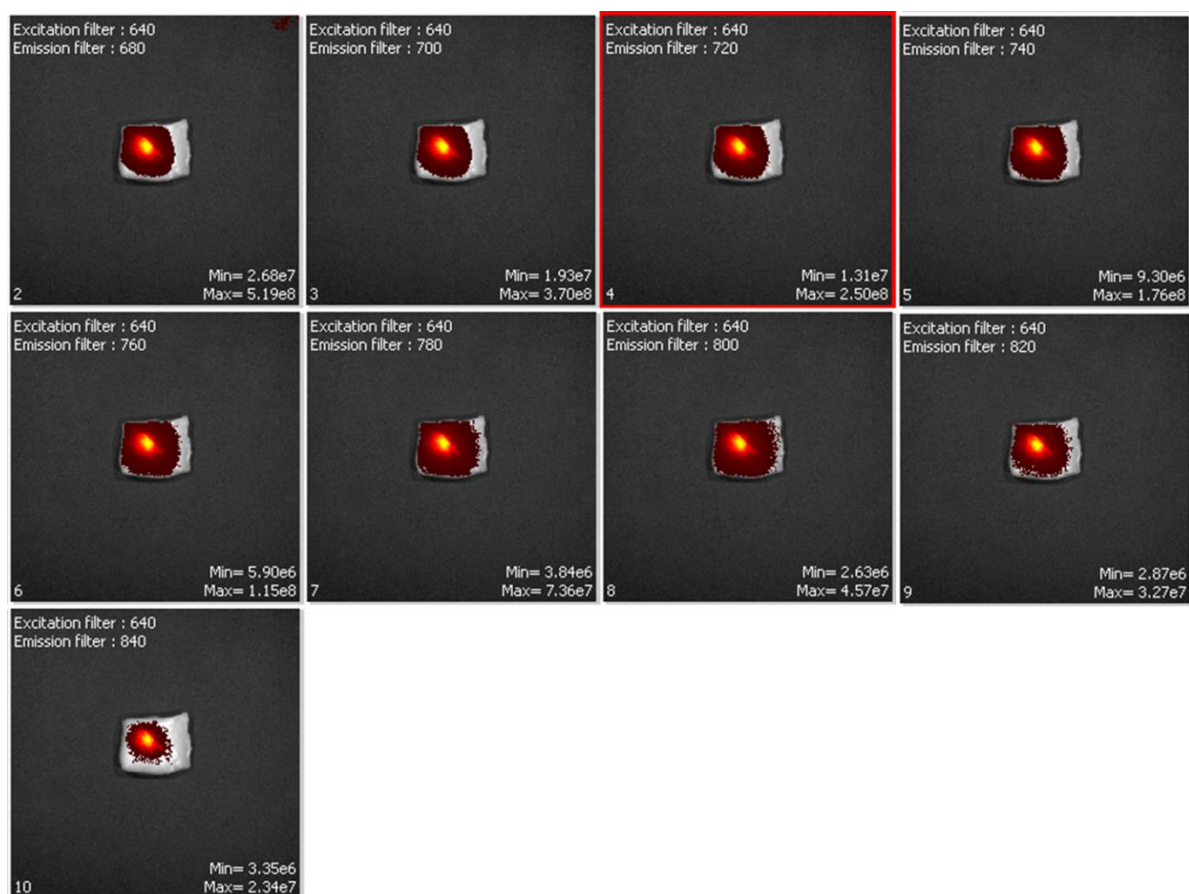
Figure H7. IVIS tissue phantom images of surface-injected BR-CDots for excitation wavelength of 640 nm and emission wavelengths in the range of 680 nm-840 nm.
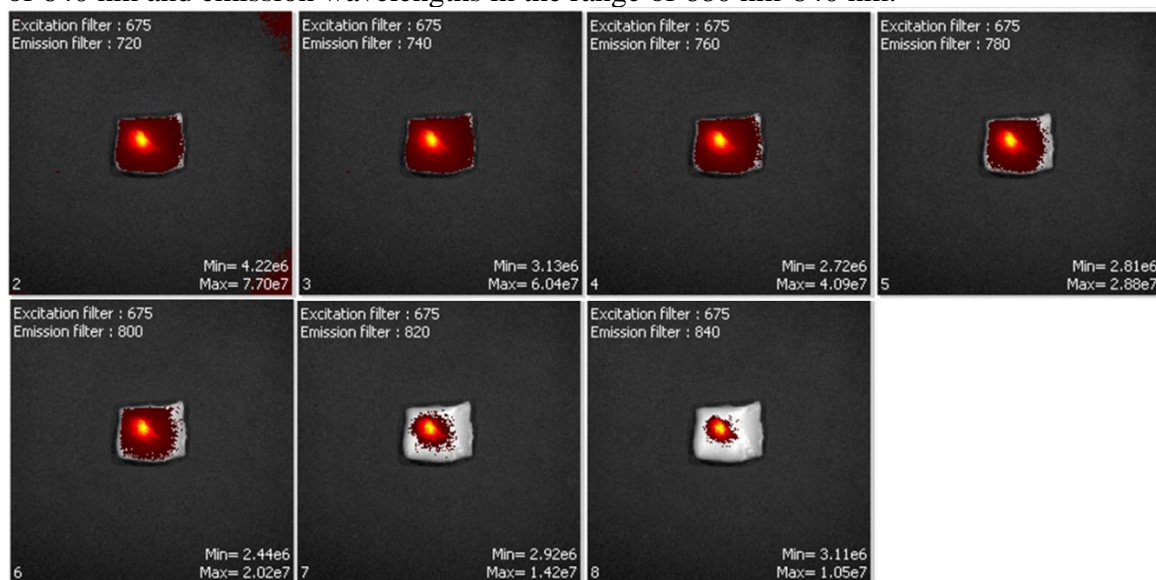
Figure H8. IVIS tissue phantom images of surface-injected BR-CDots for excitation wavelength of 675 nm and emission wavelengths in the range of 720 nm-840 nm.
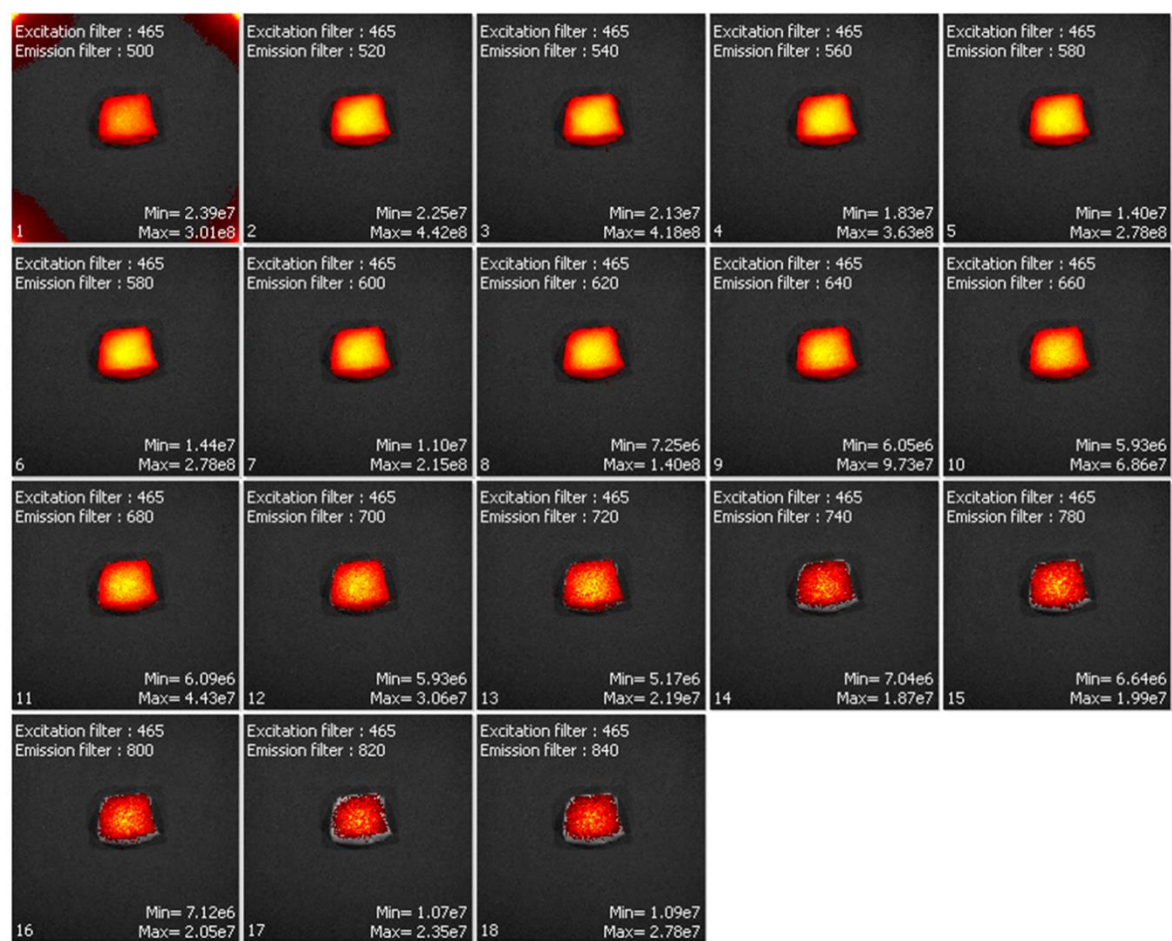
Figure H9. IVIS tissue phantom images of 8.5-mm deep BR-CDots for excitation wavelength of 465 nm and emission wavelengths in the range of 500 nm-840 nm.
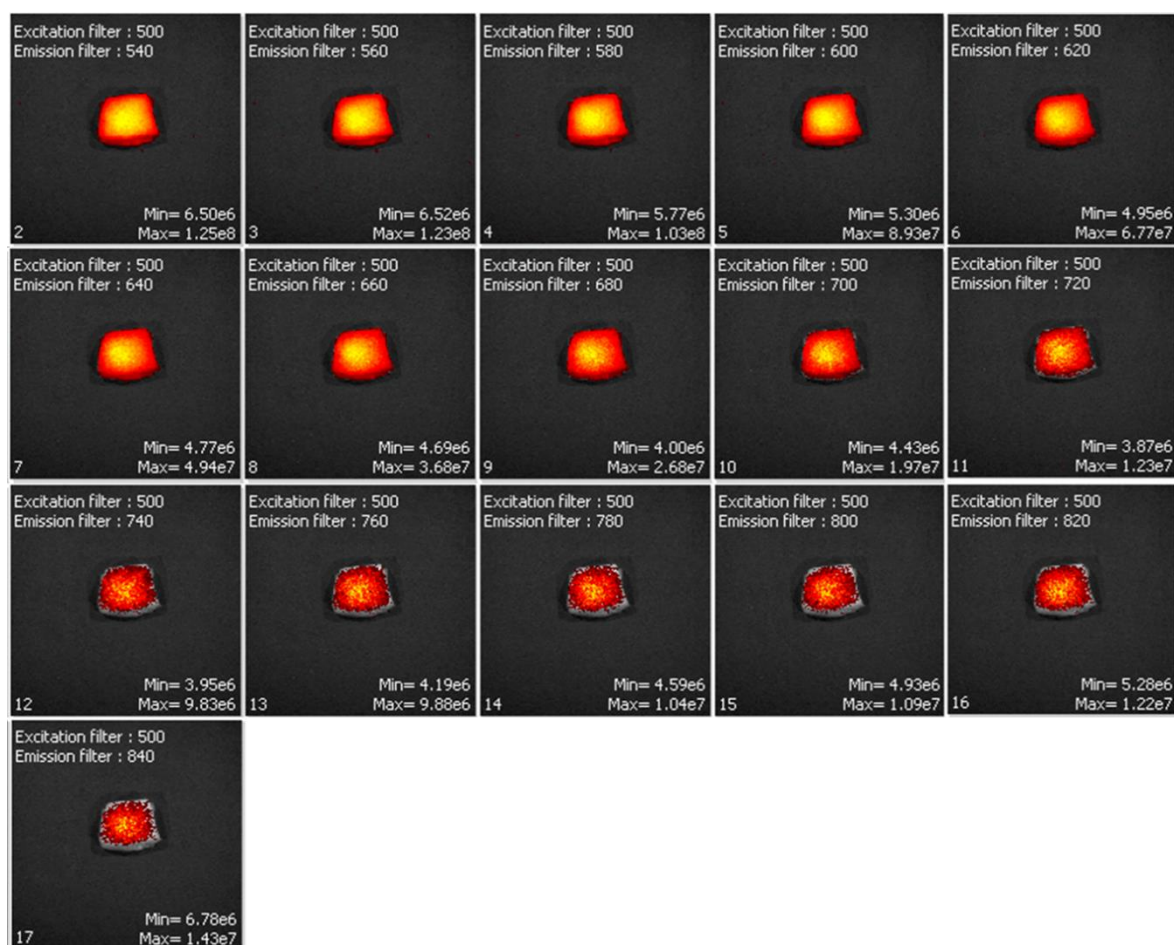
Figure H10. IVIS tissue phantom images of 8.5-mm deep BR-CDots for excitation wavelength of 500 nm and emission wavelengths in the range of 540 nm-840 nm.
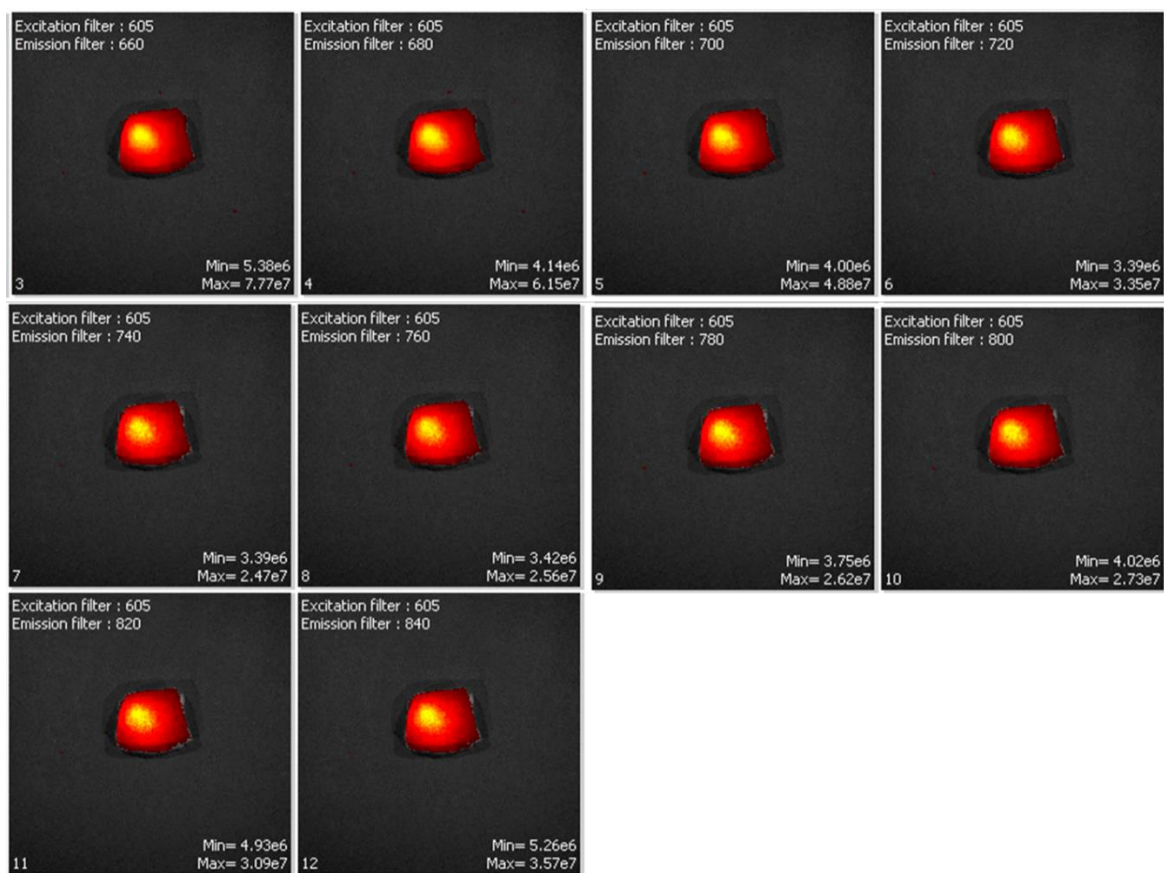
Figure H11. IVIS tissue phantom images of 8.5-mm deep BR-CDots for excitation wavelength of 605 nm and emission wavelengths in the range of 660 nm-840 nm.
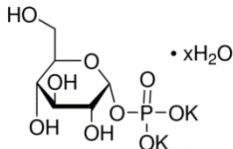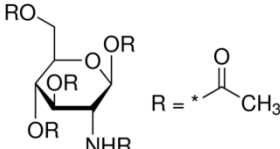
Figure H12. IVIS tissue phantom images of 8.5-mm deep BR-CDots for excitation wavelength of 640 nm and emission wavelengths in the range of 680 nm-840 nm.

Figure H13. IVIS tissue phantom images of 8.5-mm deep BR-CDots for excitation wavelength of 675 nm and emission wavelengths in the range of 720 nm-840 nm.
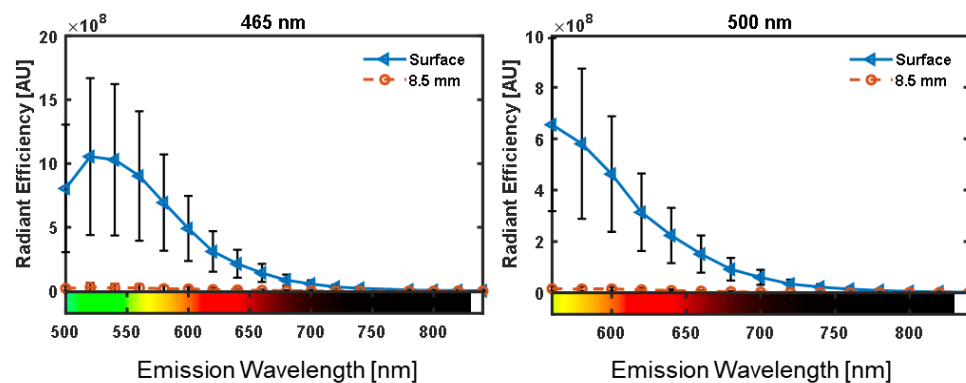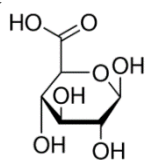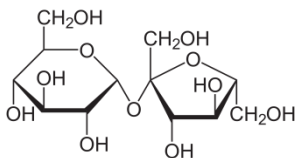

**Figure H14.** ROI analysis for BR-CDots in chicken tissue at excitation wavelengths of 465 nm and 500 nm.
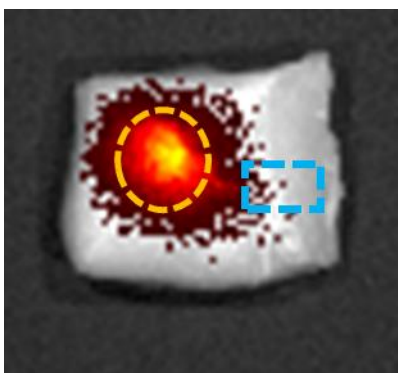
Figure H15. Example ROIs for tissue phantom image. Yellow oval outlines BR-CDot ROI and blue rectangle outlines background ROI.

Table I1. % Concentration of elements as determined by XPS

| Carbon Source	Temperature	% Concentration					
		C 1s	N 1s	O 1s	S 2p	P 2p	K 2p
α-D-Glucose 1-phosphate dipotassium salt hydrate	200 ˚C	60.91	0.29	19.32	1.19	2.96	15.34
	150 ˚C	57.27	0	38.44	1.10	3.19	0
β-D-Glucosamine pentaacetate	200 ˚C	67.02	3.3	20.33	5.09	0	4.26
	150 ˚C	57.98	2.16	30.60	9.27	0	0
D-glucuronic acid	200 ˚C	44.59	0	47.7	5.33	0	2.37
	150 ˚C	58.43	1.97	33.25	2.63	0	3.73
Sucrose	200 ˚C	50.47	1.17	44.72	3.65	0	0
	150 ˚C	71.93	0.55	26.53	1	0	0
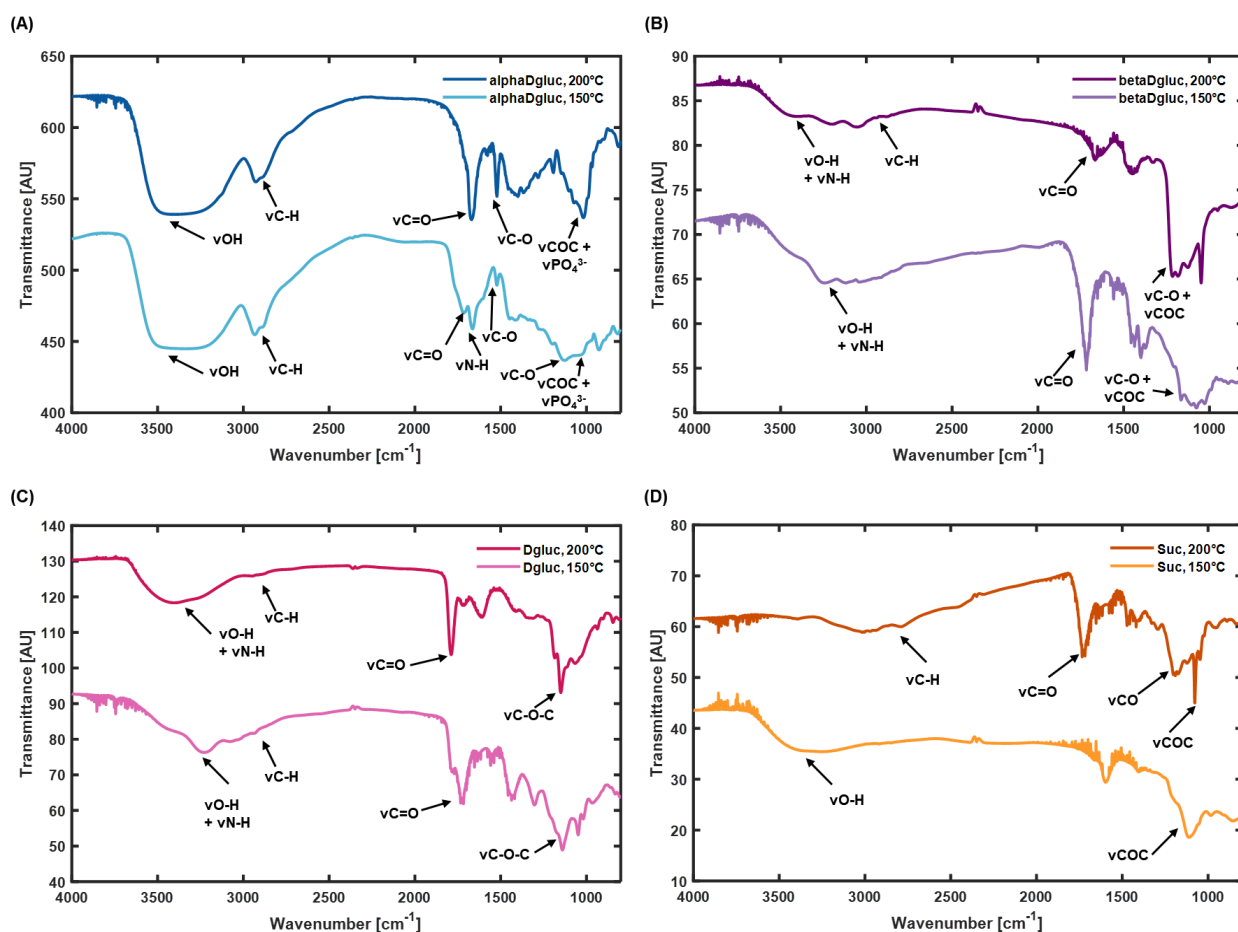
Figure I1. FT-IR spectroscopic features of CDots synthesized from **(A)** α-D-gluc, **(B)** β-D-gluc, **(C)** D-gluc, and **(D)** sucrose, at different temperatures. Signature characteristic peaks have been highlighted. α-D-gluc CDots had characteristic peaks for PO_4^{3-}, and β-D-gluc CDots had characteristic peaks for NH, corresponding to functional groups present in their respective carbon sources.
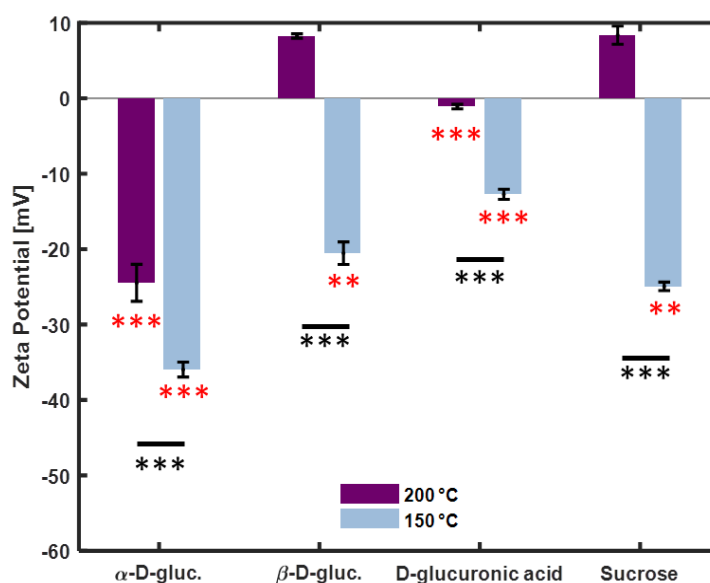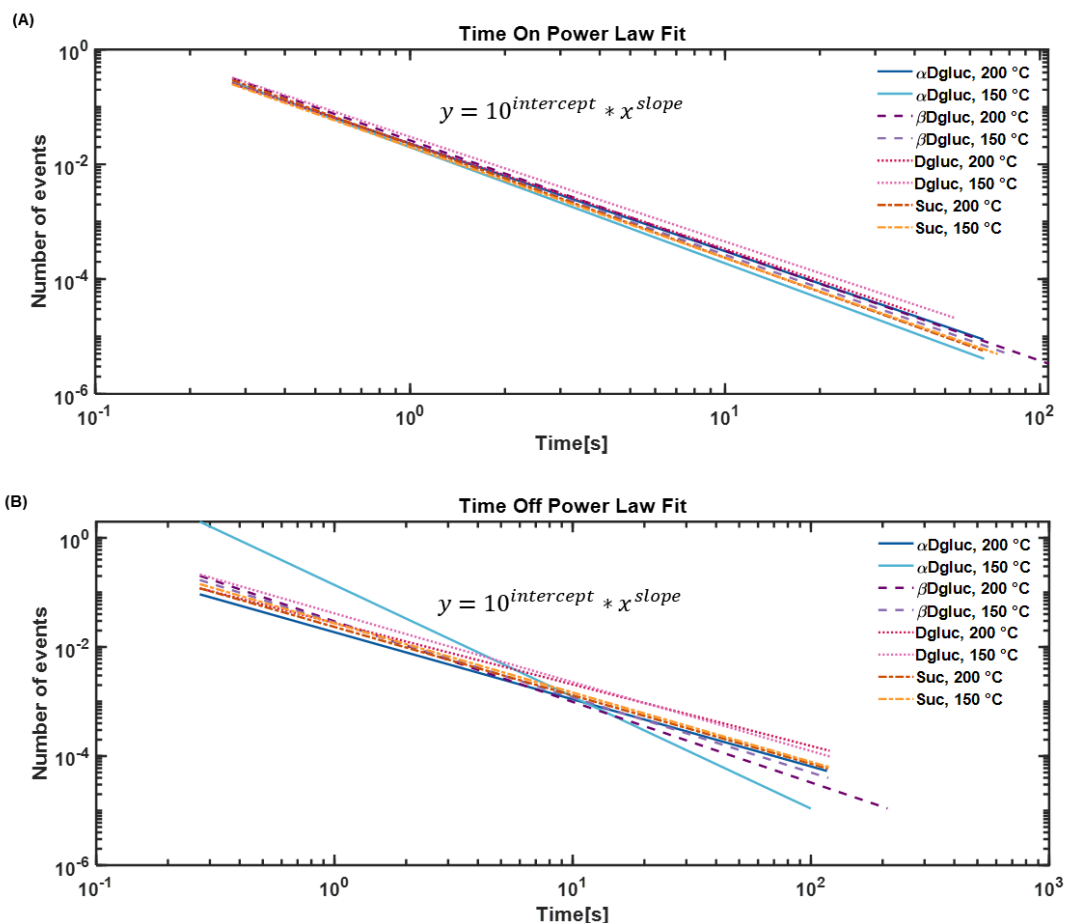
Figure I2. Zeta potential measurements. Red asterisks indicate statistical significance when compared to CDots of other carbon sources synthesized at the same temperature. Black asterisks indicate statistical significance when compared to CDots of the same carbon source synthesized at different temperatures. Triple asterisks denote P value of < 0.01, while double asterisks denote P value of < 0.1. Measurements were conducted in triplicate, with 10 or more runs per measurement. Further details of statistical analysis can be found in table S.4.
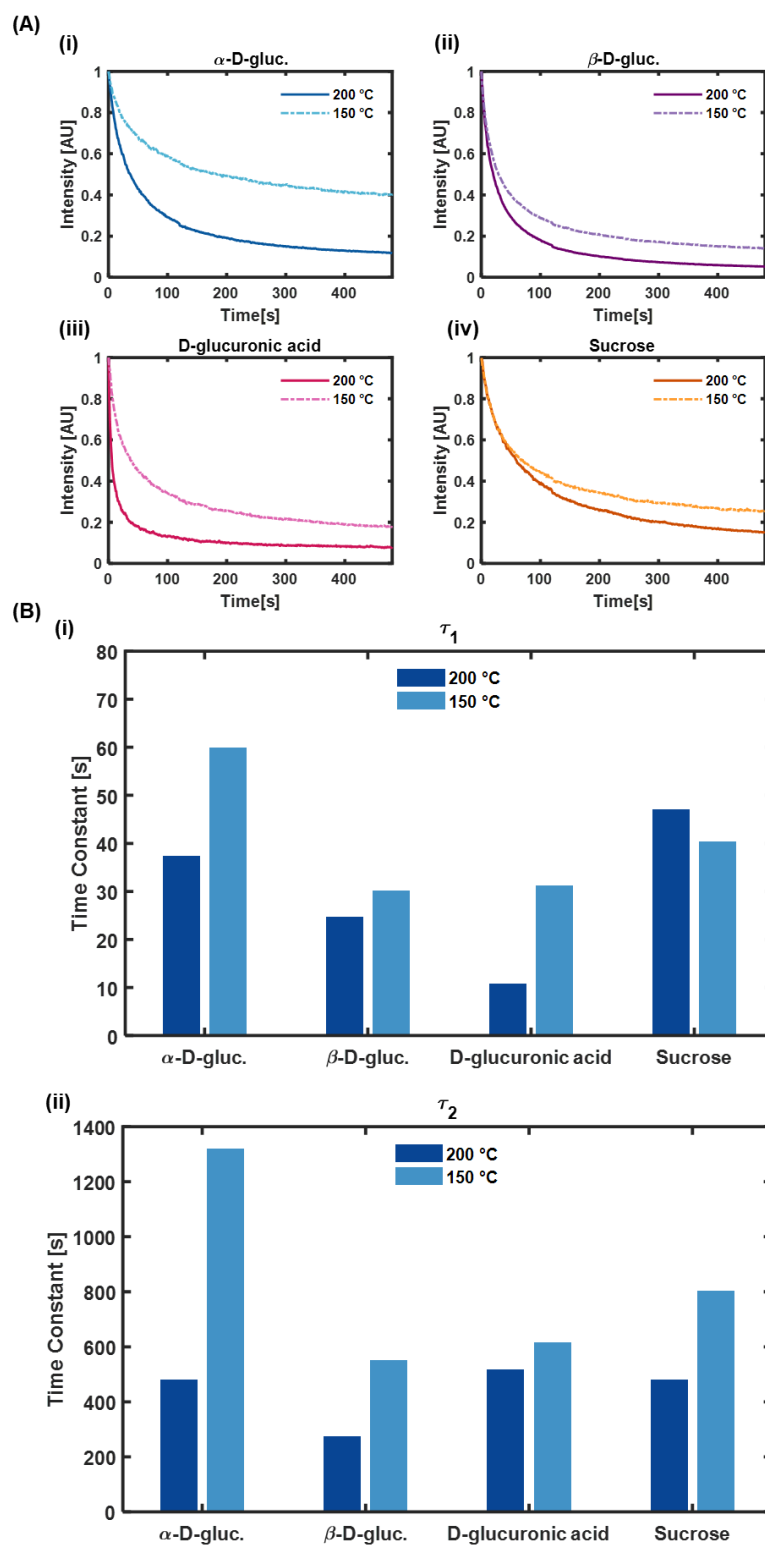
Figure I3. (A) Time to photobleaching curves for bulk nanoparticle measurements. **(B)** Bulk photobleaching time constants determined from a second order exponential fit of the time to photobleaching curves.

440

(A)

Time On Power Law Fit

$$y = 10^{intercept} * x^{slope}$$

Legend:
- αDgluc, 200 °C
- αDgluc, 150 °C
- βDgluc, 200 °C
- βDgluc, 150 °C
- Dgluc, 200 °C
- Dgluc, 150 °C
- Suc, 200 °C
- Suc, 150 °C

Axes: Number of events vs Time[s]

(B)

Time Off Power Law Fit

$$y = 10^{intercept} * x^{slope}$$

Legend:
- αDgluc, 200 °C
- αDgluc, 150 °C
- βDgluc, 200 °C
- βDgluc, 150 °C
- Dgluc, 200 °C
- Dgluc, 150 °C
- Suc, 200 °C
- Suc, 150 °C

Axes: Number of events vs Time[s]

Figure I4. t_{on} and t_{off} power law fits **(A)** Time on power law fitted line for each carbon source and synthesis temperature. **(B)** Time off power law fitted line for each carbon source and synthesis temperature.

Table I2. Absorbance at 365 nm for diluted samples. Blue shaded values indicate absorbance for a solvent:solute dilution of 980:20 instead of 998:2

	200C	150C
alphaDgluc	0.01700	0.02600
betaDgluc	0.01300	0.02700
Dgluc	0.00300	0.03700
Sucrose	0.01500	0.01400
Quinine sulfate, more dilute	0.0180	
Quinine sulfate, more concentrated	0.1720	

Table I3. Integrated Fluorescence Intensity for undiluted samples excited at 365 nm

	200C	150C
alphaDgluc	184803	90876
betaDgluc	646880	261050
Dgluc	17622	110347
Sucrose	338942	42215
Quinine sulfate	994287	

Table I4. P values from T-tests conducted on zeta potential measurements

	alphaDgluc, 200	alphaDgluc, 150	betaDgluc, 200	betaDgluc, 150	Dgluc, 200	Dgluc, 150	Sucrose, 200	Sucrose, 150
alphaDgluc, 200		0.004834325	0.001891928	0.098421027	0.003701783	0.015252658	0.00024169	0.778418872
alphaDgluc, 150	0.004834325		0.000181105	0.000658454	0.000292033	4.5653E-06	1.00574E-06	0.000460668
betaDgluc, 200	0.001891928	0.000181105		0.000941172	2.8444E-06	1.78261E-05	0.885365372	3.07625E-06
betaDgluc, 150	0.098421027	0.000658454	0.000941172		0.002064483	0.003759375	1.29373E-05	0.017728287
Dgluc, 200	0.003701783	0.000292033	2.8444E-06	0.002064483		0.000105181	0.005659842	8.3866E-06
Dgluc, 150	0.015252658	4.5653E-06	1.78261E-05	0.003759375	0.000105181		0.000116552	1.74875E-05
Sucrose, 200	0.00024169	1.00574E-06	0.885365372	1.29373E-05	0.005659842	0.000116552		2.69536E-05
Sucrose, 150	0.778418872	0.000460668	3.07625E-06	0.017728287	8.3866E-06	1.74875E-05	2.69536E-05	

Table I.5. Parameters for single particle photobleaching exponential fit

	Tau1	Tau2	a	c	R-square
alpha-D-gluc, 200	8.190008	111.1852	0.5057	0.3269	0.9671
alpha-D-gluc, 150	22.64493	1177.163	0.5358	0.1849	0.924
beta-D-gluc, 200	11.03266	94.96676	0.3646	0.4951	0.9871
beta-D-gluc, 150	8.53971	125.9446	0.6209	0.2596	0.9813
D-gluc, 200	10.06948	3910.833	0.5922	0.1976	0.8586
D-gluc, 150	9.442871	198.8467	0.7359	0.1983	0.9733
Sucrose, 200	20.75981	1196.888	0.4552	0.2944	0.907
Sucrose, 150	15.98465	589.6226	0.5266	0.2199	0.9719

Table I.6. Parameters for single particle time on fit

Slope	200	150
alpha-D-gluc	-1.87381	-2.02309
beta-D-gluc	-1.91978	-1.92068
D-gluc	-1.84065	-1.82481
sucrose	-1.9776	-1.93395
Intercept	200	150
alpha-D-gluc	-1.63974	-1.70141
beta-D-gluc	-1.58221	-1.65604
D-gluc	-1.63367	-1.52021
sucrose	-1.64944	-1.69786
R^2	200	150
alpha-D-gluc	0.988599	0.947362
beta-D-gluc	0.982591	0.984184
D-gluc	0.988712	0.984738
sucrose	0.980278	0.978213

Table I7. Parameters for single particle time off fit

Slope	200	150
alpha-D-gluc	-1.22978	2.049834
beta-D-gluc	-1.47692	-1.37518
D-gluc	-1.12641	-1.26112
sucrose	-1.25369	-1.26986
Intercept	200	150
alpha-D-gluc	-1.73013	-0.86351
beta-D-gluc	-1.53028	-1.55063
D-gluc	-1.56134	-1.38423
sucrose	-1.63309	-1.56577
R^2	200	150
alpha-D-gluc	0.939406	0.959555
beta-D-gluc	0.982147	0.979059
D-gluc	0.978529	0.970183
sucrose	0.973172	0.968484

Experimental Details

Any mention of commercial products is for information only; it does not imply recommendation or endorsement by NIST.

Particle Synthesis

Probe sonication was conducted using a Qsonica Sonicator. Lyophilization was done using a Labconco FreeZone 2.5-liter benchtop freeze dryer. A JEOL Cryo 2100 TEM was used for TEM imaging.

Photophysical Characterization

UV-Vis spectra were collected using a Thermo Scientific Genesys 10S UV-Vis Spectrophotometer. Fluorescence spectra were collected using a TECAN infinite M200 PRO fluorescence spectrometer. MirrIR IR-reflective glass slides (Kevley Technologies, Chesterland, Ohio, USA) were used as the substrate for Fourier Transform Infrared (FT-IR) measurements. FT-IR spectra were collected using a Nicolet Nexus 670 FTI-IR (Fredrick Seitz Material Research Laboratories (FSMRL), Urbana, Illinois, USA). A Phyiscal Electronics PHI 5400 spectrometer was utilized for the collection of XPS spectra. Zeta potential measurements were taken points using a Malvern Zetasizer.

Single-Particle Imaging

The inverted microscope (IX73) and 100× oil immersion objective (PlanApo) were purchased from Olympus. The 488-nm continuous wavelength laser was purchased from Spectral Physics. The exciter (FF01-482/563-25), dual-band dichroic filter (Di01-R488/561-25x36), and emitter

(FF01-523/610-25) were purchased from Semrock. A iXon U797 (Andor. Technology) Electron

Multiplying Charge Coupled Device (EMCCD) camera was utilized for imaging. The 400-mm

focal length lens (LA1725-A) was purchased from Thorlabs.

APPENDIX J: UNSUCCESSFUL BVNP EXPERIMENTS

J.1 ADVENTURES WITH HCL (AKA THE NANONETWORKS THAT NEVER WERE)

In preliminary BVNP experiments, we were not dialyzing the particles. In order to quench the reaction at a particular timepoint, we would add 50 µL 2N HCl into 1 mL of the as-prepared particle solution. However, we didn't realize that the particles would not be stable long-term in the presence of HCl, which led to the observation of a variety of nanoscale features when these samples were imaged with TEM weeks after synthesis. These shapes included apparent nanonetworks and nanofibers.

In an attempt to recreate the biliverdin nanonetworks, we tried first forming the particles, and then utilizing EDC-NHS crosslinking with a long-chain PEG diamine, Polyoxyethylene bis(amine) (M.W.=1000). No variation of this experiment was successful.

J.2 THE COBALT BVNPs THAT COULDN'T

In preliminary cobalt-BVNP experiments, I originally tried chelating cobalt within the biliverdin before conducting the crosslinking reaction. However, I wasn't able to form particles with this synthesis method. I later realized that the crosslinker itself likely competed with biliverdin for the chelation of cobalt, which prevented the formation of biliverdin. This problem was solved when we chelated cobalt into the BVNPs after the particles were already formed. We also found that the chelation of cobalt into the BVNPs appeared not to take place efficiently unless the solution pH was very basic.

J.3 IOHEXOL AND BILIVERDIN DON'T MIX WELL

Iohexol is a very common iodine-based CT contrast agent. As others have reported the formation of crosslinked iohexol particles, the concept of forming nanoparticles by inter-crosslinking iohexol and biliverdin seemed plausible. However, extensive experimentation revealed that things were not quite so simple. We tried multiple methods of crosslinking of iohexol and biliverdin, including using EDC-NHS crosslinking and diisocyanatohexane in a variety of synthesis solvents. After none of these succeeded, we moved on to forming the Si-BVNPs. I suspect that armed with the knowledge I've gained these past few years, I could make the iohexol-biliverdin reaction work now. However, there is no time to repeat these experiments and I hope that someone will work on this in the future.

J.4 I DON'T SPY ANY RED FRACTIONS

Two of the carbon sources that I utilized in my carbon dot projects appeared to have very promising fluorescence under the UV lamp: D-glucuronic acid and o-benzoic sulfimide. Under 365 nm excitation, they emitted a bright yellowish-orange fluorescence. We thought that they might contain some red fractions, but column chromatography revealed that they in fact did not.

APPENDIX K: THE ROTATING PLATFORM

**K.1 ORIGINAL DESIGN**

The original rotating platform was a simple motor hooked up to a 28 Volt power source. The power source continuously supplied a motor control chip that used PWM to control the motor speed. This design allowed for continuous motion, but would not allow for the motor to stop at a particular position. A potentiometer was used to change the motor speed, but there was a lower bound on how slow the platform could rotate.

K.2 PROTOTYPE OF MODIFIED DESIGN

In the modified design, an Arduino Uno, breadboard, transistor, and proximity sensor were utilized to allow the platform to rotate 180°, hold the position for 30 seconds, and rotate for another 180°, repeating this continuously for as long as desired. The circuit schematic is shown in **Fig. K.1**. Two magnets were placed 180°apart from each other on the back of the rotating platform. The proximity sensor was placed on top of the platform base. The transistor was used to selectively cut off or complete the motor circuit based on instructions from the Arduino. The entire system was set up such that the platform would begin rotating once powered. This was done by sending a high signal (i.e. "on") to the leftmost pin of the transistor, causing the motor circuit to be properly grounded and thus begin rotating. When the proximity sensor detects that it has reached one of the magnets, the Arduino sends a low signal (i.e. "off") to the leftmost pin of the transistor, causing the motor ground wire to disconnect and the motor to stop rotating. The code then has the motor wait a set amount of time before beginning to rotate again. The sensors do not take any new readings until a second after this rotation has restarted. The sensors then begin collecting new readings to detect whether the sensor has reached one of the magnets. Once the magnet is detected, the rotation stops,

and the entire process repeats again. The proximity sensor circuit was made using a simple voltage divider with the sensor in series with a 10 kΩ resistor. An input of 5V is given from the Arduino to the input of the proximity sensor. The output of the proximity sensor is connected to one end of a resistor, and this node is read by an analog pin. The other end of the resistor is grounded.
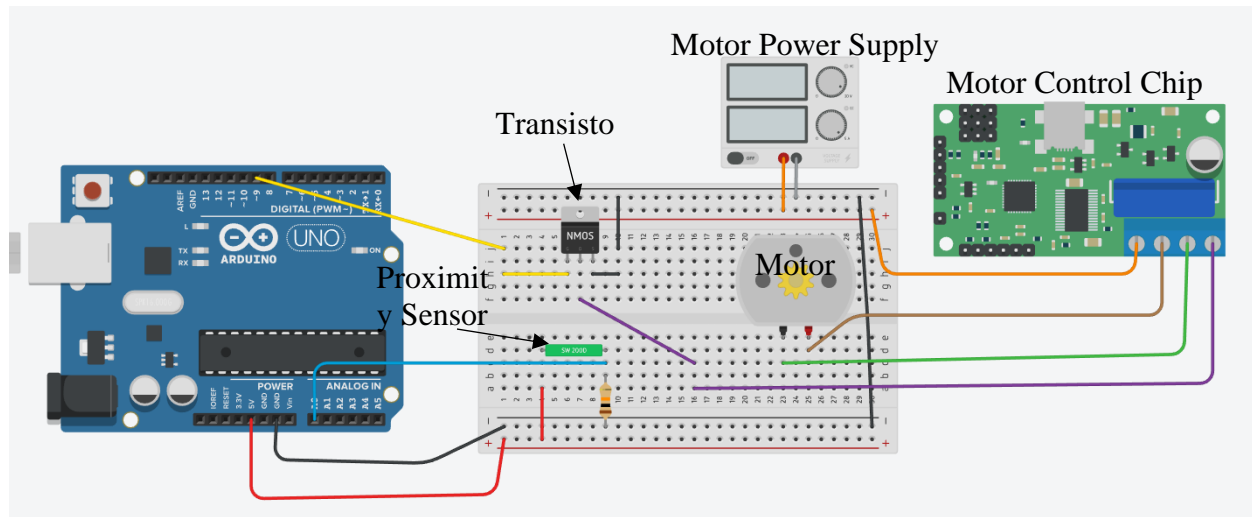
Figure K.1. Circuit diagram for the complete system. Orange wires indicate positive power from the motor power supply to the motor control chip. Gray wires indicate ground from the motor power supply. The brown wire indicates the positive control signal sent from the motor control chip to the motor. The green wire indicates the ground connected between the motor control chip and the motor. Black wires indicate the ground provided by the Arduino. The purple wire indicates the connection between the motor ground and the transistor. The yellow wire indicates the digital signal connected to the transistor. The blue wire indicates the output of the proximity sensor circuit as read by an analog pin. Red wires indicate positive 5V supplied by the Arduino. The Arduino itself is connected to a 12V wall outlet power supply. In this diagram, the proximity sensor is simulated by a tilt switch for ease of modelling.
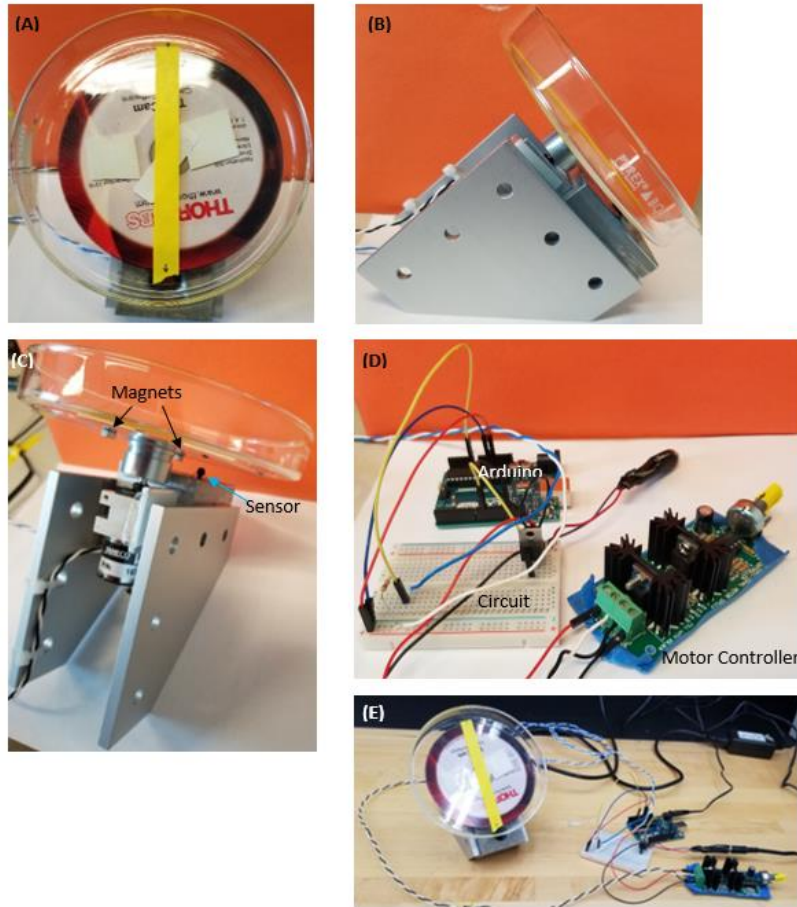
Figure K.2. Platform design. **(A)** Front view. **(B)** Side view. **(C)** Back view. Arrows indicate magnet and sensor position. **(D)** Interface between Arduino, circuit, and the motor controller. **(E)** Full setup.

K.3 ARDUINO CODE FOR PROTOTYPE

A screenshot of the Arduino code used for the rotating platform is provided in the image below.

Comments are provided within the code to explain the function of each line.

```
int sensorpin=A0; // Define sensor pin as analog pin 0
int transistorpin=9; // Define transistor activation pin as digital pin 9
int cutoff=1000; // define cutoff reading as 1000 (0 is min, 1023 is max)

void setup() {
  pinMode(transistorpin, OUTPUT); // Set transistor pin to output
Serial.begin(9600); // begin the serial monitor
}

void loop() {
int thevalue=analogRead(sensorpin); // read the sensor
Serial.println(thevalue); // print the sensor value to the serial monitor

if (thevalue<cutoff) // if the sensor didn't sense the magnet
{
  digitalWrite(transistorpin, HIGH); // keep rotating
}

else // otherwise
{
  digitalWrite(transistorpin, LOW); // stop rotating
  delay(10000); //pause for a set number of seconds
  digitalWrite(transistorpin, HIGH); // start rotating again
  delay(1000); // wait for 1 second before taking any more readings
}

}
```

Figure K.3. Arduino code used for the rotating platform. The "delay(10000)" line indicates the number of microseconds of delay used by the Arduino. It can be altered to any desired value.

APPENDIX L: A MOUSE NAMED FRED

In the last stages of the ACS Nano revisions for the BVNP paper, we were asked to replace the mouse clipart we had used for the figures with one which we had drawn ourselves. I was able to draw one using the stylus on my laptop and edited the figures accordingly. However, the mouse, which I named Fred, took on a personality of its own and became a mascot of sorts as I went through the remainder of my graduate career.
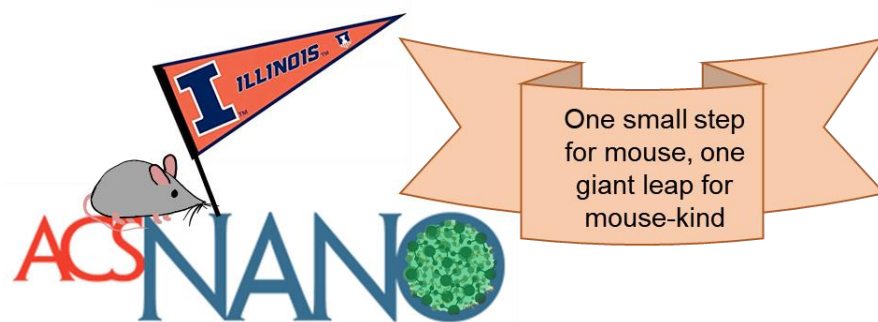

The original Fred

Fredina (aka Fredette), the female version of Fred
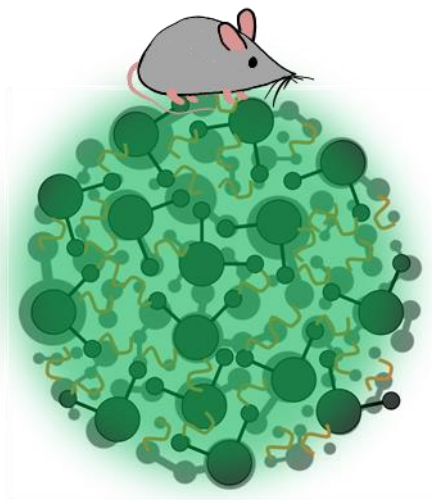
Fred on top of a biliverdin nanoparticle

Fred after the ACS Nano paper was accepted

Another version of Fred after the ACS Nano paper was accepted

Fred as a teaching assistant

Fred busy writing

Fred dreaming of the biliverdin-derived carbon dots

Fred experiencing an existential crisis with the passage of time

Fred celebrating a birthday

Fred tired after many long days in lab

Fred taking a well-deserved vacation
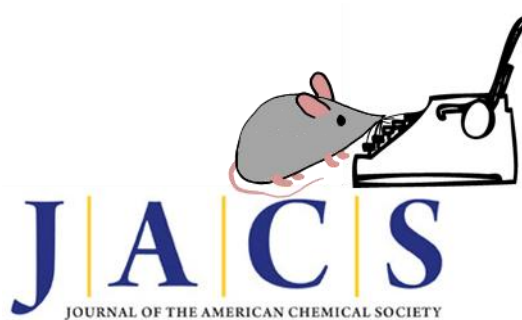
Fred helping write up a JACS paper, which was later rejected.

Fred as a computer mouse

APPENDIX M: SCIENTIFIC ART

Throughout grad school, I've had the opportunity to take many exciting images of my research.

I'm including some of those images, which have been used in art exhibits or finalists/semi-finalists
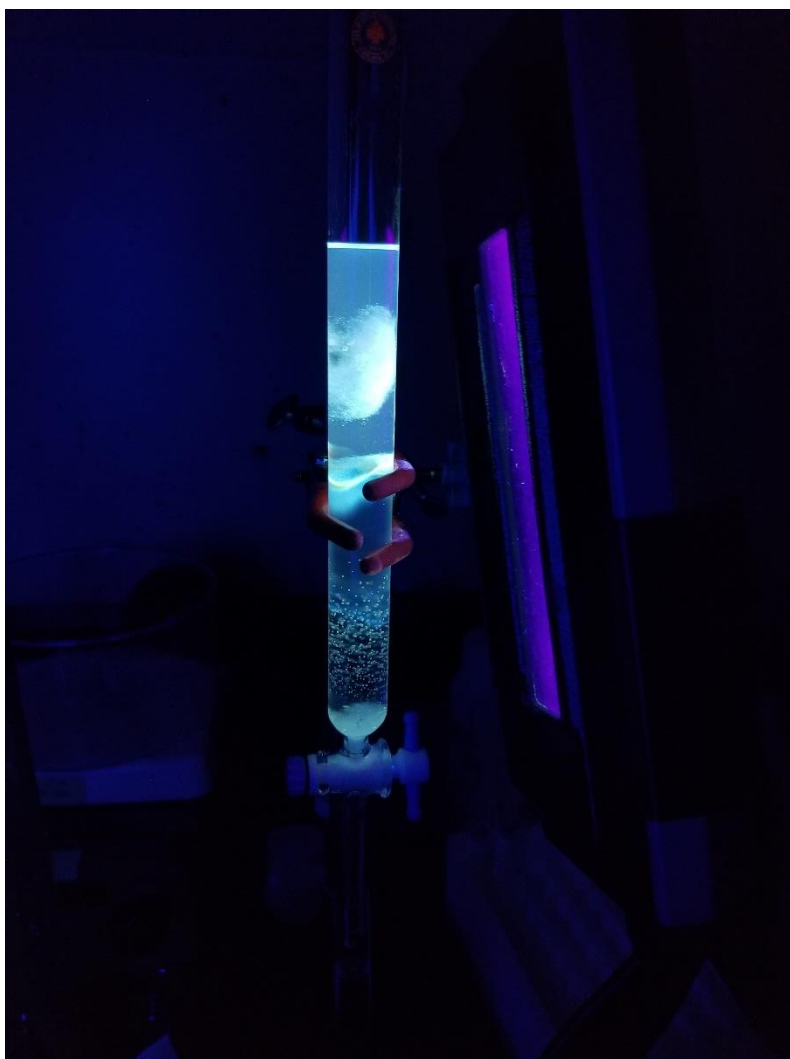
in image competitions here.

"Microscopic Roses and Thorns on a Metal Surface"

Semi-finalist for 2020 UIUC Image of Research Competition
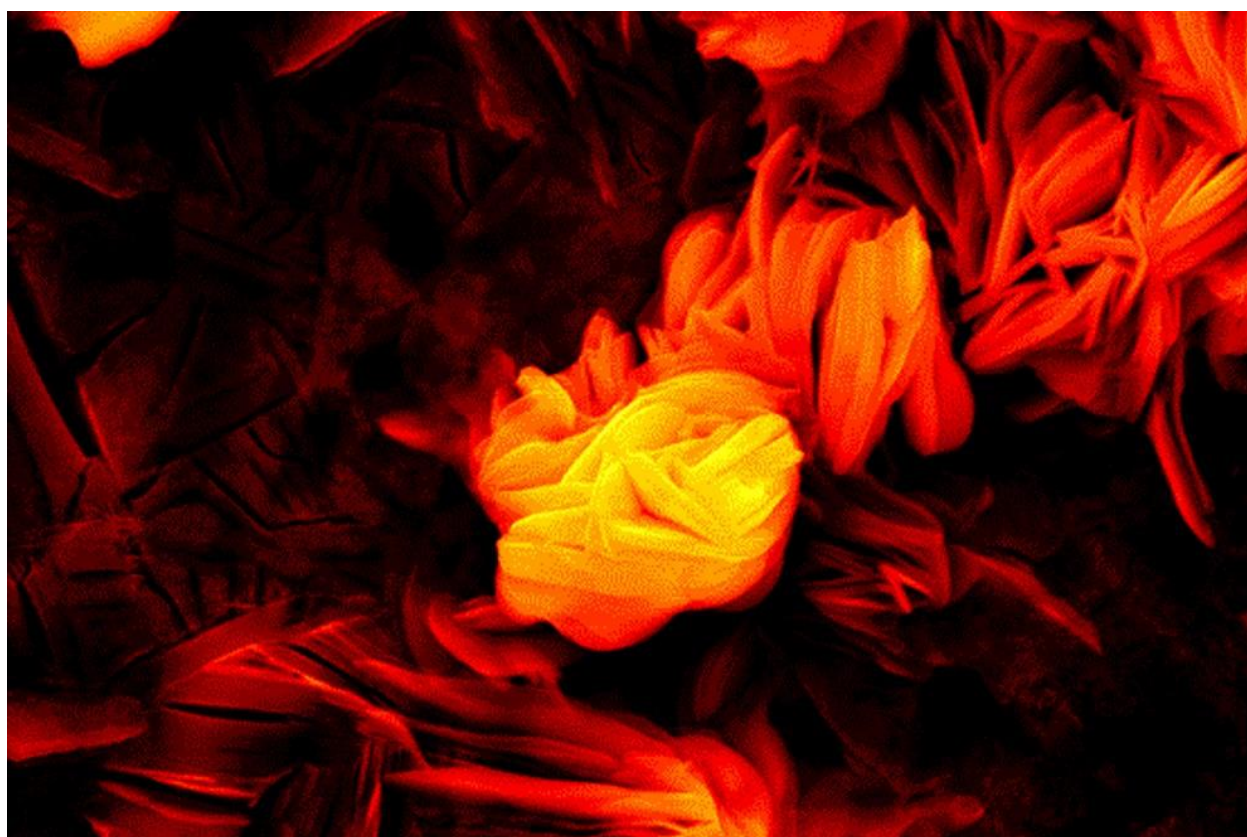
"Totally Tubular"

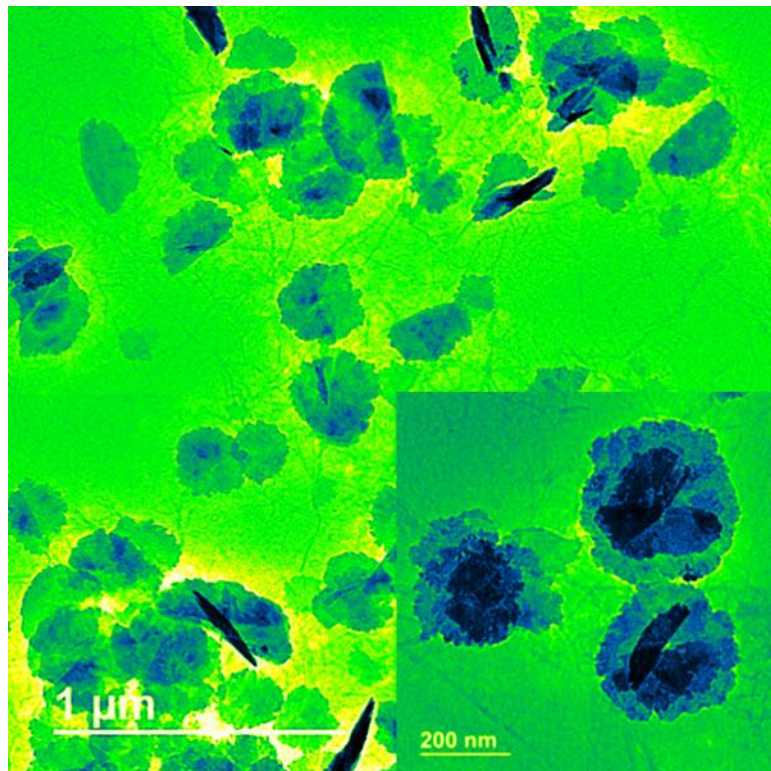C&EN Chemistry in Pictures; Science Meets Art Shanghai Tech Exhibit

"3D Image of a Human Heart"

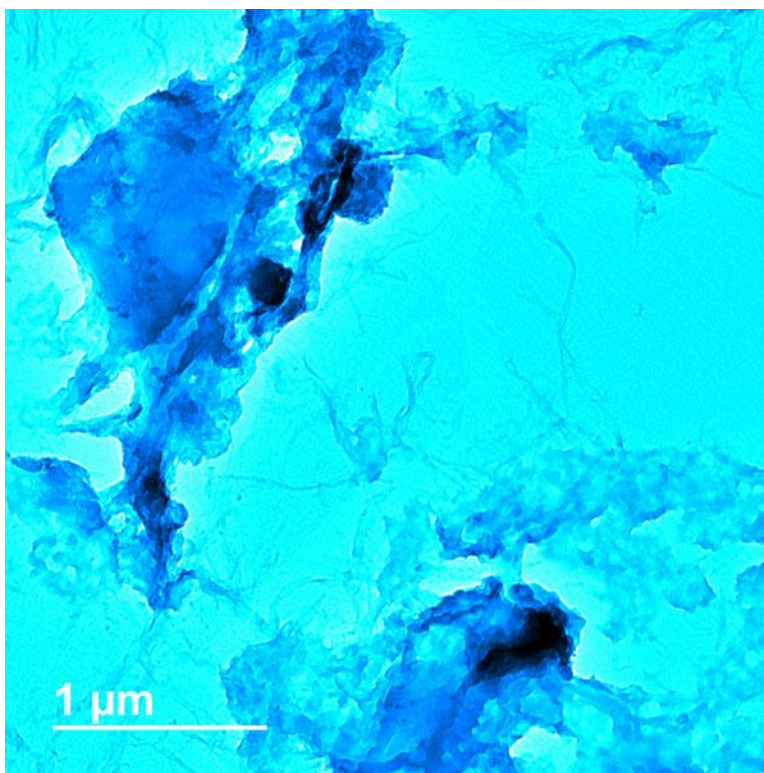FASEB 2018 BioArt winner

"Nanoflowers"

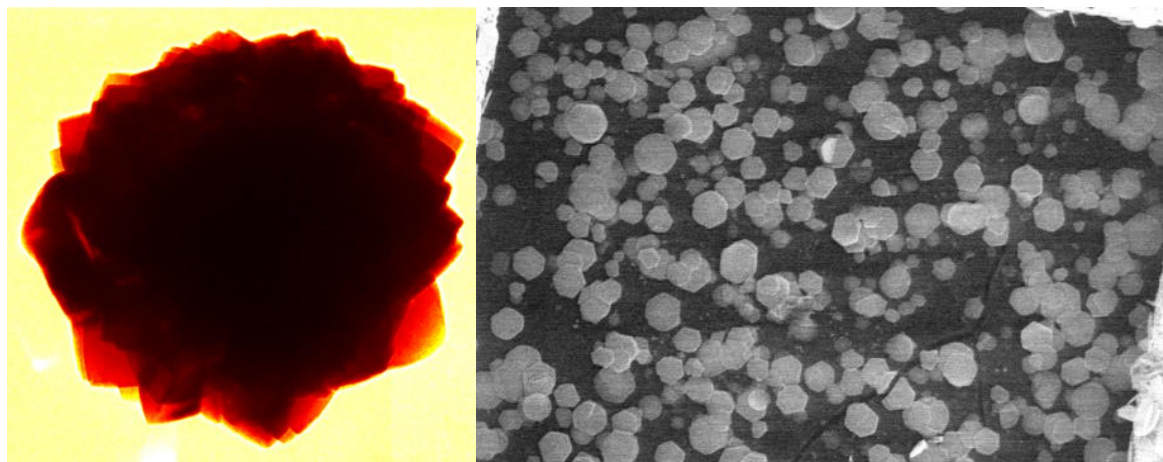2017 JEOL Image Contest Finalist; Featured in 2018 JEOL calendar

459

"Nanosquid"

2017 JEOL Image Contest Finalist

2018 UIUC non-majors art exhibit

"Biliverdin Nanoparticle Pattern"

Materials Research Society Spring 2018 Science as Art Finalist